Lecture Notes in Electrical Engineering 263

Angui Li
Yingxin Zhu
Yuguo Li
Editors

Proceedings of the 8th International Symposium on Heating, Ventilation and Air Conditioning

Volume 3: Building Simulation and Information Management

Springer

Lecture Notes in Electrical Engineering

Volume 263

For further volumes:
http://www.springer.com/series/7818

Angui Li · Yingxin Zhu · Yuguo Li
Editors

Proceedings of the 8th International Symposium on Heating, Ventilation and Air Conditioning

Volume 3: Building Simulation and Information Management

Springer

Editors
Angui Li
Xi'an University of Architecture
and Technology
Xi'an
People's Republic of China

Yuguo Li
The University of Hong Kong
Hong Kong
People's Republic of China

Yingxin Zhu
Tsinghua University
Beijing
People's Republic of China

ISSN 1876-1100 ISSN 1876-1119 (electronic)
ISBN 978-3-642-39577-2 ISBN 978-3-642-39578-9 (eBook)
DOI 10.1007/978-3-642-39578-9
Springer Heidelberg New York Dordrecht London

Library of Congress Control Number: 2013945148

Printed on acid-free paper

Springer is part of Springer Science+Business Media (www.springer.com)

Preface

The 8th International Symposium on Heating, Ventilation, and Air Conditioning—ISHVAC2013 is held in Xi'an, China from October 19 to 21, 2013, organized by Xi'an University of Architecture and Technology, and co-organized by Tsinghua University and The University of Hong Kong. The proceedings consist of over 220 peer-reviewed papers presented at the ISHVAC2013. We sincerely hope that the 8th International Symposium of Heating, Ventilation, and Air Conditioning will provide a good platform again to HVAC experts and researchers in China and elsewhere share their latest research findings and new technology development, and looking into the future of HVAC.

Xi'an has more than 3000 years of history as one of the four great ancient capitals of China. Xi'an has now re-emerged as one of the important cultural, industrial, and educational centers in China. History tells us a lot. The history of HVAC is much shorter. Addington (2001) wrote, after the 1918–1919 influenza pandemic, which killed more people than World War I, "*Engineers and manufacturers were quick to capitalize on the public's concern with cleanliness, and pointed out that the air handler could produce 'manufactured weather' that was cleaner and purer than what nature provided (Carrier 1919). In spite of the continued work of open-air enthusiasts such as Winslow and Dr. Leonard Hill during the next several decades to challenge mechanical systems, most of the early ventilation laws remained in place and the air-handler-based system became the standard for conditioning interior environments*." The new revitalization of natural ventilation and new development of mixed-mode ventilation in the last 10 years confirms the wisdom of Winslow and Dr. Leonard Hill.

The success of HVAC is and will also be judged in the balance of providing people a comfortable and healthy indoor environment and using the minimum resources and energy. The key to the success of HVAC is in understanding the human physiological needs in thermal comfort and healthy air, and the roles played by human behavior, which is dynamical in nature. We cannot just focus on the HVAC technologies as we have done in the past 100 years.

Urbanization is a huge thing in rapidly developing countries such as in China. More than 50 % of the world's population now lives in cities. The urban population will reach 1 billion by 2030 in China. In the next 10 years, it is expected at least 1 % of the population will become urban dwellers every year. The expectation for better indoor environment is also on the rise in China and other

developing countries as the living standard rises. Building consumes a large proportion of our energy in the world. Efficient HVAC is the key in high performance buildings. Continuing urban warming has been observed and studied in many megacities in the world. Just imagine if you are asked to cool the air in a Mong Kok district in Hong Kong or Wang Fu Jing Street in Beijing by a few degrees, what would you do? When shall we design a city just like a designing a building? What can HVAC engineers and researchers help?

Xi'an literally means "Peaceful in the West" in Chinese, and it was historically known as Chang An ("Perpetually Peaceful"). We also wish that the world will not only peaceful, but also sustainable. The HVAC engineers and researchers have a great role to play.

Finally, the conference organizing and the high quality of the proceedings are the result of many people's hard work, dedication, and support. The first appreciation goes to the members of the International Scientific Committee. Great appreciation should also go to many people who worked tirelessly on the Organizing Committee. We greatly appreciate for their special contributions of all the sponsors and cooperators.

We also express our thanks to the authors who enthusiastically presented their works, ideas, and results.

Angui Li
Yingxin Zhu
Yuguo Li

International Scientific Committee

Yi Jiang (China)
Jiaping Liu (China)
Phillip J. Jones (UK)
Hazim B. Awbi (UK)
William Bahnfleth (USA)
Pradeep Bansal (NZ)
Mark Bomberg (USA)
Qingyan Chen (USA)
Zhenqian Chen (China)
Qihong Deng (China)
Shiming Deng (HK, China)
Lei Fang (DK)
Leon R. Glicksman (USA)
Yanling Guan (China)
Per Heiselberg (DK)
Jan Hensen (NL)
Sture Holmberg (SE)
Xiang Huang (China)
Shinsuke Kato (JP)
Angui Li (China)
Baizhan Li (China)
Xianting Li (China)
Yuguo Li (HK, China)
Zhiwei Lian (China)
Martin W. Liddament (UK)
John C. Little (USA)
Weiding Long (China)
Shuzo Murakami (JP)
Vincenzo Naso (IT)
Jianlei Niu (HK, China)
Bjarne W. Olesen (DK)
Saffa Riffat (USA)
Dirk Saelens (BE)
Jan Sundell (China)

Shin-ichi Tanabe (JP)
Kwok wai Tham (SG)
Peter V. Nielsen (DK)
Markku Virtanen (FI)
Fenghao Wang (China)
Ruzhu Wang (China)
Shengwei Wang (HK, China)
Yew Wah Wong (SG)
Hongxing Yang (HK, China)
Xudong Yang (China)
Yang Yao (China)
Harunori Yoshida (JP)
Hiroshi Yoshino (JP)
Shijun You (China)
Chuck Yu (UK)
Guoqiang Zhang (China)
Jensen Zhang (USA)
Xiaosong Zhang (China)
Xu Zhang (China)
Yinping Zhang (China)
Jianing Zhao (China)
Rongyi Zhao (China)
Xudong Zhao (UK)
Neng Zhu (China)
Yingxin Zhu (China)

Organizing Committee

Angui Li
Yingxin Zhu
Yuguo Li
Lei Zhao
Yi Wang
Yanfeng Liu
Zhiwei Wang
Yuesheng Fan
Qiuhui Yan
Xiaohong Nan
Xiong Liu
Qinghong Zheng

Contents

Part I
Modeling and Simulation

Chapter 1
Study of the Environmental Control of Sow Farrowing Rooms by Means of Dynamic Simulation

Enrico Fabrizio, Gianfranco Airoldi and Roberto Chiabrando

Abstract While there has been a great reduction of the energy demand of civil buildings in recent years, the energy demand for the environmental control of livestock buildings is still high, due to high outdoor air changes. In a livestock building, a compromise between different requirements (reducing the heating energy in winter season, avoiding heat stress for animals in summer season, controlling the relative humidity, controlling ammonia and hydrogen sulfide concentrations) has to be done and contributes to complicate the design of the structures and the operation of the ventilation system. Moreover, depending on the animal species, ages and type of housing, the environmental control requirements change considerably. In the present work, dynamic building simulation is applied to a portion of a swine unit, in particular the sow farrowing room and weaned pigs nursery, where the effects of some important construction and HVAC system choices that influence the temperature and humidity conditions and the sow thermal comfort were investigated. The results show that the use of variable flow rate fans, able to implement in the summer season free cooling with the outside air, coupled to a building structure sufficiently massive to exploit the effect of free cooling, is surely promising. The thermal insulation is useful to reduce the energy consumption for heating in winter and does not affect the summer overheating.

Keywords Free cooling · Swine farm · Sow farrowing room · Dynamic simulation

E. Fabrizio (✉) · G. Airoldi
Department of Agricultural, Forest and Food Sciences, University of Torino, via Leonardo da Vinci 44 10095 Grugliasco, TO, Italy
e-mail: enrico.fabrizio@unito.it

G. Airoldi
e-mail: gianfranco.airoldi@unito.it

R. Chiabrando
Department of Regional and Urban Studies and Planning, University and Politecnico di Torino, 10129 Turin, Italy
e-mail: roberto.chiabrando@unito.it

A. Li et al. (eds.), *Proceedings of the 8th International Symposium on Heating, Ventilation and Air Conditioning*, Lecture Notes in Electrical Engineering 263,
DOI: 10.1007/978-3-642-39578-9_1,

1.1 Introduction

The numerical simulation of the building energy performance, in particular the dynamic building simulation, that is able to verify the energy performance of a building under the operating conditions and evaluate the effects of various design choices, is widely used in research works and in many professional applications in the civil sector. This is due to many factors, including the spread of computer codes increasingly detailed and freely available online, the study of simulation models of building components and innovative plant designs, the need to meet long-term energy performance requirements imposed by law or such as to give a score within the tools for sustainable building. Conversely, the use of dynamic simulation appears limited as regards the manufacturing buildings such as livestock and greenhouse buildings. In such cases, in which the use of the active indoor climate control is limited for reasons of technological and economic opportunities, the use of instruments which enable the evaluation of passive climate control strategies (linked to the building structure) such as the dynamic energy simulation would be particularly useful. For livestock buildings, usually self-made calculation tools are employed, see for example [1] and [2] in case of swine buildings. In the present work, the dynamic building simulation was applied to a sow farrowing room and the effects of some important construction and HVAC system choices were investigated.

1.2 Materials and Methods

1.2.1 The Calculation Tool

The dynamic simulation of the sow farrowing room was conducted by means of the EnergyPlus software (www.apps1.eere.energy.gov/buildings/energyplus), one of the most recent and updated software tool for the simulation of the energy performance of the building and of the primary and secondary systems, widely used at international level. Even though the software was not designed for particular buildings such as livestock buildings and greenhouses, this simulation was conducted exploiting the capabilities of the software and adopting the pertinent assumptions. An example of application of EnergyPlus for the study of the thermal behaviour of a greenhouse can be found in [3].

In EnergyPlus the thermal load is determined by computing the Air Heat Balance on a time step of 1/6 of an hour. The thermal conduction through heat transfer surfaces is computed by means of the CTFseries method. The radiative heat exchange is computed in detail, distinguishing between the short-wave and long-wave radiation. Due to the fact that the indoor humidity was also studied in the simulation, the effect of the vapour inertia of the indoor surfaces was taken into account by means of the effective moisture penetration depth (EMPD) model.

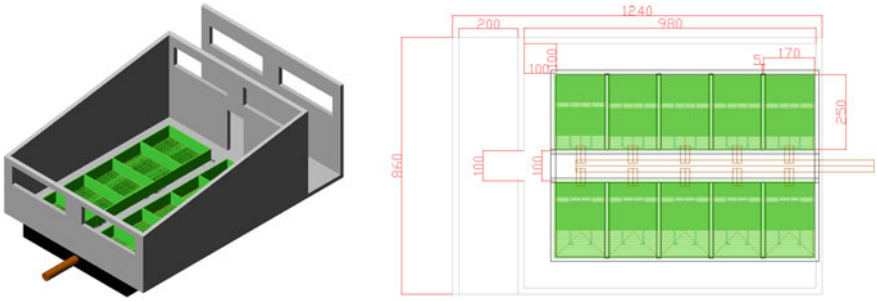

Fig. 1.1 View and dimensions of the sow farrowing room under consideration

1.2.2 The Reference Building

A reference building consisting of a sow farrowing room in a swine farm, equipped with forced ventilation, for a total of 10 sow and 84 m^2 (Fig. 1.1 left) was assumed. The dimensions are reported in Fig. 1.1 right; the room is configured as a portion of a building whose longitudinal axis is oriented along the direction east–west; the side walls are therefore adiabatic. The pent roof is oriented to the south. In the initial configuration, the constructions are made of gas concrete (30 cm) for the external walls, insulated plate (10 cm) for the roof and polycarbonate single pane windows for the openings. The floor is a plastic grid that separates the indoor environment from the sewage pit, that is 90 cm deep and made of concrete. There is an air heating HVAC. The mitigation of the thermal conditions during the summer is made by increasing the outside air flow rate (free cooling).

1.2.3 Boundary Conditions

The use of the sow farrowing room is as follows:

- 7 days: presence of the pregnant sows in each pen;
- 28 days: presence of the lactating sows and 11 piglets for each sow/pen;
- 7 days: cleaning and disinfection.

The above cycle is repeated 8.7 times during a calendar year. The sensible and latent heat loads due to the presence of the animals were estimated on the basis of CIGR values [4], assuming a body weight of pregnant and lactating sow of 200 kg and a variable weight of piglet from 1.2 kg—at birth—to 8 kg, with a daily average increase of 240 g. To evaluate the total load and split it between sensible and latent, a winter season, a summer season and an intermediate season were identified. The profiles of the sensible and latent heat loads due to animals were

normalized to a maximum value of 6,190 W for the sensible load and of 6,500 W for the latent load.

The contribution to the energy balance due to the manure was estimated from the CIGR data of daily defecation [4], by evaluating the accumulated liquid manure and the evaporation, proportionality to the difference between the saturation vapor pressure at the surface temperature of the floor and the vapor pressure of the indoor air, as reported in [5] and in the references cited there. In heating mode, a set point temperature of 18 °C was fixed, while for the piglets heating at higher temperatures in the first weeks of life, radiative lamps were considered. In summer conditions, the internal temperature of activation of the free cooling was set to 26 °C. This is the temperature above which the outdoor air flow rate is increased, provided that the dry bulb temperature is sufficiently lower, to maintain the indoor environment to 26 °C (to this regard see the following graphs of Fig. 1.4). On the basis of the maximum production of carbon (1,647 l/h) the minimum ventilation air flow rate was estimated as

$$\dot{V} = \frac{\dot{q}_{CO_2}}{C_{in} - C_{out}} = \frac{1,647 \cdot 10^{-3}}{0.032} = 514.79 \text{ m}^3/\text{h} \;=\; 0.143 \text{ m}^3/\text{s} \qquad (1.1)$$

The maximum ventilation flow rate was estimated on the basis of the summer thermal load of the building and was fixed equal to 10 times the minimum value. Different simulations were conducted adopting a two-speed fan or a variable flow fan.

The variables that were analyzed are the followings:

- heating energy requirement (set point 18 °C);
- electricity requirement for air circulation (heating and ventilation in winter, and ventilation with optional free cooling in summer);
- sum of the two previous quantities in terms of primary energy by adopting a weighting factor equal to 1 for the thermal energy and 2.17 for the electricity;
- index of overheating of the building during the summer. In the absence of a mechanical control of the internal temperature, this index is a parameter for the evaluation of the different design solutions and was defined as

$$I_s = \sum_j \left(t_{i,j} - t_R\right) = \sum_j \left(t_{i,j} - 26\right) \quad [^\circ\text{C} \cdot \text{h}] \qquad (1.2)$$

that is the sum of the positive differences between the hourly indoor air temperature and a reference temperature fixed at 26 °C (equal to the temperature of the activation of the free cooling). This sum represents the time during which the indoor air temperature exceeds the limit temperature, weighted for the entity of the deviation.

The weather conditions refer to the IWEC file of the Torino location (north–west of Italy). The running period is one year. The following cases were analyzed:

Case (1) building construction as in Sect. 2.2, two flow steps fan (step 1: 0.715 m^3/s; step 2: 1.43 m^3/s) with flow regulation with deflector;
Case (2) building construction as in Sect. 2.2, variable flow fan in all outside air, controlling the flow from a minimum of 0.143 m^3/s to a maximum of 1.43 m^3/s;
Cases (2.1–2.3) as case (2) with an increase of the thermal insulation (10, 15, 20 cm) of the roof;
Case (3) concrete walls, for both heat transfer and adiabatic surfaces, (20 cm, 1,200 kg/m^3 specific mass, 0.39 W/mK thermal conductance), ventilation as in case (2);
Cases (3.1–3.5) as case (3) with thermal insulation respectively of 5, 10, 15, 20, 25 cm;
Case (4) concrete walls with low insulation—as in case (3.1)—and roof insulated as in case (2.2).

Finally, the hourly electricity production of a monocrystalline PV plant (design efficiency of modules of 18 %) on the on the south-oriented pent roof was calculated assuming a consumption for the fans and the selling of the exceeding electricity.

1.3 Results

In Figs. 1.2 and 1.3 the time profiles of the average indoor air temperature and the outside air ventilation flow rate are represented; for clarity the trend of the outdoor air temperature is also shown in the background. In case (1), in which the ventilation flow rate is equal to only two values, we see that it is necessary to activate the higher ventilation flow rate at the beginning of May, and maintain it until mid-September. The energy consumption of this and the following configurations are reported in Table 1.1. In the graph of Fig. 1.3 it can be noted that with the variable flow fan it is possible to reduce to the minimum the flow rate during the winter period, with a consequent reduction of electricity consumption for the air movement (from 6,478 to 3,757 kWh) while the maximum flow rate is achieved when the free cooling is needed. This solution is instead comparable with that of case (1) for the other quantities.

To better understand the operation of the free cooling, in Fig. 1.4 weekly trends of the indoor parameters in two periods of activation of the free cooling in different modes are shown. In both cases the periods of activation for the free cooling can be recognized by the rising of the outside air flow rate above the lower limit (fuchsia curve). In the week on the left, with outside temperatures lower than the one that is fixed as internal set point (26 °C), free cooling is active during the day, and it is almost always possible to maintain the indoor temperature at 26 °C (horizontal sections of the blue curve); at night vice versa there is a drop in the indoor temperature due to the base ventilation.

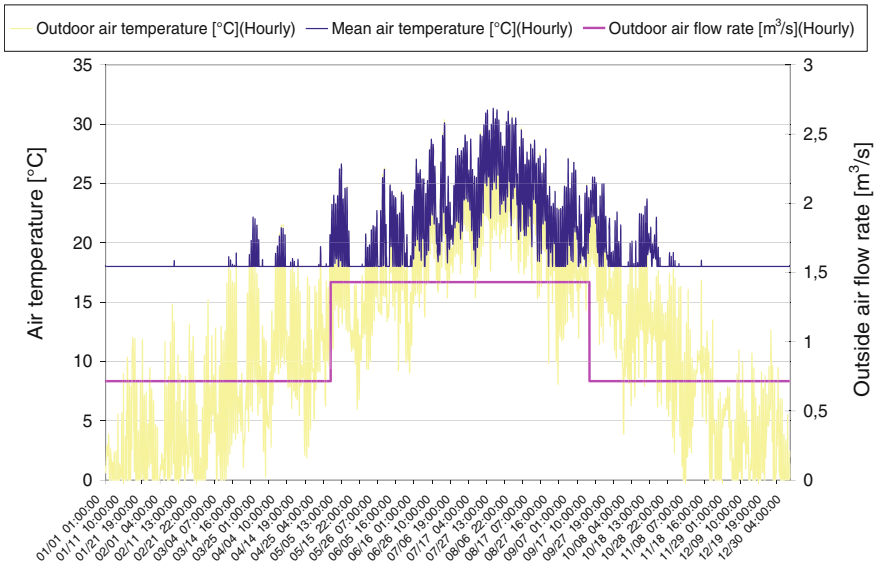

Fig. 1.2 Hourly profiles of indoor air temperature and flow rate for case 1

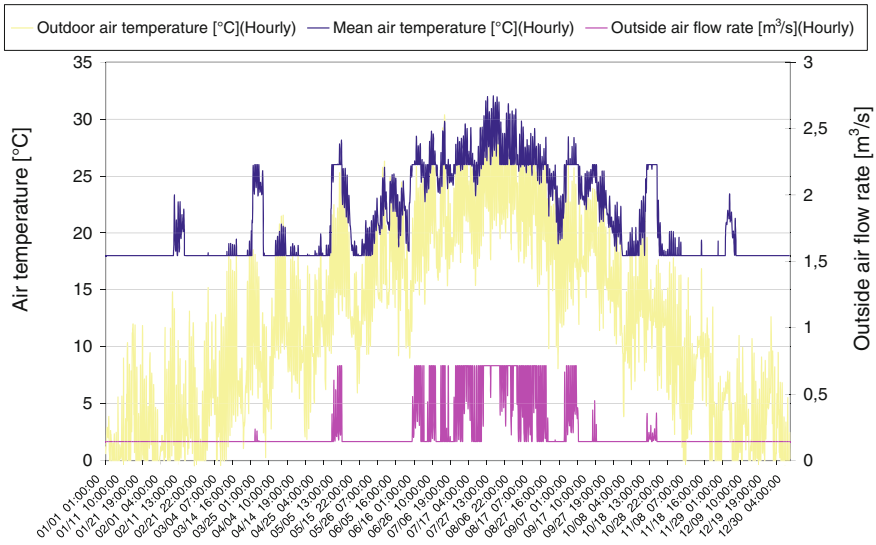

Fig. 1.3 Hourly profiles of indoor air temperature and flow rate for case 2

In the week on the right, in which the outside air temperature is often higher than 26 °C, the ventilation flow rate is almost always to the maximum permissible value and tends to decrease—although never to the value of the base ventilation—only at

Table 1.1 Summary of the results for the main case studies (sensitivity analysis on the thermal insulation are omitted)

	Case 1	Case 2	Case 3	Case 4
Fan	Constant flow (2 steps)	Variable flow	Variable flow	Variable flow
Free cooling	No	Yes	Yes	Yes
Heating energy (kWh_t)	10,143	10,150	13,328	11,148
Electricity for fans (kWh_e)	6,478	3,757	3,728	2,951
Primary energy (kWh)	24,200	18,302	21,418	17,552
Index of overheating (°C · h)	1,053	1,164	293	255

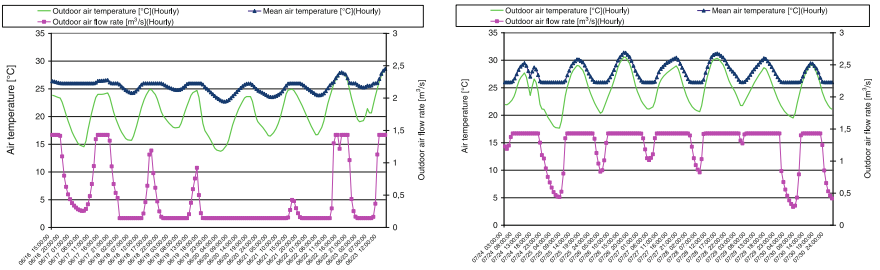

Fig. 1.4 Hourly profiles of indoor air temperature and outdoor air flow rate for case 2 for one week in June (*left*) and one week in August (*right*)

night, when the indoor air temperature equals the set point (26 °C). During the central hours of the day the ventilation system keeps the indoor air temperature 1–2 °C above the outdoor air temperature.

The adoption of the concrete walls of case (3) makes it possible to greatly reduce the index of overheating of the structure, compared with a modest increase in the energy consumption for heating, which in any case can be reduced through the thermal insulation (Table 1.1).

From the parametric analyses on the insulation thickness of the walls and on the roof (cases 2.1–2.3, 3.1–3.4), it can be seen that beyond 5–10 cm there is not any additional benefit, and the effect on the summer behavior is negligible. A greater reduction of the energy needs for heating can be obtained with the increase of the thermal insulation of the roof in case (2), since the roof is the larger heat transfer surface.

Following the previous results, a further configuration was analyzed (case 4) which is characterized by the use of concrete walls, weakly insulated (5 cm), and the roof insulated with 15 cm. This case has (Table 1.1) a low heating energy consumption (11,148 kWh), a low electricity consumption for ventilation (2,951 kWh) and a summer behavior which limits considerably the overheating (index equal to 255 °C · h).

Finally, the last evaluation was conducted on the installation of a monocrystalline PV array on the pitch roof. It emerged that, given the large available surface area (over 90 m^2) the amount of the total annual electricity is high (14,788 kWh_e/y) and equal to about 4 times the ventilation consumption (of case 2), however, the analysis of the time variable profiles of electricity production and fans electricity requirement, showed that only a modest amount of electricity produced by photovoltaic (1,795 kWh_e or 12 %) is consumed, and therefore up to 52 % of the electricity required for ventilation (1,962 kWh_e) has still to be taken from the electricity grid.

1.4 Conclusions

In the present work, dynamic simulation methodologies, widely adopted in the sector of civil buildings, were applied to a building for animal production characterized by a high degree of standardization. A series of critical issues that merit further investigations are related to the consideration of the latent load due to animals and animal manure, whose values are dependent on the values of indoor temperature and relative humidity, quantities that in turn are unknowns at each time step of the simulation in free running conditions. The results emerged in this study are similar to the ones of other research works, for example [6], and in particular the need to use building materials with sufficient thermal capacity in order to ensure the cooling of the structure through mechanical ventilation with outside air. Optimization of the building structure will then be associated with appropriate measures, where necessary, for the dedicated cooling of sows [7]. The study also revealed that it is necessary to move from a design approach based on few points or, at most, design days, to long-term analysis of the indoor temperature and humidity, in order to take into account the critical behavior of the structure and plants in mid-seasons, when warmer and colder days may alternate.

References

1. Axaopoulos P, Panagakis P, Kyritsis S (1992) Computer simulation assessment of the thermal microenvironmet of growing pigs under summer conditions. Trans ASAE 35(3):1005–1009
2. Panagakis P, Axaopoulos P (2008) Comparing fogging strategies for pig rearing using simulations to determine apparent heat-stress indices. Biosyst Eng 99:112–118
3. Fabrizio E (2012) Energy reduction measures in agricultural greenhouses heating: envelope, systems and solar energy collection. Energy Build 53:57–63
4. Bartali EH et al (1999) CIGR handbook of agricultural engineering, volume 2: animal production and aquacultural engineering. Am.Soc/Agricultural Engineers, Michigan
5. Liberati P, Zappavigna P (2006) Un software per la simulazione dinamica del clima interno degli edifici zootecnici. In: Cascone G (ed) Soluzioni edilizie, impianti e attrezzature per il miglioramento del benessere degli animali negli allevamenti intensivi. GeoGrafica, Ragusa, pp 30–44

6. Candura A, Scarascia Mugnozza G, Schettini E, Vox G (2006) Contenimento delle temperature e gestione dei reflui nei fabbricati per l'allevamento suinicolo intensivo. In: Cascone G (ed) Soluzioni edilizie, impianti e attrezzature per il miglioramento del benessere degli animali negli allevamenti intensivi. GeoGrafica, Ragusa, pp 155–167
7. Barbari M, Conti L (2009) Use of different cooling systems by pregnant sows in experimental pen. Biosyst Eng 103(2):239–244

Chapter 2
Numerical Model of a Slurry PCM-Based Solar Thermal Collector

Sara Baronetto, Gianluca Serale, Francesco Goia and Marco Perino

Abstract Flat-plate solar thermal collector is the most common device to convert solar energy into heat. This technology, which mostly adopts water-based fluids, has been widely investigated and improved since it was introduced, yet the exploitation of solar energy is limited by innate technological constraints. An interesting approach to overcome the limitations of these systems is based on the exploitation of the latent heat of fusion/solidification of the fluid—e.g., using a microencapsulated PCM suspended in a water fluid phase, also called slurry PCM. In this chapter, the numerical model of a PCM-based flat-plate solar thermal collector is presented and discussed. Starting from the well-known Hottel–Whillier equation, the physical–mathematical model of a water-based flat-plate solar is suitably modified to incorporate the phase change equations and to account for the different thermophysical properties of a non-Newtonian fluid, such as the slurry PCM. Examples of applications are also given, developing the simulation of the solar collector for different boundary conditions and showing the improved performance of the PCM-based technology in comparison with a conventional solar thermal collector.

Keywords Slurry PCM · Solar thermal collector · Numerical model · Simulation

S. Baronetto · G. Serale · F. Goia · M. Perino (✉)
TEBE Research Group, Department of Energy, Politecnico di Torino,
Corso Duca degli Abruzzi 24 10129 Turin, Italy
e-mail: marco.perino@polito.it

F. Goia
The Research Centre on Zero Emission Buildings, Faculty of Architecture
and Fine Arts, Norwegian University of Science and Technology,
Alfred Getz vei 3 7491 Trondheim, Norway

A. Li et al. (eds.), *Proceedings of the 8th International Symposium on Heating, Ventilation and Air Conditioning*, Lecture Notes in Electrical Engineering 263,
DOI: 10.1007/978-3-642-39578-9_2,

2.1 Introduction

Flat-plate solar thermal collector is the most common device to convert solar energy into heat. Conventional solar thermal collectors, which adopt water-based fluids, have been widely investigated since the 1940s [1], and improvements have been achieved in overall performance and efficiency. However, this technology suffers from constraints due to the mechanism that is exploited to harvest solar energy. Indeed, flat-plate solar collectors need relatively high irradiation levels to provide an acceptable efficiency, while with low irradiance their capability of exploiting solar energy is limited. A side effect of the present-day technologies is thus that when a relevant increase in the temperature of the water-based heat carrier fluid occurs, and then substantial solar energy exploitation takes places, the inefficiency of the system due to heat dissipation toward the outdoor increases too. Moreover, the exploitation of solar energy for space heating purpose through solar collector is often not profitable, since higher heat demands take place when low (or no) solar energy is available.

An interesting approach to overcome these limitations is based on the exploitation of the latent heat of fusion/solidification of the fluid. In this way, the isobaric process of phase change within the heat carrier fluid occurs at an almost constant temperature, and a large amount of heat is involved. Therefore, two of the main drawbacks of the present-day technology can be potentially contrasted: On the one hand, solar energy is exploited at lower thermal levels (and thus also when solar irradiance is not particularly high); on the other hand, heat losses for dissipation are reduced too.

The utilization of the heat carrier fluid phase change in solar collector applications is not a complete novelty. Experiments on this concept date back to the 1970s, where solar water pumps integrated with solar collectors [2] exploited of the heat carrier fluid phase change. After these first applications, other researches dealing with phase change-based solar collectors can be found in literature [3–5]. It is worth mentioning that all these applications made use of the liquid-to-gas phase change and that the heat carrier fluids were of different nature. Coupling a phase change material (PCM) layer and a water-based solar collector [6] is another strategy explored in the previous decades. In this concept, the phase change occurs in a material that is stored and contained inside the solar collector, while the heat carrier fluid remains in liquid state during the heat exchange process.

All the past experiences that took advantage of the latent heat of the heat carrier fluid were based on the exploitations of the liquid-to-gas transition. However, thanks to the advancements in PCM technologies, an alternative solution can be nowadays conceived: A particular heat carrier fluid (called slurry PCM), where the solid-to-liquid phase change is exploited instead, can be employed. Slurry PCM consists microencapsulated PCM (mPCM), suspended in a mixture of water and ethylene glycol, in fluid phase. In this way, the circulation of the heat carrier fluid is always guaranteed—the two-phase fluid has constant rheological properties.

There is no evidence in the literature of previous studies concerning the investigation of slurry PCM-based solar thermal system, and the aim of the research activity is to propose a simplified physical–mathematical model of slurry PCM-based flat-plate solar thermal collector in order to preliminary compare its performance with conventional flat-plate collectors.

It is worth mentioning that the whole slurry PCM-based system which has been conceived includes a PCM-based heat storage unit coupled with the solar collector and a secondary, water-based circuit to supply heating to the indoor environment. In this paper, the numerical model of the solar collector alone is presented and illustrated, while implications of coupling such a technology with a latent heat storage systems and a low-temperature heating system are not herewith investigated.

2.2 Physical–Mathematical Model

The physical–mathematical description of the flat-plate, slurry PCM-based solar thermal collector originates from the well-known Hottel-Whillier (HW) model [7]. The main assumptions of this model are as follows: quasi-steady-state (energy storage term is negligible) and step updates of the forcing parameters at each time step; internal emissions ignored; one-dimensional heat flux through the covers and the back insulation; uniform conditions over the collector; all heat losses from the collector surfaces toward the same heat sink, at the outdoor air temperature T_a.

The energy balance equation of the solar thermal collector is Eq. (2.1) (nomenclature adopted in [7] is used throughout the entire paper): The left-hand side of the equation represents the enthalpy flux of the heat carrier fluid and the right-hand side, the useful heat flux $\left(\dot{Q}_u\right)$ converted and delivered by the solar thermal collector. The efficiency of the system (Eq. 2.2) is given by the ratio of the useful heat to the solar irradiation on the collector plate.

$$\dot{m}_c c_c (T_{c,\text{out}} - T_{c,\text{in}}) = A_{col} F_R \left[G_T (\tau\alpha)_e - U_L (T_{c,\text{in}} - T_a) \right] \tag{2.1}$$

$$\eta = \left[\int \dot{Q}_u dt \right] \cdot \left[A_{col} \int G_T dt \right]^{-1} \tag{2.2}$$

The set of equations of the HW model is developed for a liquid heat carrier fluid that does not change its state of aggregation. In order to consider the physical phenomena related to the exploitation of the latent heat, changes need to be implemented.

The main change concerns the structure of the model itself: The temperature of the heat carrier fluid when it enters the solar collector ($T_{c,\text{in}}$) can be lower temperature than the initial temperature of the phase change T_l (with mPCM completely solid); moreover, the slurry PCM can leave the solar collector with a higher temperature than the final temperature of the phase change T_h (mPCM completely

melted). The solar collector can be thus virtually divided in three areas along the y-axis (i.e., along the riser tubes):

1. Δy_1 ($\Delta y_{1,\text{eff}}$) represents the segment of panel between the inlet of the heat carrier fluid and the point where it reaches the lower limit of the mPCM melting temperature range, T_l (sensible heat exploitation);
2. Δy_2 ($\Delta y_{2,\text{eff}}$) corresponds to the segment where the whole amount of mPCM completes the phase change, and the heat carrier fluid temperature thus rises from T_l to T_h (latent heat exploitation);
3. Δy_3 ($\Delta y_{3,\text{eff}}$) represents the segment where the heat carrier fluid increases further its internal energy and reaches the temperature $T_{c,\text{out}}$ (sensible heat exploitation).

The lengths of the three virtual sections (along the y-axis) depend on the boundary conditions and are calculated at each time step. The first segment Δy_1 is given by

$$\Delta y_1 = \left[\ln \left(\frac{T_{c,in} - T_a - \left(G_T(\tau\alpha)_e\right)/U_L}{T_l - T_a - \left(G_T(\tau\alpha)_e\right)/U_L} \right) \right] \cdot \left[\frac{N \cdot W \cdot F' \cdot U_L}{\dot{m}_c c_c} \right]^{-1} \tag{2.3}$$

Since the real length of the solar thermal collector along the y-axis L can be shorter than the virtual Δy_1 (if the boundary conditions are so that the heat carrier fluid cannot reach the lower limit of the phase change T_l before it leaves the collector), the effective length of the first segment $\Delta y_{1,\text{eff}}$ can be obtained imposing

$$\Delta y_{1,\text{eff}} = \min \begin{Bmatrix} \Delta y_1 \\ L \end{Bmatrix} \tag{2.4}$$

The length of the segment Δy_2, where the mPCM completes the phase change, is obtained by means of Eq. (2.5). The fictitious latent heat r'' is introduced (Eq. 2.6): It includes the mPCM latent heat contribution (r') and the sensible heat contribution of the ethylene glycol–water solution within the temperature range $T_l - T_h$, α_{pcm} being the mass fraction of mPCM in the slurry and c_{gw} is the specific heat capacity of the ethylene glycol–water solution.

$$\Delta y_2 = -\frac{\dot{m}_c r''}{N \cdot W \cdot F' \cdot U_L \cdot \left[\left(T_h + T_l\right)/2 - \left(G_T(\tau\alpha)_e\right)/U_L - T_a \right]} \tag{2.5}$$

$$r'' = r' + \frac{1 - \alpha_{\text{pcm}}}{\alpha_{pcm}} \cdot c_{gw} \cdot (T_h - T_l) \tag{2.6}$$

Considering that, due to boundary conditions, slurry PCM can leave the solar collector with a fraction of the mPCM still in solid phase (the entire phase change potential is not exploited), and thus, $\Delta y_{1,\text{eff}} + \Delta y_2 > \text{L}$, and it is necessary to identify the effective length $\Delta y_{2,\text{eff}}$, according to Eq. (2.7); the fraction of mPCM that has completed the phase change x_{pcm} is given by Eq. (2.8). Finally, the

effective length of the third segment $\Delta y_{3,\text{eff}}$ is obtained by subtracting from the length of the solar collector, L:

$$\Delta y_{2,\text{eff}} = \min \begin{cases} \Delta y_2 \\ L - \Delta y_{1,\text{eff}} \end{cases} \tag{2.7}$$

$$x_{\text{pcm}} = \Delta y_{2,\text{eff}} \cdot \Delta y_2^{-1} \tag{2.8}$$

$$\Delta y_{3,\text{eff}} = L - \Delta y_{1,\text{eff}} - \Delta y_{2,\text{eff}} \tag{2.9}$$

The full set of HW model equations is used in sections $\Delta y_{1,\text{eff}}$ and $\Delta y_{3,\text{eff}}$ to calculate F_R and U_L—each section has its own F', and thus, different F_R are obtained for each section. The useful heat fluxes $dQ_{u,1}$ and $dQ_{u,3}$ for those areas ($A_{1,\text{eff}}$ and $A_{3,\text{eff}}$, respectively) can be calculated by means of the right-hand side of Eq. (2.1), setting $T_{c,\text{in}} = T_{c,\text{in}}$ and $T_{c,\text{in}} = T_h$ for $A_{1,\text{eff}}$ and $A_{3,\text{eff}}$, respectively, and using the effective areas in place of the solar thermal collector area A_{col}, according to Eq. (2.10):

$$A_{\text{eff}=}A_{\text{col}} \cdot \Delta y_{\text{eff}} \cdot L^{-1} \tag{2.10}$$

On the contrary, in section $\Delta y_{2,\text{eff}}$, a constant temperature field along the y-axis is imposed due to the isothermal phase change process (i.e., collector flow factor $F'' = 1$): The collector heat removal factor F_R is thus equal to the collector efficiency factor F' for that section.

The useful heat flux in section $A_{2,\text{eff}}$ can be calculated using a slightly different version (Eq. 2.11) of the left-hand side of the energy balance equation of HW model (Eq. 2.1), assuming that the heat carrier fluid temperature increases linearly in section $\Delta y_{2,\text{eff}}$, between the two limit temperatures (T_l and T_h) of the phase change (Eq. 2.12), following the fraction of the mPCM that is melted x_{pcm}.

$$\dot{Q}_{u,2} = x_{\text{pcm}} \cdot \dot{m}_c \cdot r'' \tag{2.11}$$

$$T_{h,\text{eff}} = T_l + x_{\text{pcm}} \cdot (T_h - T_l) \tag{2.12}$$

The total useful heat flux (dQ_u) converted by the slurry PCM-based solar thermal collector is thus given by the sum of the useful heat fluxes converted in each section (Eq. 2.13); the efficiency of the collector (Eq. 2.14) is given by applying Eq. (2.2):

$$\dot{Q}_u = \dot{Q}_{u,1} + \dot{Q}_{u,2} + \dot{Q}_{u,3} \tag{2.13}$$

$$\eta = \left[\int \dot{Q}_u dt\right] \cdot \left[(A_{1,\text{eff}} + A_{2,\text{eff}} + A_{3,\text{eff}}) \int G_T dt\right]^{-1} \tag{2.14}$$

The slurry PCM-based solar thermal collector model needs also some changes in some subsidiary equations, in order to take into account the nature of the heat carrier fluid (a biphase, two components' fluid). In particular, the formulation of Nusselt number Nu, which plays a role in the calculation of the collector flow

factor *F'*, is changed, considering that the most-likely flow regime of the slurry PCM is laminar flow. The typical equation for a pseudoplastic non-Newtonian fluid in laminar flow (Eq. 2.15) is used, where n is the rheological behavior index (which is, in turn, function of heat carrier fluid temperature and mPCM concentration):

$$Nu = [8 \cdot (5n + 1) \cdot (3n + 1)] \cdot \left[31n^2 + 1\right]^{-1} \tag{2.15}$$

Moreover, since the slurry PCM is a suspension of mPCM in an ethylene glycol–water mixture, the thermophysical properties of the heat carrier fluid (e.g., conductivity, density, specific heat capacity) are obtained as mass-weighted average between properties of the mPCM and of the glycol–water mixture.

The physical–mathematical models of the slurry PCM-based solar collector and of the water-based solar collector (HW model) have been implemented in MATLAB-Simulink environment for numerical solution of algebraic loops.

2.3 Parametric Analysis

The performance of the slurry PCM-based solar thermal collector has been thus numerically assessed by means of parametric analysis. The typical meteorological year of Turin, Italy, (45°4′0″N, 7°42′0″E) was used and solar collector efficiency during January (η_{jan}), the heating season ($\eta_{heating}$), i.e., between mid-October and mid-April, and the entire year (η_{year}) were calculated.

In order to provide a reference and to allow a direct comparison of the performance, a water-based solar thermal collector was also simulated, under the same boundary conditions. The simulated flat solar thermal panels have an effective collector area of 1,965 m^2 ($\alpha = 0.95$; $\varepsilon = 0{,}05$), rock wool insulation (50 mm below, 20 mm along the edge), and a single transparent glass top ($\tau = 0.904$).

The heat carrier fluid for the water-based solar collector was a mixture of water and ethylene glycol (20 %). The slurry PCM was a suspension of microencapsulated PCM (n-eicosane, with a nominal melting temperature 37 °C and a latent heat storage capacity of 190–200 J/g in the melting range 35–39 °C) in water ethylene glycol; mPCM was 60 % of the total mass of the heat carrier fluid. A constant flow rate equal to 7.4 10^{-2} m^3/h was used for both cases. Parametric analyses included the following:

- the influence of the tilt angle β—from 0° (horizontal) to 90° (vertical), for a south-oriented panel;
- the influence of the azimuth angle γ—from −40° (east) to +40° (west), being 0° south, for a tilt angle $\beta = 45°$.

2.4 Results

The outcomes of the simulations, shown in Tables 2.1 and 2.2, highlight the considerable improvement in the efficiency of the solar thermal collector when the slurry PCM is used. An absolute increase in the annual efficiency η_{year} of about 0.07 is achieved, almost regardless the tilt angle and the azimuth angle.

The maximum annual efficiency is reached, for a south-exposed panel, when the tilt angle is in the range 40–50°, with a value of 0.49 and 0.56, for the water-based and the slurry PCM-based solar collector, respectively (Table 4.1). In January, the advantage given by the slurry PCM is slightly further increased: The absolute value of the highest efficiency (i.e., with almost vertical tilt angle) is 0.09 higher than the highest efficiency with a water solar thermal collector.

Table 2.1 Efficiency of sPCM and water solar collectors during the year (η_{year}), January (η_{jan}), and the heating period ($\eta_{heating}$), for different tilt angles (south-oriented solar thermal collectors)

β	η_{year}		η_{jan}		$\eta_{heating}$	
	water	sPCM	water	sPCM	Water	sPCM
90°	0.40	0.46	0.40	0.49	0.41	0.49
80°	0.45	0.52	0.41	0.50	0.43	0.51
70°	0.47	0.54	0.40	0.49	0.44	0.52
60°	0.48	0.55	0.38	0.47	0.43	0.51
50°	0.49	0.56	0.37	0.45	0.42	0.50
45°	0.49	0.56	0.35	0.43	0.42	0.49
40°	0.49	0.56	0.34	0.41	0.41	0.48
30°	0.49	0.55	0.30	0.37	0.39	0.45
20°	0.48	0.54	0.26	0.32	0.36	0.42
10°	0.46	0.52	0.19	0.24	0.32	0.37
0°	0.44	0.50	0.10	0.13	0.26	0.31

Table 2.2 Efficiency of sPCM and water solar collectors during the year (η_{year}), January (η_{jan}), and the heating period ($\eta_{heating}$), for different tilt angles (south-oriented solar thermal collectors)

γ	η_y		η_{jan}		η_{jul}	
	water	sPCM	water	sPCM	water	sPCM
-40°	0.45	0.51	0.21	0.27	0.42	0.49
-30°	0.46	0.53	0.27	0.34	0.40	0.48
-20°	0.47	0.54	0.29	0.36	0.42	0.50
-10°	0.48	0.55	0.36	0.44	0.39	0.46
0°	0.49	0.56	0.35	0.43	0.42	0.49
10°	0.50	0.56	0.42	0.51	0.37	0.44
20°	0.50	0.57	0.37	0.45	0.42	0.49
30°	0.50	0.57	0.37	0.45	0.42	0.49
40°	0.50	0.57	0.43	0.52	0.35	0.42

In the heating season, difference in efficiency between the two systems is similar to the annual one, ranging from +0.04 to 0.07, depending on the tilt angle. The parametric analysis on the orientation shows that the best performance, for $\beta = 45°$, is reached for both the sPCM and the water-based collector for an S–W exposition: η_{year} of the sPCM 0.07 higher than that of the conventional system.

2.5 Conclusion

A physical–mathematical model of a flat-plate slurry PCM-based solar thermal collector has been conceived, developed, and implemented in MATLAB/Simulink. The model was verified (the water-based version) and tested, showing a good numerical stability and a satisfactory computational speed—some seconds for each simulated time step. Thanks to these features, the model was then used to carry out sensitivity analyses about the behavior of the slurry PCM collector.

The efficiency of this novel solar panel was assessed under different boundary conditions (tilt and azimuth angle) and compared against that of a conventional water-based solar thermal collector. The analysis show that the adoption of the slurry PCM as heat carrier fluid determines an increase in the annual efficiency of the collector of about 0.07, regardless of the orientation and the tilt angle.

Acknowledgments This research was developed in the frame of the activities of SolHe_PCM project, cofunded by Regione Piemonte (Polo di Innovazione Polight, FESR 2007–2013).

References

1. Hottler MC, Woertz BB (1942) Performance of flat plate solar-heat collectors. ASME Trans 64:91–104
2. Rao DP, Rao KS (1976) Solar water pump for lift irrigation. Sol Energy 18:405
3. Soin RS, Sangameswar Rao K, Rao DP, Rao KS (1979) Performance of flat plate solar collector with fluid undergoing phase chance. Sol Energy 23:69–73
4. Kaushika ND, Bharadwaj SC, Kaushik SC (1982) Analysis of a flat plate collector with fluid undergoing phase change. Appl Energy 11:233–242
5. Kishore VVN, Gandhi MR, Marquis C, Rao KS (1984) Testing flat-plate collectors charged with phase-changing fluids. Appl Energy 17:155–168
6. Bansal NK, Buddhi D (1992) Performance equations of a collector cum storage system using phase change materials. Sol Energy 48:185–194
7. Duffie JA, Beckman WA (1974) Solar engineering of thermal processes. Wiley, New York

Chapter 3
Energy Performance Assessment of Advanced Integrated Façades by Means of Synthetic Metrics

Francesco Goia, Lorenza Bianco, Valentina Serra and Marco Perino

Abstract Façades play an important role in architecture, with deep implications in both the quality of the indoor environment and the appearance of the building. R&D in the field of energy conservation is moving toward advanced integrated façades (AIFs): these are innovative and dynamic façades deeply connected with the building equipment. Their dynamic features allow the energy performance of the façade to be optimized, adapting its behavior to different boundary conditions. The substantial lack of synthetic performance parameters to assess and to characterize the energy performance of AIFs is one of the main limitations to the widespread of these technologies. This inconvenience is due to the fact that conventional synthetic metrics (such as U-value and g-value) cannot be fully applied with these technologies. The research activity presented in the paper is an attempt to investigate new synthetic metrics able to characterize the thermal behavior of an AIF. A multiple linear regression (MLR) approach is adopted to identify synthetic parameters able to replicate the energy performance of the façade as a function of the main boundary conditions, e.g., solar irradiance and thermal gradients.

Keywords Advanced integrated façade · Synthetic metrics · Multiple linear regression · Imulation · Energy performance assessment

F. Goia · L. Bianco · V. Serra (✉) · M. Perino
TEBE Research Group, Department of Energy, Politecnico di Torino, Turin, Italy
e-mail: valentina.serra@polito.it

F. Goia
The Research Centre on Zero Emission Buildings, Faculty of Architecture and Fine Arts, Norwegian University of Science and Technology, Trondheim, Norway

A. Li et al. (eds.), *Proceedings of the 8th International Symposium on Heating, Ventilation and Air Conditioning*, Lecture Notes in Electrical Engineering 263,
DOI: 10.1007/978-3-642-39578-9_3,

3.1 Introduction

Highly glazed façades have widely spreading and gaining popularity in the last decades, due to their architectural appeal. From the energy point of view, the transparent envelope is the weakest component of the building and may also increase discomfort risk. In order to overcome these drawbacks, advanced integrated façade (AIF) concept has been developed, introducing dynamic and responsive behavior that improves the energy performance of the glazed envelope [1]. The physical phenomena involved in an AIF are complex; thus, its energy performance assessment is a challenging task [2, 3]. The adoption of conventional performance parameters (e.g., *U-value* and *g-value*) is still a common practice in energy performance characterization of innovative transparent components [4], as shown by some studies on total solar transmittance in DSF [5].

In a recent paper [6], the authors first estimated the *U-value* and the *g-value* of a reference glazing and of an AIF, and then assessed the capability of such parameters to replicate the energy performance of those glazing systems through the comparison of long-term monitoring data. The reference fenestration was a double-glazed system (8/15/6 mm) made with an external reflective pane and an internal clear glass, and the AIF a climate façade (CF). Robust data sets of field-measured temperatures, heat fluxes, and solar irradiances were used. The procedure made use of a linear regression model (ordinary least squares method, imposing that the constant term is zero) and the first-order coefficient is interpreted as *U-value* or *g-value*, according to the involved physical quantities.

The results showed that although the adoption of *U-value* and *g-value* in case of conventional glazing systems may result in some errors, it is still acceptable to use these parameters. On the contrary, the adoption of such parameters in case of more advanced façade technologies, coupled with a simplified heat balance equation that does not include transient effects, often leads to considerable inaccuracies in the estimation of the heat flux and energy that cross the glazing surface.

The aim of this paper is to explore a different strategy to estimate synthetic parameters: Multiple linear regression (MLR) approach is adopted to identify new metrics able to replicate the energy performance of glazing systems as a function of the main boundary conditions (e.g., solar irradiance and thermal gradients).

3.2 The Glazing Technology

A CF, installed on a two-story height office building and operating under actual conditions, was used as a case to assess the adoption of MLR techniques for characterizing the thermo-physical and energy behavior of advanced integrated façades. The CF is the same advanced glazing technology used in [6], i.e., a double-skin façade made with an external single pane glazing, an internal double-glazed unit (4/12/4) with low-e coating, and a high reflective roller screen is

located in the 70 cm façade cavity. The façade works as an exhaust ventilation system: the air (with variable flow rate, depending on the season and the time of the day) flows from the room through the façade cavity and then to the HVAC exhaust channels. The schedule of the ventilation system is usually 8 am to 8 pm, Monday to Friday [7].

3.3 Methods

3.3.1 Experimental Data Collection

For the sake of brevity, data collection procedure used during the experimental campaign is not reported here, detailed information can be found in [6, 7]. Surface and air temperatures were measured with T-type/J-type thermocouples (accuracy: ±0.3 °C); heat fluxes were measured with heat flux meters (accuracy: ±5 %); incident (on the vertical plan) and transmitted solar irradiance was measured with integral pyranometers (accuracy ±2 %). Thermocouples and heat flux meters were shielded with aluminum foils to reduce solar radiation influence. All the physical quantities were recorded with sub-hourly rate, but data analysis was later carried out on hourly values, obtained as average of sub-hourly readings.

3.3.2 Data Analysis Procedure and Metrics Identifications

The available experimental data of the CF were split into two different data sets (SET1 and SET2), characterized by the same representativeness of the original data, i.e., each data set had approximately the same amount of days for each season, with different boundary conditions each season. One data set (SET1) was used to identify metrics by means of MLR techniques (adopting the OLS method), while the other data set (SET2) was then used to estimate the ability of these metrics to replicate the energy performance and thermo-physical behavior.

MLR attempts to model the relationship between two or more independent variables (x_1, x_2, x_n) and a dependent variable (y) by fitting to observed data, a linear equation, whose general form is:

$$y = \alpha_0 + \alpha_1 x_1 + \alpha_2 x_2 + \cdots + \alpha_n x_n \tag{3.1}$$

In the research activity, MLR was developed for both the case of constant term ($\alpha_0 \neq 0$) and the case without constant term ($\alpha_0 = 0$). However, for the sake of brevity, only the MLR that includes the constant term is illustrated in this paper, since the results of those with $\alpha_0 = 0$ were less accurate than those with $\alpha_0 \neq 0$.

Two different MLRs were developed. A basic model (Eq. 3.2) correlates the specific heat flux entering the façade ($\dot{q}$) with the solar irradiance I and the thermal

gradient between the outdoor and the indoor ($T_{out} - T_{in}$). By integrating both sides of Eq. 3.2 over the time (along 24 h), a simple model that correlates the daily energy across the façade q_{24} with the daily irradiation (H, [Wh/m^2]) and the daily thermal gradient (degree-day, ΔT_{24}, [h °C]) is obtained.

$$\dot{q} = \beta + \beta' I + \beta''(T_{out} - T_{in}) \tag{3.2}$$

$$\begin{aligned} q_{24} &= \int_{24h} \mathrm{d}q\mathrm{d}t = \beta_{24} + \beta'_{24} \int_{24h} I\mathrm{d}t + \beta''_{24} \int_{24h} (T_{out} - T_{in})\mathrm{d}t \\ &= \beta_{24} + \beta'_{24} H + \beta''_{24} \Delta T_{24} \end{aligned} \tag{3.3}$$

In these formulations, the unit of coefficients β is [W/m^2], that of β_{24} is [Wh/m^2], that of β' and β'_{24} is [-], and that of β'' and β''_{24} is [W/m^{2}K]. β' and β'_{24} are dimensionally equal to a *g-value*, while β'' and β''_{24} are equal to an *U-value*.

A more advanced model (Eq. 3.4) is instead conceived by splitting the thermal gradient between the outdoor and the indoor in two different contributions: the thermal gradient between the outdoor environment and the cavity of the CF (i.e., $T_{out} - T_{cav}$), and the thermal gradient between the cavity and the indoor (i.e., $T_{cav} - T_{in}$). Following the same procedure of the simple model, the specific daily energy model can be obtained (Eq. 3.5), where ΔT_{24}^{o-c} [h °C] is the daily thermal gradient between the outdoor and the air cavity, and ΔT_{24}^{c-i} [h °C] is the daily thermal gradient between the air cavity and the indoor environment.

$$\dot{q} = \gamma + \gamma' I + \gamma''(T_{out} - T_{cav}) + \gamma'''(T_{cav} - T_{in}) \tag{3.4}$$

$$q_{24} = \gamma_{24} + \gamma'_{24} H + \gamma''_{24} \Delta T_{24}^{o-c} + \gamma'''_{24} \Delta T_{24}^{c-i} \tag{3.5}$$

The unit of coefficient γ is [W/m^2] and that of γ_{24} is [Wh/m^2], while that of γ' and γ'_{24} is [-] and that of $\gamma'', \gamma''_{24}, \gamma''', \gamma''_{24}$, is [W/m^{2}K].

Considering that great differences in boundary conditions (e.g., solar position and indoor air temperature) occur along the year, three sets of metrics are assessed during the year namely for winter, summer, and mid-season.

3.3.3 Model Validation and Evaluation of Metrics Performance

Once the metrics (the linear coefficients of the MLR) were assessed, their capability of replicating the thermo-physical behavior of the CF was assessed by comparing the experimental data with data obtained by means of the above-mentioned performance parameters. In particular, specific heat flux ($_e\dot{q}$) and specific daily energy ($_eq_{24}$) measured during the experimental campaign (SET2) were compared against the correspondent quantity ($_s\dot{q}$ and $_eq_{24}$, respectively) obtained through the application of β and γ metrics to readings (irradiances and air temperatures) of SET2, according to the linear Eqs. 3.2–3.5

In order to quantitatively assess the performance of the metrics, root mean square error (RMSE) [W/m^2 or Wh/m^2] and absolute percentage error ($|\varepsilon_{\%}|$)[%] are used, defined according to Eqs. 3.6 and 3.7, respectively, where s refers to the simulated datum ($_s\dot{q}$ or $_sq_{24}$) and e refers to the experimental datum ($_e\dot{q}$ or $_eq_{24}$):

$$\text{RSME} = \sigma = \sqrt{n^{-1} \cdot \sum_{i}^{n} (\text{s}_i - \text{e}_i)^2} \tag{3.6}$$

$$|\varepsilon_{\%}|_i = 100 \cdot |\text{s}_i - \text{e}_i| \cdot (\text{e}_i)^{-1} \tag{3.7}$$

3.4 Results and Discussion

The values of the metrics β and γ, determined by means of the two MLR models (simple and advanced), on SET1, are shown in Tables 3.1 and 3.2, respectively, together with the adjuster R^2, i.e., $\bar{R}^2$. Although this parameter cannot be strictly interpreted as a measure of fit (as R^2 in linear regression), it still gives a qualitative information about the capability of the MLR of approximating experimental data. The RMSE, calculated during the validation of the model with SET2, is also given in Tables 3.1 and 3.2.

In Fig. 3.1, the simulated specific heat flux $_s\dot{q}$ (*a, right*) and the simulated specific daily energy $_sq_{24}$(*b, left*) are plotted against the correspondent experimental datum (i.e., $_sdq$ and $_sq_{24}$, respectively) in the case of the simple MLR model (β coefficients). In Fig. 3.2, the same data are shown in the case of the more advanced model (γ coefficients). In Fig 3.3, the cumulated frequency of the absolute percentage error is also given, for the two MLR models, and compared against the

Table 3.1 Metric values for the specific heat flux $\dot{q}$, and daily energy q_{24}, simple model

RSME: 7.6	W/m^2	$\dot{q} = \beta + \beta' I + \beta''(T_{\text{out}} - T_{\text{in}})$		
		Winter	Midseason	Summer
β	W/m^2	−1.039	3.461	3.790
β'	–	0.079	0.074	0.060
β''	W/m^{2}K	0.560	0.788	0.810
$\bar{R}^2$	–	0.85	0.79	0.81
RSME: 61.3	Wh/m^2	$q_{24} = \beta_{24} + \beta'_{24} H + \beta''_{24} \Delta T_{24}$		
		Winter	Midseason	Summer
β_{24}	Wh/m^2	−46.510	−1.351	−27.36
β'_{24}	–	0.098	0.092	0.095
β''_{24}	W/m^{2}K	0.632	0.640	0.311
$\bar{R}^2$	–	0.95	0.82	0.62

Table 3.2 Metrics values for the specific heat flux $\dot{q}$, and daily energy q_{24} advanced model

RSME: 7.1	W/m^2	$\dot{q} = \gamma + \gamma' I + \gamma''(T_{out} - T_{cav}) + \gamma'''(T_{cav} - T_{in})$		
		Winter	Midseason	Summer
γ	W/m^2	−3.092	4.831	3.24
γ'	–	0.059	0.039	0.04
γ''	W/m^{2}K	−0.258	−0.250	0.12
γ'''	W/m^{2}K	0.867	1.588	1.45
$\bar{R}^2$	–	0.86	0.82	0.88
RSME: 59.6	Wh/m^2	$q_{24} = \gamma_{24} + \gamma'_{24} H + \gamma''_{24} \Delta T_{24}^{o-c} + \gamma'''_{24} \Delta T_{24}^{c-i}$		
		Winter	Midseason	Summer
γ_{24}	Wh/m^2	−16.850	53.782	5.424
γ'_{24}	–	0.134	0.058	0.073
γ'''_{24}	W/m^{2}K	2.004	−0.183	0.041
γ'''_{24}	W/m^{2}K	−0.027	1.413	0.870
$\bar{R}^2$	–	0.93	0.87	0.73

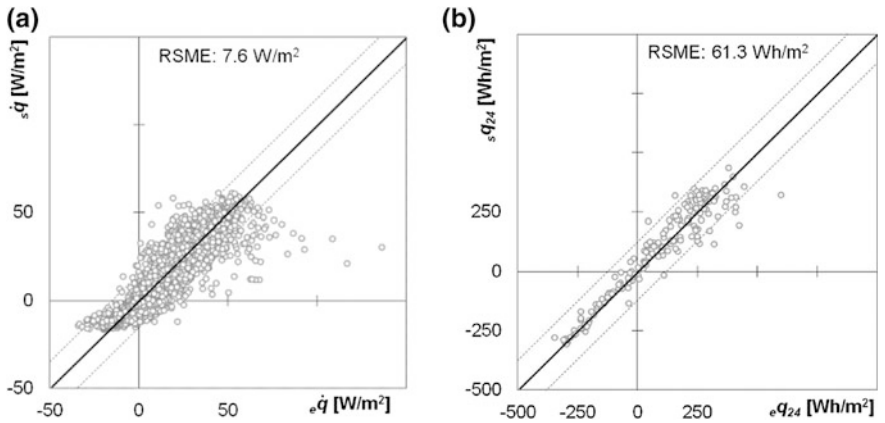

Fig. 3.1 Results for the simple model. **a** Comparison between simulated and experimental specific hourly heat flux (*left*). **b** Comparison between simulated and experimental daily energy (*right*)

outcome of a previous research activity on the same façade technology [6], where the same physical quantities (q_{24} and $\dot{q}$) were evaluated through the simulation of the energy performance of the AF by means of measured *U-value* and *g-value*.

The results show that the metrics change considerably from the simple to the advanced model, and a physical interpretation of the linear regression coefficients is difficult and probably meaningless. In general, the prediction of the specific daily energy through the adoption of the metrics determined by MLR is more reliable than that of the specific heat flux, for both the simple and the advanced models. This fact can be explained considering that inertial effects are quite relevant when $\dot{q}$ is concerned, but are less relevant when the entire daily energy is concerned.

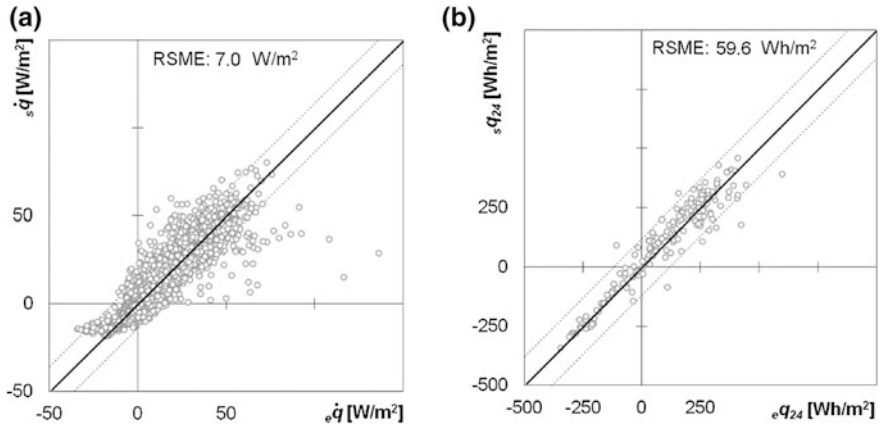

Fig. 3.2 Results for the advanced model. **a** Comparison between simulated and experimental specific hourly heat flux (*left*). **b** Comparison between simulated and experimental daily energy (*right*)

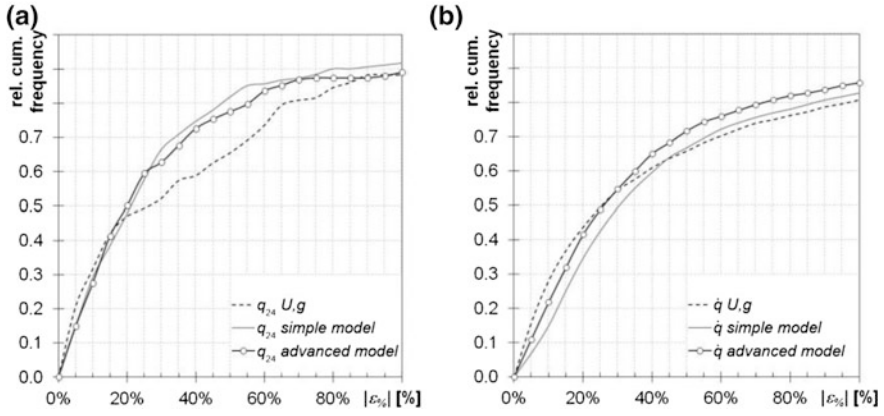

Fig. 3.3 Relative errors cumulative frequency of the three models. **a** q_{24} (*left*). **b** $\dot{q}$ (*right*)

The metrics and the adoption of the advanced model seem to slightly better replicate the phenomena than the simple model, but the difference is not substantial.

A more detailed analysis reveals that both the simple and advanced models are particularly capable of replicating the winter behavior, especially as far as q_{24} is concerned, but as far less degree of accuracy is reached in summer and mid-season.

In winter, the RMSE for both the models is about 20 Wh/m^2, while the annual RMSE is about 60 Wh/m^2. The analysis of $\bar{R}^2$ also confirms that the most critical seasons are summer and mid-season, when the data simulated with MLR models show the largest discrepancy from experimental data—another sign that the adopted MLR models and coefficients are not fully reliable when transient effects become relevant.

If compared to the outcome of the previous step of this research (q_{24} and $\dot{q}$ U,g) [6], MLR seems to increase the accuracy in the prediction of the daily energy (Fig. 3.3), but just a very slight improvement is revealed, if the advanced model is used, as far as $\dot{q}$ is concerned.

3.5 Conclusion

MLR technique was used to determine synthetic metrics able to replicate the thermo-physical behavior of an advanced integrated façade. The results show that although some improvements with respect to the adoption of conventional parameters (*U-value* and *g-value*) can be achieved, the metrics (for both the advanced and the simple models) are not fully able to replicate the behavior of the façade (not the specific heat flux, nor the specific daily energy). For more than 50 % of the time, the estimated heat flux or daily energy is more than 20 % higher/lower than the experimental one.

References

1. Annex 44—IEA—ECBCS Report, EXPERT GUIDE—PART 2: RBE, editors: Øyvind Aschehoug, Marco Perino, 2010, http://annex44.civil.aau.dk/
2. Hensen JLM, Bartak M, Drkal F (2002) Modeling and simulation of double-skin facade systems. ASHRAE Trans 108:2
3. Manz H (2005) Thermal simulation of buildings with double skin façades. Energy Build 37:1114–1121
4. Jelle BP, Hynd A, Gustavsen A, Arasteh D, Goudey H, Hart R (2012) Fenestration of today and tomorrow: A state of the art review and future research opportunities. Solar Energy Mater Solar Cells 96:1–28
5. Manz H (2004) Total solar energy transmittance of glass double façades with free convection. Energy Build 36:127–136
6. Bianco L, Goia F, Serra V (2013) Energy performance assessment of advanced glazed façades in office buildings. In: Proceedings of the 11th REHVA world congress, 16–19 June 2013, Prague, Czech Republic (in press)
7. Zanghirella F, Serra V, Perino M, Sossai C (2010) Active transparent façade integrated with a well water cooling system: an experimental analysis. In: Proceedings of the 10th REHVA world congress, 9–12 May 2010, Antalya, Turkey, pp 1–8

Chapter 4
Simulation of the Natural Smoke Filling in Subway Tunnel Fire

Wenjun Lei, Angui Li, Jie Yang, Ran Gao and Baoshun Deng

Abstract Smoke movement during a fire in subway tunnel was conducted in this study, when the heat release rate was 7.5 MW. The smoke temperature, smoke concentration and smoke velocity were also analyzed, respectively. If we recognize that the fire is the center, the temperature of the ceiling jet is almost symmetrically distributed. When the fire is in the stable combustion stage, the smoke concentration is high at the closed end of the subway tunnel. Because the plume was limited by the wall, the hot gases will move back after flow along the wall. Therefore, an obvious eddy will be produced. Meanwhile, we can see that the smoke velocity close the ground was also increased.

Keywords Subway tunnel fire · Smoke temperature · Smoke concentration · Smoke velocity · FDS

4.1 Introduction

Nowadays, subway has already been the mainstay and the lifeline of the urban traffic. However, the environment control problems of the subways are the key points scholars always focus on. In all the disasters happening in subway rail transit system, fire occupies the highest proportion.

W. Lei · A. Li (✉) · J. Yang · R. Gao
School of Environmental and Municipal Engineering,
Xi'an University of Architecture and Technology,
Xi'an 710055 Shaanxi, China
e-mail: Liag@xauat.edu.cn

B. Deng
China Railway First Survey and Design Institute Group Limited,
Xi'an 710043 Shaanxi, China

A. Li et al. (eds.), *Proceedings of the 8th International Symposium on Heating, Ventilation and Air Conditioning*, Lecture Notes in Electrical Engineering 263,
DOI: 10.1007/978-3-642-39578-9_4,

On fire, previous scholars have done many researches. Many researches have been carried out to predict smoke behavior or movement and related topics in underground space such as tunnel [1, 2] and subway systems [3–5]. Numerical prediction of smoke movement has once been studied by Park [6] in a subway station. Following their study, experiment and computational fluid dynamics (CFD) were both carried by Rie et al. [7] to investigate smoke control strategy in subway station under fire case.

In this study, smoke movement during a fire in subway tunnel was conducted, when the heat release rate was 7.5 MW. The smoke temperature, smoke concentration and smoke velocity were also analyzed, respectively.

4.2 Simulation Method

4.2.1 The Physical Model

The dimensions of the subway tunnel are 37.5 m (L) × 6.0 m (W) × 6.0 m (H), see Fig. 4.1. The right end of the tunnel is closed, and the left end is opened. The heat release rate of the fire is 7.5 MW. The ambient temperature is 15 °C. The influence of the different calculation grid number on the simulated result was also considered in this study. And then we determined that the grid number was 150 × 24 × 24.

4.2.2 The Turbulent Airflow Model

Fire dynamics simulator (FDS) is used to carry out CFD simulations [8]. In simulation of fire-induced smoke transportation, the predicted results of the software have been thoroughly validated [9]. Currently, turbulence models commonly used in the simulation of fire-induced smoke transportation are based on Reynolds-averaged Navier–Stokes equation (RANS) method, large eddy simulation (LES) and direct numerical simulation (DNS). It is reported LES is able to predict

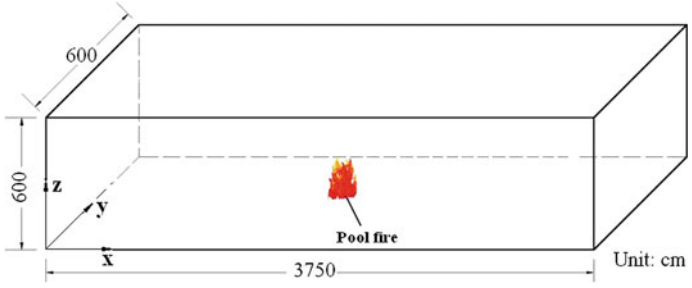

Fig. 4.1 The configuration and dimension of the subway tunnel

instantaneous flow characteristics and turbulent flow structures. Therefore, LES, which is now more widely used and reported to give better predictions on some cases of buoyancy driven flow, is used here [9].

4.2.3 Boundary Conditions

The smoke dispersion induced by a near-wall fire in a road tunnel has been studied by Hu et al. [10]. In that study, the thermally thick boundary condition rather than fixed temperature or fixed heat flux boundary condition is used to predict the tunnel wall temperature rise due to radiative and convective heat transfer from the surrounding smoke. Here, we also used this boundary condition for the wall and ceiling of the tunnel. In addition, the material of the wall and ceiling is concrete with material properties of density = 2,400 kg/m3, conductivity = 2.0 W/m/K, and specific heat = 0.9 kJ/kg/K [11]. The left end of the tunnel was set to be naturally opened with no initial velocity boundary condition specified for it. The longitudinal wind velocity was set by the "MISC" command provided by FDS [12], which can directly prescribe an initial wind through the domain.

The growth of fire is modeled by the power law using an appropriate constant to simulate low, medium, fast and ultra-fast growing fires. A typical t-square growth fire [13] is employed in the study to represent the variation of fire heat release rates with time.

4.3 Results and Discussion

4.3.1 Temperature Field

Variations of smoke temperature during smoke filling are shown in Fig. 4.2. From Fig. 4.2, we can see that the gradient of longitudinal temperature distribution is large. However, the transverse temperature distribution is relatively uniform at the same height.

4.3.2 The Temperature of the Ceiling Jet

Figure 4.3 is the variations of the ceiling jet temperature in the subway tunnel, when the heat release rate is 7.5 MW. The fire is located at the center of the subway tunnel. At the time $t = 60$ s, the ceiling jet is in the beginning stages of development. And the temperature of the measuring point is about 25 °C. After 120 s, there is considerable temperature rising at the both ends of the tunnel. At the time $t = 300$ s and $t = 600$ s, the fire is in the stable combustion stage. Therefore,

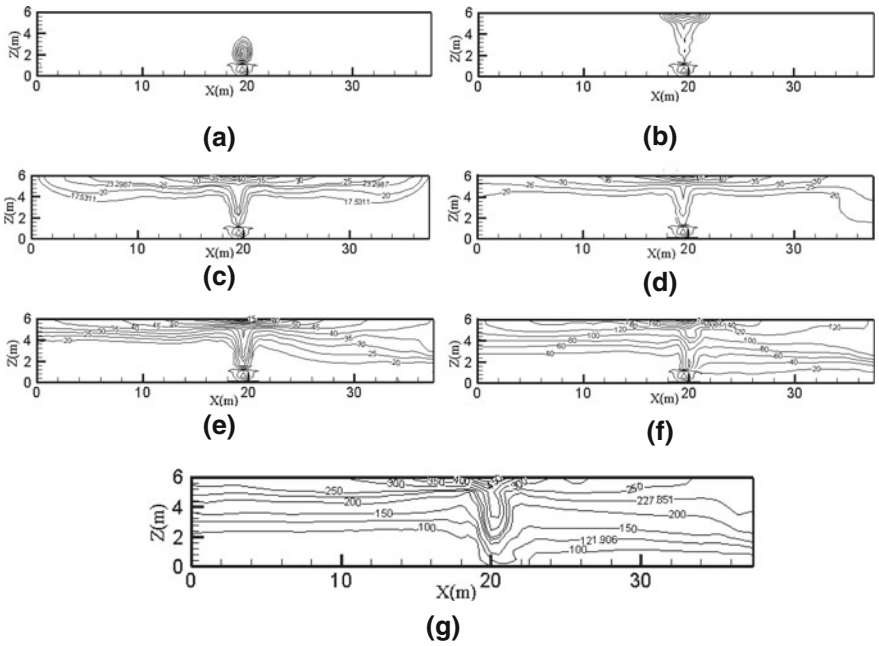

Fig. 4.2 Variations of smoke temperature at the cross-section of y = 2 m, when the fire heat release rate is 7.5 MW in subway tunnel. **a** 13 s, **b** 18 s, **c** 48 s, **d** 60 s, **e** 81 s, **f** 162 s, **g** 330 s

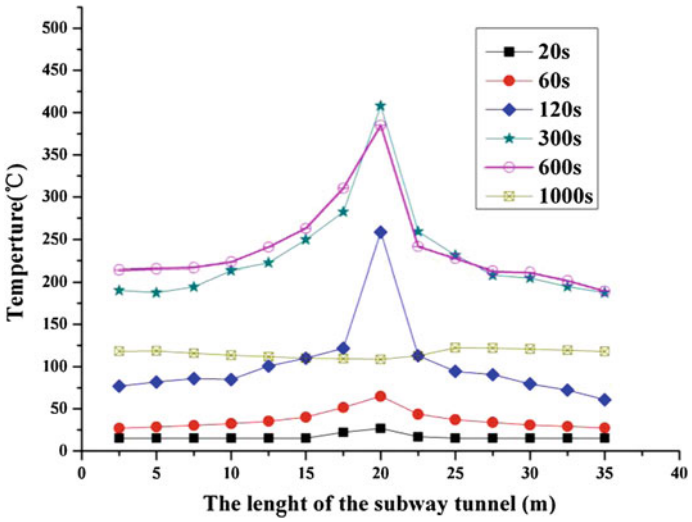

Fig. 4.3 Variations of the ceiling jet temperature in the subway tunnel

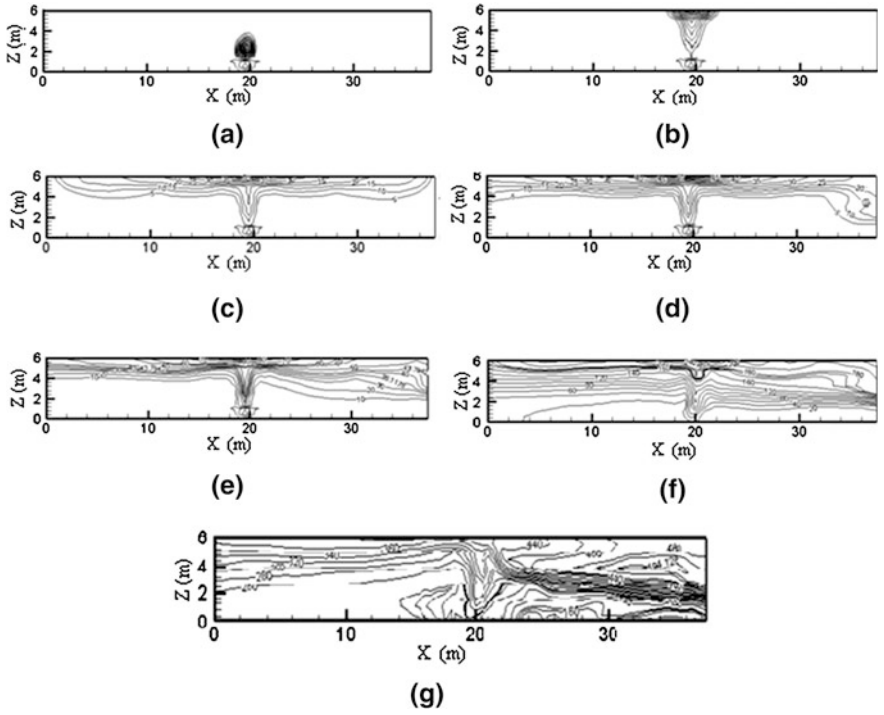

Fig. 4.4 Variations of smoke concentration at the cross-section of $y = 2$ m, when the fire heat release rate is 7.5 MW in subway tunnel. **a** 13 s **b** 18 s **c** 51 s **d** 60 s **e** 81 s **f** 162 s **g** 330 s

the two curves are consistent with each other. However, at the time $t = 1{,}000$ s, the fire was burnt out. And then the temperature of the measuring point above the fire fell sharply. Meanwhile, the residual smoke was not completely cleared. So the temperature is maintained at about 120 °C.

If we recognize that the fire is the center, from Fig. 4.3, we also could see that the temperature of the left side (close to the open end) is a little higher than that of the right side (close to the closed end). The reason is that at the open end, the hot gases keep moving, making the temperature constant renewal. However, at the closed end, the smoke continuously accumulates, making the right side reach saturation. Therefore, the temperature of the right side will not have much change.

4.3.3 Concentration Field

Figure 4.4 is the variations of smoke concentration, when the fire heat release rate is 7.5 MW in subway tunnel. We can see that it only took 18 s for the smoke to reach the ceiling. The hot gases diffuse along the ceiling (51 s). When the hot gases completely cover the ceiling (80 s), the hot layer will begin to subside. Then,

the subway tunnel will be gradually filled up with hot gases from top to bottom. When the fire is in the stable combustion stage (Fig. 4.4g $t = 330$ s), the iso-concentration line is relatively dense at the closed end of the tunnel. That is to say that the smoke concentration is high at the closed end. And the concentrations reach to 320–440 mg/m^3. At the same time, the concentration also reaches to 160 mg/m^3 for the bottom of the closed end.

4.3.4 Velocity Field

The law of the smoke flowing and the distribution of the smoke velocity at the vertical section of $y = 2$ m are investigated in this section.

In the subway tunnel fire, hot gases rise above the fire forming a plume. As the plume rises, the plume will hit the roof and forms collision zone. The plume is limited by the side wall and then diffuses vertically along the subway tunnel. As the plume rises, it entrains air from the tunnel so that the diameter and mass flow rate of the plume increase with elevation. Accordingly, the plume temperature and velocity both decrease with elevation. The fire gases from the plume flow up to the ceiling and form a hot stratified layer under the ceiling. This will form the ceiling jet.

Then, the law of the smoke flowing near the closed end was also investigated in this section. Because the plume was limited by the wall, the hot gases will move back after flow along the wall. And the reversed flow region is called the eddy region. This phenomenon is clearly shown in Fig. 4.5b. The hot gases entrain the

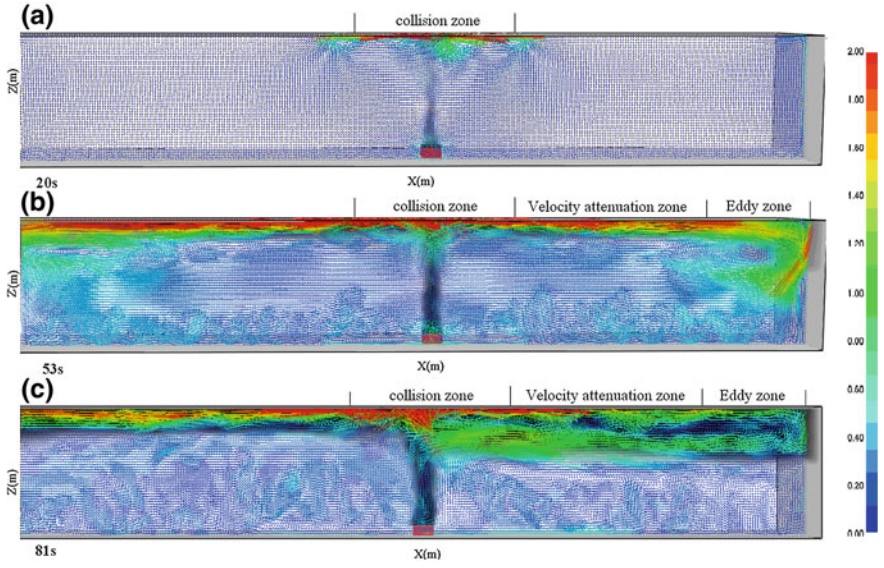

Fig. 4.5 Smoke movement and velocity field **a** 20 s, **b** 53 s, **c** 81 s

cold air from the tunnel. And the velocity of the reversed flow is high. Therefore, an obvious eddy will be produced. Meanwhile, we can see that the smoke velocity close the ground was also increased.

4.4 Conclusions

Smoke movement during a fire in subway tunnel was conducted in this study, when the heat release rate was 7.5 MW. The smoke temperature, smoke concentration and smoke velocity were also analyzed, respectively. And the main conclusions are as follows:

When the heat release rate was 7.5 MW, the progress of the natural smoke filling in subway tunnel fire was simulated in this study. If we recognize that the fire is the center, the temperature of the ceiling jet is almost symmetrically distributed.

When the fire is in the stable combustion stage, the isoconcentration line is relatively dense at the closed end of the tunnel. That is to say that the smoke concentration is high at the closed end.

Because the plume was limited by the wall, the hot gases will move back after flow along the wall. Therefore, an obvious eddy will be produced. Meanwhile, we can see that the smoke velocity close the ground was also increased.

Acknowledgments This research project is sponsored by "13115" Science and Technology Innovation Key Project in Shaanxi Province, "Study on the fire induce smoke transportation, occupant evacuation and engineering practices in huge transit terminal subway station", No. 2009ZDKG-47

References

1. Oka Y, Atkinson GT (1995) Control of smoke flow in tunnel fires. Fire Saf J 25:305–322
2. Wu Y, Bakar MZA (2000) Control of smoke flow in tunnel fires using longitudinal ventilation systems–a study of the critical velocity. Fire Saf J 35:363–390
3. Cha CH, Kim JK (1999) Smoke control in subway tunnels. Korean J Air-Conditioning Refrig Eng 28(6):425–432
4. Kang K (2007) A smoke model and its application for smoke management in an underground mass transit station. Fire Saf J 42:218–231
5. Yuan FD, You SJ (2007) CFD simulation and optimization of the ventilation for subway side-platform. Tunneling Underground Space Technol 22:474–482
6. Park WH, Kim DH, Chang HC (2006) Numerical predictions of smoke movement in a subway station under ventilation. Tunneling Underground Space Technol 21:304
7. Rie D-H, Hwang M-W, Kim S-J, Yoon S-W, Ko J-W, Kim H-Y (2006) A study of optimal vent mode for the smoke control of subway station fire. Tunneling Underground Space Technol 21:300–301

8. McGrattan KB, Forney GP (2006) Fire dynamics simulator (Version 4.07)—user' s guide. NIST Special Publication 1019, National Institute of Standards and Technology, Gaithersburg, MD
9. Friday PA, Mowrer FW (2001) Comparison of FDS model predictions with FM/SNL fire test data. NISTGCR01-810, National Institute of Standards and Technology, Gaithersburg, MD
10. Hu LH, Peng W, Huo R (2008) Critical wind velocity for arresting upwind gas and smoke dispersion induced by near-wall fire in a road tunnel. J Hazard Mater 150:68–75
11. Predvoditelev AS, Pomerantsev AA, Bubnov VA (1972) Heat and mass transfer (Handbook). Energiya, Moscow
12. McGrattan K, Klein B, Floyd J et al (2008) Fire dynamics simulator user's guide. NIST Special Publication, Baltimore, pp 30–56
13. Heskestad Q (1975) Physical modeling of fire. J Fire Flammability 6:253–273

Chapter 5
Heat Transfer Characteristics of Various Plastic–Steel Triple–Glazed Windows

Jianing Zhao, Yi Chen and Bo Sun

Abstract With the increasing demand for energy efficiency, triple-glazed windows are becoming widely used in severe cold regions in China to reduce internal heat loss in winter. There are three combinations of triple glazing and frames: triple glazing sharing one frame; a single-glazed window and a double insulating unit using two separate frames; and three single-glazed windows with three separate frames. There is a need to study the heat transfer characteristics of different types of triple-glazed windows in order to make better use of such units and provide appropriate reference designs. THERM and WINDOW software were used to simulate the total heat transfer coefficient of triple-glazed window units for variations in the number of frames, glass thickness, glazing arrangements, and air chamber width. The results show that the total heat transfer coefficient varies from 1.35 to 1.95 w/m^2; the number of frames has the greatest effect on the heat transfer coefficient and the air chamber width has the least effect.

Keywords Triple-glazed windows · Heat transfer coefficient · Stimulation · Combination between glass and frame

5.1 Introduction

In severe cold regions, heating energy accounts for a large proportion of energy consumption in buildings. The heat transfer performance of the building envelope is the major factor in determining heating energy consumption. As the heat transfer coefficient of windows is much higher than those of the walls and roof, energy consumption was reported to represent more than 50 % of the whole building,

J. Zhao (✉) · Y. Chen · B. Sun
School of Municipal and Environmental Engineering, Harbin Institute of Technology, Harbin, P. R. China
e-mail: zhaojn@hit.edu.cn

A. Li et al. (eds.), *Proceedings of the 8th International Symposium on Heating, Ventilation and Air Conditioning*, Lecture Notes in Electrical Engineering 263,
DOI: 10.1007/978-3-642-39578-9_5,

becoming the bottleneck in improving building insulation [1]. Therefore, the developments of new types of windows as well as studies of the heat transfer characteristics of windows have received much attention nowadays.

Sun Bo [2] established a numerical model to compute the heat transfer characteristics of triple glazing systems and used 2D simulation software THERM to analyze the heat transfer characteristics of dual airflow windows. Fang [3] used CFD to simulate the heat transfer characteristics of various frame materials windows, and used hot-box to verify the simulation results.

In severe cold regions, there is an increasing use of three-layer insulating glass, double or even multilayer window structures. However, previous studies have focused on single-frame insulating windows; therefore, there is limited data on the heat transfer characteristics of different combinations of multilayer glasses and window frames. As a result, there is a lack of design guidance regarding the optimum spacing and glazing sequence of multilayer window units.

The paper examines plastic–steel triple-glazed windows. THERM and WINDOW are used to calculate the heat transfer coefficients of various plastic–steel triple-glazed windows (single-frame, double-frame, and triple-frame window units). Four factors are studied for their effect on the heat transfer coefficient: number of frames, glass thickness, glazing arrangement (the sequence of panes used in each glazing unit) and air chamber width. The results will provide reference data for the design of multilayer window units and optimization of insulation properties.

5.2 Methods

Theoretical calculation is used to obtain the heat transfer coefficient for different forms of plastic–steel triple-glazed windows.

5.2.1 Calculation Method

The present study uses the ASHRAE method [4] of calculating the window heat transfer coefficient, which is widely used all over the world. In the ASHRAE method, spacer bars between window panes have effect on both the frames and the region of glass close to the frames. The glass area close to the frame is called the *edge-of-glass* and is defined as a 63.5-mm-wide perimeter region extending to the boundary between the glass and the frame. The remaining part of the glass is called *center-of-glass*. Therefore, calculation of the heat transfer coefficient for the whole window can be divided into three areas: frame, edge-of-glass, and central glass. Finally, the heat transfer coefficient for the entire window can be calculated by area-weighted average, as shown in Eq. (5.1).

$$U_{W,\mathrm{ASHRAE}} = \frac{U_g A_c + \sum U_{\mathrm{fr}} A_f + \sum U_{\mathrm{eg}} A_{\mathrm{eg}}}{A_t} \tag{5.1}$$

Here, U_g is the heat transfer coefficient of central glass (W/m^2·K); U_{fr} is the heat transfer coefficient of frame (W/m^2·K); U_{eg} is the heat transfer coefficient of edge-of-glass (W/m^2·K); A_c is central glass area (m^2); A_f is frame area (m^2); A_{eg} is the edge-of-glass area (m^2); and A_t is the total area of the window (m^2).

The frame is divided into the top border, bottom border, and side border. The edge-of-glass is divided into the upper edge, lower edge, and side edge. In this study, WINDOW software, which is based on the lumped parameter method, is used to model the central glass area, and THERM software, which is based on the finite element method, is used to model the edge-of-glass and the frame. The various parts of the window area ratio are computed according to Building Standard Design Atlas.

Six kinds of commonly used plastic–steel windows of different sizes and structures [5] were used to calculate area ratio (frames, edge area, and central area). From the results, frame area ratio is 19.44–38.49 %, the central glass area ratio is 38–58.53 %, and the edge area is 14.54–31.03 %.

The plastic–steel triple-glazed window types examined in this study comprise single-frame (type A), double-frame (type B), and triple-frame (type C). The double-frame window type includes (B1), with a double insulating glass window facing the exterior and a single interior pane, and the opposite arrangement (B2), as shown in Figure 5.1.

5.2.2 Determination of Basic Parameters

This study examined the number of frames, glass thickness, position and arrangement of each window, and air chamber width as influencing factors. Constraint factors include frame material, the structure and size of the window, and the air gap thickness of insulating glass. There is a need to determine the constraint factors and magnitudes of the four influence factors.

This study utilized plastic–steel windows, which are currently used in most cold regions. The heat transfer coefficients of 70-mm casement profiles with dual-chamber and triple-chamber window frames are 2.058 and 1.653 W/m^2·K, respectively [6]. The range of heat transfer coefficients for PVC plastic–steel

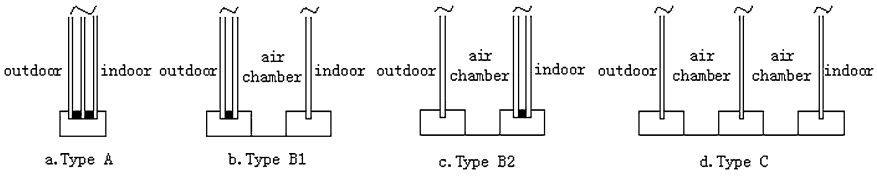

Fig. 5.1 Different forms of triple-glazed window

Table 5.1 Value Levels of influencing factors

No.	1	2	3		4
Level	Frame number	Glass thickness (mm)	Air chamber width (mm)		Glazing arrangement *
			double-frame	triple-frame	
1	1	3	100	50	1
2	2	6	150	75	2
3	3	–	200	100	–
4	–	–	250	125	–
5	–	–	300	150	–

*Glazing arrangement is only for type B: 1 represents B1, 2 represents B2

windows given in Residential Energy Conservation is 2.0–2.8 W/m^2·K [7]. This study therefore used a compromise value of 2.2 W/m^2·K as the heat transfer coefficient of the plastic–steel frame. Previous research on insulating glass reported that the energy-saving effect was greatest for units with an air gap of 12 mm [8].

From above, the constraint conditions were as follows: plastic–steel frame material, 12 mm air gap thickness of insulating glass, and 6 kinds of commonly used window statistical results.

Four thicknesses of window glass are specified in civil construction: 3, 4, 5 and 6 mm. But 3 mm single glass window cannot meet the required strength and insulation criteria in severe cold regions. We selected two extreme levels: 3, and 6, and 3 mm cannot be used as a single-glazed window.

When considering the size of the air chamber width, it is necessary to consider the max available width. According to the survey, 49 mm brick wall is usually used in cold regions. Considering the installation space, the max available width for window is 300 mm and the min width is 100 mm.

The value levels of influencing factors are shown in Table 5.1. Based on Table 5.1, different forms of triple-glazed windows can be classified, as shown in Table 5.2.

From Table 5.2, there are five air chamber levels in types B and C, but no chamber in type A. The number of simulations is A + (B × 5) + (C × 5), giving 27.

5.2.3 Boundary Conditions

It is necessary to define a standard indoor and outdoor environment when designing or evaluating the heat transfer performance of windows. The *Building Fenestration Thermal Calculation Procedures (JCJ/T15)* provides boundary conditions for windows in China. The specific values are listed in Table 5.3.

Indoor and outdoor integrated surface heat transfer coefficients (h_{in}/h_{out}) refer to the convective heat transfer coefficient ($h_{c.in}$/$h_{c.out}$) and radiation heat transfer coefficient ($h_{r.in}$/$h_{r.out}$), respectively.

If indoor and outdoor glass is ordinary float glass, the hemisphere emissivity of the glass surface is 0.837; surface emissivity of the frame material is 0.9; the

Table 5.2 Classification of triple-glazed windows

Type		Form	Explanation
A	A1	3 + 12 + 3 + 12 + 3	3-mm glass and 12-mm air gap
	A2	6 + 12 + 6 + 12 + 6	6-mm glass and 12-mm air gap
B	B11	3 + 12 + 3/6	Outer: 3 mm glass, 12 mm air gap; inside: 6 mm glass
	B12	6 + 12 + 6/6	Outer: 6 mm glass, 12 mm air gap; inside: 6 mm glass
	B21	6/3 + 12 + 3	Outer: 6 mm glass; inside: 3 mm glass, 12 mm air gap
	B22	6/6 + 12 + 6	Outer: 6 mm glass; inside: 6 mm glass, 12 mm air gap
C	C1	6/6/6	Triple-frame window with glass thickness 6 mm

Table 5.3 Standard environmental parameters for calculation

Location	Convective heat transfer coefficient ($W/m^2 \cdot K$)			Temperature
	Central glass	Edge-of-glass	Frame	°C
Outdoor	16	12	8	−20
Indoor		3.6		20

Table 5.4 Heat transfer coefficient of different areas of window($W/m^2 \cdot K$)

Name of area	Outdoor		Indoor		Outdoor integrated	Indoor integrated
	$h_{c,out}$	$h_{r,out}$	$h_{c,in}$	$h_{r,in}$	h_{out}	h_{in}
Central glass	16	3.9	3.6	4.0	19.9	7.6
Edge-of-glass	12	3.9	3.6	4.0	15.9	7.6
Frame	8	4.2	3.6	4.3	12.2	7.9

average emissivity of indoor environment material is 0.9. Calculate according to the Eqs. (2.2) to (2.5) in the Ref. [2].The surface heat transfer coefficient of the central glass, edge-of-glass, and frame are shown in Table 5.4.

5.3 Results and Discussion

The study examined 27 simulations for 6 common window types, giving a dataset of 162 results. As an example, a part of results are shown in Table 5.5.

5.3.1 Calculation Results

5.3.2 Discussion of Results

As shown in Table 5.5, the heat transfer coefficient of single-frame windows ranges from 1.84 to 1.95 $W/m^2 \cdot K$; that of double-frame windows ranges from 1.38 to 1.68 $W/m^2 \cdot K$; and that of triple-frame windows ranges from 1.35 to 1.54 $W/m^2 \cdot K$.

Table 5.5 Heat transfer coefficient of plastic–steel triple-glazed window

Type		Air chamber width (mm)	Heat transfer coefficient(W/m^2·K)					
			Frame ratio 19.4 %	Frame ratio 21.0 %	Frame ratio 25.9 %	Frame ratio 29.2 %	Frame ratio 29.6 %	Frame ratio 38.5 %
A	A1	–	1.851	1.860	1.885	1.896	1.899	1.949
	A2	–	1.836	1.846	1.871	1.886	1.889	1.942
B	B11	100	1.587	1.573	1.527	1.510	1.506	1.422
		300	1.568	1.554	1.509	1.482	1.478	1.400
	B21	100	1.679	1.671	1.669	1.641	1.640	1.621
		300	1.665	1.659	1.661	1.621	1.620	1.612
	B12	100	1.570	1.556	1.511	1.493	1.488	1.407
		300	1.551	1.538	1.494	1.465	1.461	1.385
	B22	100	1.643	1.635	1.625	1.596	1.594	1.564
		300	1.629	1.621	1.615	1.575	1.573	1.553
C	C1	50	2.376	2.350	2.288	2.232	2.225	2.096
		150	2.357	2.333	2.278	2.204	2.197	2.089

Therefore, the heat transfer coefficient for plastic–steel triple-glazed windows ranges from 1.35 to 1.95 W/m^2·K. According to the Chinese 65 % energy efficiency standards in cold regions, the heat transfer coefficient of exterior windows must be less than 2.0 W/m^2·K. The results indicate that plastic–steel triple-glazed windows can meet energy efficiency standards when installed in cold regions of China.

Figure 5.2 shows the heat transfer coefficient of the window with changes in air chamber width for a frame ratio of 25.93 %. As seen from Fig. 5.2, air chamber width has little effect on the heat transfer coefficient.

It is necessary to analyze the heat transfer process of the window to explain why air chamber width has little influence on the heat transfer coefficient. The composite heat transfer coefficient between two adjacent layers of a window comprises the radiation and convective heat transfer coefficient, in addition to the thermal

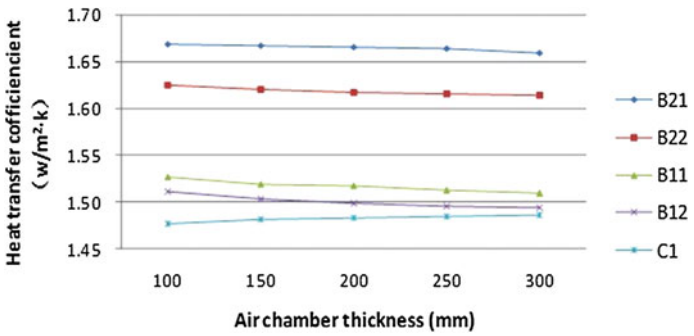

Fig. 5.2 Heat transfer coefficient with changes of air chamber thickness

conductivity. When the air gap is narrow, heat transfer mainly occurs via conduction. But when the air chamber is increased beyond a certain extent (> 30 mm), heat transfer mainly occurs via convection, and conduction can be ignored. It is equivalent to that of natural convection within infinite space, so heat transfer remains the same. The average surface temperature of both glazing panes is unchanged, so the radiation remains constant. Therefore, the heat transfer coefficient remains almost unchanged when the air chamber width increases.

Figure 5.3 shows the heat transfer coefficient of different forms of triple-glazed windows with changes in frame ratio. The heat transfer coefficient of the double- and triple-frame windows decreases when the frame ratio increases, whereas the heat transfer coefficient of the single-frame window increases when the frame ratio increases. This is due to the low heat transfer coefficient of the plastic–steel frame, which has greater insulation performance than the double insulating glass. With the use of an additional frame, the heat transfer coefficients of both the frame and the edge-of-glass will decrease. However, for the single-frame glass window, the heat transfer coefficient of the frame is greater than that of the triple insulating glass, so an increase in the frame ratio will lead to higher heat transfer coefficient.

In Fig. 5.3, we can also obtain the heat transfer coefficient of B1 is smaller than B2, indicating better insulation performance. To explain it, we need to analyze the heat transfer process in the air chamber. Table 5.6 lists the air parameters of four B-type windows when chamber thickness is 100 mm. As seen from Table 5.6, when the double-frame window is arranged as B1, the average temperature T_0 in the air chamber is about 10 °C, higher than arranged as B2, leading to a change in the air physical properties and the convection intensity. The result for *Gr*, which measures natural convection intensity, is nearly 30 % higher in B2 than in B1; the average convection heat transfer coefficient *h* is also greater in B2, leading to lower total thermal resistance. So the B1 arrangement achieves superior insulation performance to B2.

To analyze how big the influence will bring to heat transfer coefficient by each influencing factor, we should classify seven forms of windows as in Table 5.7 and

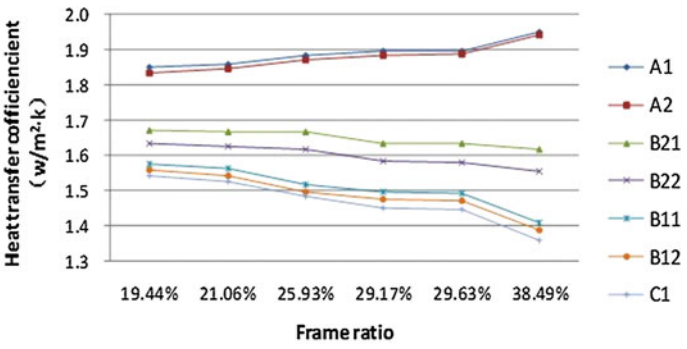

Fig. 5.3 Heat transfer coefficient with changes in frame ratio

Table 5.6 Air parameters of four B-type windows

Type	Average temperature on both sides (°C)		Air parameters in chamber			
	Side 1	Side 2	Nu	T_0	Gr(10^6)	h
B21	−14.7	−2.7	12.18	−8.7	2.82	2.9
B11	−2.2	9.2	11.39	3.5	2.18	2.8
B22	−14.8	−3.0	12.13	−8.9	2.79	2.9
B12	−1.8	9.4	11.28	3.8	2.15	2.8

Table 5.7 Classification results of factor analysis

Glass thickness		Glazing arrangement		Frame number	
Reference	Comparison	Reference	Comparison	Reference	Comparison
A1	A2	B21	B11	A2	B12
B11	B12	B22	B12	C1	B12
B21	B22	–	–	A2	B22
–	–	–	–	C1	B22

Table 5.8 Calculation results of factor analysis

Influencing factor	Heat transfer coefficient differential value (W/m^2·K)	Change of factor
Air chamber width	0.009–0.029	100–300 mm
Glass thickness	0.007–0.064	3–6 mm
Glazing arrangements	0.073–0.212	–
Frame number	0.007–0.558	Add one frame

calculate the heat transfer coefficient differential between comparison and reference types according to Table 5.5. The calculation results are shown in Table 5.8.

As seen from Table 5.8, the four factors that affect the heat transfer coefficient of triple-glazed windows are found to be as follows: number of frames > glazing arrangement > glass thickness > air chamber width.

5.4 Conclusion

The following conclusions are drawn from the study.

1. The heat transfer coefficient of a plastic–steel triple-glazed window ranges from 1.35 to 1.95 W/m^2·K, and can meet the Chinese 65 % energy efficiency standards in cold regions.
2. For double- and triple-frame windows, air chamber width has little effect on the heat transfer coefficient; the heat transfer coefficient reduces by 0.009 ∼ 0.029 W/m^2·K when the air chamber width varies from 100 to 300 mm. Therefore, designer needs to be more focused on the actual needs and stability of the structure when designing or installing windows;

3. The heat transfer coefficient of a triple-glazed window reduces by 0.007 ~ 0.064 W/m^2·K when glass thickness increases from 3 to 6 mm.
4. For the double-frame structure combining a single- and double-insulating window, insulation performance improves with the single-glazed window on the interior and the double insulating window on the exterior; the heat transfer coefficient reduces by 0.073 ~ 0.212 W/m^2·K.
5. For the plastic–steel triple-glazed windows tested in the present study, the insulation performance follows the sequence: triple frame > double frame > single frame. The heat transfer coefficient reduces by 0.007 ~ 0.558 W/m^2·K when add a frame.
6. The four factors that affect the heat transfer coefficient of triple-glazed windows follow the sequence: number of frames > glazing arrangement > glass thickness > air chamber width.

Acknowledgments This work was supported by the Ministry of Science and Technology of China via the 12th Five-Year Supporting Plan of the National Science and Technology Supporting Project, "The village building heating and indoor environmental security integration technology and engineering demonstration."

References

1. Zou H, Wang G (2009) Window's thermal performance analysis of building energy consumption in cold regions. Acad Press Shenyang Archit Univ 25(5):982–986 (in Chinese)
2. Sun B (2011) Heat transfer performances of dual airflow window. Dissertation for the Doctoral Degree. Harbin Institute of Technology (in Chinese)
3. Fang Y, Eames PC, Hyde TJ, Norton B (2005) Complex multimaterial insulating frames for windows with evacuated glazing. Sol Energy 79:245–261
4. Standard ASHRAE (1998) Standard method for determining and expressing the heat transfer and total optical properties of fenestration products, Public Review Draft of Standard 142P. American Society of Heating, Refrigerating and Air Conditioning Engineers
5. 05 Series Building Standard Design Atlas. Commonly Used Windows and Doors. DBJT03-22-2005, 05J4-1 (in Chinese)
6. Wang L (2008) Energy-saving design of the exterior windows of residential buildings in northern cold regions. Dissertation for Master's Degree, Tianjin University (in Chinese)
7. Jiang Y, Lin B (2006) Residential energy conservation. China Architecture and Building Press (in Chinese)
8. Ma Y, Deng S, Wu P (2007) Thermal performance of insulating glass windows. In: Nationwide Building Environment and Energy Conservation Conference 2007, Chengdu

Chapter 6
Simulation and Energy Economic Analysis of an Air-Conditioning System with Energy Recovery Ventilator in Summer

Li Li, Yaping Li, Qingling Zhang and Qiuhua Tao

Abstract The energy recovery ventilator (ERV) is an important equipment for indoor air conditioning, where outdoor fresh air is pre-cooled when passing through the heat reclamation equipment in summer. The building energy-consuming simulation software eQUEST is used to analyze the load change of a building in Xiamen. For the commercial building of 6,912 m^2, the air-conditioning system with ERV has an electric power saving of 13,298 kW·h in July and 12,927 kW·h in August, and then about 8,205 Yuan can be saved in July and 7,976 Yuan can be saved in August. When ERV fan power consumption is considered, the electric power saving is 3,680 kW·h in July and 3,312 kW·h in August. Comprehensive comparison shows that, installation of ERV for an air-conditioning system is more economical by recovering additional cooling energy.

Keywords Energy recovery ventilator · Energy saving · Air quality · Simulation

L. Li (✉) · Y. Li · Q. Zhang · Q. Tao
Jimei University, Xiamen, 361021 Fujian, China
e-mail: lilijmdx@163.com

Y. Li
e-mail: lyp199028@live.cn

Q. Zhang
e-mail: 06zhangqingling@163.com

Q. Tao
e-mail: ttaojiangshui@163.com

L. Li
Cleaning Combustion and Energy Utilization Research Center of Fujian Province, 361021 Xiamen, China

A. Li et al. (eds.), *Proceedings of the 8th International Symposium on Heating, Ventilation and Air Conditioning*, Lecture Notes in Electrical Engineering 263,
DOI: 10.1007/978-3-642-39578-9_6,

6.1 Introduction

For the building with air conditioning, in order to keep the appearance of the building and reduce the energy consumption, the designers and the operators of the air-conditioning system always tend to reduce the volume of the outdoor fresh air provided, which definitely arouses uncomfortable feeling of the indoor persons. From the year 1971 to 1987, 346 sites were measured by the NIOSH, with the results indicating that the reason of the low quality of the indoor air is the lack of outdoor fresh air and the poor ventilation. From then on, the problem of fresh air has drawn the attention of the building and conditioning areas [1]. In 1980, World Health Organization formally named such diseases due to lack of fresh air as "Sick Building Syndrome," so-called "Air-conditioning disease". In 1989, ANSI/ASHRAE 62-1989 formally defined the "acceptable indoor air quality," and set the minimum volume of the fresh air. On 15 November 1990, U.S. Congress passed the Law of Air Purify. Because of this law, the IAQ and fresh air supply become the issue that the architects and the air-conditioning system designers should consider, and meanwhile, the supply of the outdoor fresh air and the building energy-saving are a pair of contradictions [2–5], so an energy-saving outdoor fresh air system and device become a common problem that the designers and users all take into account.

The appearance of the ERV can help solve this problem. In ERV, energy transfers between the outdoor air and the indoor exhaust air. In summer, the indoor air pre-cools the outdoor fresh air, and in winter, the indoor air pre-heats the outdoor air, and thus, the load of the fresh air can be reduced to make a lower energy consumption and then to reach the target of energy-saving and solve the contradiction [6–9].

6.2 Related Meteorological Parameters

The building is located in Xiamen, 118.06°E, 24.45°N, belonging to the subtropical region. The detailed meteorological parameters are listed in Table 6.1 and the indoor design parameters are set, as shown in Table 6.2.

Table 6.1 The outdoor meteorological parameters in Xiamen

Summer atmospheric pressure (hPa)	999.10
Summer outdoor daily average temperature (°C)	29.90
Summer outdoor dry bulb temperature (°C)	33.40
Summer outdoor wet bulb temperature (°C)	27.60
The hottest month average relative humidity (%)	81.00
Winter atmospheric pressure (hPa)	1,013.80
Winter air-conditioning calculated temperature (°C)	6.00
Winter relative humidity of the outdoor air (%)	73.00
Outdoor mean wind speed (m/s)	3.00

Table 6.2 The indoor design parameters

	Temperature (°C)	Relative humidity (%)	Max wind speed (m/s)	Minimum fresh air volume (m^3/h·p)
Mall	28 ± 2	60 ± 10	0.25	8.5
Guest room	27 ± 1	60 ± 10	0.25	30

6.3 Simulation and Analysis of the ERV Used in the Building

6.3.1 Simulation

The building energy-consuming simulation software eQUEST is used to describe the load changes in the building. First, the basic model of the building is built according to the CAD figure of it, and then, the climate data are introduced to the software. After setting the calculation parameters, the load changes throughout the whole year can be obtained. The parameters used in our calculation are listed in Table 6.3 and the three-dimensional figure of the building is shown in Fig. 6.2. The load changes throughout the whole year are shown in Fig. 6.3, from which we can know the load change under Xiamen's meteorological conditions. From the hour–hour simulation of the building load, we can know that the maximum cooling load of this building in summer is 1,242 kW, which appears in the 4,582nd hour, 9:00 pm in July 10 (Fig. 6.1).

Table 6.3 The U-value of the building envelop (W/m^2·K)

Name of the envelop	External wall	External window	Roof
U-value	1.32	1.66	1.06

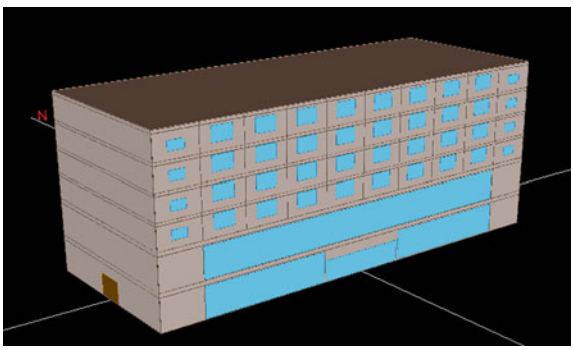

Fig. 6.1 The 3D figure of the typical building

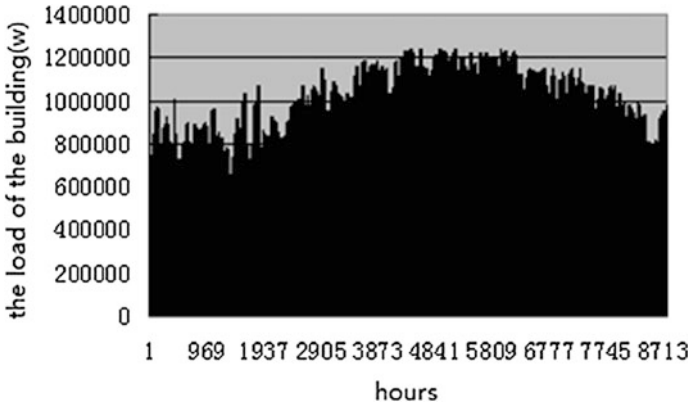

Fig. 6.2 The load changes of a building in Xiamen throughout the whole year

6.3.2 *Calculation and Analysis of the Energy-Saving Effect of ERV*

The building has six stories. The first and the second stories are commercial malls, with each area of 1,152 m^2. Assuming that the occupant density in each storey is 0.8 person/m^2, and the fresh air for each person is 8.5 m^3/(h·p), the volume of fresh air that each storey needed is calculated to be 7,833.6 m^3/h. According to the calculated volume of outdoor air, and referring to the product catalogue of the fresh air ventilation equipment of an air-conditioning company, four KRV-40Ds, two for each storey, are selected. Table 6.4 shows the detailed parameters.

The stories from third to sixth are hotel, with 28 guest rooms in each storey. Assuming that there are two people in each room, and the volume of the fresh air for each person is 30 m^3/h, then the total volume of fresh air needed in each storey is 1,680 m^3/h, According to the calculated volume of outdoor air, and referring to product catalogue of fresh air ventilation equipment, four KRV-20Ds, one for each storey, are selected, with the detailed parameters shown in Table 6.4.

The total cooling load of the building is 1,242 kW. The water-cooled screw chillers are selected, with the EER of 4.60. In Fig. 6.3, the typical hour (July 10) is analyzed, with energy-saving effect listed below (Table 6.5).

Table 6.4 The detailed parameters of KRV-40D and KRV-20D

Type	Rated air flow (m^3/h)	Motor power (kW)	Equipment enthalpy exchange efficiency (%)
KRV-40D	4,000	2.25	60
KRV-20D	2,000	0.98	59

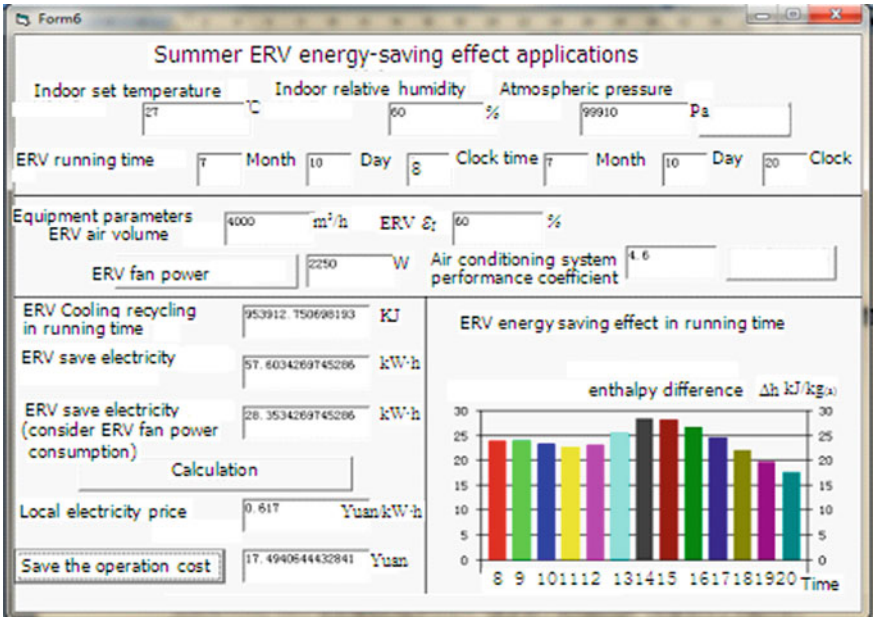

Fig. 6.3 The energy-saving effect of a KRV-40D (the operation time is 8:00–20:00)

Table 6.5 The energy-saving effect of the energy recovery ventilator

Type	Number	Cooling recovery (kJ)	Total cooling recovery (kJ)	Total electric power saving (kW·h)
KRV-40D	4	49,586 per unit	198,344	2.8
KRV-20D	4	24,379 per unit	97,516	2.0

In this hour, 295,860 kJ cooling is recovered by the energy recovery ventilator, and the total electric power saving is 4.8 kW·h. Supposing that the electricity price of Xiamen is 0.617 Yuan/(kW·h), then during this hour, 2.96 Yuan is saved.

The energy saving on July 10 is analyzed, with the result shown in Figs. 6.3 and 6.4. After running the ERV, the energy-saving effect on 10 July is listed in Table 6.6. Assuming the price of electricity in Xiamen is 0.617 Yuan/(kW·h), then after one day's operation, 120.68 Yuan will be saved. Similarly, we used this computer program to analyze the energy-saving effect in July, with the results listed in Table 6.7.

The air-conditioning system with ERV has an electric power saving of 13,298 kW·h in July, and the electric power saving is 3,680 kW·h when ERV fan power consumption is considered. When local electricity price is 0.617 Yuan/(kW·h), 8,205 Yuan can be saved. After one month's (July) operation, 2,271 Yuan will be saved when ERV fan power consumption is considered. Similarly, we used this program to analyze the energy-saving effect in August, with the results listed in Table 6.8.

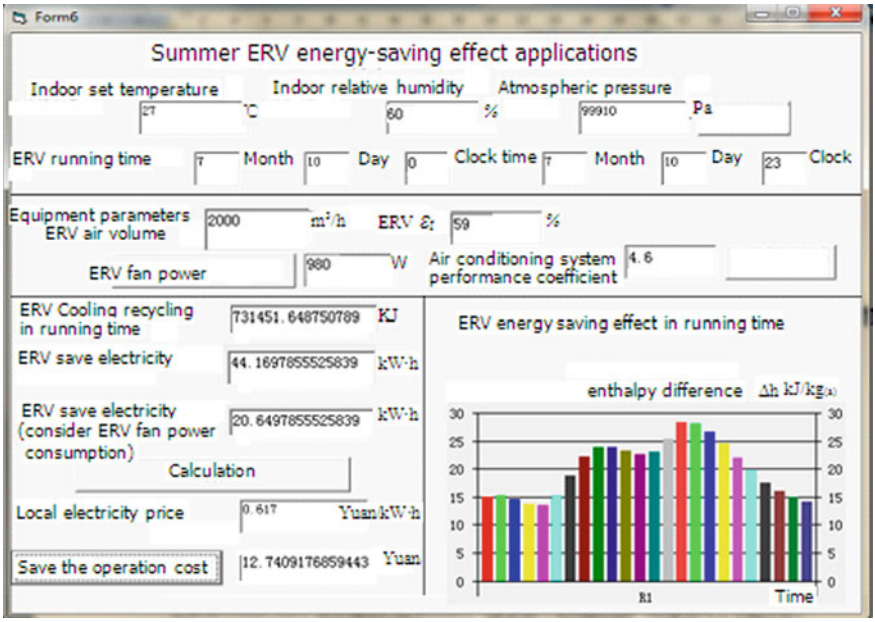

Fig. 6.4 The energy-saving effect of each KRV-20D (the operation time is 0:00–23:00)

Table 6.6 The energy-saving effect of the ERV on July 10

Type	Number	Cooling recovery (kJ)	Total cooling recovery (kJ)	Total electric power saving (kW·h)
KRV-40D	4	953,912 per unit	3,815,648	113.2
KRV-20D	4	731,451 per unit	2,925,804	82.4

Table 6.7 The energy-saving effect of the ERV in July

Type	Number	Cooling recovery (kJ)	Total cooling recovery (kJ)	Total electric power saving (kW·h)
KRV-40D	4	36,908,916 per unit	147,635,664	8,915/2,216
KRV-20D	4	18,146,884 per unit	72,587,536	4,383/1,464

Table 6.8 The energy-saving effect of the ERV in August

Type	Number	Cooling recovery (kJ)	Total cooling recovery (kJ)	Total electric power saving (kW·h)
KRV-40D	4	35,879,247 per unit	143,516,988	8,666/1,968
KRV-20D	4	17,640,630 per unit	70,562,520	4,261/1,344

The air-conditioning system with ERV has an electric power saving of 12,927 kW·h in August, and 7,976 Yuan can be saved. When ERV fan power consumption is considered, the electric power saving is 3,312 kW·h, and 2,043 Yuan can be saved after one month's (August) operation. Ventilation function is mainly for winter and transition seasons in Xiamen, not for heat recovery. Because Xiamen is the air region with hot summer and warm winter, it is considered that air-conditioning systems run in summer only. On the one hand, ERVs supply fresh air for the building, and on the other hand, recycled exhaust air provides cooling energy for energy saving.

6.4 Conclusion

The building energy-consuming simulation software eQUEST is used to analyze the load change of a building located in Xiamen, and the computer language Visual Basic is used to calculate and analyze the energy-saving effect of using ERV. The results for a commercial building with area of 6,912 m^2 shows that, the air-conditioning system with ERV has an electric power saving of 13,298 kW·h in July and 12,927 kW·h in August. When local electricity price is 0.617 Yuan/(kW·h), 8,205 Yuan can be saved in July and 7,976 Yuan can be saved in August. When ERV fan power consumption is considered, the electric power saving is 3,680 kW·h and 2,271 Yuan can be saved in July, and the electric power saving is 3,312 kW·h and 2,043 Yuan can be saved in August. So, using ERV in the buildings of Xiamen has a great energy-saving and economic effect.

For an air-conditioning system, the cost of installing an ERV and that of installing a fresh air unit and exhaust system are nearly the same, but ERV has the advantage of recovering additional cooling energy. Comprehensive comparison shows that the system with ERV is more economical.

Acknowledgments This work was supported by the Xiamen Science Technology Foundation (3502Z20103022) and Fujian technology innovation platform project (2009H2006).

References

1. ASHRAE (1992) ANSI/ASHRAE Standard 55-1992, thermal environmental conditions for human occupancy, Atlanta: American society of heating, refrigerating, and air-conditioning engineers, Inc
2. Fauchoux MT, Simonson CJ, Torvi DA (2007) The effect of energy recovery on perceived air quality, energy consumption, and the economics of an office building. ASHRAE Trans 113(2):437–449
3. EIA (2003) Commercial building energy consumption survey, energy information administration. U.S. Department of Energy
4. Li JR, Yang L (2008) Numerical simulation of fresh air exchanger effecting IAQ. Fluid Mach 36(7):29–33

5. Liu CW (2005) The influence of the outdoor air volume, quality and treatment for indoor air quality. J Electric Power 20(3):227–229, 232
6. Besant RW, Simonson CJ (2000) Air-to-air energy recovery. ASHRAE J 42(5):31–38
7. Besant RW, Simonson CJ (2003) Air-to-air exchangers. ASHRAE J 45(4):42–52
8. Brandemuehl MJ, Braun JE (1999) The impact of demand-controlled ventilation strategies on energy use in buildings. ASHRAE Trans 105(2):39–50
9. Rasouli M, Simonson CJ, Besant RW (2010) Applicability and optimum control strategy of energy recovery ventilators in different climatic conditions. Energy Build 42(9):1376–1385

Chapter 7
Analysis of Heat Transfer by Pile and Borehole Ground Heat Exchangers: Composite-Medium Line-Source Approach

Min Li and Yi Yang

Abstract Heat transfer by pile and borehole ground heat exchangers (GHEs) involves transient heat conduction in composite media together with complex geometry arrangements. This paper develops a composite-medium line-source approach to analyzing thermal responses of pile and borehole GHEs. The central idea of applying this new approach is that the downward and upward channels of U-shaped tubes (not the borehole) are approximated as line sources of heat placed in a composite medium. By the new method, effects of both heat capacity of grout/concrete and the difference between properties of soil and piles/grout on heat transfer can be fully addressed. More importantly, this approach is enough general and flexible to model various configurations of ground loops, including single and double U-shaped tubes, W-shaped channels, spiral-coils, etc. Therefore, the method developed here may contribute to providing a viable approach to modeling transient thermal processes of vertical GHEs.

Keywords Ground heat exchanger · Short-time response · Composite-medium line-source model · Ground-coupled heat pump

7.1 Introduction

Analysis of heat transfer by borehole and pile ground heat exchangers (GHEs) forms the theoretical basis for design, analysis, and simulation of GHEs and ground-coupled heat pumps (GCHPs) [1–4]. A borehole GHE is a vertically buried

M. Li (✉)
Central South University, 410083 Changsha, Hunan, China
e-mail: cnlimin@csu.edu.cn; minli.csu@gmail.com

Y. Yang
Guangdong Ocean University, 524088 Zhanjiang, Guangdong, China

A. Li et al. (eds.), *Proceedings of the 8th International Symposium on Heating, Ventilation and Air Conditioning*, Lecture Notes in Electrical Engineering 263,
DOI: 10.1007/978-3-642-39578-9_7,

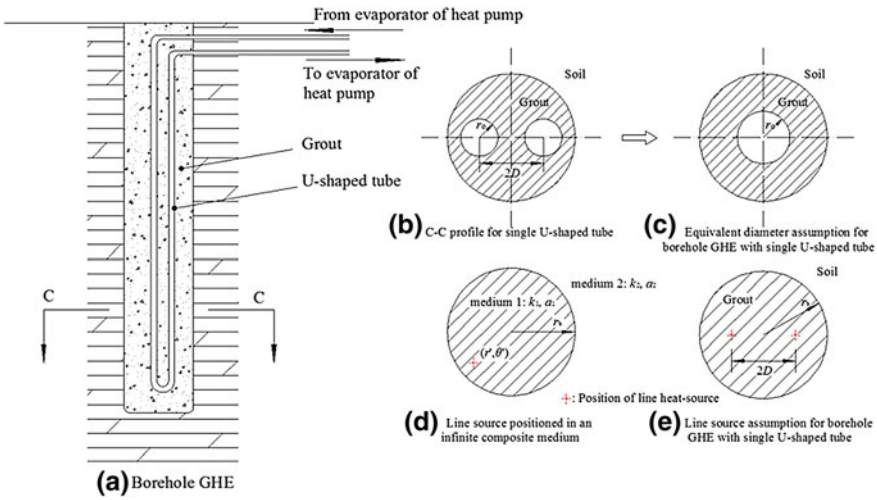

Fig. 7.1 Schematic layout of borehole GHE with a single U-shaped tube

duct or channel whereby heat-carrying fluid, with or without antifreeze, is circulated for exchanging heat between the fluid and the ground (Fig. 7.1a and b). In pile GHEs (i.e., energy piles), heat transfer tubes are arranged near the steel frame of building foundation piles in various forms (Fig. 7.2). Since energy piles can reduce the costs of boring and required land area, this technology has evoked increasing interest in research community [5, 6].

However, heat transfer analysis of GHEs remains a great challenge because of involvement with transient heat conduction in composite media, together with intricate geometric forms. A great number of studies have been performed to resolve this difficult task in analytical or numerical ways. This work tends to focus on analytical methods rather than on numerical ones; therefore, only analytical work is reviewed here. A traditional way of analyzing heat transfer of borehole GHEs is to decompose the thermal process into a steady and an unsteady part. Heat conduction in the bore is generally assumed to be steady state due to small dimensions and heat capacity compared with those outside the borehole. Heat transfer models for this steady process include two- and quasi-three-dimensional models [7]. It is worth noting that these models depend on solutions to steady heat conduction in composite media. As shown later, this paper constructs a model based on solutions to unsteady heat conduction in composite media.

Recently, many researchers have focused their attention on short-time responses of GHEs [1–4, 8–10]. Small-time responses of GHEs involve transient processes within boreholes, thus the above steady assumption is unsuitable for this purpose. To the best of the author's knowledge, most analytical models for short-time behaviors of borehole GHEs exclusively use the equivalent-diameter assumption [2, 9, 10], an assumption that reduces the original problem to a transient heat conduction in a finite or infinite hollow cylindrical composite region

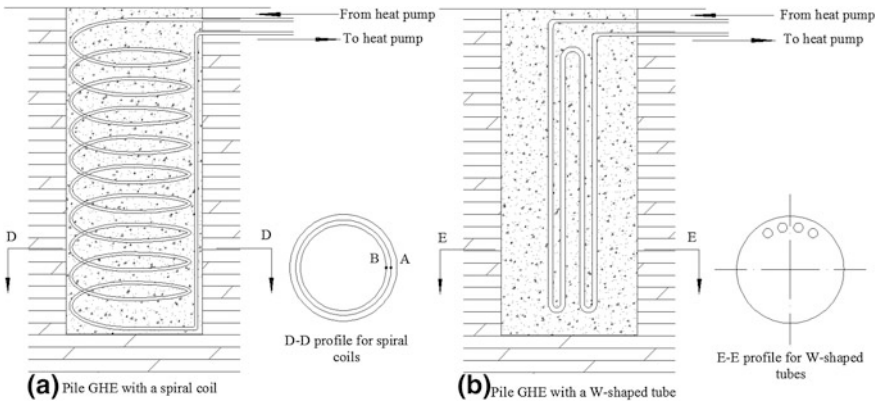

Fig. 7.2 Schematic layout of energy piles with (**a**) a spiral coil and (**b**) a W-shaped tube

(Fig. 7.1c). The equivalent diameter approach is an empirical method and cannot treat GHEs with heat transfer channels of other forms, for example, a pile GHE with W-shaped or spiral-shaped tubes.

Several studies have attempted to analytically model thermal responses of energy piles. Most of them used the common heat-source theory, ignoring the difference between properties of soil and foundation piles. For instance, spiral line source [5] and ring coil source models [6] have been proposed for pile GHEs with spiral coils. Soil composition varies widely not only with locations but also with moisture content; heat conduction associated with an energy pile occurs in a composite medium. This property difference cannot be treated by the common heat-source theory.

There are two knowledge gaps that need to be filled in the field of modeling heat transfer of pile and borehole GHEs. The first is that no satisfactory analytical solution is available for modeling the short-term unsteady behaviors of borehole GHEs. The second gap is that no analytical model can explicitly consider the influence of the difference between properties of soil and piles or grouting materials.

This paper aims to fill these two gaps by introducing the line-source theory for composite media to GCHP applications based on our previous work (see [1, 4]). The advantages of this theory are that it can be used to analyze transient heat conduction inside and outside boreholes, and it includes the effect of the difference between properties of soil and piles/grout. Further, it is flexible enough to model many configurations of heat transfer tubes, including single and double U-shaped tubes, W-shaped tubes and spiral coils.

7.2 Composite-Medium Line-Source Model

It should be noted that the medium form shown in Fig. 7.1d resemble exactly those occurring in GHEs as the grouting material inside the borehole differs from the surrounding soil or rocks (Fig. 7.1b), and the material of foundation piles is also different from the soil or rocks (Fig. 7.2); thus, they are all the cylindrical composite medium. This section presents an analytical solution for a line source of heat placed in such a medium (Fig. 7.1d), which can serve a potential better way of modeling heat transfer by GHEs than the common line-source solutions.

7.2.1 Infinite Composite-Medium Line-Source Solution

Figure 7.1d shows that an infinite line source of heat is placed in an infinite composite cylinder, of which region $r < r_b$ is of one medium (k_1, a_1, ρ_1, and c_1) and region $r > r_b$ of another (k_2, a_2, ρ_2, and c_2). The line source is parallel to the height direction, z-axis, and is positioned through a point (r', θ'). Initially, the temperatures of the medium are zero. If the infinite line source continuously releases heat into the composite solid from zero time at a rate of q_l (W/m), the temperature responses in the composite medium can be obtained by the method of heat sources. Since the mathematical details of the derivation are somewhat complicated; thus, they are ignored here and can be found in [1, 4]. The final dimensionless forms are:

$$\Theta_1(\mathrm{Fo}, R, \theta) = \frac{\varepsilon^2 \mathrm{Fo}}{2k} + \sum_{n=-\infty}^{+\infty} \cos n(\theta - \theta') \int_{\varepsilon}^{V} [1 - \exp(-\upsilon^2 \mathrm{Fo})] \times \frac{J_n(\upsilon R) J_n(\upsilon R')(\varphi g - \psi f)}{\upsilon(\varphi^2 + \psi^2)} \mathrm{d}\upsilon \tag{7.1a}$$

$$\Theta_2(\mathrm{Fo}, R, \theta) = \frac{\varepsilon^2 \mathrm{Fo}}{2k} + \frac{2}{\pi} \sum_{n=-\infty}^{+\infty} \cos n(\theta - \theta') \int_{\varepsilon}^{V} [1 - \exp(-\upsilon^2 \mathrm{Fo})] \times \frac{J_n(\upsilon R')[\psi J_n(a\upsilon R) - \varphi Y_n(a\upsilon R)]}{\upsilon^2(\varphi^2 + \psi^2)} d\upsilon \tag{7.1b}$$

Here, θ denotes azimuth; integral limits ε and V are chosen being a very small and larger numbers, respectively; J_n and Y_n denote the Bessel functions of the first kind and the second kind of order n; υ is dimensionless integral variable; subscripts 1 and 2 denote regions $r < r_b$ and $r > r_b$; and the definitions of the dimensionless variables are $k = k_2/k_1$, $a = \sqrt{a_1/a_2}$, $\mathrm{Fo} = a_1 t / r_b^2$, $\Theta(\mathrm{Fo}, R, \theta) = 2\pi k_1 T / q_l$, $R = r/r_b$, $R' = r'/r_b$, and

$$\varphi = akJ_n(\upsilon)J_n'(a\upsilon) - J_n'(\upsilon)J_n(a\upsilon) \tag{7.2a}$$

$$\psi = akJ_n(\upsilon)Y_n'(a\upsilon) - J_n'(\upsilon)Y_n(a\upsilon) \tag{7.2b}$$

$$f = akY_n(\upsilon)J_n'(a\upsilon) - Y_n'(\upsilon)J_n(a\upsilon) \tag{7.2c}$$

$$g = akY_n(\upsilon)Y_n'(a\upsilon) - Y_n'(\upsilon)Y_n(a\upsilon) \tag{7.2d}$$

Eqs. (1) ignore terms of order $O(\mathrm{Fo}\varepsilon^4)$ and terms of order $O(V^{-1})$ [4]. Therefore, the small number ε and the large limit V should be chosen reasonably according to Fo number and accuracy requirement.

7.2.2 Modeling of GHEs

Having this composite-medium solution, one can reasonably assume the descending and ascending legs of U-shaped tubes (not the borehole) to be line sources of heat, releasing heat into surrounding composite materials (Fig. 7.1e). Based on this assumption, the temperatures on the pipe wall of U-tube can be obtained by substituting the corresponding coordinates into Eqs. (7.1a), and a simplified method for calculating the average temperature on the U-tube wall T_p is suggested in Ref. [1]. Once T_p is calculated, the temperatures of circulating fluid can be obtained by the concept of thermal resistance:

$$T_f = T_p + q_l R_p \tag{7.3a}$$

$$T_{f,i}(t) = T_f(t) + \frac{q}{2C_f V_f} \tag{7.3b}$$

$$T_{f,o}(t) = T_f(t) - \frac{q}{2C_f V_f} \tag{7.3c}$$

Here, T_f, $T_{f,i}$, and $T_{f,o}$ denote the average, supply, and return temperatures of circulating fluid, respectively. Eq. (7.3b) and (7.3c) imply that T_f is equal to the algebra average of $T_{f,i}$, and $T_{f,o}$. q is total heating or cooling load of a borehole GHE; C_f and V_f are volumetric heat capacity and average volumetric flow rate of fluid; Thermal resistance of pipe R_p is evaluated by

$$R_p = \frac{1}{2\pi k_p}\ln\frac{r_o}{r_i} + \frac{1}{2\pi r_i \alpha} \tag{7.4}$$

where k_p, r_o, r_i denote thermal conductivity, outer and inner radii of heat transfer pipes, respectively; α is convective heat transfer coefficient (W m^{-2} K^{-1}).

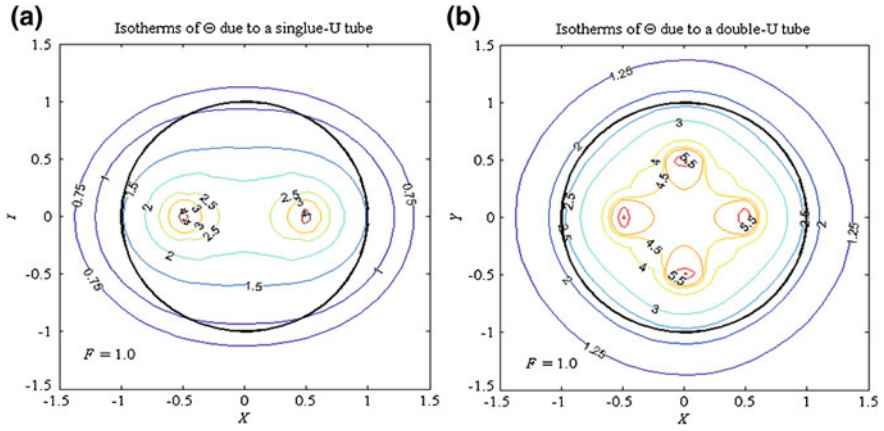

Fig. 7.3 Distributions of the temperatures of borehole GHEs with $R_b = 1$ (**a**) single U-shaped pipe, $R' = 0.5$, $\theta' = 0$, π; (**b**) double U-shaped pipe, $R' = 0.5$, $\theta' = 0$, $\pi/2$, π, $3\pi/2$

7.3 Results and Discussions

It is interesting to analyze the temperature distribution around a GHE. Figure 7.3 shows some contours of temperatures near borehole GHEs. These temperature fields are obtained by Eqs. (7.1a)–(7.4) with prescribed positions of heat sources, that is, the legs of U-shaped tube (not the bore) are approximated as line sources of heat (Fig. 7.1e); each line source is assumed to be of the same strength. Obviously, temperature fields around boreholes (Fig. 7.3a and b) are symmetric because of the symmetrical arrangements of the U-tubes or line sources.

Figure 7.4 compares three model predictions—the new composite-medium model, the common line-source model, and a numerical model—with the experimental data reported by Beier et al. [11]. Their experimental facility consists primarily of a testing unit containing electric heaters and a large sandbox containing a modeled borehole in which a U-shaped pipe is centered. The data set comprises temperature responses of circulating water and sand at different radial positions within the sandbox. More details of this reference data set can be found in the paper [11].

Two salient facts observed from Fig. 7.4 are deserved to be highlighted. First, the composite-medium line-source model can reproduce the trend of fluid temperatures over the almost entire testing period within an acceptable accuracy. Second, the traditional line-source model produces the same prediction as the composite-medium model only at late times, for example, at times larger than 600–1,000 min. During early times, the prediction of the traditional model is considerably larger than those of the experiments and the composite-medium model.

A complex set of factors can affect the thermal behaviors of borehole GHEs, model accuracy, as well as experiment reliability, of which heat input rate q,

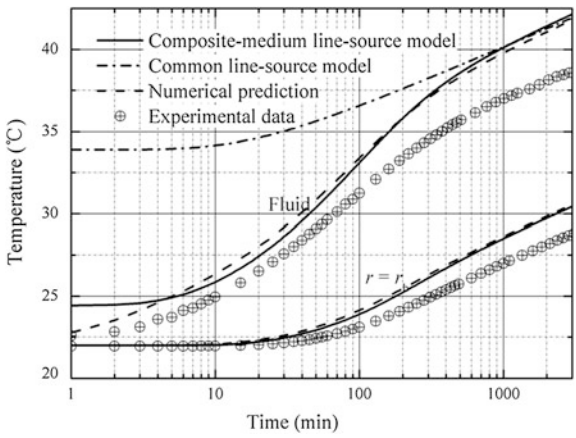

Fig. 7.4 Comparisons of temperatures between model predictions and sand-box measurements

thermal conductivities, and diffusivities of the sand and grouting material are the most possible. Our computation and sensitivity analysis show that 5 % decreases in the heating rate, thermal conductivities, and diffusivities of the sand and grouting material can lead to decreases in predicted fluid temperatures of approximately 1.1, 0.8, and 0.3 °C, respectively [4, 12]. It seems, to conclude, that the three uncertainties are likely responsible for a total discrepancy between modeling and experimental data of more than 2°. Given these uncertainties and the complexity of the problem, the temperature disparities shown in Fig. 7.4 are within a rational and acceptable range of magnitude.

It is well known that the traditional line-source approach is unsuitable for modeling short-time responses of borehole GHEs [1–4]. To use the common line-source model, one should assume that heat transfer in the borehole reaches a steady state. An estimate of the time scale for reaching this steady state is $t \geq 5r_b^2/a_b$, which is usually of a magnitude of order of 5–10 h. Figure 7.4 confirms this point again, showing that this approach overrates temperature responses during the early times.

In contrast, the fundamental presumption of the composite line-source model is that the legs of the U-shaped tube are modeled as line sources of heat (Fig. 7.1e); the effect of the heat capacities of the materials within the borehole can be addressed, except heat capacities of circulating fluid and U-shaped tubes. These heat capacities can delay the temperature rises of circulating fluid at the immediately initial times (about 5 min in Fig. 7.4), which is the source of the prediction difference between the numerical and the composite-medium models.

7.4 Conclusions

This work presents a composite-medium line-source approach to modeling pile and borehole GHEs. The central ideal of this approach is that the pipe legs of U-shaped or W-shaped tubes used in GHEs are approximated as heat sources,

differing from the traditional method, whereby borehole is modeled as heat sources. Comparison study shows that the new method can give reasonable prediction of GHE responses at times as short as 5 min and is obviously more suitable for the prediction of short-term behaviors of GHEs than the common line-source model.

References

1. Li M, Lai ACK (2012) New temperature response functions (G functions) for pile and borehole ground heat exchangers based on composite-medium line-source theory. Energy 38:255–263
2. Javed S, Claesson J (2011) New analytical and numerical solutions for the short-term analysis of vertical ground heat exchangers. ASHRAE Trans 117:3–12
3. De Carli M, Tonon M, Zarrella A, Zecchin RA (2010) Computational capacity resistance model (CaRM) for vertical ground-coupled heat exchangers. Renew Energy 35:1537–1550
4. Li M, Lai ACK (2013) Analytical model for short-time responses of ground heat exchangers with U-shaped tubes: model development and validation. Appl Energy 104:510–516
5. Li M, Lai ACK (2012) Heat-source solutions to heat conduction in anisotropic media with application to pile and borehole ground heat exchangers. Appl Energy 96:451–458
6. Cui P, Li X, Man Y, Fang ZH (2011) Heat transfer analysis of pile geothermal heat exchangers with spiral coils. Appl Energy 88:4113–4119
7. Zeng HY, Diao NR, Fang ZH (2003) Heat transfer analysis of boreholes in vertical ground heat exchangers. Int J Heat Mass Transf 46:4467–4481
8. Pasquier P, Marcotte D (2012) Short-term simulation of ground heat exchanger with an improved TRCM. Renew Energy 46:92–99
9. Beier RA, Smith MD (2003) Minimum duration of in situ tests on vertical boreholes. ASHRAE Trans 109:475–486
10. Bandyopadhyay G, Kulkarni M, Mann M (2008) A new approach to modeling ground heat exchangers in the initial phase of heat-flux build up. ASHRAE Trans 114:428–439
11. Beier RA, Smith MD, Spitler JD (2011) Reference data sets for vertical borehole ground heat exchanger models and thermal response test analysis. Geothermics 40:79–85
12. Li M, Lai ACK (2012) Parameter estimation of in situ thermal response tests for borehole ground heat exchangers. Int J Heat Mass Transf 55:2615–2624

Chapter 8
A Comparison Study of the Short-Time Responses of Borehole Ground Heat Exchangers by Using Numerical and Analytical Methods

Yi Yang and Min Li

Abstract In this paper, short-time performance of borehole GHEs is examined by using numerical and analytical methods. The numerical model can account for effect of heat capacities of circulating water, U-shaped tubes, as well as grouting materials, by using a novel time-varying boundary condition on the inner walls of U-tube legs. Both the numerical and the analytical composite-medium models are validated by an independent sandbox experiment. Comparisons between the two models are also made for different parameters, including heating rate, spacing of U-tube legs, thermal properties, and borehole radius. Overall, the composite-medium line-source model gives the virtually same results as the numerical model except for very early times: the analytical solution overestimates temperature responses for the first several min (about 5 min). This discrepancy is caused by the composite-medium line-source assumption, ignoring heat capacities of circulating fluid and U-shaped pipe.

Keywords Composite-medium line-source model · Borehole ground heat exchanger · Ground-coupled heat pump · Finite-volume model · Short-time response

M. Li (✉)
Central South University, 410083 Changsha, Hunan, China
e-mail: cnlimin@csu.edu.cn; minli.csu@gmail.com

Y. Yang
Guangdong Ocean University, 524088 Zhanjiang, Guangdong, China
e-mail: cnyangy@gmail.com

A. Li et al. (eds.), *Proceedings of the 8th International Symposium on Heating, Ventilation and Air Conditioning*, Lecture Notes in Electrical Engineering 263,
DOI: 10.1007/978-3-642-39578-9_8,

8.1 Introduction

In recent years, HVAC researchers and engineers have become increasingly aware of the importance of short-time temperature responses of borehole ground heat exchangers (GHEs) [1–5]. Knowledge of short-time responses plays an important part in design of hybrid ground-coupled heat pump systems (GCHPs), in situ response tests of GHEs, control, optimization, and hourly simulation of GCHPs. Predicting short-term heat transfer by borehole GHEs, however, remains a great challenge because of involvement with transient heat conduction in composite media, together with various U-shaped tube installations. A great number of studies have been performed to resolve this problem in analytical [1–5] or numerical ways [6–8].

Most analytical models for short-term behaviors of borehole GHEs have used an equivalent-diameter assumption [3–5], assuming U-shaped tubes as a pipe with an "equivalent" diameter (Fig. 8.1c). By this empirical assumption, the original problem in a multi-circle region reduces to one in a concentric annular region; various analytical solutions are possible. But the equivalent-diameter approach is an empirical method and may cause some errors in determining GHEs short-step responses.

In our previous work, an analytical composite-medium line-source model is created for modeling thermal processes of borehole and pile GHEs [1, 2]. The composite-medium model enables the empirical "equivalent-diameter" assumption to be abandoned. This model can accurately evaluate not only the influence of the heat capacity of grouting materials but also impact of the difference between properties of soil and grout/foundation piles, while it is flexible enough to model

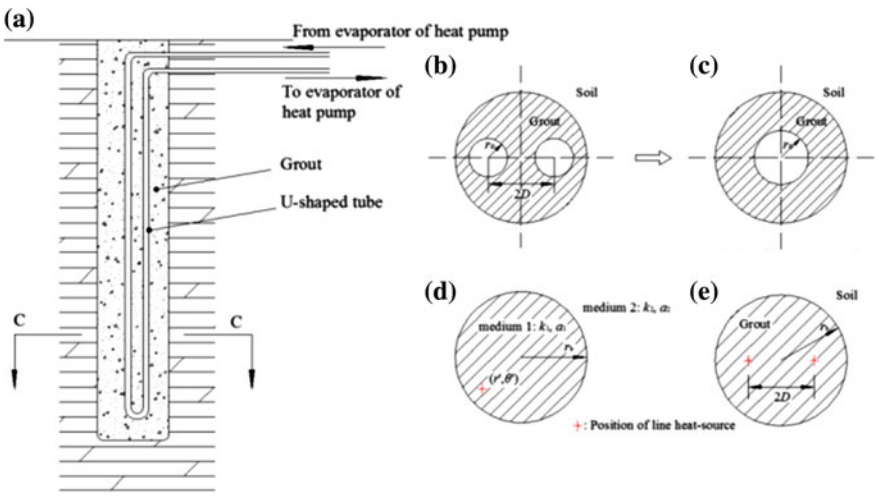

Fig. 8.1 Schematic layout of a borehole GHE with a single U-shaped tube

various configurations of heat transfer channels such as single and double U-shaped tubes, W-shaped channels, spiral-coils, etc. [2]. But this line-source model ignores the impact of heat capacities of circulating fluid and U-pipe material; this simplification can induce some errors when applied to very early times. Recent comparison with a well-controlled sandbox experiment indicates that the composite-medium model can reproduce the experimental profiles for times as short as 5 min [1]. The experimental data inevitably comprises some uncertainties and errors, and it provides the validation of the model only for one set of parameters. Therefore, it still remains indeterminate how the performance is when applying the new line-source model to very short times with various system parameters.

Models based on numerical methods, for example, finite difference methods [6], finite-volume methods [7], and finite-element methods [8], are elaborate enough for describing all physical mechanisms. To study the short-time performance of borehole GHEs, this paper first builds for borehole GHEs an elaborate two-dimensional finite-volume model, whereby the effect of heat capacities of circulating fluid and U-shaped pipe can be included. Next, both numerical and analytical models are verified by each other and validated by an independent laboratory data set. Then, detailed comparisons between the numerical and the analytical models are performed for different input parameters, which is helpful to quantitatively determine influence of these parameters on model performance.

8.2 Numerical and Analytical Models for GHEs with U-Shaped Tubes

8.2.1 Finite-Volume Model

Since we are only interested in short-time thermal processes around a borehole GHE, influence of the ground surface can be ignored, and thus, heat transfer between the circulating fluid and the ground is essentially a two-dimensional problem in the plane perpendicular to the borehole. Figure 8.2a and b show the computational domain, which is only the upper half of the actual space domain due to the symmetry of the problem. The computational domain consists of three parts: pipe wall, grouting material, and soil zone. In view of the simulated time period, an outer boundary is chosen large sufficiently (1×2 m) to model the infinite ground, and thus, it can be treated as an infinite far boundary condition.

The governing equations of temperature T in these solid zones are

$$\frac{\partial T_i}{\partial t} = \alpha_i \nabla^2 T_i \tag{8.1}$$

where subscript i can be p, g or s, respectively, for domains of pipe, grout or soil; t is time; and a denotes thermal diffusivities of these media. The initial conditions

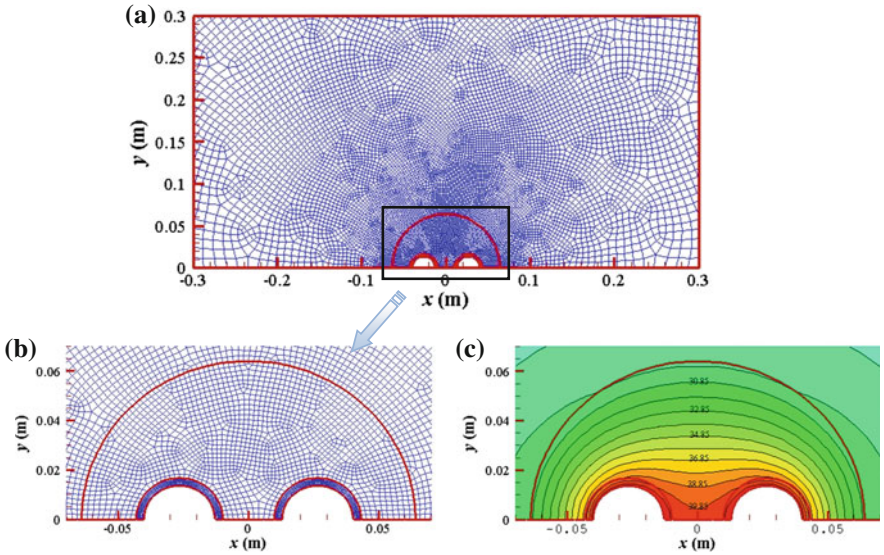

Fig. 8.2 **a** The used mesh of the computational domain. **b** Local enlarged view of borehole mesh. **c** Contours of a computed temperature field

in these solids are the undisturbed temperature of the ground. The equations are discretized by the finite-volume method.

A key step of developing the numerical model is how to deal with the boundary condition on inner surfaces of U-tubes, which the circulating fluid contacts. The governing equations for circulating fluid in the descending and ascending pipes of U-shaped tube can be written as

$$\pi r_i^2 C_f \frac{\partial T_{f,+}}{\partial t} = 2\pi r_i h_+ \left(T_{p,+} - T_{f,+}\right) + q_{l,+} \tag{8.2a}$$

$$\pi r_i^2 C_f \frac{\partial T_{f,-}}{\partial t} = 2\pi r_i h_- \left(T_{p,-} - T_{f,-}\right) + q_{l,-} \tag{8.2b}$$

where subscripts f, p, $+$, and $-$ denote fluid, U-pipe, descending leg, and ascending leg of U-pipe, respectively. C is volumetric heat capacity; r_i denotes the inner radius of heat transfer pipes; q_l is heat transfer rate into or from heat-carrier fluid (from heat pump units) per unit bore length. $q_{l,+}$ and $q_{l,-}$ are heat flux distribution over the downward and upward pipes; they may be different or not; h is convective heat transfer coefficient in the U-pipe and can be estimated by [9]

$$Nu = \frac{2hr_i}{k_f} = 0.023\mathrm{Re}^{0.8}\mathrm{Pr}^{0.3} \tag{8.3}$$

where k_f is thermal conductivity of fluid. The exponent of Pr number equals 0.3 for cooling. Re number of pipe flows is defined as

$$\mathrm{Re} = \frac{2M}{\pi\mu r_i} \tag{8.4}$$

Here, μ is dynamic viscosity of fluid (kgm^{-1} s^{-1}); M is mass flow rate (kg s^{-1}).

Functionally, Eqs. (8.2) are the boundary conditions on the inner surfaces of U-shaped pipe. Differing from the common forms (the first, second, or third kind boundary conditions), Eqs. (8.2) have two outstanding characteristics. First, it can account for effect of heat capacity of fluid by the terms on the left hand sides. If ignoring the heat capacity of fluid, Eqs. (8.2) can reduce to the common second or third kind boundary conditions. Second, the heating or cooling load, q_l, occurs in the boundary condition equations in an explicit way. Thus, our computation procedure follows the philosophy of heat transfer computation of line-source theory, computing the temperature differences under the condition of a given heat flux. This approach clearly is more natural and convenient, because the loads ql usually are known before beginning heat transfer computation of ground heat exchangers. This approach is also identical to the problem solved by the composite-medium line-source model [1, 2].

8.2.2 *Infinite Composite-Medium Line-Source Model*

Figure 8.1d shows that an infinite line source of heat is positioned in an infinite composite cylinder, of which the region $r < r_b$ is of one medium having conductivity k_1, diffusivity a_1, density ρ_1, and heat capacity c_1 and the region $r > r_b$ of another, the corresponding quantities are k_2, a_2, ρ_2, and c_2. The line source is parallel to the height direction, z-axis, and is located through a point (r', θ'). Initially, the temperatures of the medium are zero. If the infinite line source continuously releases heat into the composite solid from the initial time at a rate of q_l(W/m), the temperature responses in the composite medium can be obtained by the method of heat sources, and the solution process and the final results can be found in Ref. [1, 2].

8.3 Results and Discussions

The numerical and analytical models can verify each other, because they describe a basically same heat conduction problem. For the purpose of validation, a set of experimental data of Beier et al. [10] is used. This data set, obtained from a series of sandbox tests, consists of temperature responses at the inlet and outlet of U-loop and at different radial positions within the sandbox. More details of the data set can be found in the paper of Beier et al. [10].

In Fig. 8.3, the sandbox measurements are compared with predictions of the numerical and analytical models, showing that both models can yield predictions

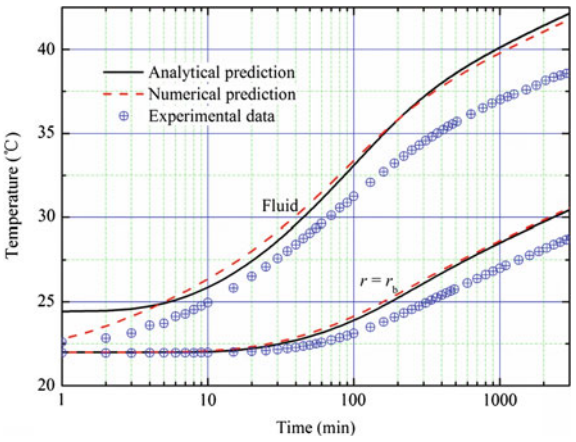

Fig. 8.3 Comparisons of temperatures between model predictions and sandbox measurements

matching the experimental temperature profiles within an acceptable accuracy, relative errors being smaller than 8 %. Both models give temperatures somewhat larger than experimental values, especially at late times. This discrepancy has already been observed when the data set was used to validate the composite-medium line-source model in our previous work [1]. We have analyzed three potential uncertainties in the experiment parameters which may contribute to the discrepancies: heating rate q_l, thermal conductivities k, and diffusivities a of the used sand and grout [1]. The analysis, however, is indeterminate because the analytical model and the sandbox test are performed independently by two research groups. In this context, a third independent work is needed to further identify the underlying reasons causing these discrepancies. Numerical models developed in this work can serve this interest.

The close match between the analytical and the numerical models at large times (Fig. 8.3) implies that the difference between model predictions and experimental data may be mainly due to some uncertainties of the sandbox experiment. The most important uncertainty (and also highly possible) is the heating rate q_l. In an ideal situation, the heat from electrical heater should entirely diffuse into sands (modeled ground); however, there always is part of heat diffusing into surrounding air through connecting pipes of the experimental facility. Previous sensitivity analysis has indicated that only a 5 % decrease in the heating rate can cause a decrease in the computed fluid temperatures of approximately 1.1 °C [11]. Therefore, we infer that the inevitable heat loss contributes to a major part of the discrepancies between the model predictions and the experimental data, though we cannot estimate the extent to which heat diffuses into the air. Other potential uncertainties, such as the position of U-shaped tube, thermal properties of used materials, size of borehole, etc., may also account for parts of the discrepancy. Considering these complexities, we conclude that the numerical and analytical models are essentially valid for modeling borehole GHEs.

The main difference in predictions between the two models occurs only at very early times (within the first 5 min). The numerical model can give a more appropriate temperature profile of circulating fluid at the extremely early times. This result is in line with expectation: the new line-source model ignores heat capacities of circulating fluid and U-shaped pipe wall. At the immediately initial times, these heat capacities can delay the temperature rises of circulating fluid, thus ignoring them leads to an overestimate of temperature responses. Corresponding to the experimental case, the period of the initial time is 5 min.

Figure 8.4 shows comparisons between numerical and analytical predictions with different parameter inputs, including various values of q_l, k, D, and r_b. These results again verify that heating load q_l is a very sensitive parameter. Parameters k and D also have important influence on temperature responses. In contrast, fluid temperature is relatively insensitive to borehole radius r_b. But these influences center mainly on the period of late times. Surprisingly, at extremely short times, variations in these parameters play a relatively minor role in influencing thermal responses, permitting analyzing these curves as a whole.

As reviewed in the introduction, our previous studies cannot determine a time limit beyond which the composite-medium line-source model is applicable. Experimental data show an excellent performance that the analytical model is

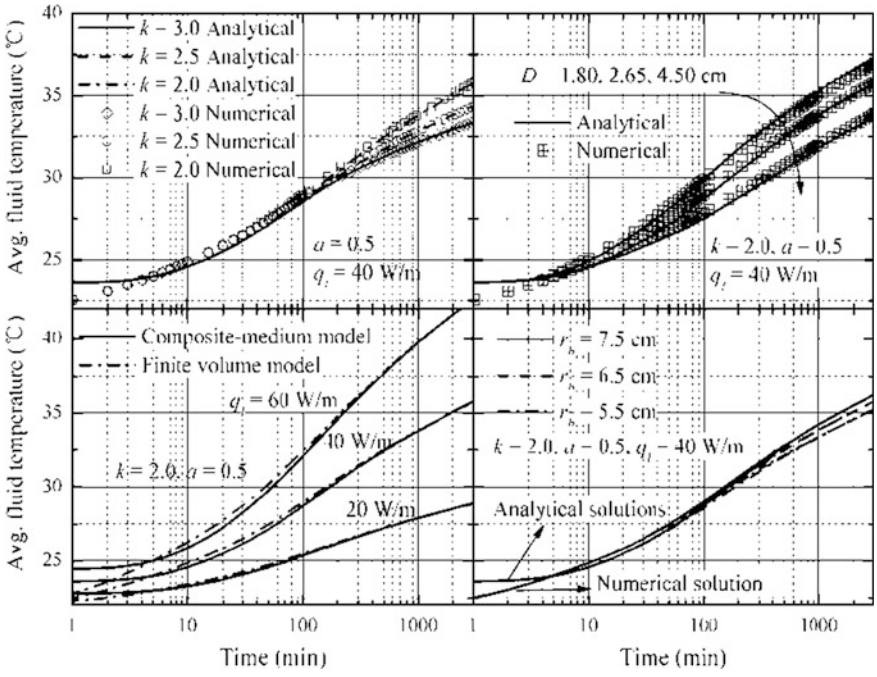

Fig. 8.4 Comparisons of the numerical and analytical computations with parameters: q_l, k, D and r_b

applicable for times as short as 5 min [1]. The numerical model further confirms this short-time performance (Fig. 8.4), illustrating that the temperatures obtained from the analytical model are virtually identical to the results of the finite-volume model except the initial several minutes, during which the analytical model overrates fluid temperatures. Thus, the comparison with the finite-volume model provides us evidence that the first 5 min can be used as a minimum time beyond which the composite-medium line-source model is applicable.

8.4 Conclusions

To examine the short-term performance of the composite-medium line source model, this paper builds a two-dimensional numerical model by the finite-volume method. In the numerical model, heat capacities of circulating fluid and U-pipe wall are treated by a transient boundary condition on the inner surface of U-shaped tub. A reported reference experiment data are used to validate the numerical model. A detailed comparison of the numerical and the line-source models is also performed, and main conclusions drawn from this study are that

With the exception of very early times, the numerical and the analytical models yield results matching each other very well; but they all give predictions somewhat larger than the laboratory data. Considering the highly consistency of the models and unavoidable uncertainties in the experiment, we infer that the two models are essentially valid for modeling thermal responses of borehole GHEs.

For different parameter inputs, comparison between the two models also shows that the main differences between them occur only within the first 5 min in all the case studies; therefore, 5 min can be used as the general minimum threshold for applying the composite-medium line-source model.

References

1. Li M, Lai ACK (2013) Analytical model for short-time responses of borehole ground heat exchangers: model development and validation. Appl Energy 104:510–516
2. Li M, Lai ACK (2012) New temperature response functions (G functions) for pile and borehole ground heat exchangers based on composite-medium line-source theory. Energy 38:255–263
3. Claesson J, Javed S (2011) An analytical method to calculate borehole fluid temperatures for time-scales from minutes to decades. ASHRAE Trans 117:279–288
4. Bandyopadhyay G, Kulkarni M, Mann M (2008) A new approach to modeling ground heat exchangers in the initial phase of heat-flux build up. ASHRAE Trans 114:428–439
5. Beier RA, Smith MD (2003) Minimum duration of in situ tests on vertical boreholes. ASHRAE Trans 109:475–486
6. Mottaghy D, Dijkshoorn L (2012) Implementing an effective finite difference formulation for borehole heat exchangers into a heat and mass transport code. Renew Energy 45:59–71

7. Li Z, Zheng M (2009) Development of a numerical model for the simulation of vertical U-tube ground heat exchangers. Appl Therm Eng 29:920–924
8. Kim EJ, Roux JJ, Rusaouen G et al (2010) Numerical modeling of geothermal vertical heat exchangers for the short time analysis using the state model size reduction technique. Appl Therm Eng 30:706–714
9. Bejan A (2004) Convection heat transfer, 3rd edn. Wiley, Hoboken
10. Beier RA, Smith MD, Spitler JD (2011) Reference data sets for vertical borehole ground heat exchanger models and thermal response test analysis. Geothermics 40:79–85
11. Li M, Lai ACK (2012) Parameter estimation of in situ thermal response tests for borehole ground heat exchangers. Int J Heat Mass Transf 55:2615–2624

Chapter 9
Comparing Condensation Theory with Hygrothermal Models for the Mixed Climate Region of China

Shui Yu, Xu Zhang, Mark Bomberg and Guohui Feng

Abstract Calculations of the coupled heat and moisture transfer are necessary for energy-efficient buildings, improving IAQ and durability of building materials. While correct approach requires simultaneous consideration of heat, air and moisture transports, many architects and designers still use the water vapor transport theory without considering other environmental factors. This paper applies either of these two methods to three wall types over summer and winter seasons and compares results highlighting the limitation of the traditional method.

Keywords Coupled heat and moisture transfer · Hygrothermal models · HAM models · CHAMPS-BES model · Temperature field · Humidity field

9.1 Introduction

With the increased stress on airtight, highly insulated buildings we encounter growing are needed for hygrothermal calculations [1–3]. We realize that in Eastern China region of mixed climate, with high relatively humidity (RH) in winter, the

S. Yu (✉) · G. Feng
School of Municipal and Environmental Engineering, Shenyang Jianzhu University, No. 9, Hunnan East Road, Hunnan New District 110168 Shenyang, China
e-mail: yushui19832002@gmail.com

G. Feng
e-mail: fengguohui888@163.com

X. Zhang
College of Mechanical Engineering, Tongji University, 200092 Shanghai, China
e-mail: zhangxu-hvac@tongji.edu.cn

M. Bomberg
Toronto U, Canada and Southest Universiy, Nanjing, China
e-mail: mark.bomberg@gmail.com

A. Li et al. (eds.), *Proceedings of the 8th International Symposium on Heating, Ventilation and Air Conditioning*, Lecture Notes in Electrical Engineering 263,
DOI: 10.1007/978-3-642-39578-9_9,

risk for condensation and mold growth on the surface of the building enclosure is high. Furthermore, the long-term operation of air conditioning in summer season increases this potential. When the temperature on the inner face of the external wall is lower than the dew point, the condensation takes place often leading to a mold growth [3–6].

Most designers, however, are focused on the thermal performance of buildings without considering moisture effects. Yet, moisture has a big influence on a number of performance aspects including the heat transfer. To highlight these issues, three types of wall characteristics to China are selected, namely 240 mm clay brick, 180 mm concrete and 190 mm aerated autoclaved concrete (AAC) with exterior and interior insulation layers (Fig. 9.1).

While HT models use hourly weather data from the metrological station that is representative for each region, the condensation methods are typically using a steady state approximation [7–9]. The weather data used in this case are shown in Table 9.1 and Fig. 9.2.

9.2 Comparison of Steady State Moisture Profiles in Sum and Win

Below, comparison between manual- and computer-generated profiles of relative humidity for (a) summer and (b) winter day for a selected wall including normal wall, ETIS and ITIS in Shanghai climate is displayed. Note: (1)When RH $>$ 90 %, there is capillary condensation and liquid transfer on the mechanism of capillary function; (2) Shadow zone is condensation zone by simulation; (3) Only relative humidity distribution is displayed; and temperature distribution is not showed because there is no obvious difference (From Figs. 9.3, 9.4, 9.5, 9.6, 9.7, 9.8, 9.9, 9.10, and 9.11)

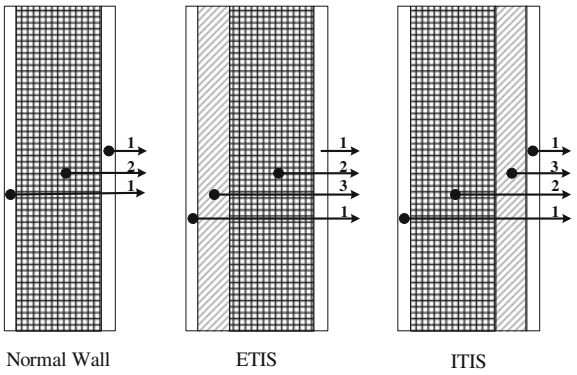

Fig. 9.1 Considered wall types: normal wall, wall with ETIS, wall with ITIS

Table 9.1 Boundary conditions for Shanghai used for condensation methods for steady state

Design parameters	Tem (°C)	RH (%)	Heat transfer coefficient ($W/m^2 \cdot K$)	WV diffusion coefficient (s/m)
Winter-indoor	18	60	8.7	3×10^{-8}
Winter-outdoor	−4	75	23	2×10^{-7}
Summer-indoor	26	60	8.7	3×10^{-8}
Summer-outdoor	34	65	23	2×10^{-7}

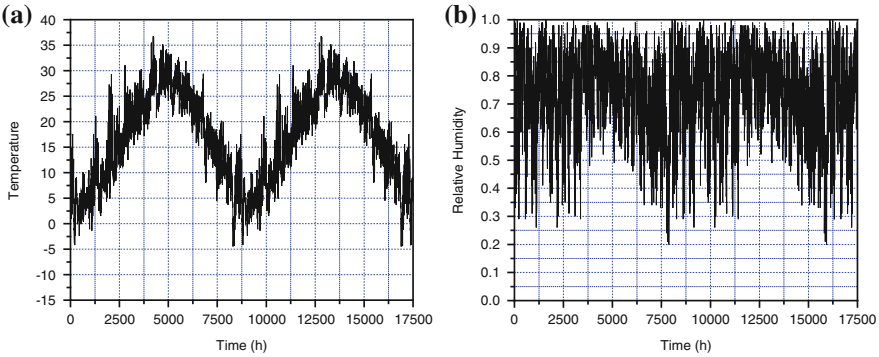

Fig. 9.2 Outdoor temperature **a** and relative humidity **b** in two year

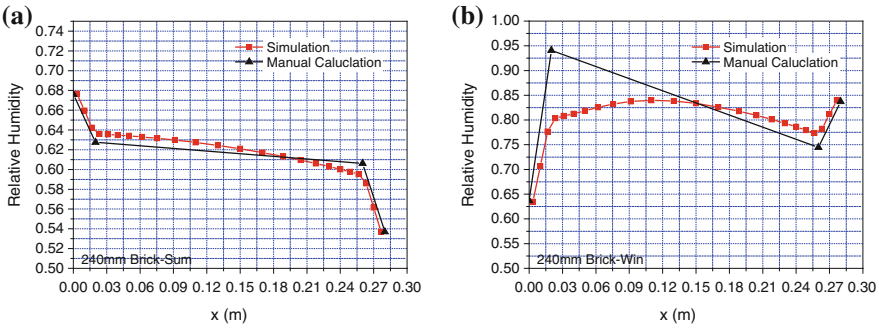

Fig. 9.3 Distribution of RH in normal brick wall in **a** summer and **b** winter

9.3 Moisture Profiles of L-type Wall in Winter

Below, computer-generated profiles of relative humidity in winter for a selected L-type wall including normal wall and wall with ETIS in Shanghai climate is displayed. (From Figs. 9.12, 9.13, and 9.14)

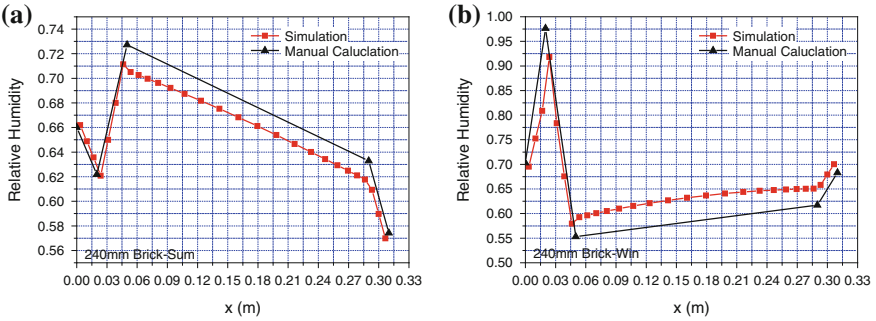

Fig. 9.4 Distribution of RH in brick wall with ETIS in **a** summer and **b** winter

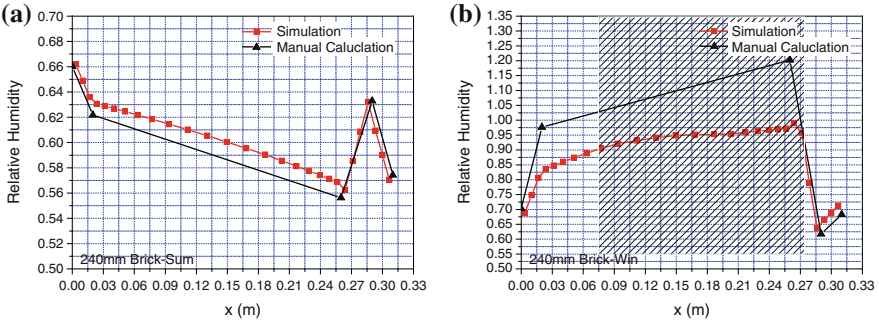

Fig. 9.5 Distribution of RH in brick wall with ITIS in **a** summer and **b** winter

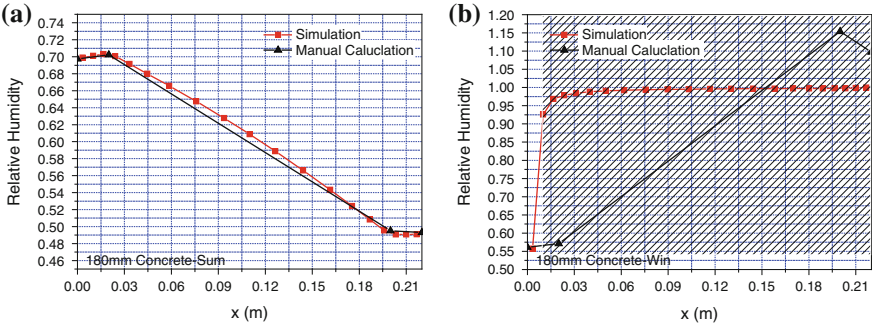

Fig. 9.6 Distribution of RH in normal Concrete wall in **a** summer and **b** winter

9.4 Moisture Profiles of Unsteady State

Below, computer-generated profiles of relative humidity for two year for a selected wall including normal wall and wall with ETIS in Shanghai climate is displayed. (From Figs. 9.15, 9.16, and 9.17). It is easily reached to 90 % on the exterior of the

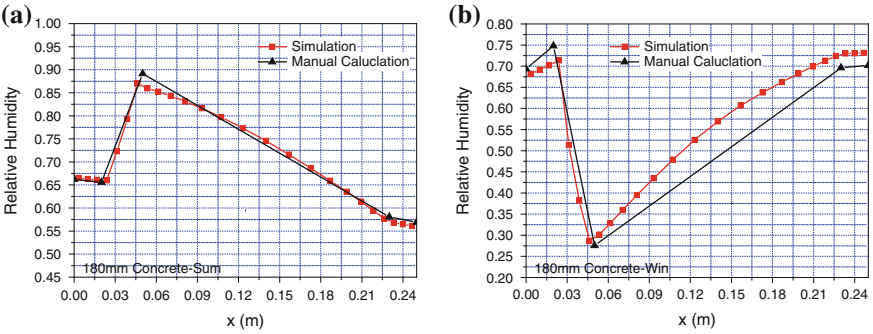

Fig. 9.7 Distribution of RH in Concrete wall with ETIS in **a** summer and **b** winter

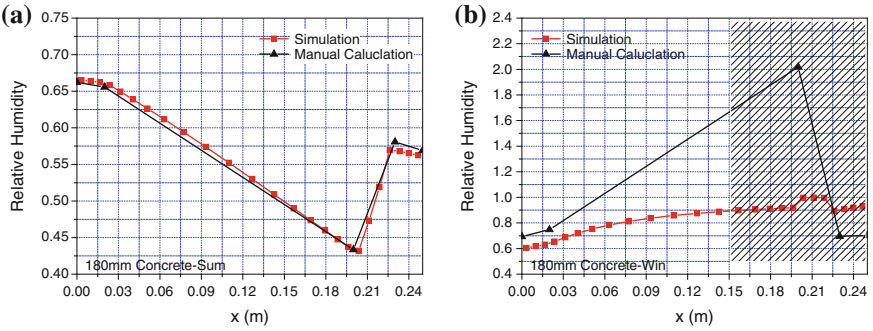

Fig. 9.8 Distribution of RH in Concrete wall with ITIS in **a** summer and **b** winter

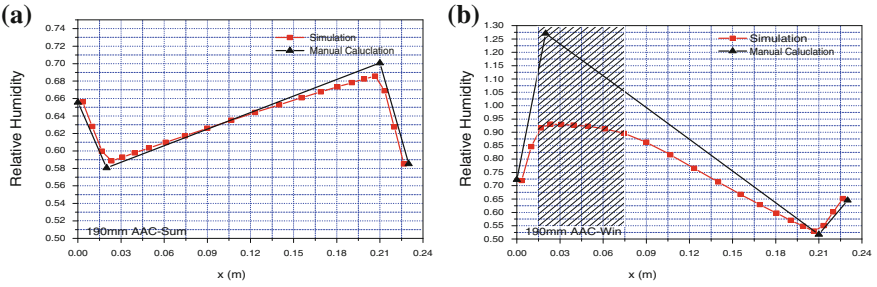

Fig. 9.9 Distribution of RH in normal AAC wall in **a** summer and **b** winter

wall that means capillary condensation often occur on the surface of outside wall for all kinds of wall. That is one reason exterior surface of outside wall is usually destroyed first.

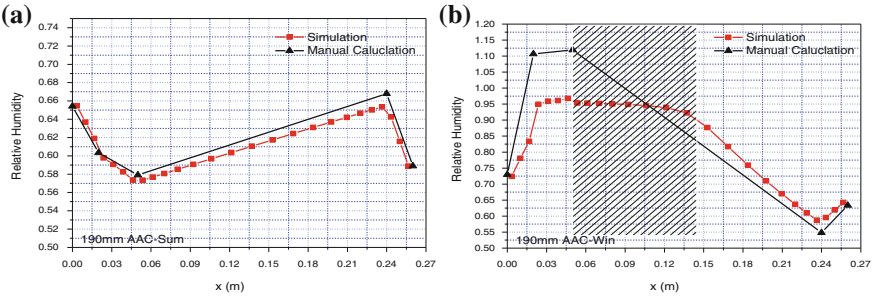

Fig. 9.10 Distribution of RH in AAC wall with ETIS in **a** summer and **b** winter

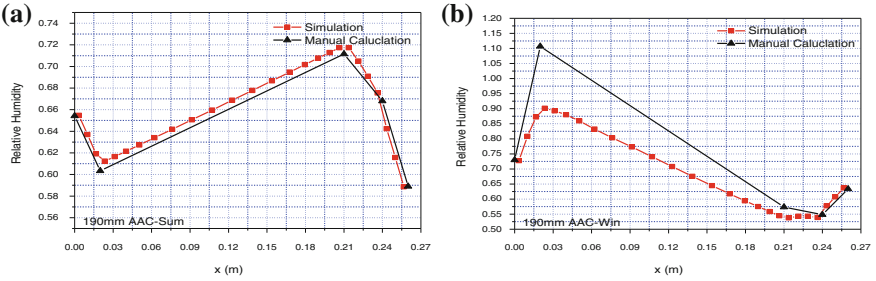

Fig. 9.11 Distribution of RH in AAC wall with ITIS in **a** summer and **b** winter

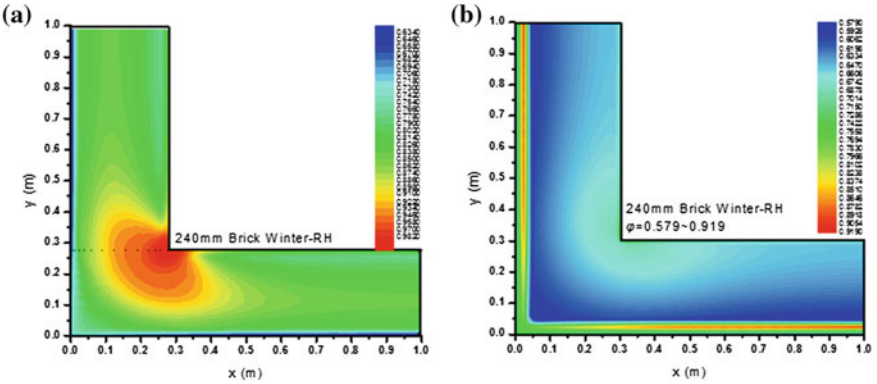

Fig. 9.12 Distribution of RH in normal brick wall **a** and wall with ETIS **b**

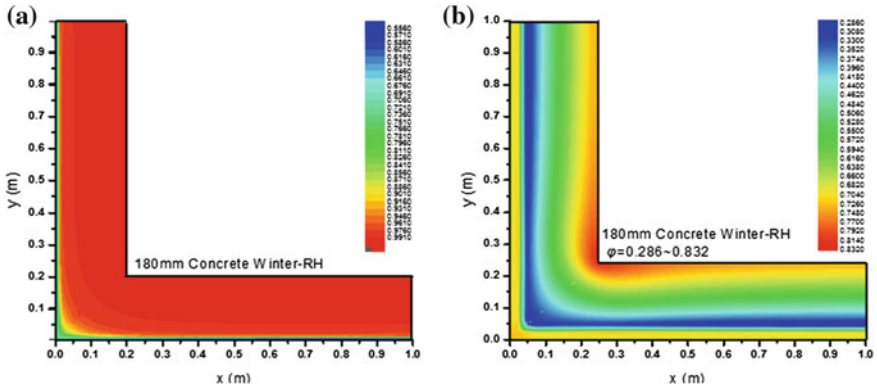

Fig. 9.13 Distribution of RH in normal concrete wall **a** and wall with ETIS **b**

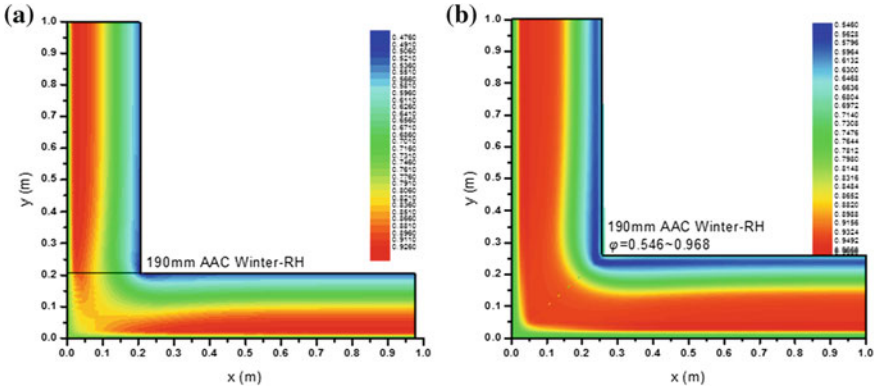

Fig. 9.14 Distribution of RH in normal AAC wall **a** and wall with ETIS **b**

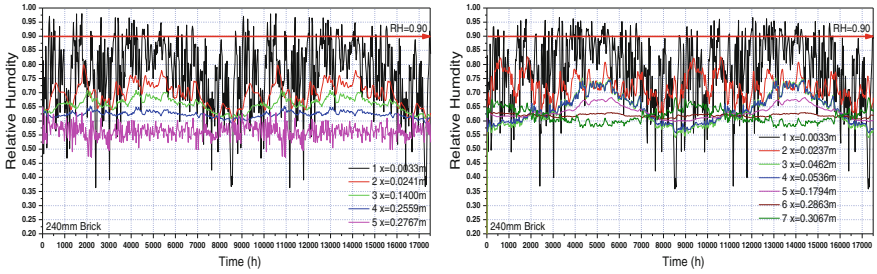

Fig. 9.15 RH of key points in the normal brick wall and wall with ETIS

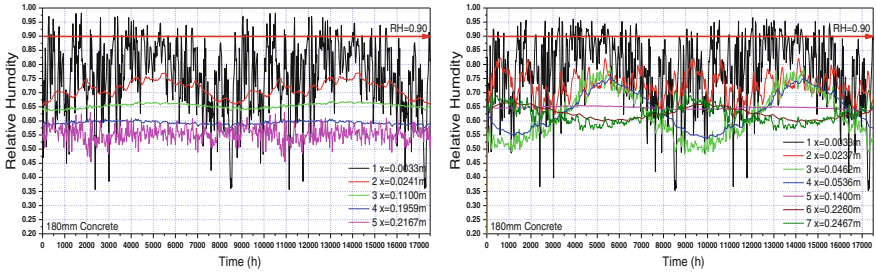

Fig. 9.16 RH of key points in the normal concrete wall and wall with ETIS

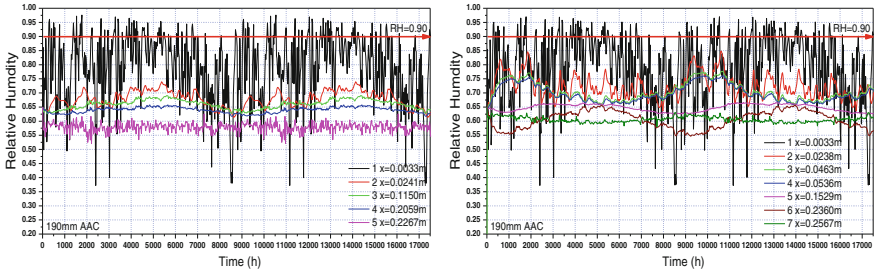

Fig. 9.17 RH of key points in the normal AAC wall and wall with ETIS

9.5 Discussions and Conclusions

1. Comparing RH distribution by condensation theory with hygrothermal models, there is no obvious difference in summer, so condensation theory could be used in summer.
2. When RH is larger than 90 %, the capillary condensation lead to liquid water transfer by capillary mechanism or liquid drop exists in porous. So, condensation theory is not suitable to calculate RH distribution in the wall when Max RH is larger than 90 %, especially in winter.
3. Brick and concrete wall is suitable to use ETIS to avoid condensation and increase thermal resistance.
4. AAC wall is suitable to use ITIS to avoid condensation and increase thermal resistance.
5. It is easily reached to 90 % on the exterior of the wall that means capillary condensation often occur on the surface of outside wall which is one reason that the durability of the exterior surface of the wall is weak.

Acknowledgments The authors would like to thank both of the National Eleventh Five-year Plan for Science and Technology (2006BAJ01A05) of China and Building Energy and Environmental Systems Laboratory at Syracuse University for their financial support to the project.

References

1. Rode Pedersen C (1990) Combined heat and moisture transfer in building constructions, Ph.D. Thesis. Thermal Insulation Laboratory, Technical University of Denmark
2. Straube J, Burnett E (2005) Building science for building enclosures. Building Science Press Inc, Westford, pp 293–365
3. Bomberg MT, Shirtliffe CJ (2009) Moisture control in buildings: the key factor in mold prevention. Baltimore, MD, pp 16–37
4. Van Schijndel AWM (2007) Integrated heat air and moisture modeling and simulation, PhD thesis.Eindhoven, Technische Universiteit, 2007
5. Yu S, Bomberg M, Zhang X (2012) Integrated methodology for evaluation of energy performance of the building enclosures: part 5-application of the proposed hygrothermal characterization. J Build Phys 36(2):178–197
6. Yu S, Bomberg M, Zhang X (2012) Integrated methodology for evaluation of energy performance of the building enclosures: part 4-material characterization for input to hygrothermal models. J Build Phys 35(3):194–212
7. Miller EE, Miller RD (1995) Theory of capillary flow: I. practical implications. Proc Soil Sci Soc Am 19:267–271
8. Miller EE, Miller RD (1955) Theory of capillary flow: II. experimental information. Proc Soil Sci Soc Am 19:272–275
9. Miller JD (1984) Development of validation of a moisture mass balance model for predicting residential cooling energy consumption. ASHRAE Trans 90(2):275–293

Chapter 10
Numerical Simulation and Evaluation of Mechanical Smoke Exhaust in a Loop Corridor of a High-Rise Hotel

Wei Shi and Fusheng Gao

Abstract The mechanical smoke exhaust is as acknowledged as an effective smoke control manner by making use of some necessary exhaust facilities, also with more stability than natural exhaust. In this paper, the field model Fire Dynamic Simulator (FDS) with a combination of zone model Consolidate Fire and Smoke Transport (CFAST) were used to simulate the mechanical smoke exhaust in a loop corridor of the fire floor in a high-rise hotel, for the propose of evaluate fire safety of mechanical smoke exhaust. There were several factors under discussion, such as the arrangement of smoke vents, quantity of smoke vents, the volume of smoke exhaust, the position of the smoke vents and height of ceiling indoor. The conclusions were obtained as followed. When two exhaust vents were set symmetrically in the loop corridor, one of which was located nearby the fire room, the smoke exhausted better. The volume of smoke exhaust per unit area with 60 m^3/h according to regulations could always ensure safety of smoke exhaust. The smoke exhausted worse within the corridor when ceiling height reduced. It was recommended that the lowest ceiling height limit should be provided in correlative regulation.

Keywords Building fire · Mechanical smoke exhaust · Loop corridor · FDS · CFAST

W. Shi (✉)
Northeast Petroleum University, Daqing 163318, China
e-mail: sw_dqpi@126.com

F. Gao
Harbin Institute of Technology, Harbin 150001, China
e-mail: fushenggao@126.com

A. Li et al. (eds.), *Proceedings of the 8th International Symposium on Heating, Ventilation and Air Conditioning*, Lecture Notes in Electrical Engineering 263,
DOI: 10.1007/978-3-642-39578-9_10,

10.1 Introduction

In high-rise building fires, mechanical exhaust was an effective and significant way for persons to evacuate, and was widely used in design. Specification states that "if there is no direct natural ventilation, or internal corridor with length of more than 20 m, or direct natural ventilation but internal corridor with the length of more than 60 m" [1], then the place should be set with mechanical exhaust facilities. When the building was on fire, the fire area produced large amounts of high-temperature flue gas and the pressure would be higher than in other areas, which averages about 10–l5 Pa, which in short term may reach about 35–40 Pa. The pressure differences and reading prompted the flue gas leakage through the gap of doors, windows, opening and pipe also through gap of the wall. Mechanical exhaust was an effective manner to exclude smoke in time. At the same time, causing the negative pressure, it could prevent the spread of the smoke to the security zone, creating the conditions of time and space for the evacuation.

Smoke control design in high-rise buildings usually used a combination of positive pressure air supply in the atria and stairwells, and mechanical exhaust in the corridor. In this paper, the field model Fire Dynamic Simulator (FDS) with a combination of zone model Consolidate Fire and Smoke Transport (CFAST) were used to simulate the mechanical smoke exhaust [2] in a loop corridor of the fire floor in a high-rise hotel, for the propose of evaluate fire safety of mechanical smoke exhaust.

The general view of simulation model in 2D was represented in Fig. 10.1. The loop corridor was 60 m in length, and 1.8 m in width, with ceiling height of 2.5 m. There were two doors in the corridor, connected with atria, with the width 1.2 m and the height 2.1 m. The high-rise hotel was in urban district of Beijing, which had 30 floors and each floor height was 3 m. The fire room was on the 20th floor. Room 1 was on fire, with the fire source in corner.

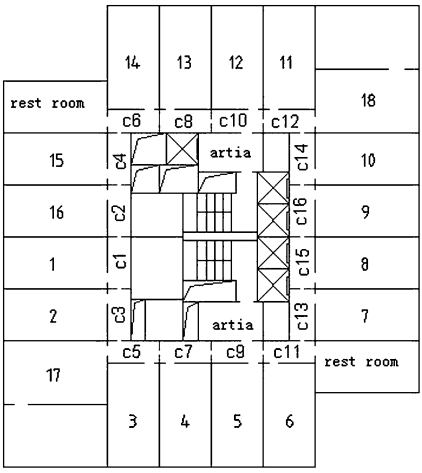

Fig. 10.1 Floor plan of building in simulation

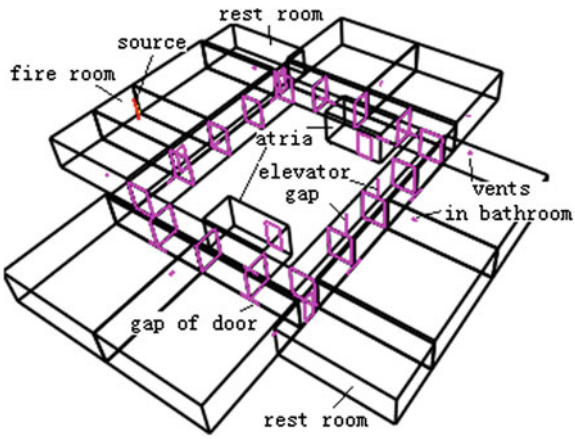

Fig. 10.2 3D view of model in simulation

The study showed that with the increase in the fire room door's open size, the peak of HRR increased [1]. The corresponding smoke speed, temperature and concentration of the flue gas would also increase. After the fire, if a non-fire room door opened, it would save a certain amount of smoke. In this article, the condition of fire room with door fully open and non-fire room with door fully closed was simulated.

The door from corridor to atria was always closed, only opened for a short time for evacuation through the doors. According to provisions in GB50045-95, the door to atria should be kept at a wind speed of 0.7 m/s to block the intrusion of smoke when opening. When the door opened, the influx of air from atria to corridor would improve the pressure of lower layer air, which could accelerate the exhaust of the smoke. There were several factors that were considered in the simulation, as infiltration of doors and exhaust windows in bathroom, in order to maximize and reflect the real situation of the hotel building. The model was reasonable and simplified as shown in Fig. 10.2, also considering the limit of CFAST settings [2]. Relative size of opening and leakage were shown in Table 10.1.

There were several factors under analyzing, such as the arrangement of smoke vents, quantity of smoke vents, the volume of smoke exhaust, the position of the smoke vents and height of ceiling indoor. With intent of providing more accurate results, the loop corridor was divided into several regions [3], and contour vents were set between regions. These vents were set with the same dimensions of the length and height of corridor. There were 16 regions that were divided and named

Table 10.1 Size of gap under considering

	Width of gap of the door/m	Width of gap of the elevator door/m	Size of vents in bathroom/m × m
Size	0.015	0.030	0.12 × 0.12

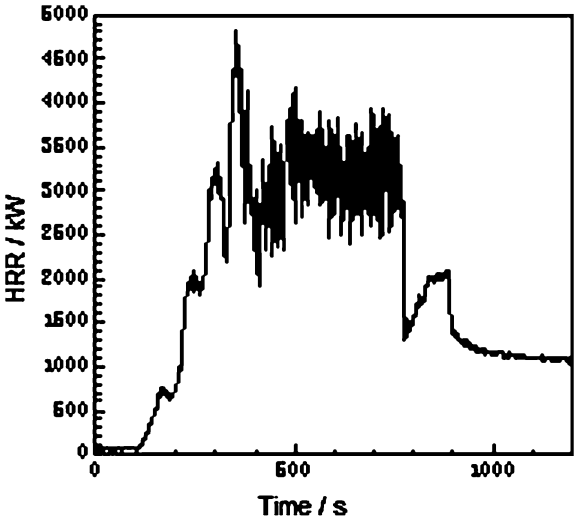

Fig. 10.3 Input parameters of HRR

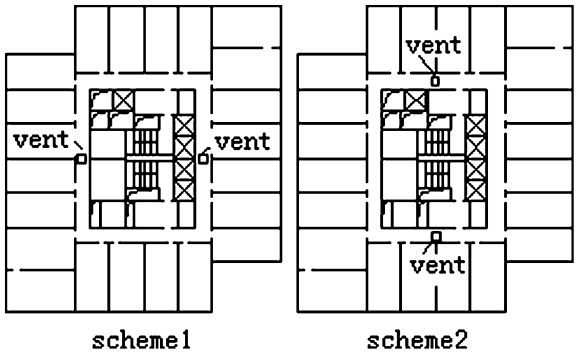

Fig. 10.4 Two schemes under simulation

by c1, c2… c16. And c1, c3, c5… c15 were called access1 and c2, c4, c6… c16 were called access2. Height of smoke layer interface is used to evaluate the effect of smoke exhaust, which was less than 1.5 m, considered to be safe.

Fire development in fire room was simulated by FDS. Heat release rate (HRR) was set as Fig. 10.3 by calculations of FDS, which was transmitted to CFAST. Smoke spread was simulated by CFAST. The simulation time was 1,200 s. Height of smoke layer interface was used to evaluate the effect of smoke exhaust, with the limit of 1.5 m. Different schemes were set (in Fig. 10.4), the exhaust vent was located in the ceiling at the height of 2.5 m and exhaust system parameter settings are shown in Table 10.2.

Table 10.2 Exhaust system parameter settings

Exhaust volume per unit area/m^3/h	Exhaust volume/m^3/h	Exhaust velocity of each vent/m^3/s
40	8,600	1.20
60	13,000	1.80
80	17,200	2.39

10.2 Analyzing Simulation Results

10.2.1 Impact of Exhaust Vents Arrangement

The simulations were made by two schemes, as shown in Fig. 10.4. In the first scheme, the exhaust vents were set further away from the entrance to atria, than the second scheme. Exhaust volume per unit area was set with 60 m^3/h. The results of two schemes simulated were represented in Fig. 10.5.

As seen in the results, in the two exhaust schemes, the smoke layer interface could maintain a safe altitude above, which could ensure the safe evacuation. Combined with the architectural pattern demonstrable, the first scheme was better than the second. In the first scheme, exhaust vents were located away from the exits to the atria, which benefited cooperation of the pressurization system in atria.

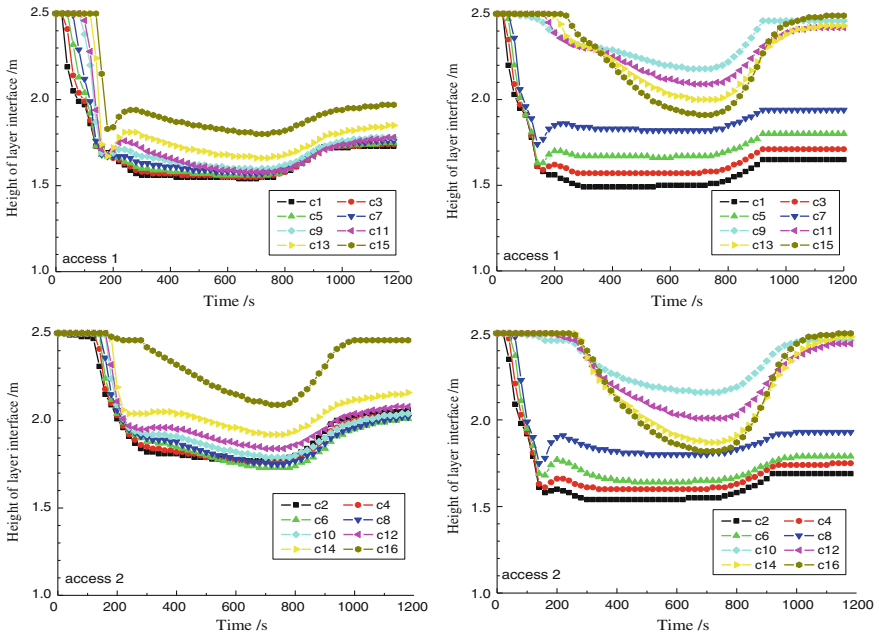

Fig. 10.5 Smoke exhaust effect comparison with different projects (*Left* scheme1, *Right* scheme2)

Especially when the atria door was opened in a short time for the evacuation of staff, it was easy to form a reasonable airflow organization. The pressure distribution of the corridor along the persons' evacuation increased. Control of the smoke concentration near the exits was conducive to the evacuation.

In addition, it was found in the domestic experiments that, when the mechanical exhaust system was running, there would be smoke gathered in the exhaust vents, seriously affecting people to identify safe evacuation export position, and also affecting people who went through the security exit. Therefore, the exhaust vents are supposed to be designed as far as possible from the evacuation exit.

10.2.2 Impact of Smoke Exhaust Volume

The simulations were made under scheme1, using exhaust volume per unit area set with 40 m^3/h and 80 m^3/h separately. The resulting curves are shown in Fig. 10.6. Compared with the two situations, when the smoke exhaust volume was small, a large number of flue gas gathered in the corridor, and smoke layer interface within the entire corridor was relatively low. Under the exhaust volume per unit area set

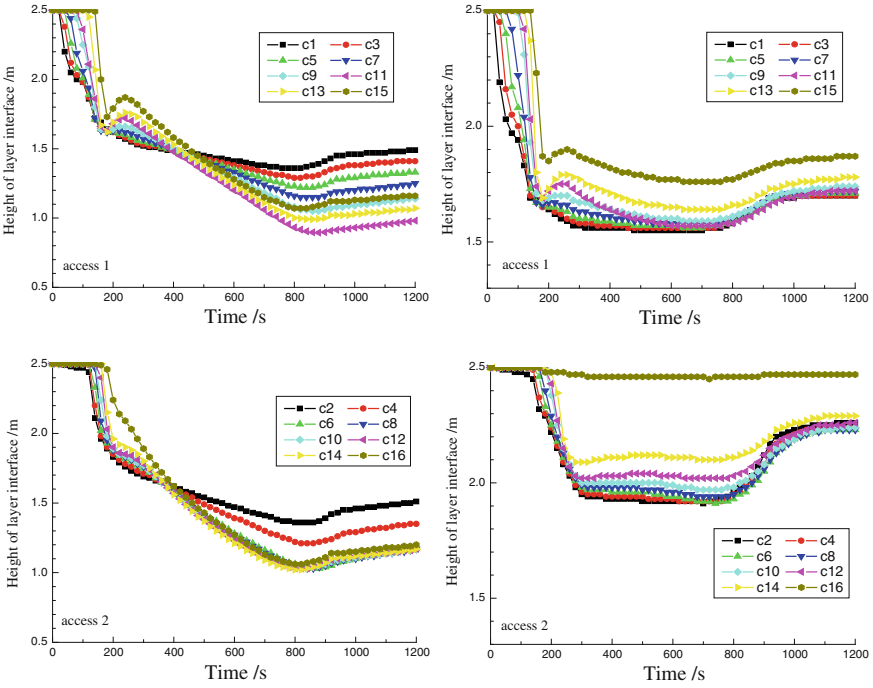

Fig. 10.6 Smoke exhaust effect with changing exhaust volume per unit area (*Left* 40 m^3/h, *Right* 80 m^3/h)

with 40 m^3/h, smoke layer could be reduced to close to floor. Compared with the curves in Fig. 10.5 which set exhaust volume per unit area as 60 m^3/h, when it increased to 80 m^3/h, the smoke layer interface height of access1 increased little, of which smoke layer interface was located between 1.5 and 2.0 m height. In access2, as the smoke exhaust volume added, smoke effect is improved obviously. Smoke layer interface of access2 could be increased to more than 1.9 m.

10.2.3 Impact of Location of Exhaust Vents

The simulations were made under scheme1 with exhaust volume per unit area as 60 m^3/h, with the exhaust vents set in the ceiling or in side wall. When vents were in the side wall, middle point of the vents was 2.0 m in height, and the results were shown in Fig. 10.7. As seen in curves, whether the vents set in ceiling or in side wall, smoke exhaust effect of the two cases could satisfy people's evacuation safety conditions. It was because, in scheme1, the vents were set symmetrically. One of them was nearby the fire room, and another vent was located in the area that was far away from the fire room. Though the area was far away from the fire room, the smoke layer interface would reduce because the smoke temperature was brought down by cooling. Due to the pumping action of the exhaust vents, the smoke layer interface was able to maintain a certain height. Mechanical exhaust affects the entire corridor.

10.2.4 Impact of Ceiling Height

There were always a large number of lines, water pipes, duct laying in the ceiling of corridor, which lead to the construction of ceiling at low altitudes, maybe less than 2.5 m. This would greatly affect much of the mechanical smoke exhaust.

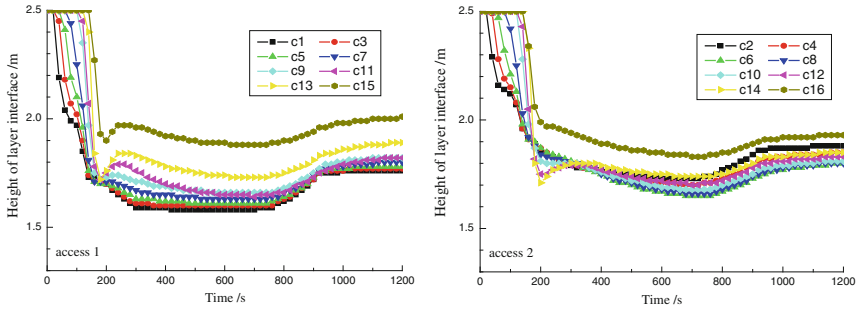

Fig. 10.7 Smoke exhaust effect comparison with exhaust vents in side wall

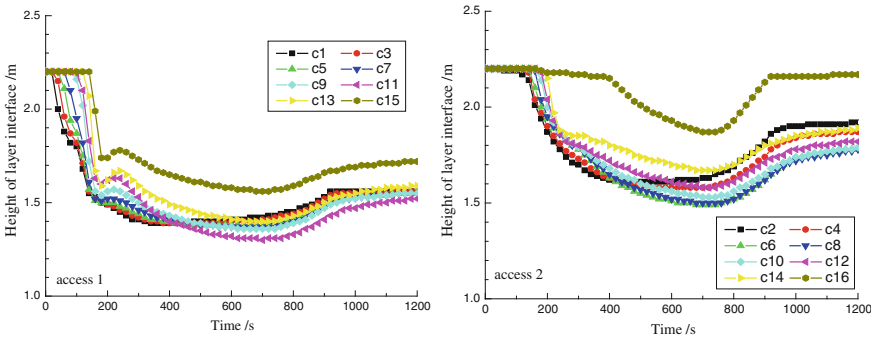

Fig. 10.8 Smoke exhaust effect with ceiling height changed as 2.2 m (Scheme1, vents in ceiling)

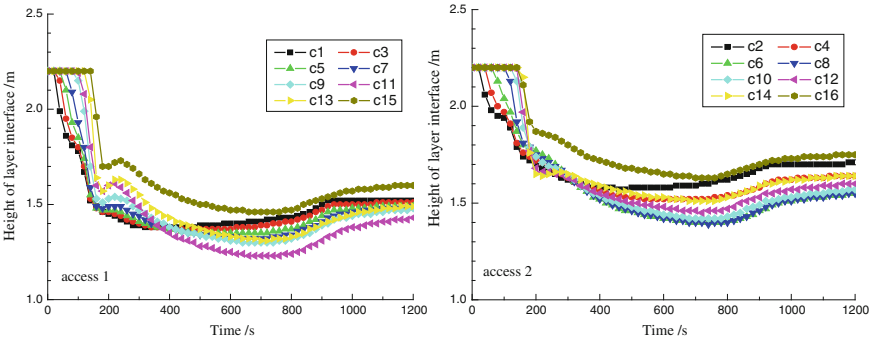

Fig. 10.9 Smoke exhaust effect with ceiling height changed as 2.2 m (Scheme1, vents in side wall)

The simulations were made by changing the height of the ceiling, with a lower height of 2.2 m. The exhaust vents were set in ceiling and side wall, with the exhaust volume per unit area as 60 m^3/h. When the vents were in the side wall, middle point of the vents was 1.8 m in height. The simulation results are shown in Figs. 10.8, 10.9.

In contrast, when the ceiling height was 2.2 m and the vents were in ceiling, smoke layer interface height of the regional decline overall in the corridor. Smoke layer interface of most areas of access1 had been reduced to between 1.3 and 1.5 m. Compared with the results of 2.5 m of ceiling height, it was found that after reducing the ceiling height, the evacuation of people in the building would be threatened. In Fig. 10.9, the vents were in the side wall and the smoke layer height of most of the area within the corridor fell below 1.5 m, mainly distributed in the 1.2–1.5 m, which was difficult to guarantee the safe evacuation. Smoke exhaust vents in sidewall should not be used at this time. Therefore, to recommend to the GB50045-95, the exhaust vents location should require the height of vents and ceiling top be minimum, to ensure the effective operation of the mechanical exhaust system.

10.3 Conclusions

The conclusions were obtained as followed. When two exhaust vents were set symmetrically in the loop corridor, one of which was located nearby the fire room, the smoke exhausted better. The volume of smoke exhaust per unit area with 60 m^3/h according to regulations always could ensure safety of smoke exhaust. There would be no further effect with more volume. With the smoke exhaust vents in ceiling, effect of mechanical exhaust would be better than with vents in slide wall. The smoke exhausted worse within the corridor when ceiling height reduced. It was recommended that the ceiling lowest height limit should be provided in correlative regulation.

References

1. Qiu X (2003) Fire numerical simulation in high-rise building. Dissertation for the master degree. Harbin Institute of Technology, Harbin
2. Jones WW, Forney GP, Peacock RD et al (2009) CFAST: consolidated model of fire growth and smoke transport (Version 6). Technical reference guide, vol 1026, NIST SP, pp 13–17
3. Long-hua HU, Ran HUO, Bin YAO et al (2003) Preliminary study on engineering method to predict smoke movement in very long-narrow spaces with two closing ends. Fire Saf Sci 12(1):36–39

Chapter 11
The Effect of Fresh Air Opening Locations on Natural Ventilation and Thermal Environment in Industrial Workshop with Heat Source

Yaxin Su and Chao Miao

Abstract The buoyancy-driven natural ventilation was numerically simulated based on computational fluid dynamics (CFD) method in a typical industrial plant with heat source. Heat stress index (HSI) was used to evaluate the thermal environment. The influence of fresh air opening locations, i.e., the distance between fresh air opening and ground, H, on the natural ventilation performance and thermal environment was discussed. Results showed that when the distance between fresh air inlet and ground increased from 0.3 to 1.2 m, the ventilation rate and the air velocity in working zone increased, the convection heat loss from human body changed very slightly, the radiation heat received by human body decreased obviously, and the required sweat rate decreased. The HIS decreased as H increased and the allowed exposure time of workers to continuously work increased. Therefore, when there is a heat source above the ground in the workshop, it is helpful to improve the thermal environment by increasing the distance between the fresh air inlet and ground.

Keywords Industrial workshop · Natural ventilation · Thermal environment · Heat stress index · Numerical simulation

11.1 Introduction

Natural ventilation has been widely applied to both industrial plants and variable buildings as a passive ventilation technology. Many authors conducted both experimental investigation and theoretical modeling on natural ventilation in laboratory-scale building models and commercial buildings [1–5]. Natural

Y. Su (✉) · C. Miao
School of Environmental Science and Engineering, Donghua University, Shanghai, China
e-mail: suyx@dhu.edu.cn

A. Li et al. (eds.), *Proceedings of the 8th International Symposium on Heating, Ventilation and Air Conditioning*, Lecture Notes in Electrical Engineering 263,
DOI: 10.1007/978-3-642-39578-9_11,

ventilation is usually adopted in many workshops, e. g., iron and steel processing workshops, due to its energy-saving merit. Generally, natural ventilation is suitable for workshops with heat sources due to the large air temperature difference inside and outside of the workshop which forms the thermal pressure. However, very little papers are available to report the natural ventilation performance of workshops.

Reliable information on the air flow and the pressure distribution around and inside a naturally ventilated building is very important for a reasonable design and could be obtained by experimental test on full-scale measurements [6, 7]. However, most of the tests are conducted on small-scale models in laboratory due to the cost and difficulties in full-scale test. Computational fluid dynamics (CFD) simulation to predict the internal air flow and temperature field inside buildings has increased dramatically in the last two decades and has become a powerful tool for engineering design and understanding of the mechanism of natural ventilation. CFD-based simulation could provide detailed description of the air flow, temperature, and pressure distribution inside the buildings, and more and more CFD simulation has been carried out recently to investigate the natural ventilation [8–10].

The assessment of thermal environment is important to evaluate the design of natural ventilation. The thermal environment is rather uncomfortable in an industrial workshop with a strong heat source. The traditional indexes, such as the predicted mean vote (PMV) and predicted percentage of dissatisfied (PPD) [11], are not suitable to describe the thermal environment in the workshop. Heat stress index (HSI) will be introduced as a thermal index to evaluate the thermal environment.

The present study presents the CFD simulation of the buoyancy-driven natural ventilation in an industrial workshop with heat source. The effect of fresh air opening locations, i.e., the distance between fresh air inlet and ground, on the natural ventilation performance and thermal environment will be discussed.

11.2 Model and Method

Figure 11.1 presents a typical workshop in Shanghai, China, which is $50 \times 30 \times 10$ m (length $\times$ width $\times$ height). The heat source size was set in the right center of the workshop and its size was $40 \times 7 \times 1.5$ m (length $\times$ width $\times$ height). There are two fresh air openings on the left and right sides of the workshop wall, as noted '1' in Fig. 11.1. The height of fresh air opening is $h_1 = 3$ m. The distance between fresh air opening and ground is noted as H, which is a variable parameter in this study. There is a skylight on the workshop ceiling with two air outlets on each side, as noted as '2' in Fig. 11.1. Its height is noted as h_2. The width of the skylight is noted as 'W.' In the present simulation, $h_2 = 1.0$ m and $W = 7.0$ m. Fresh air comes into the workshop from the two fresh air openings and is heated when it flows over the heat source. The heated air rises to exit from the skylight air outlets to outdoor.

The basic conservation equations for the air flow were numerically solved by the Fluent 6.3 CFD code [12]. For a steady incompressible flow, the time-averaged

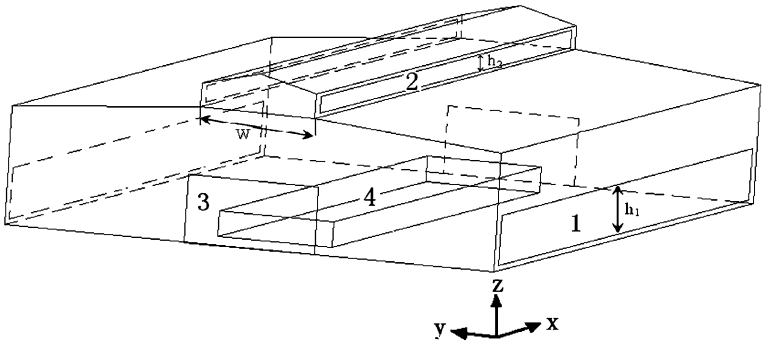

Fig. 11.1 Sketch of workshop *1*: fresh air opening; *2*: air outlet; *3*: workshop entrance; *4*: heat sources)

continuity equation and the Reynolds-averaged Navier–Stokes equations in Cartesian coordinates can be referred to textbooks. Realizable $k - \varepsilon$ turbulent model [13] was selected for the CFD calculation after several trial calculations and comparison to related experimental data. Full buoyancy effects were added to the realizable $k - \varepsilon$ turbulent model. Discrete ordinate (DO) radiation model was used to calculate the radiation heat transfer. The emissivity of the wall surface was set as 0.85. The boundary condition for the upwind side of the workshop was set at velocity inlet condition, while the boundary condition for the leeward side of the workshop was set at pressure inlet condition. Free outflow condition was set at air outlet. Standard wall function was used for the near wall calculation. Grid refinement was locally adopted near the heat source, air outlet, and air inlet. Hexahedral cell was used to mesh the whole workshop space except the region near the skylight where the tetrahedral cell was adopted.

11.3 Results

The calculation was carried out with second-order upwind scheme for the discretization and SIMPLEC algorithm. Grid-independent results were ensured during the calculation trial. Three grids were used for the trial calculation, i.e., a total mesh cells of 420.000, 850.000, and 1,160. 000, respectively. The calculated ventilation rates for the 3 grids were 76. 8, 78.9, and 78.2 kg/s. The difference of the ventilation rate between the grids of 850,000 and 1,160.000 was very small, and therefore, the grid system of 850 000 mesh cells was finally adopted for the simulation. The comparison of the tested air temperature by Deng et al. [14] in a steel wire production workshop and the present CFD calculated temperatures validated the present CFD model that can be used to further simulate the natural ventilation in the workshop(see [15]).

11.3.1 Ventilation Performance

The ventilation performance relates to several parameters, including the ventilation rate, the air velocity and temperature in the working zone, and the pollutant concentration distribution. These parameters were calculated when the distance between fresh air inlet and ground, H, varied from 0.3 to 1.2 m, and Table 11.1 presents the results.

Results showed that the calculated ventilation rate listed in Table 11.1 increased when the distance between fresh air inlet and ground, H, increased from 0.3 to 1.2 m. When H increased from 0.3 to 0.8 m, the ventilation rate increased 2.27 %. When H increased further, the ventilation rate increased only very slightly. According to the principle of natural ventilation due to thermal pressure [16], the thermal pressure difference between the indoor and outdoor air is in proportion to the altitude difference between the air inlet and outlet openings, i.e., the larger the altitude difference is, the more ventilation the rate becomes. According to this theory, the natural ventilation rate will decrease when the distance between fresh air opening and ground increases. However, in the present study, there is a heat source that is 1.5 m above the ground. When the air inlet opening lies in a lower position, e.g., $H = 0.3$ m, the fresh air entering the workshop will be partly blocked by the heat source. When H increases, the fresh air enters into the workshop and will directly flow over the heat source and be heated to rise. So, the ventilation rate will increase as H increases. The location of fresh air opening has generally only a moderate effect on the ventilation rate, which agrees with Ref [17].

The mean air velocity in the working zone, u, increased as the distance between fresh air inlet and ground increased. As listed in Table 11.1, u increased by 7.4, 6.8, and 13.3 %, respectively, when H increased from 0.3 to 0.5, 0.8, and 1.0 m. When H exceeded 1.0 m, u increased very slightly. The air flow pattern in the workshop is shown in Fig 11.2. When H increased, the air above the heat source rose at a higher velocity; this is because more fresh air could directly flow over the heat source as it entered the workshop when H is higher.

The mean air temperature in working zone increased very slightly when H increased, as listed in Table 11.1. When H increased, the amount of air that flows over the heat source increased. At the same time, the air velocity in the working zone also increased, while the air temperature in working zone kept almost unchanged, which suggested that the worker would fell more comfortable due to the improved natural 'wind' there.

Table 11.1 Ventilation performance

Distance between fresh air opening and ground, H (m)	1.2	1.0	0.8	0.5	0.3
Ventilation rate, G(kg/s)	80.06	79.18	79.60	77.96	77.83
Mean air velocity in working zone, u(m/s)	0.336	0.335	0.303	0.290	0.268
Mean air temperature in working zone, T_a(K)	305.79	305.58	305.69	305.39	305.34

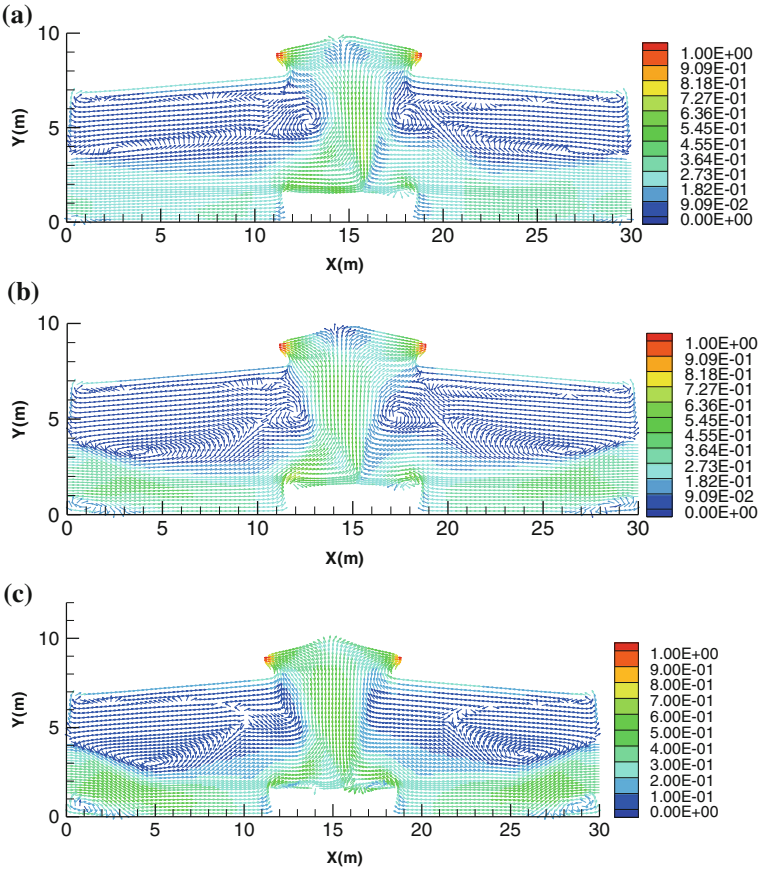

Fig. 11.2 Air flow patterns versus distance between fresh air inlet and ground, *H*. (**a**) $H = 0.3$ m; (**b**) $H = 0.8$ m; (**c**) $H = 1.2$ m

11.3.2 Thermal Environment

Belding and Hatch [18] proposed a climatic index based on the energy balance, i.e., the HSI. Although some researchers claimed that HIS is rather a step toward a useable index for evaluating climatic conditions rather than an established climatic index that is applicable in practice [19], HIS was considered as one major index to assess the thermal comfort and sensation in hot environment by ISO [20], and many authors conducted further modification on the calculation method of required sweat rate for HSI [21]. HIS is used in the present study to calculate the thermal environment since there are no any other better methods. Table 11.2 lists the parameters and the calculation formulas for HIS. The maximum evaporation loss, E_{max}, is set at 390 W/m^2, which equals to the sweat rate of a man, about 1L/h. If $E_{req} > E_{max}$, human body could not keep body thermal balance and the body

Table 11.2 Parameters and the calculation formulas for HSI (naked)

Parameters	Calculation formula
Radiation loss, R(W/m^2)	7.3(35-T_{MRT})
Convection loss, C(W/m^2)	7.6u$^{0.6}$(35-T_a)
Maximum *evaporation loss,* E_{max} (W/m^2)	11.7u$^{0.6}$(56-P_a)
Required sweat rate, E_{req} (W/m^2)	E_{req} = M-R–C
HSI (%)	HIS = E_{req}/E_{max} × 100 %
Allowed exposure time, AET (min)	AET = 2,440/(E_{req} − E_{max})

Note T_{MRT}/T_a: working zone mean radiation temperature/averaged temperature,°C; u: working zone-averaged air velocity, m/s; P_a: water vapor partial pressure in the air, Pa; M: metabolic heat generation in human body, W/m^2 , when doing moderate physical work, M = 123 W/m^2 [22]. Assume that human skin keeps constantly 35 °C, heat loss by breathing ignored. Water vapor partial pressure in the air is set at 3,200 Pa

temperature will rise. It is impossible to work for a long time in such a thermal environment.

Table 11.3 lists the calculated HSI parameters in the working zone ($Z \leq 2$ m). In Table 11.3, when the heat loss is positive, it means that human body dissipates heat; when the heat loss is negative, it means that human body receives heat. The larger the absolute of the heat is, the more the dissipated or received heat is. The convection heat loss depends on the air temperature and velocity in the working zone. The calculated convection heat loss from human body changed very slightly. The radiation heat loss completely relates to the inner surface temperature of the workshop. As H increased, the ventilation increased and more waste heat was brought away by the ventilation. The inner surface temperature of the workshop then decreased; as listed in Table 11.3, there was about 5.5 °C drop of the working zone mean radiation temperature when H increased from 0.3 to 1.2 m. Hence, the human body received less radiation heat, about a reduction of 32.85 W/m^2 radiation heat when H increased from 0.3 to 1.2 m. This result suggested that the necessary heat dissipation from human body decreased and led to a decreased required sweat rate. In addition, the water vapor partial pressure in the air is

Table 11.3 Effect of fresh air opening location on HSI

Distance between fresh air opening and ground, H (m)	1.2	1.0	0.8	0.5	0.3
Working zone mean temperature, T_a(K)	305.79	305.58	305.69	305.39	305.34
Working zone mean radiation temperature, T_{MRT} (°C)	42.60	43.70	44.61	45.89	47.10
Mean air velocity in working zone, u (m/s)	0.336	0.335	0.303	0.290	0.267
Radiation heat loss, R (W/m^2)	−55.48	−63.51	−70.15	−79.5	−88.33
Convection heat loss, C (W/m$^{2)}$	8.73	9.54	8.58	9.44	9.15
Maximum evaporation loss, E_{max} (W/m^2)	145.95	145.69	137.17	133.61	127.15
Required sweat rate, E_{req} (W/m^2)	169.75	177.00	184.58	193.07	202.18
HSI (%)	116.31	121.49	134.56	144.51	159.01
Allowed exposure time, AET (min)	102.52	77.93	51.47	41.03	32.52

assumed constant, so the maximum evaporation loss of human body depends totally on the air velocity and is directly proportional to the air velocity. When H increased, the mean air velocity in working zone increased, and therefore, the maximum evaporation loss of human body increased, which suggested that human could dissipate more heat through sweat evaporation. The radiation heat loss and the required sweat rate had the decisive effect on the reduction in HSI. HSI decreased as H increased and the allowed exposure time of workers to continuously work increased. Therefore, when there is a heat source above the ground in the workshop and the fresh air opening location lies in a lower position, it is helpful to improve the thermal environment by increasing the distance between fresh air inlet and ground.

11.4 Conclusion

Results based on CFD calculation of the natural ventilation in the workshop with heat source showed that the location of fresh air opening had important influence on the ventilation performance. Results showed that when the distance between fresh air inlet and ground increased from 0.3 to 1.2 m, the ventilation rate and the air velocity in working zone increased, the convection heat loss from human body changed very slightly, the radiation heat received by human body decreased obviously, and the required sweat rate decreased. The HIS decreased as H increased and the allowed exposure time of workers to continuously work increased. Therefore, when there is a heat source above the ground in the workshop, it is helpful to improve the thermal environment by increasing the distance between fresh air inlet and ground.

Acknowledgments The work was supported by National Natural Science Foundation (No. 51278095) and Shanghai Natural Science Foundation (No.11ZR1401000).

References

1. Andersen KT (1995) Theoretical considerations on natural ventilation by thermal buoyancy. Ashrae Trans 101(2):1103–1117
2. Li Y (2000) Buoyancy-driven natural ventilation in a thermally stratified one-zone building. Build Environ 35:207–214. doi:10.1016/S0360-1323(99)00012-8
3. Chen ZD, Li Y (2002) Buoyancy-driven displacement natural ventilation in a single-zone building with three-level openings. Build Environ 37:295–303. doi:10.1016/S0360-1323(01)00021-X
4. Ei-Agou SAZ (2008) The effect of internal heat source and opening locations on environmental natural ventilation. Energy Build 40:409–418. doi:10.1016/j.enbuild.2007.03.009
5. Letan R, Dubovsky V, Ziskind G (2003) Passive ventilation and heating by natural convection in a multi-storey building. Build Environ 38:197–208. doi:10.1016/S0360-1323(02)00070-7

6. Koinakis CJ (2005) Combined thermal and natural ventilation modeling for long-term energy assessment: validation with experimental measurements. Energy Build 37:311–323. doi:10.1016/j.enbuild.2004.06.022
7. Straw MP, Baker CJ, Robertson AP (2000) Experimental measurements and computations of the wind-induced ventilation of a cubic structure. J Wind Eng Ind Aerodyn 88:213–230. doi:10.1016/S0167-6105(00)00050-7
8. Gan G (2010) Simulation of buoyancy-driven natural ventilation of buildings—impact of computational domain. Energ Build 42:1290–1300. doi:10.1016/j.enbuild.2010.02.022
9. Gan G (2010) Impact of computational domain on the prediction of buoyancy-driven ventilation cooling. Build Environ 45:1173–1183. doi:10.1016/j.buildenv.2009.10.023
10. Jiang Y, Chen Q (2001) Study of natural ventilation in buildings by large eddy simulation. J Wind Eng Ind Aerodyn 89:1155–1178. doi:10.1016/S0167-6105(01)00106-4
11. Fanger PO (1970) Thermal comfort. Danish Technical Press, Copenhagen
12. Inc Fluent (2005) FLUENT user's guide. New Hampshire, USA
13. Shih TH, Liou WW, Shabbir A et al (1995) A new k-ε eddy viscosity model for high Reynolds number turbulent flows. Comput Fluids 24:227–238. doi:10.1016/0045-7930(94)00032-T
14. Deng G, Zhang D, Li K (2004) Numerical simulation and experimental research of natural ventilation in heat workshop (in Chinese). Build Energ Environ 2(23):70–73
15. Su Y, Wan X (2012) CFD simulation and retrofit of natural ventilation in a steel workshop. Adv Mater Res 383–390:6608–6613. doi:10.4028/www.scientific.net/AMR.383-390.6608
16. Sun YJ (1994) Industrial ventilation, 3rd edn. China Architecture & Building Press, Beijing
17. Zhao HZ (2010) Indoor convection and ventilation. China Architecture & Building Press, Beijing
18. Belding HS, Hatch TF (1955) Index for evaluating heat stress in terms of resulting physiological strains. Heat Piping Air Cond 27:29–136
19. Kampmann B, Piekarski C (2000) The evaluation of workplaces subjected to heat stress: can ISO 7933 (1989) adequately describe heat strain in industrial workplaces? Appl Ergon 31:59–71
20. ISO 7933(1989) Hot environments—analytical determination and interpretation of thermal stress using calculation of required sweat rate. International Organization for Standardization, Geneva
21. Mehnert P, Brode P, Griefahn B (2002) Gender-related difference in sweat loss and its impact on exposure limits to heat stress. Int J Ind Ergon 29:343–351. doi:10.1016/S0169-8141(02)00073-2
22. Huang C (2007) Building environment. Mechanical Industry Press of China, Beijing

Chapter 12
Dynamic Modeling of HVAC System with State-Space Method

Ye Yao, Mengwei Huang and Kun Yang

Abstract The design of an efficient HVAC controller that maintains an anticipated indoor thermal environment at minimum energy consumption largely depends on the availability of a valid dynamic model of the system. This paper presents a state-space-based dynamic model for a HVAC system whose components are mainly air-to-water surface heat exchangers, air-supply ducts and water pipes. Firstly, the dynamic models for the components are developed according to the principle of energy and mass conservation. By introducing the vector–matrix notation, the ordinary differential equations describing the component dynamics are converted into the state-space form. Then, the state-space model for the whole HVAC system is developed based on the component models and model connection algorithms. Afterward, experiments have been performed to verify the HVAC system state-space model in predicting the transient responses of exit air temperature and humidity as well as outlet water temperature of the surface heat exchanger under inlet perturbations. The proposed modeling procedure can be especially useful for the development of the dynamic toolbox for the control design of HVAC system.

Keywords State space · Dynamic modeling HVAC system

12.1 Introduction

The design of successful controllers for HVAC systems primarily depends on the availability of good dynamic models of the systems. Many dynamic models of HVAC components have been developed for control applications [1–5]. In this

Y. Yao (✉) · M. Huang · K. Yang
Institute of Refrigeration and Cryogenics, Shanghai Jiao Tong University, Shanghai 200240, China
e-mail: yeyao10000@sjtu.edu.cn

A. Li et al. (eds.), *Proceedings of the 8th International Symposium on Heating, Ventilation and Air Conditioning*, Lecture Notes in Electrical Engineering 263,
DOI: 10.1007/978-3-642-39578-9_12,

paper, the dynamic models of the HVAC components and the HVAC system are presented in the state-space form. A state-space representation is a mathematical model of a physical system as a set of input, output and state variables related by first-order differential equations. To abstract from the number of inputs, outputs and states, the variables are expressed as vectors. Additionally, if the dynamical system is linear and time invariant, the differential and algebraic equations may be written in matrix form. The state-space representation (also known as the "time-domain approach") provides a convenient and compact way to model and analyze systems with multiple inputs and outputs. The general state-space representation can be found in Ref. [6] for detail.

12.2 Model of HVAC Components

Due to limitations of space, only the state-space models of three HVAC components are presented in this paper. These are the air-to-water heat exchanger, the air-supply duct and the water pipe. The model is firstly formulated with the ordinary differential equations from mass continuity, energy conservation and heat transfer physical fundamentals by using a lumped-parameter formulation and physical relations. These equations are then transformed into a representation form of the state space by using vector–matrix notation and linearization. For the basic modeling procedure with the state-space method, please refer to literature [7].

12.2.1 Water-to-Air Surface Heat Exchanger

According to Ref. [7], the dynamic model of water-to-air heat exchanger can be expressed in the state-space form as below:

$$\dot{x}_{\text{coil}} = A_{\text{coil}} \cdot x_{\text{coil}} + B_{\text{coil}} \cdot u_{\text{coil}} \tag{12.1}$$

$$y_{\text{coil}} = C_{\text{coil}} \cdot x_{\text{coil}} + D_{\text{coil}} \cdot u_{\text{coil}} \tag{12.2}$$

For dry-condition process: $x_{\text{coil}} = [\Delta t_{w,L}, \Delta t_{a,L}, \Delta t_g]^T$; $y_{\text{coil}} = [\Delta t_{w,L}, \Delta G_{w,L} \Delta t_{a,L}, \Delta W_{a,L}, \Delta G_{a,L}]^T$; $u_{\text{coil}} = [\Delta t_{w,E}, \Delta G_{w,E}, \Delta t_{a,E}, \Delta W_{a,E}, \Delta G_{a,E}]^T$ For wet-condition process: $x_{\text{coil}} = [\Delta t_{w,L}, \Delta t_{a,L}, \Delta W_{a,L}, \Delta t_g]^T$; $y_{\text{coil}} = [\Delta t_{w,L}, \Delta G_{w,L}, \Delta t_{a,L}, \Delta W_{a,L}, \Delta G_{a,L}]^T$; $u_{\text{coil}} = [\Delta t_{w,E}, \Delta G_{w,E}, \Delta t_{a,E}, \Delta W_{a,E}, \Delta G_{a,E}]^T$.

The matrixes, A_{coil}, B_{coil}, C_{coil} and D_{coil}, are related to the physical structure of heat exchanger and initial conditions.

12.2.2 Air-Supply Duct

The following equations can be obtained based on the law of mass and energy conservation.

Mass equation for the air flow:

$$G_{da,L} = G_{da,E} = G_{da} \tag{12.3}$$

Energy equation for the air:

$$\begin{aligned}\frac{1}{2}\rho_a A_d l_d \frac{d\left(h_{da,L} + h_{da,E}\right)}{d\tau} &= G_{da,E}\left(h_{da,E} - h_{da,L}\right) + a_{da}A_{da}\left(t_{dg} - \frac{t_{da,E} + t_{da,L}}{2}\right) \\ &+ q_r \lambda_m A_{da}\left(W_{db} - \frac{W_{da,E} + W_{da,L}}{2}\right)\end{aligned} \tag{12.4}$$

Moisture equation for the air:

$$\begin{aligned}\frac{1}{2}\rho_a A_d l_d \frac{d(W_{da,L} + W_{da,E})}{d\tau} &= G_{da,E}(W_{da,E} - W_{da,L}) \\ &+ \lambda_m A_{da}\left(W_{db} - \frac{W_{da,E} + W_{da,L}}{2}\right)\end{aligned} \tag{12.5}$$

Energy equation for the air duct:

$$\begin{aligned}c_{dg}M_{dg}\frac{dt_{dg}}{d\tau} &= \frac{l_d}{R_{dg}}(t_{env} - t_{dg}) + a_{da}A_{di}\left(\frac{t_{da,E} + t_{da,L}}{2} - t_{tg}\right) \\ &+ q_r \lambda_m A_{di}\left(\frac{W_{da,E} + W_{da,L}}{2} - W_{db}\right)\end{aligned} \tag{12.6}$$

After linearization, Eqs. (12.3) through (12.6) can be transformed into the state-space representation as follows:

$$\dot{x}_{\text{zduct}} = A_{\text{zduct}} \cdot x_{\text{zduct}} + B_{\text{zduct}} \cdot u_{\text{zduct}} \tag{12.7}$$

$$y_{\text{zduct}} = C_{\text{zduct}} \cdot x_{\text{zduct}} + D_{\text{zduct}} \cdot u_{\text{zduct}} \tag{12.8}$$

where, $x_{\text{zduct}} = [\Delta t_{da,L}, \Delta W_{da,L}, \Delta t_{dg}]^T$; $y_{\text{zduct}} = [\Delta t_{da,L}, \Delta W_{da,L}, \Delta G_{da,L}]^T$; $u_{\text{zduct}} = [\Delta t_{da,E}, \Delta W_{da,E}, \Delta G_{da,E}]^T$. The matrixes, A_{zduct}, B_{zduct}, C_{zduct} and D_{zduct}, are related to the physical structure of air duct and initial conditions.

12.2.3 Water Pipe

Mass equation for the water flow:

$$G_{zpw,L} = G_{zpw,E} = G_{zpw} \tag{12.9}$$

Energy equation for the water:

$$\frac{1}{2}\rho_w c_w A_p l_p \frac{d(t_{pw,L}+t_{pw,E})}{d\tau} = G_{pw,E}(t_{pw,E}-t_{pw,L}) + a_{pw}A_{pi}\left(t_{pg}-\frac{t_{pw,E}+t_{pw,L}}{2}\right) \tag{12.10}$$

Energy equation for the water pipe:

$$c_{pg}M_{pg}\frac{dt_{pg}}{d\tau} = \frac{l_p}{R_{pg}}(t_{env}-t_{pg}) + a_{pw}A_{pi}\left(\frac{t_{pw,E}+t_{pw,L}}{2}-t_{pg}\right) \tag{12.11}$$

After linearization, Eqs. (12.3) through (12.6) can be transformed into the state-space representation as follows:

$$\dot{x}_{\text{zpipe}} = A_{\text{zpipe}} \cdot x_{\text{zpipe}} + B_{\text{zpipe}} \cdot u_{\text{zpipe}} \tag{12.12}$$

$$y_{\text{zpipe}} = C_{\text{zpipe}} \cdot x_{\text{zpipe}} + D_{\text{zpipe}} \cdot u_{\text{zpipe}} \tag{12.13}$$

where, $x_{\text{zpipe}} = [\Delta t_{pw,L}, \Delta t_{pg}]^T$; $y_{\text{zpipe}} = [\Delta t_{pw,L}, \Delta G_{pw,L}]^T$; $u_{\text{zpipe}} = [\Delta t_{pw,E}, \Delta G_{pw,E}]^T$. The matrixes, A_{zpipe}, B_{zpipe}, C_{zpipe} and D_{zpipe}, are related to the physical structure of water pipe and initial conditions.

12.3 Model of HVAC System

12.3.1 Component Model Connection

The HVAC system consists of numerous components, which are often in parallel or series connection (Please see Fig. 12.1). In Fig. 12.1, the components S_1 and S_2 are expressed, respectively, by Eqs. (12.14) and (12.15).

$$\text{Component } S_1 : \begin{cases} \dot{x}_1 = A_1 x_1 + B_1 u \\ y_1 = C_1 x_1 + D_1 u_1 \end{cases} \tag{12.14}$$

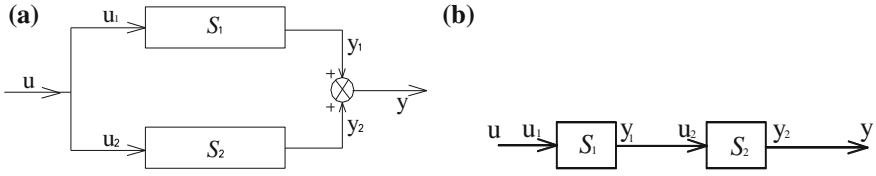

Fig. 12.1 Schematic diagram for the component model connection. **a** Parallel connection. **b** Series connection

$$\text{Component } S_2 : \begin{cases} \dot{x}_2 = A_2 x_2 + B_2 u_2 \\ y_2 = C_2 x_2 + D_2 u_2 \end{cases} \tag{12.15}$$

12.3.1.1 Parallel Connection

If the output vector of components S_1 and S_2 shares the same parameter type and dimension, then the output vector of the parallel system can be written as $[y] = [y_1] + [y_2]$. In such case, the state-space model of the parallel system can be obtained as follows:

$$\begin{bmatrix} \dot{x}_1 \\ \dot{x}_2 \end{bmatrix} = \begin{bmatrix} A_1 & 0 \\ 0 & A_2 \end{bmatrix} \cdot \begin{bmatrix} x_1 \\ x_2 \end{bmatrix} + \begin{bmatrix} B_1 & 0 \\ 0 & B_2 \end{bmatrix} \cdot \begin{bmatrix} u_1 \\ u_2 \end{bmatrix} \tag{12.16}$$

$$y = \begin{bmatrix} C_1 & C_2 \end{bmatrix} \cdot \begin{bmatrix} x_1 \\ x_2 \end{bmatrix} + \begin{bmatrix} D_1 & D_2 \end{bmatrix} \cdot \begin{bmatrix} u_1 \\ u_2 \end{bmatrix} \tag{12.17}$$

If the output vector of components S_1 and S_2 is different from each other in the parameter type and dimension, then the output vector of the parallel system can be written as $[y] = [y_1, y_2]^T$. In such case, the state-space model of the parallel system can be gotten as follows:

$$\begin{bmatrix} \dot{x}_1 \\ \dot{x}_2 \end{bmatrix} = \begin{bmatrix} A_1 & 0 \\ 0 & A_2 \end{bmatrix} \cdot \begin{bmatrix} x_1 \\ x_2 \end{bmatrix} + \begin{bmatrix} B_1 & 0 \\ 0 & B_2 \end{bmatrix} \cdot \begin{bmatrix} u_1 \\ u_2 \end{bmatrix} \tag{12.18}$$

$$[y] = \begin{bmatrix} C_1 & 0 \\ 0 & C_2 \end{bmatrix} \cdot \begin{bmatrix} x_1 \\ x_2 \end{bmatrix} + \begin{bmatrix} D_1 & 0 \\ 0 & D_2 \end{bmatrix} \cdot \begin{bmatrix} u_1 \\ u_2 \end{bmatrix} \tag{12.19}$$

12.3.1.2 Series Connection

It is easily known from Fig. 12.4b that the state-space model of series system can be written as follows:

$$\begin{bmatrix} \dot{x}_1 \\ \dot{x}_2 \end{bmatrix} = \begin{bmatrix} A_1 & 0 \\ B_2 C_1 & A_2 \end{bmatrix} \cdot \begin{bmatrix} x_1 \\ x_2 \end{bmatrix} + \begin{bmatrix} B_1 \\ B_2 D_1 \end{bmatrix} \cdot u \tag{12.20}$$

$$y = \begin{bmatrix} D_2 C_1 & C_2 \end{bmatrix} \cdot \begin{bmatrix} x_1 \\ x_2 \end{bmatrix} + D_2 D_1 u \tag{12.21}$$

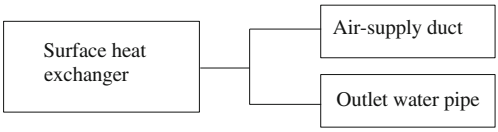

Fig. 12.2 Connection of components in a AHU system for the case study

12.3.2 Case Study

Figure 12.2 gives the schematic diagram of connection of components in a simple AHU system, which consists of the water-to-air heat exchanger, the air-supply duct and the outlet water pipe. According to the method of component model connection, the state-space representation of the system can be obtained as follows:

$$\dot{x}_{\text{sys}} = A_{\text{sys}} X_{\text{sys}} + B_{\text{sys}} \cdot u_{\text{coil}} \tag{12.22}$$

$$Y_{\text{sys}} = Y_{\text{duct\&pipe}} = C_{\text{sys}} \cdot X_{\text{sys}} + D_{\text{sys}} \cdot u_{\text{coil}} - \xi_{Y\text{sys}} \tag{12.23}$$

where $X_{\text{sys}} = \begin{bmatrix} X_{\text{coil}} \\ X_{\text{duct\&pipe}} \end{bmatrix}$; $A_{\text{sys}} = \begin{bmatrix} A_{\text{coil}} & 0 \\ B_{\text{duct \& pipe}} C_{\text{coil}} & A_{\text{duct \& pipe}} \end{bmatrix}$; $B_{\text{sys}} = \begin{bmatrix} B_{\text{coil}} \\ B_{\text{duct \& pipe}} D_{\text{coil}} \end{bmatrix}$; $C_{\text{sys}} = [D_{\text{duct \& pipe}} C_{\text{coil}} \quad C_{\text{duct \& pipe}}]$; $D_{\text{sys}} = D_{\text{duct \& pipe}} D_{\text{coil}}$.

12.3.3 Experimental Results

An experimental air-conditioning system is built for the system model validation. The system mainly consists of a water-to-air surface heat exchanger, a heat pump (for chilled or hot water supply), a circulating water pump, fans, air ducts and water pipes. The test instruments mainly include the temperature sensors (measurement precision ±0.1 °C), the water flow sensor (accuracy of measurement 0.5 magnitude) and the hotwire anemometer (accuracy of measurement ±2 % reading data). The perturbations of inlet variables of the system are presented in Fig. 12.3. The experimental and calculated results of the change responses of the system exit variables are plotted in Fig. 12.4. As shown in Fig. 12.4, the calculated responses of the system exit variables under the perturbations of inlet variables have a favorable agreement with the experimental ones. The average error of the model calculation is estimated as 12.6, 22.2 and 9.5 %, respectively, for the response of the exit air temperature, the exit air humidity and the exit water temperature of the system.

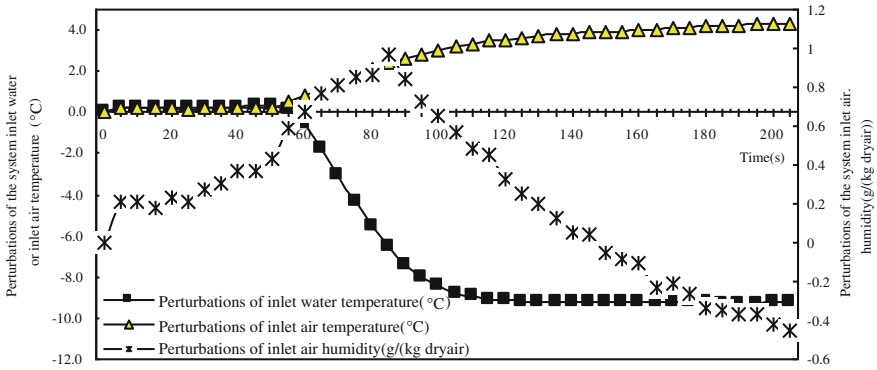

Fig. 12.3 Perturbations of inlet variables of the AHU system

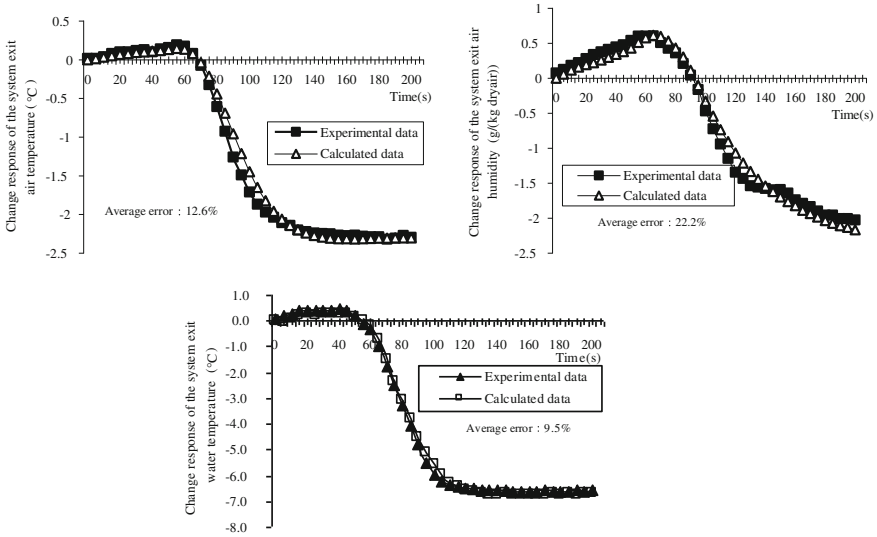

Fig. 12.4 Responses of the AHU system exit variables (experimental versuss calculated)

12.4 Conclusions

The state-space method is employed to develop the dynamic response model of the HVAC system. Basically, the state-space models of the components in the HVAC system should be firstly developed. Then, the system state-space model can be integrated based on the component models according to the model connection method. A case study is given to illustrate the system model development, and experiments have been performed for the model validation. State-space model

developed in this paper will have good applicability in studying the dynamic thermal characteristics and designing good performance control system for the central air-conditioning system.

Acknowledgments This work was supported by a Grant from the National Natural Science Foundation of China (No. 51076100).

References

1. Clark DR, Hurley CW, Hill CR (1985) Dynamic models for HVAC system components. ASHRAE Trans 91(1):737–751
2. Underwood DM, Crawford RR (1990) Dynamic nonlinear modeling of a hot-water-to-air heat exchanger for control applications. ASHRAE Trans 96(1):149–155
3. Kasahara M, Kuzuu Y, Matsuba T, Hashimoto Y, Kamimura K, Kurosu S (2000) Stability analysis and tuning of PID controller in VAV systems. ASHRAE Trans 106(2):285–296
4. Kasahara M, Kuzuu Y, Matsuba T, Hashimoto Y, Kamimura K, Kurosu S (2000) Physical model of an air-conditioned space for control analysis. ASHRAE Trans 106(2):307–317
5. Tashtoush B, Molhim M, Al-Rousan M (2005) Dynamic model of an HVAC system for control analysis. Energy 30(10):1729–1745
6. http://en.wikipedia.org/wiki/State_space_representation
7. Dai S, Mo J, Yao y (2012) Dynamic modeling for surface heat exchanger based on state-space method. J Refrige 33(2):1–6

Chapter 13
Research on Building Configuration Adapt to Natural Ventilation

Weijie Zhang, Yingying Ma, Yu Du and Meiyuan Yang

Abstract To achieve the objective building of low energy consumption and good air quality, the perception of "Natural first and mechanical second" should be highly preferred, and optimization should be started from the inception of the design work. Building configuration that can well adapt to natural ventilation should be paid much more attention to utilize (including control) the natural force as large as possible. In this paper, some building configurations adapt to natural ventilation have been suggested and discussed. Different ventilation effect depends on different thermal pressure has been studied and presented by simulation work. Multi-scheme comparison and optimization have been done by utilizing some evaluation indexes such as time of air exchange, average air age, energy available coefficient, etc. Further, research on regional adaptation has been also done by selecting four different meteorological regions in China from east to west. Based on our research work, some building configurations adapt to natural ventilation can be obtained and demonstrated.

Keywords Building configuration · Adapt to · Natural ventilation · Simulation · Comparison · Regional adaptation

13.1 Introduction

Building environment is very important to peoples' safety, health, thermal pleasure, and productivity. Mechanical approaches are emphasized in our era to artificially create a so-called thermal comfortable building environment that yields great amount of building energy consumption. Reducing building energy consumption to the minimum and meanwhile improving the building environment to the most satisfied state is an urgent and main assignment to architects and building

W. Zhang (✉) · Y. Ma · Y. Du · M. Yang
College of Urban Construction, Hebei University of Engineering, Handan 056038, China
e-mail: zhangweijie_5@sina.com

A. Li et al. (eds.), *Proceedings of the 8th International Symposium on Heating, Ventilation and Air Conditioning*, Lecture Notes in Electrical Engineering 263,
DOI: 10.1007/978-3-642-39578-9_13,

services engineers. Many ideas have been proposed, and many schematic approaches have been suggested in this sphere. Among all of these, the perception of "Natural first and mechanical second" should be highly preferred. To achieve the objective building of low energy consumption and good air quality, optimization should be started from the inception of the design work. Building configuration that can well adapt to natural ventilation should be paid much more attention to utilize (including control) the natural force as large as possible.

Thermal pressure and wind pressure are the motive power of building natural ventilation, and they are not constant and sometimes be unexpected less. Only the resistance of air flow within the building is very small can air be well circulated in the building. So the main problem and the crucial work of building configuration design for natural ventilation is to arrange the air tunnel (or passageway) reasonably including following items: optimal establishment of ventilation shafts and air tunnels including position, number, dimension, wall roughness, etc.; optimal allocation of air inlets and outlets including position, number, dimension, coefficient of resistance, etc. [1]; In order to make the ventilation adjustable, air valves and dampers in the air passageway are necessary.

In this paper, some building configurations adapt to natural ventilation have been suggested and discussed. Different ventilation effect depends on different thermal pressure has been studied and presented by simulation work. Multi-scheme comparison and optimization have been done by utilizing some evaluation indexes such as time of air exchange [2], average air age, energy available coefficient, etc. Further, research on regional adaptation has been also done by selecting four different meteorological regions in China from east to west (Shanghai, Wuhan, Xi'an, and Urumqi).

Based on our research work, some building configurations adapt to natural ventilation can be obtained and demonstrated. It is convinced of that this kind of research work is valuable and helpful to the design work of energy-efficient buildings and green buildings.

13.2 Establishment of Model Building and Model Room

13.2.1 The Model of an Office Building

A model office building is established. It is a five-storey office building; Each floor has the area of 320.58 m^2, and floor height of each floor is 3.5 m. Each floor has office and meeting rooms. The outlook of the model building is shown in Fig. 13.1. The plan of the second floor of the model building is shown in Fig. 13.2.

The model building configuration above is a common and typical configuration of office building in China, and this kind of building configuration is defined as A.

To achieve the objective building of low energy consumption and good air quality, optimization should be started from the inception of the design work.

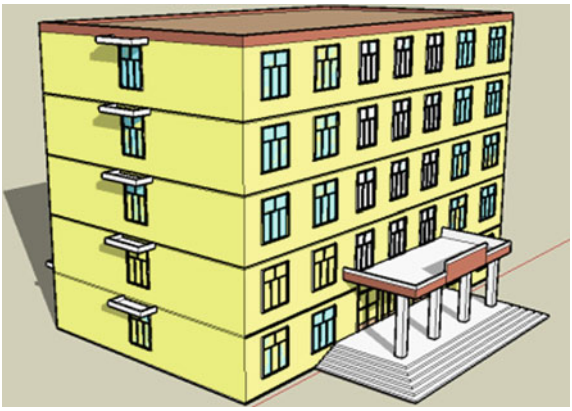

Fig. 13.1 Outlook of the model building

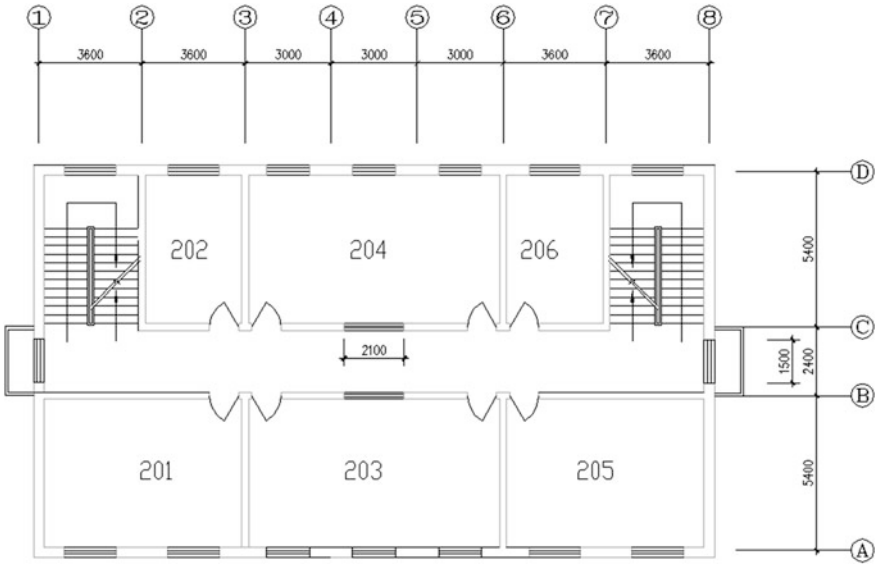

Fig. 13.2 The plan of the second floor

Building configuration that can well adapt to natural ventilation should be paid much more attention to utilize (including control) the natural force as large as possible.

A new improved building configuration (Defined as B) was initiated and presented in this paper,which is shown in Figs. 13.3, 13.4, and 13.5. Building configuration B has the following main characteristics:

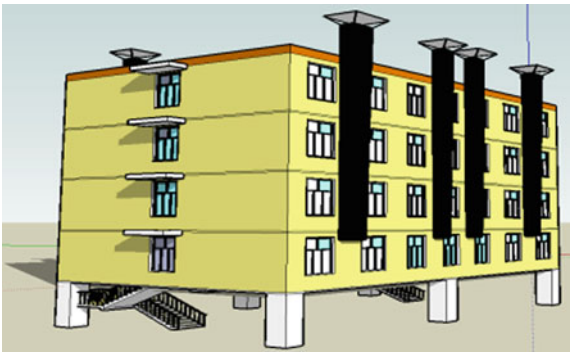

Fig. 13.3 Outlook of B

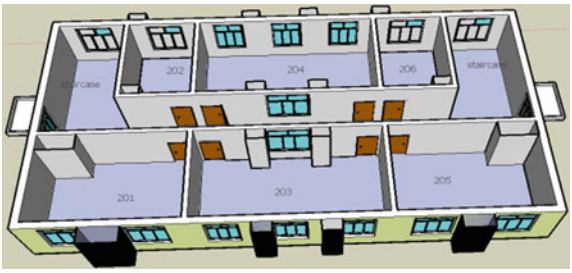

Fig. 13.4 A view of the second floor of B

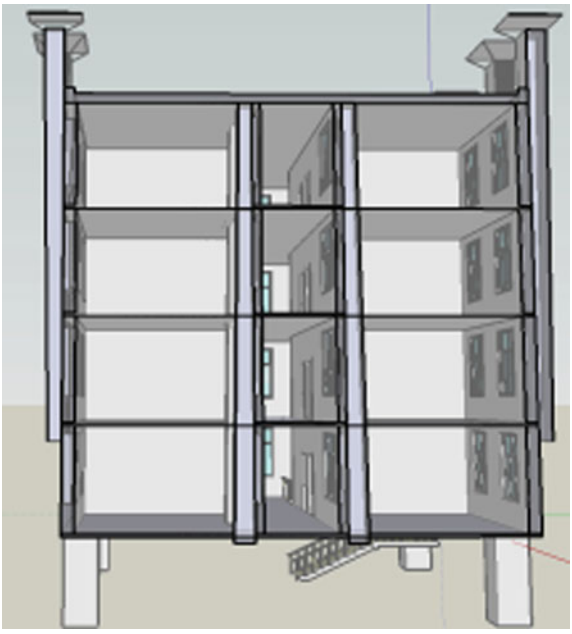

Fig. 13.5 The profile of B

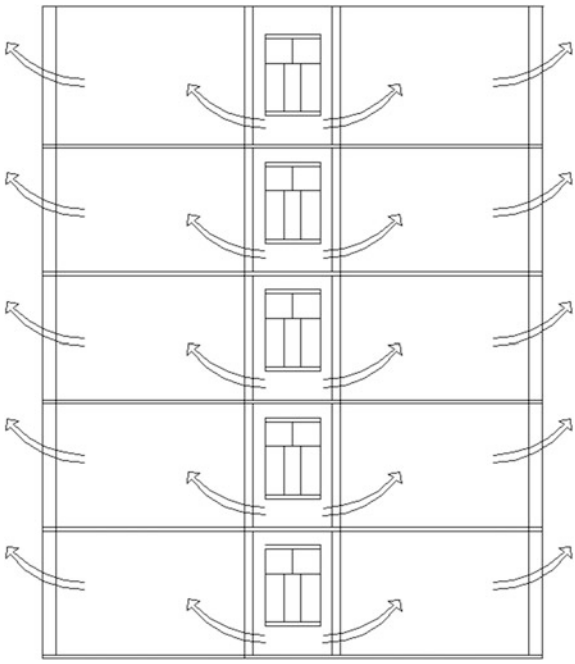

Fig. 13.6 Ventilation principle of A

1. Make the first floor as an empty space [3];
2. Ventilating shafts are established in the core area of the building;
3. Solar chimneys are established outside the building facade [4].

All of these measures are deemed as optimal measures that can well adapt to natural ventilation, but to obtain and demonstrate the concrete improved effect and the accurate indexes of natural ventilation, simulation work is necessary and unavoidable.

The natural ventilation principle (thermal pressure only) of building configuration A and B is demonstrated in Figs. 13.6 and 13.7.

13.3 Simulation Work

To demonstrate the process and results of simulation work, a model room (room 202, length × width × height, 5.4 × 3.6 × 3.5 m) within the model building is selected as the objective case for simulation and the position and dimensions of the model room are illustrated in Fig. 13.12.

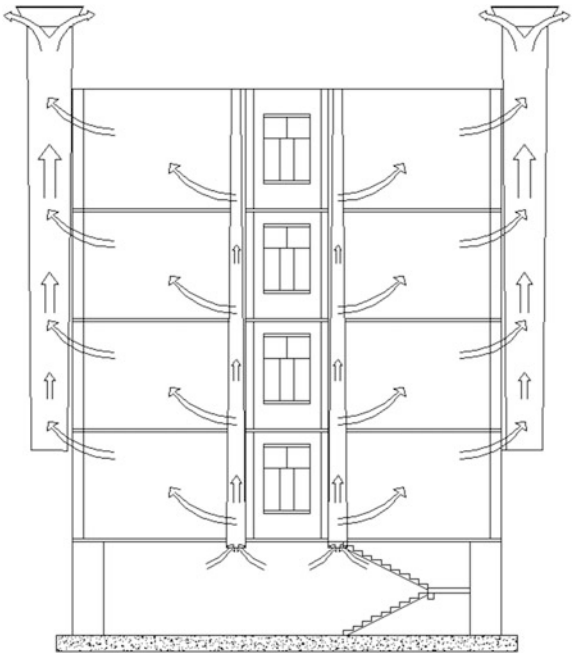

Fig. 13.7 Ventilation principle of B

13.3.1 Parameter Descriptions of the Model Room

Parameters of the model building are listed in Table 13.1.

13.3.2 Simulation Work

DeST is employed to simulate the natural indoor air temperature of the model room, and Fluent is employed to simulate the air velocity distribution and the air temperature distribution within the model room [5].

Table 13.1 Parameters of the model building

Information of building configuration	Ordinary office size: (length × width × height) 5.4 × 3.6 × 3.5(m)
	Senior office size: (length × width × height) 5.4 × 7.2 × 3.5 (m)
	Meeting room size: (length × width × height) 5.4 × 9 × 3.5 (m)
	The size of the window: (length × width) 2 × 1.8 (m)
	The size of the door: (length × width) 2 × 1 (m)
	The height of windowsill: 1 (m)
	Corridor area of each floor: 95.04 m^2
	External window: Double clear glazing,U-value = 2.68 W/m^2 k

Table 13.2 Simulation presetting parameters of building configuration A

Region Parameters	Shanghai	Wuhan	Xi'an	Urumqi
Atmospheric pressure (Pa)	100,573	99,967	95,707	93,213
Inlet temperature (°C)	35	36.8	35.7	36.8
Inlet pressure (Pa) (relative pressure)	0	0	0	0
Outlet temperature (°C)	38	40	39.12	38.6
Outlet pressure (Pa) (relative pressure)	−11.56	−11.39	−11.43	−11.42
Wall thickness (m)	0.2	0.24	0.37	0.49
U-Value (W/m^2 k)	2.31	1.97	1.5	1.22
Turbulence model	k-epsilon standard			

Table 13.3 Simulation presetting parameters of building configuration B

Region Parameters	Shanghai	Wuhan	Xi'an	Urumqi
Atmospheric pressure (Pa)	100,573	99,967	95,707	93,213
Inlet temperature (°C)	30.8	32	30.7	27.4
Inlet pressure (Pa) (relative pressure)	0	0	0	0
Outlet temperature (°C)	38	40	38	38.2
Outlet pressure (Pa) (relative pressure)	−24.95	−23.55	−28.9	−31.21
Wall thickness (m)	0.2	0.24	0.37	0.49
Solar radiation intensity (W/m^2)	291	280	345	395
Air temperature in ventilation tower (°C)	41.22	39.66	48.87	55.95
Turbulence model	k-epsilon standard			

Simulation presetting parameters of the building configuration A and B are illustrated in Tables 13.2 and 13.3. The maximum natural indoor air temperature within the typical year and the corresponding outdoor air temperature are selected as the presetting parameters of the Fluent ventilation simulation. Based on some research results, the air temperature within the solar chimney is nearly proportional to the in situ solar radiation intensity. In Shanghai area with a certain type solar chimney, the air temperature within the solar chimney can reach the value of 41.22 °C at 14:00 p.m. [6, 7]. So the air temperature within the solar chimney in the four different meteorological regions is listed in Table 13.3.

The simulation results of natural indoor air temperature (model room) within the typical year and the corresponding outdoor air temperature are illustrated in Figs. 13.8, 13.9, 13.10, and 13.11.

Before Fluent simulation,take the air pressure at air inlet and outlet as the boundary condition and only thermal pressure is considered in this case. To demonstrate the maximum natural ventilation capacity, all windows, doors, and draft passage are set fully opened and the maximum meteorological parameters are selected. Dimensions of room 202 in building configuration A are illustrated in Figs. 13.12 and 13.13; Dimensions of room 202 in building configuration B are illustrated in Figs. 13.14 and 13.15.

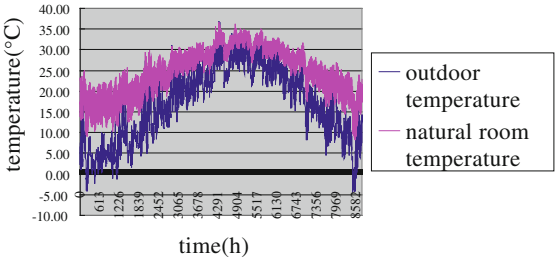

Fig. 13.8 The temperature in Shanghai

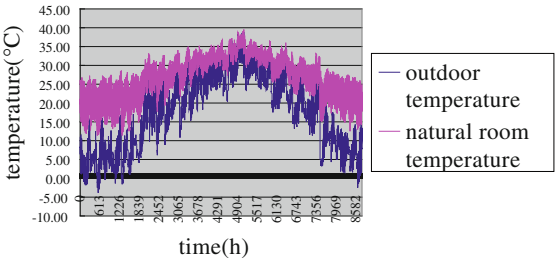

Fig. 13.9 The temperature in Wuhan

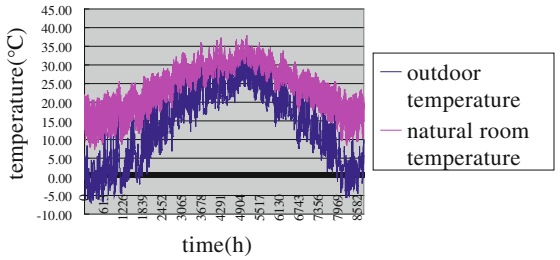

Fig. 13.10 The temperature in Xi'an

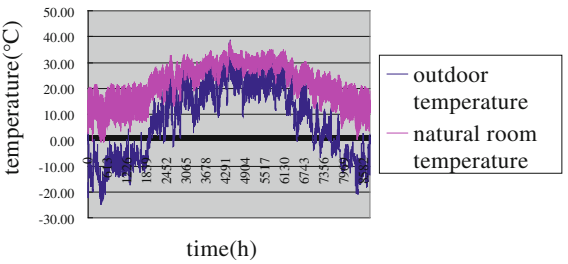

Fig. 13.11 The temperature in Urumqi

The calculation of thermal pressure (as the driving force of natural ventilation) is as follows:

$$\Delta P = (\Delta)\rho \times (\Delta)h \times g \tag{13.1}$$

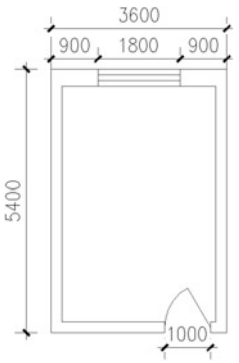

Fig. 13.12 The plan of room 202 of A

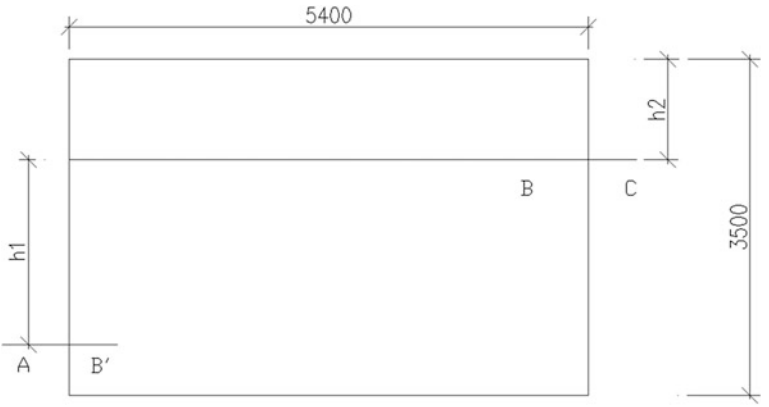

Fig. 13.13 The profile of room 202 of A. *note* h1' is the altitude difference from the center of the air inlet to the air outlet; h2' is the altitude difference from the center of the air outlet to the room ceiling

where

ΔP thermal pressure difference (Pa);
ρ air density (kg/m^3);
h altitude above the horizontal reference plane (m);
g acceleration of gravity (m/s^2)

In building configuration A

$$P_B - P_C = (\rho_B - \rho_C) \times h_2 \times g = M_1 \tag{13.2}$$

h_2: altitude difference from the center of the window to the room ceiling (m).

$$P_{B'} - P_B = (\rho_{B'} - \rho_B) \times \mathrm{h}_1 \times g = M_2 \tag{13.3}$$

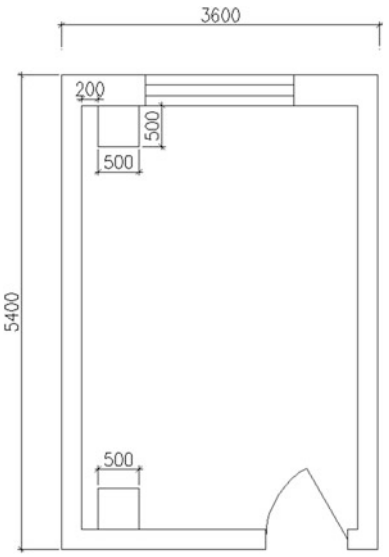

Fig. 13.14 The plan of room 202 of B

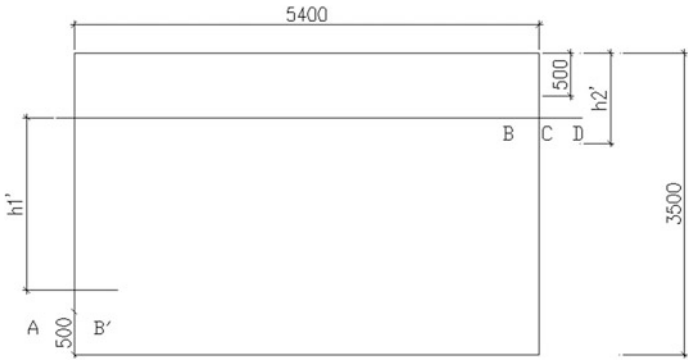

Fig. 13.15 The profile of room 202 of B. *note* h1' is the altitude difference from the center of the air inlet to the air outlet; h2' is the altitude difference from the center of the air outlet to the room ceiling

$$P_A - P_{B'} = (\rho_A - \rho_{B'}) \times \mathrm{h}_1 \times g = M_3 \tag{13.4}$$

h_1: altitude difference from the center of the door to the center of the window (m).

Take air inlet pressure as the atmospheric P_A,

Make Eq. (13.2) + Eq. (13.3) + Eq. (13.4),we can have

$$P_A - P_C = M_1 + M_2 + M_3 \tag{13.5}$$

Then, the air pressure at the air outlet P_C can be obtained.

In building configuration B

$$P_C - P_D = (\rho_C - \rho_D) \times h \times g = M_4 \tag{13.6}$$

h: height of the solar chimney (m);

$$P_A - P_D = M_1{}' + M_2{}' + M_3{}' + M_4{}' \tag{13.7}$$

Then, the air pressure at the air outlet P_D can be obtained.

13.3.3 Analysis on regional adaptation

The natural ventilation effect is not only based on the building configuration, but also depends on meteorological parameters. The simulation results in the four different meteorological regions of China are demonstrated as follows:

The simulation results of natural ventilation effect in Shanghai area: (Figs. 13.16, 13.17, 13.18, and 13.19).

The simulation results of natural ventilation effect in Wuhan area: (Figs. 13.20, 13.21, 13.22, and 13.23).

The simulation results of natural ventilation effect in Xi'an area: (Figs. 13.24, 13.25, 13.26, and 13.27).

The simulation results of natural ventilation effect in Urumqi area: (Figs. 13.28, 13.29, 13.30, and 13.31).

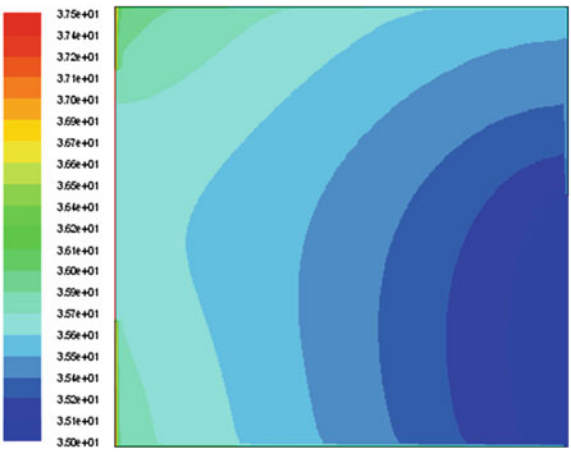

Fig. 13.16 Temperature contours of A

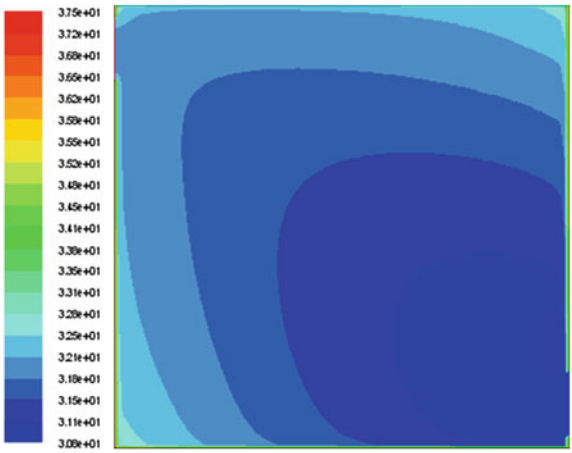

Fig. 13.17 Temperature contours of B

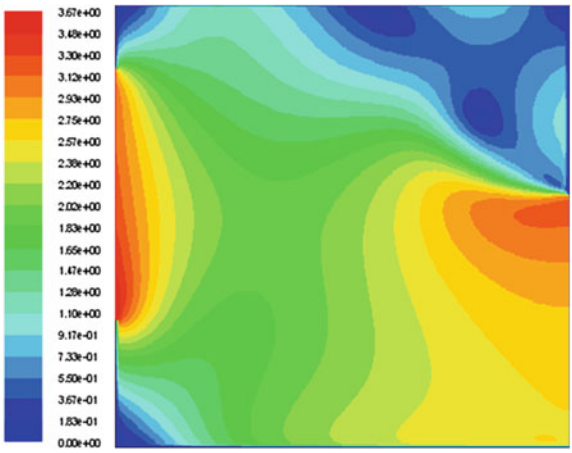

Fig. 13.18 Velocity contours of A

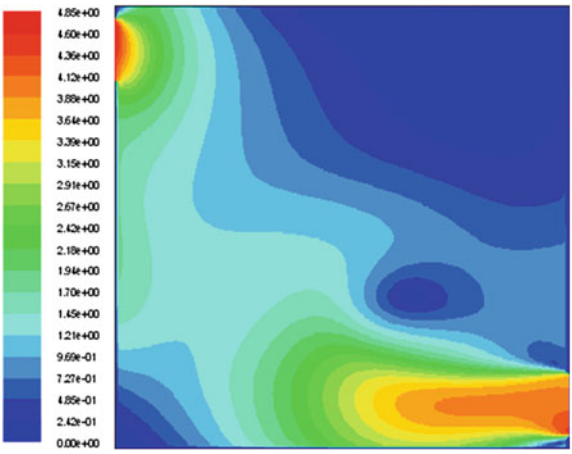

Fig. 13.19 Velocity contours of B

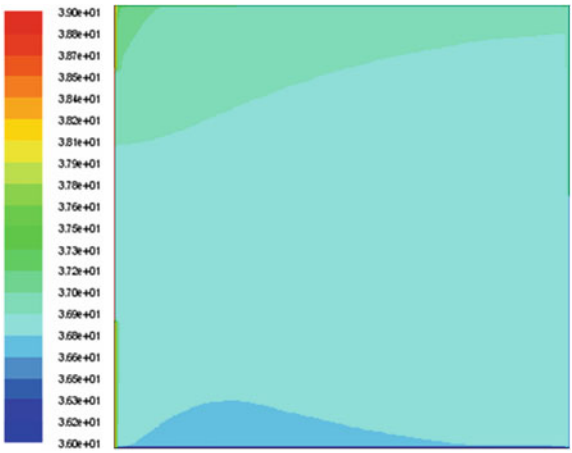

Fig. 13.20 Temperature contours of A

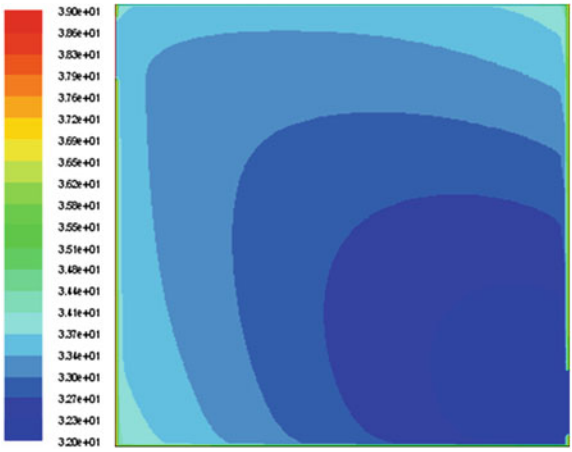

Fig. 13.21 Temperature contours of B

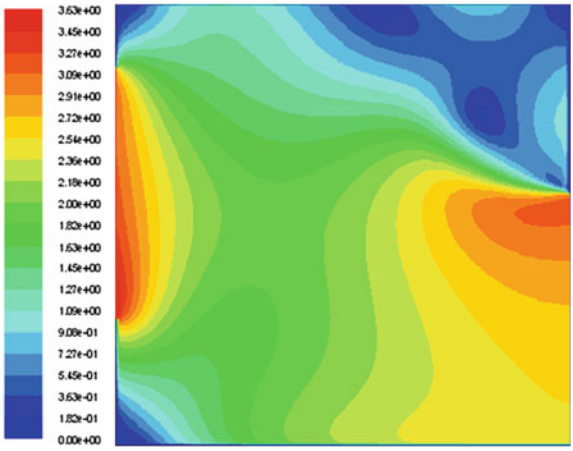

Fig. 13.22 Velocity contours of A

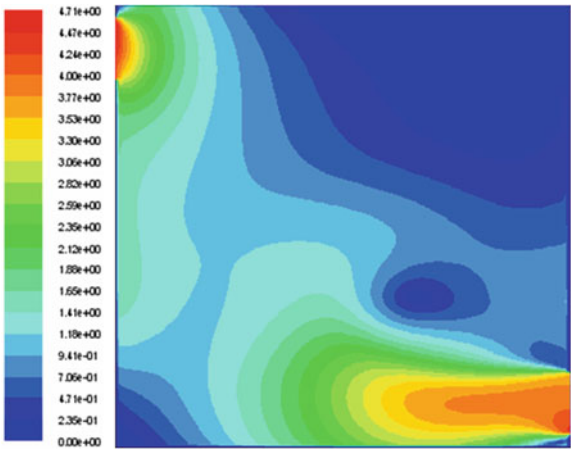

Fig. 13.23 Velocity contours of B

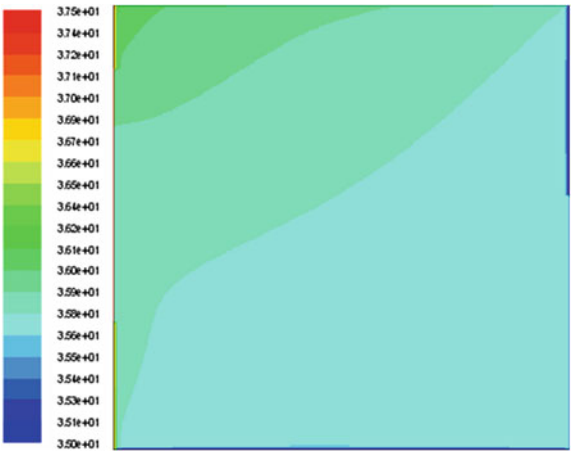

Fig. 13.24 Temperature contours of A

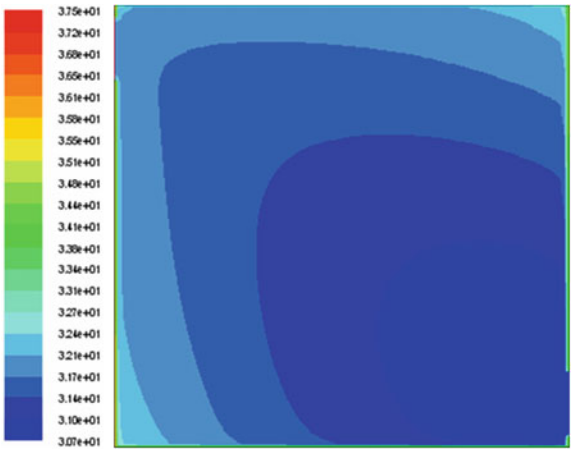

Fig. 13.25 Temperature contours of B

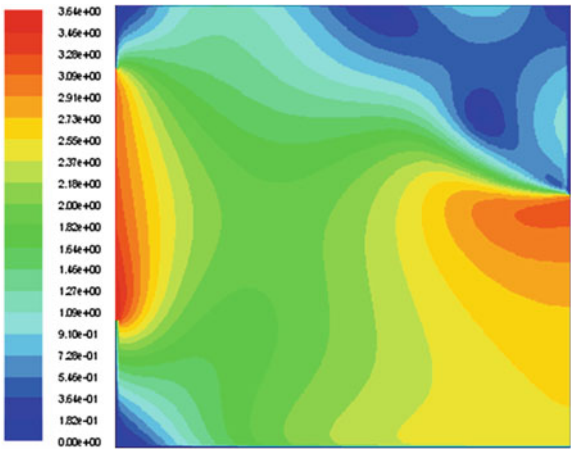

Fig. 13.26 Velocity contours of A

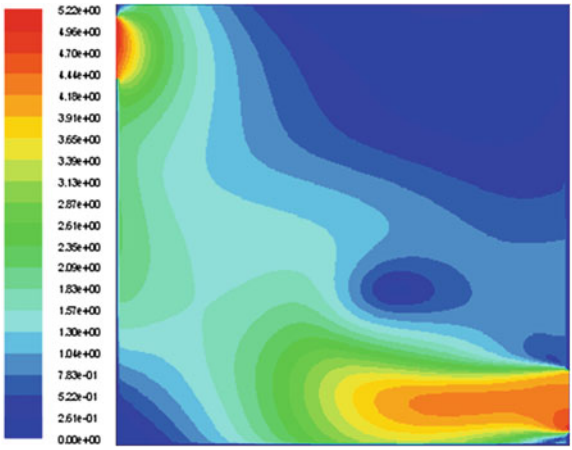

Fig. 13.27 Velocity contours of B

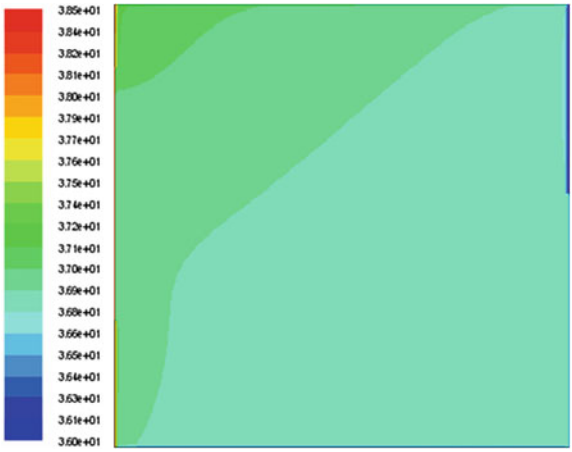

Fig. 13.28 Temperature contours of A

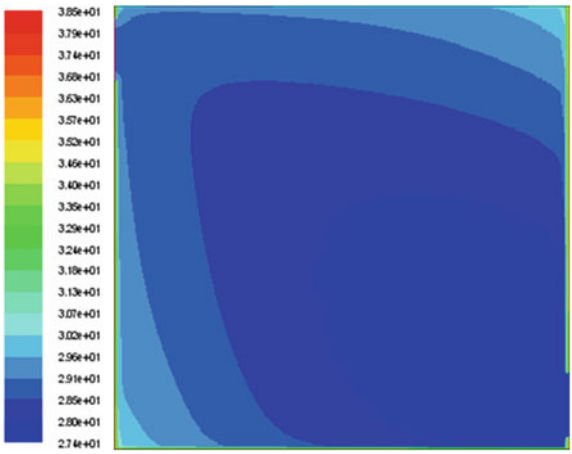

Fig. 13.29 Temperature contours of B

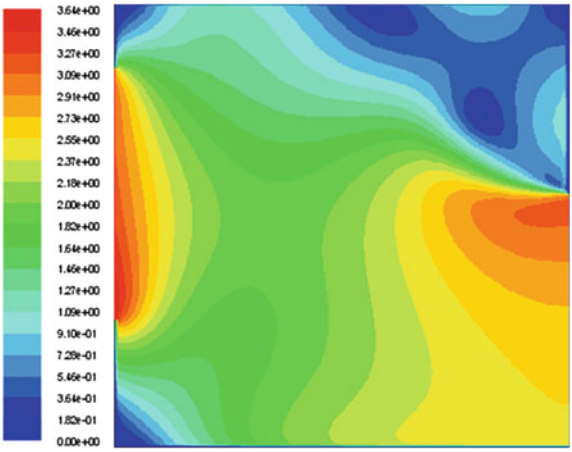

Fig. 13.30 Velocity contours of A

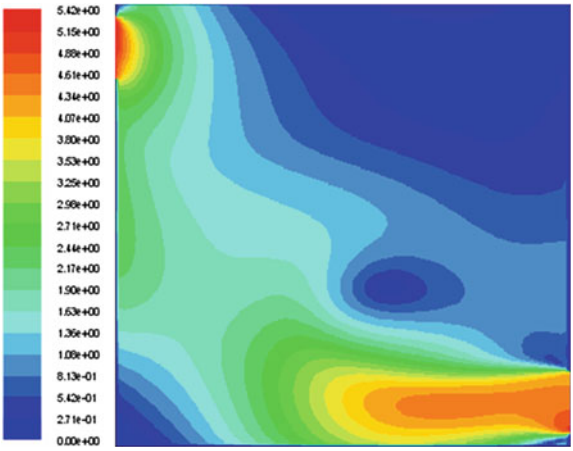

Fig. 13.31 Velocity contours of B

13.3.4 Comparison Work

For schematic comparison and optimization, three evaluation indexes are employed:

1. Time of air exchange N:

$$N = \frac{Q}{V} \text{ (times/}h\text{)} \tag{13.8}$$

where

Q: ventilation quantity, m^3/h;

V: room volume, m^3.

The comparison of N between A configuration and B configuration in four different meteorological regions of China is shown in Fig. 13.32.

2. Average air age $\overline{\tau_p}$:

Take the air flow within the room as the ideal piston flow, then:

$$\overline{\tau_p} = \frac{1}{2}\tau_n \ (s) \tag{13.9}$$

where τ_n: room nominal time constant;

$$\tau_n = \frac{V}{Q} \ (s) \tag{13.10}$$

Q:ventilation quantity, m^3/s.

The comparison of $\overline{\tau_p}$ between A configuration and B configuration in four different meteorological regions of China is shown in Fig. 13.33.

3. Energy available coefficient η_N

$$\eta_N = \frac{t_p - t_0}{t_N - t_0} \tag{13.11}$$

where

t_p: Outlet air temperature (°C);

t_N: Room air average temperature (°C);

t_0: Inlet air temperature (°C).

The comparison of η_N between A configuration and B configuration in four different meteorological regions of China is shown in Fig. 13.34.

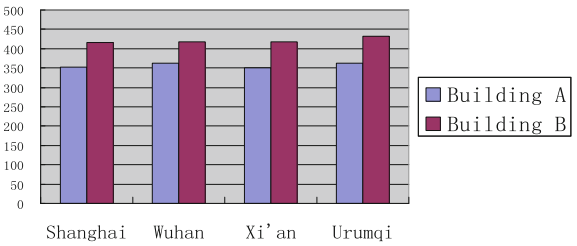

Fig. 13.32 Time of air exchange of A and B

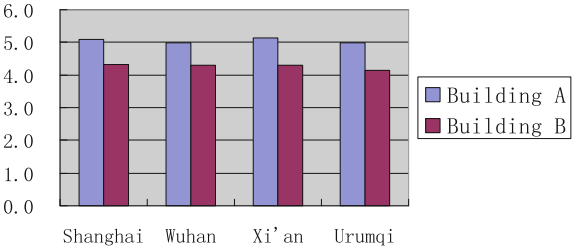

Fig. 13.33 Average air age of A and B

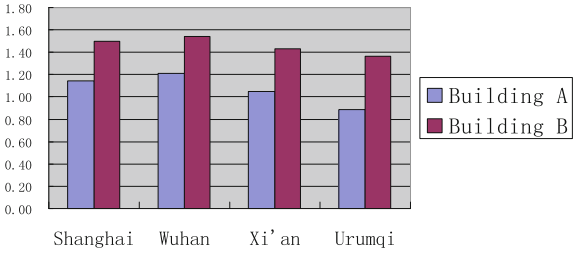

Fig. 13.34 Energy available coefficient of A and B

Let

$$\Delta N = N_A - N_B \quad \Delta N' = \frac{N_A - N_B}{N_A} \times 100\,\%;$$

$$\Delta \overline{\tau}_p = \overline{\tau}_{p_A} - \overline{\tau}_{p_B} \quad \Delta \overline{\tau}'_p = \frac{\overline{\tau}_{p_A} - \overline{\tau}_{p_B}}{\overline{\tau}_{p_A}} \times 100\,\%;$$

$$\Delta \eta_N = \eta_{NA} - \eta_{NB} \quad \Delta \eta_N{}' = \frac{\eta_{NA} - \eta_{NB}}{\eta_{NA}} \times 100;$$

Results of indexes comparison between A configuration and B configuration within four regions are illustrated in Table 13.4.

Table 13.4 Results of indexes comparison between A configuration and B configuration

Parameters	N (times/h)		$\overline{\tau_p}$ (s)		η_N	
Region	ΔN	$\Delta N'$ (%↑)	$\Delta\,\overline{\tau_p}$	$\Delta\overline{\tau}'_p$ (%↓)	$\Delta\,\eta_N$	$\Delta\,\eta'_N$ (%↑)
Shanghai	62.17	17.59	0.76	14.96	0.36	31.50
Wuhan	56.88	15.72	0.68	13.58	0.33	26.92
Xi'an	68.78	19.64	0.84	16.41	0.38	36.29
Urumqi	71.43	19.74	0.83	16.64	0.40	37.27

13.4 Conclusions

From the simulation work and analysis above, some conclusions can be obtained:

1. Building configuration is very important to improve the natural ventilation effect which pay off in the improvement of indoor environment and the reduction in building HVAC energy consumption, so building configurations adapt to natural ventilation are worth studying;
2. Under certain building configuration adapt to natural ventilation, the real improved effect of natural ventilation depends on the in situ thermal pressure and wind pressure (only thermal pressure is considered in this paper, and further study should be taken in the future including wind pressure);
3. Different area has the different meteorological parameters, so the real improved effect of natural ventilation with certain building configuration adapt to natural ventilation differs from the different meteorological regions of China;
4. To well obtain and demonstrate the advantages and the regional adaptation of the building configuration adapt to natural ventilation, simulation and optimal work are necessary and unavoidable in the inception of the building design work;
5. Making the first floor as an empty space,ventilating shafts are established in the core area of the building,and solar chimneys that were established outside the building façade are proved as the advantageous measures to improve natural ventilation.

References

1. Gao CF, Lee WL (2011) Evaluating the influence of openings configuration on natural ventilation performance of residential units in Hong Kong. Build Environ 46:961–9
2. Jiang Y, Chen Q (2001) Study of natural ventilation in buildings by large eddy simulation. J Wind Eng Ind Aerodyn 89(13):1155–78
3. Du G, Hu W, Yang C (2008) Numerical simulation on arial patterns effect on outdoor wind environment of pedestrian field in residential quarter. Build Sci (12):40–45 (in Chinese)
4. Khedari J, Boonsri B, Hirunlabh J (2000) Ventilation impact of a solar chimney on indoor temperature fluctuation and air change in a school building. Energy Build 32:89–93

5. Chen Q (2004) Using computational tools to factor wind into architectural environment design. Energy Build 36:1197–1209
6. Liu Z, SU Y (2011) A one-dimensional unsteady model for natural ventilation in a solar chimney. Build Energy Environ 6:37–40 (in Chinese)
7. SU Y, Liu Z (2011) One dimensional steady model for natural ventilation of solar chimney. Archit Environ Eng 5:102–107 (in Chinese)

Chapter 14
Simulation and Analysis of Low-Energy Consumption of Office Building

Huixing Li, Wei Wang, Guohui Feng, Hongyu Ding and Xingzhi Zheng

Abstract Taking a low-energy consumption of office building that adopts the water source heat pump system as cold and heat source in Shenyang as an example, we investigated the whole building energy condition and system operation situation and collected the energy consumption data of building in former years. The energy consumption of the whole office building is simulated based on Design Builder software; it is proved that the numerical simulation method is reliable compared with the previous collected data. Operating energy consumption of air-conditioning system, other power system, indoor lighting system, and office equipment system in this office building is simulated with the Design Builder software. The energy utilization efficiency of low-energy consumption of office building is evaluated. The results show that the office building annual energy consumption per unit area index is less than ordinary office building. It reflects the advantages of water source heat pump air-conditioning system than others. Energy consumption index of lighting and office equipment reflects the characteristics about energy consumption of the office building.

Keywords Simulation · Analysis · Evaluate · Low-energy consumption of office building

14.1 Introduction

14.1.1 Basic Situation of Building

The office building is located in Shenyang. The building is oriented south to north. Total height of the building is 19.8 m. There are five storeys on the ground and one underground storey. And there is an atrium in the middle of the building. The total

H. Li · W. Wang · G. Feng (✉) · H. Ding · X. Zheng
School of Municipal and Environment Engineering, Shenyang Jianzhu University, Shenyang 110168, China
e-mail: fengguohui888@163.com

A. Li et al. (eds.), *Proceedings of the 8th International Symposium on Heating, Ventilation and Air Conditioning*, Lecture Notes in Electrical Engineering 263,
DOI: 10.1007/978-3-642-39578-9_14,

construction area of the building is 10,997.38 m^2, with 200 workers in the building.

A frame structure is adopted in the office building. The bricks of 370 mm thick are used for the exterior wall and the bricks of 180 mm thick are used for the interior wall. Exterior window is a hollow two-layer glass window, the window frame materials are of plastic steel window frame, degree specifications are of 5 + 9 + 5 mm with ordinary transparent glass, and plant polyurethane foam materials be used for outer insulation. Heat transfer coefficient of roofing is 0.25 W/(m^2K), heat transfer coefficient of outer wall is 0.51 W/(m^2K), and heat transfer coefficient of exterior window is 2.2 W/(m^2K) [1].

The underground layer of the building has the duty room, variable control room, air-conditioning room, and warehouse and tool room. One layer of the building mainly has showroom, reception room, archives, mail room, and office. The main function of two to five layers of building is the office room, the second floor has two small conference rooms, and the third layer has a big conference room. The building operation time is from 8:00 a.m. to 5:00 p.m. every day, all used for private and utilization rate 100 %, the holidays are in August, and the building is closed.

14.1.2 Air-Conditioning System

There are many different kinds of air-conditioning systems in the office building. The all-air system is used in the archives with humidification in winter. The all-air system is also used in the conference room. Atrium adopts fan coil unit plus fresh air system and uses the vertical dark attire air blower serpentines. Offices adopt the fan coil system with fresh air system. And there is an independent fresh air system for each floor. Fire control room takes cold and hot source split air conditioners, respectively. Cold and hot source device of the building is water source heat pump units; the water is from the shallow groundwater, using vacuum recharge of groundwater recharge mode. The runtime of water source heat pump is 24 h in winter, using temperature control in summer and turning off at summer night.

14.2 Design Builder

Design Builder is a user-friendly modeling environment where you can work (and play) with virtual building models. It provides a range of environmental performance data such as energy consumption, carbon emissions, comfort conditions, daylight luminance, maximum summertime temperatures, and HVAC component sizes [2].

14.2.1 Input Parameters for Simulation

Building energy consumption simulation is based on the latest building drawings provided by architect and building materials list and design descriptions, the HVACs and artificial lighting drawings provided by mechanical and electrical engineers, design description and equipment list, and the landlord to provide technology and equipment requirements, personnel, operation time and so on [2, 3].

The actual and the simulated energy consumption of the building are compared, as shown in Fig. 14.1. The simulated electricity consumption is 1,099,123 kW·h.

As seen in Fig. 14.2, the numerical simulation and actual values did not differ quite, which confirmed the credibility of simulation.

Fig. 14.1 Contrast diagram of simulate power consumption in 2011.4–2012.3 (kWh)

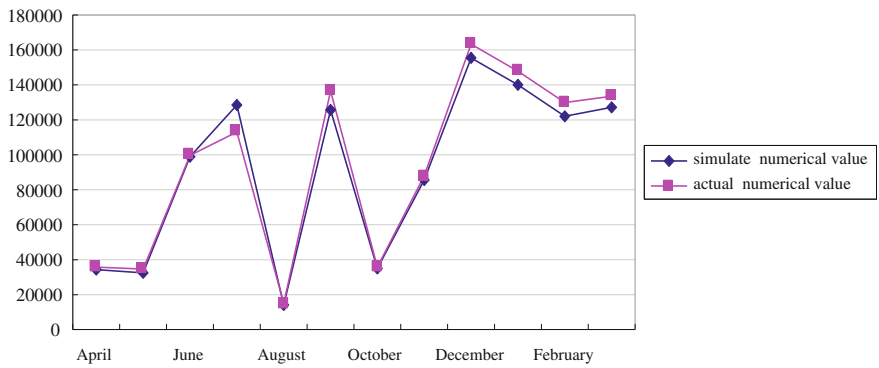

Fig. 14.2 Contrast diagram of simulate numerical value and actual numerical value (kWh)

14.2.2 Simulate Power Consumption of the Other System

Heating power consumption by simulation of the building in November 2011 to March 2012 month by month, the total used in this part of the total annual heating power consumption is 441,532.8 kWh. From Fig. 14.3, we can see that the power consumption of heating is peak in December and January; the power consumption is 105,000 kWh; power consumption reaches the valley value; energy consumption value is 46,836 kWh in November; the difference between peak and valley value is 58,164 kWh; and heating power consumption is 92,000 kWh to achieve balance in February and March.

Cooling power consumption by simulation of the building is in June 2011 to September 2011, and the total cooling power consumption is 262,329.42 kWh. Figure 14.4 shows cooling power consumption up to peak in July, and power consumption is 98,419.06 kWh. The main reason is that most of the air-conditioning equipment works in July. Energy consumption of air-conditioning systems in building is one of the main reasons for the rise of the electricity consumption. So the energy consumption is larger in summer for cooling [4]. The air-conditioning systems stop working in August and the energy consumption becomes lower then.

Simulated annual building office equipment total power consumption is 144,950 kWh. Figure 14.5 shows office equipment power consumption fluctuation is not big and in a relatively average level, and the office equipment power consumption up to peak and power consumption is 18,719.63 kWh in December. In February and August, the power consumption is low and is the result of the operation characteristics of the building itself; the building stops using in this period. The equilibrium consumption shows power consumption of building office

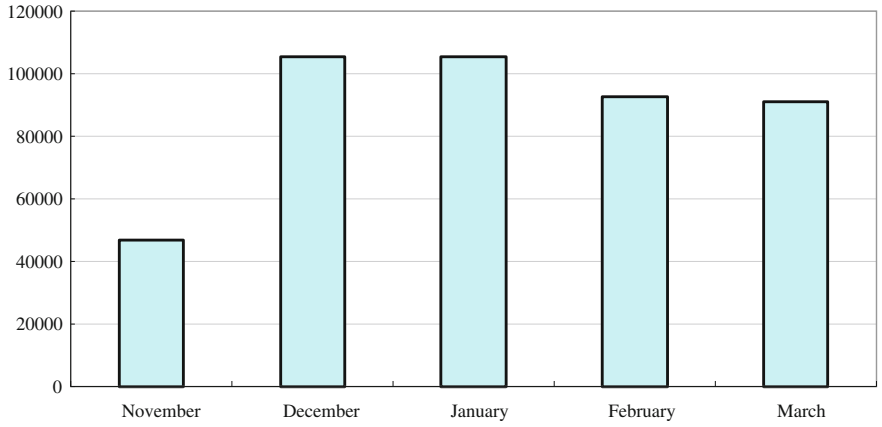

Fig. 14.3 Heating power consumption of air-conditioning in 2011.11–2012.3 (kWh)

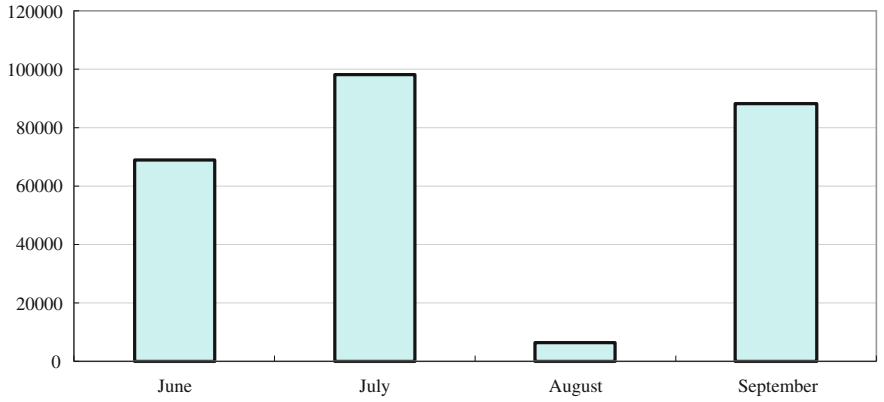

Fig. 14.4 Cooling power consumption of air-conditioning in 2011.6–2011.9 (kWh)

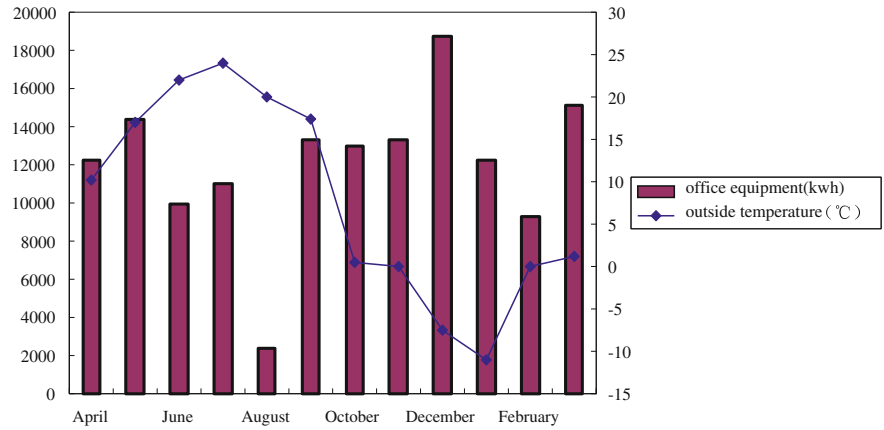

Fig. 14.5 Power consumption of office equipment in 2011.4–2012.3

equipment only concerned building personnel demand, which has nothing to do with the outdoor meteorological parameters.

Simulation of building lighting energy consumption is shown in Fig. 14.6, and the total power consumption is 149,689.86 kWh. Lighting electric power consumption and outdoor temperature have positive correlation obviously. The annual electricity consumption of the building changes with the variation of the outdoor temperature. This is because the building is in hot summer and cold winter area, summer nights are short, winter days are short, and the nights are long.

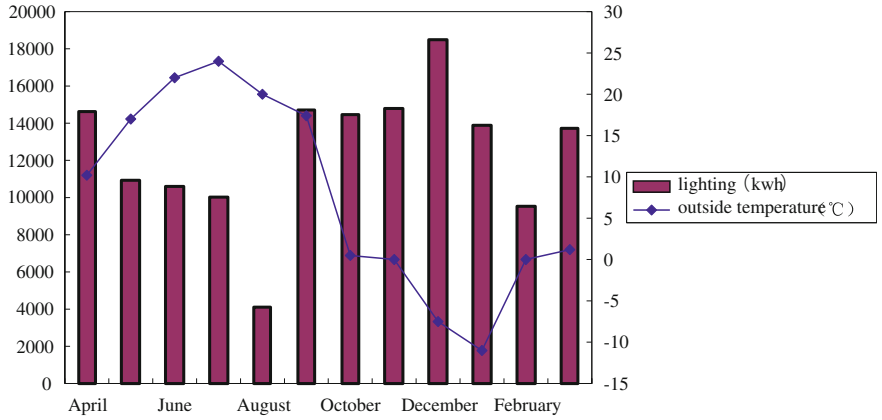

Fig. 14.6 Power consumption of lighting in 2011.4–2012.3

Table 14.1 Index of energy consumption

Subentry	Annual energy consumption (kWh)	Energy consumption index of unit area [kWh/(m^2·a)]
Heating system of air-conditioning	441,532.75	40.15
Cooling system of air-conditioning	262,329.42	23.85
Lighting system	149,689.86	13.61
Office equipment system	144,950.99	13.18
Other system	100,620.72	9.15
Total	1,099,123.74	99.94

14.3 Conclusions

1. The simulation results in Table 14.1 shows annual energy consumption per unit area index in low-energy consumption of office building is 99.94 kWh/(m^2•a) and reflects the basic information of office building.
2. Air-conditioning of heating energy consumption per unit area index is 40.15 kWh/(m^2•a), the better the office building heating in winter, the higher the indoor temperature.
3. Air-conditioning of cooling unit area energy consumption indicators is 23.85 kWh/(m^2•a) and embodies the advantages of water source heat pump air-conditioning system.
4. Lighting energy consumption index and office equipment energy consumption indicators reflect the characteristic of energy consumption of office building, indoor computer, printer, etc. Various kinds of office equipment utilization rate are higher.

Acknowledgments This research was supported by National Twelfth Five-Year plan cooperation project (2010DFA72740-06-04) building energy efficiency of China–USA clean energy research center.

References

1. Liaoning provincial standard DB21/T1476-2011 living building are energy-saving design standard (2011) (in Chinese)
2. Tsinghua University Architecture Energy-saving Research Center (2010) China building energy saving annual development research report (in Chinese)
3. Zhaojiang L (2006) Jiang Yinchuan's building energy consumption status analysis and thinking. J Arch (7):30–33 (in Chinese)
4. DB21/T1476—2011 (2011) Energy saving design standard for residential buildings. Liaoning Provincial Department of housing and Urban-Rural Development, Liaoning (in Chinese)

Chapter 15
Heating Transfer Characteristics Analysis on the Flooded Refrigerant Evaporator Using Untreated Sewage Heat Energy

Zhaoyi Zhuang and Haiying Pang

Abstract Sewage evaporator is the critical component which affects the performance of the direct sewage source heat pump unit. The sewage directly flows into the evaporator and exchanges heat with the refrigerant. The performance of sewage evaporator is different from the general water source heat pump units because of the characteristic of sewage. This paper developed a theoretical model with sewage FRE distribution parameters based on some reasonable simplifications, and this model was applied to predict the performance of some sewage evaporator and analyze the influence of different tubes and pass arrangements and different sewage inlet temperature and flux on evaporator performance. The results show that there is little effect on the sewage FRE performance with different pass arrangement. The evaporator heat exchange increases linearly with the rise of sewage inlet temperature when the sewage flux and refrigerant inlet conditions are fixed. The evaporator heat exchange and flow resistance increase with the sewage flux raises when the sewage inlet temperature and refrigerant inlet conditions are constant. In addition, the change extent of heat exchange is similar to that of the flux change.

Keywords Untreated sewage · Flooded refrigerant evaporator (FRE) · Inlet temperature · Flux · Heat exchange

Z. Zhuang (✉)
School of Thermal Energy Engineering, Shandong Jianzhu University, Jinan 250101, China
e-mail: hit6421@126.com

H. Pang
Design Institute of Electrical Division, Hebei Dadi Construction Technology Co. Ltd, Shijiazhuang 050035, China

A. Li et al. (eds.), *Proceedings of the 8th International Symposium on Heating, Ventilation and Air Conditioning*, Lecture Notes in Electrical Engineering 263,
DOI: 10.1007/978-3-642-39578-9_15,

15.1 Introduction

In FRE, sewage flows in the tube, while refrigerant boils and evaporates outside the tube bundle. In engineering design, calculation of the shell side is based on the methodology of adding modified value to the pool boiling data. Additionally, researches confirm that the heat transfer coefficient of tubes in upper part of FRE is more than 7 times that of pool boiling [1]. This equates integral calculation with conservative estimate of the evaporator performance [2]. For this reason, Webb [3] come up with a thermal calculation method of FRE distribution parameters, based on Chen's additive flow boiling model, and simulate the cooling pass set both horizontally and vertically, of FRE with low threaded pipes. Particularly, for vertically arranged FRE, Webb [4] assumes that the refrigerant flow is evenly distributed along the axis of heat transfer tubes, and applies this model to the analysis of FRE with horizontal layout and various types of tubes. Huang [5] sets up a thermal calculation model by modifying Webb's modern and runs simulations on the performance of FRE, involving horizontal and vertical pass arrangement, as well as different choices in the tube types. Because of the characteristics of sewage, the sewage FRE employs tubes with smooth inner walls. With no enhancement measures of heat transfer adopted in the sewage source side, increasing tube passes creates higher sewage speed, which is pivotal to improve the performance of the evaporator. This paper develops two-dimensional grid cells in both axial direction and alongside the tube rows, and by applying the thermal calculation model of distribution parameters, it simulates the FRE performance with four-pass tubes fixed up horizontally and vertically (the sewage either enters at the top and leaves at the bottom or vice versa).

15.2 Mathematical Model of Sewage FRE

15.2.1 Establishment of Unit Model

One single pass is divided into N_x grid cells, which means for a horizontal heat exchanger of N_p passes, there are $N_p \times N_x$ grid cells along the tube direction. In the direction of the tube row, it is divided into N_t grid cells. Therefore, a horizontal heat exchanger of N_p passes contains $\left(N_p \times N_x\right) \times N_t$ meshes. As is shown in Fig. 15.1, i and j mark the grid numbers in axial and tube row direction of the heat exchanger.

15.2.2 Heat Transfer Equations of Grid Cells

For any element within the model, the following equations are valid:

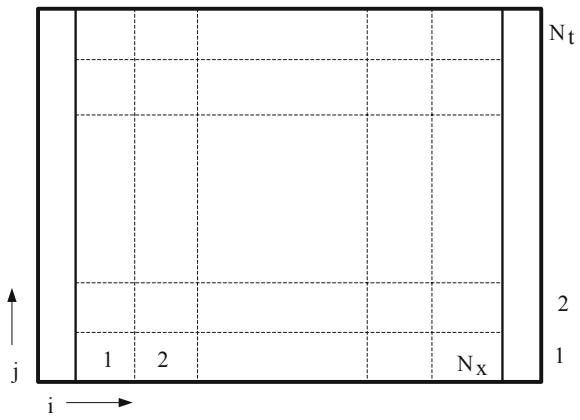

Fig. 15.1 Grid distribution of sewage flooded refrigerant evaporator

Flow heat transfer equation at the sewage side:

$$Q_{ij,w} = m_{we}c_{pw}\left(t_{w,\text{in}} - t_{w,\text{out}}\right) \tag{15.1}$$

Flow heat transfer equation at the refrigerant side:

$$Q_{ij,r} = m_r(h_2 - h_1) \tag{15.2}$$

Based on the method of e-NTU, the thermal load within each cell is:

$$Q_{ij} = \left(m_{we}c_{pw}\right)_w \varepsilon\left(t_{w,\text{in}} - t_{r,\text{in}}\right) \tag{15.3}$$

$$\varepsilon = 1 - \mathrm{e}^{-\text{NTU}} \tag{15.4}$$

$$\text{NTU} = \frac{K_{ij}A}{\left(m_{wc}c_{pw}\right)_{cw}} \tag{15.5}$$

Heat transfer equilibrium equation between the internal and external of the tube:

$$Q_{ij,w} = Q_{ij,r} = Q_{ij} \tag{15.6}$$

Overall heat transfer coefficient of the heat exchanger:

$$K = \frac{1}{A\left(\frac{1}{h_iA_i} + \frac{R_f}{A_i} + \frac{R_w}{A_w} + \frac{1}{A_oh_r}\right)} \tag{15.7}$$

For sewage evaporator, two-phase pressure drop is composed of friction pressure drop Δp_f, accelerated pressure drop Δp_a, and gravitational pressure drop Δp_g. The details of the calculation method refer to documentation [5].

15.2.3 Solution of the Model

To solve the model of FRE with horizontally set pass, the idea is to calculate each cell in axial direction based on the sewage flow direction. In one axial grid cell, the calculation starts from the bottom tube row, up straight to the top row of the evaporator. The specific steps are as follows:

1. Input known conditions: structural parameters of the evaporator, total number of tube row N_t, number of passes N_p; inlet mass flow and temperature of the sewage; inlet pressure, enthalpy h_1 and dryness x_{in} of the refrigerant.
2. Calculate the first axial cell in the first pass ($i = 1$, $j = 1$, as is shown in Fig. 15.1), assuming that the refrigerant inlet evaporation is $m_{r,i}$.
3. Assume that the refrigerant outlet dryness is x in this cell. Calculate the gas porosity, the refrigerant pressure drop and outlet temperature, as well as the overall heat transfer coefficient of the tube. Based on the results of Eq. (15.3), solve for the thermal load Q_{ij} in one cell, and sewage outlet temperature for all cells.
4. Figure out the refrigerant outlet enthalpy h_2 with outlet temperature and dryness. Then calculate the thermal load $Q_{ij,r}$ in one cell with the Eq. (15.2).
5. Test the convergence of the thermal load of the cell. If not, turn to step (3) and adjust the refrigerant outlet dryness; if it is convergent, carry on with the steps set.
6. Judge whether the algorithm has reached the top bundle row of the evaporator. If not, $j = j + 1$ and move on to the next tube row, going to step (3); if indeed, move to the next step.
7. Judge whether the refrigerant outlet dryness of the top tube row in this cell is 1. If not, adjust the refrigerant evaporation and turn to step (3). Calculate the cell from the beginning with $j = 1$ all over again. If it is indeed 1, then move to the next step.
8. Judge whether all the cells in axial direction of this pass have been discussed and calculated. If not, turn to step (2) with $i = i + 1$ and $j = 1$, and carry on with the calculation with the next cell. If it is done in this pass, then calculate the refrigerant outlet temperature of this pass.
9. Judge whether all the passes have been discussed and calculated. If not, turn to step (2) with $i = i + 1$ and j = 1, and carry on with the calculation with the next cell in the next pass. If it is all done, output the result.

Table 15.1 Structural parameters of the sewage FRE

External surface parameters			Internal surface parameters			
Outside diameter/mm	Height of fins/mm	Number of fins/m^{-1}	Inner diameter/mm	Height of fins mm	Internal surface are(m^2/m)	Wall thickness/mm
19.05	0.62	1575	16.54	–	–	0.635
Material	Tube length/m	Number of tubes	Heat transfer area/m^2		Axial distance/mm	Number of passes
Naval brass	3.55	116	24.62		28.58	4

15.3 Simulation Results and Analyses of the Sewage FRE

15.3.1 Simulation Conditions

The structural parameters of the sewage FRE are given in Table 15.1, Take 5 as number of axial grid cells and 10 for the tube rows. This grid meets the requirement of precision [6]. Therefore, there are 200 horizontal cells and 50 vertical ones.

15.3.2 Simulation Results and Analyses

The sewage inlet temperature is 12 °C. The sewage flux is 40 m^3/h. The refrigerant inlet pressure is 548.06 kPa. The refrigerant dryness is 0.15, and the inlet enthalpy is 233.967 kJ/kg.

1. Characteristics of the parameter distribution of the sewage FRE

The simulation results are shown in Table 15.2, and from there we know that: Change in the arrangement of pass does not have much influence on the overall performance of the sewage FRE, nor on the heat transfer coefficient of various evaporators. Because the heat transfer resistance mainly comes from the sewage side in the tube, and when the flow velocity is fixed in the tube, the heat transfer

Table 15.2 Simulation results of different tube row arrangement

		Q/ kW	K W/ (m^2 K)	$h_{r,e}$ W/ (m^2 K)	m_r (kg/s)	$\triangle P_f$ pa	$\triangle P_a$ pa	$\triangle P_g$ pa	$\triangle P$ pa
Horizontal		308.4	2621.9	13594.8	1.782	14.2	47.3	478.2	539.7
Vertical	From bottom	310.1	2626.3	13643.1	1.791	13.7	45.9	465.5	525.1
	From top	303.8	2624.2	13632.6	1.755	14.9	46.5	479.7	541.1

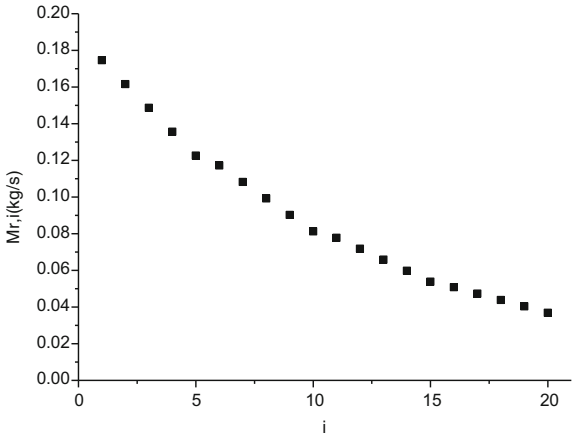

Fig. 15.2 Axial distribution of the refrigerant evaporation when the pass is horizontal

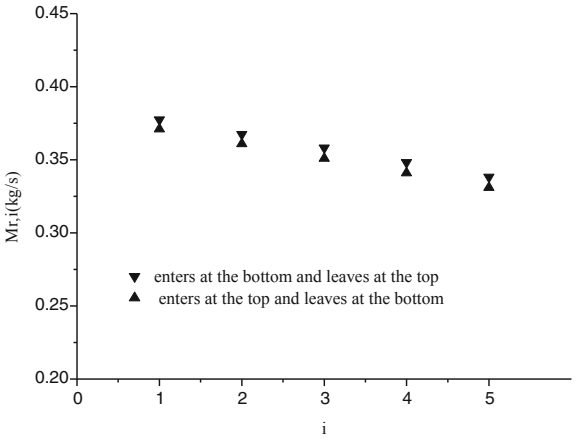

Fig. 15.3 Axial distribution of the refrigerant flux with difference inlet and outlet positions for the sewage when a pass is vertical

coefficient remains at a stable value. There is also not much difference shown in the refrigerant evaporation in various evaporators.

Figures 15.2 and 15.3 give information about the axial distribution of the refrigerant evaporation when the tube row is horizontally and vertically arranged. According to Fig. 15.2, the refrigerant evaporation gradually decreases along the axial direction, and the declining trend is getting gentler in the flowing direction of the sewage. As is shown in Fig. 15.3, the refrigerant axial distribution is even, although the sewage inlet and outlet positions vary. This is because in vertical arrangement like this, the high temperature side and the lower one compensate each other when the sewage temperature changes along the pass. This can lead to the axial even distribution of the refrigerant evaporation.

Figure 15.4 shows how the heat transfer coefficient outside of the tube changes when the tube row is arranged differently. According to Fig. 15.4, for horizontal

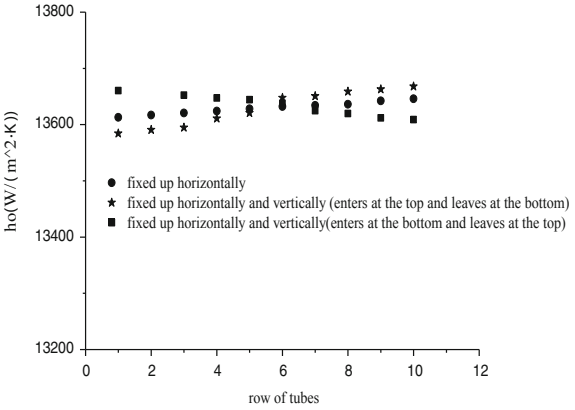

Fig. 15.4 The variation range of the heat transfer coefficient on the refrigerant side when the number of tube rows is different

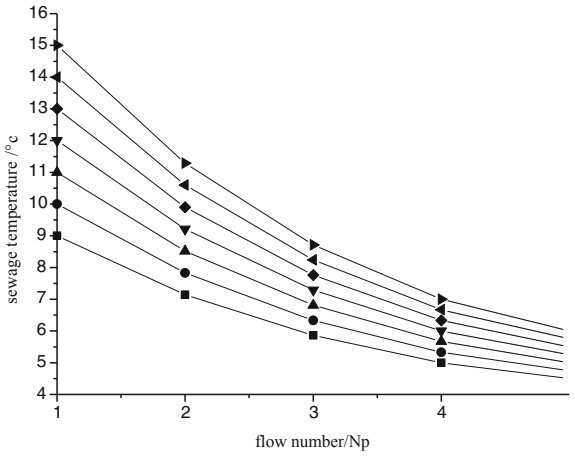

Fig. 15.5 Sewage inlet temperature along the passes

passes, when the height of the row rises, the heat transfer coefficient increases outside of the tube. For vertical passes, the observation is consistent. When the sewage enters at the top and leaves at the bottom, the heat transfer coefficient increases with the growing height of the tube row. Conversely, when the sewage enters at the bottom and leaves at the top, the coefficient experiences the opposite trend to that of the height of the tube row.

2. Influence on the heat transfer performance of the evaporator from the sewage inlet parameter changes

Assume that the sewage flux and the refrigerant inlet status remain stable. Take the horizontal pass as an example, and examine the change of the evaporator performance when the sewage inlet temperature is 9–15 °C. Figure 15.5 depicts how the temperature in each pass changes with different sewage inlet temperature. As shown below, the outlet temperature of all passes increases when the sewage

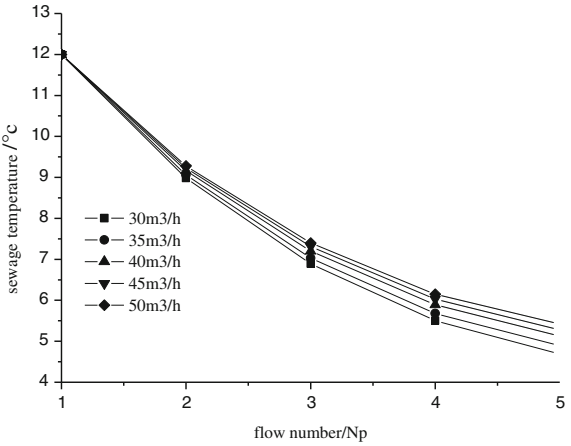

Fig. 15.6 Variation in the sewage temperature with different sewage flux along the pass

inlet temperature rises. These two share similar trend. When the sewage inlet temperature is 9 °C, the outlet temperature reaches to 4.51 °C; when the inlet temperature is 12 °C, the outlet amounts to 5.25 °C. When the inlet temperature increases to 15 °C, the outlet temperature is 6.01 °C.

Assume that the sewage inlet temperature levels out at 12 °C. The refrigerant inlet parameters are constant. Examine the evaporator performance when the sewage flux is 30, 35, 40, 45 and 50 m^3/h. Figure 15.6 depicts how the sewage temperature changes with different sewage flux along the passes. The graph shows that the sewage flux and the sewage outlet temperature have similar trend. But the variation range is rather limited. In other words, the flux does not affect the sewage outlet temperature in a decisive way. The major reason for this is that within the change span of heat exchange, the heat transfer coefficient and flux play a leading role.

15.4 Conclusions

This paper focuses on developing a simulation model of the distribution parameters of the sewage FRE, and writing corresponding programs for design and simulation. The following conclusions can be drawn via numerical simulation:

1. Smooth tubes are installed at the sewage side of the heat transfer tube, and no enforcement measures are taken. By adding the passes of the sewage, the flow velocity will experience an escalation and therefore bring about improvement in the heat transfer property. With respect to the sewage within the evaporator, four-pass process is the most recommendable.
2. The simulation results of the sewage evaporator show that the arrangement of passes or the inlets and outlets of the sewage has little effect on the heat exchange.

3. Simulation results also show that the changing sewage velocity has affected the heat exchange to a considerable extent. According to further analyses, that results from the significant effects of the sewage velocity, on the convection resistance and the fouling resistance on the sewage side.

Acknowledgments Supported by Doctoral Research Fund of Shandong Jianzhu University (XNBS1226)

References

1. Casciaro S, Tome JR (2001) Thermal performance of flooded evaporators, part 1: review of boiling heat transfer studies. ASHRAE Trans 107(1):903–918
2. Browne MW, Bansal PK (1999) Heat transfer characteristics of boiling phenomenon in flooded refrigerant evaporators. Appl Therm Eng 19:595–624
3. Webb RL, Choi KD, Apparao TR (1989) A theoretical model for prediction of the heat load in flooded refrigerant evaporators. ASHRAE Trans 95(1):326–338
4. Webb RL, Apparao TVVR, Choi KD (1989) Prediction of the heat duty in flooded refrigerant evaporators. ASHRAE Trans 95(1):339–348
5. Huang X, Wang Q, Wang R (2004) Prediction of the performance of flooded refrigerant evaporators based on a distributed parameter model. J Shanghai Jiaotong Univ 38(7):1164–1169
6. Webb RL, Choi KD, Apparao TR (1989) A theoretical model for prediction of the heat load in flooded refrigerant evaporators. ASHRAE Trans 95(1):326–338

Chapter 16
"Cross-Ventilation" Effect of Piston Wind and Energy-Saving Evaluation for the Ventilation and Air Condition in Subway Station

Zhenzhen Li, Chao Chen, Le Yan, Song Pan and Lili Zhang

Abstract This study takes a subway station of line 2 in Beijing as study object, based on the piston wind flow characteristics of a field test and a 1:8 scale model experiment combining the theoretical research and the numerical simulation, specially analyzed the influence on the piston wind flow characteristic of the different setting heights of the Semi-enclosed platform doors (SPDs), and based on the test results of air temperature and humidity in and out of the subway station analyzed the "cross-ventilation" effect of piston wind and evaluated its contribution to the energy consumption of the ventilation and air condition in subway station. Results show that little difference in the piston-wind volume exists when height of the SPDs changes [Enclosed platform doors (EPDs) or Semi-enclosed platform doors (SPDs)]; according to the summer weather condition of the large day–night temperature difference and the lower enthalpy in Beijing, a SPD can improve the indoor air quality and reduce the energy consumption of ventilation and air condition in subway stations in Beijing.

Keywords Piston wind · "Cross-ventilation" effect · Subway station environment · Field test and model · Energy consumption evaluation

16.1 Introduction

How to select an appropriate PDS according to the structure of the subway station and the characteristics of the subway operation system and the feature of annual weather variation in Beijing is of great meaning in safety and economic operation reducing the construction costs in the subway system.

Z. Li · C. Chen (✉) · L. Yan · S. Pan · L. Zhang
Beijing University of Technology, 100124 Beijing, China
e-mail: chenchao@bjut.edu.cn

A. Li et al. (eds.), *Proceedings of the 8th International Symposium on Heating, Ventilation and Air Conditioning*, Lecture Notes in Electrical Engineering 263,
DOI: 10.1007/978-3-642-39578-9_16,

Many scholars have done much work on the influence on the thermal environment and the air quality in subway station with the PDS. Hu and Lee [1] showed that little difference in EPDs exists in the overall energy consumption. Cao et al. [2] proposed a EPD system with the adjustable vents on it; this system can use the piston process to introduce outside air; thereby, it is obvious for energy-saving effect. Dong [3] considered that the heat extraction by the piston effect should be popularized in northern China. Zhang [4] showed SPD with the height of 1.7 m is appropriate in northern China. Xu [5] studied the energy consumption, and results showed that ventilation energy consumption of EPDs in the whole year is larger than that of SPDs in subway station of Tianjin. Ding and Zhu [6] concluded that PSDs can play an active role in energy saving of ventilation and air-condition system in subway stations in Nanjing.

In order to grasp the effect on air quality and thermal environment of different platform doors, in this study, it is combined with theoretical analysis, model experiment and numerical simulation to analyze the influence of piston wind on subway station air environment with different SPDs setting heights and the influence of the weather variation in summer in Beijing on the subway station environment to study the adaption condition of the SPDs. The relevant results obtained would provide some references for the energy saving and safety design of the subway system in Beijing.

16.2 The Piston Effect and the Improvement of the Air Environment in Subway

Due to the piston effect, when the train enters the station, the positive pressure in front of the train pushes some air in the tunnel flow into the platform of the station and then exhausts to outdoor through the way of "platform–concourse–corridor–ground exits" (Fig. 16.1a).

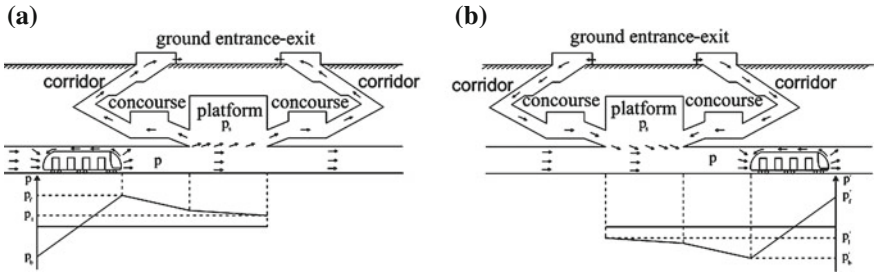

Fig. 16.1 Air flow characteristic analysis in the tested station. **a** Train entering into the tested station. **b** Train leaving the tested station

Likewise, when the train leaves the station, the negative pressure in the back of the train sucks the outdoor air into the tunnel through the converse path, thereby resulting in a "cross-ventilation" effect of "tunnel–platform–concourse–corridor–ground exits" (Fig. 16.1b), and improves the air quality of the relatively close subway station effectively.

16.3 Influence on the Piston Effect Flow of the Subway PDs

16.3.1 Typical Structure Characteristics of the Subway Station

This study takes the Beijing subway as the study object. Figure 16.2a shows the typical structure of the one-layer subway station in Beijing. Their characteristics are that the storey of the platform is higher, there are no PDs (Fig. 16.2 shows the supposed PDs), and the two concourses are on both ends of the station with a smaller area. Figure 16.2b shows the typical structure of the two-layer subway station in Beijing (H_0 is the height of air flow). Their main characteristics are that the platform and the concourse are separate, the storey of the platform is lower, there are PDs, and the area of the concourse is far greater than that of lines 1 and 2.

16.3.2 Analysis of the Piston Effect Flow Resistance in the Subway Station

In order to analyze the influence of the different station structures on the flow characteristics of piston wind, a one-layer subway station of the line 2 subway in Beijing (Fig. 16.2a) is taken as the key study object based on the team's previous work.

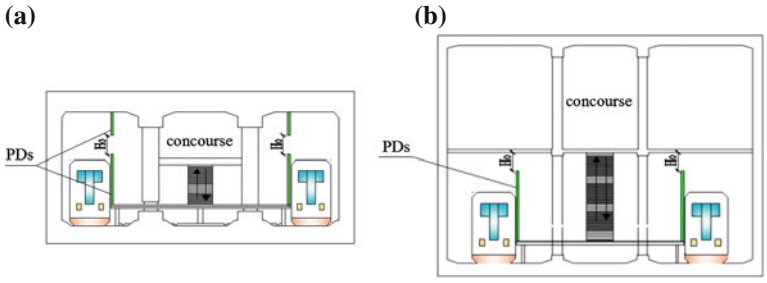

Fig. 16.2 Structure section of inland-type station. **a** One floor inland-type station. **b** Two floors inland-type station

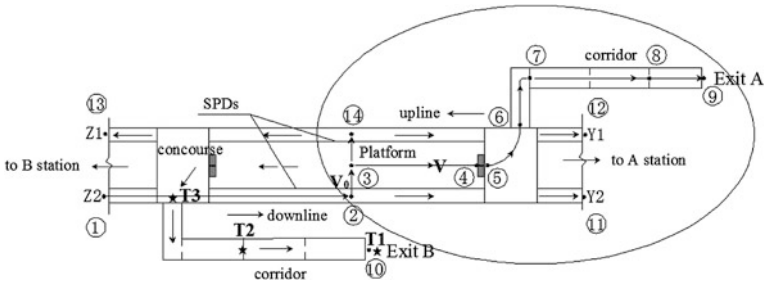

Fig. 16.3 Path of the subway piston wind through exit A

From Fig. 16.3, when train enters the station from the down line, due to the piston effect, air flow path from the station to ground exit A can be simplified as ①–⑨. Table 16.1 shows the resistance characteristics of the component H_0 above the SPDs (②–③); the pressure loss along can be obtained from formula (16.1). The cross-sectional velocity of the flow path in the platform supposes as V (③–④), and the cross-sectional velocity above the SPDs supposes as V_0 (②–③).

$$\Delta P_{\mathrm{SPDs}} = (0 \sim 8.91)\frac{v^2}{2g} \tag{16.1}$$

where ΔP represents pressure loss, Pa; Ψ friction coefficient of SPDs (Table 16.1); v_0 sectional velocity above the SPDs, m/s; and v sectional velocity along the flow path, m/s

$$\phi = \frac{\Delta P_{\mathrm{SPDs}}}{P_{\mathrm{total}}} = \frac{(0 \sim 8.91)}{(0 \sim 8.91) + 179.23} \approx 0 \sim 5\% \tag{16.2}$$

From formula (16.2), the pressure loss of the SPDs is only 5 % of the whole path with various H_0, and the pressure loss from the platform to the stairs in the concourse and from corridor to the ground exit A are 45 and 50 % of the whole line, respectively. That is, even if H_0 is 500 mm, it has very limited influence on the piston effect.

Table 16.1 Characteristics of difference semi-enclosed platform door heights

Air flow height above the SPDs H_0 (m)	Width of SPDs (m)	local resistance coefficient ζ_0	Sectional velocity $v_{0\ (v)}$	Ψ
0.5	138.8	4.29	1.44	8.91
1.0	138.8	2.98	0.70	1.46
2.0	138.8	1.37	0.41	0.23
No SPDs	138.8	0	1.00	0

Note $\zeta_0(v_0^2/2g) = \Psi(v^2/2g)$

16.3.3 1:8 Model Scale Verification Experiment

To verify the results that the SPDs have a little influence on the whole path pressure loss, an experiment on a 1:8 scale model (Fig. 16.4a) subway station of BJUT is conducted.

16.3.3.1 Similarity between the Model and the Prototype

Because this experiment mainly focuses on the flow of air, based on the similarity theory [7], there should be geometric similarity, kinematic similarity and dynamic similarity between the model and the prototype.

Arrow symbol in Fig. 16.4b represents flow direction of the air. When the exhaust fan is working, on the one hand, the air flows into the track area through a duct connected to the outdoor (black symbols). On the other hand, the outdoor air flows into the concourse through the four exits connected to the outdoor (red symbols).

16.3.3.2 Basic Program of the Experiment

Investigate on the air volume of the points 1 and 2 in Fig. 16.4 by changing the height of the SPDs and the frequency of the fan.

Hot Ball Anemometer testo-435 and Air Quantity Calculation 8317 of USA TSI Company are used in the test; each case repeats three times to reduce the accidental data.

16.3.3.3 Analysis of the Experiment Result

As shown in Fig. 16.5, the velocity of point 1 and the air volume of point 2 show almost no change when installing full-height SPDs, half-height SPDs or even no PDs corresponding to the frequency of the fan 40, 25 and 10 Hz. The results get a

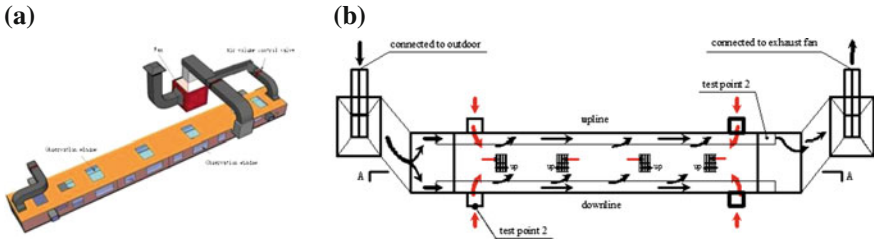

Fig. 16.4 1:8 scale model system. **a** Model; **b** the schematic diagram of air flow

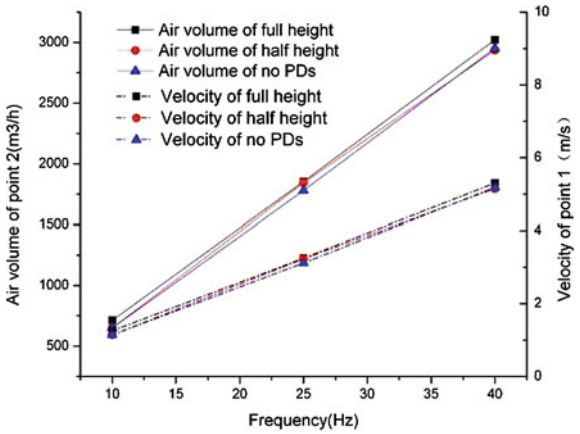

Fig. 16.5 The relationship between SPD height changes and the piston air volume

verification that the influence on the volume of the air flowing from the station to the ground exits is very limited when height of the SPDs changes.

The analysis result above shows that the influence on the air volume flowing from the station to the ground exits is very limited whether there are SPDs or not or its height changes.

16.4 The "Cross-Ventilation" Effect in the Subway Station

Based on the result of Sect. 2, the SPDs exit and the change of its height have little effect on the air flow in the ground exits of the subway station. For evaluating the influences of the "cross-ventilation" effect, it also takes the same station shown in Fig. 16.2a as the study object. It analyzes the characteristics of the sucked fresh air in the ground entrance–exits based on the piston effect combining field test with the simulation of Subway Environmental Simulation Program.

According to the results of the field test and the calculation of Fluent [8, 9], the change of fresh air volume in each zone of the station with time during one cycle (300 s) of the off-peak time is (Fig. 16.6) that the outdoor fresh air being sucked into through the ground exits (Fig. 16.7a) is during the first half-cycle (0–150 s); the foul air in the station is pushed out (Fig. 16.7b) during the latter half-cycle (150–300 s). During this period, the fresh air constantly mixes with the piston air from the tunnel in each area; then it is mixed up and exhausted to outside until the next cycle.

According to Fig. 16.7, due to the piston effect in the calculation cycle (300 s), a total outdoor fresh air volume of 7,820 m^3 can be sucked into the station through the ground exits. According to [10] mentioned, the suction fresh air volume can basically meet the fresh air demand for 3,860 people on the platform in an off-hour, while 71.4 % of the piston air from tunnel flows into the opposite tunnel and then the remaining piston air (4,566 m^3) flows into the station and finally flows through the entrance to outside.

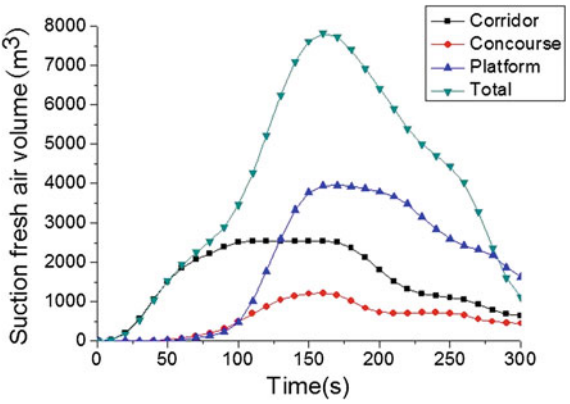

Fig. 16.6 Suction outdoor fresh air volume flow variation with time in each station area

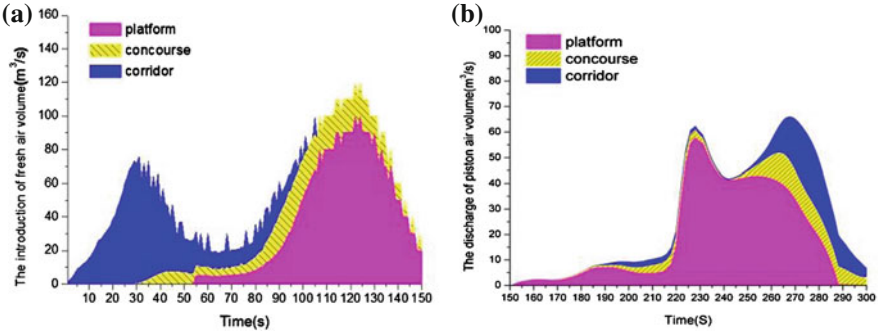

Fig. 16.7 The introduced and discharged amount of air through the ground exits in a cycle (300 s). **a** Fresh air flow (150 s). **b** Air flow exhaust (150 s)

The analysis above shows that a SPD in subway stations can make the piston-wind flow through tunnel–platform–concourse–corridor–ground entrances–outdoor, forming a "cross-ventilation" effect, achieving the goal of ventilation and air exchange in the subway station.

16.5 Energy-Saving Evaluation of "Cross-Ventilation" Effect

In the condition of installing the SPDs, "cross-ventilation" effect generated by the piston wind can introduce fresh air into the subway station through the ground entrances; it also can bring the cooling capacity when the outdoor enthalpy is

lower than the indoor enthalpy, thereby decreasing the energy consumption of ventilation and air-condition system; however, without the separation of the EPDs between tunnel and platform, braking heat from locomotive and condense heat from air-conditioning in the tunnel can increase the air-condition cooling load. That is, compared with the EPDs, SPDs can bring the cooling capacity from the exits and the heat that piston wind brings from tunnel of the subway.

16.5.1 Cooling Capacity into the Station from Ground Entrances

When train leaves the station with SPDs, the hot outdoor air can flow inside easily due to the piston effect. With the air being sucked into each station area, the air parameters change. Heat of the piston wind from ground entrances can be expressed by the formulae (16.3) and (16.4).

$$\begin{aligned} Q^f n = {} & M^{\text{corridor}} n\left(i^f - i^{\text{corridor}} n\right) + M^{\text{concourse}} n\left(i^f - i^{\text{concourse}} n\right) \\ & + M^{\text{platform}} n\left(i^f - i^{\text{platform}} n\right) \end{aligned} \tag{16.3}$$

$$Q^f = \sum_{n=1}^{150} Q^f n \tag{16.4}$$

where $Q^f n$ is the total heat from the fresh air in the moment of n, kJ; $M^{\text{corridor}} n, M^{\text{concourse}} n, M^{\text{platform}} n$ is fresh air volume introduced into corridor, concourse and platform in the moment of n, kg/s; i^f is enthalpy of the fresh air, kJ/kg; $i^{\text{corridor}} n, i^{\text{concourse}} n, i^{\text{platform}} n$ is air enthalpy in corridor, concourse and platform in the moment of n, kJ/kg; and Q^{f} is total heat from fresh air in a cycle (300 s), kJ.

16.5.2 Heat into the Station from the Tunnel

When train enters the station, the piston air from the tunnel flows into the station. With the piston air being introduced into each station area, the air parameters change. Heat of the piston air from tunnel can be expressed by the formulas (16.5) and (16.6).

$$\begin{aligned} Q^p n = {} & G^{\text{corridor}} n\left(i^p n - i^{\text{corridor}} n\right) + G^{\text{concourse}} n\left(i^p n - i^{\text{concourse}} n\right) \\ & + G^{\text{platform}} n\left(i^p n - i^{\text{platform}} n\right) \end{aligned} \tag{16.5}$$

$$Q^p = \sum_{n=151}^{300} Q^p n \tag{16.6}$$

where $Q^p n$ is the total heat from the piston wind in the moment of n, kJ; $G^{\text{corridor}} n, G^{\text{concourse}} n, G^{\text{platform}} n$ is piston-wind volume flow into corridor, concourse and platform in the moment of n, kg/s; $i^p n$ is enthalpy of the piston air in the moment of n, kJ/kg; and Q^p is total heat from piston air in a cycle (300 s), kJ.

16.5.3 Energy-Saving Evaluation from the Piston Effect

Based on Sects. 4.1 and 4.2, test data of the first express on July 27, 2011, were chosen for calculation, which is in the subway air-conditioning season; the air parameters in the public area are the design parameters, that is, temperature of the concourse/platform is 29/30 °C and the enthalpy is 70.8/74.3 kJ/kg; there is no air control system in the corridor, the test air temperature in the tunnel is 35 °C , and the enthalpy is 86.2 kJ/kg; the test outdoor temperature is 35 °C , and the enthalpy is 86.2 kJ/kg. Calculation result is shown in Fig. 16.8.

Figure 16.8a shows that the outdoor fresh air is being sucked into the station during the first half-cycle (0–150 s), as the outdoor enthalpy is lower than that of the each station area; ultimately, the cooling capacity from the ground exits into the corridor, concourse and the platform is 38,683, 32,342 and 1,093,l00 kJ, respectively (giving a total of 180,325 kJ). During the latter cycle (150–300 s), the piston air from the tunnel flows into the station, while the foul air in the station is exhausted to the outside, as the enthalpy of the piston air is higher than that of the each station area; the heat capacity from the piston air totals up to 67,045 kJ. After heat imbalance, the piston wind brings a total cooling capacity of 41,280 kJ for the station in a cycle (300 s).

Similarly, Fig. 16.8b shows that even in the hot summer months, the comprehensive effect of piston wind is a cooling capacity of 691,037 kJ/day to the station. Using the method mentioned above, a cooling capacity of 5.1×10^5 is introduced

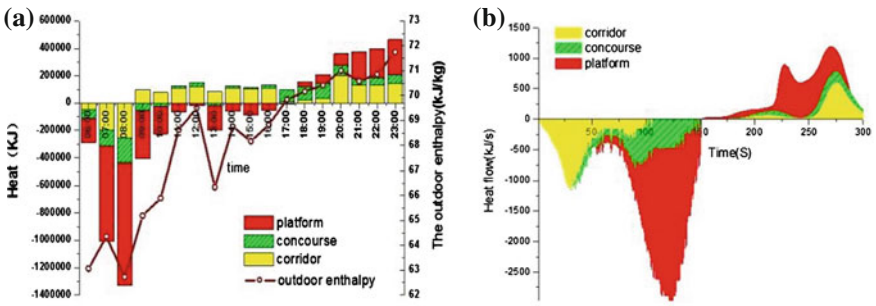

Fig. 16.8 Cooling capacity into the station from piston wind. **a** One calculation cycle in morning rush hour (300 s). **b** Whole day of July 27

into the station during the summer in Beijing (June 15–September 15, 2011). Obviously, installing SPDs achieve advantages in the energy saving of ventilation and air-conditioning in the subway station.

16.6 Conclusions

1. Theoretical analysis and experiment of 1:8 scale model show that the influence of the height of Semi-enclosed Platform Doors (full height, half-height or no platform doors) on the volume of the air flowing from the station to the ground exits is very limited.
2. A Semi-enclosed Platform Doors system in subway stations can make the piston-wind flow through tunnel–platform–concourse–corridor–ground entrances–outdoor, forming a "cross-ventilation" effect, achieving the goal of ventilation and air exchange in the subway station.
3. The results show that even in the hot summer months, a cooling capacity of 5.1×10^5 kJ/(per summer) is introduced into the station during the summer in Beijing. Installing SPDs achieve advantages in the energy saving of ventilation and air-conditioning in the subway station.

Acknowledgments This study is funded by Specialized Research Fund for the Doctoral Program of Higher Education of China (3B0040201201).

References

1. Hu SC, Lee JH (2004) Influence of platform screen doors on energy consumption of the environment control system of a mass rapid transit system: case study of the Taipei MRT system. J Energy Convers Manage 45(5):639–650
2. Cao RG, You SJ, Dong SY (2009) Energy consumption analysis and reconstruction of subway platform screen doors in northern cities for energy-saving. J Chongqing Univ 32(2):218–222
3. Dong SY (2008) Piston effect on the subway station and its' utilization in the north of China, Tianjin, China
4. Zhang L (2006) Measurement and simulation of piston wind in the subway station, Tianjin, China
5. Xu B (2007) The study of comfort and energy-consumption of platform bailout doors system and platform screen doors system in subway, Tianjin, China
6. Ding DY, Zhu PG (2008) Energy consumption of ventilating and air conditioning system of subway with platform safety gate. J Build Energy Environ 27(10):64–66
7. Long TY, CAI ZJ (2004) Fluid mechanics. Architecture and Building Press, China
8. Xu L (2011) Research on subway piston wind and its thermal environment, Beijing, China
9. Zhang LL (2012) Fresh air flow characteristics introduced through subway station passageway based on piston wind, Beijing, China
10. Code for Design of Metro GB50157-2003

Chapter 17
Numerical Simulation of Heat Transfer and Fluid Flow Characteristics of Server Rack in Datacenter

Jianfei Zhang, Donghao Liu, Xiping Qiao, Xu Du and Kaizhen Zhu

Abstract This chapter is studying the fluid mechanics and heat transfer of single server rack using the computational fluid dynamics software. The major study is the effect of the different structure parameters of server rack in datacenter, including the grille inlet size of under-floor air distribution, the blade angle of grille inlet, the size of return outlet, and the height of return outlet. And drawing the following conclusions: (1) the size of grille inlet has a significant influence, the temperature variation is nearly 3°; (2) when the inlet velocity is below 1 m/s, the blade angle of grille has a little influence on the air distribution, but the velocity is more than 1.0 m/s; the blade angle should be below 60°, never more than the limit value which is the arc tangent of the height of server rack and distance between server rack and grille inlet; (3) when keeping the height of suspended ceiling fixed and changing the height of return outlet, the height should be close to the top of server rack; and (4) the size of return outlet has a significant influence on air distribution of servicer rack, the temperature variation is around 2°.

Keywords Datacenter · Server rack · Size of grille inlet · Size of return outlet · Height of return outlet · Blade angle of grille inlet

J. Zhang (✉) · D. Liu · X. Qiao · X. Du · K. Zhu
Green Technology Center, SIPPR Engineering Group Co., Ltd, 450007 Zhengzhou, China
e-mail: hnzjf08@163.com

D. Liu
e-mail: xmldh1014@163.com

X. Qiao
e-mail: qxpsunny114@126.com

X. Du
e-mail: chinaduxu@yahoo.cn

K. Zhu
e-mail: hnzjf08@163.com

A. Li et al. (eds.), *Proceedings of the 8th International Symposium on Heating, Ventilation and Air Conditioning*, Lecture Notes in Electrical Engineering 263,
DOI: 10.1007/978-3-642-39578-9_17,

17.1 Introduction

The datacenter occupies an important position in the lifeblood of business; it would cause irreversible loss if problem arises. Through running practice of data center, the reliability and service life of server are closely related to its temperature. Along with the advance in technology, the heat-flow density of server is rising rapidly, so the reasonable air distribution plays a critical role in functional operation of data-center. Meanwhile, the price of data equipment and room-dedicated air-conditioning is very expensive, and the energy consumption of air-conditioning is huge; the unscientific running mode of air-conditioning would cause a great waste of equipment investment and energy. Then, it will be extremely valuable in researching the operation mode of air-conditioning in datacenter deeply.

The technology that modeling the actual problem using the CFD has achieved rapid development, the cooling of datacenter is the most excellent application of CFD [1]. This chapter is studying the fluid flow mechanics and heat transfer process along the surface of server rack in the datacenter using the simulation software; the major study is the effect of different structure parameters for air distribution of server rack, including the size of grille inlet, the blade angle of grille inlet, the size of return outlet, and the height of return outlet.

17.2 Physical Model

In the datacenter, the main heat source is the server rack. In order to cool server cabinets effectively, the arrangement of server rack adopts array-based layout in order to form cold aisles where the front of adjacent server racks are facing each other and hot aisles where the back of adjacent server racks are facing each other. Because of the symmetry plane existing among adjacent server rack and adjacent ranks, it is an ideal condition for studying single sever rack [2]. The model which is built using CFD software is showed in Fig. 17.1, and the structural size is shown in Fig. 17.2 and Table 17.1.

The dimensions of server rack are 600 × 1000 × 2000 mm, and there are many slots which can place servers in the server rack. In order to simplify the model, it is assumed that there exists ten servers in the server rack. The height of each server is 0.08 m, the gap between the servers is passageway of air circulation, and its height is 0.12 m. When designing the datacenter, the heat energy which is produced by each rack is usually supposed to be 3 kW; this is considered to include all kinds of factors and is a maximum value. The following are some assumptions: (1) The heat flow cannot go out neither through the bottom nor the top of the heat source. This is based on that the bottom of the heat source contacts the directly. So we need a frame for the server rack. (2) The heat flux of each server escapes from the surface, and primarily from the upper and nether surfaces of server, the right and left surfaces of server are assumed to be heat insulation

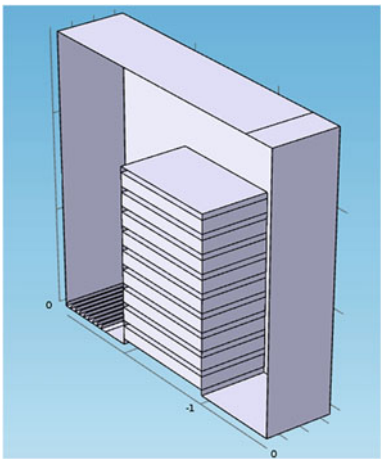

Fig. 17.1 Physical model built in CFD software

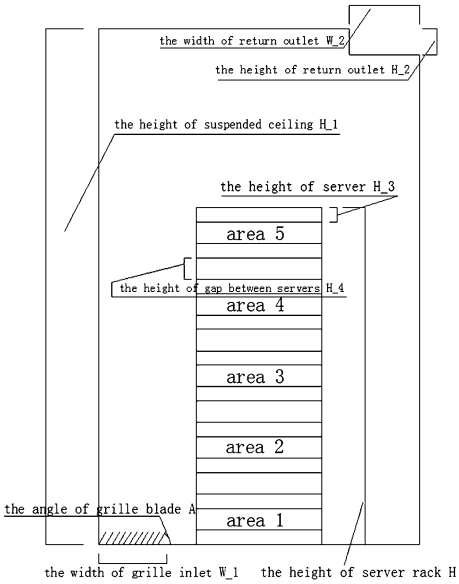

Fig. 17.2 The structural size of single server rack

Table 17.1 Structural size of server rack

H (m)	H_1 (m)	H_2 (m)	H_3 (m)	H_4 (m)	W_1 (m)	W_2 (m)	A (deg)
2	2.8	0	0.8	1.2	0.605	0.605	60

face. Because there are ten servers in server rack, there exists twenty surfaces, and excluding the upper and nether surfaces, there will be eighteen surfaces which are used to dissipate heat. The size of each surface is $0.605 \times 1.015 = 0.614075\ m^2$,

the total size of all surfaces is $0.614075 \times 18 = 11.05335\ m^2$, so the heat flux escaped from the surface is $3{,}000/11.05335 = 271.4\ W/m^2$. Because of assuming the surface heat source, it is unnecessary to set the body heat source; it is beneficial to save a lot of gridding because of removing away the domain which used to be the body heat source.

When running the numerical calculation for single serve rack, the grille inlet volume flow rate and temperature of supply air of under-floor air distribution are kept constant. The air volume flow rate is fixed at $0.244318\ m^3/s$, while the temperature is fixed at 14 °C; the return outlet is set to outlet of heat flux and pressure; the right and left faces of fluid are set to periodic flow boundary condition and periodic thermal boundary condition; buoyancy force exists in all domain; the surface of each server is set to surface heat source, and the heat flux is $271.4\ W/m^2$.

17.3 Results of Numerical Simulation and Discussion

In order to cool down the temperature of server rack, the traditional way is increasing the air quantity of air-condition. This measure can cool the temperature of server rack, but it costs more energy consumption, initial investment, and operating cost. Many studies show that reasonable air distribution can effectively decrease the temperature without increasing the air quantity of air condition to reach win–win situation. The following analysis analyzes the influence of different parameters under the condition of verifying the rationality of model and reliability of computing method. The temperature of five main areas will be measured to be the criterion to respond to the effect of different parameters, the five areas are shown in Fig. 17.2.

17.3.1 The Size Effect of Grille Inlet on Air Distribution

There are eighty-eight server racks in datacenter; the cooling capacity is provided by three dedicated precision air-conditioning, the cooling capacity of each is 100 kW, and the air output is $215{,}800\ m^3/h$; so the average quantity of air supply for each server rack is $25{,}800 \times 3/3{,}600/88 = 0.244318\ m^3/s$. Keeping the length fixed and changing the width, the inlet velocity can be determined through different width. The width of grille outlet changes from 0.242 to 0.762 m. Because of the fixed volume flow rate, the inlet velocity changes from 0.53 to 1.668 m/s.

From the Table 17.2 and Fig. 17.3, it can be concluded as follows: the width of grille inlet has a significant influence on the air distribution, the temperature of five areas decreases with the width increase of the grille inlet. The temperature variation is very obvious and almost 3°. The major reason for this phenomena is that the inlet velocity is very high when the width of grille inlet is kept low under the condition of

Table 17.2 The average temperature of each area under different width of grille inlet

Width of grille inlet (m)	Average temperature (K)				
	Area 1	Area 2	Area 3	Area 4	Area 5
0.242	302.2	302.58	302.73	302.93	303.5
0.3025	302.06	302.22	302.47	302.66	303.02
0.363	301.71	301.96	302.13	302.35	302.72
0.4235	301.43	301.51	301.66	301.92	302.48
0.484	301.19	301.23	301.39	301.79	302.17
0.5445	300.71	300.94	300.91	301.51	301.84
0.605	300.21	300.69	300.77	301.22	301.51
0.6655	299.57	299.86	300.12	300.76	301.12
0.726	299.22	299.34	299.72	299.8	300.25

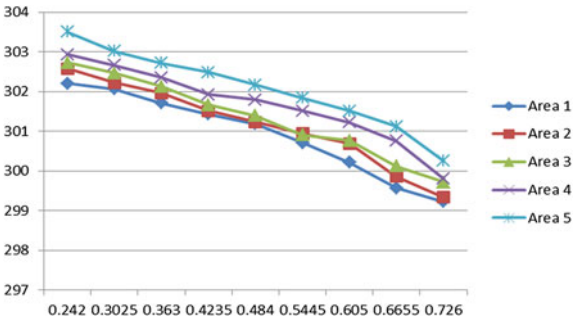

Fig. 17.3 The temperature variation of each area under different width of grille inlet

fixed volume flow rate; in other words, the inertia force is very high, and far more than the buoyancy force, leading to most of air flow reaching the return outlet through the space on top of server rack instead of the passageway between servers and resulting in cold short circuit. When the width of grille inlet increases gradually, the inlet velocity decreases correspondingly; the difference between inertia force and buoyancy force reduces, resulting in most of the air volume flow rate passing the server rack and cooling down the server rack. Taking into account the overall performance of heat exchange, it can be concluded that if the length of grille inlet is 0.6 mm, the width should be more than 0.5 mm; in other words, the inlet velocity should be between 0.5 and 1.8 m/s when the volume flow rate is fixed.

17.3.2 The Angle Effect of Grille Blade on Air Distribution

From the Table 17.3 and Fig. 17.4, it can be concluded as follows: the average temperature of each area decreases, when the angle of grille blade exceeds 70°, the average temperature of area 1 increases slightly, the average temperature of area 2 is constant first and then decreases gradually, the average temperature of areas

Table 17.3 The average temperature of each area under different degree of grille blade

Angle of grille blade (rad)	Average temperature (K)				
	Area 1	Area 2	Area 3	Area 4	Area 5
0.34907	300.98	300.95	301.25	301.93	302.30
0.5236	300.76	300.81	301.12	301.86	302.14
0.69813	300.50	300.93	300.86	301.63	302.04
0.87266	300.27	300.62	300.75	301.47	301.84
1.04719	300.15	300.63	300.80	301.50	301.78
1.2217	300.09	300.59	300.65	301.36	301.69
1.3963	300.44	300.30	300.56	300.98	301.54

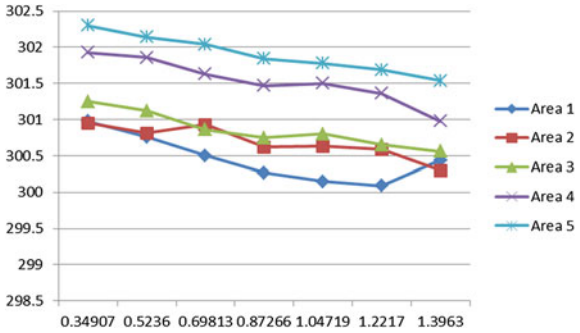

Fig. 17.4 The temperature variation of each area under different degree of grille blade

3, 4, and 5 always decreases. And the temperature variation of areas 1, 2, and 3 which is less than 0.6 K is relatively small compared with the average temperature of areas 4 and 5 which is around 1 K. The reason for the temperature variation of area 1 is that area is located on the bottom of server rack; the angle variation of grille blade had very small influence on air volume flow rate of area 1, so the temperature variation is not obvious, and the reason for temperature elevation when the angle of grille blade is above 70° is that the air volume flow rate which passes through area 1 decreases, while the air volume flow rate which passes through the top of server rack increases. The height of server rack is 2 m, the distance between air supply inlet and server rack is 0.8 m, and the angle of grille blade is not more than a $\cot(2/0.8) = 1.19103$ rad. The angle variation of grille blade has a small influence on the temperature of areas 1, 2, and 3, but has a great influence on the temperature of areas 4 and 5 because the air flow rate was kept small on the condition of low angle of grille blade while more on the condition of high angle of grille blade.

Table 17.4 The average temperature of each area under different height of return outlet

Height of return outlet (m)	Average temperature (K)				
	Area 1	Area 2	Area 3	Area 4	Area 5
0.1	300.32	300.55	300.69	301.21	301.83
0.2	300.29	300.20	300.28	301.13	301.52
0.3	300.17	299.97	300.03	301.05	301.16
0.4	300.21	299.83	299.73	300.74	300.93
0.5	300.01	299.76	299.52	300.44	300.66
0.6	299.89	299.88	299.49	300.33	300.20
0.7	299.56	299.73	299.21	299.77	299.99

17.3.3 The Height Effect of Return Outlet on Air Distribution

From the Table 17.4 and Fig. 17.5, it can be concluded as follows: the average temperature of each area decreases gradually along with the distance increase between the return outlet and the top of server rack, the degree of temperature change of areas 1 and 2 is relatively small compared with the degree of temperature change of areas 3, 4, and 5. It is obvious that the more lower the height of return outlet above the hot aisle is, the more faster the heat flux can run out of the room, and the negative pressure will be higher when the height is kept low, resulting in most of the cooling air passing through the server rack; this can optimize the air distribution. When designing the datacenter, this method is adopted if the quantity of heat of server rack is great, reducing the height of return outlet close enough to top of server rack.

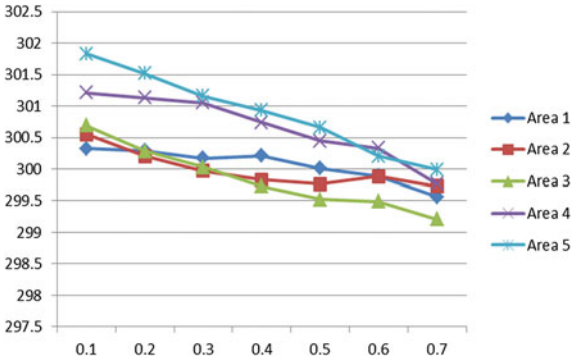

Fig. 17.5 The temperature variation of each area under different height of return outlet

Table 17.5 The average temperature of each area under different width of return outlet

Width of return outlet (m)	Average temperature (K)				
	Area 1	Area 2	Area 3	Area 4	Area 5
0.3	301.54	301.69	301.93	302.21	302.32
0.4	301.28	301.55	301.57	301.77	301.93
0.5	300.85	301.12	301.12	301.51	301.79
0.6	300.17	300.45	300.67	301.24	301.63
0.7	299.75	300.23	300.22	300.83	301.11
0.8	299.35	299.63	299.82	300.35	300.71

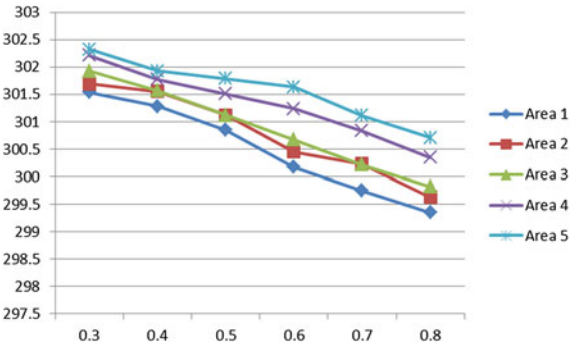

Fig. 17.6 The temperature variation of each area under different width of return outlet

17.3.4 The Width Effect of Return Outlet on Air Distribution

From the Table 17.5 and Fig. 17.6, it can be concluded as follows: the average temperature of each area decreases gradually along with the width of return outlet increase; the temperature variation is almost 2°, so the width of return outlet will have a great influence on the air distribution of server rack. When the width of return outlet is low, the velocity of return outlet is high; the air flow on the top of server rack and cold aisle will be entrained by the air flow of return outlet, leading to the confusion and cold short circuit of air flow on the top of server rack and cold aisle, it is evident that there exists the air-entraining vortex when the width of return outlet is small. When the width of return outlet is large, the velocity of air flow of return outlet is small; the air flow of whole area is well-distributed.

17.4 Conclusion

This chapter has simulated the sole server rack using the CFD software and studied the influence of structural parameter of datacenter to the heat transfer and fluid flow characteristics of server rack in datacenter, including the grille inlet size of under-floor air distribution, the blade angle of grille inlet, the return outlet size, the

return outlet height, and the height of suspended ceiling. And drawing the following conclusion:

1. the size of grille inlet has a significant influence; the temperature variation is nearly 3°; if the length of grille inlet is 0.6 mm, the width should be more than 0.5 mm; in other words, the inlet velocity should be between 0.5 and 1.8 m/s when the volume flow rate is fixed;
2. when the inlet velocity is below 1 m/s, the blade angle of grille has a little influence on the air distribution; but if the velocity is more than 1.0 m/s, the blade angle should be below 60°, never more than limit value which is the arc tangent of the height of servicer rack and distance between servicer rack and grille inlet;
3. when keeping the height of suspended ceiling fixed and changing the height of return outlet, the height of return inlet should be close to the top of server rack; it is better to keep the distance between the top of server rack and height of return inlet around 100 mm;
4. the size of return inlet has a significant influence on air distribution of servicer rack; the temperature variation is around 2°; when the length of return inlet is 0.6 mm, the width should be more than 300 mm; in other words, the velocity of return inlet should be less than 3 m/s; this will promote the cool air through the server rack.

References

1. Pan Y, Yin R, Huang Z (2008) Energy modelling of two office buildings with data center for green building design. Energy Build 40:1145–1152
2. Karki KC, Patankar SV (2006) Airflow distribution through perforated tiles in raised-floor data center. Build Environ 2006(41):734–744
3. Su Y, Long T, Xiang W (2007) Computational fluid dynamics, Central South University Press
4. Anderson JD (1995) Computational fluid dynamics. The basics with applications. McGraw Hill, New York, Tsinghua University Press, Beijing

Chapter 18
Study on Thermal Resistance of Basement Exterior Wall in Hot Summer and Cold Winter Zone

Huizhi Zhong and Ya Feng

Abstract With the growing of high-rise building in hot summer and cold winter zone, dew retardation measures of building basement are becoming more and more important. The problem of dew retardation is appeared in some buildings, which built before the code of design standard for energy efficiency of public buildings putting into practice. With the implementation of the code of design standard for energy efficiency of public buildings, the problem of dew retardation is not appeared any more. But the regulations of limits for the thermal resistance of basement exterior wall in hot summer and cold winter zone are 1.2 m^2 k/w, which did not find the relevant basis. In this paper, the inner surface temperature of basement exterior wall in Chengdu was studied by using numerical simulation program, energyplus, under given outside weather conditions in summer. After analyzing and comparing the calculated results, the basement exterior wall will be condensed despite the thermal resistance of basement exterior wall, which is inconsistent with the actual. After analyzing the results, there are three reasons. First, the underground soil temperature is missing, and the temperature provided by software is not accurate. Second, because the basement is connected outdoor through the underground garage entrance, the ventilation frequency is very difficult to determine. Third, the meteorological data is wrong.

Keywords The thermal resistance of basement exterior wall · Design standard for energy efficiency of public buildings · Dew retardation

H. Zhong · Y. Feng (✉)
China Southwest Architecture Design and Research Institute, Chengdu 610042, China
e-mail: fc10@xnjz.com

A. Li et al. (eds.), *Proceedings of the 8th International Symposium on Heating, Ventilation and Air Conditioning*, Lecture Notes in Electrical Engineering 263,
DOI: 10.1007/978-3-642-39578-9_18,

18.1 Introduction

The moisture content of air is commonly described as the "relative humidity" (RH). This is expressed as a percentage and compares the moisture content of air to the maximum moisture capacity of air at a specified temperature. The air temperature is important since air's capacity to hold moisture is lower at reduced temperatures. When warm outdoor air contacts cold surfaces, its temperature falls, causing the RH to increase. If RH reaches 100 %, condensation occurs. Because the surfaces of basement influenced by the soil temperature, the moisture problem of basement is worse. Several investigators have studied on the moisture problem of basement. Ponessa [1] researched when to ventilate the basement to reduce moisture problems. King and Meyer [2] advised to insulate the wall, raise the inside surface temperature much closer to the indoor air temperature, and reduce the risk of condensation. Bo et al. [3] analyzed and calculated the site inspection results based on an exterior-protected construction of an energy conservation construction in cold area. Zhang [4] found out the cause of condensation based on the analysis for the condensation of an underground garage in Suzhou Industrial Park (SIP).

In fact, above-described studies are mainly focused on the measures of reduced moisture problems. The problem of dew retardation was appeared usually in public buildings. And the regulations of limits for the thermal resistance of basement exterior wall in hot summer and cold winter zone are 1.2 m^2 k/w, which is determined in the code of design standard for energy efficiency of public buildings [5]. But the reason for the regulations of limits for the thermal resistance is not clear. So the building energy simulation program (EnergyPlus) was used to verify the thermal resistance of basement exterior wall in hot summer and cold winter zone.

18.2 Methodologies

Because the public building structure is complex, the research building must be simplified. In Fig. 18.1, the simplified building model is shown. The building is one story under and over ground, the height between floors is 4 m, and the area ratio of window to wall is 0.3.

18.2.1 The Thermodynamic Parameters

The external thermal insulation system was used in the external wall; the structure and the materials' parameter of external wall are presented in Table 18.1. The flat roof was used in the building; the roof structure and the materials' parameter of flat roof are presented in Table 18.2. The outside wall of basement was also presented in Table 18.3.

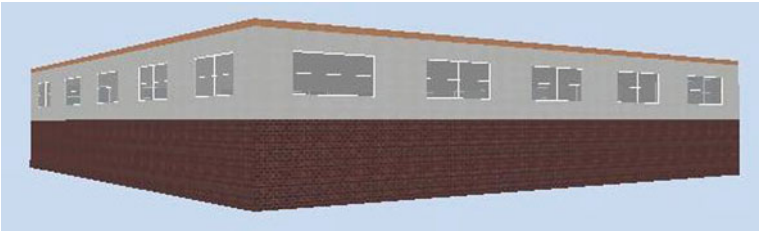

Fig. 18.1 Building model

Table 18.1 The structure and the materials' parameter of external wall

external wall	Thickness (mm)	Thermal conductivity (W/m K)	Specific heat [KJ/(kg K)]	Materials density (kg/m^3)
EPS of outside	25	0.04	1.4	15
Cement mortar	20	0.93	0.84	2,000
Brick	240	0.84	0.80	1,700
Cement mortar	20	0.93	0.84	2,000

Table 18.2 The structure and the materials' parameter of flat roof

flat roof	Thickness (mm)	Thermal conductivity (W/m K)	Specific heat [KJ/(kg K)]	Materials density (kg/m^3)
EPS of outside	40	0.04	1.4	15
Cement mortar	20	0.93	0.84	2,000
Concrete	200	1.58	0.84	2,500
Cement mortar	20	0.93	0.84	2,000

Table 18.3 The structure and the materials' parameter of outside wall of basement

External wall	Thickness (mm)	Thermal conductivity (W/m K)	Specific heat [KJ/(kg K)]	Materials density (kg/m^3)
brick of outside	100	0.84	0.80	1,700
XPS	30–60	0.04	1.4	15
concrete	100	1.58	0.84	2,500
cement mortar	13	0.93	0.84	2,000

18.2.2 The Heat Comes from Light and the Room Air Change per Hour

Room heat gain only includes lights heat gain in basement. The lights heat gain is from 0 w/m^2 to 8 w/m^2 [6]. And the room air change per hour (ACH) is assumed to be 1.0–6.0 h^{-1}.

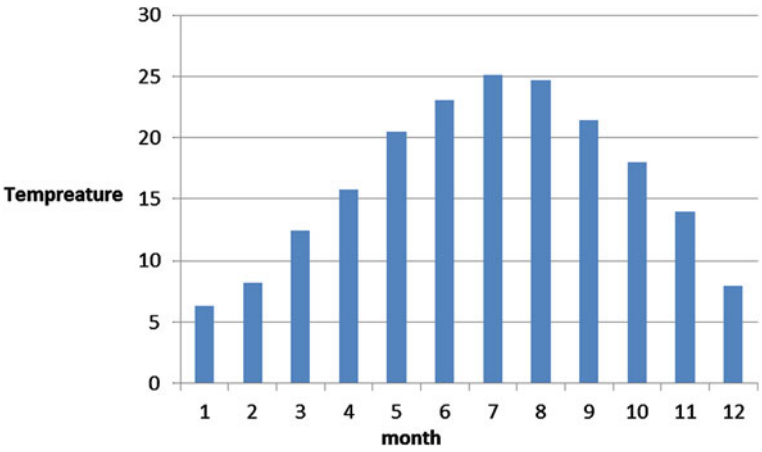

Fig. 18.2 Monthly mean temperature of underground soil

18.2.3 The Typical Cities and Underground Soil Temperature

The hot summer and cold winter zone covers large cities; it is not possible to put every city to study. Hence, Chengdu is chosen to be studied. The underground soil temperature was presented in Fig. 18.2, which is calculated by basement program. The basement program used to calculate the results is included with the Energy-Plus distribution.

18.2.4 Calculation Modes

For verifying the thermal resistance of basement exterior wall in hot summer and cold winter zone, the insulated materials' (eps) thickness of outside wall of basement was set to 30, 40, 50, and 60 mm, and the thermal resistance of basement exterior wall is 1.168, 1.418, 1.668, 1.918 (m^2 K)/W, respectively. The room ACH was set to be 1.0, 2.0, 3.0, 4.0, 5.0 and 6.0 h^{-1}, respectively. And the lights heat gain was set to 0, 2, 4, 6, 8 w/m^2, respectively.

18.2.5 Results and Discussion

The Fig. 18.3 presents the dew retardation hours of different insulated materials' thickness of outside wall of basement. The dew retardation hours reduce with the thickness increasing. And the dew retardation hours are not reduced when the

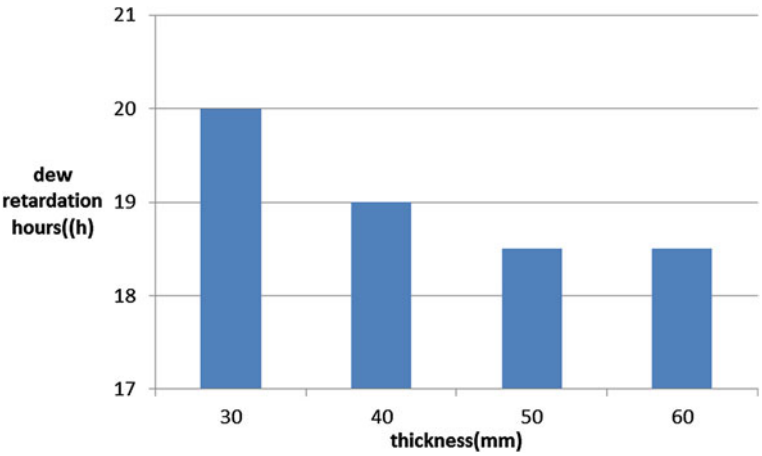

Fig. 18.3 The dew retardation hours of different insulated materials' thickness of outside wall of basement

thickness of insulated materials reach 50 mm. In other words, the dew retardation hours are steady when the thermal resistance of basement exterior wall is 1.668 (m^2 K)/W. And it is unnecessary to enhance the thermal resistance any more.

The Fig. 18.4 presents the dew retardation hours of different ACH. The dew retardation hours increase with the ACH increasing. And the dew retardation is not increased when the ACH reach 5. That is to say, the ACH must be reducing for reducing moisture problems of outside wall of basement.

The Fig. 18.5 presents the dew retardation hours of different heat gain. The dew retardation hours reduce with the heat gain increasing. And the dew retardation hours is 0 when the heat gain reaches 5.

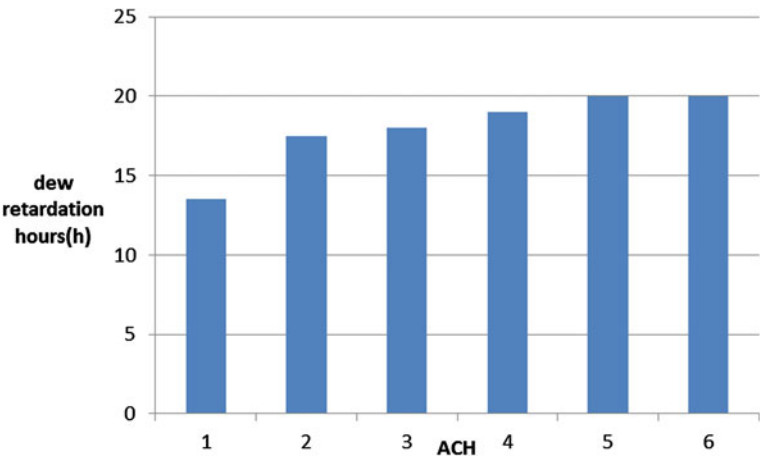

Fig. 18.4 The dew retardation hours of different ACH

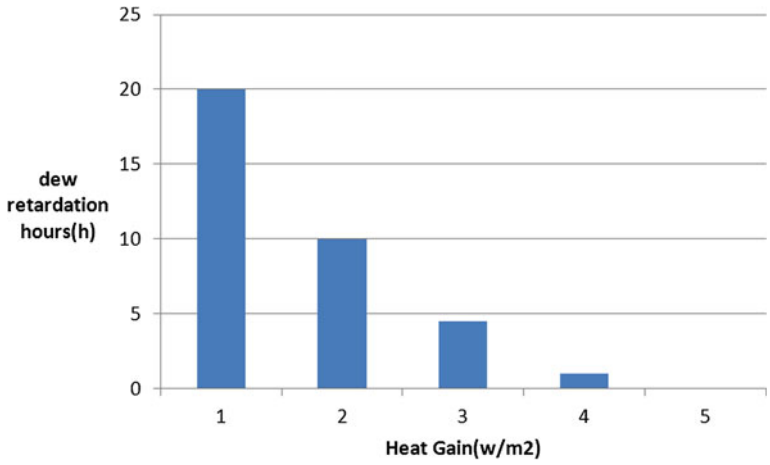

Fig. 18.5 The dew retardation hours of different heat gain

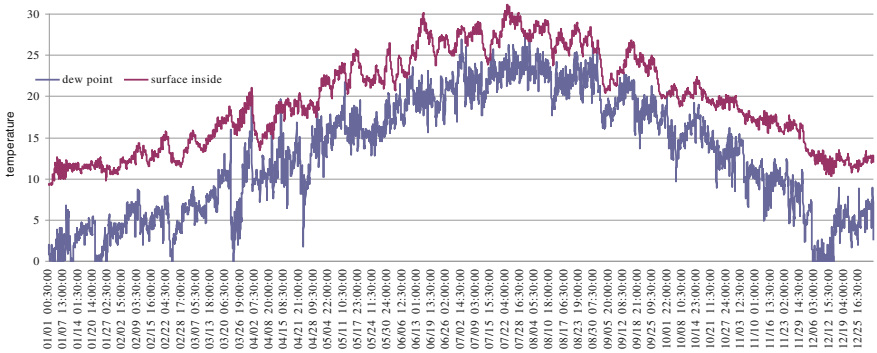

Fig. 18.6 The comparison between the dew point temperature and the surface inside temperature of basement

In the fact, the heat gain of basement is usually below 2 w/m^2. The Fig. 18.6 presents the comparison between the dew point temperature and the surface inside temperature of basement when heat gain is 2 w/m^2. The dew retardation hours appear in 13/4 and 1/10 from Fig. 18.6.

18.3 Conclusions

The moisture problems of outside wall of basement in chengdu were studied using the building energy simulation program (EnergyPlus) under given outside weather conditions. And the conclusion could be drawn as follows:

1. The dew retardation hours reduce with the thickness increasing. And the dew retardation hours are steady when the thermal resistance of basement exterior wall is 1.668 (m^2 K)/W.
2. The ACH must be reducing for reducing moisture problems of outside wall of basement.
3. The dew retardation hours is 0 when the heat gain reaches 5. In the fact, the heat gain of basement is usually below 2 w/m^2. When heat gain is 2 w/m^2, the dew retardation hours appear in 13/4 and 1/10.

In actual building, the moisture problems of outside wall of basement will not appear when the thermal resistance of basement exterior wall reaches 1.2 m^2k/w. But the calculated results show that the dew retardation hours will appear in 13/4 and 1/10, which is inconsistent with the actual. After analyzing the results, there are three reasons. First, the underground soil temperature is missing, and the temperature provided by software is not accurate. Second, because the basement is connected outdoor through the underground garage entrance, the ventilation frequency is very difficult to determine. Third, the meteorological data is error.

Acknowledgments The authors gratefully acknowledge the financial support of the State Natural Sciences Foundation 51038005.

References

1. Ponessa JT (2002) When to ventilate the basement to reduce moisture problems. www.rce.rutgers.edu
2. King JE, Meyer G (1999) A builder's guide to residential foundation insulation. Energy Programs, Kansas Corporation Commission, Topeka, KS
3. Bo H, Pan Y, Li H (2009) Analysis and counter measures on condensation of energy conservation construction in cold area. J HUST (Urban Sci Ed) 26:3
4. Zhang H (2010) Analysis and solution for the condensation of the basement. Build Energy Effi 38:228
5. GB501189-2005 (2005) The code of design standard for energy efficiency of public buildings
6. Lu Y (2007) Practical heating air conditioning design manual

Chapter 19
A CFD Study of Convective Heat Transfer at an Isothermal Surface with Horizontal Louvers

Fujian Jiang, Zhengrong Li, Qun Zhao, Qiuhua Tao and Xiaobin Li

Abstract Louvers blind can change its surrounding airflow and temperature field, which will affect the convective heat transfer of a vertical surface near louvers. In order to correctly predict HVAC load and building energy consumption, it is important to calculate the convective heat transfer coefficient of interior and exterior surfaces with louvers. The present study has been conducted on a CFD simulation for laminar and steady natural convective heat transfer in an approximated system that consists of an isothermal vertical surface with louvers blind. The effects of louvers blind on the natural heat transfer are obtained by the two-dimensional CFD model, which is validated with the previous experimental data. It is found that the louvers can promote or restrain the natural convective heat transfer of an isothermal surface. Such effects are periodic distributed along the vertical direction, which is partially determined by the geometry and physical properties of louvers. The impact of distance from louvers to surface b, temperature difference between surface and ambient air ΔT as well as louvers angle φ on the heat transfer coefficient distribution will be discussed in this research.

Keywords Louvers blind · Natural convection · Local heat transfer coefficient · CFD simulation

Nomenclature

b	Distance from louvers to surface
w	Width of louver blade

Z. Li (✉)
Tongji University, Room 413-3, Jiyang Building, 1239# Siping Road, Yangpu disctrict 200092 Shanghai, China
e-mail: ZhengrongLi@tongji.edu.cn

F. Jiang · Z. Li · Q. Tao · X. Li
School of Mechanical Engineering, Tongji University, Shanghai, China

Q. Zhao
College of Architecture and Urban Planning, Tongji University, Shanghai, China

A. Li et al. (eds.), *Proceedings of the 8th International Symposium on Heating, Ventilation and Air Conditioning*, Lecture Notes in Electrical Engineering 263,
DOI: 10.1007/978-3-642-39578-9_19,

t	Thickness of louver blade
p	Blade spacing
u, v	x, y velocity components
g	Gravitational acceleration
c_p	Specific heat
k	Thermal conductivity
I	Radiation intensity
F_{kj}	View factor from surface k to surface j
A	Surface area for radiation calculation
r	Distance from surface k to surface j
h	Convective heat transfer coefficient

Greek symbols

φ	Louvers angle, degrees
ρ	Density
μ	Dynamic viscosity
β	Volumetric expansion coefficient
T	Temperature
ε	Emissivity
σ	Stefan-Boltzmann constant

Subscripts

∞	Associated with ambient air
s	Associated with the isothermal surface
b	Associated with blinds
l	Associated with local heat transfer

19.1 Introduction

Shading device is widely used in buildings to control solar heat gain and sunlit. The application of shading, such as louvers blind, will affect the convective heat transfer at the indoor or outdoor surface of envelops, which is important for accurate analysis of envelops' thermal performance. In this research, a CFD solution is presented to examine the complex thermal effects of louvers blind on the natural convective heat transfer at an adjacent vertical isothermal surface for the simulation of "nighttime" conditions.

Several previous studies have been done for the convective heat transfer between vertical surface and louvers blind. Fang and Ge [1] used side-by-side test boxes to investigate the U-value of glass window with louvers blind. The result of this study showed the significant influence of the louvers on the U-value of the whole fenestration system. Machin [2] has got the temperature and steam fields

between louvers and an isothermal surface by Mach–Zehnder interferometer and flow visualization. This study indicated that under this experiment condition, the louver blades produced reduction on the average convective heat transfer from the surface to the air around (for 0, ±45 blade angle) and a periodic variation in the local convective heat transfer distribution along the isothermal surface. It also showed the blade angle and blind-to-plate spacing will determine the extent of the impact. Based on Machin's experimental work, some numerical simulations have been carried out on effects of geometry and physical properties to the convection at the isothermal surface with louvers [3, 4]. These simulations extended convective heat transfer research of this fenestration system. Phillips [3] developed a two-dimensional modeling of a louvers blind adjacent to vertical isothermal plate. The result reported that the louver blades enhance the free convection at low Rayleigh number while inhabit the free convection at high Rayleigh number. Shahid [4] extended the simulation work to complete fenestration with louvers blind to evaluate the heat transfer and energy efficiency of these systems.

In the present study, a CFD model is developed for an isothermal surface with louvers blind, which is similar to Phillips's work. The influence of some parameters on the natural local heat transfer coefficient distribution will be discussed in this study.

19.2 CFD Modeling and Analysis

At present, most fenestration calculation models of energy simulation software are in steady state. The temperature difference and feature dimension of fenestration system are not large, so the flow is always laminar along the surface of windows at natural convection. Taken together, present CFD modeling is set up in steady state and laminar flow conditions. Thermal properties of the flow are assumed constant, except that the density difference of flow, which is the force of natural convection, is treated with the Boussinesq approximation.

The two-dimensional model geometry is shown in Fig. 19.1 for a surface with louvers blind. In this modeling, boundaries AB, BC, and CD are fluid entrance/exit for natural convection, where the values of first derivatives of velocity and temperature are both zero. DE and GA are fixed to be the surfaces with no influence on the convection. EF and FG are set to be isothermal surfaces with no slip/impermeability velocity conditions to simulate the surface of envelope. The louvers are present at a distance b from the surface, with width w, thickness t, louvers angle φ, and blade spacing p. In this study, the louvers were set at the width of $w = 25.4$ mm, thickness of $t = 0.17$ mm, and spacing $p = 22.2$ mm, the same as louvers in Machin's experiment.

With these physical and geometry conditions, the governing equations by the finite volume model are developed to solve the problem:

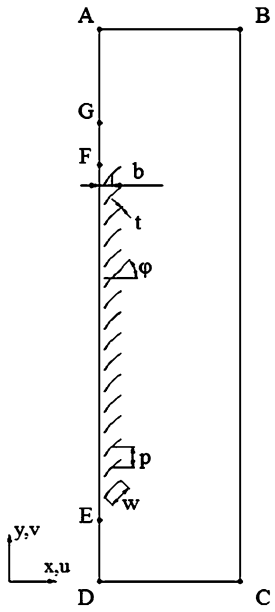

Fig. 19.1 Model geometry of the computation domain

$$\frac{\partial u}{\partial x}+\frac{\partial v}{\partial y}=0 \tag{2.1}$$

$$\rho\left(u\frac{\partial u}{\partial x}+v\frac{\partial u}{\partial y}\right)=-\frac{\partial p}{\partial x}+\mu\left(\frac{\partial^2 u}{\partial x^2}+\frac{\partial^2 u}{\partial y^2}\right) \tag{2.2}$$

$$\rho\left(u\frac{\partial v}{\partial x}+v\frac{\partial v}{\partial y}\right)=-\frac{\partial p}{\partial y}+\mu\left(\frac{\partial^2 v}{\partial x^2}+\frac{\partial^2 v}{\partial y^2}\right)+\rho g\beta(T-T_\infty) \tag{2.3}$$

$$\rho c_p\left(u\frac{\partial T}{\partial x}+v\frac{\partial T}{\partial y}\right)=k\left(\frac{\partial^2 T}{\partial x^2}+\frac{\partial^2 T}{\partial y^2}\right)+S \tag{2.4}$$

Equations (2.1)–(2.4) describe the incompressible and laminar flow of this model. For radiation, in this model, radiative heat transfer between isothermal surfaces and louvers will have effects on the temperature distribution of the louver blades. The long-wave radiation heat transfer from each surface to the air is negligible. In order to simply the calculation, the solid surfaces are assumed to be diffuse, gray, and opaque to radiation. The radiation heat transfer in this simulation was calculated by surface-to-surface (S2S) modeling. In this model, the energy balance of a surface k is expressed by Eq. (2.5):

$$I_{\text{out},k}=\varepsilon_k\sigma T_k^4+\rho_k\sum_{j=1}^{N}F_{kj}I_{\text{out},j} \tag{2.5}$$

In this equation, F_{kj} is the view factor between surface j and surface k. The total number of surfaces in the model is N. The view factor F_{kj} is given by Eq. (2.6):

$$F_{kj} = \frac{1}{A_k}\int_{A_k}\int_{A_j}\frac{\cos\theta_k \cos\theta_j}{\pi r^2}\delta_{kj} dA_k dA_j \tag{2.6}$$

For δ_{kj}, if dA_j is visible to dA_k, $\delta_{kj} = 1$; otherwise, $\delta_{kj} = 0$. θ_k are angles between line of centers for each two surfaces and normal line of surface k and so as to θ_j. With the convection and radiation models above, the boundary conditions of computational domain are listed as follows:

$$T = T_\infty,\ \frac{\partial v}{\partial y} = u = 0, \quad \text{for AB and CD} \tag{2.7}$$

$$T = T_\infty,\ \frac{\partial u}{\partial x} = v = 0, \quad \text{for BC} \tag{2.8}$$

$$\frac{\partial T}{\partial x} = v = u = 0, \quad \text{for DE and GA} \tag{2.9}$$

$$T = T_s,\ v = u = 0, \quad \text{for EF and FG} \tag{2.10}$$

In this study, Eqs. (2.1)–(2.10) were simultaneously solved by general CFD software Fluent 6.3. The number of grid nodes used to calculate was around 105,000. The simulation of convection and radiation is nearly grid independent under this number of nodes.

19.3 Validation

To validate the numerical method and boundary conditions, the simulation results are compared with the experimental data published. For the current study, the comparison is made between physical fields and convective heat transfer coefficient of the isothermal surface of CFD work and Machin's experiment under similar geometric and boundary conditions.

Figure 19.2 shows the temperature and stream function contours of experimental work and present simulation study for $b = 14.5$ mm, $\varphi = 0°$, $\varepsilon_s = \varepsilon_b = 0.81$, and $\Delta T = 20$ °C($\Delta T = T_s - T_\infty$). It can be seen from the figure that the simulation result has a good agreement with Machin's experimental work. In Fig. 19.2 (left), the isothermals from infinite fringe interferogram are similar to the simulated ones. Figure 19.2 (right) shows that two rotating eddies are present between each two louver blades. The left eddy is larger than the right one, which is the same as the flow visualization photograph shown in experiment.

The local average and local convective heat transfer coefficient of isothermal surface is compared with that in experiment in Fig. 19.3 for $b = 14.5$ mm, $\varphi = 0°$, and $\Delta T = 20$ °C. It shows that the average convective heat transfer

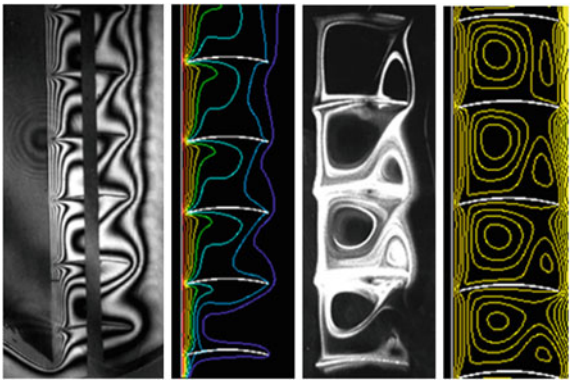

Fig. 19.2 Comparison of simulated temperature and flow field with infinite fringe interferogram (*left*) and flow visualization (*right*) photograph in Machin's experiment ($b = 14.5$ mm, $\varphi = 0$, $\varepsilon_s = \varepsilon_l = 0.81$, and $\Delta T = 20$ °C)

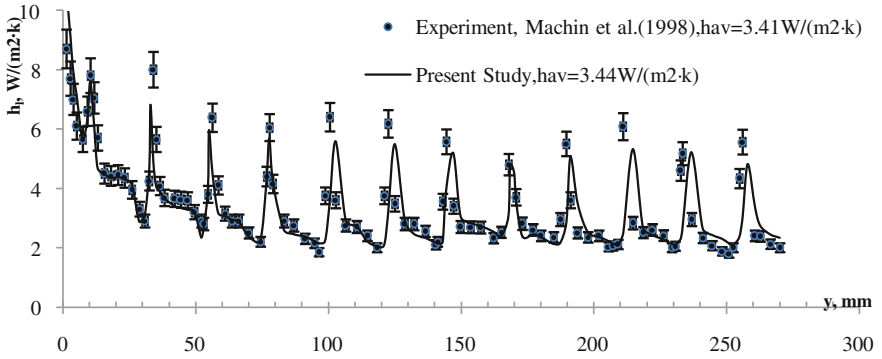

Fig. 19.3 Comparison of simulated average and local heat transfer coefficient with the results of Machin's experimental data ($b = 14.5$ mm, $\varphi = 0$, $\varepsilon_s = \varepsilon_l = 0.81$, and $\Delta T = 20$ °C)

coefficient in simulation is very close to the experimental one, and the local convective heat transfer coefficient is periodically distributed along the isothermal surface, with deviation blow 10 % to experimental data.

19.4 Results and Discussion

The heat transfer between isothermal surface and air is influenced by many factors. To simplify the analysis, some parameters are considered to be constant. The influence of temperature difference between the surface and air ΔT, distance from surface to louvers b, and blade angle φ on the local heat transfer is shown in

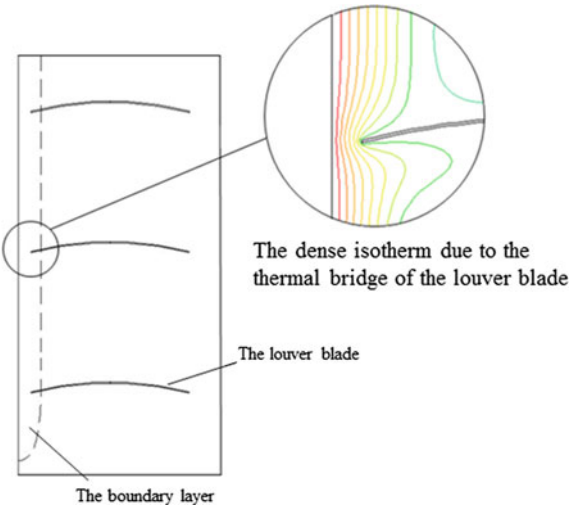

Fig. 19.4 The thermal bridge of the louver blade to the surface heat transfer

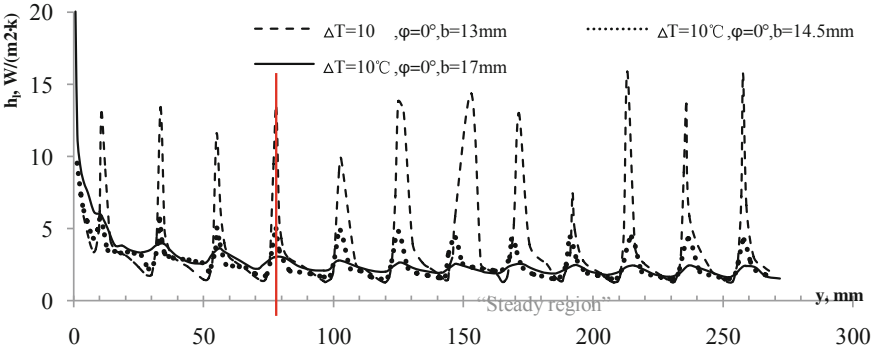

Fig. 19.5 The local heat transfer coefficient distribution along the isothermal surface with different distance from surface to louvers b ($\Delta T = 10$ °C, $\varepsilon_s = \varepsilon_b = 0.81$, and $\varphi = 0°$)

Figs. 19.5, 19.6, 19.7. It is worth noting from these figures that the period length of the local convective heat transfer coefficient is about 22.2 mm, which is equal to the blade spacing p. Furthermore, for a certain period, the local convective heat transfer coefficient climbs to the peak at the surface point which is the closest to the louver blades. It is mainly because the heat transfer of the air in the boundary layer attached to the surface chiefly depends on heat conduction. When the louver blades are set into the boundary layer, the blades will become thermal bridges and results in high local heat transfer coefficient (see in Fig. 19.4), since the thermal conductivity of louver ($k_b = 200$ W/(m·K)) is far larger than that of air ($k_\infty = 0.024$ W/(m·K)). On the other hand, louver blade will impede the airflow rising along the surface, which will cause the local heat transfer coefficient decreased in the area far away from louver blade in a period. For the blades

Table 19.1 Effects of b, ΔT, and φ on the average amplitude for the local heat transfer coefficient distribution along the "steady region" ($\varepsilon_s = \varepsilon_b = 0.81$)

The average amplitude for the local heat transfer coefficient distribution along the "steady region," W/(m^2·K)

φ	0°			+45°			−45°		
	b = 13 mm	b = 14.5 mm	b = 17 mm	b = 13 mm	b = 14.5 mm	b = 17 mm	b = 13 mm	b = 14.5 mm	b = 17 mm
ΔT									
1 °C	15.40	3.64	1.03	2.25	0.92	0.39	0.79	0.52	0.18
10 °C	15.25	3.23	0.87	2.20	0.82	0.37	0.74	0.49	0.19
20 °C	15.87	3.25	0.89	2.08	0.87	0.36	0.76	0.47	0.21

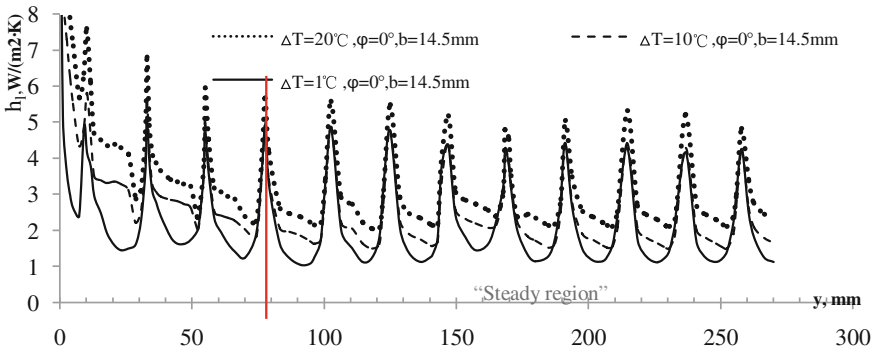

Fig. 19.6 The local heat transfer coefficient distribution along the isothermal surface with different ΔT ($b = 14.5$ mm, $\varepsilon_s = \varepsilon_b = 0.81$, and $\varphi = 0$)

arranged every p distance, the influence of blades on local convective heat transfer is periodically distributed by cycle length p.

Another interesting thing from these figures is that the local heat transfer coefficient shows a decreased trend along the surface. In the first three periods, the local convective heat transfer coefficient dumps sharply, while the decrease in this coefficient is not obvious in the following period, which is named "steady region" and will be focused on in the subsequent study. In this region, the amplitude and average of local heat transfer coefficient distribution change little with x changes.

Figure 19.5 illustrates the impact of the distance from louvers to surface b on the local convective heat transfer coefficient distribution along the isothermal surface. It can be seen from this figure that the distance b has a significant influence on the amplitude for a certain period, which can be also concluded from Table 19.1. This is because when the louvers are set close to the surface, the interference of blades on the airflow will increase, so as to promote the thermal bridge and airflow impeding for different region along the surface. As a result, the amplitude of the local heat transfer coefficient will increase as the difference between peak and valley becomes large.

The impact of temperature difference between surface and ambient air ΔT on the local heat transfer coefficient distribution is illustrated in Fig. 19.6. In this figure, the temperature difference varies from $\Delta T = 1$ to 20 °C. The result shows that ΔT has weak effect on the amplitude of the local convective heat transfer coefficient's periodic distribution, while it has stronger influence on the average of this distribution. This conclusion can be confirmed by Tables 19.1 and 19.2. With certain distance b, louvers angle φ but different ΔT, local heat transfer coefficient changes little in average amplitude, but it changes so much in the average local heat transfer coefficient. It is because ΔT has little effect on the thermal conductivity of louver blade, and it also has no contribution to the louver impeding to the airflow. As a result, the amplitude of local heat transfer coefficient is barely affected by ΔT for the peak and valley of heat transfer coefficient varies little with

Table 19.2 Effects of b, ΔT, and φ on the average local heat transfer coefficient distribution along the "steady region" ($\varepsilon_s = \varepsilon_b = 0.81$)

The average local heat transfer coefficient distribution along the "steady region," W/(m^2·K)									
φ	0°			+45°			−45°		
	$b = 13$ mm	$b = 14.5$ mm	$b = 17$ mm	$b = 13$ mm	$b = 14.5$ mm	$b = 17$ mm	$b = 13$ mm	$b = 14.5$ mm	$b = 17$ mm
ΔT									
1 °C	2.75	2.09	1.63	2.28	1.92	1.59	2.56	2.31	2.67
10 °C	3.11	2.63	2.46	2.71	2.80	2.76	2.83	2.94	3.03
20 °C	4.02	3.28	3.20	3.53	3.40	3.59	3.61	3.77	3.88

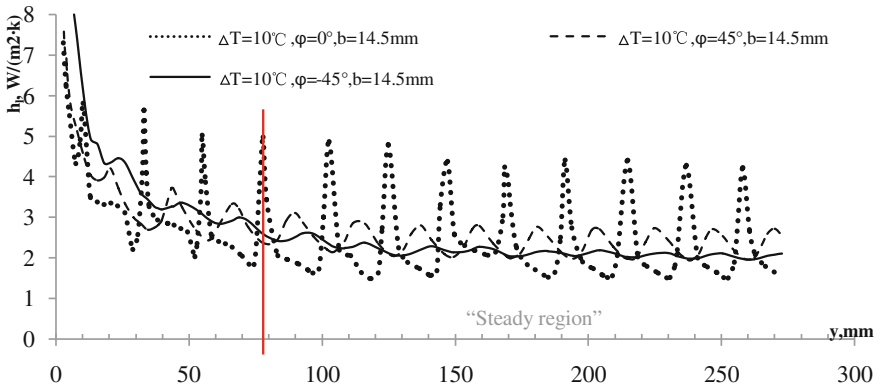

Fig. 19.7 The local heat transfer coefficient distribution along the isothermal surface with different φ ($b = 14.5$ mm, $\varepsilon_s = \varepsilon_b = 0.81$, and $\Delta T = 10$ °C)

ΔT changes. On the other hand, with large ΔT, the density difference between air attached to surface and ambient air increases, so the buoyancy of airflow becomes stronger. Consequently, the average of natural heat transfer coefficient becomes large as the buoyancy-driven convection become strong.

Figure 19.7 shows the distribution of local convective heat transfer coefficient along the isothermal surface with different louvers angle φ. In Fig. 19.6, the amplitude of coefficient periodic distribution is largest when $\varphi = 0°$. If the louvers are set to a certain distance b, the louvers blade will have great effect on the airflow attached to the surface when the louver angle's absolute value is small. This will cause large amplitude of the periodic distribution. On the other hand, different louvers angles also lead to different position for each period, for the location of blade change as the louvers angle changes.

19.5 Conclusion

A CFD simulation solution has been obtained for the natural convective heat transfer from the isothermal surface to louvers blind. The result shows that the local convective heat transfer coefficient of the surface will vary periodically with close-set louvers blind, which will make heat transfer inhomogeneous along the surface. Furthermore, distance from louvers to surface b, temperature difference between the surface and the ambient ΔT, and louvers angle φ will have great effects on the periodic distribution of convective heat transfer coefficient. In the future, some measures should be taken to the louvers blind in order to prevent cold bridge or hot bridge along the building envelops (e.g., turn the louvers vertically when there is no need for natural lighting, such as in nighttime).

References

1. Fang X, Ge X (1993) Experimental study of overall heat transfer coefficients of a window with venetian blinds. J Solar Energy 14(2):138–141 (in Chinese)
2. Machin AD, Naylor D, Harrison SJ, Oosthuizen PH (1998) Experimental study of free convection at an indoor glazing surface with a venetian blind. Int J HVAC&R Res 4(2):153–166
3. Phillips J (1999) Numerical study of the effects of venetian blinds on radiation and convection heat transfer from a window glazing. M.E.Sc.Thesis, University of Western Ontario, London, Ontario, Canada
4. Shahid H, Naylor D (2005) Energy performance assessment of a window with horizontal Venetian blinds. Energy Build 37:836–843

Chapter 20
Study on the Optimal Control Strategy for Condensing Side of Chiller Systems

Zheliang Chen, Pinshu Yang and Fulin Wang

Abstract The performance curves of typical chillers available from the present market are investigated. These performance curves are fitted to develop a chiller model, which together with pump and cooling tower models are used to study the optimal control strategy for condensing side of chiller systems. The optimization objective is to minimize the total energy use of chillers, condensing pumps, and cooling tower fans. The optimization problem is solved by traversing all possible combinations of chiller water flow rates, cooling tower air flow rates, and ambient air wet-bulb temperatures. Then the optimal solutions are analyzed to find out applicable rule-based control strategies that are not far from optimal solutions and reliable as well. The rule-based control strategy is to keep one or two constant cooling water flow rates during whole operational season according to the number of running chillers and to keep cooling tower air flow rate at a constant ratio to cooling water flow rate. Because this rule-based control strategy does not use sensor measured data, such as wet-bulb air temperature, it is free of sensor faults and can be more robust and reliable than the currently used control strategies, most of which use cooling water temperature or ambient air wet-bulb temperature to decide the cooling water flow rate or air flow rate of cooling tower fans.

Keywords Control strategy · Optimization · Rule-based · Condensing side of chillers · Energy consumption

Nomenclature

a_i, b_j, c_j, $i = 1, 2, j = 1, 2, 3$	fitted coefficients using manufacturers' specification data
AWR	air–water ratio of cooling tower
COP	coefficient of performance of chiller

Z. Chen · P. Yang · F. Wang (✉)
Department of Building Science, School of Architecture, Tsinghua University, Beijing 100084, China
e-mail: flwang@tsinghua.edu.cn

A. Li et al. (eds.), *Proceedings of the 8th International Symposium on Heating, Ventilation and Air Conditioning*, Lecture Notes in Electrical Engineering 263,
DOI: 10.1007/978-3-642-39578-9_20,

c_p	water specific heat capacity (kJ/(kg·°C))
E_{25}, E_{50}, E_{75}, E_{100}	energy consumption under 25, 50, 75, 100 % part load ratio (kW)
E_{ave}	annual weighted average energy consumption (kW)
E_{pump}	power consumption of condensing pump (W)
E_{tower}	power consumption of cooling tower (W)
$E_{tower,r}$	rated power consumption of cooling tower (W)
L	cooling tower water mass flow rate (kg/s)
G	cooling tower air mass flow rate (kg/s)
G_r	rated cooling tower air mass flow rate (kg/s)
H	air enthalpy in cooling tower (kJ/kg)
H_s	saturated air enthalpy (kJ/kg)
NTU	number of transfer units
PFR	part flow ratio (ratio of actual flow rate to rated flow rate of condensing water)
PLR	part load ratio
$RMSD$	root-mean-square difference
T_{EF}	condenser inlet water temperature (°C)
V	pump water volume flow rate (m^3/s)
η_{imp}	pump impeller efficiency
η_{inv}	pump inverter efficiency
η_m	pump motor efficiency
η_t	total efficiency of pump

20.1 Introduction

The condensing side of a chiller system, also known as the condenser water loop, is an indispensable part of the heating, ventilation, and air conditioning (HVAC) system in a building. It consists mainly of chillers, condensing pumps, and cooling towers. As an important module in the HVAC system, it contributes greatly to the overall energy consumption, making the enhancement of its energy efficiency necessary. Researchers have conducted a lot of study in this field to find better control strategies. Among the existing control strategies, there are two traditional methods, the fixed set-point control method and the fixed approach control method [1–3]. The fixed set-point control method changes the cooling tower air flow rate to maintain a constant condenser inlet water temperature, while the fixed approach control method changes the cooling tower air flow rate to maintain a constant difference between condenser inlet water temperature and the ambient air wet-bulb temperature. But in recent years, more energy-efficient control methods are developed [1–6], and they consume less energy when compared with the above-mentioned two methods. They utilize a certain algorithm to calculate the optimal

condenser inlet water temperature according to the cooling load and the ambient air wet-bulb temperature. This optimal temperature is achieved by varying the cooling tower air flow rate and sometimes by varying the condenser water flow rate.

Though the advantage of the optimal control method is obvious, it faces problems in the process of practical application. The operation of this method relies heavily on sensors and the frequent changes of flow rate can give rise to problems of less-facility life span. Once any fault occurs, the repairing costs quite an amount of money and time, both of which are of vital importance in the management of a building. With these potential problems, the stability of this method is questionable, and its actual efficiency in practical application may cause disappointment.

So a method is in urgent need which is energy-efficient and, in the meantime, can overcome the application problems. This chapter proposes a method as an attempt to fulfill the task by seeking a rule-based near-optimal control strategy using simulation.

20.2 Models

Condensing side simulation model includes three parts: the chiller model, the pump model, and the cooling tower model. The chiller model is a regression model by fitting the data of chiller performance curves provided by chiller manufacturers. The pump model is developed using the method proposed by Wang et al. [7]. The cooling tower model is a theoretical model [8].

20.2.1 Chiller Model

Typical chiller manufacturers' performance data are investigated to develop chiller model. Regarding condensing side, three variables influence a chiller's COP: chiller's part load ratio (PLR), condensing water part flow ratio (PFR), and condensing water inlet temperature T_{EF}. Manufacturer data are shown in Table 20.1. Each value of COP in Table 20.1 is the average value of the typical manufacturers' chiller samples in the same condition.

In order to simulate the performance of a chiller, this paper uses a three-variable equation [9], as shown in Eq. 20.1, to fit the performance data.

$$\mathrm{COP} = (a_1\mathrm{PLR}^2 + b_1\mathrm{PLR} + c_1)(a_2\mathrm{PFR}^2 + b_2\mathrm{PFR}^2 + c_2)(b_3 T_{\mathrm{EF}} + c_3) \quad (20.1)$$

The coefficients in Eq. 20.1, i.e., a_i, b_j, c_j, $i = 1, 2, j = 1, 2, 3$, can be determined using least-square difference method. The fitted coefficients are shown in

Table 20.1 Data of chiller samples selected from typical manufacturers

PLR (%)		30	40	50	60	70	80	90	100
T_{EF} (°C)	PFR	COP							
28	0.65	4.70	5.32	5.77	6.02	6.19	6.19	6.11	5.92
	0.85	4.80	5.46	5.91	6.22	6.40	6.44	6.39	6.22
	1.00	4.84	5.50	5.97	6.30	6.49	6.54	6.51	6.35
30	0.65	4.44	5.02	5.44	5.69	5.87	5.87	5.78	5.57
	0.85	4.53	5.14	5.57	5.86	6.03	6.07	6.01	5.85
	1.00	4.67	5.26	5.68	5.96	6.15	6.21	6.17	6.01
32	0.65	4.17	4.69	5.07	5.30	5.44	5.50	5.43	5.25
	0.85	4.20	4.82	5.25	5.52	5.71	5.75	5.69	5.48
	1.00	4.31	4.92	5.32	5.60	5.78	5.82	5.77	5.62

Table 20.2 Coefficients of a fitted chiller model

a_1	b_1	c_1	a_2	b_2	c_2	b_3	c_3
−1.6190	2.5732	0.5501	−0.0336	0.1001	0.2566	−0.3611	23.0467

Table 20.2. In the simulation, by inputting cooling load, PFR, and T_{EF}, chiller's COP can be achieved.

The model accuracy is evaluated using root-mean-square difference (RMSD) between model simulation data (COP_m) and sample data (COP_s). The RMSD is calculated using Eq. 20.2. The value of RMSD is 4.15 %, so that the model can be considered accurate. The model's accuracy is also shown in Fig. 20.1.

$$\mathrm{RMSD} = \sqrt{\frac{\sum_{i=1}^{n} (\mathrm{COP}_{m,i} - \mathrm{COP}_{s,i})^2}{n}} \tag{20.2}$$

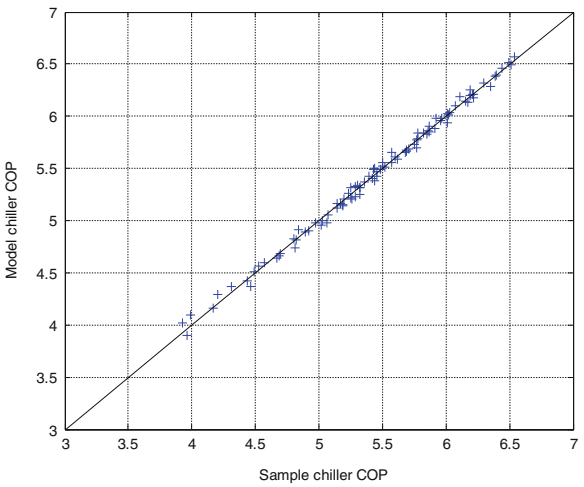

Fig. 20.1 Chiller model accuracy verification by comparing the model-calculated data with sample data

20.2.2 Pump Model

In order to realize variable condensing water flow rates, a variable-speed pump model is considered in this paper. The pump energy consumption model is shown in Eqs. 20.3–20.4 [7], in which the efficiencies of a pump's impeller, motor, and inverter are all taken into consideration.

$$E_{\text{pump}} = \frac{V\Delta P}{\eta_t} \tag{20.3}$$

$$\eta_t = \eta_{\text{imp}}\eta_m\eta_{\text{inv}} \tag{20.4}$$

The impeller efficiency (η_{imp}) model can be fitted using the performance curve of a pump with parameters of flow rate, head pressure, and rotation speed. The motor efficiency (η_m) and the inverter efficiency (η_{inv}) models are fitted using the motor and inverter performance curves [7].

20.2.3 Cooling Tower Model

Considering the increasing use of variable speed drive (VSD), the cooling tower model used in this paper is a variable-speed fan instead of commonly used multi-speed fan. The cooling tower's heat transfer model is based on an energy balance equation and Merkel's formula [8], as shown in Eqs. 20.5 and 20.6. By dividing cooling tower packing into several layers, an approximate solution of cooling tower water outlet temperature (T_{EF}) can be achieved.

$$Lc_p\mathrm{d}T = G\mathrm{d}H \tag{20.5}$$

$$\text{NTU} = \int \frac{c_p dT}{H_s - H} \tag{20.6}$$

Cooling tower's energy consumption is approximately calculated using Eq. 20.7. Cooling tower's air–water ratio (AWR) is calculated using Eq. 20.8.

$$E_{\text{tower}} = E_{\text{tower},r}\left(\frac{G}{G_r}\right)^3 \tag{20.7}$$

$$\text{AWR} = \frac{G}{L} \tag{20.8}$$

20.3 Simulation and Discussion

With its modular structure and ease of use in modeling process, Simulink is used to conduct the simulation. The main structure of the simulation model is shown in Fig. 20.2. Simulink's built-in solvers and standard blocks make it flexible and convenient to build a model and achieve results.

Four variables influence the total energy consumption of the condensing side. Ambient air wet-bulb temperature varies from 22 to 35 °C with an interval of 1 °C to simulate different periods and weather conditions during the cooling season. PLR varies from 25 to 100 % with an interval of 25 % to simulate different loads. PFR varies from 0.4 to 0.8, and the AWR varies from 0.6 to 1.4, with an interval of 0.1 and 0.2, respectively, to find out the optimal PFR and AWR.

The simulated total energy consumptions of AWR = 1.0 are shown (Fig. 20.3) as an example. The Y-axis represents a dimensionless energy consumption, which is the ratio of actual energy consumption to the rated one (with the wet-bulb temperature of 28 °C, full load and rated water and air flow rates). From Fig. 20.3, it can be seen that energy consumptions of the condensing side follow certain rules despite the variation of ambient wet-bulb temperature. Though the energy consumption of condensing side increases with the cooling load and the wet-bulb temperature, increasing trends can be seen while the PFR and AWR vary. However, for each PLR condition, a pair of values of PFR and AWR which is most energy-efficient can be found, as listed in Table 20.3. Thus, a rule-based control strategy can be built. During the whole cooling season, chiller's output can be used to get the value of PLR. When PLR < 50 %, the near-optimal pump speed is to keep PFR at 0.5; when PLR ≥ 50 %, the near-optimal pump speed is to keep PFR at 0.6. This rule-based control strategy does not use temperature, humidity, and flow rate sensors, so it is free of the faults of temperature and humidity sensors, which are not so reliable because of measurement drift and being easy to damage.

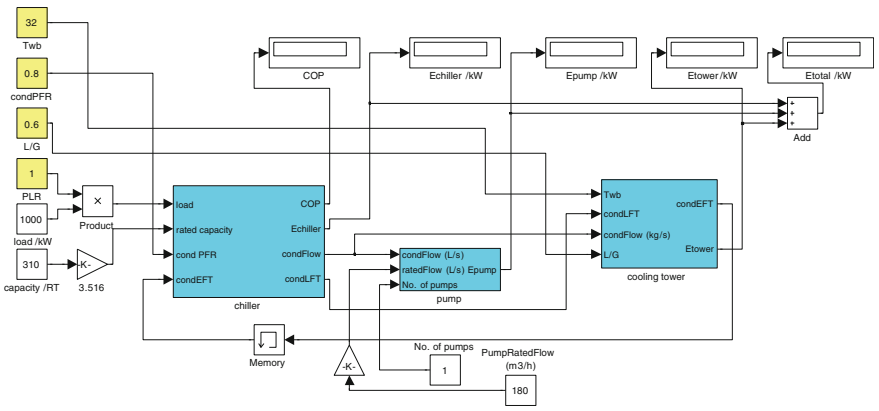

Fig. 20.2 Simulation model built in Simulink

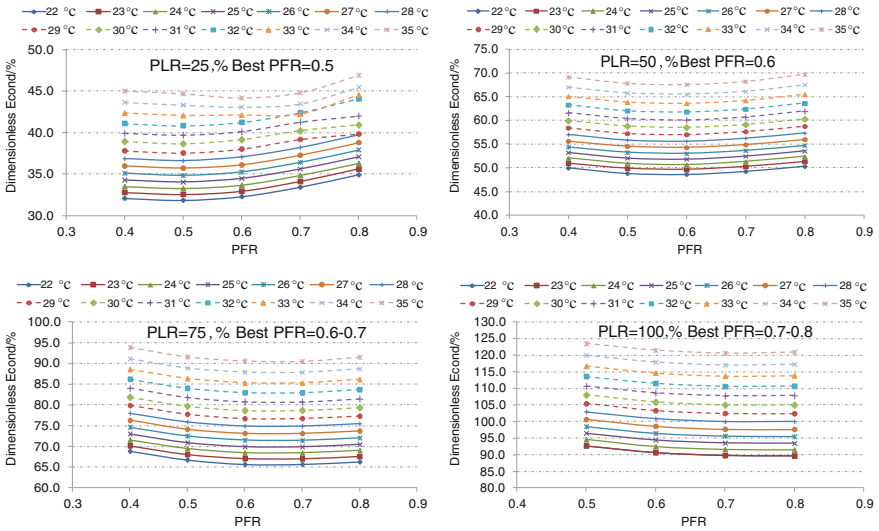

Fig. 20.3 Simulation results keeping AWR = 1.0

A common method of condensing side control is to fix flow rate at the rated value, which keeps condensing water flow rate and cooling tower air flow rate constant. Another commonly used strategy of condensing side control is the fixed cooling water supply temperature strategy, which keeps condensing water flow rate constant but varies cooling tower air flow rate to maintain condenser inlet water temperature at certain set points. Using non-standard part load value (NPLV) [9] weights, the approximate annual energy consumption can be calculated with Eq. 20.9. The weights of different PLRs are listed in Table 20.3.

$$E_{\text{ave}} = 0.12E_{25} + 0.45E_{50} + 0.42E_{75} + 0.01E_{100} \tag{20.9}$$

The energy consumptions of the proposed rule-based strategy and the other two control methods are compared to evaluate the proposed control method, as shown in Fig. 20.4. The total energy consumption of chiller, condensing pump, and cooling tower running with the proposed rule-based strategy is less than that with the fixed flow rate control and the fixed cooling water temperature set-point strategy by 4.2–5.2 and 1.6–3.3 %, respectively, mainly because of the benefit from lower pump flow rate and cooling tower fan speed.

Table 20.3 Most energy-saving PFRs and AWRs, NPLV weights for different PLRs

PLR/(%)	25	50	75	100
PFR	0.5	0.5	0.6	0.6
AWR	1.0	1.2	1.2	1.4
NPLV weight	0.12	0.45	0.42	0.01

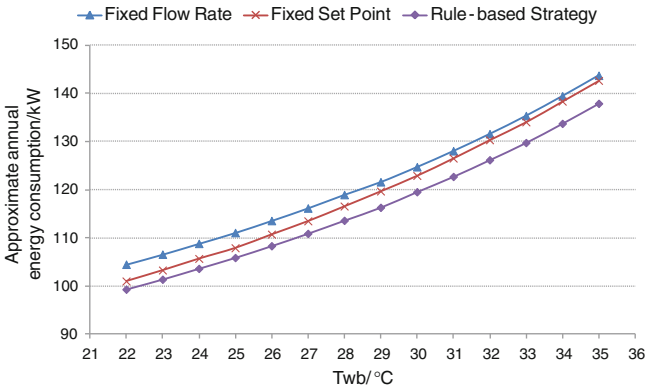

Fig. 20.4 Energy consumption of different strategies

20.4 Conclusions

A rule-based near-optimal control strategy for condensing side of chillers is presented. Chiller model based on performance data together with pump and cooling tower models is built using Simulink to find out the optimal cooling water flow rates and cooling tower air flow rates under different ambient wet-bulb temperatures and PLRs to minimize the total energy consumption of condensing side. NPLV weights are applied to estimate annual energy-saving potential of the proposed control strategy.

Simulation results show that the control strategy proposed is able to achieve 4.2–5.2 and 1.6–3.3 % of reduction in the chiller system's energy consumption compared to two commonly used strategies: the fixed flow rate strategy and the fixed cooling water temperature set-point strategy, respectively. In the meantime, by keeping condensing water PFR and cooling tower AWR at several constant values, the proposed control method can simplify the chiller systems' control and management and avoid non-energy-efficient even wrong running caused by temperature and humidity sensor faults.

References

1. Yu FW, Chan KT (2009) Comprehensive environmental assessment for cooling towers with various controls. Indoor Built Environ 18(1):5–23
2. Ma Z, Wang S, Xiao F (2009) Online performance evaluation of alternative control strategies for building cooling water systems prior to in situ implementation. Appl Energy 86:712–721
3. Braun JE (2007) A general control algorithm for cooling towers in cooling plants with electric and/or gas-driven chillers. HVAC&R Res 13(4):581–598

4. Ma Z, Wang S, Xu X, Xiao F (2008) A supervisory control strategy for building cooling water systems for practical and real time applications. Energy Convers Manage 49:2324–2336
5. Lu L, Cai W, Soh YC, Xie L, Li S (2004) HVAC system optimization: condenser water loop. Energy Convers Manage 45:613–630
6. Crowther H, Furlong J (2004) Optimizing chillers and towers. ASHRAE J 46(7):34–44
7. Wang F, Yoshida H, Miyata M (2004) Total energy consumption model of fan subsystem suitable for continuous commissioning. ASHRAE Trans 110:357–364
8. Ye M (1999) Design of cooling towers. Chem Eng Equip Technol 20(3):34–40 (in Chinese)
9. Wang F, Yoshida H, Masuhara S, Kitagawa H, Goto K (2005) Simulation-based automated commissioning method for air-conditioning systems and its application case study. In: Proceedings of international IBPSA conference 2005, Montreal
10. ARI (2003) Standard for performance rating of water chilling packages using the vapor compression cycle. Air-conditioning & Refrigeration Institute, Virginia

Chapter 21
Application of Multizone Model and CFD Method in Ventilation System Design of Soft Sleeper Car

Gang Wang and Songtao Hu

Abstract Airflow in the high-speed soft sleeper car of passenger train is complex. To balance the air volume distribution between different rooms, multizone model combined with Computational fluid dynamics (CFD) method is used to guide the design. Multizone network model of the ventilation system including ducts and rooms is established, and CFD method is used to get necessary data for solution of the model, e.g., determine the flow resistance characteristic in irregular duct components. According to the calculating results, ventilation system is adjusted for several times till air volume distribution meets the design requirement. Then, prototype model of the car is set up, and experimental test is carried out to verify the multizone model and calculating results. It proved that method of this paper can be applied to the design of ventilation system of soft sleeper car and similar places.

Keywords Ventilation system · Soft sleeper car · Multizone model · CFD method

21.1 Introduction

Ventilation system is an important part of environmental control system for passenger train, and good design of ventilation system is vital for good environment of the carriage.

Hydraulic calculation is necessary for design of the ventilation system in buildings, but because of the complexity of the ducts and rooms in the passenger train, it is hard to carry out the calculation just by traditional method.

G. Wang (✉) · S. Hu
Qingdao Technological University, Qingdao 266033, China
e-mail: grant414@gmail.com

A. Li et al. (eds.), *Proceedings of the 8th International Symposium on Heating, Ventilation and Air Conditioning*, Lecture Notes in Electrical Engineering 263,
DOI: 10.1007/978-3-642-39578-9_21,

Computational fluid dynamics (CFD) method now acts as a useful tool for duct design in the field of railway car because it can simulate the flow in the duct and give air volume distribution of the openings [1–3].

Each opening has the same external condition in seat car, so good design of air supply ducts only can meet the requirement of air volume distribution. But for soft sleeper car, the carriage is divided into several boxes, which makes the openings have different condition, and then affected the air volume distribution. So, calculation domain of CFD simulation must include the whole carriage and all the ducts in order to get accurate results, which will cause huge computing load.

Design of the ventilation system also includes several times of adjusting and computing procedure. To accelerate the process, multizone network model is introduced to balance the air volume distribution in soft sleeper car, and the model is proved to be useful in airflow simulation and ventilation design [4, 5]. Because there are many irregular or non-standard components in passenger car and their resistance characteristic is unknown, CFD method is used to study the relationship between pressure drop and air volume of those special components, which is necessary for multizone modelling.

CFD method can also simulate the airflow in boxes and aisle based on given air supply volume, and it can also work coupled with multizone simulation [6, 7], but in this paper, just for design purpose, CFD method is only used to provide basic data for multizone model. Most data used in the simulation are accumulated during previous work and already verified by experiments.

21.2 Scheme of the Ventilation System

The soft sleeper car is divided into 10 sleeper boxes, and the rooms also include 1 train crew room, 1 electrical room, and 1 toilet, which are shown in Fig. 21.1.

During conceptual design, structure and space of the car are analyzed as well as the air distribution and thermal comfort, up-inlet and down-outlet flow scheme are adopted.

As shown in Fig. 21.2, the supply airflow path includes main duct 6 run through the car, branch duct 4 of each room, static pressure box and orifice plate 2, while the return airflow path includes ventilation grille 9 at the box door, slot opening 8 at the corridor ceiling, static pressure interlayer 7, branch duct 5, ceiling space 3, and main air return 1.

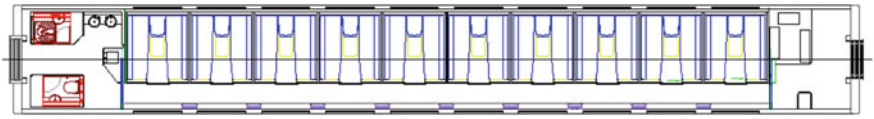

Fig. 21.1 Floor plan of the soft sleeper car

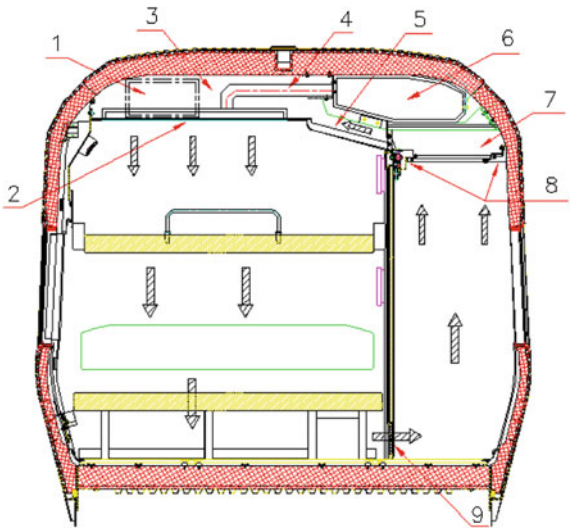

Fig. 21.2 Airflow schematic diagram

The main duct adopts variable cross section structure, and other parts of each box keep same size for convenience of batch processing. At the base of preliminary design, size of each segment of duct can be changed in order to achieve air volume balance. Adjusting mechanism is set in junction of main duct and branch duct, and its open ratio should also be decided by calculation.

21.3 Multizone Model

According to the airflow condition of the sleeper car, the ventilation system and special components are abstracted and simplified by analysis of the duct system and carriage, and then, the multizone model is established.

21.3.1 Overview of the Model

- Nodes

The model includes the ducts and rooms, so there are two kinds of nodes: zone node and duct node.

Each box, train crew room, electrical room, toilet, and corridor is treated as zone node. Air parameters are assumed uniform in same zone.

Duct node is set at the duct junction in order to calculate flow in the ducts, and it has the same character as zone node.

- Flow path

Pressure difference between boxes will mainly affects airflow from boxes to corridor, so ventilation grille at the box door is treated as the main flow path. Ceiling space between corridor and main air return is also considered as flow path because of its flow character.

Each flow path between duct nodes is handled separately because their character is influenced by many factors, hard to set a same value.

The multizone model of ventilation system is shown in Fig. 21.3, and flow path between duct nodes use the arrow symbol.

21.3.2 Flow Path Characteristic

Resistance characteristic of regular duct is easy to determine, but for irregular and non-standard component, the parameter must determined by CFD simulation and experiments.

Most components are studied in previous work, and a database has already been set up. The components include duct of common dimensions, elbow, gradually reducing, sudden contraction, tee joint, opening, grille, orifice plate. Some special components such as adjusting mechanism still need additional computing.

21.3.3 Solution of the Model

Based on the model, flow and pressure equations are set and solved using MATLAB.

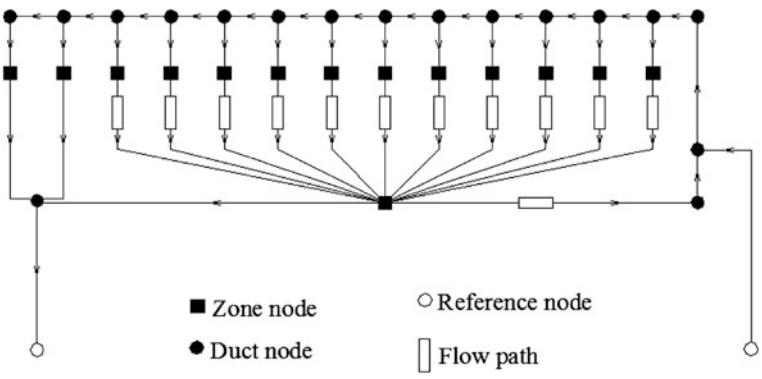

Fig. 21.3 Mutizone model of ventilation system

The air volume results of each zone with design value are compared, and then adjusted corresponding parts according the deviation, till it less than a set upper limit.

Pressure drop of each segment should also be considered when adjusting the size, avoid too large value. While small value means potential of space saving and can provide advice to latter design.

After two times of global and several times of minor adjustment, final scheme is put forward, deviation of simulation result and design value controlled in 5 % of all zones.

21.4 Experimental Tests

To evaluate the design, a prototype car with all the furniture and ventilation system is set up according to the final scheme. Test item includes, but not limited to:

- Total air volume of the ventilation system
- Air volume and pressure of each zone
- Air volume and pressure of key section of the duct
- Air distribution of 3 typical boxes and the corridor

Resistance characteristic of special components is also tested on local resistance experiment station as routine and expand the database.

Test instruments include standard nozzle flowmeter, Pitot tube, DP-CALC micromanometer 8705, ACCUBALANCE air capture hood 8373, and KANOMAX anemomaster model 6242.

Figure 21.4 shows comparison of design and test value of air volume.

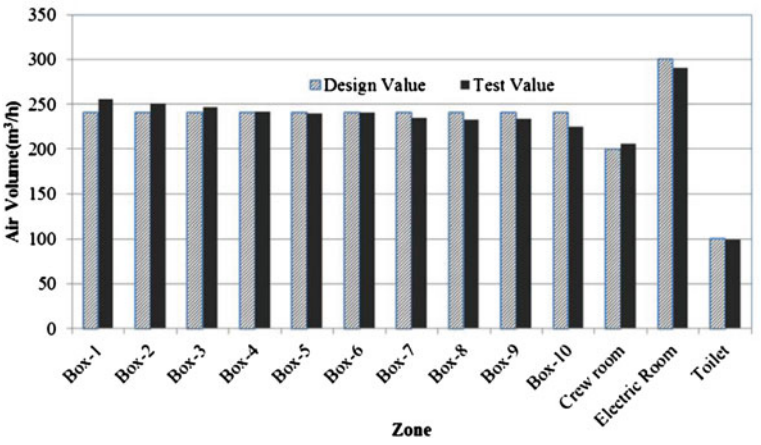

Fig. 21.4 Air volume comparison of design and test value

21.5 Conclusion

Adoption of multizone network model can speed up the design and optimization process of the ventilation system, and CFD method can provide flow details which could be used to study flow path characteristic and air distribution in the room. Combination of them is suitable in design of the ventilation system of soft sleeper car.

This method is now introduced to subsequent design process of other car and proved to be reasonable and high efficiency.

References

1. Gang W, Huihui Y, Songtao H (2011) Uniform air supply system adjusted by perforated plate. In: Proceedings of international conference on computer distributed control and intelligent environmental monitoring, CDCIEM 2011, pp 2379–2382
2. Zhou A (2008) Study on variable cross-section duct air supply system with spiral duct used in trains. Dissertation for the master degree in engineering, Qingdao Technological University, p 6
3. Zhang B (2010) Study on uniformity of train air supply system and air distribution optimization of car. Dissertation for the master degree in engineering, Qingdao Technological University 2010, p 6
4. Chen Q (2009) Ventilation performance prediction for buildings: a method overview and recent applications. Build Environ 44(4):848–858
5. Johnson MH, Zhai Z, Krarti M (2012) Performance evaluation of network airflow models for natural ventilation. HVAC&R Res 18(3):349–365
6. Wang LL, Dols WS, Chen Q (2010) Using CFD capabilities of CONTAM 3.0 for simulating airflow and contaminant transport in and around buildings. HVAC&R Res 16(6):749–763
7. Wang H, Wang F, Li D (2010) Developments and applications of coupled CFD and multizone simulations. Build Energy Environ 29(6):7–10

Chapter 22
Numerical Simulation of Aerosol Particles Distribution in a Classroom

Yi Zhang, Guohui Feng, Kailiang Huang and Guangyu Cao

Abstract This chapter studies the concentration distribution and particle tracks of students talking continuously in a classroom with two air distribution methods, including mixing ventilation (MV) and displacement ventilation (DV) using CFD simulations. The classroom is occupied by 10 students with a seating arrangement of 5 rows and 2 columns. RNG k-ε model is used to simulate the velocity field and temperature field, and the Lagrange method is used to deal with the particles. The simulation results indicated that the DV could remove the respiratory aerosol droplets and minimize the risk of infections effectively compared with MV. Under the same concentration threshold, the contaminant spread farther, when the flow field is weak Furthermore, high particle-releasing velocity would make the contaminant stay in the classroom for a long time.

Keywords Aerosols · Airflow · Concentration distribution · Particle tracks · Numerical simulation

22.1 Introduction

The outbreak of influenza A (H1N1) influenza in March 2009, the emergence of severe acute respiratory syndrome (SARS) in November 2002, and the global resurgence of tuberculosis (TB) during the last decade remind us that the airborne infectious diseases remain a serious threat to human health [1]. Respiratory aerosol was one of the spreading ways. There is a strong and sufficient evidence to demonstrate the association between the ventilation in buildings and the transmission of infectious diseases [2]. Poorly designed ventilation system and

Y. Zhang · G. Feng (✉) · K. Huang · G. Cao
School of Municipal and Environment Engineering, Shenyang Jianzhu University, Shenyang 110168, China
e-mail: fengguohui888@163.com

A. Li et al. (eds.), *Proceedings of the 8th International Symposium on Heating, Ventilation and Air Conditioning*, Lecture Notes in Electrical Engineering 263,
DOI: 10.1007/978-3-642-39578-9_22,

unreasonable ventilation strategy could lead serious health risks, and people who inhaled contaminated air would result in epidemic outbreak [3]. There are studies on respiratory aerosol diffusion and transmission in public places now, such as isolation rooms, clinics, high-speed rail, and aircraft cabin [4–7], but still there is lack of studies on classroom. The classroom is personnel intensive place and the main place for students' learning. Hence, it is important to find out an effective ventilation mode to weaken the exposure risk to other students.

22.2 Classroom Model

The classroom is occupied by 10 students with a seating arrangement of 5 rows and 2 columns and ventilated by two modes, including MV and DV. The geometry of the classroom is $X \times Y \times Z = 800 \times 360 \times 300$ cm. Figure 22.1 shows the schematic of the ventilated classroom. The window is on the back wall of the classroom with the geometry of $Y \times Z = 300 \times 90$ cm. The desks are simplified as the cuboid with the geometry of $X \times Y \times Z = 40 \times 120 \times 5$ cm. The desk is 70 cm above the floor.

22.3 Thermal Manikins

There are no standards for the size of the thermal manikins. The height of most thermal manikins is about 1.65 m^2, and the surface area ranges from 1.594 to 1.688 m^2 [8]. The study generally simplifies the thermal manikin as four parts: head, torso, leg, and mouth to simulate the students. Detailed geometry is shown in Fig. 22.2. To simplify the calculation, it is assumed that the students are talking continuously, that is, ignored the influence on mouths open and close, and supposed that the particles are injected at constant speed [9].

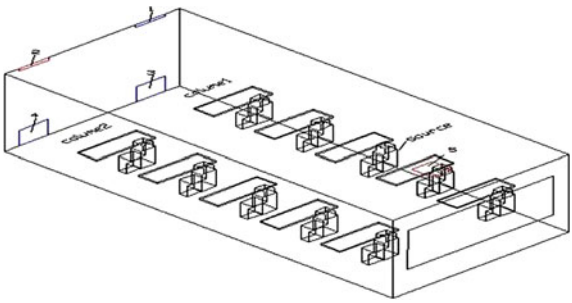

Fig. 22.1 Schematic of the ventilated classroom 1, MV inlet (60 × 10 cm); 2, MV outlet (60 × 10 cm); 3, DV inlet (60 × 60 cm); 4, DV inlet (60 × 60 cm); 5, DV outlet (43 × 43 cm)

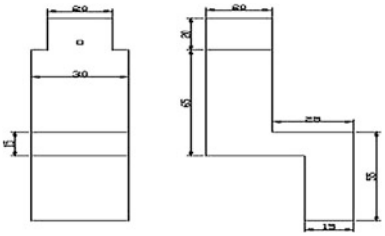

Fig. 22.2 Geometry of the thermal manikin

22.4 Boundary Conditions and Simulation Cases

Detailed boundary condition is shown in Table 22.1.

This study simulates the particles concentration distribution and tracks under three cases:

Case 1: Set the mouth of the student sitting in the third row first column as the source, releasing 5 μm particles when student talks continuously. Compare the particles concentration distribution and tracks of typical plane under MV and DV.

Case 2: Set the mouth of the student sitting in the row 1, row 3, and row 5 as the source, respectively, releasing 5 μm particles when student talks continuously. Study the influence of source positions on particles concentration distribution and tracks under DV.

Case 3: Set the mouth of the student sitting in the third row first column as the source. Study the influence of particle-releasing velocities on particles concentration distribution and tracks under DV.

Table 22.1 Boundary conditions

Items	Description
Wwindow	Wall, uniform 36 °C
Floor, ceiling, walls	Wall, adiabatic
Body surface	Wall, uniform 31 °C
Desks	Wall, adiabatic
MV inlet	Velocity inlet, 3 m/s, temperature 292 K
DV inlet	Velocity inlet, 0.25 m/s, temperature 294 K
Outlet	Outflow
Mouths	Velocity inlet, 1 m/s, temperature 308 K
Particles	Density 600 kg/m^3, 5 μm, flow rate 0.085 μm/s [4], temperature 35 °C

22.5 Governing Equations and Computational Method

Indoor airflow is generally turbulent. At present, there are three simulation methods for turbulence, which are direct numerical simulation (DNS), large eddy simulation (LES), and Reynolds-averaged Navier–Stokes (RANS). The application of DNS and LES to turbulent simulation requires very demanding computer memory and calculation speed, but the RNG k-ε model based on RANS is more applicable to simulate the indoor airflow. The simulation results could be in good agreement with experiment results using RNG k-ε model, so this study uses RNG k-ε model to simulate the indoor airflow.

The governing equations, including continuity, momentum, energy, turbulent kinetic energy k, and turbulent dissipation rate ε, can be written in the general format as follows:

$$\frac{\partial(\rho\phi)}{\partial t} + \nabla \cdot \left(\rho\phi\overrightarrow{v}\right) = \nabla \cdot \left(\Gamma_\phi \nabla\phi\right) + S_\phi \tag{22.1}$$

where ρ is the air density, $\overrightarrow{v}$ is the velocity vector, ϕ represents each of the three velocity components (u, v, w). When $\phi = 1$, the equation becomes the continuity equation. Γ_ϕ is the effective diffusion coefficient for each dependent variable. S_ϕ is the source term.

The respiratory aerosols released by people talking are composed of inner particles and outer mucus. The mucus evaporation has influence on the aerosols distribution and deposition. But the research shows that [10] the shrinkage time from the original respiratory aerosols to particles is rapid and is in the order of 0.5 s, especially to small particles with the size smaller than 20 μm. So, this study ignores the influence of respiratory aerosols evaporation and simplifies the respiratory aerosols as particles. In order to obtain the particle tracks, Lagrange method is used to track the moving particles. The Lagrange approach tracks particle phase separately through the flow domain by solving the force balance equations of particle movement. For a particle, the force balance in i direction can be written as:

$$\frac{\mathrm{d}u_{pi}}{\mathrm{d}t} = F_d + \mathrm{G} + F_{ai} \tag{22.2}$$

where u_{pi} is the velocity of particles in i direction, F_d is the drag force, G is the gravitation, F_{ai} is the additional forces (besides drag force and gravitation) exerted on unit particle mass in i direction, mainly including pressure gradient force, Basset force, and virtual mass force caused by unsteady flow, Brownian force, Saffman's lift force due to shear, and thermophoretic force due to temperature gradient. For room airflow involving fine particles, only the Brownian force and Saffman's lift force are relatively large. The thermophoretic force due to temperature gradient can be important in the case of nonisothermal airflow. Therefore, in this study, the Brownian force, Saffman's lift force, and thermophoretic force have been included in the additional force term.

Use the first-order upwind scheme to discrete and use the SIMPLE algorithm to solve the steady-state flow.

22.6 Results

22.6.1 Case 1 Results

Figure 22.3 shows the concentration distributions and particle tracks of plane y-300 under MV and DV. In Fig. 22.3a and b, under mixing ventilation (MV), the particles injected from mouth are diluted fast, leading to a low concentration distribution and short transportation distance. Because of the high turbulence intensity and the small particle with the size of 5 μm used in the simulation, the particles' movement is mostly influenced by the indoor airflow. However, the turbulence intensity is low under displacement ventilation (DV), so the particles could not be diluted fast when injected from the mouth and transported to a large distance along the straight line.

In Fig. 22.3c and d, because of the low velocity and low turbulence of the DV, the airflow mixing degree is weak, leading to high ventilation efficiency. However, the MV with high turbulence intensity makes the airflow well mixed. Though the particles move fast, they could stay in the classroom for a long time and distribute in the classroom widely. So, it is easy to inhale the particles, increasing the possibility of cross infection. Compared with MV, the ventilation modes of the bottom-up airflow with the low velocity and low turbulence such as the displacement and the under floor air distribution might eliminate the particles and reduce the possibility of the infections among students.

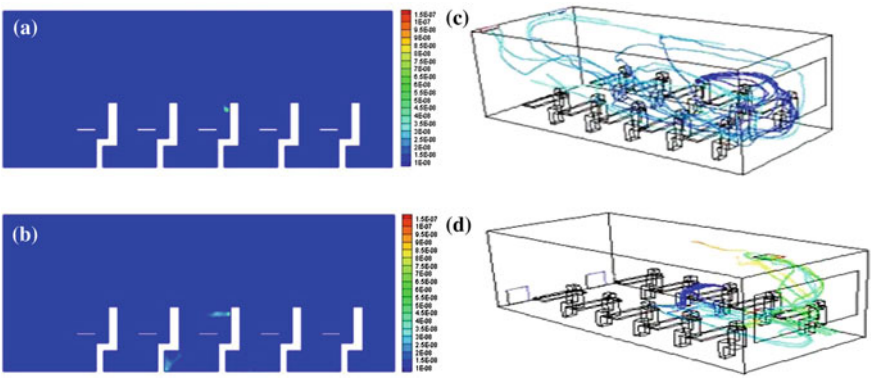

Fig. 22.3 The concentration distribution and particle tracks of plane $y = 300$. **a** MV concentration distribution, **b** DV concentration distribution, **c** MV particle tracks, and **d** DV particle tracks

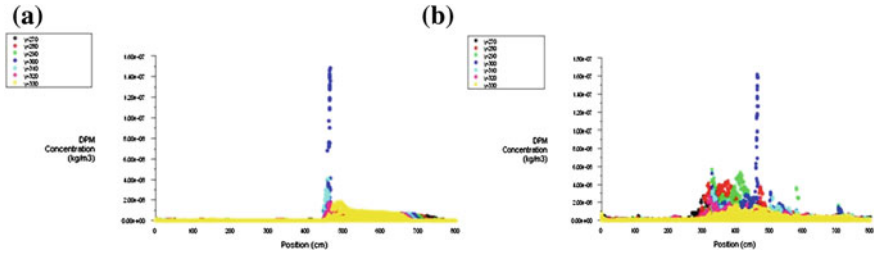

Fig. 22.4 The concentration distribution of typical plane. **a** MV. **b** DV

Figure 22.4 shows the concentration distribution of the typical plane of $y = 270$, $y = 280$, $y = 290$, $y = 300$, $y = 310$, $y = 320$, and $y = 330$ under MV and DV. In Fig. 22.4a and b, under MV, the concentration value is about 1.5e–07 kg/m^3 at the source, and the particles are diluted fast by indoor air, making a low concentration distribution around the students. So, it mainly has influence on the students sitting behind the source, and the concentration value is under 4.0e–08 kg/m^3. Under DV, because of the low turbulence and low velocity, the particles could not be diluted fast when injected from the mouth, and the particles spread along the directions of the length and the width of the classroom. But from the particle tracks, we could see that under DV, the particles are distributed in the area 70 cm above the floor, so it has limited influence on breathing zone which is about 110 cm above the floor.

22.6.2 Case 2 Results

In Fig. 22.5a, the concentration distributions have great difference under different source positions. When set the mouth of the students sitting in the row 1 and row 5 as the sources, the particles spread farther, because the air flow is weak around the source, and the particles could not be diluted fast. When set the mouth of the student sitting in the row 3 as the source, the particles generated a dense area near the hind legs of student in row 2. When set the mouth of the student sitting in row 5 as the source, the particles generated a dense area near the hind legs of students in row 1 and 2.

22.6.3 Case 3 Results

Figure 22.6 shows the concentration distributions and particle tracks of plane $y = 300$ under DV when the particles' releasing velocities are 1 m/s and 2 m/s, respectively. In Fig. 22.6a and b, set the concentration threshold from 1e–08 kg/m^3

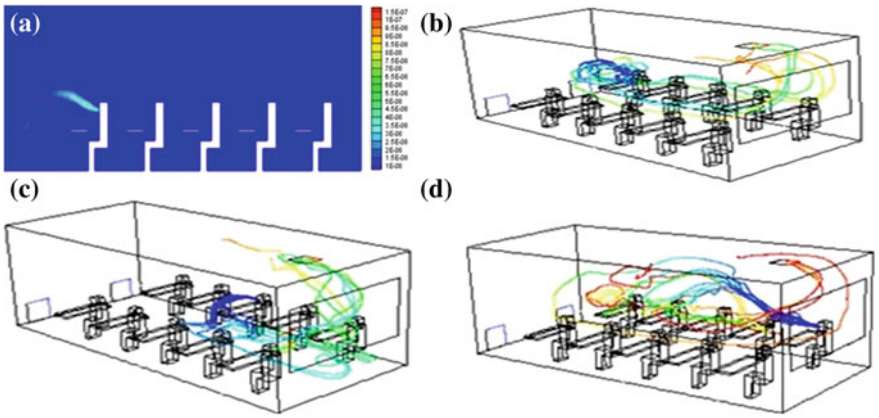

Fig. 22.5 The concentration distribution and particle tracks under different sources of plane $y = 300$. **a** row 1 concentration distribution. **b** Row 1 particle tracks. **c** Row 3 particle tracks, and **d** Row 5 particle tracks

to 1.5e–07 kg/m^3 as the study range considering the comparison. When the releasing velocity is 1 m/s, the particles have no concentration distribution in the front row breathing area while the releasing velocity is 2 m/s; the particles above the head have obvious concentration distribution in the breathing area of the student sitting in row 2.

In Fig. 22.6c and d, when the releasing velocity is 1 m/s, the particles spread 65 cm along the –X axis, and because of the velocity attenuation and the dilution of the indoor airflow, the moving particles follow the indoor airflow. When the

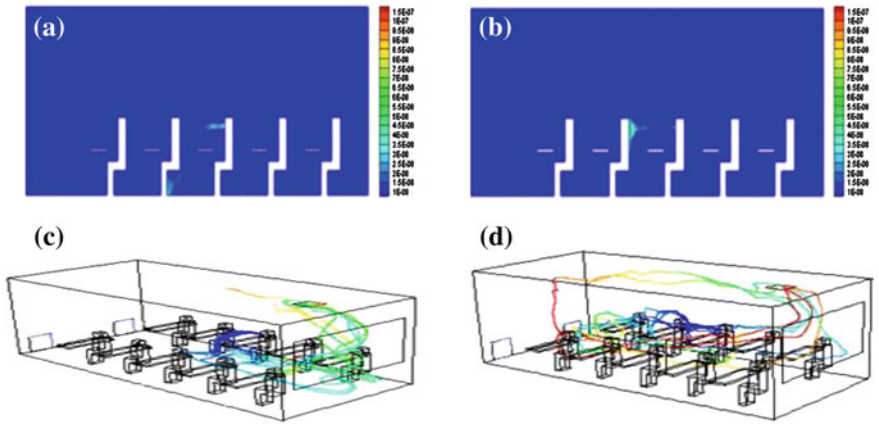

Fig. 22.6 The concentration distribution and particle tracks under different sources of plane $y = 300$. **a** 1 m/s concentration distribution. **b** 2 m/s concentration distribution. and **c** 1 m/s particle tracks. **d** 2 m/s particle tracks

releasing velocity is 2 m/s, the particles spread along the –X axis until they reached student's head of row 2. By the blocking of the student's head of row 2, the velocity reduced fast, and the particles are exhausted and followed the airflow. If there is no block, the particles would spread farther along the –X axis and stay in the classroom for a long time.

22.7 Conclusions

(1) The ventilation modes of the bottom-up airflow with the low velocity and low turbulence such as the displacement air distribution might eliminate the particles effectively and reduce the possibility of the infections among students.
(2) The source positions have great influence on concentration distribution and particle tracks. Under the same concentration threshold, the contaminant spread farther, when the flow field is weak.
(3) Under the same concentration threshold, high particle-releasing velocity would make the contaminants stay in the classroom for a long time.

Acknowledgments This research was supported by The Natural Science Foundation of Liaoning (20101088). Scientific and technical fund project subsidy of Shenyang City (F11-264-1-17), and scientific and technical fund project subsidy of Shenyang City (F10-208-1-00).

References

1. Qian H, Li Y, Nielsen PV et al (2009) Spatial distribution of infection risk of SARS transmission in a hospital ward. Build Environ 44:1651–1658
2. Li Y, Leung GM, Tang JW et al (2007) Role of ventilation in airborne transmission of infectious agents in the built environment-a multidisciplinary systematic review. Indoor Air 17:2–18
3. Cheremisinoff NP (2002) Handbook of air pollution prevention and control. Butterworth-Heinemann, pp 188–280
4. Qian H, Li Y (2010) Removal of exhaled particles by ventilation and deposition in a multibed airborne infection isolation room. Indoor Air 20(4):284–297
5. Zhang L, Li Y (2012) Dispersion of coughed droplets in a fully-occupied high-speed rail cabin. Build Environ 47:58–66
6. Zhu S, Srebric J, Spengler J et al (2012) An advanced numerical model for the assessment of airborne transmission of influenza in bus microenvironments. Build Environ 47:67–75
7. Yan W, Zhang Y, Sun Y et al (2009) Experimental and CFD study of unsteady airborne pollutant transport within an aircraft cabin mock-up. Build Environ 44:34–43
8. Gao N (2006) Numerical and experimental study of personalized ventilation. The Hong Kong Polytechnic University
9. Deng W, Shen J, Tang X (2005) The Study on the Optimization of Indoor Air Distribution for SARS Isolation Wards. Build Energy Environ 24(2):9–14. (In Chinese)
10. Nicas M, Nazaroff W, Hubbard A (2005) Toward understanding the risk of secondary airborne infection: emission of respirable pathogens. J Occup Environ Hyg 2:143–154

Chapter 23
A Numerical Investigation of Mechanical Smoke Exhaust in the Powerhouse of an Underground Hydropower Station

Jiangyan Ma, Angui Li, Yeqiu Wu and Bin Xiao

Abstract A fire dynamics simulator (FDS) was used to investigate mechanical smoke exhaust in the powerhouse of an underground hydropower station. Initially, the simulation results were validated through comparison with experimental data from a powerhouse fire. Then, the influence of the smoke exhaust vent locations on the mechanical smoke exhaust efficiency was studied. Simulated results showed that the location of the exhaust ports had little effect on the smoke exhaust. In addition, the effects of the exhaust rates and heat release rates were discussed. Results showed that both the soot density and the temperature of the smoke layer decreased with larger smoke exhaust rates. The smoke temperature and density both increased rapidly with increasing heat release rates, for the same exhaust rates.

Keywords Mechanical smoke exhaust · Powerhouse · Underground hydropower station · Numerical simulation

23.1 Introduction

Until the end of 2012, the installed capacity of hydropower in China was 1.7 million kW, ranking first in the world [1]. With the development of hydropower, the safety problems of hydropower related to the safety of regional and also

J. Ma (✉)
School of Environmental and Municipal Engineering, Xi'an University of Architecture and Technology, China Railway First Survey and Design Institute Group Ltd, Xi'an 710043, China
e-mail: majiangyan2008@126.com

A. Li · Y. Wu
School of Environmental and Municipal Engineering, Xi'an University of Architecture and Technology, Xi'an 710043, China

B. Xiao
China Hydropower Engineering Consulting Group Co., Xi'an 710065, China

A. Li et al. (eds.), *Proceedings of the 8th International Symposium on Heating, Ventilation and Air Conditioning*, Lecture Notes in Electrical Engineering 263,
DOI: 10.1007/978-3-642-39578-9_23,

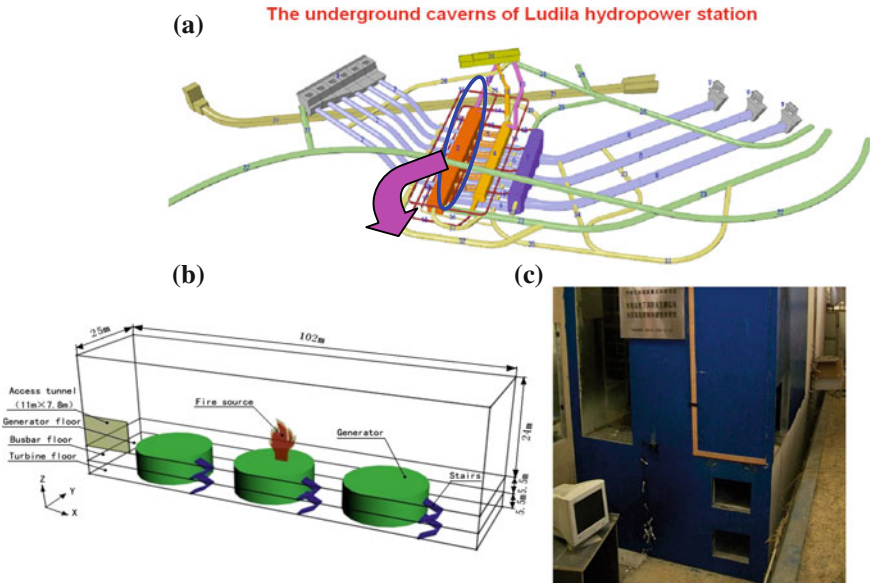

Fig. 23.1 Underground caverns of the Ludila Hydropower Station **a**, a schematic diagram of the main workshop of the Ludila Hydropower Station **b**, a picture of a 1:12 model **c**

national power have received more and more attention, particularly the safety problems of hydropower station facilities during fires. How to identify and control smoke movement in the large enclosed underground spaces typical of the main generator halls of underground hydropower stations, remains an issue to be solved and is of realistic significance.

Early investigations focused on smoke characteristics in large spaces such as atriums [2–7, 14, 15], sports centers [8], and road tunnels [9–13]. Full-scale experimentation is an important method in studying the characteristics of mechanical smoke exhaust of fires in large areas [4, 5, 16, 17]. Due to the large size of powerhouses, it is difficult to conduct full-scale experiments on their smoke exhaust systems. Numerical simulations have been widely applied to the research of smoke movement in large space fires, as a scientific method that can proficiently predict the smoke movement in actual fires [18, 19].

In this paper, the research is based on the actual Ludila Hydropower Station, located on the Jinsha River (see Fig. 23.1a, b). The aim is to validate the accuracy of a fire dynamics simulator (FDS) simulation through a 1:12 similarity model test, and then, the characteristics of the mechanical smoke exhaust can be studied in three parts: the influence of the amount of smoke exhaust, the location of the exhaust, and the fire intensity. This paper simulates the spread of the smoke with different heat release rates, using the FDS code [20], based on large-eddy simulations (LES).

23.2 Validation of the FDS Model

An approximate form of the Navier–Stokes equation appropriate for low Mach number applications, as outlined by McGrattan et al. [20], is used in the FDS model. In this paper, the 1:12 model of the main workshop (see Fig. 23.1c) is determined according to Froude modeling [16, 21]. To ensure the similitude between the model and the actual application, the following three similarity criteria must be the same:

Time similarity:

$$\pi_1 = \frac{L}{V\tau} = \frac{\sqrt{L/g}}{\tau} \tag{23.1}$$

Kinematic similarity:

$$\pi_2 = \frac{gL}{V^2} = \frac{1}{\mathrm{Fr}} \tag{23.2}$$

Heat release rate similarity:

$$\pi_3 = \frac{\dot{Q}_0}{\rho_0 c_p g^{1/2} T_0 L^{5/2}} \tag{23.3}$$

Heat loss through envelope similarity:

$$\pi_4 = \frac{(\rho C \lambda)_s}{C_1^2 g^{0.3} \lambda^2 \left(\frac{\rho_0}{\mu}\right)^{1.6} L^{0.9}} \tag{23.4}$$

The scales of the actual application and the model are given in Table 23.1.

In order to validate the accuracy of the model, FDS is applied to simulate the fire experiment, which was carried out on a reduced-scale model of the Ludila experiment (see Fig. 23.1). The experiments were mainly carried out in the generator layer, the actual size of which was 102 × 25 × 24 m, while the size of the 1:12 model is 8.5 × 2.1 × 2.0 m. The thermocouples were placed along the top of the generator floor as shown in Fig. 23.2. The FDS simulation and experiment conditions are compared in Table 23.2. The heat release rates and geometric lengths are obtained through conversion according to the heat release rate scale λ_Q and geometric scales λ_L in Table 23.1.

Comparing the simulated results with the predicted results of Eq. (25.5) [22] and NFPA 92B [23], as shown in Fig. 23.3, it can be seen that the FDS simulated results agree well with the experimental results and the predicted results of

Table 23.1 Scales of each parameter

Name	Temperature	Length	Velocity	Time	Exhaust flow rate	Heat release rate
Symbol	λ_T	λ_L	λ_V	λ_t	λ_{Ve}	λ_Q
Scale	$\frac{1}{1}$	$\frac{1}{12}$	$\frac{1}{3.456}$	$\frac{1}{3.456}$	$\frac{1}{500}$	$\frac{1}{500}$

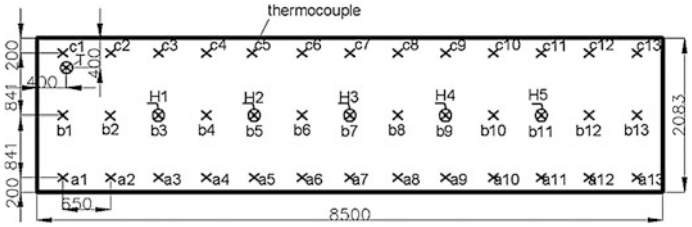

Fig. 23.2 The layout of the thermocouples on the ceiling of the generator floor

Table 23.2 The model experimental conditions and the FDS simulated conditions

	Fire location	Heat release rate/kW	Model	Fire type	Ambient temp/°C
Experimental conditions	At the center	3	1:12 model (8.5 × 2.1 × 2.0 m)	Diesel	19.7
		6			19.3
Simulated conditions	At the center	1,500	Full-scale model (102 × 25 × 24 m)	Diesel	20.0
		3,000			20.0

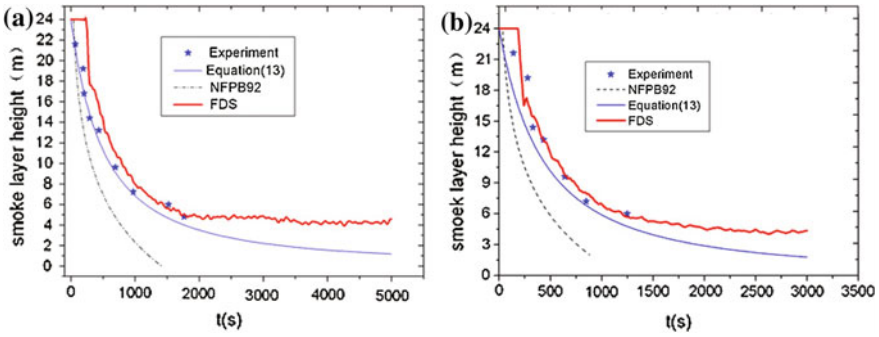

Fig. 23.3 The height of the smoke layer. **a** Heat release rate of 1,500 kw, **b** Heat release rate of 3,000 kw

Eq. (23.5), but the agreement with NFPB 92 is not so good, because NFPA 92B mainly predicts the height of smoke interface. So, it can be concluded that the 1:12 model tests can be a useful tool to verify the correctness and accuracy of the FDS simulation.

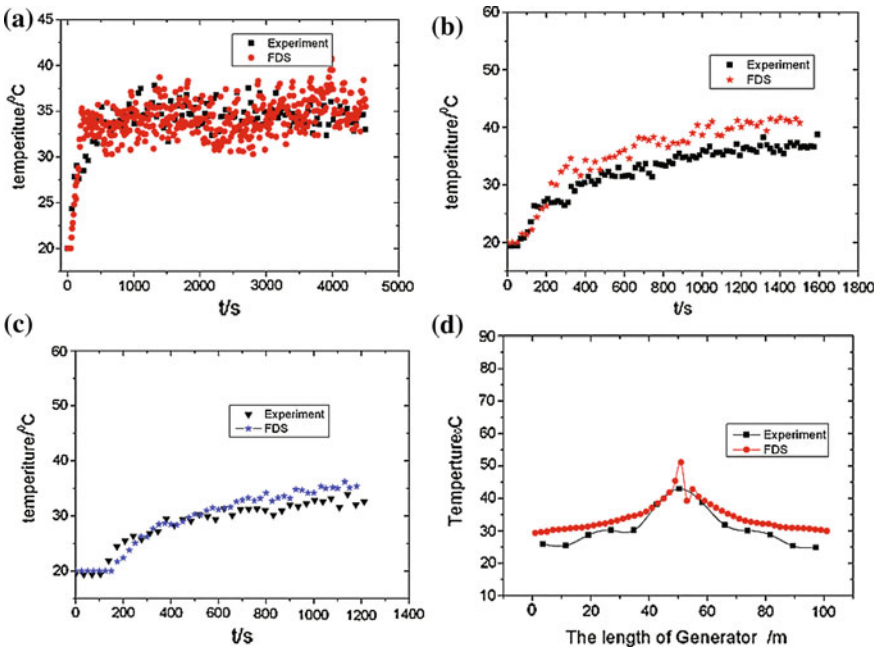

Fig. 23.4 The temperature distribution when the heat release rate is 1,500 kW. **a** Measure point b7, **b** Measure point b9, **c** Measure point b1, **d** Ceiling jet temperature at time 500 s

$$Z = \left[0.035\left(\frac{Q^{\frac{1}{3}}}{A}\right)t + H^{\frac{-2}{3}}\right]^{\frac{-3}{2}} \tag{23.5}$$

$$\frac{z}{H} = 1.11 - 0.28\ln\left(\frac{tQ^{1/3}/H^{4/3}}{A/H^2}\right) \tag{23.6}$$

where Z is the smoke layer height, m; Q is the heat release rate, kW; A is the ground area of generator floor, m^2; H is the height of the generator floor and m; t is time, s.

Figure 23.4 shows the comparison between simulation and experiment temperatures measured by different thermocouples, where b1 is far away from the smoke center, b7 is above the smoke plume, and b9 is close to the center. It can be seen that the simulated results of the temperature distribution at 500 s agrees well with the measured values, and that there is a steep temperature gradient along the horizontal direction of the generator floor.

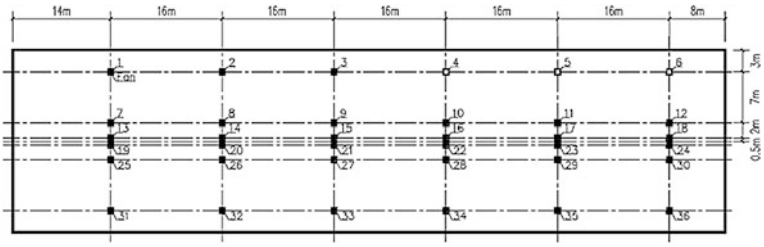

Fig. 23.5 Layout of the exhaust port on the ceiling of the generator floor

23.3 Results and Discussion

There are some provisions for smoke exhaust of main workshops in the "Hydropower Engineering Design Standard" of China [24], which state that mechanical smoke exhaust systems should be applied in the generator floors of closed underground workshops, and smoke exhaust rates should not be less than 120 $m^3/(h\ m^2)$ based on the ground area of one unit. In this paper, the design exhaust rate per exhaust port is 2.93 m^3/s, based on the area of each unit of the Ludila generator floor. In order to determine the impact of the exhaust rate, simulations were conducted under different criteria, with different exhaust port locations. Figure 23.5 shows the layout of the exhaust ports on the ceiling of the generator floor.

23.3.1 The Impact of the Exhaust Rate

In this paper, the effects of different smoke exhaust systems on the spread of smoke above the generator floor were simulated. To simulate the spread of the smoke in a fire scenario, a 2 m × 2 m oil burner with a heat release rate of 375 kW per unit area was placed in the center of the floor to form a symmetric fire plume. In order to learn the impact of the exhaust rate on the smoke exhaust, five cases were simulated in this paper as, outlined in Table 23.3, in which the locations of the exhaust ports were the same (exhaust ports 13–24). When fire breaks out on the generator floor of the main workshop, the hot smoke rises to the ceiling, by buoyancy. When smoke reaches the ceiling, a "ceiling jet" phenomenon occurs, and the spread of smoke covers the entire ceiling. In Fig. 23.6, comparisons of the mean characteristics of the smoke layer at the ceiling, at different exhaust rates, are shown. Figure 23.6a shows that when the location of the exhaust port and the fire and heat release rates are the same, the descent rate of the smoke layer decreases as the exhaust rates increase. Therefore, it can be concluded that due to the huge volume of the main workshop (about 61,200 m^3), the smoke layer descends slowly, and the descent rate decreases as the exhaust rates increase.

Table 23.3 Simulation conditions for different exhaust rates

Case	Heat release rate/kW	Exhaust rate per exhaust port/m^3/s	Location of the fire	Exhaust port	Environment temperature/°C
1	1,500	1.465($0.5G_0$)	Center of the generator floor	13–24	20
2	1,500	2.344($0.8G_0$)	Center of the generator floor	13–24	20
3	1,500	2.93($1.0G_0$)	Center of the generator floor	13–24	20
4	1,500	3.516($1.2G_0$)	Center of generator floor	13–24	20
5	1,500	4.395($1.5G_0$)	Center of the generator floor	13–24	20

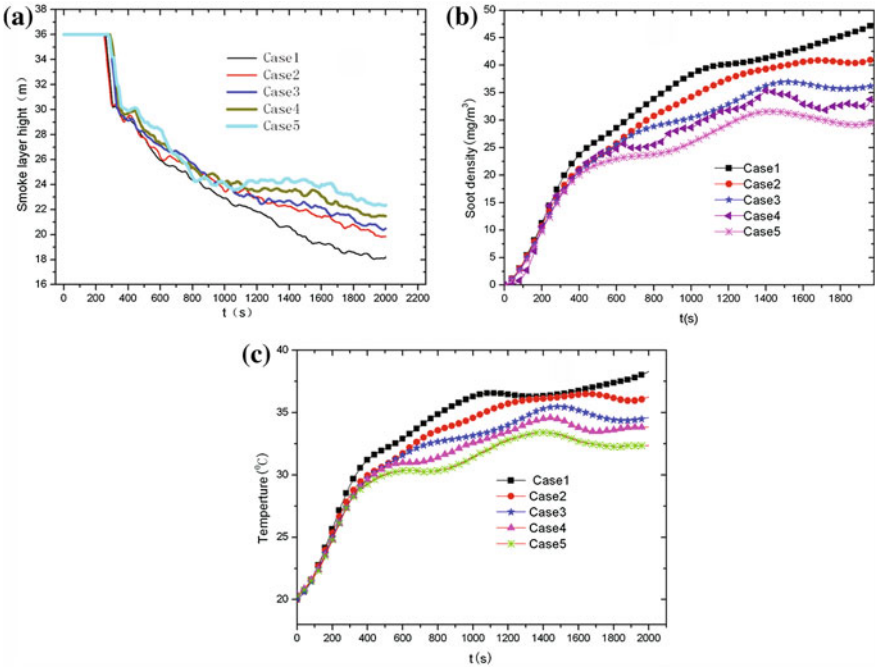

Fig. 23.6 Mean characteristics of smoke for different flux volumes on the roof: **a** descent of smoke layer, **b** distribution of mean soot density, and **c** distribution of mean temperature

In general, more ambient air is allowed to be drawn onto the generator floor with a greater exhaust rate, and the smoke in the main workshop will be diluted and cooled. Therefore, the mean soot density of the smoke layer is reduced when the exhaust rate of the smoke is increased, as shown in Fig. 23.6b. In addition, as more ambient air is drawn into the generator floor room, the mean temperature of the smoke layer decreases as the smoke exhaust rate increases, as shown in Fig. 23.6c. It can be seen that higher exhaust rates lead to lower mean soot densities and mean temperatures of the smoke layer.

Table 23.4 Simulation conditions with different locations of exhaust ports

Case	Heat release rate/kW	Exhaust rate/m^3/s	Location of the fire	Environment temperature/°C	Exhaust port
A	5,000	2.93	Center of the generator floor	20	13–24
B	5,000	2.93	Center of the generator floor	20	1–6, 31–36
C	5,000	2.93	Center of the generator floor	20	11, 12, 17, 18, 23, 24, 29, 30, 35, 36
D	5,000	2.93	Center of the generator floor	20	1, 2, 7, 8, 19, 20, 25, 26, 31, 32

23.3.2 The Impact of the Location of the Exhaust Ports

In this paper, four mechanical smoke exhaust systems were investigated. In cases A and B, the exhaust ports were laid out uniformly along the length of the generator, and in cases C and D, they are arranged centrally, see Table 23.4.

Comparisons of the mean characteristics of the smoke layer for the four cases are shown in Fig. 23.7. It can be seen that, regardless of the location of the exhaust ports, whether uniformly or centrally, the descent velocities of the smoke layer are almost the same. Thus, there is little impact made by the location of the exhaust ports, under the stipulation that the exhaust rates and heat release rates are the same, and there is no short circuit between the exhaust air and supplementary air. As the exhaust rates under the different cases are equal, the fresh air supplemented from the traffic tunnel is almost equal, and the diluted and cooling effects are also the same. Therefore, the average smoke density and temperatures are almost the same for different locations of the exhaust ports.

23.3.3 The Impact of the Heat Release Rate

In this paper, the effects on the spread of the smoke due to the different release rates of the fire source were simulated, as described in Table 23.5. In all cases, the locations of the exhaust ports and the exhaust rates of each port are the same. The fire is at the center of the generator floor, and the heat release rates are, respectively, 5, 8, and 10 MW, as shown in Fig. 23.8. It can be seen that the heat release rates are becoming stable after 200 s. Comparisons of the mean characteristics of the smoke layers for the three cases are shown in Fig. 23.9. It can be seen that the heat release rate has the greatest impact on the descent velocity of the smoke layer, and the smoke layer descends faster with a greater heat release rate. When a fire breaks out, the heat release rate is rather large, so the smoke accumulates with

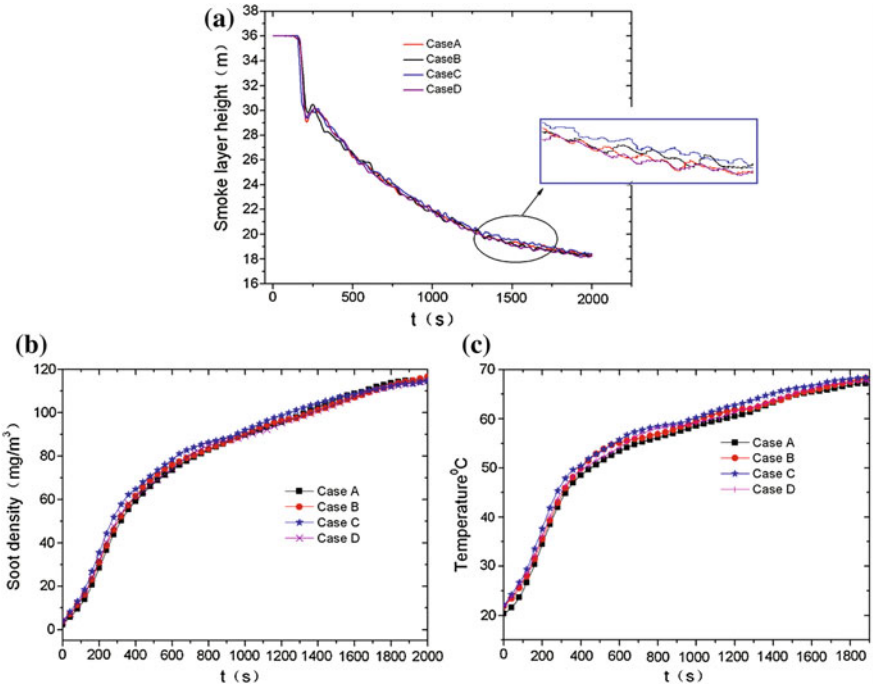

Fig. 23.7 Mean characteristics of smoke for different exhaust systems on the ceiling: **a** descent of smoke layer, **b** distribution of mean soot density and **c** distribution of mean temperature

Table 23.5 Simulation conditions with different heat release rates

Case	Heat release rate/kW	Exhaust rate/ m^3/s	Location of the fire	Environment temperature/°C	Exhaust port
a	5,000	2.93	Center of the generator floor	20 °C	13–24
b	8,000	2.93	Center of the generator floor	20 °C	13–24
c	10,000	2.93	Center of the generator floor	20 °C	13–24

more and more air involved near the fire, and then, the smoke layer descends more quickly. It also leads to an increase in the average density and temperature of the smoke layer, as shown in Figs. 23.10 and 23.11.

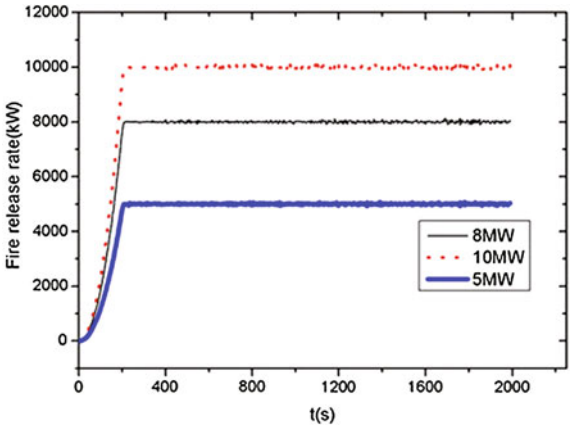

Fig. 23.8 The release rate of fire source

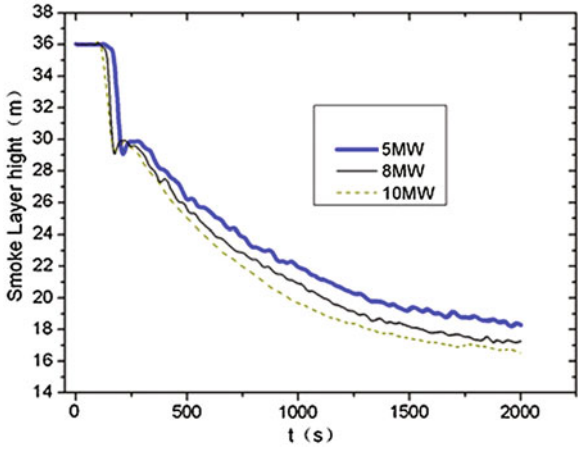

Fig. 23.9 Smoke layer height with different fire release rates

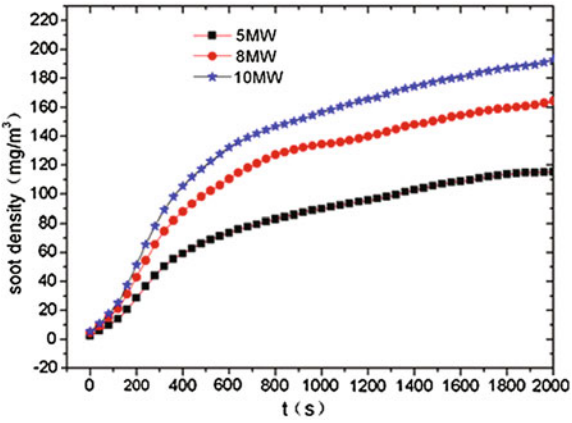

Fig. 23.10 Distribution of mean soot density

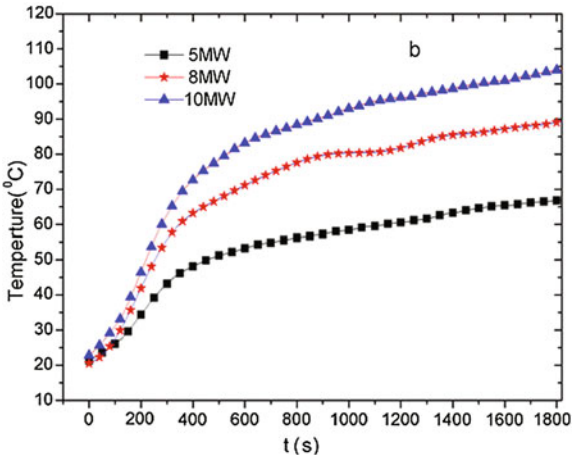

Fig. 23.11 Distribution of mean temperature

23.4 Conclusions

The FDS code is used to simulate the smoke filling process in the generator room of the Ludila Hydropower Station. Results show that the simulated results of the FDS and the experimental results of a 1:12 model are in good agreement, and the FDS model can effectively predict the smoke movement in hydropower station fires.

It can be concluded from simulations of the characteristics of mechanical smoke exhaust for different cases that, because the generator floor of a hydropower station is huge, when a fire breaks out, the smoke layer descends rather slowly, and the smoke temperature and density are relatively low. The smoke exhaust rate is a major factor impacting the smoke exhaust, while the exhaust port locations have little effect on the smoke exhaust. Under the same exhaust rates, the smoke temperature and density both increase rapidly with increasing heat release rates.

Acknowledgments This research was sponsored by the National Key Scientific for Hydropower Industry (No. CHC-KJ-2007-21-12) and Shaanxi Province 13115 Technology Innovation Project (No. 2009ZDKG-47).

References

1. http://www.ocn.com.cn/reports/2006062shuidian.htm
2. Chow WK, Cui E (1997)·Plume equation for studying smoke-filling process in atria with a zone model. Fire Mater 21:235–244
3. Chow WK, Li J (2001) Simulation on natural smoke filling in atrium with a balcony spill plume. J Fire Sci 19:258–283
4. Shi CL, Lu WZ et al (2007) An investigation on spill plume development and natural filling in large full-scale atrium under retail shop fire. Int J Heat Mass Transf 50:513–529

5. Cándido GM et al (2008) Numerical model and validation experiments of atrium enclosure fire in a new fire test facility. Build Environ 43:1912–1928
6. Chow WK, Li SS et al (2009) Numerical studies on atrium smoke movement and control with validation by field tests. Build Environ 44:1150–1155
7. Qin TX, Guo YC et al (2009) Numerical simulation of the spread of smoke in an atrium under fire scenario. Build Environ 44:56–65
8. Chen JG, Chen HX, Fu S (2005) Numerical investigation of fire smoke transport in the Tsinghua University Sports Center Tsinghua. Sci Technol 5:618–622
9. Gao PZ, Liu SL, Chow WK et al (2004) Large eddy simulation for studying tunnel smoke ventilation. Tunn Undergr Space Technol 19:577–586
10. Hu LH, Huo R, Chow WK et al (2005) Full-scale burning tests on studying smoke temperature and velocity along a corridor. Tunn Undergr Space Technol 20:223–329
11. Hu LH, Huo R, Chow WK et al (2006) On the maximum smoke temperature under the ceiling in tunnel fires. Tunn Undergr Space Technol 21:650–655
12. Hu LH, Peng W, Huo R (2008) Critical wind velocity for arresting up wind gas and smoke dispersion induced by near-wall fire in a road tunnel. J Hazard Mater 150:68–75
13. Hu LH (2006) Studies on thermal physics of smoke movement in tunnel fires. Dissertation for Ph.D degree of University of Science and Technology of China
14. Huo R, Chow WK, Jin XH et al (2005) Experimental studies on natural smoke filling in atrium due to a shop fire. Build Environ 40:1185–1193
15. Tanaka T, Yamana T (1985) Smoke control in large scale spaces-part 2: smoke control in large scale spaces. Fire Sci Technol 5(1):41–54
16. Quintiere JG (1989) Scaling application in fire research. Fire Saf J 15:3–29
17. Liu F, Fu XZ, Liao SJ, Hu B (2001) A scaling model for smoke flow in atrium fires. China Saf Sci J 11(4):17–20
18. Chow WK (1997) On the use of time constants for specifying the smoke filling process in atrium halls. Fire Saf J 28:165–177
19. Hua NK, Fong LZ et al (2007) Modeling fire-induced smoke spread and carbon monoxide transportation in a long channel: fire dynamics simulator comparisons with measured data. J Hazard Mater 140:293–298
20. McGrattan K, Hostikka S (2008) Fire dynamics simulator—technical reference guide. NIST Special Publication 1019-5. National Institute of Standards and Technology, Gaithersburg, MD
21. Huo R, Hu Y, Li YZ (2009) Introduction to building fire safety engineering. Press of University of Science and Technology of China, Hafei
22. Heskestad G (2002) Fire dymanics, SFPE handbook of fire protection engineering, 3rd edn. National Fire Protection Association, Quincy, MA
23. NFPA (2000) NFPA 92B, Guide for smoke management system in malls, atria and large area. National Fire Protection Association, Quincy, Mass
24. Code for Design of Fire Protection of Hydraulic Engineering (1990) SD1278-90, water resources and hydropower planning and design general institute. Ministry of Public Security, Department of energy of the People's Republic of China

Chapter 24
An Overview of the Applications of Particle Image Velocimetry for Indoor Airflow Field Measurement

Xiaodong Cao, Junjie Liu and Nan Jiang

Abstract Particle image velocimetry (PIV) is a promising technique for quantifying the airflow fields in buildings, which is crucial for creating a thermal comfortable and healthy indoor environment. This investigation summarized the state-of-the-art applications of PIV in measuring indoor airflow fields. The overview shows that PIV has gradually become the most popular and versatile tools for measuring various indoor airflow fields. The quantitative and detailed turbulent flow information obtained by PIV is critical for analyzing turbulent properties and validating numerical simulations. Specifically, we analyzed the pros and cons of PIV applications and gave the typical parameters of PIV systems used in indoor airflow field measurements. For indoor PIV measurements, small-scale models are the most convenient and appropriate, but may suffer from scaling problems. Large-scale PIV measurements are still necessary, for the data obtained from full-scale models are the most realistic and reliable. The researchers should pay much more attention to the selection of an appropriate PIV system according to their specific needs.

Keywords Indoor environment · Airflow · Particle image velocimetry (PIV) · Measurement technology

X. Cao · J. Liu (✉)
School of Environmental Science and Engineering, Tianjin University, Tianjin 300072, China
e-mail: jjliu@tju.edu.cn

N. Jiang
School of Mechanical Engineering, Tianjin University, Tianjin 300072, China

A. Li et al. (eds.), *Proceedings of the 8th International Symposium on Heating, Ventilation and Air Conditioning*, Lecture Notes in Electrical Engineering 263,
DOI: 10.1007/978-3-642-39578-9_24,

24.1 Introduction

Quantifying the airflow field in a room is crucial for creating a thermal comfortable and healthy indoor environment. Nevertheless, indoor airflow field is normally characterized by high turbulent level and unsteady due to the relatively low air velocity from the diffuser, thermal plume of heat source and unsteady perturbation of occupants' behavior. Therefore, it is not easy to conduct accurate airflow field measurement in indoor environment. Sun and Zhang [1] summarized various kinds of modern indoor air motion measurement techniques. In general, the velocimetry can be divided into pointwise and global-wise. The traditional pointwise velocimetry can only obtain the velocity information at the point of the probe sensor. Generally, it is very difficult to conduct accurate and detailed measurement of the global airflow field with this kind of velocimetry. Meanwhile, most of the pointwise velocimetry is thought to have perturbations on the local airflow. In contrast, global-wise velocimetry can obtain the velocities and related statistical information in a global domain without disturbing the airflow, which makes the whole instantaneous and mean velocity field measurement possible. Particle image velocimetry (PIV) is one of the most robust and widely used global-wise velocimetry [2, 3]. Specifically, PIV has gradually become the alternative tools for measuring indoor airflow distributions during the last decade. This paper aims to provide an overview of the state-of-the-art applications of PIV in measuring indoor airflow fields.

24.2 Applications in Indoor Airflow Field Measurements

24.2.1 Ventilation Devices

Ventilation devices play an important role as the air supply boundary conditions for the ventilated rooms. However, conventional velocimetry cannot fulfill the measurement requirement of the complex airflows generated by ventilation devices, such as the jet flows. In contrast, PIV is an ideal measurement tool to investigate the jet dynamic behavior, such as the spatial vortex structure and the turbulent transitional process.

Cao et al. [4] used PIV to reveal the structure of a turbulent attached plane jet in the entrainment process of the ambient air downstream from an active chilled beam in a full-scale climate chamber. The PIV system was capable of measuring the attached plane jet at a low Reynolds number with high-turbulence intensity quantitatively and instantaneously. Figure 24.1 shows their PIV measurement results of the jet velocity fields at different slot average velocities. The results provided a precise visualization of the structure of the attached jet during the turbulent transition and entrainment process after leaving the supply slot. During the measurement, it was observed that the optimization of the measurement

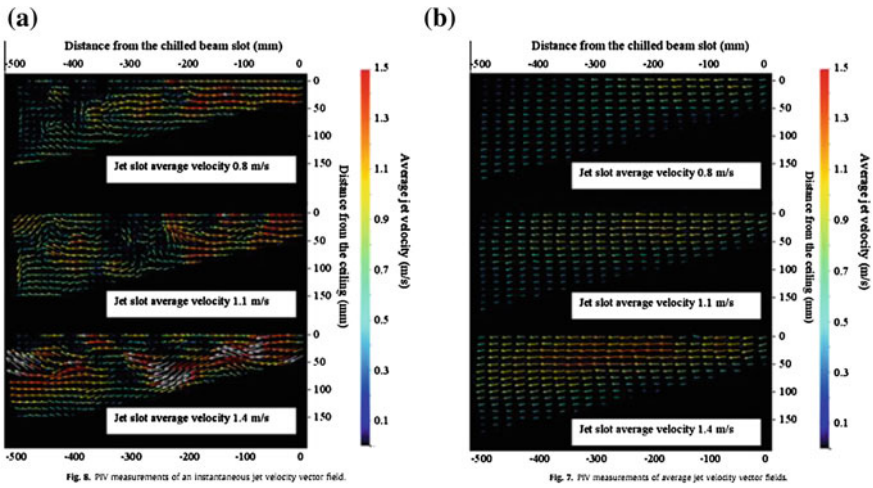

Fig. 24.1 PIV measurements of a turbulent attached plane jet discharged from an active chilled beam in a room by Cao et al. [4]: **a** Instantaneous jet velocity vector fields, **b** time-averaged jet velocity vector fields

parameters, such as the time delay between pulses and the seeding density, has to be performed with extreme caution. Meslem et al. [5] employed a PIV system to acquire instantaneous spatial velocity distributions of two different kinds of jet. They also used PIV to measure the flow field of a turbulent twin cross-shaped jet on a perforated panel diffuser [6]. Elvsén and Sandberg [7] used PIV to study the entrainment into the buoyant jet close to a diffuser for displacement ventilation. Montoya et al. [8] demonstrated the application of synthetic jet actuators for controlling indoor air quality in a dedicated closed chamber. The flow field in the chamber was determined using PIV. Nastase et al. [9] employed PIV system to measure the flow fields from two different kinds of grills. Besides, PIV also can be used to measure the flow fields inside the ventilation devices. Sanjuan et al. [10] used PIV to measure the velocity field inside the air cavity of an open joint ventilated facades (OJVF) model. Chami and Zoughaib [11] used PIV system to characterize the buoyancy-driven airflow inside the thermosyphon. It is found that most of these investigations were based on 2D-PIV systems. In fact, the airflow fields generated by many devices, such as split air conditioners, usually have significant three dimensional flow structures. Thus, it is more desired to measure these airflows by using volumetric PIV [5, 6].

24.2.2 Human Airflows

Knowledge of the behaviors and physics of human airflows, such as thermal plumes, coughing flows and breathing flows, are very critical to create high indoor

environment quality. However, it is very difficult to capture the instantaneous (e.g., coughing and sneezing) and unsteady (e.g., thermal plume) human airflows by pointwise anemometry. Thus, PIV is certainly more suitable for measuring the human airflows.

Özcan et al. [12] obtained mean velocity data around the head of a real-life size breathing thermal manikin for two cases of 'no breathing' and 'continuous exhalation' through nose by using PIV. Marr et al. [13] employed TR-PIV and stereoscopic PIV to obtain the quantitative velocity information in the breathing zone of a thermal manikin placed within a chamber with simulated breathing. The results suggested that the airflow due to breathing is both unsteady and highly anisotropic. The above investigations were based on thermal manikins. However, it would be more meaningful to conduct measurements based on human volunteers to study the physics of human airflows or obtain accurate boundary conditions for further simulations. Craven et al. [14] used PIV to characterize the velocity field around a human volunteer in the temperature-stratified room. Zhu et al. [15] used PIV to measure the velocity distribution around the mouth of the coughing subject with flour as the tracer particle. Chao et al. [16] presented the PIV data of expiration air jet velocities from volunteers during coughing and speaking. Similarly, the initial velocity and angle of exhaled airflow from coughing and speaking was measured with 26 tested subjects using PIV by Kwon et al. [17]. VanSciver et al. [18] also applied PIV system to measure the velocity field of human cough from 29 subjects. Cough flow velocity profiles, average widths of the cough jet, and maximum cough velocities were obtained. The recent applications indicate that the trend in this area is to use human volunteers instead of manikins. If using volunteers as the subjects, the tracer particles should be non-toxic and similarly represent the particles expelled from a human's mouth during breathing and coughing. In this case, theatrical fog seems a good choice for the measurements of thermal plumes [14] or coughing flows [18]. Figure 24.2a and b show the results of these two investigations, respectively. Nevertheless, it is worthy to mention that the laser beam in PIV system is a safety hazard and may harm eyes and skin.

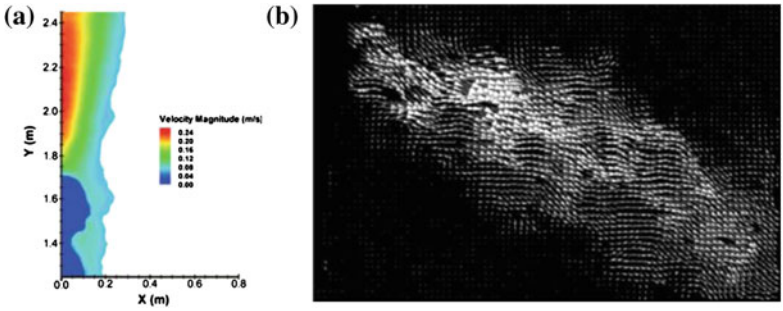

Fig. 24.2 PIV investigations of actual human airflows: **a** Velocity magnitude contours of human thermal plume in the sagittal plane obtained by Craven et al. [14], **b** velocity field of a typical cough flow measured by VanSciver et al. [18]

Thus, the PIV experiments involving human volunteers should be paid great attention to the safety problems.

24.2.3 Indoor Airflow Fields

The measurements of indoor airflow fields can use both small-scale models and full-scale models. Generally, small-scale models are more suitable for PIV measurements. The dimensions of small-scale models are similar to the field of view (FOV) of typical PIV systems and the enclosures can be easily made transparent. Therefore, PIV is able to straightforwardly measure the airflow field in the whole cross section in a small-scale model. Besides, the controllable boundary conditions of small-scale models can be easily changed for studying different cases.

Li et al. [19] used PIV to study the air distribution in a powerhouse. It would be impossible to conduct such a measurement in a full-scale model. Therefore, a 1/50 scale-down model was built up to mimic the real building. In order to ensure the similarity under non-isothermal condition, Archimedes number was chosen to be the similar dimensionless parameter. The averaged velocity field measured at a cross section is shown in Fig. 24.3a. Their research found that the supply air velocity and the air inlet location had a remarkable effect on air distribution characteristics of the large space and occupant zone velocity. Kang and Lee [20] used PIV to investigate the natural ventilation of entrained air inside a scale-down factory building using a louver ventilator. Hooff et al. [21] presented detailed PIV measurements and an analysis of transitional flow in a ventilated enclosure model. Karava et al. [22] employed the PIV technique for the evaluation of the air velocity field in a generic single-zone building model with cross-ventilation under isothermal flow conditions. Rouaud et al. [23] made an assessment on the influence of external perturbations on an original minienvironment. The PIV measurements were initially carried out in order to describe the steady flow in the minienvironment. Poussou et al. [24] conducted PIV and PLIF measurements in a one-tenth-scale, water-based model to investigate the effects of a moving body on

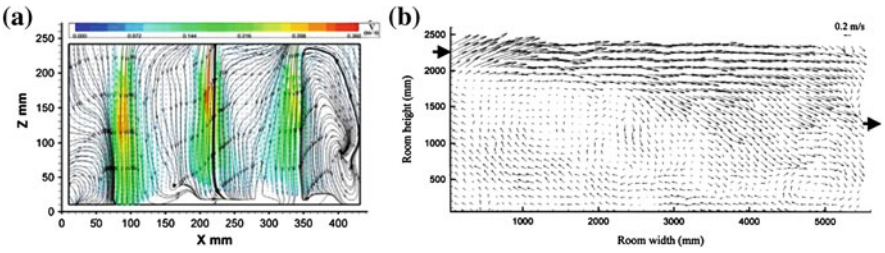

Fig. 24.3 PIV investigations of indoor airflow fields: **a** Stream line of velocity field in a 1/50 scale-down powerhouse model obtained by Li et al. [19], **b** airflow pattern in a full-scale room for cross-flow ventilation measured by Zhao et al. [25]

airflow and contaminant transport inside an airliner cabin. Various applications indicate that PIV is popular and appropriate for small-scale model experiments. However, small-scale models may suffer from scaling problems associated with combined modeling of inertial and buoyancy forces, and simplified geometries.

Measurements of the airflows in full-scale models are also critical for analyzing ventilation performances and validating numerical simulations. Compared with small-scale models, full-scale models can better represent the real conditions but more expensive and complex. Generally, the applications of PIV in full-scale models are much more difficult than small-scale models due to the large space, non-transparent enclosures and inside obstructions. The research group led by Yuanhui Zhang has performed some large-scale PIV measurements in a full-scale test room (5.5 × 3.7 × 2.4 m). They developed both large-scale 2D-PIV system [25] and large-scale stereoscopic PIV system [26] to obtain the full-scale room airflow fields for validating numerical models. Helium-filled bubbles of neutral buoyancy were used to seed room airflow, and a bank of projector lamps were used to offer illumination. Figure 24.3b shows an example of their measurement result by 2D-PIV system. As shown in Fig. 24.3b, the large-scale PIV results can directly give the realistic prediction of indoor air distribution without scaling and simplification problems. Besides the large-scale applications, PIV were also available to obtain local airflow fields in real-size rooms. Caciolo et al. [27] used PIV to measure the flow field on a vertical plane orthogonal to the opening in a full-scale room. Mortensen et al. [28] performed a PIV investigation of the airflow pattern in the microclimate behind furniture placed next to exterior walls. The above applications indicate that using PIV in full-scale rooms seems to be less popular than small-scale models. In full-scale models, the research emphasis was also switched to local airflows rather than entire flow patterns. However, it is still meaningful to conduct large-scale PIV measurements in full-scale rooms, for they can give the most realistic predictions of ventilation performances in buildings.

It is also worth mentioning that no universally applicable PIV system is available for different indoor applications. Table 24.1 lists the applicable range of three typical 2D-PIV systems that the authors have used in indoor airflow measurements. The researchers should pay more attention to the selection of appropriate PIV system parameters for their specific needs, such as the measuring area, the spatial and temporal resolution, and the required accuracy. In addition, PIV is not always the optimum choice when conducting detailed turbulence investigations. For instance, a high-frequency hot-wire anemometer is obvious better than PIV for analyzing the turbulent energy spectrum of inlet airflow.

Table 24.1 Typical 2D-PIV systems used in indoor airflow field measurements

PIV system	Main parameters	Advantage	Disadvantage	Applicability
TR-PIV	10 MJ lasers; 1 M CMOS camera	Very high time resolution(2 kHz); High spatial resolution	Restricted FOV (0.15 × 0.13 m); Bulky	Small-scale model
Mini-PIV	5 MJ lasers; 0.3 M CMOS camera	High time resolution(200 Hz); Portable	Restricted FOV (0.08 × 0.06 m); Low spatial resolution	Critical area in large space (e.g., air inlet)
High power PIV	350 MJ lasers; 11 M CCD camera	High spatial resolution; large FOV (0.9 × 0.6 m)	Low time resolution(3.5 Hz); Bulky	Full-scale model

24.3 Conclusions

PIV has gradually become the most popular and versatile tools for measuring various indoor airflow fields. The quantitative and detailed flow visualization information obtained by PIV is critical for analyzing turbulent properties and validating numerical simulations. Volumetric PIV is suggested for the further investigations of ventilation devices. The PIV experiments involving human volunteers should be paid great attention to the safety problems. For indoor PIV measurements, small-scale models are the most convenient and appropriate, but may suffer from scaling problems. In contrast, it is much more difficult to perform PIV measurements in full-scale models. Even so, large-scale PIV measurements are still necessary, for the data obtained from full-scale models are the most realistic and reliable. The selection of an appropriate PIV system is dependent on researchers' specific needs.

Acknowledgments The research presented in this paper was financially supported by the National Basic Research Program of China (The 973 Program) through grant No. 2012CB720100.

References

1. Sun Y, Zhang Y (2007) An overview of room air motion measurement: technology and application. HVAC&R Res 13(6):929–950
2. Adrian RJ (2005) Twenty years of particle image velocimetry. Exp Fluids 39(2):159–169
3. Raffel M, Willert CE, Wereley ST et al (2007) Particle image velocimetry: a practical guide. Springer
4. Cao G, Sivukari M, Kurnitski J et al (2010) PIV measurement of the attached plane jet velocity field at a high turbulence intensity level in a room. Int J Heat Fluid Fl 31(5):897–908
5. Melsem A, Nastace I, Allard F (2010) Passive mixing control for innovative air diffusion terminal devices for buildings. Build Environ 45(12):2679–2688
6. Meslem A, Dia A, Beghein C et al (2011) A comparison of three turbulence models for the prediction of parallel lobed jets in perforated panel optimization. Build Environ 46(11):2203–2219
7. Elvsén P, Sandberg M (2009) Buoyant jet in a ventilated room: velocity field, temperature, field and airflow patterns analyzed with three different whole-field methods. Build Environ 44(1):137–145
8. Montoya LD, Jackson JL, Amitay M (2010) Control of aerosol dispersion and removal in a room using synthetic jet actuators. Build Environ 45(1):165–175
9. Nastase I, Meslem A, Vlad I, Colda I (2011) Lobed grilles for high mixing ventilation—an experimental analysis in a full scale model room. Build Environ 46(3):547–555
10. Sanjuan C, Sánchez MN, Heras MR et al (2011) Experimental analysis of natural convection in open joint ventilated facades with 2D PIV. Build Environ 46(11):2314–2325
11. Chami N, Zoughaib A (2010) Modeling natural convection in a pitched thermosyphon system in building roofs and experimental validation using particle image velocimetry. Energy Buildings 42(8):1267–1274
12. Özcan O, Meyer KE, Melikov AK (2005) A visual description of the convective flow field around the head of a human. J Visual 8(1):23–31

13. Marr DR, Spitzer IM, Glauser MN (2008) Anisotropy in the breathing zone of a thermal manikin. Exp Fluids 44(4):661–673
14. Craven BA, Settles GS (2006) A computational and experimental investigation of the human thermal plume. J Fluid Eng 128(6):1251–1258
15. Zhu SW, Kato S, Yang JH (2006) Study on transport characteristics of saliva droplets produced by coughing in a calm indoor environment. Build Environ 41(12):1691–1702
16. Chao CYH et al (2009) Characterization of expiration air jets and droplet size distributions immediately at the mouth opening. J Aerosol Sci 40(2):122–133
17. Kwon SB et al (2012) Study on the initial velocity distribution of exhaled air from coughing and speaking. Chemosphere 87(11):1260–1264
18. VanSciver M, Miller S, Jean Hertzberg (2011) Particle image velocimetry of human cough. Aerosol Sci Tech 45(3):415–422
19. Li A, Qin E, Xin B, Wang G, Wang J (2010) Experimental analysis on the air distribution of powerhouse of Hohhot hydropower station with 2D-PIV. Energ Convers Manage 51(1):33–41
20. Kang JH, Lee SJ (2008) Improvement of natural ventilation in a large factory building using a louver ventilator. Build Environ 43(12):2132–2141
21. van Hooff T, Blocken B, Defraeye T et al (2012) PIV measurements and analysis of transitional flow in a reduced-scale model: ventilation by a free plane jet with Coanda effect. Build Environ 56:301–313
22. Karave P, Stathopoulos T, Athienitis AK (2011) Airflow assessment in cross-ventilated buildings with operable facade elements. Build Environ 46(1):266–297
23. Rouaud O, Havet M, Solliec C (2004) Influence of external perturbations on a minienvironment: experimental investigations. Build Environ 39(7):863–872
24. Poussou SB, Mazumdar S, Plesniak MW et al (2010) Flow and contaminant transport in an airliner cabin induced by a moving body: model experiments and CFD predictions. Atmos Environ 44(24):2830–2839
25. Zhao L, Zhang Y, Wang X et al (2001) Measurement of two-dimensional air velocities in a full-scale room using particle image velocimetry. ASHRAE T 107(2):434–444
26. Sun Y, Zhang Y (2003) Development of a stereoscopic particle image velocimetry system for full-scale room airflow studies, part II: experimental setup. ASHRAE T 2:540–548
27. Caciolo M, Pascal Stabat, Marchio D (2011) Full scale experimental study of single-sided ventilation: analysis of stack and wind effects. Energy Buildings 43(7):1765–1773
28. Mortensen LH, Rode C, Peuhkuri R (2008) Investigation of airflow patterns in a microclimate by particle image velocimetry (PIV). Build Environ 43(11):1929–1938

Chapter 25
Optimized Analysis of Lightweight Wall Outfitted with PCM in Hot Summer Zone

Yuan Zhang, Kai Du and Jiapeng He

Abstract A new type of lightweight wall outfitted with expanded polystyrene (EPS) layer and phase change material (PCM) layer was built for improving the thermal performance of building enclosure. The main purpose of this paper is to analyze the thermal performance of different walls in order to find the optimum wall structure. The enthalpy model has been established to solve the transient nonlinear heat transfer process using MATLAB program. The results show that 31 °C is the optimum phase change temperature in the hot summer zone of China. Meanwhile, the use of traditional thermal insulation material, such as EPS, is necessary for satisfying the demand of the heat transfer resistance. The integration of EPS layer and PCM layer with proper thicknesses can produce the optimum thermal performance. Finally, the optimum wall structure has been obtained in which the thicknesses of the PCM layer and EPS layer are 0.01 and 0.02 m, respectively.

Keywords Building enclosure · Energy conservation · Phase change material · Thermal performance · Phase change temperature · Enthalpy model

25.1 Introduction

Traditional insulation materials are widely used in building enclosures for energy saving. However, due to the low thermal capacity, this type of wall produces large fluctuations of indoor temperature and heat flux, which reduces thermal comfort

Y. Zhang · K. Du (✉)
School of Energy and Environment, Southeast University, 2# Sipailou, Nanjing 210096, China
e-mail: du-kai@seu.edu.cn

J. He
College of Urban Construction and Safety Engineering, Nanjing University of Technology, Nanjing, China

A. Li et al. (eds.), *Proceedings of the 8th International Symposium on Heating, Ventilation and Air Conditioning*, Lecture Notes in Electrical Engineering 263,
DOI: 10.1007/978-3-642-39578-9_25,

degree and increases the energy consumption of air-conditioning device [1–3]. To solve this problem, phase change material (PCM) with high latent heat has been used to improve the thermal capacity in recent years [4–6].

Castell [7] carried out an experiment to test PCM under the condition of cold winters and warm summers. The results showed that the n-octadecane and the salt hydrates compounds produced indoor air peak temperature reductions of about 0.9 and 0.73 °C, respectively, and an energy reduction of approximately 15 and 17 %, respectively. Cabeza [8] evaluated the thermal performance of a conventional concrete wall outfitted with microencapsulated PCM. The field tests were carried out under a hot summer Mediterranean (CSa) climate according to the Koppen–Geiger climate classification [9]. The results showed that the surface temperature of the PCM-outfitted wall was reduced between 0 and 2 °C at peak times when compared to the wall without PCM. The PCM-outfitted wall produced a peak thermal shift about two hours to the surface temperature.

In this paper, a new type of wall outfitted with traditional thermal insulation material expanded polystyrene (EPS) layer and PCM layer has been setup for improving the thermal performance of building external wall. The enthalpy model has been built to solve the transient nonlinear heat transfer process. The calculations of three walls, which are the wall outfitted with EPS layer (EPS wall), the wall outfitted with PCM layer (PCM wall), and the wall outfitted with EPS layer and PCM layer (compound wall), have been performed using MATLAB program. The comparative analysis and the optimum phase change temperature and wall structure have been presented.

25.2 Methods

25.2.1 Governing Equation and Boundary Conditions

To simplify the calculation reasonably, the assumptions are applied: (1) All the materials are considered to be thermally homogeneous and isotropic media. (2) The volume change of PCM during phase change process is ignored. (3) The super-cooling effect and the natural convection effect of PCM are ignored. (4) The heat transfer is one dimensional.

The heat transfer problems of PCM building enclosure can be solved by enthalpy model [10]. The governing equation is as follows:

$$\rho \frac{\partial H}{\partial \tau} = \lambda \frac{\partial^2 T}{\partial x^2} \tag{1.1}$$

where ρ, λ, H are the density, thermal conductivity, and enthalpy of PCM, respectively. The thickness is represented by x, and the temperature at any point in time τ is T. The enthalpy of PCM can be calculated by Eq. (1.2)

$$H = \begin{cases} c_{p,s} \cdot T & T < T_m - \varepsilon \\ c_{p,s} \cdot (T_m - \varepsilon) + \frac{L}{2\varepsilon} \cdot [T - (T_m - \varepsilon)] & T_m - \varepsilon \le T \le T_m + \varepsilon \\ c_{p,s} \cdot (T_m - \varepsilon) + L + c_{p,l} \cdot [T - (T_m + \varepsilon)] & T > T_m + \varepsilon \end{cases} \quad (1.2)$$

where $c_{p,s}$ and $c_{p,l}$ are the specific heat of the PCM in its solid and liquid states, respectively, T_m is the mean temperature of the phase transition temperature range. The phase change radius ε represents the half length of the phase change temperature range, and L is latent heat. The temperature range of phase transition is from $T_m - \varepsilon$ to $T_m + \varepsilon$.

The initial condition is as follows:

$$T(x, \tau)|_{\tau=0} = T_{\text{init}} \quad (1.3)$$

where $T(x, \tau)$ is the temperature at point x at time, τ. T_{init} is the initial temperature (=26.0 °C).

The heat transfer on the two boundary surfaces along the thickness direction, x, is calculated using the third-type thermal boundary condition in Eqs. (1.4) and (1.5).

$$\lambda \frac{T_2 - T_1}{\Delta x} + h_{w,\text{out}}(T_z - T_1) = \rho c \frac{\Delta x}{2} \left(\frac{\partial T}{\partial \tau} \right)_{x=1} \quad (1.4)$$

$$\lambda \frac{T_{N-1} - T_N}{\Delta x} + h_{w,\text{in}}(T_{\text{in}} - T_N) = \rho c \frac{\Delta x}{2} \left(\frac{\partial T}{\partial \tau} \right)_{x=N} \quad (1.5)$$

where ρ, λ, c are the density, thermal conductivity, and specific heat of wall, respectively, $h_{w,\text{in}}$ and $h_{w,\text{out}}$ are the heat convection coefficient on the interior and exterior surfaces of wall, respectively, $h_{w,\text{in}} = 8.7$ W/(m^2 K), $h_{w,\text{out}} = 19.0$ W/(m^2 K), T_z is the outdoor sol–air temperature (Fig. 25.1) during a typical day in the hot summer zone of China, T_{in} is the indoor temperature, T_1 and T_N are the temperatures on the exterior and interior surfaces of wall, respectively.

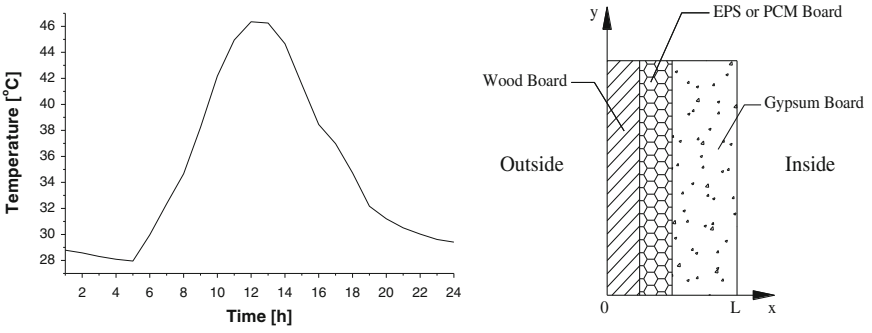

Fig. 25.1 Outdoor sol–air temperature condition and wall structure

The governing equations and the boundary conditions are discretized using finite differences method. Central differences are applied in space, and a fully implicit finite difference scheme and forward differences are applied in time. The size of the space grid is 0.001 m, and the time step is 3,600 s. The equation system is solved using a tri-diagonal matrix algorithm (TDMA) method. The entire calculation process is performed using MATLAB program.

25.2.2 Validation of Model

The herein proposed experimental approach used for the validation of the model is called temperature-change hot chamber method. A PCM specimen (Fig. 25.2) has been prefabricated. The PCM was inserted between every two red copper plates (six red copper plates in all). EPS boards were placed on four of the six sides of the PCM specimen to force the heat transfer to be one dimensional. Thermocouples were installed at the centers of each copper plate. The distance between every two neighboring plates was 12 mm. In the experiment, the temperatures were controlled in the hot and cold chambers. After a complete cycle (a melting and freezing process had completed), the experiment finished. The calculation results (Ent) show a good agreement with the experimental data (Exp) at each point along the thickness of the PCM specimen, which validated the accuracy of the model.

25.2.3 Physical Model

There are four layers of the compound wall. The EPS layer and the PCM layer both take the half thickness of the central layer in Fig. 25.1, and the PCM layer is outside the EPS layer. The physical parameters of each material are shown in

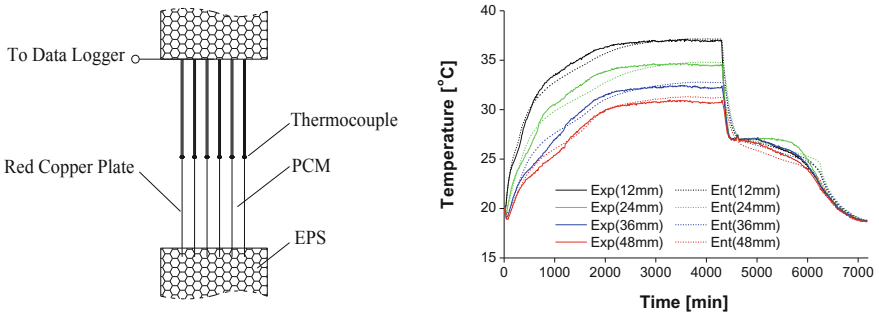

Fig. 25.2 PCM specimen and experimental and calculation data

Table 25.1 Physical parameters of materials

Name	Wood	EPS	Gypsum	PCM
Thickness (m)	0.03	0 ~ 0.03	0.06	0 ~ 0.03
Density (kg m^{-3})	700	30	1,050	1,000
Specific heat (J kg^{-1} K^{-1})	2,510	1,380	2,010	2,000
Thermal conductivity (W m^{-1} K^{-1})	0.17	0.042	0.33	0.2
Latent heat of PCM (kJ kg^{-1})	150			
Phase change temperature of PCM (°C)	28, 30, 31, 32, 33, 34			
Phase change radius of PCM (K)	1.0			

Table 25.1. To find the optimum phase change temperature of PCM, 28, 30, 31, 32, 33, and 34 °C are selected and calculated.

25.3 Results and Discussions

25.3.1 Optimum Phase Change Temperature

The varied temperatures and heat fluxes on the interior surfaces of walls with different phase change temperatures are shown in Fig. 25.3. For the EPS wall, the temperature and heat flux amplitudes are large (0.76 K and 6.64 W m^{-2}, respectively); the time lag relative to the temperature of the outdoor air is 6 h, which is the smallest of all. Different phase change temperatures (28, 30, 32, and 34 °C, respectively) produce different situations (Fig. 25.3a, b, d, and f). In Fig. 25.3a, the phase change temperature is low, which makes the PCM be always in liquid state. The thermal conductivity of the PCM (0.2 W m^{-1} K^{-1}) is higher than that of the EPS (0.042 W m^{-1} K^{-1}), and the specific heat of the EPS (1,380 J kg^{-1} K^{-1}) is nearly to that of the liquid PCM (2,000 J kg^{-1} K^{-1}), which makes the thermal performance of the EPS wall be superior to the PCM wall; therefore, the amplitudes of the PCM wall and the compound wall are large. The melting and freezing processes take place periodically in Fig. 25.3b, which stabilizes the fluctuations of the PCM wall and the compound wall; 32 °C is a proper phase change temperature for the compound wall in Fig. 25.3d, as the amplitudes are smooth and stable. However, the phase change temperature of 34 °C is too high, and most of the PCM is always in solid state, which make the amplitudes become large again (Fig. 25.3f). Therefore, the optimum phase change temperature is around 32 °C. Through the comparison of 31, 32, and 33 °C in the Fig. 25.3c, d, and e, 31 °C is the optimum phase change temperature as a result of the smooth amplitudes and the relatively low temperatures and heat fluxes.

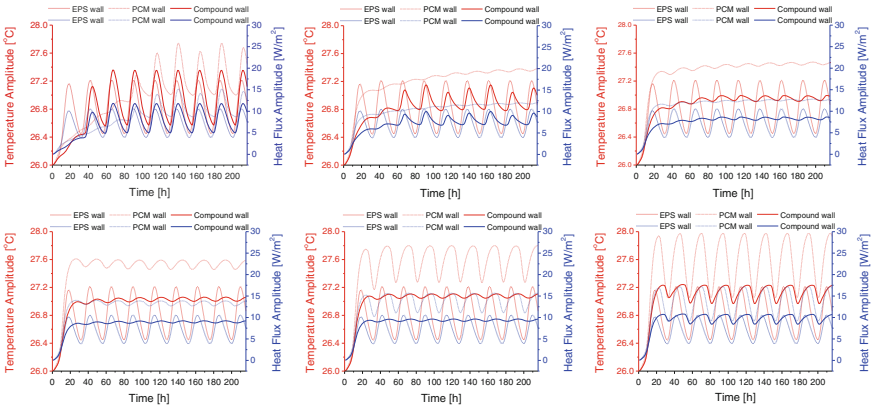

Fig. 25.3 Temperature and heat flux on the interior surfaces of the walls

25.3.2 Thermal Performance of Walls

The heat transfer resistance of wall can be calculated by Eq. (1.6).

$$R = R_{\text{out}} + R_{\text{wood}} + R' + R_{\text{gypsum}} + R_{\text{in}} \tag{1.6}$$

where R is the heat transfer resistance of wall, R_{in} and R_{out} are the thermal resistance of the convection at the interior and exterior surfaces, respectively, the sum of them is 0.15 W m^{-2} K^{-1}, R_{wood} and R_{gypsum} are the thermal resistance of the wood and gypsum layers, R' is the thermal resistance of EPS layer (EPS wall), PCM layer (PCM wall) or the sum of the two layers (compound wall).

With the optimum phase change temperature of 31 °C, the thermal performance of walls with varied thickness of EPS layer and PCM layer is shown in Table 25.2 and Fig. 25.4. As a result of the low heat transfer resistance, the temperature and heat flux on the interior surface of the PCM wall are pretty high (nearly 27.50 °C and 13 W m^{-2} in Fig. 25.3). Therefore, the use of EPS layer is necessary. According to the demand of the heat transfer resistance, only the wall 1, wall 2 and wall 3 (1.22, 1.13 and 1.03 W m^{-2} K^{-1}, respectively) are satisfactory. The temperature and heat flux amplitudes are decreased rapidly (from 0.76 to 0.04 °C, from 6.64 to 0.33 W m^{-2}, respectively) in Fig. 25.4 when the EPS layer is gradually replaced by the PCM layer, especially from wall 1 to wall 3. The main reason for this is that the latent heat of the PCM was much higher than the specific heat of the EPS when the phase transition takes place; namely, more amount of heat is needed to increase the temperature of the PCM for 1 °C. The thicker the PCM layer is, the smaller the temperature and heat flux amplitudes are, the longer the time lag is, and the lower the heat transfer resistance is. However, the speed of the amplitudes decreases gradually as the thickness of PCM layer increasing. Because of the high latent heat, the time lags of the PCM wall and the compound

Table 25.2 Thermal performances of walls with the phase change temperature of 31 °C

Order of wall	Structure of wall	Temperature amplitude (°C)	Heat flux amplitude (W m^{-2})	Time lag (h)	Heat transfer resistance (W m^{-2} K^{-1})
1 (EPS wall)	EPS (30 mm)	0.76	6.64	6	1.22
2	PCM (5 mm) + EPS (25 mm)	0.40	3.47	7	1.13
3	PCM (10 mm) + EPS (20 mm)	0.17	1.50	8	1.03
4	PCM (15 mm) + EPS (15 mm)	0.09	0.76	9	0.94
5	PCM (20 mm) + EPS (10 mm)	0.05	0.42	14	0.85
6	PCM (25 mm) + EPS (5 mm)	0.03	0.28	17	0.75
7 (PCM wall)	PCM (30 mm)	0.04	0.33	17	0.66
Demand of heat transfer resistance					1.00 [11]

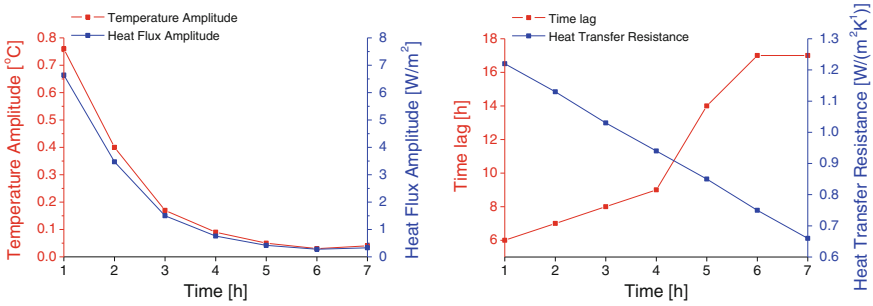

Fig. 25.4 Varied parameters of walls with the phase change temperature of 31 °C

wall are longer than that of the EPS wall. That implies that the peak temperature at day will affect the indoor environment at night when the temperature and the price of electricity are low; consequently, the indoor thermal comfort increases and the energy consumption decreases. Considering the thermal performance and economy, the wall 3 (the thicknesses of PCM layer and EPS layer are 0.01 and 0.02 m, respectively) is the optimum wall structure.

25.4 Conclusions

In this paper, the enthalpy model has been established to solve the transient nonlinear heat transfer process of the walls outfitted with PCM under the typical hot summer condition of China using MATLAB program. The typical lightweight external wall is provided as the physical model. The results show that, for the lightweight external wall in the hot summer zone of China, 31 °C is the optimum

phase change temperature. If the phase change temperature is higher or lower than this point, the PCM will not be fully used. Meanwhile, the use of traditional thermal insulation material, such as EPS, is necessary for satisfying the demand of the heat transfer resistance. Proper thicknesses of EPS layer and PCM layer can decrease the average levels and smooth the fluctuations of temperature and heat flux on the interior surface of wall; the integration of the two materials can produce the optimum thermal performance. By using the wall 3 (the thicknesses of PCM layer and EPS layer are 0.01 and 0.02 m, respectively), it produces relatively low values of temperature and heat flux, smooth amplitudes, long time lags; meanwhile, the heat transfer resistance are satisfactory. With these factors, the energy saving, the thermal load shifting, and the indoor thermal comfort increasing are produced. Therefore, the wall 3 is performed as the optimum option.

Acknowledgments This work was financially supported by The 12th Five Year National Science and Technology Support Key Project of China (No. 2011BAJ03B05) and (No. 2011BAE14B06).

References

1. Cabeza LF, Castell A, Barreneche C et al (2011) Materials used as PCM in thermal energy storage in buildings: a review. Renew Sust Energ Rev 15:1675–1695
2. Baetens R, Jelle BP, Gustavsen A (2010) Phase change materials for building applications: a state-of-the-art review. Energ Build 42:1361–1368
3. Farid MM, Khudhair AM, Razack SAK et al (2004) A review on phase change energy storage: materials and applications. Energ Convers Manage 45:1597–1615
4. Kuznik F, David D, Johannes K et al (2011) A review on phase change materials integrated in building walls. Renew Sust Energ Rev 15:379–391
5. Regin AF, Solanki SC, Saini JS (2008) Heat transfer characteristics of thermal energy storage system using PCM capsules: a review. Renew Sust Energ Rev 12:2438–2458
6. Sharma A, Tyagi VV, Chen CR et al (2009) Review on thermal energy storage with phase change materials and applications. Renew Sust Energ Rev 13:318–345
7. Castell A, Martorell I, Medrano M et al (2010) Experimental study of using PCM in brick constructive solutions for passive cooling. Energ Build 42:534–540
8. Cabeza LF, Castellon C, Nogues M et al (2007) Use of microencapsulated PCM in concrete walls for energy savings. Energ Build 39:113–119
9. Kottek M, Grieser J, Beck C et al (2006) World map of the Koppen-Geiger climate classification updated. Meteorol Z 15:259–263
10. Lin K, Zhang Y, Di H et al (2007) Study of an electrical heating system with ductless air supply and shape-stabilized PCM for thermal storage. Energ Convers Manage 48:2016–2024
11. Ministry of Housing and Urban-Rural Development of the People's Republic of China (2010) Design standard for energy efficiency of residential buildings in hot summer and cold winter zone. China Architecture & Building Press, Beijing (JGJ134-2010)

Chapter 26
Modeling and Simulation of Ventilated Double-Skin Facade Using EnergyPlus

Sha Le, Youming Chen, Yuan Bi and Xiang Lu

Abstract Double-skin facade systems (DSF), as one of the newest kind of envelops of buildings, is attracting more and more architects and investors' attention in China. The skins can be air tight or ventilated. As for the ventilated DSF, airflow passing through the cavity can be naturally driven, mechanically driven, or a combination of both. According to some previous studies, buildings constructed with DSF may have better energy performance than the conventional single-skin facade. The problem is that, presently, there are still no official specifications which can help the engineers to thoroughly understand the complex thermal and airflow behavior of DSF. This paper presents a detailed simulation process for an office building equipped with naturally ventilated DSF under the climatic condition in Changsha. A theoretical model is developed via the EnergyPlus simulation program to evaluate the thermal performance of double-skin facade with different configurations. The results obtained in this paper can be valuable for engineers to do some optimization work during the design process under the hot summer and cold winter climates. It indicates that a reasonably constructed DSF can provide an annual saving of around 30 % in building cooling energy, and up to 10 % as for the heating energy, compared to a conventional single-skin facade.

Keywords Double-skin facade systems · EnergyPlus · Airflow network model · Simulation

S. Le · Y. Chen (✉) · Y. Bi · X. Lu
College of Civil Engineering, Hunan University, Changsha 410082, China
e-mail: ymchen@hnu.edu.cn

S. Le
Guangxi Hualan Design and Consulting Group, Nanning 530011, China

A. Li et al. (eds.), *Proceedings of the 8th International Symposium on Heating, Ventilation and Air Conditioning*, Lecture Notes in Electrical Engineering 263,
DOI: 10.1007/978-3-642-39578-9_26,

26.1 Introduction

While energy consumption of buildings is becoming an escalating concern around the world, double-skin facade systems (DSF) have become a potential option to control the energy consumption of buildings, especially for the fully air-conditioned buildings. Presently, the conventional single-skin facade is widely used in all kinds of commercial buildings, while the DSF is usually utilized in order to obtain better acoustic and thermal insulation. According to some previous researches, buildings which are enveloped by reasonably configured DSF will improve the indoor air quality as well as reducing the energy consumption in air-conditioned system [1].

Outdoor air curtain, which have openings at bottom and upper lever installed at the outer pane, is the most popular type of DSF. In the hot summer, natural ventilation takes place through outdoor air entering at low level, absorbing heat energy inside the air cavity and then exhausting at high lever opening. In cold winter, the openings are closed, and then, the cavity is like a temperature buffer layer, which can reduce the heating load [2].

At present, there are about two methods to study the DSF. One is the method of experiment, that is, a test room equipped with DSF is constructed, and then, the parameters and variables are measured by some experimental instruments; finally, researchers can make a qualitative analysis on the airflow patterns and thermal behavior of the DSF. Manz et al. [3, 4] made an experimental investigation of two mechanically ventilated DSF built in an outdoor test facility, and he reported that a spectral optical model combined with a CFD model that includes convection, conduction, and radiation is recommended for analyzing and optimizing DSF. Heiselberg et al. [5] indicated that the air velocity of the cavity is difficult to measure, because of the complex three-dimensional geometry of the naturally ventilated DSF, but the experimental data can be used to validate the mathematical model and simulation results. Gavan et al. [6] set up a test facility under controlled climatic conditions, which provided valuable experimental data for the validation of numerical models dealing with ventilated double-skin facade with sun-shading device.

The other method for studying DSF is to model and simulate the DSF by some computer programs. Haase et al. [7] assessed the energy performance of the DSF buildings using thermal building simulations (TRNSYS), and he proved that a careful facade design can play an important role in highly glazed buildings and provide potential for energy efficiency. Chan et al. [2] indicated that a double-skin facade with optimization configurations can provide an annual saving of around 26 % in building cooling energy as compared to a conventional single-skin facade via the EnergyPlus simulation program in Hong Kong. Jiru [8] used computational fluid dynamics (CFD) with RNG turbulence model to analyze airflow and heat transfer in DSF.

Enormous researches are performed on the DSF in Europe and some other regions, but widespread application of the DSF in buildings still has a long way to

go. There are quite a lot reasons which may account for the situation, and there are still no official guidelines aiming to help the design community to make a decision that under what kind of climates the DSF can be adopted and how to establish DSF with reasonable configurations. Literatures show that lots of studies have been done in the cold and warm regions. Studies in cold winter and hot summer regions are rare. This paper reports a detailed computer simulation of an air-conditioned office building equipped with naturally ventilated DSF under the climatic condition in Changsha. Based on building energy simulations, the energy performances of different cases were studied. Finally, the energy saving efficiency of the DSF was investigated, and the results were reported herewith.

26.2 Simulation Model

Since the DSF is a sophisticated system that many factors are highly coupled with each other, it is really no easy task to figure out how it runs. EnergyPlus 7.0, developed by the US-DOE, which is a whole building energy simulation tool, is applied in this study. The methodology adopted in this paper is essentially an iterative process comprising the following steps.

1. Make a thorough analysis of the issue and then re-express the target building constructed with DSF in a validated and appropriate simulation model in terms of extent, complexity, and time and space resolution levels.
2. Add the weather data into the simulation model, and then, the inside and ambient boundary conditions of the model are established.
3. Perform simulations during a suitable length of time, and calibrate the model based on the results, if the results are reasonable then go to step 4 directly, if not, then go back to step 1 and step 2, do this operation repeatedly until the results meet the requirement.
4. Analyze and report the results, if some further researches are needed, modify the model and then repeat the simulation again.

26.2.1 Solar Radiation

Solar transmission, reflection, and absorption are important features that distinguish the glazing facade from other envelops of building. According to DOE, there are five solar distribution options: minimal shadowing, full exterior, full interior and exterior, full exterior with reflections, full interior and exterior with reflections. In the case of full interior and exterior, the program calculates the amount of beam radiation falling on each surface in the zone by projecting the sun's rays through the exterior window and taking into account the effect of window shading devices. It also calculates how much beam radiation falling on the inside of an

exterior window (from other window in the zone) is absorbed by the window, how much is reflected back into the zone, and how much is transmitted to the outside. So, in the study, full interior and exterior option is chosen since it is well suited for the DSF that has multiple reflections between glazing and blind slats in the cavity zone.

26.2.2 Thermal Model

In order to obtain a more precise simulation, reasonable convective heat transfer coefficients should be adopted (Fig. 26.1).

26.2.2.1 Exterior Convective Heat Transfer Coefficient (h_{out})

The Mobile Window Thermal Test (MoWiTT) model is based on measurements taken at the MoWiTT facility. The correlation applies to very smooth vertical surfaces (e.g., window glass) in low-rise buildings. Since there is no accepted superior algorithm for the DSF, the MoWiTT is chosen and has the form:

$$h_{\text{out}} = \sqrt{\left[C_t(\Delta T)^{1/3}\right]^2 + \left[aV_z^b\right]^2} \tag{1.1}$$

where ΔT is the temperature difference between the surface and the air constants a and b, and turbulent natural convection constant C_t is given by Yazdanian and Klems's experimental work [9]

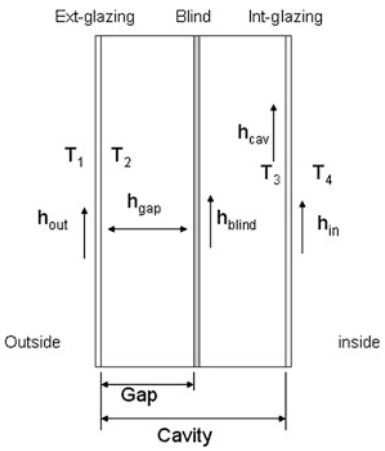

Fig. 26.1 Section view of the DSF with convective heat transfer coefficients and temperatures

26.2.2.2 Interior Convective Heat Transfer Coefficient (h_{blind}, h_{cav}, h_{in})

There are several methods in EnergyPlus for the calculation of the interior convective heat transfer coefficients (h_{blind}, h_{cav}, h_{in} in Fig. 26.1). However, none of those methods considers the cavity airflow pattern for the calculation of the convective heat transfer. This is the limitation of the tool and will affect the simulation result to some extent. In this study, the ASHRAE Vertical Wall algorithm is chosen which has the form:

$$h_{\text{blind}} \quad \text{or} \quad h_{\text{cav}} \quad \text{or} \quad h_{\text{in}} = 1.31\Delta T^{1/3} \tag{1.2}$$

26.2.2.3 "Gap" Convective Heat Transfer Coefficient (h_{gap})

In EnergyPlus, the gap means the space between the bind and the exterior glazing. The cavity means a space between the exterior glazing and the interior glazing. The gap velocity, a function of the pressure drop factor, is used to calculate h_{gap}. The"gap" convective heat transfer coefficient (h_{gap}) has the form:

$$h_{\text{gap}} = 2h_c + 4v \tag{1.3}$$

where h_c is the surface-to-surface heat transfer coefficient for closed cavity (W/m^2K), 4 is an empirical coefficient (J/m^3K), and v is the mean air velocity in the gap (m/s).

26.2.3 Airflow Model

In order to simulate the energy performance of the DSF, the airflow in the cavity between the external and internal facades requires to be modeled. To figure out the sophisticated relationship between the airflow and the transient heat transfer phenomena, an airflow network model is adopted by EnergyPlus, which consists of several nodes connected by airflow components through linkages. The entire process of airflow simulation can be described as shown in Fig. 26.2. Firstly, the air cavity and the room are divided into several stacked zones, and each zone refers to an airflow network node. Then, those nodes are linked by airflow components implemented in EnergyPlus, which can mimic the airflow through the cavity and the room. That is, a relationship between pressure and airflow among the nodes and linkages is built. Finally, the multi-zone airflow calculations, which can fully model the process of long-wave radiant exchange, surface convection, solar transmission, reflection, and absorption, are performed at each HVAC system time step.

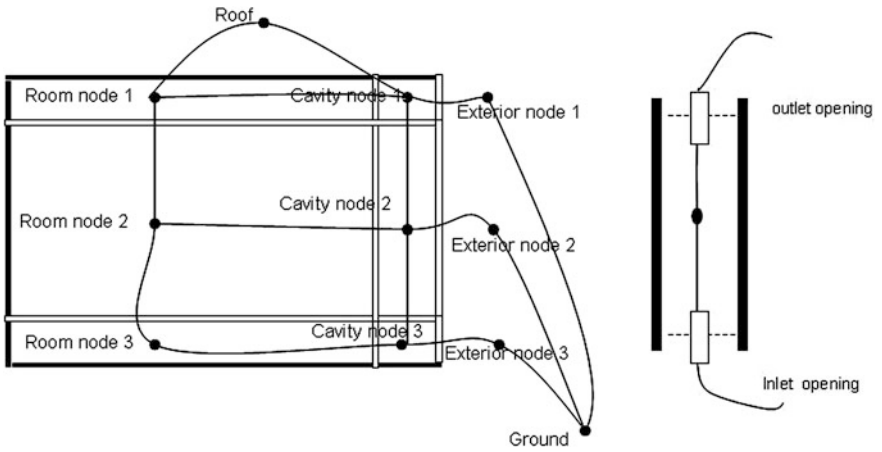

Fig. 26.2 Section view of modeled cavity and room divided into three stacked zones. Each zone represents an airflow network node. The *left graph* shows the connection of the airflow nodes. The *right graph* shows airflow path in the cavity

26.3 Case Studies

In order to evaluate the energy performance of a DSF, a single-story office building equipped with DSF was modeled via EnergyPlus. Figure 26.3 shows the perspective view of the room. The dimensions of the room are width 2.4 m, depth 6 m, height 4 m. The DSF is face to the true east. Both the external and internal facades are a single 6 mm clear glass. The dimensions of the DSF are width 2.4, depth 0.5 m, height 4 m. The openings installed on the external facade at bottom and upper lever. The height of the opening is 0.3 m. The EnergyPlus weather data (.epw file) is downloaded from the EnergyPlus office website. Location is Changsha, Hunan, China. The other constructions of the room are in line with national energy efficiency standards. No internal heat source is included. Simulation time is through the whole year, from day to night.

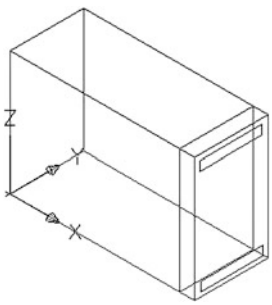

Fig. 26.3 Perspective view of the room of DSF

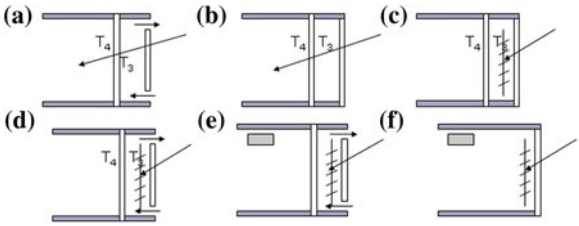

Fig. 26.4 Cross-sectional view of simulation cases

Table 26.1 Description of the cases (e.g., case D means a room equipped with a natural ventilated DSF, and there is a blind positioned in the air cavity (as shown in Fig. 26.4)

Case	Blind	Ventilation	Air-conditioner	DSF	Single-skin facade
A		√		√	
B				√	
C	√			√	
D	√	√		√	
E	√		√		√
F	√	√	√	√	

The internal facade temperature is a typical facade performance parameter, because it has a large effect on the thermal comfort of the perimeter zone. In order to figure out the influence of sun-shading device, ventilation on the DSF, the flowing cases, except case E and case F, which are explained later, have been studied (as shown in Table 26.1) and the inside and outside temperatures of the internal facade are output as comparisons.

The days from July 20 to 22 are chosen to perform the simulation, which represents the most hot summer days. Figure 26.5 shows the solar radiation on the exterior glazing which is acquired from the simulation result.

26.3.1 Influence of Ventilation

A comparison of case A with case B and a comparison of case D with case C would show the influences that the natural ventilation impact on the DSF.

It is clear that both the internal facade and indoor temperatures of case A is lower then the case B. But the difference is not so enormous, about 1 °C. During the time of strong solar radiation, the difference of the temperature of the internal facade is getting larger. The ventilation accounts for the phenomena directly (Fig. 26.6).

With the same sun-shading device, a comparison of case D with case C shows nearly the same result with the above (Fig. 26.7). The indoor temperature of case C is a little bit higher than that of the case D. Blind heat accumulation cannot be ventilated away.

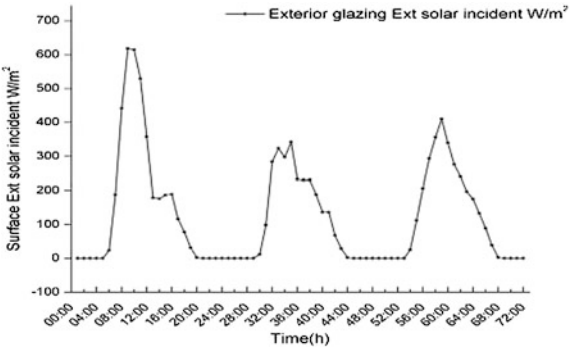

Fig. 26.5 Solar radiation on exterior glazing

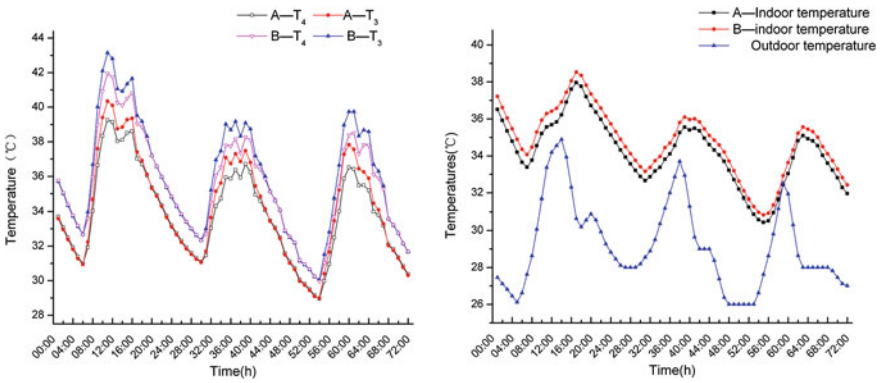

Fig. 26.6 The comparison of case A with case B. The *left graph* shows the comparison of the temperatures of the internal facade. T_3 represents the inside temperature of the internal facade, while T_4 represents the outside (as shown in Fig. 26.4). The *right graph* shows the comparison of the indoor temperature of the rooms. The *upper lines* represent the indoor temperature of case B, while the *middle lines* represent the case A and the *lower lines* represent the outdoor temperature

26.3.2 Influence of Sun-Shading Device

A comparison of case B with case C and a comparison of case D with case A would show the influences that the sun-shading device lays on the DSF.

As the Fig. 26.8 shows, when the cavity of the DSF is closed, the temperature of the internal facade of case C is about 5 °C lower, the indoor temperature of case C is about 2.7 °C lower. Meanwhile, a comparison of case D with case A is given (Fig. 26.9). The openings at bottom and upper are opened respectively. And then, the cavity is naturally ventilated, which shows nearly the same temperature difference with the above.

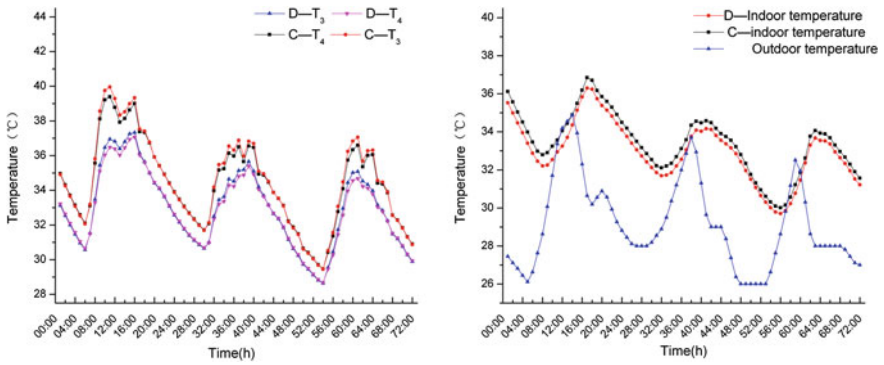

Fig. 26.7 The comparison of case D and case C. The *left graph* shows the comparison of the temperatures of internal facade. T_3 represents the inside temperature of the internal facade, while T_4 represents the outside (as shown in Fig. 26.4). The *right graph* shows the comparison of the indoor temperature of the rooms. The *upper lines* represent the indoor temperature of case C, while the middle lines represent case D and the *lower lines* represent the outdoor temperature

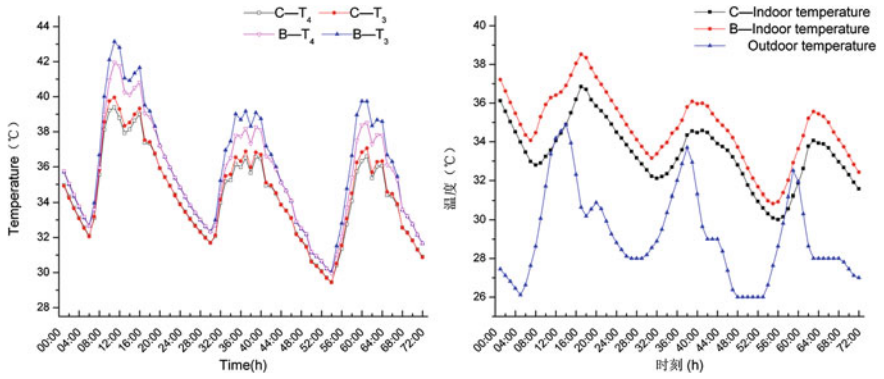

Fig. 26.8 The comparison of case B and case C. The *left graph* shows the comparison of the temperatures of internal facade. T_3 represents the inside temperature of the inner facade, while T_4 represents the outside (Fig 26.4). The *right graph* shows the comparison of the indoor temperature of the rooms. The *upper lines* represent the indoor temperature of case B, while the *middle lines* represent case C and the *lower lines* represent the outdoor temperature

26.3.3 Evaluation of Energy consumption

In order to assess the energy consumption of a room with a naturally ventilated DSF, case E, an air-conditioned room equipped with natural ventilated DSF and blind positioned in the cavity, case F, an air-conditioned single glazing facade with interior blind room, are modeled. The temperature of the room is maintained at 26 °C in cooling season and at 20 °C in heating season by using the Ideal Air Loads System object in EnergyPlus. The coefficient of performance (COP) of the

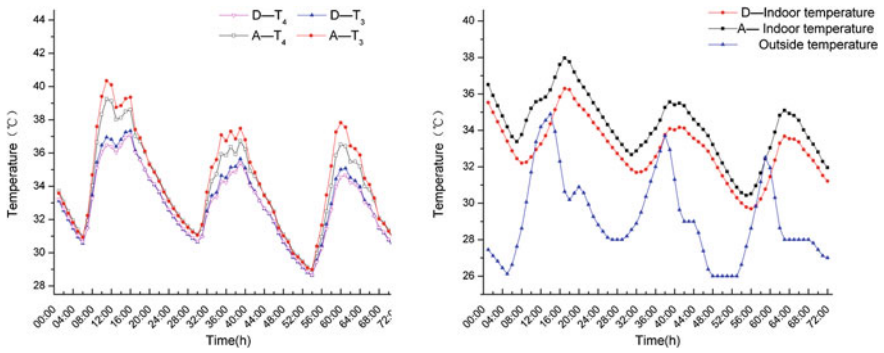

Fig. 26.9 The comparison of case D and case A. The *left graph* shows the comparison of the temperatures of internal facade. T_3 represents the inside temperature of the internal facade, while T_4 represents the outside (as shown in Fig 26.4). The *right graph* shows the comparison of the indoor temperature of the rooms. The *upper lines* represent the indoor temperature of case A, while the *middle lines* represent case D and the *lower lines* represent the outdoor temperature

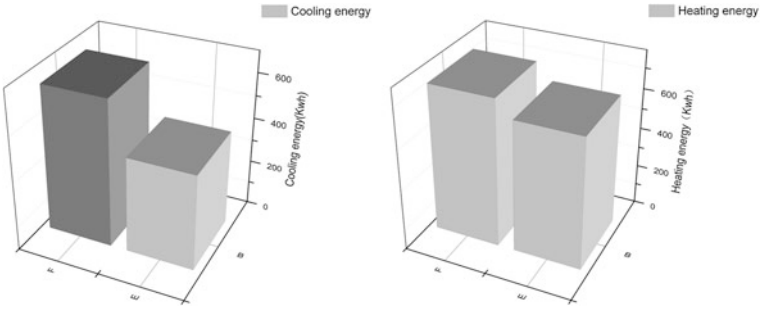

Fig. 26.10 The comparison of energy consumption. The *left graph* shows the comparison of cooling energy between the case E and case F. The *right graph* shows the comparison of heating energy between the case E and case F

air-conditioning system was assumed as 2.6 in summer cooling season, while 3.0 in winter heating season. A comparison of case E with case F shows that a saving of annual cooling energy up to 30 % and annual heating energy up to 10 % can be achieved as compared to a room with a single facade system, which makes an obvious sense that DSF has a big potential for energy saving in hot summer and cold winter climate regions (Fig. 26.10).

26.4 Conclusions

In this study, a room constructed with DSF was modeled under a typical hot summer and cold winter climate in Changsha via the EnergyPlus program. Some conclusions can be drawn as follows:

1. Both sun-shading device and ventilation have influences on the thermal behavior of the DSF. While the DSF with the same sun-shading device, the influence of ventilation is relatively small. While the DSF with the same ventilation, the influence of sun-shading device is relatively large. So, the impact of sun-shading devices takes the priority.
2. Double-skin facade system has great energy saving potential in the hot summer and cold winter weather climate regions.
3. A proper facade design plays an important role in the energy conservation performance of green building. It is worth an effort to conduct some optimization work during the design process.
4. This paper presents a simulation method via EnergyPlus for DSF, less computing time, high efficiency, which is suitable for designers to establish some optimal configurations of DSF. The simulation method and results reported in this paper can basically reflect some basic principles of the DSF. But some simplifications and assumptions of the reality are made during the simulation process, which may make the simulation result less accuracy. It should be noticed that the method presented in this paper is far from perfection. A more detail calibration study has to be done and lots of jobs still need to be continued in the near future.
5. Since the existing simulation tools are insufficient to model the transient heat and mass transfer phenomena that occur in the complex three-dimensional geometry of DSF in detail. The authors suggest that integration of CFD and building energy simulation, a zonal approach and flexibility of the convection correlation according to the condition of the cavity ventilation condition may be useful approaches for this matter.

References

1. Singh MC, Garg SN, Jha R (2008) Different glazing systems and their impact on human thermal comfort—Indian scenario. Build Environ 43:1596–1602
2. Chan ALS, Chow TT, Fong KF, Lin Z (2009) Investigation on energy performance of double skin facade in Hong Kong. Energy Build 41:1135–1142
3. Manz H, Schaelin A, Simmler H (2004) Airflow patterns and thermal behavior of mechanically ventilated glass double facades. Build Environ 39:1023–1033
4. Manz H (2004) Total solar energy transmittance of glass double facades with free convection. Energy Build 36:127–136
5. Heiselberg P, Kalyanova O, Jensen RL (2008) Measurement and modeling of air flow rate in a naturally ventilated double sin facade. In: Proceedings of the 1st international conference on building energy and environment, Dalian, pp 1895–1902

6. Gavan V, Woolsey M, Kuznik F, Roux JJ (2010) Experimental study of a mechanically ventilated double-skin facade with Venetian sun-shading device: a full-scale investigation in controlled environment. Sol Energy 84:183–195
7. Haase M, Da Silva FM, Amato A (2009) Simulation of ventilated facades in hot and humid climates. Energy Build 41:361–373
8. Jirua TE (2011) Airflow and heat transfer in double skin facades. Energy Build 43:2760–2766
9. Yazdanian M, Klems JH (1994) Measurement of the exterior convective film coefficient for windows in low-rise buildings. ASHRAE Trans 100(1):1087–1096

Chapter 27
Study on the Effect of Enclosed Balcony Partition on Indoor Heating Load in Xi'an

Zhewei Li, Zengfeng Yan and Shuyun Wu

Abstract In this paper, we focus on the effect of partition setting between enclosed balcony and its directly connected room. In residential buildings, the heat lose through balcony components makes disadvantage for energy saving. In order to avoid these adverse effects of enclosed balcony, *Design Standard for Energy Efficiency of Residential Buildings in Severe Cold and Cold Zones* rules that partition should be set between enclosed balcony and its directly connected room; if there is no partition, the heat transfer coefficients of the enclosed balcony envelope, as well as window to wall ratio, should be controlled within a reasonable range. To evaluate the effect of balcony partition, we use DeST-h software to simulate these two situation—balcony with partition and without partition. According to the simulation results, we come to such a conclusion that the heating load of the room with balcony partition is lower than that without, and the outside surface of balcony should be set with insulation.

Keywords Enclosed balcony partition · Heating load · Indoor air temperature

27.1 Introduction

In residential buildings, the heat lose through balcony components makes disadvantage for energy saving. Because of its high window to wall ration, enclosed balcony increases the contact surface area of the building and outdoor air, which can accelerate convention between indoor and outdoor air, increase indoor energy consumption, and affect heat insulation of building envelope. In order to avoid these adverse effects of enclosed balcony, *Design Standard for Energy Efficiency*

Z. Li (✉) · Z. Yan · S. Wu
Institute of Arch, Xi'an University of Architecture and Technology,
Xi'an 710055, China
e-mail: 676750981@qq.com

A. Li et al. (eds.), *Proceedings of the 8th International Symposium on Heating, Ventilation and Air Conditioning*, Lecture Notes in Electrical Engineering 263,
DOI: 10.1007/978-3-642-39578-9_27,

of Residential Buildings in Severe Cold and Cold Zones rules that partition should be set between enclosed balcony and its directly connected room; if there is no partition, the heat transfer coefficients of the enclosed balcony envelope, as well as window to wall ratio, should be controlled within a reasonable range. To evaluate the effect of balcony partition, we use DeST-h software to simulate these two situation—balcony with partition and without partition.

In China, insulation of enclosed balcony should meet the following four qualification requirements depending on *Design Standard for Energy Efficiency of Residential Buildings in Severe Cold and Cold Zones* [1]:

1. Partition, door, and window should be set between balcony and its directly connected room.
2. Balcony should be considered as part of its directly connected room, if there is no partition, door, and window between them. And the heat transfer coefficient of Balcony's outside wall panel, roof, and floor must be consistent with the requirements of ; window to wall ratio of balcony must be consistent with the requirements.
3. If the heat transfer coefficient of balcony's outside wall panel, roof, and floor, and window to wall ratio of balcony are controlled below the limit value, there is no special requirement for balcony's outside surface.
4. If the heat transfer coefficient of the partition, door, and window of balcony exceed the limit value is shown, as well as the heat transfer coefficient of balcony's outside surface exceed 120 % of limit value is shown in Table 1, the heat transfer coefficient of balcony's window in severe cold and cold zones should be, respectively, controlled below 2.5 W/(m^2·K) and 3.1 W/(m^2·K), and window to wall ratio of balcony should be not exceed 60 %.

Based on above, DeST-h software is used to simulate the thermal effect of the partition on residential building. Through simulation, we can get the building heating load and the room base temperature. Then, this paper compares the difference in simulation results through different partition types. Finally, design recommendation of enclosed balcony insulation on energy saving are proposed.

27.2 Simulation Procedure

27.2.1 Simulation Software

Designer's simulation toolkits (DeST), a quick building energy simulation tool that is developed by Tsinghua University, is a sophisticated, yet easy to use, building energy use analysis tool that allows detailed analysis of building thermal processes and HVAC system performance. DeST comprises a number of different modules for handling different functions: Medpha (weather data), VentPlus (natural ventilation), Bshadow (external shading), Lighting (lighting), and CABD (CAD interface). BAS (Building Analysis and Simulation) performs hourly calculations for indoor air

temperatures and cooling/heating loads for buildings, including complicated buildings of up to 1000 rooms. There are five versions in the DeST family: DeST-h (residences), DeST-c (commercial), DeST-e (building evaluation), DeST-r (building ratings), and DeST-s (solar buildings). DeST has been widely used in China for various prestige large structures such as the State Grand Theater and the State Swimming Center. In this study, DeST-h was adopted as an analysis tool [2].

27.2.2 Study Objective

The area studied in this research was located within Xi'an, which is suited in the cold zone of China. A south-oriented residential building with 11 stories, within this city was chosen as the main simulation target. The primary space allocation in the target building includes an enclosed balcony, a living room, three bedrooms. The plan for standard floor of the target building is shown in Fig. 27.1. And a computer model, shown in Fig. 27.2, was established by using software DeST-h that was adopted to analyze the thermal performance of the balcony's partition.

27.2.3 Thermal Performance of Building Envelope

The structure material set in this research is mainly reinforced concrete. Outside thermal insulation material was adopted for the exterior wall. In terms of window glass, the material is low-e glass with a thermal transmittance (U-value) of

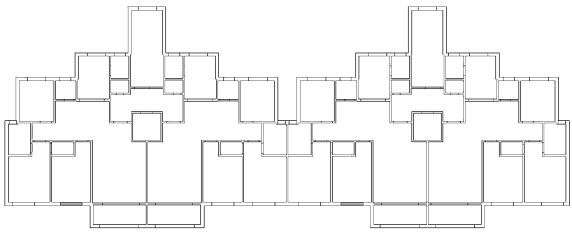

Fig. 27.1 Standard floor plans of the main simulation target

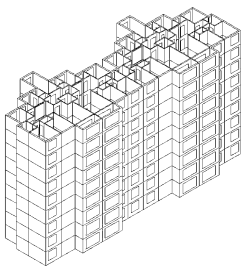

Fig. 27.2 Model base

Table 27.1 Thermal properties of building envelope

Building envelope	U-value ($W/m^2 \cdot K$)
External wall	0.53
Interior wall	2.7
Window glass	2.1
Floor	3.0
Roof	0.43

2.1 $W/m^2 \cdot K$. Table 27.1 presents the thermal properties of the building's envelope.

27.2.4 Determining the Indoor Thermal Disturbance

According to different living conditions and needs, DeST-h determined the umber of residents and power consumed in different rooms. And the value of indoor thermal disturbance is dynamic, which can be reflected the actual condition of building. In this research, default values of DeST-h for indoor thermal disturbance were adopted.

27.2.5 Balcony Partition

According to the norms of *Design Standard for Energy Efficiency of Residential Buildings in Severe Cold and Cold Zones,* the enclosed balcony with partition and without partition can be set as following 4 conditions, respectively, shown in Tables 27.2 and 27.3.

The partition of No. 1 and No. 2 is equipped with thermal insulation layer and low-e medi-empty window filled with inert gas. And No. 1 and No. 3 use insulated wall and window as outside surface.

According to *Design Standard for Energy Efficiency of Residential Buildings in Severe Cold and Cold Zones*, the thermal properties of balcony envelope without partition should be controlled within reasonable range. Therefore, the outside wall of balcony is equipped with thermal insulation layer, and low-e medi-empty window filled with inert gas is used as the outside window of balcony.

Table 27.2 Thermal properties of balcony envelope partition

No.	Partition U-value ($W/m^2 \cdot K$)	Window and door of partition U-value ($W/m^2 \cdot K$)	Outside wall of balcony U-value ($W/m^2 \cdot K$)	Outside window of balcony U-value ($W/m^2 \cdot K$)	Ratio of window to partition	Ratio of window to wall of balcony
1	0.7	2.0	0.6	2.0	0.5	0.5
2	0.7	2.0	2.1	3.1	0.5	0.5
3	1.5	3.1	0.6	2.0	0.5	0.5

Table 27.3 Thermal properties of balcony envelope without partition

No.	Outside wall of balcony U-value ($W/m^2 \cdot K$)	Outside window of balcony U-value ($W/m^2 \cdot K$)	Ratio of window to wall of balcony
4	0.6	2.0	0.5

27.3 Simulation Results and Discussion

In this study, DeST-h was used to simulate the heating season load of the building, and the simulation results of heating season load, annual peak heating load, annual heating energy results, and building hourly load per area of typical day, shown in Table 27.4 and Fig. 27.3, verify that the building with partition indeed has lower heating season load than the building without.

Through this simulation, we get the heating season load of No. 1, No. 2, No. 3, and No. 4, which are 20.80, 22.89, 22.01, 24.51 w/m^2. And building hourly load per area of typical day is shown in Fig. 27.3. Based on the comparison between these simulation results, we can observe that balcony partition can reduce the heating season load from 24.51 to 20.80 w/m^2. And Fig. 27.3 illustrates that,

Table 27.4 Simulation results of heating season load, annual peak heating load, and annual heating energy

No.	Heating season load (w/m^2)	Annual peak heating load (w/m^2)	Annual heating energy (kWh/m^2)
1	20.80	38.69	67.17
2	22.89	41.41	73.74
3	22.01	40.60	71.63
4	24.51	44.62	80.34

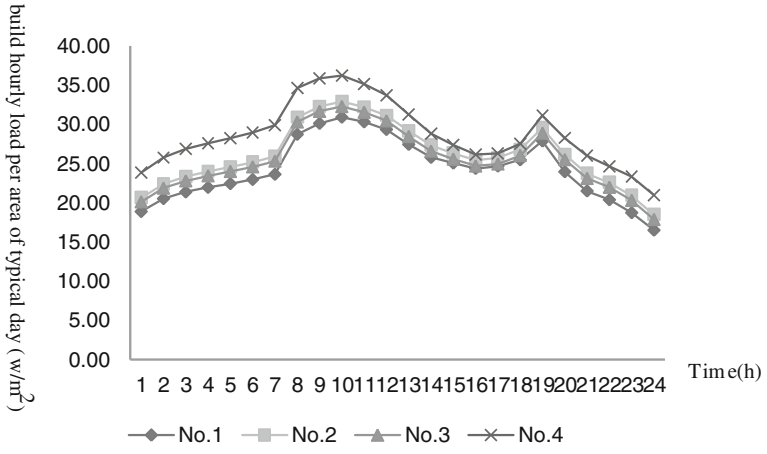

Fig. 27.3 Building hourly load per area of typical day

compared to balcony with partition, the build hourly load per area of typical day in winter of balcony without partition is larger throughout all day, especially in peak value.

The simulation results of balcony with partition, shown in Table 27.4 and Fig. 27.3, show that, compared to insulated partition, the insulation of balcony outside surface more important. Balcony with insulated outside surface can help to reduce the heat lose.

Then, compared between No. 1 and No. 3, which have insulated outside surface of balcony, No. 1 has a smaller heating season load than No. 3. Therefore, we were able to confirm that balcony's partition with insulation contribute to reduce heating season load.

27.4 Conclusion

Based on the simulation results, this paper gets some conclusions as follows:

1. Enclosed balcony partition contributes to reduce heating load of building. Under normal conditions, enclosed balcony should set up with partition.
2. Insulated treatment of balcony partition cannot be ignored. In most situations, enclosed balcony is unheating space. Therefore, in order to avoid the adverse effect of unheating space on heating space, U-value of balcony partition, which divide building space into heating space and unheating space, should be controlled with a reasonable range ruled in *Design Standard for Energy Efficiency of Residential Buildings in Severe Cold and Cold Zones*
3. The insulation of the outside surface of balcony is benefit to decrease heating load of building. Therefore, whether the partition of enclosed balcony has insulation or not, the outside surface of balcony should be set with insulation.

Acknowledgments This research was financially supported by "Twelfth Five-Year' National Technology Program" (2011BAJ03B06) and the Science and Technology Resource Coordinate Project of Shaanxi Province (2011KTCQ03-07).

References

1. JGJ26-2012 Design standard for energy efficiency of residential buildings in severe cold and cold zones
2. Peng X, Gu Q, Lin C (2008) Experimental study on the steel frame-reinforced concrete infill wall structure with semi-rigid joints. China Civ Eng J 41:64–69 (in Chinese)

Chapter 28
The Intermittent Operation Control Strategy of Low-Temperature Hot-Water Floor Radiant Heating System

Chao Ma, Yanfeng Liu, Cong Song and Dengjia Wang

Abstract The low-temperature hot-water floor radiant heating system could intermittently work without impacting the indoor thermal comfort conditions for occupants. According to the urban resident life work and rest mode and the change characteristics of indoor air temperature caused by intermittent operation of this system, the control strategies of the system of the urban residential building were proposed. The control strategies contained the average temperature adjustment of coil supply and return water and the time adjustment of system start/stop. In the different control strategies, the indoor air temperatures of the south room and the north room were analyzed by numerical simulation. The results indicated that to meet the thermal comfort requirements for most occupants, the north room needed to be heated about 18 h per day, while the south room only needed to be heated for 13–14 h per day.

Keywords Radiant floor heating · Intermittent operation · Control strategy

28.1 Introduction

As the development of the requirement for energy use efficiency and the room thermal comfort, low-temperature hot-water floor radiant heating system which is a heating method of energy saving and comfort is widely used. This heating method can realize the mutual independence of heating system between the resident families in order to meet the demand of household heat metering [1]. Meanwhile, each room of a house can be a system so that it can be timely

C. Ma (✉) · Y. Liu · C. Song · D. Wang
School of Environment and Municipal Engineering, Xi'an University of Architecture and Technology, Xi'an 710055, China
e-mail: machao9108@163.com

A. Li et al. (eds.), *Proceedings of the 8th International Symposium on Heating, Ventilation and Air Conditioning*, Lecture Notes in Electrical Engineering 263,
DOI: 10.1007/978-3-642-39578-9_28,

regulated according to the requirement, which reduces the unnecessary waste of heating and makes for building energy saving [2, 3].

Since there is vast territory in our country, there are big differences in the meteorological conditions, heating resources, and heating habits. Due to the characteristics of climates, the heating time is shorter in non-coldest season and heating transitional areas, as well as in new heating regions [4]. Besides, some public buildings and civil construction can also use intermittent heating because they are not used all-day long, and the usage time is cyclical [5]. The intermittent heating system used with continuous heating equipment can save heating energy consumption and not affect the room thermal comfort to a certain extent.

The coil of the floor radiant heating system embeds into the concrete structure layer. The floor has a good heat storage performance. The storage and release heat performance of the floors and other envelope have an important influence on the regulation characteristics of the system. If it is not regulated reasonably, not only will the energy consumption be wasted, but also affects the indoor thermal comfort [6, 7]. From the perspective of energy saving and comfort, it is quite necessary to regulate and control the floor radiant heating system reasonably during the heating period.

In this paper, in order to research the system intermittent operation control on the bases of indoor air temperature change and floor storage and release performance, a common residence house is chosen to adjust and control the average temperature of coil supply and return water and the intermittent operation time.

28.2 General Situation of Building Model

One of the common residential house types in Xi'an is chosen as the object of study in the article. The six-story simulation building is oriented north and south, plat roof. The top story is selected as simulation object.

The story height is 3.0 m, and the south window–wall ratio is 0.29, and the north window–wall ratio is 0.22. EnergyPlus is used to simulate the building model. The plan of building model is shown in Fig. 28.1. The material thermal parameter of building enclosure is shown in Table 28.1.

28.3 The Typical Day and Outdoor Meteorological Parameters

The day of which the daily average outdoor temperature of the whole day is relatively close to the average outdoor temperature of the heating period. So, January 25 is chosen as the typical day in this study. The outdoor air temperature and solar radiation intensity of the typical day are shown in Fig. 28.2.

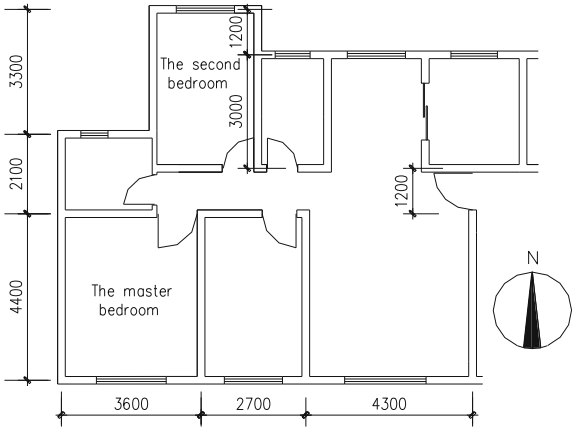

Fig. 28.1 The plan of building model

Table 28.1 The material thermal parameter of building enclosure

Material	Heat conductivity coefficient(W/m·K)	Density (kg/m^3)	Specific heat (J/kg·K)
Cement mortar	0.93	1,800	1,050.00
Expanded polystyrene board	0.046	19	2,517.34
Concrete perforated brick	0.74	1,450	673.61
Aeroconcrete	0.349	800	837.00
Expanded perlite	0.058	120	670.00
Reinforced concrete	1.74	2,500	673.61
Solid wood	0.35	550	2,512.00

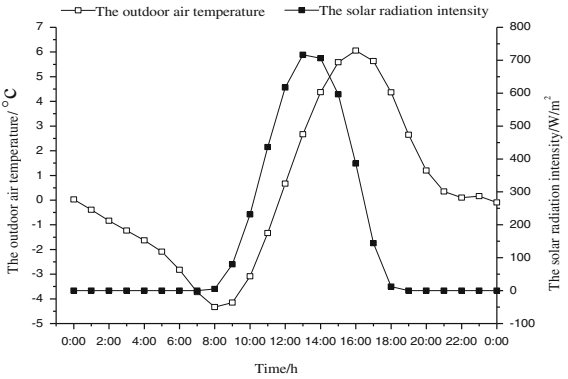

Fig. 28.2 The outdoor air temperature and solar radiation intensity of typical day

28.4 The Indoor Temperature of the North and South Rooms in the Common Intermittent Modes

The intermittent modes of the heating system are given according to the urban resident life work and rest mode [8]. The intermittent modes are as follows:

1. The first intermittent mode: 7:00–9:00 stop heating (cases of the residents retired at home)
2. The second intermittent mode: 7:00–11:00, 13:00–17:00 stop heating (cases of the residents living close to workplace and back home at noon)
3. The third intermittent mode: 7:00-17:00 stop heating (cases of the residents living far from workplace and not back home at noon).

Considering the difference in the indoor temperature variation of the north and south rooms, the master and second bedrooms were taken as example. The indoor temperatures of the south room (the master room) and the north room (the second room) of the heating system operated under the consecutive and three intermittent modes are shown in Fig. 28.3, in the condition of average temperature of coil supply and return water of 30 °C, coil spacing of 200 mm, and the filling layer thickness of 60 mm.

It is observed in Fig. 28.3 that the indoor temperature of the master bedroom under the second and third intermittent modes is slightly lower than 18 °C in 8:00–11:00; in most other periods, the indoor temperature under every operation mode stays higher than 18 °C; the first intermittent mode can reach a maximum temperature of 20.8 °C. Therefore, the master bedroom is not required the control strategies of the average temperature enhancement of coil supply and return water and the time advancement of the system start. The control strategy of the time adjustment of system start/stop can be used to adjust the heating system of the master bedroom.

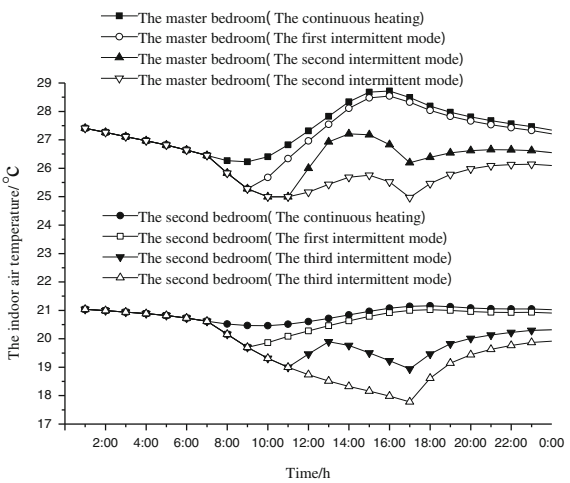

Fig. 28.3 The indoor temperature of the master and second bedrooms in different operation modes

28.5 The Control Strategy of the Intermittent Operation System

For better analyzing the control and adjustment strategy, the operating conditions of the floors of the master bedroom are chosen as the average temperature of coil supply and return water of 26 °C, the coil spacing of 300 mm, and the filling layer thickness of 70 mm and that of the second bedroom: the average temperature of coil supply and return water of 28.2 °C, the coil spacing of 200 mm, and the filling layer thickness of 70 mm. The adjustment and control of the system based on the conditions can save heating energy consumption without affecting the room thermal comfort.

28.5.1 The Control Strategy of the Average Temperature Adjustment of Coil Supply and Return Water

Changing the average temperature of coil supply and return water through changing the temperature and flow of coil supply water can enhance the indoor thermal comfort to a certain degree. For example, increasing the temperature of coil supply water can increase the rising rate of indoor temperature. However, the increase in temperature has a certain range and that of the floor surface is provided in Ref. [9]. When increasing the temperature of coil supply water is inappropriate, it is advisable to enhance the flow of coil supply water to increase the average temperature of coil supply and return water which can raise the heating rate of the system.

As is shown in Fig. 28.4, the first adjustment mode is that the average temperature of coil supply and return water is increased to 30 °C and preheated 2 h

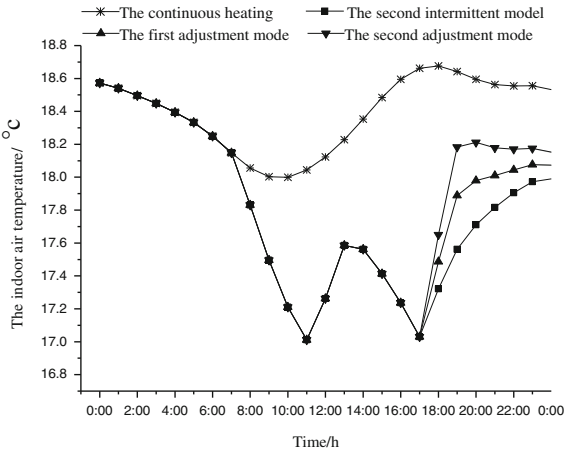

Fig. 28.4 The indoor temperature of the second bedroom as the average temperature adjustment of coil supply and return water of the heating system (in allusion to the second intermittent mode)

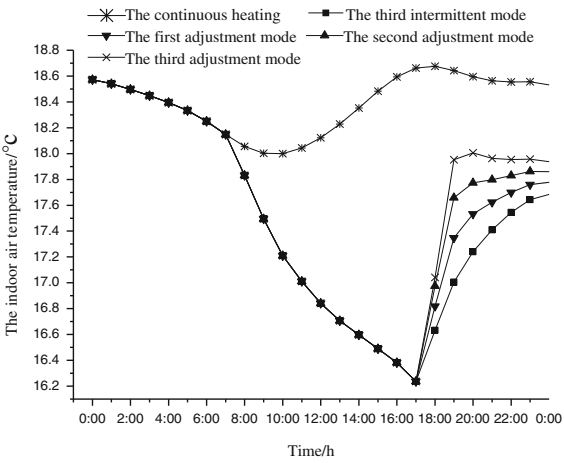

Fig. 28.5 The indoor temperature of the second bedroom as the average temperature adjustment of coil supply and return water of the heating system (in allusion to the third intermittent mode)

when the heating system is switched on at 17:00. The second adjustment mode is that the average temperature of coil supply and return water is increased to 32 °C and preheated 2 h when the heating system is switched on at 17:00. It can be concluded that after 2 h preheating of both the adjustment modes, the indoor temperature, respectively, increased 0.33 and 0.62 °C compared with the second intermittent mode. It is especially for the second adjustment mode that the indoor temperature reaches the comfort requirement with preheating less than 2 h.

As is shown in Fig. 28.5, the average temperature of coil supply and return water of the three adjustment modes relatively increase to 30, 32, and 34 °C with preheating for 2 h. It can be concluded that after 2-h preheating of the three adjustment modes, the indoor temperature, respectively, increased 0.35, 0.66, and 0.95 °C compared with the second intermittent mode. It is especially for the second adjustment mode that the indoor temperature reaches the comfort requirement with preheating for less than 2 h.

28.5.2 The Control Strategy of the Time Adjustment of the System Start/Stop

When the temperature and flow of coil supply and return water are set invariant, for the sake of diminishing the volatility of the indoor temperature, some intermittent adjustment modes are needed. At the same time, combined with the expected control, the time system start/stop is needed to do the reaction control advanced.

The expected control can ensure the stability of the indoor temperature as much as possible, but this is only when the outdoor temperature and solar radiation with the indoor heat source are in regular change. When the indoor conditions suddenly change, it is unable to make appropriate adjustment [10].

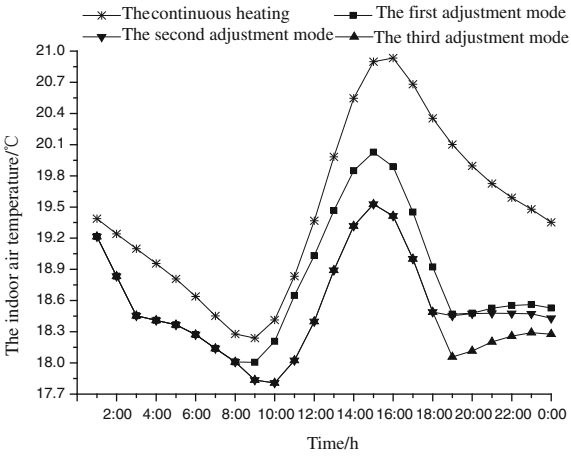

Fig. 28.6 The indoor temperature of the master bedroom as the time adjustment of system start/stop

As is shown in Fig. 28.6, the first adjustment mode is that the heating system works during 3:00–11:00 and 19:00–24:00 and switched off in the rest of the time. The second adjustment mode is that the heating system works during 3:00–8:00 and 18:00–24:00 and switched off in the rest of the time. The third adjustment mode is that the heating system works during 3:00–8:00 and 19:00–24:00 and switched off in the rest of the time. It is observed in Fig. 28.7 that compared with the consecutive operation mode, the indoor temperature decreases 1.2 °C in the first adjustment mode, while it decreases 1.6 °C in the second and third adjustment modes. The three adjustment modes can release the indoor overheating in the afternoon to some extent. The heating system is working for 13 h in the first adjustment mode, and the indoor temperature can meet the comfort of the master bedroom for most of the time. For the second and third adjustment modes, the heating system is, respectively, working for 11 and 10 h, and the indoor temperature is below 18 °C during 8:00–11:00. Therefore, the first adjustment mode can meet the demand for the residents often stay at home (e.g., the residents retired at home), and the second adjustment mode can meet the demand of the most residents.

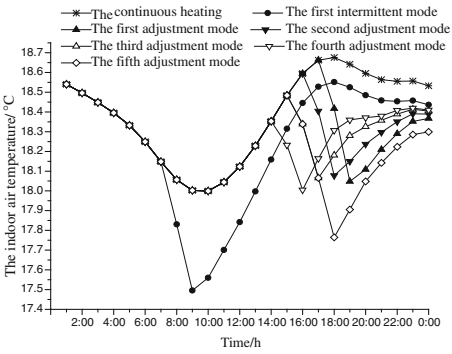

Fig. 28.7 The indoor temperature of the second bedroom as the time adjustment of system start/stop (in allusion to the first intermittent mode)

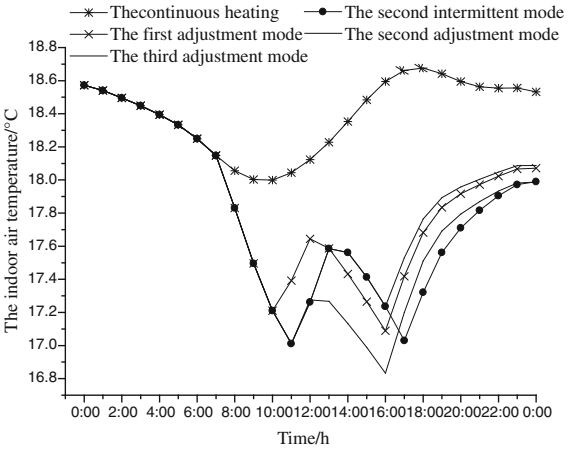

Fig. 28.8 The indoor temperature of the second bedroom as the time adjustment of system start/stop (in allusion to the second intermittent mode)

As is shown in Fig. 28.7, for the first, second, third, fourth, and fifth adjustment modes, the heating systems are, respectively, closed during 17:00–19:00, 16:00–18:00, 15:00–17:00, 14:00–16:00, and 15:00–18:00 and will work for the rest of the time. It is observed in Fig. 28.8 that for the first intermittent mode, the first, second, third, and fourth adjustment modes, the systems are closed for 2 h. For the first intermittent mode, the master bedroom does not meet the indoor comfort demand for 4.5 h, while for the first, second, third, and fourth adjustment modes, the master bedroom meets the indoor comfort demand for all-day long. For the fifth adjustment mode, the heating system is closed for 3 h, and the indoor temperature decreases in large range. It can be concluded that the different intermittent periods have the big influence on the indoor temperature. The decreasing range is relatively low when the system is switched off during the period of the temperature on rise of consecutive heating, but it is inappropriate for a long intermittent period. Compared with the first and second adjustment modes, the indoor temperatures of the master bedroom are relatively high in the third and fourth adjustment modes. Therefore, the closed time of the heating system is suggested to be selected between 14:00 and 15:00. For the residents always at home, the third and fourth adjustment modes are suggested to be selected.

As is shown in Fig. 28.8, for the first, second, and third adjustment modes, the heating systems are, respectively, closed during 7:00–10:00 and 2:00–16:00, 7:00–11:00 and 13:00–16:00, 7:00–11:00 and 13:00–17:00 and will work for the rest of the time. It is observed in Fig. 28.9 that the first adjustment mode and the second intermittent mode are set at the same heating time and both started heat 1 h in advance. Compared with the second intermittent mode, the heating time is the same, while 1 h less during the noon and 1 h earlier during the night in the third adjustment mode. However, as for the second bedroom, during the night, after 17:00, the indoor temperature in the first and third adjustment modes is higher than the second intermittent mode, and the indoor thermal environment is better when the first adjustment mode is adopted. So preheating makes for a better indoor

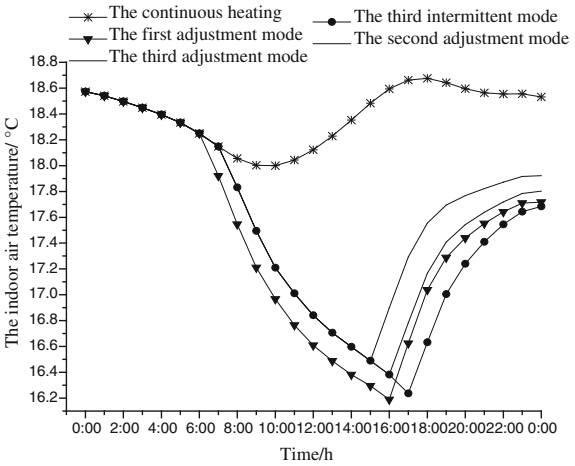

Fig. 28.9 The indoor temperature of the second bedroom as the time adjustment of system start/stop (in allusion to the third intermittent mode)

thermal environment. Compared with the first adjustment mode and the second intermittent mode, the heating time of the second adjustment mode is 1 h longer, and the indoor temperature of the second bedroom is 0.05 and 0.26 °C higher during 17:00–24:00. So the indoor thermal environment is better when the second adjustment mode is adopted. For the three adjustment modes, there is a longer time for reaching 18 °C; therefore, the control strategy of preheating and increasing the preheating temperature should be combined.

As is shown in Fig. 28.9, for the first, second, and third adjustment modes, the heating systems are, respectively, closed during 6:00–16:00, 7:00–16:00, and 7:00–15:00. Compared with the third intermittent mode, there is the same heating time, and the indoor temperature of the second bedroom during night is relatively higher for the first adjustment mode. Therefore, switching off and on the heating system both in advance can improve the indoor thermal environment. Compared with the third intermittent mode, the heating system starts 2 h earlier and the indoor temperature increased faster in the third adjustment mode, and at the same time, it needs a longer time to keep a stable indoor temperature after switching off the heating system for 10 h. Compared with the third intermittent mode, the heating system starts 1 h earlier and the indoor temperature cannot meet the demand of temperature increase for in the second adjustment mode.

28.6 Conclusions

According to the indoor temperature variation characteristic of the south room and the north room, the control strategies of the average temperature adjustment of coil supply and return water and the time adjustment of system start/stop are proposed, and it is concluded as follows:

1. Adopting the second intermittent mode for the north room, after increasing the average temperature of coil supply and return water of 3–4 °C, or maintaining the temperature of coil supply and return water, and preheating for 2 h or so, the indoor temperature can reach the thermal comfort demand.
2. For the north room, the residents always staying at home, the closing time of the heating system is suggested to select between 14:00 and 15:00. When the heating system is closed during 7:00–10:00 and 13:00–16:00, the indoor temperature can meet the demand of the most residents.
3. For the south room, the heating system is closed 2–3 h from 0:00 and 7 h or so from 11:00, working for 13–14 h of the rest of the time; then, the indoor temperature can meet the thermal comfort demand of the residents and effectively diminishes the overheating in the afternoon.
4. Compared with the original intermittent mode, switching on and off the heating system both in advance while keeping the total heating time, the indoor temperature will relatively higher at night.

References

1. Liu Y, Liu J (2004) Study of indoor thermal environment and energy consumption with floor heating and radiator heating. Energy Technol 25(1):27–30
2. Bu Y (2003) Floor heating and individual heat metering technology. China Architecture and Building Press, Beijing
3. Chen L (2010). Study on the calculation method of intermittent heating load. Harbin Institute of Technology, Harbin
4. Liu Y (2004) Study on basic theory of designing and running control of imbed pipe floor heating. Xian University of Architecture and Technology, Xi'an
5. Xiaotong W, Qiang G (2001) The relation of pipe structure measurements and temperature evenness in the floor surface to floor panel heating systems. Build Energy Environ 20(1):40–41
6. Chuangchid P (2001) Foundation heat loss from heated concrete slab-on-grade floors. Build Environ 36(5):637–655
7. Liu X, Zhang L, Xu Y (2009) Heat transfer model for floor structure layer of the low temperature water floor panel heating system. J HV&AC 39(2):19–22
8. Zhaojian L, Yi J, Da Y (2005) Simulation and analysis of intermittent heating in residential buildings. J HV&AC 35(8):110–113
9. JGJ 142-2004 (2004) Floor radiant heating technology regulations. China Architecture and Building Press, Beijing
10. Niu Z, Deng Q (2008) A parametric study on predictive control of intermittently operated radiant floor systems. Build Energy Environ 27(3):10–13

Chapter 29
Modeling on Indoor Transportation Energy Use for Large-Scale Commercial Buildings

Qi Shen, Jiang Jiang, Xiaochen Mao, Mingjin Guo and Jianjun Xia

Abstract In recent years, people pay more and more attention to large-scale commercial buildings because of the high intensity of their energy use. For these commercial buildings, the indoor transportation system is a significant energy consumption component. This chapter mainly focuses on the electricity consumption of elevators in office buildings. To summarize characteristics of running schedules and quantity, statistical methods are utilized according to the hourly energy data series from the monitoring system. The energy use of elevators nearly keeps constant during working days. To explain the steady energy use, on-site investigations and tests are implemented. A mechanical elevator model is provided to explain the nonlinear relation. In addition, a variable-element Poisson flow is modeled, aiming at obtaining visitor flow rate of elevators. At last, an hourly energy use model for elevators is degraded from the detailed mechanical model by time integral process from per minute to per hour. The hourly elevator energy model that is much simpler compared with the mechanical model not only eliminates those partial dynamic factors but also emphasizes the main hourly factors, which is very useful for both energy assessment and brief diagnosis in the total building level.

Keywords Elevator · Energy · Cluster · Building

29.1 Introduction

Nowadays, energy use of buildings accounts for 30–40 % of all energy use. As a result of the continuous development of urbanization in China, numerous large-scale modern public buildings have emerged. Among these buildings, electricity

Q. Shen (✉) · J. Jiang · X. Mao · M. Guo · J. Xia
Building Energy Research Center, Tsinghua University, Beijing 100084, China
e-mail: q-chen05@mails.tsinghua.edu.cn

A. Li et al. (eds.), *Proceedings of the 8th International Symposium on Heating, Ventilation and Air Conditioning*, Lecture Notes in Electrical Engineering 263,
DOI: 10.1007/978-3-642-39578-9_29,

consumption of elevators accounts for 5–15 % of the whole energy use in buildings [1], which ranks only second to that of building cooling and heating. As the number of elevators continuously rises, the huge electric consumption of elevators has driven governments, organizations, research institutions, and elevator enterprises to devote themselves to studying test, evaluation, and energy-saving design related to the energy consumption of elevators. Based on the building energy consumption monitoring systems which are gradually used in modern buildings, we can find the inherent law with detailed analyses on the operation of building equipment. The energy consumption data in the chapter derives from the building energy consumption monitoring systems.

As complicated electromechanical systems, neither the operating situations nor using conditions of elevators are certain. Therefore, there have not been unified methods for evaluations of the energy consumption of elevators. Methods that are widely used at present mainly include on-site testing method [2], simulation method [3, 4], and gray-box model [5]. These methods focus on simulating the energy consumption in the start-up and stop processes, so the time step is seconds and the models are complicated, which are mainly applied to product development of enterprises. In addition, other kind of researches on the energy consumption of elevators centers on forecast about the control and incoming flow of elevators, for instance, Bartz-Beielstein [6] provided a simple S-ring model to solve problems related to the supervisory group control of elevators. Besides, Siikonen [7] studied elevator traffic, especially the peak traffic.

With respect to existing researches, they have done enough work on the mechanical system, control system, and dynamic demands of elevators. However, these research results are not suitable for evaluations on energy consumption and energy-saving diagnosis of buildings. Consequently, this thesis analyzes performance in actual operation and energy consumption characters and proposes the methods that are more suitable for evaluations on energy consumption and energy-saving diagnosis of buildings.

29.2 Energy Performance of Transportation

As we all know, transportation is a significant element of public service in large-scale commercial buildings, whose energy performance displays the characteristics of high load and high utilization ratio. This thesis investigates three large-scale office buildings in all. With the energy monitoring systems, hourly energy consumption of elevators in these buildings is available. Building 1 is a government office building with a floor area of 42,000 m^2, about 2,000 people, and 2 elevators. Building 2 and Building 3 are commercial office buildings, with a floor area of 54,500 and 62,200 m^2, about 7,000 and 6,300 people, and 6 and 4 elevators, respectively.

Curves in Fig. 29.1 present the hourly energy consumption in one-day period. According to the figure, it is obvious that all daily curves are clustered in two

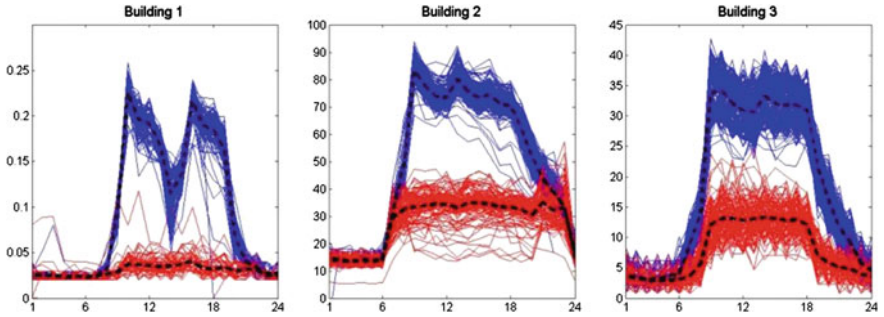

Fig. 29.1 Hourly energy consumption of elevators in the office building (unit: kW)

modes, i.e., workday and weekend. Although such typical curves are a bit different among buildings, the basic shape and aggregation degree are quite similar. Such energy consumption phenomenon may contradict with our common sense that the energy consumption of elevators should vary with visitor flow rate in buildings, while the visitor flow rate should also change as time goes, especially coming and leaving time will have a much larger number of visitors compared with working time. However, the curves are not largely influenced by changes in the total visitor flow rate but nearly keep constant during the daytime as a square wave in the one-day period.

An on-site investigation about visitor flow, startup and stop processes and destination floors were implemented in Building 1 where there are two elevators with a passenger capacity of 12 people. The sampling period is ten minutes. According to the investigation results, it is shown that the energy consumption of elevators stays in a low level when there were few people in the building during the early morning, noon time, and night. Nevertheless, in the working time, the consumption stays in a high level and nearly does not change with the number of visitors. It is obvious that the number of visitors is quite different between coming and leaving time and other periods, but energy consumption does not follow it. Thus, we can conclude that the main factor for the energy consumption of elevators may not be people but machines themselves (Fig. 29.2).

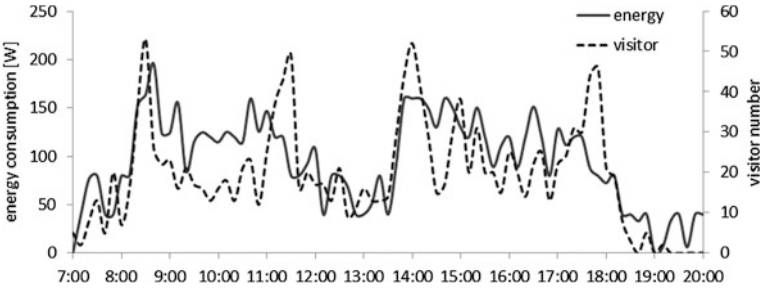

Fig. 29.2 Longitudinal data of energy consumption and the number of visitors

Although elevators transfer people to their destinations, their energy consumption only has a weak relation with the number of people. In fact, the energy use of elevator is influenced by the intensity of visitor flow rate, occupant schedule, and machine itself. However, the hourly or even daily accumulated energy use of all elevators in a building is commonly considered for energy assessment and diagnosis. And the energy curve performs a great regularity in this condition. There seems to be a cluster phenomenon on visitor flow rate, which is common in large-scale buildings.

29.3 Cluster Model

29.3.1 Mechanical Model

Being driven by a motor, an elevator runs in a linear trace, changing from circular motion of the entrainment wheel. Figure 29.3 visually presents a typical mechanical system of an entrainment elevator. The entrainment system is composed of traction machine, lift car, counter-weight, steel wire rope, and guide wheel. Generally speaking, the electricity power of a driven motor is influenced by both the passenger load in a lift car and the state of motion.

$$P_e = T\omega_m = f(m_Q, v) \tag{29.1}$$

Where P_e is the output power of the driven system, T refers to the output torque of the entrainment machine, ω_m stands for the angular velocity of the entrainment wheel, m_Q is the passenger load in the lift car, and v represents the velocity of the lift car.

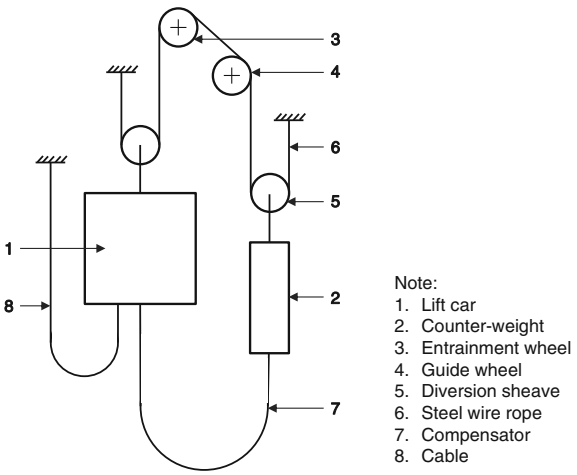

Fig. 29.3 The entrainment system of an elevator

An elevator is a kind of complex mechanical equipment whose kinetic energy and potential energy change with each other in the entrainment system when the elevator runs. For this, it is essential for the entrainment machine and the elevator control system to provide dragging force or braking force. Meanwhile, the running mode of the electrical motor is changing between a power-driven mode and a power generation mode. The power generation mode not only provides kinetic energy and potential energy but also consumes power to offer frictional resistance from braking process, guide rail, transmission, and air resistance so that the elevator can keep running at a constant velocity. In accordance with energy conservation, the mathematic model of the elevator entrainment system can be expressed as follows.

$$\begin{aligned}\text{Input power} = {} & \text{Rotational kinetic energy change} \\ & + \text{Linear kinetic energy change} + \text{Potential energy change} \\ & + \text{Resistance work}\end{aligned} \tag{29.2}$$

The input power is equal to the input power multiplied by the transmission efficiency of the entrainment wheel and driven wheels. Consequently, the energy performance of an elevator in a certain period, for instance, accumulated consumption, can be qualitatively analyzed.

29.3.2 Passenger Flow

Obviously, the phenomenon that people come to take an elevator is a typical queuing problem. In most cases, visitor flow is supposed as a *Possion* flow, and each visitor is mutually independent. Then, the number of visitors in an elevator in a unit time follows Po(λ) probability distribution function (pdf), as shown in the following equation.

$$\mathbb{P}(s = k) = e^{-\lambda}\frac{\lambda^k}{k!}, k = 0, 1, 2, \ldots \tag{29.3}$$

Where, λ is the mean number of visitors.

However, an elevator cannot contain a random number of people, so the number of passengers in an elevator follows truncation *Possion* pdf. Thus, when there are k people in an elevator with a capacity of S people, the probability is higher than that of unlimited *Possion* pdf.

When the relationship between the energy performance and the passenger load of an elevator is taken into consideration, the energy consumption of all elevators in a certain period is usually calculated. In fact, the energy performance of accumulated electricity consumption in several minutes or even in one hour is quite different from the energy use in a moment. The process of accumulation filters some dynamic disturbances at a high frequency, and then an inherent schedule will be stood out.

29.3.3 Energy Cluster Model

According to the mechanical model shown in Eq. (29.2), the accumulated energy use performance can be analyzed under the condition that both the number of passengers and their destinations are given. In an ideal assumption that the global mechanical efficiency keeps constant and independent of passenger load, the kinetic energy change during one start-up and stop processes is zero, and the potential energy change during one up and down travel is zero too. Considering this, Jin et al. [8] has tested and simulated the start-up and stop processes. As a result, it was found that the accumulated consumption in this process approached zero. Thus, the actual accumulated energy consumption of an elevator in a certain period is mainly influenced by the total running distance and changes in the potential energy.

As for one moving force and back process starting from the first floor, there are t_1 stops and t_2 stops in both force process and back process. In addition, there are s_i people going to the h_ith floor, while the differences in weight among people are ignored. Besides, the velocity of the lift car usually keeps constant ($v = const$). Based on the foregoing aspects, the accumulated energy consumption in this force and back process can be written as follows.

$$P_t = 2\alpha \cdot \max(h_{t_1}, h_{t_2}) + \beta\left(\sum_{i=1}^{t_1} s_i h_i - \sum_{i=1}^{t_2} s_i h_i\right) \tag{29.4}$$

In most cases, one moving force and back process usually last less than one minute. Consequently, there are many times in an energy sampling period, one hour commonly. When considering the relationship between data related to hourly energy and these factors, we can find expectation value is more meaningful.

$$E\{P_t\} = \alpha L + \beta T \tag{29.5}$$

Where $L = 2E\{\max(h_t|\lambda_1, h_t|\lambda_2)\}$, $T = E\left\{\sum_{i=1}^{t_1} s_i \cdot h_i \middle| \lambda_1\right\} - E\left\{\sum_{i=1}^{t_2} s_i \cdot h_i \middle| \lambda_2\right\}$.

This foregoing equation is called the elevator energy consumption cluster model, which is simplified without a kinetic energy change component compared with the mechanical model. By the energy recovery equipment, the kinetic energy change does not create any power consumption in a start-up and stop processes. In addition, when both up and down visitor flow rates are nearly the same, the energy created by the potential energy change will approach zero, which indicates that the energy of the elevator is relative to running distance standing for the resistance work component only during the working hours rather than coming and leaving time. Meanwhile, the hourly running distance L keeps relatively constant in different intensity of visitor flow.

29.4 Verification and Discussion

29.4.1 Elevator Energy Principal Component Analysis

Directing at verifying the elevator energy cluster model, this chapter utilizes principal component analysis on the longitudinal data investigated in Building 1. According to the expectation of accumulated energy in Eq. (29.4), three main factor indexes in one-hour period can be identified, i.e., the running distance L, the potential energy change T, and the kinetic energy change K, which are expressed in the following equation.

$$L = 2\max(h_{t_1}, h_{t_2}),\ T = \sum_{i=1}^{t_1} s_i h_i - \sum_{i=1}^{t_2} s_i h_i,\ K = \sum_{i=1}^{t_1+t_2} s_i \tag{29.6}$$

The on-site testing longitudinal data are shown in Fig. 29.4. According to the mechanical analysis in the above section, the importance degree of these three factors are listed in the order of $L > T > K$, and K can be approximately ignored. Thus, they are considered as principal components one by one. See details about the regression results in Table 29.1.

When only the running distance L is considered, it is a significant component for energy consumption for the high correlation coefficient. The potential energy change T is the second component, because the correlation coefficient increases observably, and its linear regression parameter is much smaller than that of L.

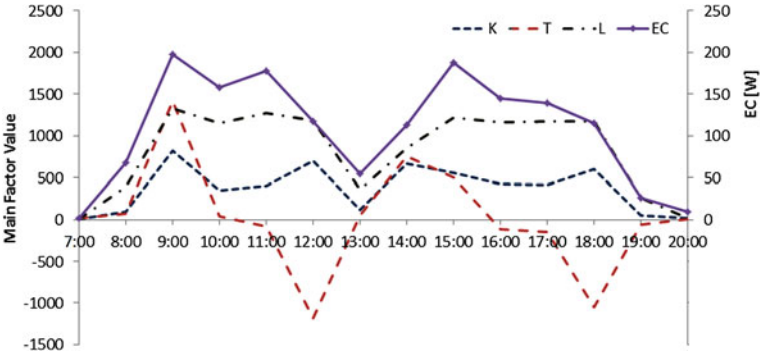

Fig. 29.4 Relation between the energy consumption and three main factors

Table 29.1 Principle component analysis of the energy consumption of an elevator

Regression equation	Correlation coefficient
$EC = 1.206 + 0.128L$	0.911
$EC = 0.562 + 0.129L + 0.026T$	0.971
$EC = -0.446 + 0.153L + 0.029T - 0.052K$	0.982

Table 29.2 Statistical characteristics of running distance at different visitor flow intensity

Visitor flow intensity λ (people/30 s)	1	2	3	4	5	6
Expectation	979	996	1,003	1,006	1,008	1,009
Standard deviation	28.7	25.9	24.7	24.4	24.1	24.1
Dispersion	2.9 %	2.6 %	2.5 %	2.4 %	2.4 %	2.4 %

At the same time, the linear regression parameter of L changes little when T is also taken into consideration, which sufficiently verifies that L is the first principle component. Furthermore, if the kinetic energy change K is considered, the correlation coefficient will create few and the regression parameter of K will be negative, which is unacceptable in accordance with physical rules.

29.4.2 Cluster of Running Distance

As noticed in the process of principle component analysis, the running distance is a major factor for the energy consumption of an elevator. It is amazing that running distance nearly keeps constant during the working hours and can resist the changes in visitor flow rate at coming and leaving time, which is also the main reason for the constant performance of energy consumption.

To simulate the visitor flow and running process of an elevator, a stochastic process in which passenger flow rate follows *Possion* pdf as shown in Eq. (29.3) is implemented. The floors that each passenger comes to and visits comply with the uniform distribution. For the common moving time in a single trip, the sampling period is 30 s and the calculation period is one hour. Thus, the running distance is an accumulated value in one-hour course. The simulation results are listed in Table 29.2. Different visitor flow intensity are considered, including conditions of few people ($\lambda = 1$) and peak traffic ($\lambda = 6$).

Apparently, the running distance is influenced by visitor flow intensity to a smaller degree, which indicates that an elevator will consume that common value that is independent of changes in the visitor flow intensity once there are some people working in the building. That is the reason why the energy consumption of an elevator nearly keeps constant in all kinds of large-scale office buildings. Furthermore, the accumulated energy under group action displays a powerful cluster phenomenon.

29.5 Conclusion

As a significant public service appliance, elevator accounts for 5–15 % of total energy use in large-scale modern building, which ranks only second to cooling and heating system. Thus, it is important to evaluate the energy use of elevator

objectively and efficiently, but not relying on energy use intensity index only. The evaluation method should display the performance of elevator itself and eliminate the influence of occupant behavior. This work seems very difficult based on the mechanical model, but changes to simple considering hourly accumulated consumption of all elevators in a building.

The energy consumption of elevators in large-scale office buildings has regular schedule which approximately looks like a square wave and is independent of the number of passengers. It indicates that the energy consumption of elevator is mainly influenced by the working time length during the daytime and total number of people in the building, but not by the passenger flow intensity. Based on the mechanical model and the stochastic process model of passenger flow, the analysis result shows that electricity power of an elevator mainly consumes in resistance work, and the running distance nearly keeps constant whatever the visitor flow intensity is. Therefore, the building height and mechanical system without the number of people serve as major factors for elevator consumption.

As a result of above theoretical and numerical analysis, an energy use evaluation method of elevator in large-scale building can be developed. Only five factors are considered, i.e., the number of elevators, operational time during the daytime, building height, and energy use intensity in daytime and night. And the two intensity factors in daytime and night stand for the appliance performance in both typical time periods. The other three factors should be normalized in benchmarking and evaluation process.

References

1. Al-Sharif L (1996) Lift power consumption. Elevator World 44:85–87
2. Doolaard DA (1992) Energy consumption of different types of lift drive system. Elevator Technol 4:214–252. In: Proceedings of Elevcon'92
3. Schroeder J (1986) Energy consumption and power requirements of elevators. Elevator World 34:28–29
4. Jin J (1999) An investigation of demand side management perspectives of elevators-electrical power consumption modeling and analysis. Korea Energy Management Administration
5. Al-Sharif L, Peters R, Smith R (2004) Elevator energy simulation model. Elevator World 54:108–111
6. Bartz Beielstein T, Preussl M, Markon S (2005) Validation and optimization of an elevator simulation model with modern search heuristics. Oper Res/Comput Sci Interfaces Ser 32:109–128
7. Siikonen ML (1993) Elevator traffic simulation. Simulation 61:257–267
8. Shen Q, Lu A, Xia J (2012) Daily energy consumption density analyzing method for hourly data monitoring system. In: Proceedings of the second international conference on building energy and environment 2012, pp 80–87

Chapter 30
Numerical Simulation for Convergent Air Curtain Under Undisturbed Area Condition

Faen Shi, Zhenying Zhu, Dahua Jiang and Wei Yuan

Abstract The formation of an "invisible, transparent, insulated airtight cover" from the convergent air curtain between pollutants and operator control pollution equivalent to increase a sealed cover to prevent the outward diffusion of pollutants, which cut off heat passed out at the environmental protection, labor protection, and health protection, is very beneficial and also has great application value in life. In this chapter, under static conditions, the air curtain in a different angle of incidence, the width of the initial wind speed, to use AutoCAD to set air curtain model, meshed it with Gambit and solved it by FLUENT software, then drawn a simulation model. On the other hand, to analyze the experimental results by the numerical simulation, software Origin was used to analyse the convergent effect of the air curtain with undisturbed outward conditions. The varying parameters are incident angle and the width of the air curtain. The incident angle, the relationship of the width of the air curtain. Gotten that the best range air curtain incident angle under undisturbed conditions is from 68 to 74, laid the theoretical and experimental bases for the actual applications of convergent air curtain.

Keywords Convergent air curtain · FLUENT · Numerical simulation · k-ε

30.1 Introduction

There are aspects of the problem of pollution in the flow field regulation; the traditional sealed cover or partial cover exhaust hood to control pollutants is used in many ventilation systems and pollutant control system, in which collection rate is very low with high energy consumption. The formation of an "invisible,

F. Shi (✉) · Z. Zhu · D. Jiang · W. Yuan
Jiangxi University of Science and Technology, HongQi Road 86, Ganzhou, Jiangxi 341000, China
e-mail: 864342579@qq.com

A. Li et al. (eds.), *Proceedings of the 8th International Symposium on Heating, Ventilation and Air Conditioning*, Lecture Notes in Electrical Engineering 263,
DOI: 10.1007/978-3-642-39578-9_30,

transparent, insulated airtight cover" from the convergent air curtain between pollutants and operator control pollution equivalent to increase a sealed cover to prevent the outward diffusion of pollutants, which cut off heat passed out at the environmental protection, labor protection, and health protection is very beneficial, and also has great application value in life [1–4] (Fig. 30.1).

Numerical results help to find the optimum convergent air curtain system to protect the industry environment. The study on the air curtain is going on for many years [5–9], but there is no simulation on convergent air curtain. In this study, a convergent air curtain model is set and its velocity flow field under undisturbed condition is simulated, the step is shown as Fig. 30.2.

30.2 Numerical Analysis

The convergent air curtain is axisymmetric; therefore, we use of 2-dimensional symmetry which simplifies the calculation; the model is mapped by AutoCAD soft and exported by *sat.* type, which was imported by Gambit and mapped in 7,500 ~ 8,200 grids as shown in Fig. 30.3. The air curtain angle was $\alpha = \beta - 90$, the values were 56°, 62°, 68°, 72°, and 80°, and the width of curtain vent was valued by $2b_0$, the values of $2b_0$ were 2, 4, 6, 8, and 10 cm for 62°; values of velocity inlet by curtain vent were 1, 1.5, 2, 2.5, and 3 m/s for 68°.

30.2.1 The Computational Domain and Grid

The convergent air curtain is axisymmetric; therefore, we use of 2-dimensional symmetry which simplifies the calculation; the model is mapped by AutoCAD soft and exported by *sat.* type, which was imported by Gambit and mapped in 7,500 ~ 8,200 grids as shown in Fig. 30.3. The air curtain angle was $\alpha = \beta - 90$, the values were 56°, 62°, 68°, 72°, and 80°, and the width of curtain vent was valued by $2b_0$, the values of $2b_0$ were 2, 4, 6, 8, and 10 cm for 62°; values of velocity inlet by curtain vent were 1, 1.5, 2, 2.5, and 3 m/s for 68°.

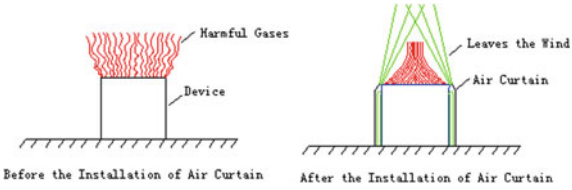

Fig. 30.1 Schematic diagram of air curtain convergent

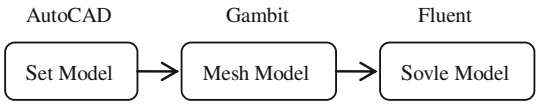

Fig. 30.2 The step to deal with convergent air curtain

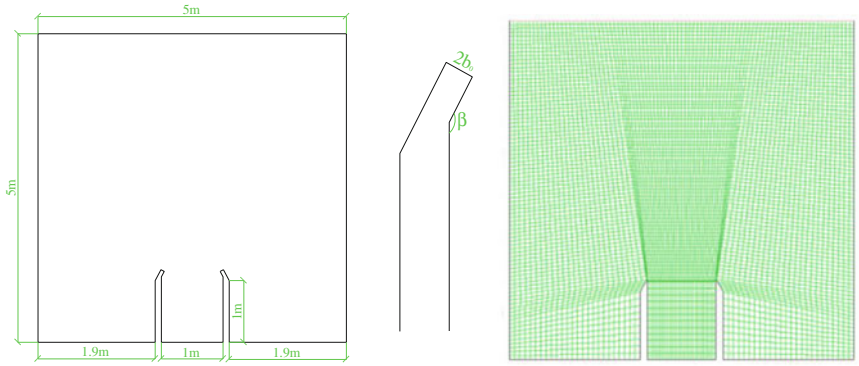

Fig. 30.3 The computational domain and grid

The computational grid was generated by structured grid; the grid around the curtain vent was made dense, which is shown in Fig. 30.3. The grid was distributed along 2 axes. A grid validation study was performed to make sure that the computed quantities were properly converged. The room size was set between −2.5 and 2.5 m in x direction, and the height was between 0 and 5 m in y direction as shown in Fig. 30.3.

30.2.2 Analysis: The Computational Tools and Turbulence Model

FLUENT CFD software is widely used to deal with a wide variety of fluid problems; the FLUENT Workbench provides the geometry and modifies the geometry read-through data formats. Standard two-equation turbulence models often fail to predict the amount of flow separation under pressure gradient conditions, as air is a low-speed flow of air between the rate range from 1 to 3 m/s); the coupled is more fitting than segregate, which has a similar degree of convergence. Simulation results are more symmetrical, and the used segregate will vary due to the choice of the initial value with both sides of asymmetrical speed. The Standard model, the RNG model and the Realized model are common method. Realized method has a higher resolution of the velocity gradient; therefore, this chapter selected Coupled + Realized method for solving.

The k-ε-based standard, RNS, and realized are all available, but the combination of coupled, implicit realized, steady time, absolute velocity, cell-based gradient option, superficial velocity, and porous, second upwind formulation are not.

The realized k-ε model's turbulent kinetic energy dissipation rate transport equation [10] is below:

$$\frac{\partial(\rho k)}{\partial t}+\frac{\partial(\rho k u_i)}{\partial x_i}=\frac{\partial}{\partial x_j}\left[\left(\mu+\frac{\mu_t}{\sigma_k}\right)\frac{\partial k}{\partial x_j}\right]+G_k+G_b-\rho\varepsilon-Y_M \qquad (30.2.1)$$

$$\frac{\partial(\rho\varepsilon)}{\partial t}+\frac{\partial(\rho\varepsilon u_i)}{\partial x_i}=\frac{\partial}{\partial x_j}\left[\left(\mu+\frac{\mu_t}{\sigma_\varepsilon}\right)\frac{\partial\varepsilon}{\partial x_j}\right]+\rho C_1 E\varepsilon-\rho C_2\frac{\varepsilon^2}{k+\sqrt{\upsilon\varepsilon}}+C_{1\varepsilon}\frac{\varepsilon}{k}G_{3\varepsilon}G_b \tag{30.2.2}$$

The realized model was designed to give highly accurate predictions of the flow separation under adverse pressure gradients by the inclusion of transport effects into the formulation of the eddy viscosity. The time derivative terms were discretized for time steady computations. The choice of the turbulence model depends on considerations of the established practice of a specific class of problem, the level of accuracy required, the available computational resources, and the amount of computing time available for the simulation.

30.2.3 Boundary and Simulation Conditions of the Computational Domain

The working fluid of the domain was ideal air at 300 K of temperature under atmospheric pressure condition as shown in Fig. 30.4.

In FLUENT software, the gas in low velocity cannot set in velocity inlet, but in pressure inlet.

The speed was set as the boundary condition. Supersonic/Initial Gauge Pressure (hydrostatic pressure) was set as 0. Gauge total pressure (pressure) was calculated as follows:

$$\frac{p_{Total}}{p}=\left(1+\frac{k-1}{2}M_a^2\right)^{k/k-1} \tag{30.2.3}$$

$$M_a=V_0/\sqrt{kRT_0} \tag{30.2.4}$$

$$\Delta p=p_{Total}-p \tag{30.2.5}$$

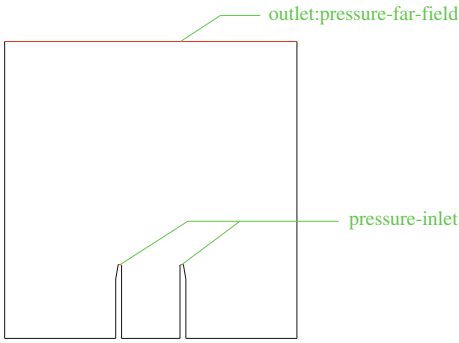

Fig. 30.4 The boundry type of curtain

In the formula, p is the static pressure, valued 101325 Pa
K is the adiabatic index, and generally 1.4
T_0 is the operating temperature, valued 300 K

The gauge pressure could be computed by Excel software as shown below.

30.3 Results and Discussion

Using computational fluid dynamics (CFD) modeling, the air curtain rates of the convergent air curtain are analyzed. These analyses are performed by means of the program FLUENT 6.2.16 ddp which uses finite volumes theory.

After iterating 2,000 ~ 2,500 times, the residuals of convergence, due to space limitations, are presented as shown in Fig. 30.5 to prove the results were credible. The do the comparison of the experimental and data, which results in correlative, drawn the velocity vector and found the entrainment and rotation and made the diffusion of the air leave from air curtain. The influence of several factors, such as the width of the bar nozzle, initial velocity, the angle of the nozzle, the variation of angle, was also researched in this paper.

30.3.1 Comparison of the Data

To test the fidelity of the simulation model, at 62°, measured data and simulated data were compared. In the horizontal direction measured the size of the air velocity magnitude. Experimental data were from the hot bulb anemometer, numerical analog data sources were from FLUENT Software; data are shown in Fig. 30.6, and the scatter plot of the experimental data and numerical data is shown as Fig. 30.7; the SPSS Software showed the comparison of the data as 0.77, which is correlative.

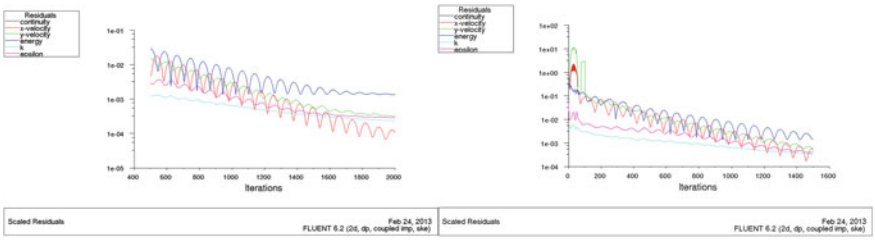

Fig. 30.5 The residuals of iteration

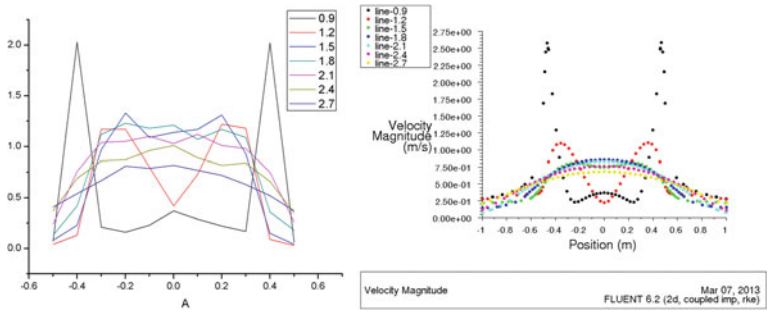

Fig. 30.6 The velocity magnitude under experimental (*left*) and numerical (*right*) condition

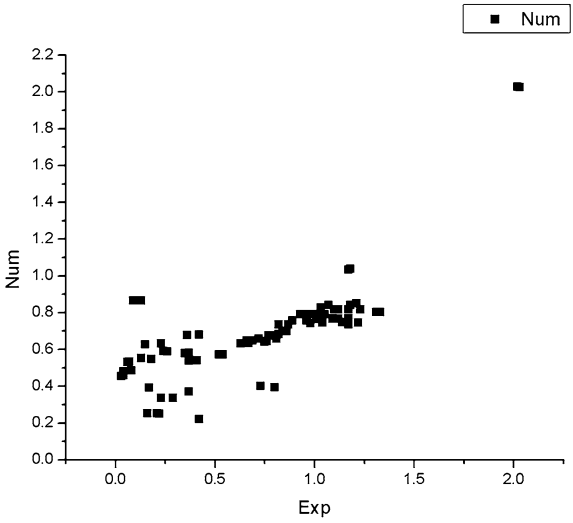

Fig. 30.7 Scatter plot of the experimental data and numerical data

Error analysis: In the experiment, there were no completely ideal conditions, but external conditions' interference, when the wind speed was low, and the holding by the testers anemometer may cause spoiler or change the wind vector.

For the simulation, completely static conditions did not exist; this was only observed in the case of interference-free distribution of the flow field of the air curtain and was bound with the actual situation (the existence of temperature, external pressure changes, and the error exist).

30.3.2 The Velocity Vector of Convergent Air Curtain

Under undisturbed area of convergent air-curtain, all range of inlet velocity and vent width ($2b_0$) and angle, the velocity also had the same shape of flow field,

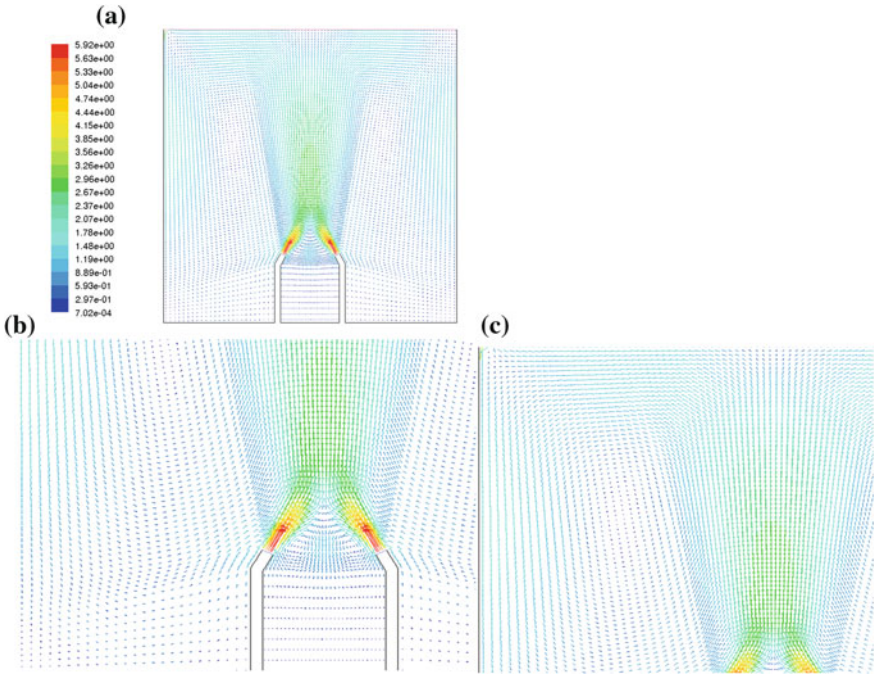

Fig. 30.8 The velocity flow field of convergent air curtain. **a** The whole velocity flow field. **b** The velocity flow field when y < y0. **c** The velocity flow field when y> and =y0

which can be presented by Fig. 30.8. In the convergent air curtain exists the entrainment as shown in Fig. 30.8b). Large eddy formed at the left and the right corner. When the distance for the top of the air curtain was $0 \sim y_0$(y = $0 \sim y_0 + 1$ m, the height of the air curtain was 1 m), the airflow closer toward the center direction, and due to entrainment, attracted the surrounding airflow of the air curtain to the curtain stream, in this range, air curtain central airflow speed was greater than the peripheral velocity, and the absolute value of the velocity magnitude and X is inversely proportional; this showed that in a certain range within converged air curtain had a good convergence effect. While the distance was longer than y_0 ($y > y_0 + 1$ m) to the top of the air curtain, out speed, airflow spread to both sides of the intermediate speed gradually smaller. The y_0 range was about 1.5 m and so the specific values of different parameters vary. The following is discussion on the relationship of the air curtain aggregation under static conditions with the mounting angle of the jet width, the ejection speed, and the ejection angle.

30.3.3 The Width and the Velocity of the Inlet Vent of the Convergent Air Curtain

From the Table 30.1, the velocity nephogram of the width of curtain vent were 2, 4, 6, 8, and 10 cm of the angle of inlet in 62° as shown in Table 30.1 and as shown in Fig. 30.9a, the velocity magnitude of y = 2.5 m(black) and y = 3.5 m(red) is shown as Fig. 30.9b,and the velocities are 1, 1.5, 2, 2.5, and 3 m/s of the curtain angle 68° (Tables 30.2, 30.3).

Table 30.1 The domain built by AutoCAD and Gambit software

Angle α (°)	Width $2b_0$ (cm)	Velocity inlet (m/s)
56	6	2
62	2,4,6,8,10	2
68	6	1, 1.5, 2, 2.5, 3
74	6	2
80	6	2

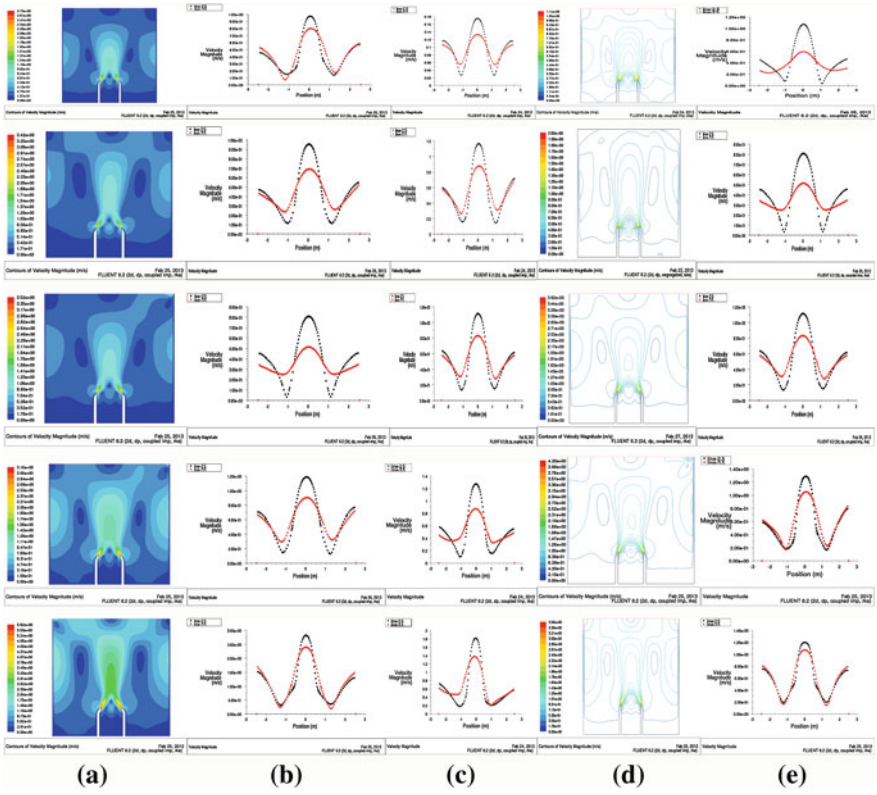

Fig. 30.9 The curtain velocity magnitude with different width and velocity: **a** with different vent size; **b** with different air velocity; **c** with different width; **d** counter with different angle; **e** y_o with different angle

Table 30.2 The convert of velocity to pressure

velocity(m/s)	1	1.5	2	2.5	3
Δp(Pa)	0.588573	1.324292	2.354305	3.678619	5.297242

Table 30.3 The velocity magnitude under experimental (*up*) and numerical (*down*) condition (m/s)

y x	−0.5 m	−0.4 m	−0.3 m	−0.2 m	−0.1 m	0 m	0.1 m	0.2 m	0.3 m	0.4 m	0.5 m
0.9 m	0.07	2.03	0.21	0.16	0.23	0.37	0.29	0.22	0.17	2.02	0.06
1.2 m	0.04	0.13	1.17	1.17	0.8	0.42	0.73	1.22	1.18	0.09	0.03
1.5 m	0.08	0.23	0.97	1.33	1.09	1.14	1.17	1.31	0.93	0.15	0.04
1.8 m	0.13	0.42	1.12	1.23	1.18	1.21	1.07	1.17	1.09	0.36	0.18
2.1 m	0.24	0.76	1.04	1.05	1.1	1.03	1.12	1.01	0.98	0.75	0.26
2.4 m	0.37	0.69	0.86	0.87	0.96	1.01	0.89	0.82	0.84	0.66	0.35
2.7 m	0.41	0.54	0.67	0.81	0.79	0.82	0.77	0.72	0.63	0.52	0.37
	−0.5 m	−0.4 m	−0.3 m	−0.2 m	−0.1 m	0 m	0.1 m	0.2 m	0.3 m	0.4 m	0.5 m
0.9 m	0.53	2.02	0.25	0.25	0.34	0.37	0.34	0.25	0.39	2.03	0.53
1.2 m	0.46	0.86	1.03	0.74	0.39	0.22	0.40	0.74	1.04	0.86	0.45
1.5 m	0.49	0.63	0.79	0.80	0.77	0.75	0.77	0.80	0.79	0.63	0.48
1.8 m	0.55	0.68	0.77	0.82	0.84	0.85	0.84	0.82	0.77	0.68	0.55
2.1 m	0.59	0.64	0.74	0.79	0.82	0.82	0.82	0.79	0.74	0.64	0.59
2.4 m	0.58	0.65	0.70	0.74	0.76	0.76	0.76	0.74	0.70	0.65	0.58
2.7 m	0.54	0.57	0.63	0.66	0.68	0.68	0.68	0.66	0.63	0.57	0.54

The outlet speed is shown in Fig. 30.9c. As the width increased, the total rate of flux increased. Once the entrainment was too big, the processing burden and economic burden would increase. The size of the air volume entrainment strength of image data processing, aggregation intensity, moderate amount of width 2 cm, and wind velocity magnitude 2 m/s were taken into account.

30.3.4 The Velocity of the Inlet Vent of the Convergent Air Curtain with Different Angle

With the inlet speed of 2 m/s, and the inlet width of 6 cm, analog 56°, 62°, 68°, 72°, and 80° of the convergent air curtain, and the velocity magnitude flow field as shown in Fig. 30.9d, it can be found that y_0 increases as α increases as shown in Fig. 30.9e. When y = 2.5 m and y = 3.5 m, it was found that velocity magnitude of 56°,62° change more significantly. At the plane of y = 3.5 m the rate of diffusion is larger. The velocity magnitude of 68°, 72°, 80° nearly didn't change. At the plane of y = 3.5 m, the diameter of the air curtain airflow is, consistent with the experimental data[1]. The conditions of angle 68° and angle 72° are better.

30.4 Conclusion

Numerical simulation are applied to understand the convergent air curtain and to improve the ventilation performance of the room. The harmful gases can be prevent by changing the velocity of the air curtain. There is a great agreement between the simulated result and the experimental data. What we need to do in the next step is as below:

a. Tanking the thermal radiation into consideration
b. Simulating the air curtain with an exhaust outlet
c. Evaluating the performance of the air curtain.

References

1. Faen S, Neng Z, Ren R, Zhao Y, Jiang D (2011) Research on the undisturbed area of convergent air curtain. In: International conference on multimedia technology (ICMT 2011), pp 4063–4066
2. Faen S, Neng Z, Jiao S, Pengfei J (2011a) The impact of the lateral force on the convergent air curtain. International conference on electrical and control engineering (ICECE 2011), pp 1819–1823
3. Faen S, Neng Z, Jiao S, Pengfei J (2011b) Establishment of the experimental model for the convergent air curtain and theoretical study. International conference on electronics, communications and control (ICECC 2011), pp 248–253
4. Shi F-E, Zhu N, Liu K-X (2011) Experimental Analysis of controlling pollutants by the convergent jet air curtain. International conference on energy, environment and sustainable development (ICEESD 2011), pp 1396–1400
5. Nakai M, Arita M (2012) An experimental study on prevention of saline wedge intrusion by an air curtain in rivers. J Hydraul Res 3:333–339
6. Ryu KJ, Juraeva M (2012) Numerical simulation in the air-curtain installed subway tunnel for the indoor air quality. The 6th international journal of mechanical and aerospace engineering, pp 414–418
7. Gerber AG, Dubay R (2006) CFD-based predictive control of melt temperature in plastic injection molding. Appl Math Model 30:884–903
8. Ichida M, Kunitomo K (2002) Control of CO2 peak position by dual lance air curtain method. ISIJ Internation 10:1077–1083
9. Jaramillo JE, Perez-Segarra CD (2010) Detailed numerical study of turbulent flows in air curtains. V European conference on computational fluid dynamics, pp 1–19
10. Zhu H-J, Lin Y, Xie L (2010) FLUNT: fluid analysis and simulation practical tutorial. Posts & Telecom Press

Chapter 31
A Practical Software for Hourly Energy Efficiency Simulation of U-Tube Ground Source Heat Pump Systems

Hua Su, Xungen Shi and Jingwen Kang

Abstract U-tube ground source heat pump systems (GSHPs) are widely used in China and other countries for building energy efficiency consideration. Because of the transient heat transfer in the ground heat exchangers, hourly simulation of GSHPs is important to the assessment of GSHPs scheme design. In this paper, proprietary simulating software is developed which includes a pretreating tool, a computing engine, and a post-treating tool. The preprocessing and post-processing tools are developed based on EXCEL and VBA. The computing engine is coded with C++ language. Text files are designed for data exchanging between modules. In the computing engine, the core model is an explicit one-dimensional transient numerical heat transfer model for the domain beyond the borehole and a steady-state heat transfer model within the borehole. Quadratic correlations for the performance of heat pump units are employed which are functions of the outlet temperature of the ground heat exchanger. Energy consumptions of the source-side pump(s), the load-side pump(s), and fans are all taken into account. Considering interactions between COP and EER, the thermal load and temperature of the ground heat exchanger, COP/EER of heat pump units is computed by an iterate algorithm. Based on hourly building loads, this software can present results of ground temperatures, fluid temperatures, energy consumptions, and energy efficiencies. One simulation case of one-year duration consumes no more than 1 min of CPU time on a common PC. Based on simulated results, one can quickly assess a GSHPs scheme or refine it if necessary. The novelty of this software is the transient numerical heat transfer model proposed by the authors. Flexibility in treating time-varying load, accuracy and fast computing speed make it a practical tool for GSHPs design and analysis.

H. Su (✉)
Key Laboratory of Fluid and Power Machinery, Xihua University, Chengdu 610039, China
e-mail: cq_suhua@163.com

X. Shi · J. Kang
China Southwest Geotechnical Investigation and Surveying Institute Co.,Ltd, Chengdu 610081, China

A. Li et al. (eds.), *Proceedings of the 8th International Symposium on Heating, Ventilation and Air Conditioning*, Lecture Notes in Electrical Engineering 263,
DOI: 10.1007/978-3-642-39578-9_31,

Keywords Ground source heat pump system · Energy efficiency · Simulation · Software

31.1 Introduction

Ground source heat pump systems (GSHPs) are widely used in China and other countries for building energy efficiency consideration. Vertical U-tube borehole heat exchangers are often used as heat sinks/sources. Because of the transient heat transfer in the ground heat exchangers (GHEs), hourly simulation is essential to the assessment of GSHPs scheme design. Many tools have been developed [1–9]. Most practical simulating tools employ analytical models for the GHE [1]. Analytical methods for time-varying heat loads often depend on a convolution scheme (superposition technique) and may be very time consuming, so accelerating methods shall be utilized [7]. Numerical models are flexible to treat time-varying heat loads [10, 11]. The numerical model for the borehole in [10] is accurate and applicable for fast simulations. Directly based on this numerical model, this paper develops a software to simulate the overall performance of a U-tube ground source heat pump system.

Section 31.2 introduces simulating method briefly. Section 31.3 describes the frame of the software. In Sect. 31.4, a case study is presented.

31.2 Brief Description of Method

31.2.1 Model of the Borehole Heat Exchanger

A two-region model [9] is used: A quasi-steady-state assumption is applied to heat transfer between water and the borehole wall; transient heat conduction in the domain outside the borehole is considered. Other than an analytical model used in [9], an explicit 1-D transient numerical model is employed here. The numerical model is based on thermal resistance and capacity formula and was described and validated in details in Ref. [10]. A similar model was used in Ref. [11]. For single borehole, the radius of the far boundary is set to 10 m; for multi-boreholes, the most disadvantage borehole in the field center is simulated and the radius of the far boundary is set to half the distance of two adjacent boreholes.

Suppose that the load on the borehole wall is Q_g and the heat flux on the far boundary of GHE is zero, the soil temperature can be computed by the 1-D numerical model.

Once the borehole wall temperature at the *j*th step, T_b^j is available, the mean fluid temperature (defined as the average of inlet and outlet temperature), T_f^j, can be calculated as follows:

$$T_f^j = \frac{Q_g^j}{L} R_b + T_b^j \tag{31.1}$$

where L is the length of GHE, m; R_b is the thermal resistance per unit length of the borehole, m·K/W. R_b can be calculated using methods in Refs [12–14].

The inlet and outlet temperature of GHE can be computed as follows:

$$\Delta T_f^j = \frac{Q_g^j}{mCp} \tag{31.2}$$

$$T_{f,\text{in}}^j = T_f^j + \Delta T_f^j/2 \tag{31.3}$$

$$T_{f,\text{out}}^j = T_f^j - \Delta T_f^j/2 \tag{31.4}$$

where m is the mass flow rate, kg/m^3; Cp is the water specific heat, J/K·kg.

The transient numerical heat transfer model is the novelty of this software. The merit of this numerical model is that it can treat time-varying load flexibly. Only if this core model is accurate, can the software be accurate. Ref. [10] has validated this model by comparison with analytical models and test data. Here, comparison of borehole wall temperature between the numerical model and the analytical models [4, 7] is presented in Fig. 31.1. It can be concluded that the transient numerical heat transfer model is accurate.

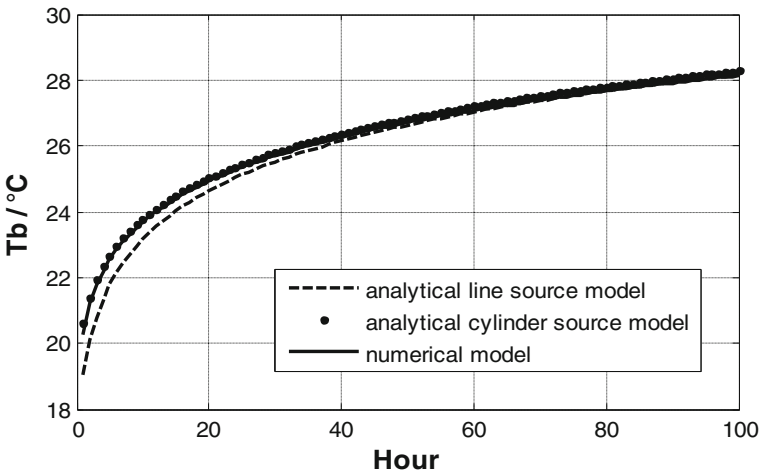

Fig. 31.1 Comparison of borehole wall temperature between the numerical model and the analytical models (L = 80 m, Db = 130 mm, λ_s = 1.8 W/(K·m), $\rho_s c_s$ = 3.5 × 106 J/(m^3·K), T_∞ = 18 °C, Q = 4,000 W, $\triangle r$ = 0.033 m, $\triangle t$ = 60 s)

31.2.2 Efficiency Model of the Heat Pump

EER or COP of heat pump unit is a quadratic function of heat pump inlet temperature (i.e., out temperature of the GHE):

$$\mathrm{EER/COP} = a + b * T_{f,\mathrm{out}} + c * T_{f,\mathrm{out}}^2 \tag{31.5}$$

where a, b, and c are fitting coefficients, which can be obtained based on production dada from manufactures.

The relationship between the GHE load and the building load is as follows:

$$Q_g^j = Q^j(1 + 1/\mathrm{EER}), \text{in cooling mode} \tag{31.6}$$

$$Q_g^j = Q^j(1 - 1/\mathrm{COP}), \text{ in heating mode} \tag{31.7}$$

where Q is the building load, W.

Electricity consumption of the heat pump unit is as follows:

$$E_{hp}^j = Q^j/\mathrm{EER}, \text{in cooling mode} \tag{31.8}$$

$$E_{hp}^j = Q^j/COP, \text{ in heating mode} \tag{31.9}$$

31.2.3 Energy Consumption of the Pump and Fan

Energy consumptions of pumps and fans are complex [15, 16], depending on the type of pumps and fans, system schemes, control strategies, etc. In this paper, a proximately proportional relationship is used.

If actual load is smaller than 25 % of the designed load,

$$E_p = E_{p0} \times 25\,\% \tag{31.10}$$

$$E_f = E_{f0} \times 25\,\% \tag{31.11}$$

If actual load is from 25 to 75 % of the designed load,

$$E_p = E_{p0} \times \frac{Q}{Q_0} \tag{31.12}$$

$$E_f = E_{f0} \times \frac{Q}{Q_0} \tag{31.13}$$

If actual load is greater than 75 % of the designed load,

$$E_p = E_{p0} \times 100\,\% \tag{31.14}$$

$$E_p = E_{p0} \times 100\,\% \tag{31.15}$$

where Q is the actual building load; Q_0 is the design load; E_{p0} and E_{f0} are the design power of pumps and fans, respectively; E_p and E_f are the actual power of pumps and fans, respectively.

31.2.4 Total Energy Consumption and Efficiency

The total energy consumption is as follows:

$$E_{\text{sys}} = E_{\text{hp}} + E_{\text{ssp}} + E_{\text{lsp}} + E_f \tag{31.16}$$

where E_{sys} is the system energy consumption; E_{hp} is the heat pump unit consumption; E_{ssp} is the energy consumption of source-side pumps; E_{lsp} is the energy consumption of load-side pumps; E_{f} is energy consumption of fans.

The system energy efficiency is as follows:

$$EE_{\text{sys}} = \frac{Q}{E_{\text{sys}}} \tag{31.17}$$

31.2.5 Algorithm for System Simulation

Considering interactions between COP and EER, the thermal load and temperature of the GHE, COP/EER of heat pump units is computed by an iterate algorithm. The overall computing algorithm is described in pseudo-code:

(1) Read basic data, such as thermal parameters of GHE, number of computational nodes, simulation step, step time, etc.;
(2) Read initial soil temperatures;
(3) For j = 1 to N (N is the simulation step)

1) Read the building load, Q_{hp}^j;
2) IF Q<>0 then

Assume COP0 or EER0
While error >eps (i.e. the convergent criteria)

Compute the load of GHE, Q_g^j using Eqs. (31.6, 31.7);
Compute soil temperature, using the numerical model;
Compute the borehole thermal resistance;
Compute the mean water temperature, using Eq. (31.2);
Compute inlet and outlet temperature, using Eqs. (31.3, 31.4);

Compute COP1 or EER1 using Eq. (31.5);
Compute error = abs(COP1−COP0) or error = abs(EER1-EER0)
COP0 ← COP1 or EER0 ← EER1

End while
Compute energy consumption;
Else
Compute soil temperature, using the numerical model;
End IF

3) Update the initial soil temperature;
Next j

31.3 Software Frame

Based on the method in Sect. 31.2, proprietary simulating software, called XHGSHP, is developed. This software includes a pretreating tool, a computing engine, and a post-treating tool as shown in Fig. 31.2.

The preprocessing and post-processing tools are developed based on EXCEL and VBA. The computing engine is coded with C++ language. The preprocessing module consists of seven worksheets for necessary data and can export data for the computing engine; the post-treating module includes six worksheets and can import results of the computing engine and generate typical charts. Text files are designed for data exchanging among the three modules. The text file format is not given for space saving. The computing engine employs the methods in Sect. 31.2.

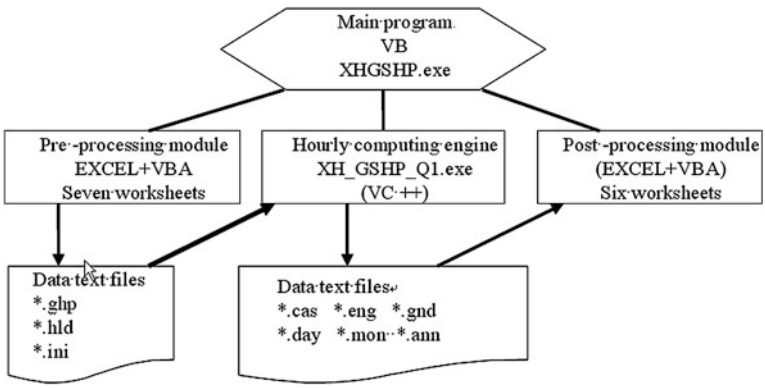

Fig. 31.2 Structure of software

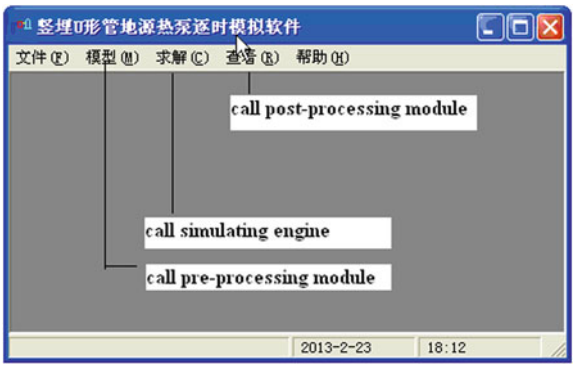

Fig. 31.3 Interface of the main program

The preprocessing tool and post-processing tool can be opened by EXCEL, and the hourly computing engine, a console program with no interface, can run in DOS mode. Three modules can be called by the main program which has a friendly interface, as shown in Fig. 31.3.

31.4 A Case Study

A case study is carried out to show the performance of XHGSHP. Only primary information is given for space saving. Readers can contact with the authors for details.

We set the building load like that in Fig. 31.4. 150 GHE with a depth of 100 m are installed and the initial soil temperature is 18.5 °C. Hourly building loads can

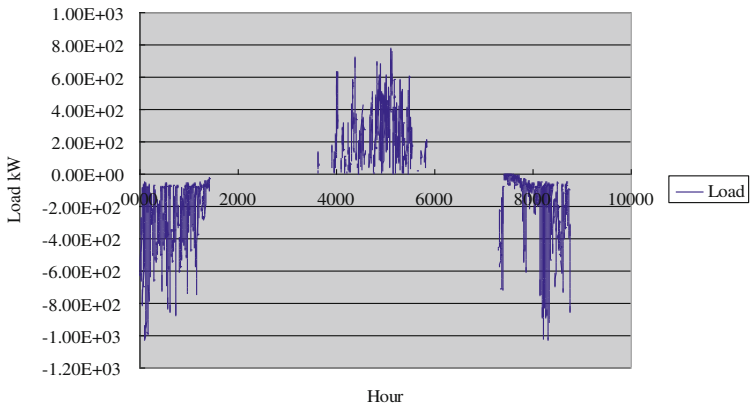

Fig. 31.4 Hourly building load

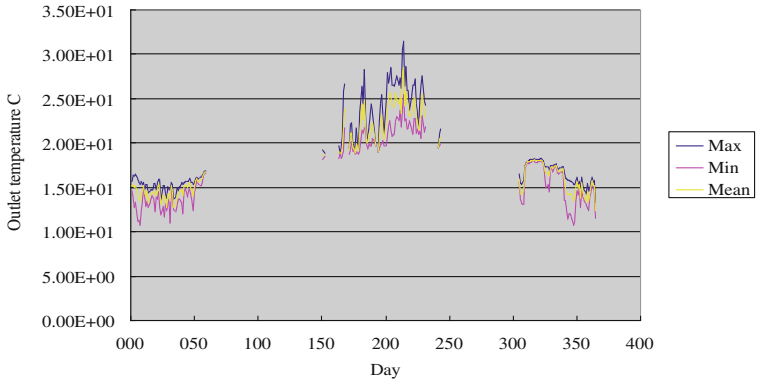

Fig. 31.5 Daily water temperature

be computed by other programs such as DOE and DEST. Once data are prepared by the preprocessing tool, the simulating engine can finish a one-year period simulation, consuming no more than 1 min of CPU time on a common PC. Typical charts can be generated by the post-processing tool.

Figure 31.5 shows the daily water temperature. Figure 31.6 shows monthly energy efficiency of the heat pump unit and system. Figure 31.7 shows the year round cooling and heating electricity consumption. It should be noted that all inputted data are not checked carefully, so the results may not be the real case. The figures in this section are only for showing the computing performance of the software.

The numerical model of GHE used here has been validated in Ref [10]. and in Sect. 2.1 of this paper. If input data are prepared correctly, reasonable simulated results can be obtained. Using the results, one can quickly assess a GSHP scheme or refine it if necessary.

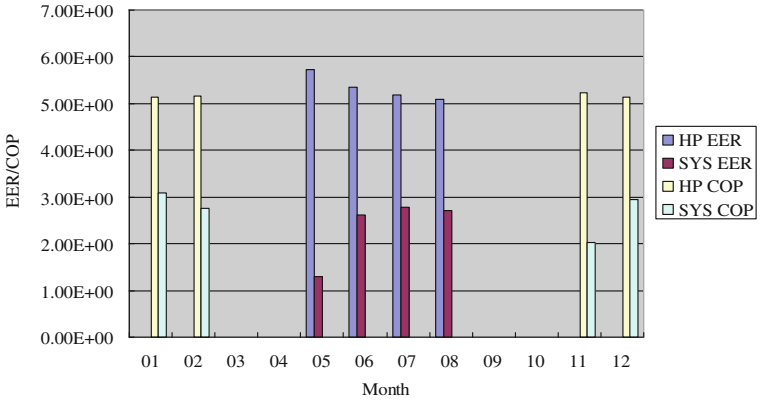

Fig. 31.6 Monthly EER/COP

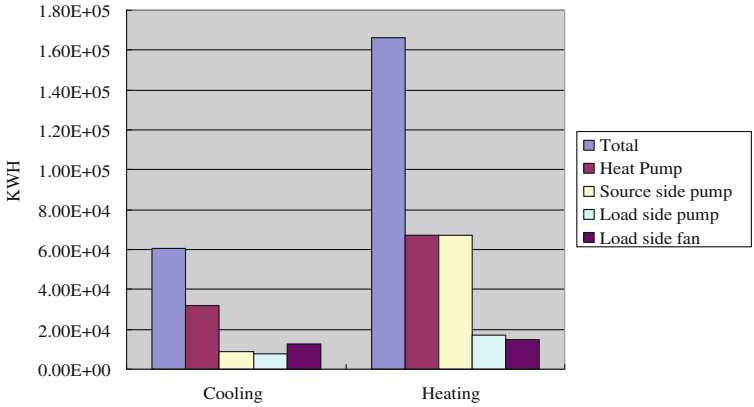

Fig. 31.7 Cooling and heating energy consumption

This software is easy to operate and can obtain results quickly. It can compute directly based on hourly loads. Thus, it may be a practical tool for GSHP design and analysis.

31.5 Concluding Remarks

In this paper, proprietary software is developed for simulating the ground source heat pump system. The method used in the software is briefly described. The structure of the software is introduced. Main results of a case study are presented. The novelty of this software is the transient numerical heat transfer model proposed by the authors. This software may be a practical tool for GSHP design and analysis because of its flexibility in treating time-varying load, accuracy, and fast computing speed.

References

1. Yang H, Cui P, Fang Z (2010) Vertical-borehole ground-coupled heat pumps: a review of models and systems. Appl Energy 87(1):16–27
2. Nam Y, Ooka R, Hwang S (2008) Development of a numerical model to predict heat exchange rates for a ground-source heat pump system. Energy Build 40(12):2133–2140
3. Lee CK, Lam HN (2008) Computer simulation of borehole ground heat exchangers for geothermal heat pump systems. Renewable Energy 33(6):1286–1296
4. Michopoulos A, Kyriakis N (2009) A new energy analysis tool for ground source heat pump systems. Energy Build 41(9):937–941
5. Nagano K, Katsura T, Takeda S (2006) Development of a design and performance prediction tool for the ground source heat pump system. Appl Therm Eng 26(14–15):1578–1592

6. Lamarche L, Dupré G, Kajl S (2008) A new design approach for ground source heat pumps based on hourly load simulations. In: ICREPQ Conference, Santander, 338/1–5
7. Lamarche L (2009) A fast algorithm for the hourly simulations of ground-source heat pumps using arbitrary response factors. Renewable Energy 34(10):2252–2258
8. Xu X, Spitler JD (2006) Modeling of vertical ground loop heat exchangers with variable convective resistance and thermal mass of the fluid. In: Proceedings of the 10th International Conference on Thermal Energy Storage—Ecostock 2006, Pomona, NJ
9. Yang W, Shi M, Liu G, Chen Z (2009) A two-region simulation model of vertical U-tube ground heat exchanger and its experimental verification. Appl Energy 86(10):2005–2012
10. Su H, Li Q, Li XH et al (2011) Fast simulation of vertical U-tube ground heat exchanger directly based on one-dimensional transient numerical model. Numer Heat Transfer, Part A 60(4):328–346
11. De Carli M, Tonon M, Zarrella A, Zecchin R (2010) A computational capacity resistance model (CaRM) for vertical ground-coupled heat exchangers. Renewable Energy 35(7):1537–1550
12. Diao NR, Li QY, Fang ZH (2004) Improvement on modeling of heat transfer in vertical ground heat exchangers. Int J HVAC&R Res 10(4):459–470
13. Hellstrom G (1991) Ground heat storage: thermal analysis of duct storage systems, Department of Mathematical Physics. University of Lund, Sweden
14. Sharqawy MH, Mokheimer EM, Badr HM (2009) Effective pipe-to-borehole thermal resistance for vertical ground heat exchangers. Geothermics 38(2):271–277
15. Guodong Y (2004) Discussion on energy consumption of variable frequency pump in air conditioning systems. HV & AC 34(6):32–34 (In Chinese)
16. Zheng H, Yingxin Z (2009) Comparison of EER_t between different terminal devices of air systems. HV & AC 39(2), 73–107(In Chinese)

Chapter 32
A Physical Model for VOC Emissions from Coating Materials Applied on Porous Substrates

Zhao Gao and Xinke Wang

Abstract A physical model for VOC emission from a coating film applied on porous substrates was proposed. In the model, the mass transfer at the air–film interface, at the film–substrate interface, and in the substrate is mathematically described and the mass change of the film because of the evaporation into indoor air and penetration into the substrate was quantified. Therefore, a whole process from "wet" state to "dry" state for the coating film can be characterized. Compared with the experimental data in the literature, the model is validated. Through a case study, it is found that VOC emissions prolong for a longer time after a sharp VOC release, and that the liquid VOC may exists in the substrate, though the film becomes "dry." After the liquid VOC evaporates completely, the gas-phase VOC in the porous substrate keeps in a relative high concentration level for a longer time.

Keywords Volatile organic compounds (VOCs) · Indoor air quality · Wet material · Coating · Model

32.1 Introduction

Indoor air quality is being concerned more and more because of lots of chemical pollutant sources applied indoors and less fresh air supply. Volatile organic compounds (VOCs) are one kind of indoor main gaseous contaminants for modern urban buildings, which tend to result in some health problems such as headache, eye, nose, or throat irritations, and other sick building symptoms (SBS) [1].

Z. Gao · X. Wang (✉)
School of Human Settlements and Civil Engineering, Xi'an Jiaotong University, Xi'an 710049, China
e-mail: wangxinke@mail.xjtu.edu.cn

A. Li et al. (eds.), *Proceedings of the 8th International Symposium on Heating, Ventilation and Air Conditioning*, Lecture Notes in Electrical Engineering 263,
DOI: 10.1007/978-3-642-39578-9_32,

As one of the important sources of VOCs, characteristics of VOC emission from interior coating materials such as wood stains, varnishes, and paints were studied including experiments and modelling [2]. Based on some chamber experiments, VOC emissions from interior coating materials were characterized by some empiric models, for example one-order decay model [2]. However, as this kind of models cannot provide insight into mechanism of VOC emissions, the application is limited. Hence, mass transfer-based models were proposed such as VB model [3], VBX model [4], and Yang's model [5]. Because of no consideration for internal diffusion in the material film and the substrate, VB and VBX models underestimate VOC emission rate after evaporation dominated emission process [5]. Yang proposed a complex mass transfer model to predict not only emission rate but also the VOC distribution in the film and the substrate. The simulated data using the model agree better with experimental data than those using VB and VBX models. Recently, a mathematic model [6] was put forward to characterize dynamic VOC emission. However, by all the mentioned models, the drying process cannot be simulated, and a key problem that what's the difference between "wet" and "dry" building materials could not be clarified. Therefore, a mass transfer-based model is presented to depict the whole process including liquid- and gas-phase mass transfer.

32.2 Model

When a paint film was applied on an indoor porous surface, VOC emission from the film will affect VOC concentration in indoor air together with penetrating into the porous substrate, which is schematically shown in Fig. 32.1.

For the sake of simplicity, the following assumptions are made before developing the model: (1) the paint film is so thin that it can be treated as homogeneous and that its diffusion resistance of mass transfer within itself is negligible; (2) the substrate is assumed to be homogenous porous materials; (3) the mass transfer in the paint film and the substrate is one dimensional, driven only by concentration difference; (4) there is no chemical reaction for the process.

The emission rate from the paint into indoor air depends on the mass convection and can be expressed as follows:

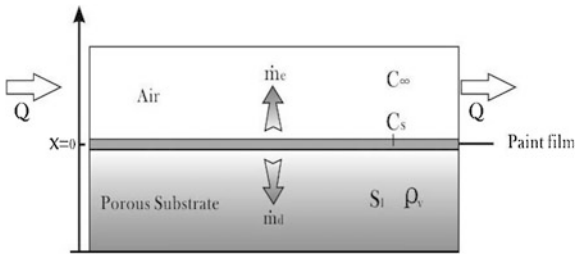

Fig. 32.1 Schematic drawing of VOC transfer from a paint film applied on a porous substrate

$$\dot{m}_e = h_m(C_v - C_\infty) \tag{32.1}$$

where $\dot{m}_e$ is the mass flux ($mg{\cdot}m^{-2}{\cdot}s^{-1}$), h_m is the convective mass transfer coefficient over the paint film ($m{\cdot}s^{-1}$), C_∞ is the VOC concentration in the bulk air ($mg{\cdot}m^{-3}$), C_v is the VOC concentration adjacent to the pain film ($mg{\cdot}m^{-3}$).

Indoor air in the room is assumed as well mixing and the VOC concentration C_∞ is governed by Eq. (32.2):

$$V\frac{dC_\infty}{dt} = \dot{m}_e A - Q(C_\infty - C_{in}) \tag{32.2}$$

where V is the volume of the room (m^3), A is the area of the paint coated surface (m^2), Q is the ventilation rate ($m^3{\cdot}s^{-1}$), and t is the time (s).

At the paint film–air interface, C_v is independent of the mass of residual VOCs in the paint film [1]:

$$C_v = C_{v,0}\frac{M}{M_0} \tag{32.3}$$

where M is the quality of the residual VOCs in the paint film (mg), M_0 is the initial quality of VOCs in the paint film, $C_{v,0}$ is the initial vapor concentration ($mg{\cdot}m^{-3}$).

The quality of the residual VOCs in the paint film, M, is determined by the emission rate from the paint into indoor air and the penetration rate from the paint into the substrate as shown in Eq. (32.4):

$$\frac{dM}{dt} = -\dot{m}_e A - \dot{m}_d A \tag{32.4}$$

where $\dot{m}_d$ is the VOCs mass flux diffusing from the paint film into the substrate ($mg{\cdot}m^{-2}{\cdot}s^{-1}$).

At the paint film–substrate interface, the following equilibrium exists between the VOC concentration in the substrate and the concentration in the paint film:

$$C_j|_{x=0} = \frac{C_s}{K_{m/w}} \tag{32.5}$$

where C_s is the VOCs concentration in the paint film, which is assumed uniform distribution ($mg{\cdot}m^{-3}$); C_j is the VOC concentration in the substrate ($mg{\cdot}m^{-3}$); x is the coordinate within the substrate (m) and the coordinate at the paint–substrate interface is assigned $x = 0$; $K_{m/w}$ is the partition coefficient between the paint film and the substrate (dimensionless).

The VOCs within the substrate exist in form of liquid and gas phases. Therefore, C_j can also be expressed as Eq. (32.6):

$$C_j = \rho_l \varphi S_l + C_g \varphi(1 - S_l) \tag{32.6}$$

where φ is the porosity of the substrate, ρ_l is the density of the VOCs liquid ($mg{\cdot}m^{-3}$), S_l is the saturation of the VOCs liquid in the micropores, C_g is the concentration of the gas-phase VOCs in the micropores ($mg{\cdot}m^{-3}$).

As described above, the transient VOCs mass transfer within the substrate can be divided in two parts:

1. The liquid part:

$$\frac{\partial(\rho_l \varphi S_l)}{\partial t} = D_l \frac{\partial^2(\rho_l \varphi S_l)}{\partial x^2} - \dot{m}_v \tag{32.7}$$

which D_l is the effective diffusion coefficient of the VOCs liquid in the porous substrate ($m^2 \cdot s^{-1}$), $\dot{m}_v$ is the evaporation rate of the VOCs liquid ($mg \cdot m^{-3} \cdot s^{-1}$) which can be obtained by the following equation:

$$\dot{m}_v = K_v\left(C_{g,\mathrm{sat}} - \mathrm{C}_g\right) S_l \tag{32.8}$$

where K_v is a mass transfer coefficient (s^{-1}), $C_{g,\mathrm{sat}}$ is the saturate VOC gas vapor ($mg \cdot m^{-3}$).

2. The gas part:

$$\frac{\partial\left[\phi(1 - \mathrm{S}_l)C_g\right]}{\partial t} = D_g \frac{\partial^2\left[\phi(1 - \mathrm{S}_l)C_g\right]}{\partial x^2} + \dot{m}_v + \dot{m}_f \tag{32.9}$$

where D_g is the effective diffusion coefficient of the VOCs gas in the porous substrate ($m^2 \cdot s^{-1}$), $\dot{m}_f$ is the adsorption rate of the VOCs gas by the wall of micropores ($mg \cdot m^{-3} \cdot s^{-1}$) described as follows:

$$\dot{m}_f = \varphi(1 - \mathrm{S}_l)\frac{\partial\left(K_f C_g\right)}{\partial t} \tag{32.10}$$

where K_f is the partition coefficient between the substrate and gas phase (dimensionless).

The boundary condition at the upper surface of the substrate is

$$\dot{m}_d = D_l \frac{\partial(\rho_l \phi S_l)}{\partial x}\Big|_{x=0} + D_g \frac{\partial\left[\phi(1-S_l)C_g\right]}{\partial x}\Big|_{x=0} \tag{32.11}$$

and the boundary conditions at the lower surface of the substrate are

$$\frac{\partial(\rho_l \varphi S_l)}{\partial x}\Big|_{x=-L} = 0 \tag{32.12}$$

$$\frac{\partial\left[\varphi(1 - \mathrm{S}_l)C_g\right]}{\partial x}\Big|_{x=-L} = 0 \tag{32.13}$$

where L is the thickness of the substrate (m).

32.3 Model Validation

The equations of the model shown in Eqs. (32.1)–(32.3) are closed and can be solved using implicit finite volume with numerical calculation. In Ref [3], there is a validating experiment conducted via chamber tests for the emission of wet coating applied on building materials substrate (oak boards), whose main experimental parameters and conditions are listed in Table 32.1. For the model simulation, the other related parameters are also estimated and listed in Table 32.1.

Based on the model, the VOC concentration in indoor air is simulated and compared with the experimental data as shown in Fig. 32.2. From that, an agreement between the simulated results and the experimental data is observed.

As the model can also be used to simulate VOCs emission from dry building materials, the experiments for dry buildings also are available for validation of the proposed model. A chamber experiment [5] for VOC emission from dry particle boards with the related parameters listed in Table 32.2 is adopted. Based on the parameters in the literature and other ones estimated, the chamber TVOC concentration is predicted as shown in Fig. 32.3. Consistence between the simulated results and the experimental data verifies the proposed model.

Table 32.1 Main parameters used for the experiment described in Ref. [3]

Parameter	Value
h_m	0.000273 $m \cdot s^{-1}$ [3]
$C_{g,\ sat}$	2.17×10^4 $mg \cdot m^{-3}$ [3]
V	0.053 m^3 [3]
A	0.021 m^2 [3]
$N(= Q/V)$	0.5 h^{-1} [3]
D_g	2.6×10^{-6} $m^2 \cdot s^{-1}$ (estimated)
D_l	7.65×10^{-9} $m^2 \cdot s^{-1}$(estimated)
K	3289 (estimated)
φ	0.001 (estimated)

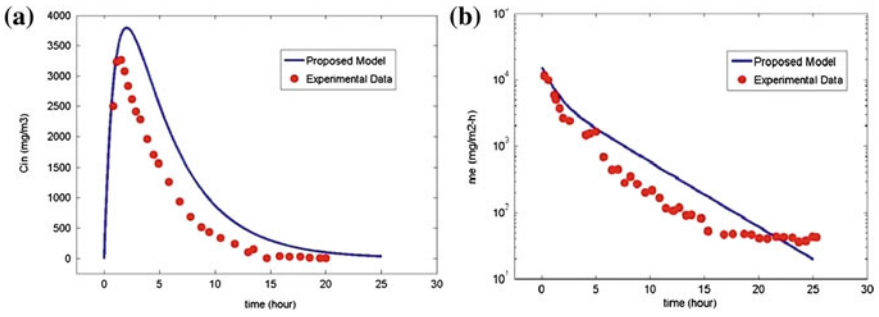

Fig. 32.2 Comparison between the experimental data in Ref. [3] and the results obtained by the model

Table 32.2 The parameters used for the prediction by the model

Parameter	Value
V [5]	$0.5 \times 0.4 \times 0.25$ m^3
A [5]	0.212×0.212 m^2
N [5]	1 h^{-1}
L [5]	0.0159 m
D_g/K [5]	7.65×10^{-11} m^2·s^{-1}
K [5]	3289
$C_{j,o}$ [5]	98.6 g·m^{-3}
φ	0.2 (estimated)

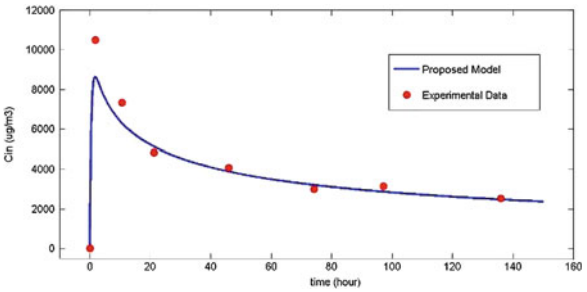

Fig. 32.3 Comparison with the experimental data in Ref. [5]

32.4 Case Study

A case is set up to depict the process of the VOCs emission from the paint on a porous substrate schematically shown in Fig. 32.4. A desk with coating painted surface emits VOCs into the room, and there is a window open for ventilation. The condition and parameters for the simulation are listed in Table 32.3, and other parameters keep the same as those in Table 32.1.

With the proposed model used, some details of the VOCs emission from coating materials painted on porous substrate are obtained as shown below. From Fig. 32.5, the VOCs concentration decays sharply after a rapid increase. But after

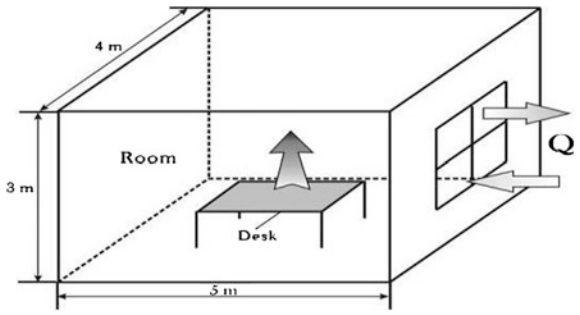

Fig. 32.4 Schematic drawing of the compositions of the case study

Table 32.3 Experimental parameters and condition of the case

Parameter	Value
V	$5 \times 4 \times 3$ m^3
A	0.8×1.5 m^2
N	1 h^{-1}
L	0.02 m
φ	0.3

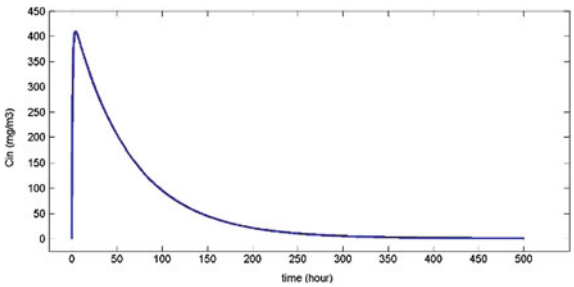

Fig. 32.5 The VOC concentration in the air obtained by the model

about 300 h, the VOCs concentration's decay slows down, which seems the emission from the coating will affect indoor VOCs centration only at the early stage. However, from the gas concentration and the liquid saturation in the substrate shown in Figs. 32.6 and 32.7, respectively, a relative high concentration of gaseous VOCs in the material is observed even after 500 h and there still is liquid VOC in the material after 300 h. It indicates that the material will affect indoor air quality for a longer time even the coating paint at the surface of the substrate looks dry.

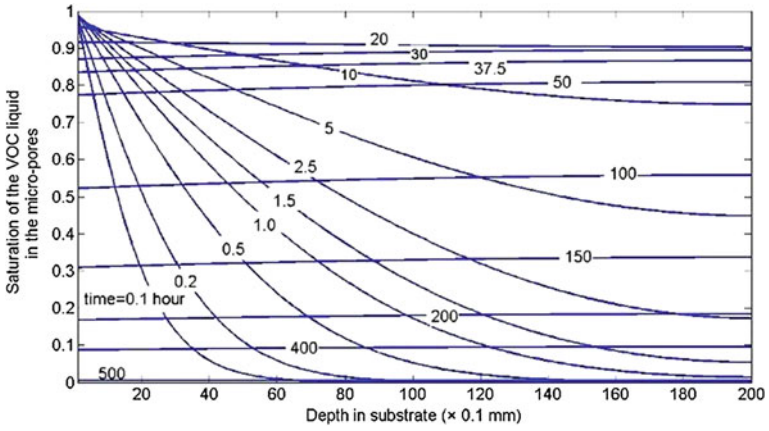

Fig. 32.6 The changes of saturation of VOC liquid in the micropores of substrate over time

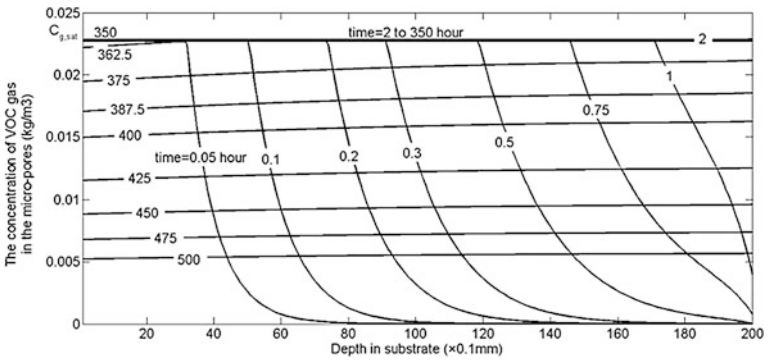

Fig. 32.7 The changes of the concentration of VOC gas in the micropores of substrate over time

32.5 Conclusion

A proposed model of VOC emissions from coating materials painted on porous substrates is built upon the physical mechanism, and by the model, the process from "wet" material to "dry" material can be pictured. Through the validation with the experimental data in the literature, the model shows a good reliability.

A case study simulated by the proposed model shows that VOC emission from the coating material painted on the porous substrate persists for a long period at a very low level after the early stage, and that the substrate keeps "wet" (that is, the saturation of VOC liquid in the micropores of substrate is not zero before 500 h) even the VOC emission into the air seems very week compared with the emission at the early stage. The concentration of gas-phase VOC in the micropores of substrate is also relative high even after 500 h. After this stage, the emission is similar to the emission for a dry building material.

References

1. Kim YM, Harrad S et al (2001) Concentrations and sources of VOCs in urban domestic and public microenvironments. Environ Sci Technol 35(6):997–1004
2. Guo Z (2002) Review of indoor emission source models. Part 1. Overview. Environ Pollut 120:533–549
3. Tichenor BA, Guo Z, Sparks LE (1993) Fundamental mass transfer model for indoor air emissions from surface coatings. Indoor Air 3(4):263–268
4. Guo Z et al (1998) Predicting the emissions of individual VOCs from petroleum-based indoor coatings. Atmos Environ 32(2):231–237
5. Yang X (1999) Study of building material emissions and Indoor Air Quality. PhD Thesis, Massachusetts Institute of Technology
6. Chang YM et al (2011) A Study on dynamic volatile organic compound emission characterization of water-based paints. J Air Waste Manag Assoc 61(1):35–45

Chapter 33
Baseline Office Building Comparison of GB Standard and ASHRAE Standard in Energy Modeling

Xing Han and Ting Shi

Abstract In order to promote the development of China green building standard and improve the level of building energy efficiency design, in this paper, the two standards, that are China *public building energy saving design standard* (*GB for short*) and American ASHRAE 90.1, are compared with the regulations and requirements in baseline building simulation to find out the potential revision part in the China's standard. Take an office building of shanghai for example, the energy consumption is compared between the two baseline buildings which are set based on the above-mentioned standards. The total energy consumption is calculated with energy simulation software EnergyPlus. The calculation results show that the building envelope and equipment efficiency requirements of GB standard are much lower than ASHRAE 90.1, but the average air-conditioning energy consumption is almost the same in two standards, for humidity control is needed in American's air-condition system which increases the reheating energy. The research also demonstrates the lack of energy simulation regulations in GB standard, which are needed to obtain the simulation results more precisely.

Keywords Office building · Energy-saving standard · EnergyPlus · Baseline building · Simulation · The energy-saving rate

33.1 Introduction

According to some statistics show that building energy consumption accounts for about 30 % of the total social energy consumption, however, energy-saving rate is less than 10 %, especially in large office buildings. Energy saving of existing

X. Han (✉) · T. Shi
University of Shanghai for Science and Technology,
Jun Gong Road 516, Shanghai, China
e-mail: hanxing@usst.edu.cn

A. Li et al. (eds.), *Proceedings of the 8th International Symposium on Heating, Ventilation and Air Conditioning*, Lecture Notes in Electrical Engineering 263,
DOI: 10.1007/978-3-642-39578-9_33,

buildings has been carried out in foreign countries, and with the increasing emphasis on building energy saving, many measures of office energy saving have been proposed, such as the use of new building envelope structural materials and parts, ventilation and exhaust heat recovery, take full advantage of the fresh air in transitional season, and the optimization of the operating mode. Since the energy crisis in 1970s, the energy utilization and application have been carried out over the world, and more than 90 countries and regions have achieved different degrees of effectiveness in building energy conservation work. Issuing and executing standards is an important means to obtain the energy-saving effect. Building Energy Conservation Code prepared by ASHRAE has become the standard specified by the Energy Policy Act of the United States Government [1]. In May 2010, United States has begun to realize that a new standard for building energy simulation should be established, and in November, they started recruiting talent to write ASHRAE STANDARD 209. The standards are mainly for buildings except the underlying residential buildings, and the purpose is to provide the minimum requirements for building energy efficiency, through the use of energy simulation and analysis. Similarly, China is also constantly improving the design standards of energy saving.

Southeast University and Hong Kong University has studied and compared the China's Green Building Evaluation Standard and the US LEED standard about the frame structure and evaluation methods, reference standards, operation mode and support system, and application status [2, 3]. Lee et al. [4] compared the baseline building, performance criteria, and simulation tools, between the US LEED, UK BREEAM, and the Hong Kong HK-BEAM, based on statistical energy assessment analysis methods. However, Asdrubali et al. [5] carried out a comparative study of building energy consumption criteria in Italy and Spain based on the semi-detached houses. Lamberto et al. [6] carried out an assessment of energy-saving rate for separate houses in Italy in three different standards (CEN-Umbrella prEN 15603 Clause 7, EN832 standard, and CEN-Umbrella prEN 15316-X prEN 15217 to prEN13790 standard). Ya Roderik et al. [7] compared the new office building energy-saving performance evaluation system between LEED, BREEAM, and Green Star, in order to understand the performance of the building better. Beijing Construction Engineering College [8] compared 6 standards and provided a reference for the development and improvement of China's green building valuation system. However, as a standard evaluation both of the comparisons are limited, and it have not compare the specific contents.

In addition, a large number of scholars researched and tested the actual energy consumption of office buildings[9, 10] and found that the energy consumption of public buildings (except heating) was complex, it is composited with air-conditioning energy consumption, lighting energy consumption, office electrical equipment and elevators and other public services equipment power consumption, in which about 40 % of the total energy consumption is air-conditioning energy consumption, about 20 % of the total energy consumption is the lighting energy consumption, and office equipment power consumption is about 25 %.

In summary, most of the current research work focuses on green building standard systems, or research and testing energy consumption for existing buildings. ASHRAE 90.1 is widely used in our public buildings to judge the building's energy efficient, but many scholars still study it yet. Therefore, in this article, the provisions and requirements of the two standards will be compared, and the typical building, according to the benchmark construction of provisions in the standard model, to study baseline building energy consumption, and contrast, pointed out that "public buildings standard" should be improved.

Here is a comparison of the reference standard in Green Evaluation System inside.

> The comparison of design standards between Chinese and the United States China's<public buildings> includes five parts, and the most important part is the last three parts. It involves the calculation parameters of indoor environment energy-saving design, architecture and building thermal design and heating, ventilation and air-conditioning energy-saving design. The three parts are also introduced in the ASHRAE 90.1, the comparison of these three parts are following.

33.1.1 The Comparison of Heat Transfer Coefficient of Building Envelope and Shading Coefficient

The office building in this research is located in Shanghai, according to the method HDD10°C and CDD18°C to determine the climate in ASHRAE 90.1, Shanghai belongs to 3A; according to the major cities climate partition in Table 4.2.1, in <Public building energy efficiency design standards>, this region is the hot summer and cold winter district. The comparisons of the heat transfer coefficient and shading coefficient are shown in Table 33.1.

Through the parameter comparison between standard of China and ASHRAE 90.1, we can find that the heat transfer coefficient limits in Public building energy efficiency design standards is more than twice of the limit in the US ASHRAE 90.1, and the limits of the shading coefficient is twice of the limit in the US ASHRAE 90.1. According to the principle of cooling and heating load calculations, the computational load of baseline building under China's standard is larger. While the high load would cause the high-conditioning energy consumption directly, so it is necessary to norm the heat transfer coefficient limit and the shading coefficient limit in China's standard.

33.1.2 The Comparison of the Lighting System

Since the object of this paper is the office building, the comparison of the lighting system is only for office buildings, but other type buildings do not compared here. The value of the lighting density in the China's standards is referred to the ≪Standards of the building lighting design≫ to determine. In the standard of

Table 33.1 The comparison of the building envelope heat transfer coefficient

Envelope portion		Heat transfer coefficient W/(m^2·K)			
		China's standard		ASHRAE 90.1	
Roof		≤0.70		≤U-0.273	
Wall (including non-transparent portion)		≤1.0		≤U-0.365	
Overhead or outside of the contact with the bottom of outdoor air to pick an empty floor		≤1.0		–	
Exterior windows (including transparent curtain wall)		Heat transfer coefficient kW/(m^2·K)	Shading coefficient	Heat transfer coefficient kW/(m^2·K)	Shading coefficient
Single area ratio of window to wall toward the exterior windows (including the transparent curtain wall)	≤0.2	≤4.7	–	≤U-3.69	≤SHGC-0.25
	0.2–0.3	≤3.5	≤0.55/-		
	0.3–0.4	≤3.0	≤050/0.60		
	0.4–0.5	≤2.8	≤0.45/0.55		
	0.5–0.7	≤2.5	≤0.40/0.55		
Roof transparent part	≤0.02 (shade)	≤3.0	≤0.40	Uall-7.38	≤SHGC-0.27
	0.021–0.05			Uall-7.38	≤SHGC-0.27
	≤0.02 (No shade)			Uall-3.92	≤SHGC-0.36
	0.021–0.05			Uall-3.92	≤SHGC-0.19
		Thermal resistance(m^2·K)/W			
		China's standard		ASHRAE 90.1	
Ground		≥1.2		≤U-1.264	
Basement exterior wall (wall in contact with the soil)		≥1.2		–	

America, there are two methods to obtain the lighting density: the building area method and the space method, the space method is taken into considerate here. The comparison of the lighting power density is as shown in the Table 33.2.

33.1.3 The Comparison of the Climate Division

The climate division in China's standard is just for our country region. According to the different temperature and humidity of different provinces, all provinces are divided into five areas: Cold region A, Cold region B, cold region, hot summer and cold winter region, and the hot summer and warm winter region. In ASHRAE 90.1, all international regions are divided into eight areas, according to the

Table 33.2 The contrast of the lighting power density (W/m^2)

Room type	China's standard	ASHRAE 90.1
General office	11	12
Conference room	11	14
Corridor	5	5
Other	11	–

difference of the humidity and the feeling of the heat and cold. 3, 4, and 5 areas are divided into A, B, and C areas, and the area 6 is divided into A and B areas. Not only the United States and Canada are divided, but also the main cities in many international countries are divided. If there is not the information of one city in the division, the method of HDD10°C and CDD18°C can be adopted to judge. So the climate division in the ASHRAE 90.1 is more comprehensive and widespread.

The Table 33.3 is the provision about the parameters of the performance of water chillers in the ≪Standards of the public buildings≫ and ASHRAE 90.1. From the table, we can find that the coefficient of the performance of American standard is about 20 % higher than the coefficient in our country under the same refrigerating capacity. So in order to obtain the same refrigerating capacity, the more energy will be consumed if according to the standard of our country and it is not energy saving enough.

The introduction about the heat source in China's standard is less, it just makes a simple introduction about the thermal efficiency and the selection of the number of boilers. The efficiency of all oil-fired boiler, gas-fired boiler, and steam boiler is 89 %. However, the introduction about it in the ASHRAE 90.1 is more detailed, it makes a general regulation about the boiler efficiency under different heating capacity. From the Table 33.4, we can find that the thermal efficiency of the fuel boiler in ASHRAE 90.1 is 10–16 % less than the China's standard. In addition, the thermal efficiency of the fuel boiler under the US standard is not mentioned, because the coal is not used in the United States.

Table 33.3 The comparison of the cold source performance requirements

Type		China's standard		ASHRAE 90.1	
		Rated cooling capacity (kW)	Coefficient of performance COP (W/W)	Rated cooling capacity(kW)	Coefficient of performance COP (W/W)
Water-cooled	Piston	<528	3.8	–	–
		528–1,163	4.0	–	–
		>1,163	4.2	–	–
	Scroll	<528	3.8	<528	4.45
		528–1,163	4.0	528–1,055	4.9
		>1163	4.2	>1,055	5.5
	Screw-type	<528	4.1	All	4.45
		528–1,163	4.3		4.9
		>1163	4.6		5.5
	Centrifugal	<528	4.4	<528	5
		528–1,163	4.7	528–1,055	5.55
		>1163	5.1	>1,055	6.1
Air-cooled or evaporative cooling	Piston/Scroll	≤50	2.4	–	–
		>50	2.6	–	–
	Screw-type	≤50	2.6	–	–
		>50	2.8	–	–

Table 33.4 The comparison of the heat source efficiency

		Heating capacity (input) (kW)	China's standard (%)	ASHRAE 90.1 (%)
Hot water boiler	Gas-fired boiler	<88	89	80
		88–733		75
		≥733		80
	Oil-fired boiler	<88	89	80
		88–733		78
		≥733		83
Steam boiler	Gas-fired boiler	<88	89	75
	Gas boiler (except natural gas)	88–733		75
		≥733		80
	Gas-fired boiler (natural gas)	88–733		75
		≥733		80
	Oil-fired boiler	<88	89	80
		88–733		78
		≥733		83

33.1.4 The Comparison of the Fan Parameters

The fan parameter is described with the consumption power of the unit volume Ws [W/(m^3/h)] in China's standard, and the formula is $W_s = P/(3,600\eta_t)$. Here, P stands for the value of the fan total pressure (Pa), η_t stands for the total efficiency including the fan, the electrical machine, and the transmission efficiency. But it should not more than the value ruled in the Table 33.5.

In ASHRAE 90.1, the efficiency of the baseline fan is different according to the formula of the different air-conditioning system, and the formulas of the part load and full load are different. Table 33.6 is the formula of the fan power of the different air-conditioning system under the full load, but there are two methods of the fan power calculation under the partial load. One of the methods is to get the fan power which is under the load by searching the chart directly, and the other one is using the formula of the fan power under the partial load, as following the Table G3.1.3.15 part-load performance for VAV Fan Systems in the ASHRAE 90.1.

Table 33.5 The limit to the consumption in unit volume of the fan [W/(m^3/h)]

System type	Office building		Commercial and hotel building	
	Coarse filter	Coarse, medium efficiency filters	Coarse filter	Coarse, medium efficiency filters
The two constant air volume system	0.42	0.48	0.46	0.52
Four constant air volume system	0.47	0.53	0.51	0.58
Two variable air volume system	0.58	0.64	0.62	0.68
Four variable air volume system	0.63	0.69	0.67	0.74
General mechanical ventilation system	0.32			

Table 33.6 The system fan power

Baseline fan motor power	
1.2 system	3–8 system
$P = CFM_S*0.3$	P = Watts*746/fan motor efficiency

where
P—fan motor power
Watts—baseline fan motor input power, in Table 33.7
Fan motor efficiency—the efficiency from Table 33.8 for the next motor size greater than the input kW using the enclosed motor at 1,800 rpm
CFM_S—the baseline system maximum design supply fan airflow rate in *L/s*

Table 33.7 The baseline fan input power

Baseline fan motor power	
Constant air volume 3–4	VAV systems 5–8
$L_S*0.0015+A$	$L_S*0.0021+A$

Note the parameters refer ASHRAE 90.1

As the Tables 33.5 and 33.6 shown, the formulas of the fan power are different. The determining factor of fan power in different air-conditioning system is different in ASHRAE 90.1. The PTAC system and PTHP system are mainly determined by the maximum flow rate. Other systems are determined by the input power and the efficiency. But all fan powers under China's standard are determined by the fan total pressure and total efficiency. At present, the design drawing in our country only gives the outside pressure of supply air units, but it does not give the total pressure. Considering the safety, the motor power is higher than the real operation power, so the requirement of air-conditioning unit drawing is not satisfied to the parameter requirement in energy simulation.

33.1.5 The Comparison of the Pump Parameters

The pumps in the air-conditioning system include the chilled water pump, cooling water pump, and hot water pump. There are not any provisions to the pump parameters in China's standard, it just makes rules to the ER of the air-conditioning cold and hot water system and the EHR of the hot water circulating pump of the concentrated hot water heating system. However, it makes rules to the power calculation methods of three kinds of pumps, respectively. Table 33.8 is the power calculation formulas of three kinds of pumps.

Table 33.8 The pump power calculation of the baseline building

Chilled water pumps	349 kW/1,000 L/s
Cooling water pump	310 kW/1,000 L/s
Hot water pump	301 kW/1,000 L/s

33.1.6 The Simulation Principle

The energy consumption simulation principle is described in ASHRAE 90.1 in detailed but is not mentioned in China's standard. The principles of the energy consumption in ASHRAE 90.1 include the following: (1) The cooling load is calculated by 115 % and the heating load is calculated by 125 % during the simulation. (2) During the yearly simulation including 8,760 h, the hours which is not satisfied for the loads of the designed buildings and the reference architectures should not be more than 300 h, and the hours which are not enough for the designed buildings should not be more 50 h than the reference architectures. If the hours which are not enough for the designed buildings are more 50 h than the reference architectures, the loads of the baseline building should be decreased and go on simulation until it reaches the requirements. (3) The requirements of the partition for the air-conditioning in the baseline buildings: the same design parameters room should be divided to the same zone. The pose angles which are in the same zone should not be more than 45 angles. Moreover, the LEED requires that the consumption of the equipment should be more than 25 %.

33.1.7 The Simple Introduction of EnergyPlus

EnergyPlus is supported by the energy department of United States and invented by the Berkeley National Laboratory, the University of Illinois, the US military construction engineering laboratory, the Oklahoma State University, and other companies. It not only absorbs the advantages of the DOE-2 and BLAST which are used for analyzing the energy consumption of the buildings, but also has a lot of new functions. It is considered as a new-generation software to analyze the consumption of buildings. In the class list, we can set the basic architectural parameters (the geographical position, the meteorological parameters, envelope, etc.), the air-conditioning system and parameters, the time step, the operation control, and the output results. EnergyPlus can be used to analyze the energy consumption of buildings and it also can simulate the load, the system, and the equipment. This software is an engine to simulate the building consumptions hourly. It adopts the simulation methods of integrated synchronous load/system/equipment. When calculating the load, users can choose the step length by themselves which is 10–15 min in general. But during the simulation, the software will set to be shorter step length automatically in order to converge easily. The simulation of the system adopts the methods of the modular system simulation, and the step length is also variable. According to the designed air loop or water loop actually, every equipment, pipeline, and rooms are connected with nodes in order to simulate the whole system. Some frequently used air-conditioning systems and configurations have been made into built-in modules and can set the parameters directly then do the simulation. The simulation of the equipment adopts the curve fitting method and can simulate the

cold and heat source equipment. The results of the simulation can be input in the table with the Excel in order to search conveniently.

In this paper, the author uses EnergyPlus to simulate the energy consumption of baseline building and design building under the above-mentioned standards and analyzes the results.

33.2 The Basic Information of the Research Case and the Setting of Baseline Building Based on the Design Standard

33.2.1 The Introduction of the Baseline Building and the Air-Conditioning

This office building contains eight floors on the ground and one floor under the ground. The total area is about 24,000 m^2, the area on the ground is 13,277 m^2, and the height is 44.95 m. The space under the ground is used as a garage and just designed with the ventilation system and exhaust system, but without air-conditioning. The lobby on the first floor adopts constant all air volume system with single duct and two fans. The large conference room adopts the VRV system. The office areas of every floor adopt variable air volume system with single duct and one air-conditioning unit is equipped to the inside and outside regions in the air-conditioning room of each layer, respectively. After the fresh air and exhausting air in outer areas are dealt by the roof full heat recovery centralized treatment, they would sent to the rooms of each floor through the shaft. The fans adopt varied conversion. The design temperature of primary supply air is 15 °C, and it can satisfy the cold and heat load yearly. The air-conditioning box adopts double fans. Individual small rooms adopt single split air-conditioning unit. The all fresh air system is used in the transition seasons, and it can adjust the fresh air ratio according to the enthalpy difference between indoor and outdoor. This office building adopts high-performance glasses, the exterior insulation, the full heat recovery, the efficient cold source, and other energy-saving technologies.

Owning to the building is built for self-use, the use rate is 100 %, which is operating from Monday to Friday, and not operating on the weekends. Everyday, the running time of lighting system and air-conditioning system is from 7 am to 9 pm, and the use rate is 50 % during 7:00–8:30 in the morning and 7:00–9:00 in the afternoon, the other time is 90 %. Every morning, the equipments turned on manually, the indoor environment parameter is auto-controlled according to the outdoor environment, and the temperature and humidity is controlled all year. The use condition set in three models according to the actual building operation.

33.2.2 The Baseline Building Under the China's Standard and America Standard

Baseline building is a model which the envelop parameters, air-conditioning system and equipment parameters are set under CN–US standard. In baseline building, the envelop parameters, lighting density, and cold and heat source parameters are set according to Tables 33.1, 33.2, 33.3, 33.4 and 33.8 .

33.2.2.1 The Air-Conditioning System of the Baseline Buildings in ASHRAE 90.1

Table 33.9 shows the air-conditioning system of the baseline buildings in ASHRAE 90.1.

Table 33.9 The air-conditioning system of the baseline buildings in ASHRAE 90.1

Architectural forms	Fossil fuel, fossil/electric hybrid, and purchase heat	Electricity or other
Residential construction	PTAC (packaged terminal air conditioner)	PTHP (packaged terminal heat pump)
Less than three or area of less than 2,300 m^2 of non-residential buildings	PSZ-AC (assembled roof air conditioner)	PSZ-HP (assembled roof heat pump)
The 4, 5 layer and the area is less than 2,300 m^2 or less than 5 layers and non-residential building area of 2,300–14,000 m^2	VAV system with preheated assembly	Assembly VAV system with PFP boxes
Higher than 5 layers or an area of more than 14,000 m^2 of non-residential buildings	VAV system with preheated	VAV system with PFP boxes

System in the form	Fan control	The form of cold source	The form of heat source
1PTAC	Constant volume	Direct expansion	Hot water fossil fuel boiler
2PTHP	Constant volume	Direct expansion	Electric heat pump
3PSZ-AC	Constant volume	Direct expansion	Fossil fuel furnace
4PSZ-HP	VAV	Direct expansion	Electric heat pump
5 VAV system with preheated closure	VAV	Direct expansion	Hot water fossil fuel
6 Closed VAV system with PFP boxes	VAV	Direct expansion	Hot water fossil fuel boiler
7 VAV system with preheated	VAV	Water-cooled	Hot water fossil fuel boiler
8 VAV system with PFP boxes	VAV	Water-cooled	Resistive

33.2.2.2 The Air-Conditioning System of the Baseline Buildings in China' Standard

The introduction of air-conditioning system of the baseline building in China' standard is not detailed; it gives a simple introduction of the division principle of air system, when to select air-conditioning system. According to the use principle of air-conditioning, the baseline building should use VAV system under China's standard.

33.3 The Input Parameter, Simulation Results, and the Analysis

33.3.1 The Input Parameters in Simulation

The accuracy of the simulation input parameter determined the simulation result. Since the simulation is under the template of the E+, the input parameter is simple, the main parameters are the pressure hand of pumps and fans, the performance value of units. The power density of lighting system and the performance value of units have been shown in Table 33.10.

In Table 33.10, the parameters are selected according to the calculation result based on the formula above, in China's standard, there is a regulation of chiller water pump, but without the heat water pump. The pump parameter is decided according to the rate of the three kind pumps mentioned in the ASHRAE 90.1. The simulation parameters are input according to the design introduction. But the excess pressure outside the fan is not given, so the parameter is the same with the China's standard.

33.3.2 The Simulation Result and Analysis

33.3.2.1 The Simulation Result of Baseline Building Under China's Standard

It can be seen from Fig. 33.1 that under the China' standard, the energy consumption of fans, pumps, and heat rejection is about 20 % of the total. Chiller

Table 33.10 The input parameter of fans and pumps

	ASHRAE 90.1	China's standard	Actual building
Fan full pressure (pa)	1,680	1,250	1,250
Chiller pump head (mmH_2O)	232,700	37,000	254,973
Cooling water pump head (mmH_2O)	189,790	333,400	229,480
Heat water pump head (mmH_2O)	184,000	320,000	219,280

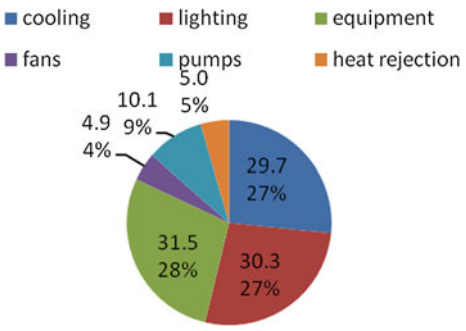

Fig. 33.1 Each part energy consumption percentage of baseline building in China's standard

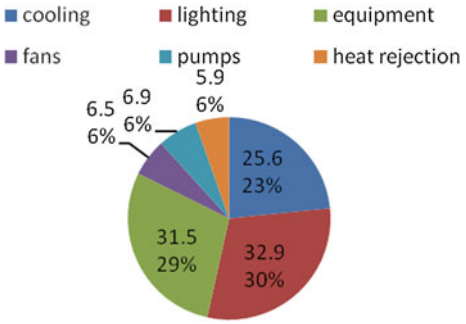

Fig. 33.2 Each part energy consumption percentage of baseline building in American standard

water units, equipment, and lighting system energy consumption are almost the same, which is 30 %, the biggest energy consumption proportion is 28 % for equipments.

It can be seen from the Fig. 33.2 that the proportion of energy consumption percentage of baseline building under china's standard is closed to America's, the percentage of lighting energy consumption is the largest; this mainly because of the indoor lighting requirement is higher than China's, but the chiller water unit's energy consumption is lower than China's. So in the same building, the energy consumption of chiller water units in America is lower than China's.

33.3.2.2 The Actual Building Simulation Result

It can be seen from the Fig. 33.3 that the energy consumption percentage of actual building is the same as the baseline building. The building energy consumption percentage is the same in three different set criteria, because energy consumption source is the same in every model,and the air-conditioning system is the same too,only the parameter setting in different standard is different.

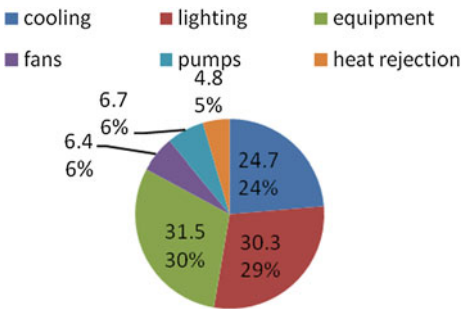

Fig. 33.3 Each part energy consumption percentage of the actual building

Here only make a comparison for building energy consumption structure analyzed the proportion of the energy consumption, which can conclude that the biggest energy-saving potential in office building is indoor equipment and lighting system.

33.3.3 The results of the simulation

Since the heat resource is gas-fired boiler, the analysis is not contained the heating energy consumption, the Table 33.11 is the comparison of heating energy.

Figure 33.4 is the energy consumption comparison in each model, it can be seen that the actual building energy consumption is the minimum, which is 105 kWh/m^2·a; the following is ASHRAE 90.1, is 110 kWh/m^2·a, and the most is China' standard, which is 112 kWh/m^2·a. The reason of the result is in actual building, it uses the high-performance glasses, the exterior insulation, the full heat recovery, the efficient cold source, and other energy-saving technologies.

In ASHRAE 90.1, the heating energy consumption is higher than the China's standard. Though the requirement of envelope thermal insulation properties in ASHRAE 90.1 is higher than public standard, but it adopt reheat in summer, so the energy consumption is higher than the public standard.

The lighting energy consumption calculated based on ASHRAE 90.1 is higher than the public standard.

The calculated fans energy consumption is higher than the public standard, because the limited value of energy consumption in ASHRAE 90.1 is higher than the public standard. Though the thermal insulation properties in ASHRAE 90.1 are better, the design air volume is bigger than the public standard. Result under the actual fan energy consumption is bigger than the energy consumption calculated under the public standard.

Table 33.11 Heating statistics

	ASHRAE 90.1	Public standard	Actual building
Heating (GJ)	1,893	1,761	2,056

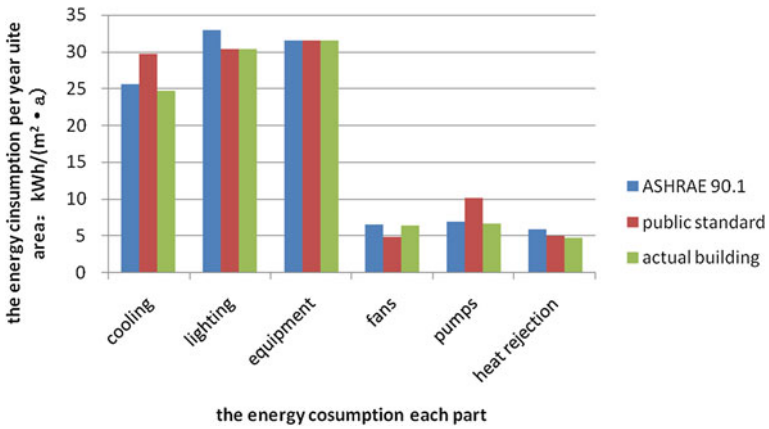

Fig. 33.4 Energy consumption situation in each building

The refrigerator energy consumption in ASHRAE 90.1 is lower than the public standard. In summer, there is much heat, the cooling, and heating balance out, but in ASHRAE 90.1, there is a higher requirement of chiller water units efficiency. So the refrigerator energy consumption is lower than the public standard. From the Tables 33.1 and 33.2, the limited value of the parameters is higher in the public standard can be found.

The limited value of pumps energy consumption in ASHRAE 90.1, the calculation pumps energy consumption is lower than the public standard.

33.4 Conclusion

According to the comparison of energy consumption of the baseline building,we can find that there is a certain gap between the public standard and ASHRAE 90.1. Each parameter limited value needs to be modified to achieve better effect of energy saving,such as reduce the heat transfer coefficient of the building envelope and improve the performance of the unit. Especially,the effect to improve the refrigerator performance is obviously for energy saving. The average energy density in the public standard is 2 kWh/(m^2·a) bigger than in ASHRAE 90.1. We also need to do more efforts to improve baseline building simulation principle, thus increasing the constraint conditions of baseline building energy consumption simulation and reducing the adjustable range of energy consumption simulation results. Because this paper only making a comparison about baseline building simulation, many other contents are not involved, some contents about control need further comparison.

References

1. Energy performance criteria in the Hong Kong Building Environmental Assessment Method 1999(02)
2. Sun Y, Yang W, Shi X The contrast of China's green building value standard and the America LEED. 2010 BEST-CN international conference
3. Zhang Z, Liu S The contrast of China's green building value standard and the America LEED 2009 NC. The sixth international conference of green building and building energy-saving
4. Lee WL, Burnett J (2008) Benchmarking energy use assessment of HK-BREEAM. BREEAM LEED Build Environ 43:1882–1891
5. Asdrubali F, Battidti M, Venegas M (2008) Comparative study of energy regulations for building in Italy and Spain. Energy Buildings 40:1805–1815
6. Tronchin L, Fabbri K (2008) Energy performance building evaluation in mediterranean countries: comparison between software simulations and opening rating simulation. Energy Buildings Schemes 40:1176–1187
7. Roderik Y, McEwan D, Wheatley C, Alonso C A comparative study of building energy performance assessment between LEED, BREEAM and Green Star. http://www.iesve.com/content/mediaassets/pdf
8. Wang Y, Wang S, Wang Q, Song X, Zhang X, Luo X (2010) The analysis of foreign green building value system. Build Energy 2:64–66
9. Wei Q, Wang X, Xiao H, Yang X (2009) The energy consumption actuality and the character in China's public building. Constr Sci Technol 8:38–43
10. Liu J, Gu Q, Wei Q (2007) The research of the big public building and the analyse of example of energy-saving Rebuilt in Shenzhen. Building Science 10:112–115

Chapter 34
Numerical Analysis of Passive Heavy Concrete Wall Cool Discharge Performance

Ping Luo, Xu Zhang, Kunming Che and Biao Zeng

Abstract Focusing on the concrete structure with rib-steel fin to enhance heat transfer, the impacts of structural feature (height of rib), thermal parameter (heat transfer coefficient), and indoor temperature set point (initial temperature of the wall) are studied by means of CFD simulation. The results indicate that the initial temperature of the wall shows the greatest effect, followed by the rib height dimensions and heat transfer coefficient with minimal impact on the cool discharged value from the heavy wall within 72 h. From the aspect of time response of the wall cool discharge, heat transfer coefficient of the wall shows the greatest impact on the time constant of the cool discharge process, followed by the rib height, and the initial temperature of the wall influences minimally. In order to ensure the acceptance of the thermal environment of the specific passive occasions, such stiffened heavy wall design process should take into account the amount of overall thermal storage to determine the structural parameters of the wall. Besides, numerical simulation methods need to be used for the wall cool discharge simulation, through which we get its fitting time constant and check whether it meets the requirements of removal of indoor thermal disturbance in the whole control period.

Keywords Rib-finned heavy concrete wall · Passive · Cool discharge characteristic · Numerical simulation · Time constant

P. Luo · X. Zhang (✉)
Department of HVAC and GAS Engineering, Tongji University, No. 1239 Siping Road Shanghai, Shanghai 200092, China
e-mail: zhangxu-hvac@tongji.edu.cn

K. Che · B. Zeng
School of Mechanical Engineering, Tongji University, Shanghai 201804, China

A. Li et al. (eds.), *Proceedings of the 8th International Symposium on Heating, Ventilation and Air Conditioning*, Lecture Notes in Electrical Engineering 263,
DOI: 10.1007/978-3-642-39578-9_34,

34.1 Introduction

Using the thermal storage capacity of the building envelope to eliminate indoor thermal disturbance is one kind of passive technologies. It is widely used in domestic fields. And it also has great potential in industrial environment controlling application especially in case of emergency. For several key occasions, such as large-scale power plant main control room, underground air defense facilities, and the main control room, indoor residence needs to be kept within a certain time in case of accident. For these control requirements, the passive technology using heavy wall of thermal storage to maintain indoor short-term residence is very suitable.

The key issue of this passive technology is that how to control the wall's cool discharge rate to offset the inner heat release during the emergency period. In this paper, ribs were attached to the inner side of the wall to enhance the heat transfer. This new heavy rib-steel wall was expected to release enough cool to offset inner heat during the accident period.

Bao [1] analyzed the efficiency of a set of passive heavy wall and emergency ventilation system for a large, new energy hub control room, and the main structure of the passive heavy wall is the rib-steel wall concerned in this paper. Zhang et al. [2] conducted a model experimental test with both rib-steel-finned heavy wall and normal heavy wall without rib-steel-finned as envelops of an environmental chamber. In the experiment, temperature distribution and cool discharge characteristic were compared between two heavy walls. The result shows that the rib steel has well made up for the discharge capacity of the heavy wall. Besides the chamber experiment, Zeng [3] analyzed the influences of indoor temperature set point, inner side convective heat transfer coefficient, and thermal conductivity of concrete on wall heat storage capacity, local time constant, and the correction time factor. He also gave out the significance analysis of the three parameters by means of orthogonal design and numerical simulation.

Those above are attempt and exploring cases for heavy wall thermal storage usage in emergency thermal environment control applications. However, such heavy wall applications lack a general design guide or reference standard about its cool discharge characteristic and thermal parameters. In this study, we used numerical simulation to model the wall cool discharge processes with different structural parameters and thermal parameters during the emergency period of 72 h. Figure 34.1 shows the structure of the rib-steel wall. The wall consisted of concrete structure, reinforcing steel inside the concrete, ribs attached to the interior surface of the wall and rivets group inserted into the structure for fixing the ribs. Considering the influence factors of the wall's cool discharge characteristic, the variable factors include rib height, wall heat transfer coefficient, and wall's initial temperature. The simulation model was designed from the actual heavy wall of our test system. Figure 34.2 indicates the temperature monitor point distribution of the test heavy wall.

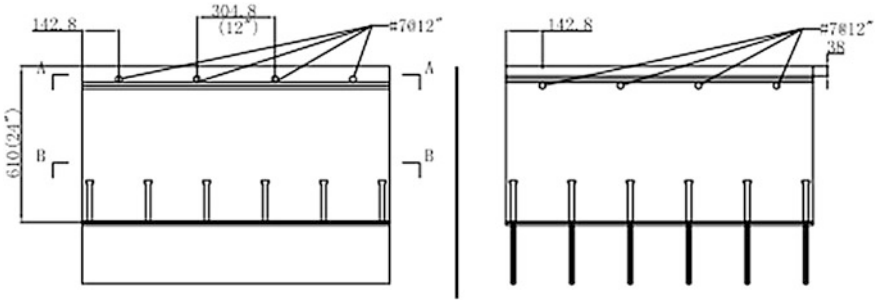

Fig. 34.1 The structure of the rib-steel-finned heavy wall

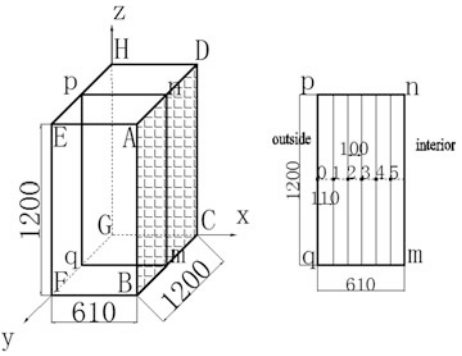

Fig. 34.2 The temperature monitor distribution of the test system

34.2 Simulation Case Setup Background

The rib height, wall heat transfer coefficient, and initial temperature of the wall play a great role in the cool discharge process of rib-steel heavy wall. In this paper, three levels were arranged for each factor according to different situations. The case details are summarized in Table 34.1.

Table 34.1 Simulation case parameters

Variable factors	Case no.	Initial temperature °C	Wall heat transfer coefficient W/m^{2}K	Rib height mm
Wall heat transfer coefficient	1	26	9.26	228.6
	2	26	6.5	228.6
	3	26	3.99	228.6
Rib height	4	24	9.26	170.5
	5	24	9.26	228.6
	6	24	9.26	306.5
Initial temperature	7	22	6.5	228.6
	8	24	6.5	228.6
	9/2	26	6.5	228.6

(*Note* the interior side boundary condition was set as fixed temperature 36 °C)

34.2.1 Variable Factor-1: The Rib Height

In the actual project application, the rib height is 228.6 mm. Thus, this value is one of the levels of the rib height factor. Considering the heat transfer strengthening effect, the fin efficiency formula [4] can be adopted to calculate another level of the rib height as follows:

$$\eta = \frac{\mathrm{th}(\mathrm{ml})}{\mathrm{ml}} \tag{34.1}$$

where th represents hyperbolic tangent function, that is

$$\mathrm{th}x = \frac{e^{x} - e^{-x}}{e^{x} + e^{-x}} \tag{34.2}$$

$$m = \sqrt{\frac{hU}{\lambda A_L}} = \sqrt{\frac{2\,\mathrm{h}}{\lambda\delta}} \tag{34.3}$$

(In this paper, it is calculated to be 2.8738), and l represents the height of the rib.

In practice, fin efficiency is treated as bigger and better. After analysis of the formula (34.1), we get that the smaller l corresponds better fin efficiency. However, enough heat exchange area requires bigger rib height. This contradiction can be handled with a conception of economic fin efficiency 80 % in field application. For the economic fin efficiency, the rib height is 306.5 mm. In addition, a smaller rib height 170.5 mm was used as the lowest level for this factor.

34.2.2 Variable Factor-2: Wall Heat Transfer Coefficient

Obviously, the wall heat transfer coefficient affects the cool discharge processes directly. Resulting from the layout difference of the wall (ceiled or vertical around placed) and the interior disturbance intensity difference (viz. interior air velocity), the wall heat transfer coefficient would be diverse. According to the Application A H O H [5], one level of the factor was set by the wall heat transfer coefficient of a cold face down steel's free convection as 9.26 W/(m^{2}K). While considering the vertical placed wall which creates vertical free heat convection, with several empirical formulas [4, 6], the lowest level of this factor was obtained as 3.99 W/(m^{2}K). And reasonable, the third level of this factor is the average of these two values, 6.5 W/(m^{2}K).

34.2.3 Variable Factor-3: The Initial Temperature of the Wall

For the emergency used heavy wall cool discharge characteristic, the initial temperature of the wall is equal to the set point of the interior temperature. Related to the field application, three set points, 22, 24, and 26 °C, were used as the three levels for this factor.

34.3 Simulation Theoretical Model

The cool discharge process of the wall mainly contains free heat convection of the inner side with a fixed free air temperature 36 °C, which is also called the third boundary condition of unsteady heat conduction problems. The control equation [7] for this heat transfer process is given here:

$$\frac{\partial t}{\partial \tau} = \frac{\lambda}{c\rho}\left(\frac{\partial^2 t}{\partial x^2} + \frac{\partial^2 t}{\partial y^2} + \frac{\partial^2 t}{\partial z^2}\right) \tag{34.4}$$

Where λ represents coefficient of thermal conductivity of the wall, $\mathrm{W}/(\mathrm{m\ k})$; c represents the specific heat of wall , $\mathrm{J}/(\mathrm{kg\ k})$; τ means variable time, s; t is the temperature inside the wall; ρ represents the density of the wall, kg/m^3

And the boundary and initial conditions for this control equation are as follows:

$$\tau = 0,\ t = t_0 \tag{34.5}$$

$$-\lambda \frac{\partial t}{\partial x}\bigg|_{x=0} = 0 \tag{34.6}$$

$$-\lambda \frac{\partial t}{\partial y}\bigg|_{y=0} = 0 \tag{34.7}$$

$$-\lambda \frac{\partial t}{\partial z}\bigg|_{z=0} = 0 \tag{34.8}$$

$$-\lambda \frac{\partial t}{\partial x}\bigg|_{x=\mathrm{l}_x} = h(t|_{x=\mathrm{l}_x} - t_f) \tag{34.9}$$

$$-\lambda \frac{\partial t}{\partial y}\bigg|_{y=\mathrm{l}_y} = 0 \tag{34.10}$$

$$-\lambda \frac{\partial t}{\partial z}\bigg|_{z=\mathrm{l}_z} = 0 \tag{34.11}$$

Where

h	wall heat transfer coefficient, W/(m^2 K)
t_f	interior room temperature, K
l_x, l_y, l_z	represent the depth, height, and width of the rib-steel heavy wall, m.

In order to study the impact of these factors on cool discharge characteristics of the wall, the following reasonable assumptions were made in the simulation:

1. The wall's initial temperature distribution is uniform and equals to indoor temperature set point due to the long-time normal operation.
2. The wall surface is a non-reflective surface, ignoring the impact of radiation heat transfer.
3. During simulation period, the wall temperature changes relatively small, so the material properties were set as constant.
4. Indoor air flow velocity is small and lies in a laminar flow state, thus the wall heat transfer coefficient can be treated as invariable parameter during the simulation period.

34.4 Simulation Results

In order to check the effectiveness of the simulation model, experiment verification for simulation case No. 5 was made. Figure 34.3 indicates that the monitor points 3/4/5 close to the interior side share a temperature difference within 0.5 °C between the simulation and experiment results. While the left 3 points 0/1/2 away from the interior side and the interior surface hold a temperature difference within 0.53 °C which is bigger than the points 3/4/5, resulting from the external environment interference and the interior measuring error. But the overall tendency of the simulation agreed well with the experiment (Fig. 34.4).

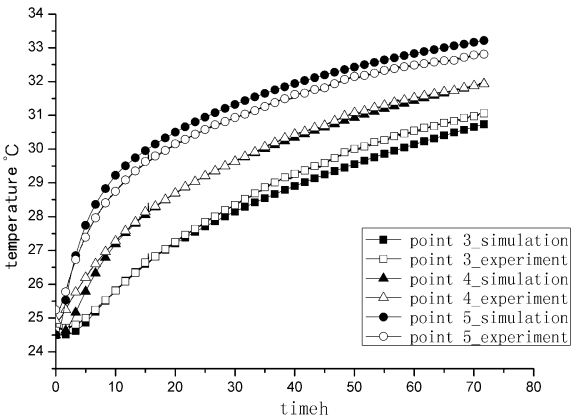

Fig. 34.3 Temperature comparison of point 3/4/5 between simulation and experiment

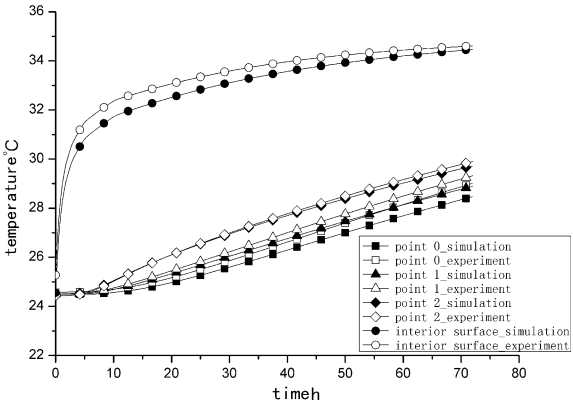

Fig. 34.4 Temperature comparison of point 0/1/2 and interior surface between simulation and experiment

34.4.1 The Influence of the Wall Heat Transfer Coefficient

Resulting from the simulation of case 1/2/3, the cool discharge rate of thee cases varies slightly (As shown in Fig. 34.5).While for its time accumulation value—cool discharge value, the increase is 11.8 % when h value changes from 3.99 to 6.50 W/(m^{2}K) and 4.6 % for h value changing from 6.5 to 9.26 W/(m^{2}K) (see Table 34.2).By use of exponential fitting, wall cool discharge rate can be formulated for the three cases, fitting formula is as follows:

$$y = A1 * \exp(-x/t1) + y0 \tag{34.12}$$

The fitting parameters summarized in the following Table 34.3:

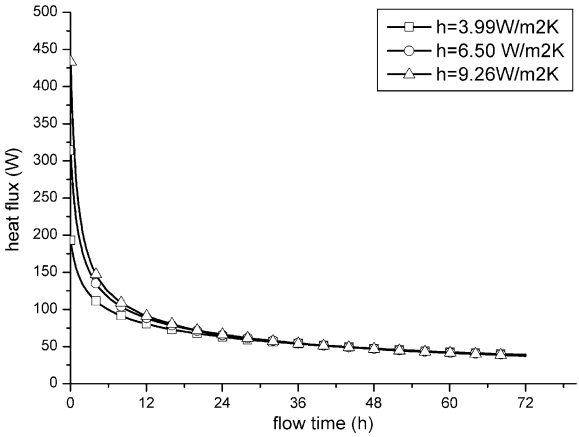

Fig. 34.5 Heat flux tendency of different wall heat transfer coefficient

Table 34.2 Wall cool discharge value of case 1/2/3

Case	1	2	3
Cool discharge value KJ	12,550.4	11,997.7	10,790.9

Table 34.3 Fitting parameters of case 1/2/3

Case	Fitting accuracy R^2	$y0$	$A1$	$t1$
1	0.95895	44.4639	103.88196	12.24605
2	0.93858	48.03911	175.44985	7.86962
3	0.92281	50.72272	251.96053	5.48132

34.4.2 The Influence of the Wall Rib Height

The simulation results (see in Fig. 34.6) of case 4/5/6 show that the cool discharge rates of the three cases vary a bit in the early 24 h. And in the latter 48 h, the cool discharge rate curves of rib height 228.6 and 170.5 mm tend to overlap each other. And the cool discharge rate curve of rib height 306.5 mm stays above other two curves. It seems that a higher enough rib can enhance the cool discharge rate during whole period. The cool discharge value of the wall increases by 5.46 % from 170.5 to 228.6 mm and 14.29 % from 228.6 to 306.5 mm (See Table 34.4). Again, exponential fitting the curve of the cool discharge rate according to formula (34.12), we get the formula parameters listed in Table 34.5.

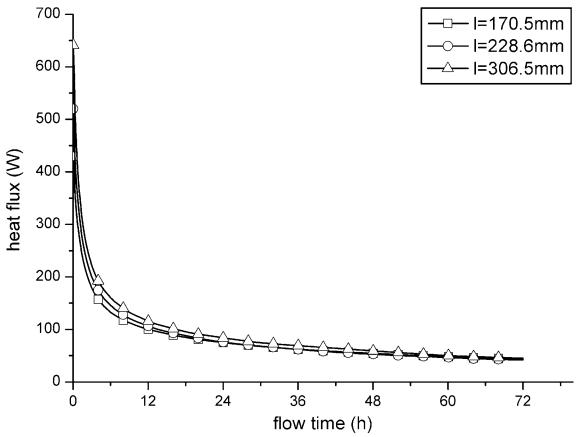

Fig. 34.6 Heat flux tendency of different rib height

Table 34.4 Wall cool discharge value of case 4/5/6

Case	4	5	6
Cool discharge value KJ	14,631.5	15,430.8	17,635.5

Table 34.5 Fitting parameters of case 4/5/6

Case	Fitting accuracy R^2	$y0$	$A1$	$t1$
4	0.92376	57.54463	245.5787	5.93541
5	0.92456	57.70925	303.59657	5.46831
6	0.91354	65.51925	377.06907	4.59666

34.4.3 The Influence of the Initial Temperature of the Wall

For the emergency used environment controlling technology, the initial temperature of the wall refers to the interior set point. In the unsteady thermal process simulation of the wall cool discharge, the initial temperature condition has a significant impact on the thermal process. And the simulation results of case 7/8/9 proved this. As the initial temperature drops from 26 to 24 °C and 24 to 22 °C, the curve of the cool discharge rate approximately moves down equivalently (See Fig. 34.7). This phenomenon leads to the cool discharge value increasing by 23.73 and 17.53 %, respectively (See Table 34.6).Exponential fitting the curve of the cool discharge rate according to formula (34.12), we get the formula parameters listed in Table 34.7.

34.5 Time Response Analysis of the Wall Discharge Processes

According to the wall cool discharge process control equation, the interpretation of the wall cooling system is a first-order linear system [8]. The interior third boundary condition corresponds to a unit pulse input signal, and the wall discharge rate corresponds to output response. Time constant of the dynamic thermal

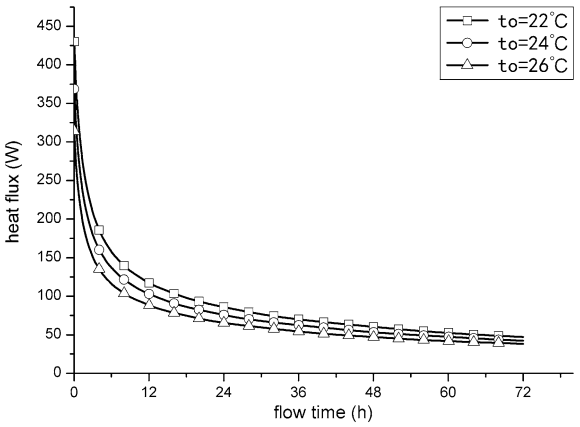

Fig. 34.7 Heat flux tendency of different wall initial temperature

Table 34.6 Wall cool discharge value of case 7/8/9

Case	7	8	9
Cool discharge value KJ	17,447.27	14,844.97	11,997.75

Table 34.7 Fitting parameters of case 7/8/9

Case	Fitting accuracy R^2	$y0$	$A1$	$t1$
7	0.94224	61.4363	251.01816	7.70373
8	0.94032	54.74354	213.63676	7.75157
9	0.93858	48.03911	175.44985	7.86962

Table 34.8 Dynamic performance index of cool discharge process

Case no.	Initial temperature °C	Wall heat transfer coefficient W/m^{2}K	Rib height mm	Time constant h
1	26	9.26	228.6	12.24605
2	26	6.5	228.6	7.86962
3	26	3.99	228.6	5.48132
4	24	9.26	170.5	5.93541
5	24	9.26	228.6	5.46831
6	24	9.26	306.5	4.59666
7	22	6.5	228.6	7.70373
8	24	6.5	228.6	7.75157
9/2	26	6.5	228.6	7.86962

response, T, equals to the fitting parameters, $t1$. This dynamic performance index T varies a lot in the nine cases (See Table 34.8). When the wall heat transfer coefficient changes from 3.99 to 9.26 W/(m^{2}K), the time constant doubles from 5.48 to 12.25 h. The rib height and initial temperature differences have not caused notable change for the time constant.

34.6 Conclusion

The cool discharge characteristic of heavy concrete wall can be influenced by a variety of factors. Within the range of simulation conditions in this study, it can be concluded as follows:

1. Judging from the wall cooling capacity discharged within 72 h, the initial temperature of the wall affects the greatest, followed by the rib height dimension, and the wall surface heat transfer coefficient holds minimal impact.
2. Referring to the dynamic thermal response characteristic within 72 h, the wall surface heat transfer coefficient affects the most, followed by the rib height dimension, and the initial temperature of the wall affects least.

3. In the actual rib-finned heavy wall design process, it can be considered initially to identify the basic wall structure parameters and indoor temperature set point at normal stage according to the storage capacity of the wall. Then numerical simulation method can be adopted to check whether the dynamic thermal response of the wall discharge processes meets actual requirements.

Acknowledgments The authors would like to acknowledge the support from the research project cooperating with Shanghai Nuclear Engineering Research & Design Institute.

References

1. Bao Q (2011) Study on thermal performance of control room emergency heat sink of large-scale new energy base. Tongji University, Shanghai
2. Zhang Y, Bao Q, Zeng B et al (2012) Thermal storage experiment of reinforced concrete specimens. HV&AC 2012(6):114–118
3. Zeng B (2012) Experiment and simulation study of charge and discharge character research on large thermal inertia wall. Tongji University, Shanghai
4. Zhang X, Ren Z, Mei F et al (2007). Heat transfer, 5th edn. China Building Industry Press, pp 45–46
5. Application A H O H (2005) American society of heating R A A E: chapter 25: thermal and water vapor transmission data
6. Mcadams WH (1954) Heat transmission. McGraw-Hill, New York
7. Tao W (2001) Numerical heat transfer, 2nd edn. Xi'an Jiaotong University Press, Xi'an
8. Wang H, Yang X, Lin J (2004) Automatic control theory. National Defense Industry Press, Beijing

Chapter 35
Coupled Heat and Moisture Transfer in Two Common Walls

Guojie Chen, Xiangwei Liu, Youming Chen, Xingguo Guo and Yingying Tan

Abstract In order to optimize building energy consumption, it is essential to reduce the heat losses and gains through the building envelope by selecting proper materials which are often porous. However, heat transfer and moisture transfer are often highly coupled, so coupled heat and moisture transfer in two common walls (aerated concrete wall and red brick wall) were studied in this paper. Aerated concrete wall is made up by aerated concrete block, cement mortar, and lime–cement mortar. It is widely used now for the superior thermal insulation of aerated concrete block. Red brick wall is made up by aerated concrete block, cement mortar, and lime–cement mortar. It was frequently used in China decades ago, and many existing building are made up by red brick wall. After a simple review of the development of models for coupled heat and moisture transfer in porous media, a dynamic model was proposed which takes into account most of the main hydro-thermal effects. It takes temperature and air humidity ratio of the porous media as the critical driving potentials. Then the model was used to simulate coupled heat and moisture transfer in both aerated concrete wall and red brick wall and then analyzed comparatively. Results show that aerated concrete wall can reduce more heat transfer than red brick wall. However, aerated concrete wall may accumulate moisture and cause moisture damage more easily.

Keywords Coupled heat and moisture transfer · Porous media · Aerated concrete wall · Red brick wall

G. Chen · X. Liu · Y. Chen (✉) · Y. Tan
College of Civil Engineering, Hunan University, Changsha 410082, China
e-mail: ymchen@hnu.edu.cn

G. Chen
College of Mechanical Engineering, University of South China,
Hengyang 421001, China

X. Guo
School of Civil Engineering and Architecture,
Nanchang University, Nanchang 330031, China

A. Li et al. (eds.), *Proceedings of the 8th International Symposium on Heating, Ventilation and Air Conditioning*, Lecture Notes in Electrical Engineering 263,
DOI: 10.1007/978-3-642-39578-9_35,

35.1 Introduction

The problems of energy consumption and environment pollution are increasing interest all over the world. In the field of building engineering, it is essential to choose building envelope material and to optimize its hydrothermal performance [1]. Aerated concrete wall is often made up by aerated concrete block and cement mortar and so on. Aerated concrete block is increasingly widely used in China in the last decades, particularly as it combines ease of construction with excellent combination of mechanical and thermal properties [2]. It was reported that the energy use in the residential buildings can be reduced by 7 % if aerated concrete block walls are used. Each square meter of this wall can save almost 350 kg of CO_2 emissions throughout its life cycle [3]. As it can also be considered environment-friendly material, it may have considerable potential for future applications [4]. However, there are also some problems for the aerated concrete wall, such as cracking of both external and internal finishes, detachment of renders from the aerated concrete block blocks, and frost failure of external render [5]. And red brick wall is often made up of red brick and cement mortar and so on. It was frequently used in China decades ago. A lot of existing buildings are red brick wall, although it has been prohibited now.

Just like most building materials, all elements of aerated concrete block wall or red brick wall are porous, composed of solid matrix and pores. In these porous materials, heat transfer is often coupled strongly with moisture transfer, especially in hot and humid climate of South China, where it is often of high value of temperature and relative humidity [6]. Accurate prediction of heat and moisture transfer in porous material is essential for optimization of building envelope with respect to energy consumption, hydrothermal performance, and indoor environment [7, 8].

Many researches have been conducted on the coupled heat and moisture transfer in porous media [9]. Glaser mold was applied widely to study the moisture damage in porous construction, but it does not take into consideration the liquid water transfer and the effect of temperature gradient [10]. Another most disseminated and accepted model is the Philip and DeVries model, which uses the temperature and moisture content gradients as driving potentials [11]. However, it is well known that there is discontinuity on the moisture content profile at the interface between two porous media. Luikov proposed a mathematical model for simultaneous heat and mass transfer in building porous materials [12]. But the solutions are either numerical or complicated involving complex eigenvalues. Also some researchers have studied coupled heat and moisture transfer in many different materials under different climate conditions [13, 14]. However, up to now, there is no enough research on coupled heat and moisture transfer in aerated concrete wall beyond hot and humid climate of South China.

In this paper, a model of coupled heat and moisture transfer in porous media was developed and used to study the coupled heat and moisture transfer in both

aerated concrete wall and red brick wall under hot and humid climate. And heat and moisture profiles in the two walls were analyzed comparatively.

35.2 Mathematical Model

This work constitutes part of an ongoing research project investigating heat and moisture transfer in building structures of South China, both experimentally and numerically. Based on the work of Budaiwi [15], a transient dynamic model is developed with the driving potentials of temperature and air humidity ratio, which is derived from conservation of mass and energy flow in a one-dimensional element volume of porous material. The phase change occurring within porous material acts as a heat source or sink, which results in the coupled heat and moisture transfer. The model is based on the following assumptions:

1. Below the maximum hygroscopic moisture content of the material, moisture content is modeled with the air moisture content as the driving potential, and instantaneous moisture equalization is assumed for higher moisture content;
2. The effect of temperature on vapor diffusion coefficients can be neglected;
3. The effect of material history and temperature on material moisture capacity can be neglected. And the average moisture equilibrium curve in terms of relative humidity will be used;
4. Moisture only exists in the form of vapor and liquid in the material and where local moisture equilibrium is always present.

The governing partial differential equations to model heat and mass transfer through porous walls are given by Eqs. (35.1) and (35.3). In the porous material, the air humidity ratio is a function of the material moisture content and temperature. The moisture transport process can be described as:

$$\frac{\partial W}{\partial t} = \frac{W_s}{\xi \rho_m}\left(D_v R_v T_m \rho_a + \frac{\xi \rho_m}{W_s} D_w\right)\frac{\partial^2 W}{\partial x^2} + \phi \frac{\partial W_s}{\partial T}\frac{\partial T}{\partial t} \tag{35.1}$$

At both sides of the wall, the corresponding boundary conditions can be written as:

$$-D_v R_v T_m \rho_a \frac{\partial W}{\partial x} = h_m (W_\infty - W_{\text{surf}}) \tag{35.2}$$

where T_m is material temperature, W air humidity ratio (W_s for saturated one), D_v material vapor diffusion coefficient, D_w material liquid water diffusion coefficient, ξ slope of moisture equilibrium curve, ρ_m density of material (ρ_a for air), R_v water vapor characteristic constant, ϕ relative humidity, h_m surface mass transfer coefficient, W_∞ ambient air moisture content, W_{surf} surface moisture content.

The thermal transport process can be described as:

$$(\rho_m c_{vm})\frac{\partial T}{\partial t} = K\frac{\partial^2 T}{\partial x^2} + h_{fg}D_v R_v T_m \rho_a \frac{\partial^2 W}{\partial x^2} \tag{35.3}$$

It shows that the temperature variation is due to heat conduction and the phase change of water.

The corresponding boundary conditions can be written as:

$$-k\frac{\partial T}{\partial t} = h_c(T_\infty - T_{\text{surf}}) + h_{fg}D_v R_v T_m \rho_a \frac{\partial W}{\partial x} \tag{35.4}$$

where K is the heat conduction coefficient, $c_{vm}$the material specific heat, h_{fg} latent heat of water vaporization, h_c surface mass transfer coefficient, T_∞ ambient air moisture content, T_{surf} surface moisture content.

This model has been proved valid for the coupled heat and moisture transfer in porous media by experiments, whose results show that the simulation results agree well with field measurements [16].

35.3 Computation and Analysis

This chapter focuses on a multi-layer porous building envelope named as aerated concrete wall, which is built up from outside to inside of cement mortar (20 mm), aerated concrete block (240 mm), and lime–cement mortar (20 mm). And the comparison object is red brick wall, which is built up from outside to inside of cement mortar (20 mm), red brick (240 mm), and lime–cement mortar (20 mm). Red brick was frequently used in China for a long time, and many existing buildings are red brick wall. However, it is gradually prohibited for its consumption of land sources and energy. Properties of these materials are obtained from IEA Annex 24, as showed in Table 35.1. It can be found that the two kinds of walls are all the same except the middle material.

The inner surface and outer surface of both two walls are named as surface one and surface two. And for both walls, the interface connecting lime–cement mortar and red brick (or aerated block) is named as interface one and the interface connecting red brick (or aerated block) and cement mortar is named as interface two. Changsha is one of the typical regions of hot and humid climate in South China. This simulation was performed for the two walls using the typical meteorological data for the outdoor condition as shown in Fig. 35.1. The temperature of

Table 35.1 Material properties of tested walls

	$\rho_v/(\text{kgm}^{-3})$	$K/(\text{Wm}^{-1}\text{K}^{-1})$	$c_{vm}/(\text{Jkg}^{-1}\text{K}^{-1})$	$D_v/(\text{kgm}^{-1}\text{Pa}^{-1}\text{s}^{-1})$
Cement mortar	1,807	1.93	780	5.4×10^{-11}
Lime–cement mortar	1,600	0.81	920	1.2×10^{-11}
Red brick	1,923.4	1.21	840	2.9×10^{-11}
Aerated concrete block	600	0.384	1,050	2.5×10^{-11}

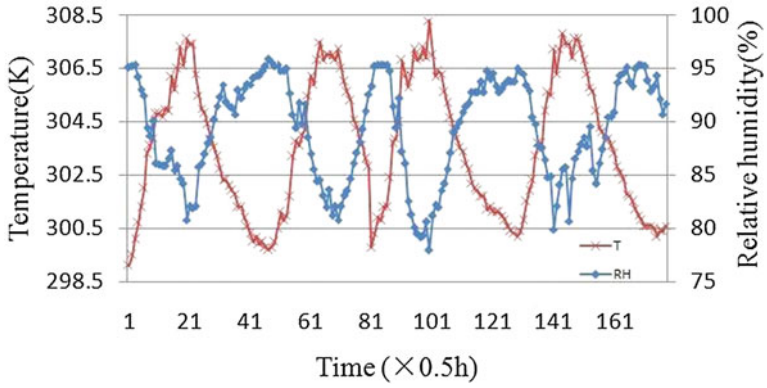

Fig. 35.1 Outdoor temperature and relative humidity

indoor air keeps 297 K and relative humidity 60 %. The temperature and moisture content of the construction layers were initially assumed to be uniform.

Figures 35.2 and 35.3 show the temperature at different sites of red brick wall and aerated concrete wall, respectively. We can find that for red brick wall the temperature gradient is located at red brick and for aerated concrete wall at aerated concrete block, which is the result of the large thickness and large thermal resistance. And the temperature gradient in aerated concrete block is larger than red brick. For both two walls, temperature fluctuation at surface two is more volatile than interface two, followed by interface one and surface one in that order. That is the result of damping effect of the materials. Also, we can find that for both two walls, interface one is mainly affected by indoor conditions and interface two by outdoor conditions.

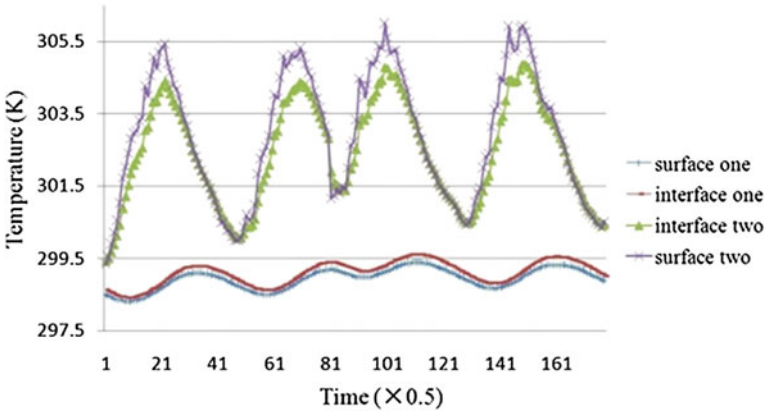

Fig. 35.2 Temperature at different sites of red brick wall

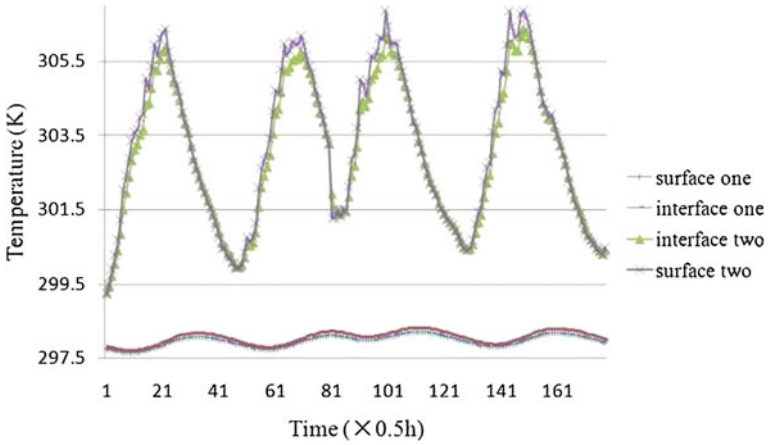

Fig. 35.3 Temperature at different sites of aerated concrete wall

Comparing Figs. 35.2 and 35.3, we can find that at surface two and interface two of aerated concrete wall, temperature is higher than that of red brick wall, and at surface two, temperature of aerated concrete wall can be 0.8 °C higher than red brick wall, at interface two about 1.5 °C. It must be the result of the larger thermal capacity and less thermal conductivity of aerated concrete block. And it is also the reason of the lower temperature at surface one and interface one of aerated concrete wall, and at surface one, temperature of red brick wall can be 1.1 °C higher than aerated concrete wall, at interface one about 1.3 °C. So, it is obvious that less heat can transfer through aerated concrete wall than red brick wall, and building built by aerated concrete block can save more energy than by red brick.

Figures 35.4 and 35.5 show air moisture content at different sites of red brick wall and aerated concrete wall, respectively. We can find that for both two walls, the air moisture content at surface one is larger than interface one and interface

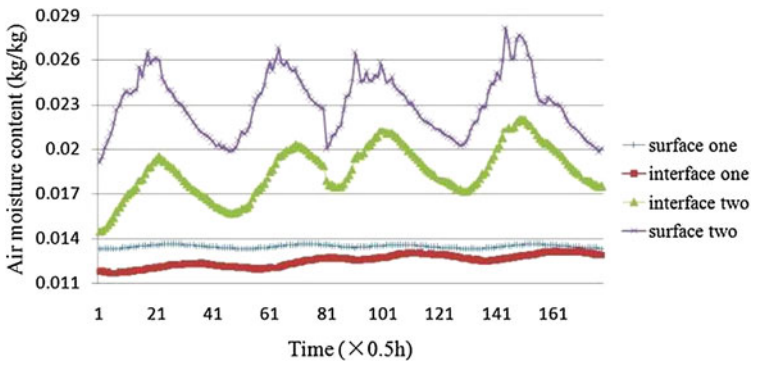

Fig. 35.4 Air moisture content at different sites of red brick wall

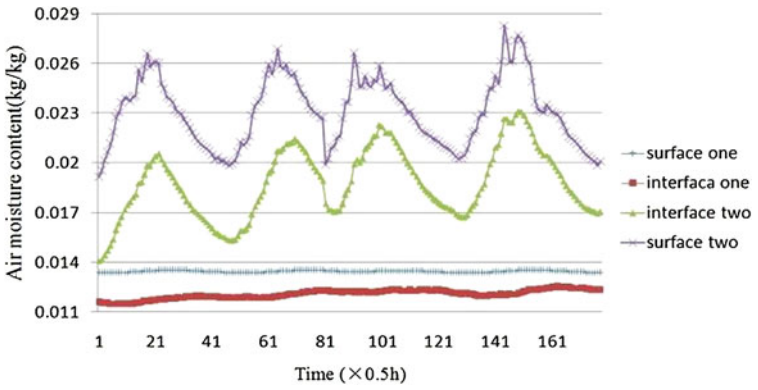

Fig. 35.5 Air moisture content at different sites of aerated concrete wall

two larger than surface two, which indicates that moisture transfer toward wall from both outside and inside under this condition.

Comparing Figs. 35.4 and 35.5, we can find that at the interface two of aerated concrete wall air moisture content is about 4.9 % larger than that of red brick wall at most. With the larger moisture content, it is easier to condensate and cause moisture damage for aerated concrete wall than red brick wall. More attention should be given on moisture transfer and moisture accumulation in aerated concrete wall.

35.4 Conclusion

In order to save energy and ease the environmental burden, there is an increasing interest to decrease the building energy consumption all over the world. Aerated concrete is widely used in building engineering for its light weight and low thermal conductivity. However, as a porous material, it easily suffers from moisture damage, especially in the hot and humid climate of South China. And red brick was frequently used in China decades ago. A lot of existing buildings are red brick wall, although it has been prohibited now.

A transient dynamic model was developed with the driving potentials of temperature and air humidity ratio. And then, this model was used to simulate coupled heat and moisture transfer in both aerated concrete wall and red brick wall. From the results, we can find that aerated concrete wall can reduce more heat transfer than red brick wall. But more attention should be given on moisture transfer and moisture accumulation in aerated concrete wall, because it more easily accumulates moisture and causes moisture damage.

Acknowledgments This research work was financially supported by a grant from the Natural Science Foundation of China (Contract No. 51078127, 51208247, 51178170). The authors wish to express their gratitude for this financial support.

References

1. Osanyintola OF, Simonson CJ (2006) Moisture buffering capacity of hygroscopic building materials: experimental facilities and energy impact. Energy Build 38(10):1270–1282
2. Chen HJ (2009) Applied research on aerated concrete wall. Constr Sci Technol 3:32–33
3. Drochytka R, Zach J, Korjenic A et al (2013) Improving the energy efficiency in buildings while reducing the waste using autoclaved aerated concrete made from power industry waste. Energy Build 58:319–323
4. Narayanan N, Ramamurthy K (2000) Structure and properties of aerated concrete block: a review. Cem Concr Block Compos 22:321–329
5. Jerman M, Keppert M, Výborný J et al (2013) Hygric, thermal and durability properties of autoclaved aerated concrete block. Constr Build Mater 41:352–359
6. Qin MH, Belarbi R, Aït-Mokhtar A et al (2009) Coupled heat and moisture transfer in multi-layer building materials. Constr Build Mater 23(2):967–975
7. Mendes N, Winkelmann FC, Lamberts R et al (2003) Moisture effects on conduction loads. Energy Build 35(7):641–644
8. Daniel A, Vries DE (1987) The theory of heat and moisture transfer in porous media revisited. Int J Heat Mass Transf 30(7):1343–1350
9. Woloszyn M, Rode C (2008) Tools for performance simulation of heat, air and moisture conditions of whole buildings. Build Simul 1(1):5–24
10. Glaser H (1958) Graphical method for investigation of diffusion process. Kalteohnik, German
11. Philip JR, DeVries DA (1975) Moisture movement in porous materials under temperature gradients. Trans Am Geophys Union 2:222–232
12. Luikov AW (1966) Heat and mass transfer in capillary-porous bodies. Pergamon Oxford, UK
13. Qin MH, Walton G, Belarbi R et al (2011) Simulation of whole building coupled hygrothermal-airflow transfer in different climates. Energy Convers Manage 52(2):1470–1478
14. Su XH, Ang HS (2003) A method to solve the multilayer non-continuity problem for heat and moisture transfer in building structures. Commun Numer Methods Eng 19:933–944
15. Bubaiwi I, EI-Diasty R, Abdou A (1999) Modeling of moisture and thermal transient behavior of multi-layer non-cavity walls. Build Environ 34:537–551
16. Guo XG, Chen YM (2008) Computational analysis of heat and moisture performance of multilayer wall in south China. J Central South Univ Technol 114(3):106–110

Chapter 36
Dynamic-Load Compensation Method and Simulation of the Heat-Supply Control System

Yanling Zhang and Yongming Song

Abstract Air temperature compensators were used currently to change the set value of the return-water temperature in heat-supply control systems according to outdoor temperature. However, the great inertia effect makes it difficult to control the return-water temperature to be stable, and changing the set value will increase disturbance factors to the system. A new method based on the dynamic-load compensation was proposed in the paper, in which the disturbance effects of outdoor temperature to indoor temperature can be overcome rapidly and the stationarity of the return-water temperature control can be improved effectively. And the simulation results have corroborated the effects of the dynamic-load compensation.

Keywords Heat-supply system · Dynamic-load compensation · Temperature control

36.1 Introduction

The control system of heating room temperature is complex with a large inertia effect. It is characterized by the adjusting time of the control system for too long and obvious overshoot. So that the traditional control strategy is difficult to achieve good quality of control [1–3]. The heating room temperature is usually taken as controlled object. The precision of heating control system is low and the dynamic characteristic is unsatisfactory. This article studies to take the return-water

Y. Zhang (✉) · Y. Song
School of Thermal Energy Engineering, Shandong Jianzhu University, Jinan, China
e-mail: sjdyanling@163.com

Y. Song
Key Laboratory of Renewable Energy Utilization Technologies in Buildings, Ministry of Education, Jinan, China
e-mail: songym99@163.com

A. Li et al. (eds.), *Proceedings of the 8th International Symposium on Heating, Ventilation and Air Conditioning*, Lecture Notes in Electrical Engineering 263,
DOI: 10.1007/978-3-642-39578-9_36,

temperature of radiator as the controlled object and the outdoor temperature as a feed-forward signal of the heating control system. The heating control system is able to quickly overcome the disturbance effects of the outdoor temperature to room temperature. It has high control precision and quick speed of response.

36.2 Mathematical Model of the Heating Room Temperature Control System

36.2.1 Mathematical Model of the Controlled Object

For a heated room, the indoor temperature field is very complex. In order to simplify the calculation, the indoor room temperature is simplified by using the method of lump heat capacity. Average temperature of the indoor heat capacity is represented by the following formula:

$$t_n = \frac{\sum_{i=1}^{n} t_{ni} C_i}{\sum_{i=1}^{n} C_i} = \frac{\sum_{i=1}^{n} t_{ni} C_i}{C} \tag{36.1.1}$$

where t_n is the average temperature of room, t_{ni} is the temperature of room at each point, C_i is the heat capacity of room at each point, and C is the total heat capacity of room.

Through the above analysis, t_n can be described the temperature of entire room. In order to analyze easily, the dynamic characteristic of the controlled object is approximately described by low-order mathematical model as long as meeting certain precision of control. According to the energy conservation law, the heat balance equation of radiator is established as follows:

$$C_r \frac{\mathrm{d}t_r}{\mathrm{d}\tau} = cq(t_s - t_{re}) - k_1 F_1 (t_r - t_n) \tag{36.1.2}$$

where C_r is the heat capacity of radiator, c is the specific heat capacity of water, t_r is the surface temperature of radiator, q is the mass flow rate of the radiator, t_s is the inlet water temperature of radiator, t_{re} is the outlet water temperature of the radiator, k_1 is the heat transfer coefficient of radiator, F_1 is the heat transfer area of radiator, and t_n is the temperature of the heating room.

Make $t_r = (t_s + t_{re})/2, q_2 = q_1 + \Delta q, t_{s2} = t_{s1} + \Delta t_s, t_{re2} = t_{re1} + \Delta t_{re}, t_{n2} = t_{n1} + \Delta t_n$ into the Eq. (36.1.2). Incremental equation is described as follows:

$$C_r \frac{\mathrm{d}(\Delta t_s + \Delta t_{re})/2}{d\tau} = c_w \Delta q(t_s - t_{re}) + c_w q_1(\Delta t_s - \Delta t_{re}) - k_1 F_1((\Delta t_s + \Delta t_{re})/2 - \Delta t_n) \quad (36.1.3)$$

The simplification of Eq. (36.1.3) is established as follows:

$$T_1 \frac{\mathrm{d}t_{re}}{\mathrm{d}\tau} + t_{re} + T_1 \frac{\mathrm{d}t_s}{\mathrm{d}\tau} + Ct_s = K_1 q + K_2 t_n \quad (36.1.4)$$

In which $T_1 = \frac{C_r}{k_1 F_1 + 2q_1 c}$, $C = \frac{k_1 F_1 - 2q_1 c}{k_1 F_1 + 2q_1 c}$, $K_1 = \frac{2c(t_{s1} - t_{re1})}{k_1 F_1 + 2q_1 c}$, $K_2 = \frac{2k_1 F_1}{k_1 F_1 + 2q_1 c}$

The Laplace transform of Eq. (36.1.4) is described as follows:

$$(T_1 s + 1)t_{re}(s) + (T_1 s + C)t_s(s) = K_1 q(s) + K_2 t_n(s) \quad (36.1.5)$$

The transfer function of controlled object is established as follows:

$$G_p(s) = \frac{t_{re}(s)}{q(s)} = \frac{K_1}{T_1 s + 1} \quad (36.1.6)$$

36.2.2 Mathematical Model of the Disturbance Object

The outdoor temperature is the main external disturbance factor of heating room temperature. According to the energy conservation law, the heat balance equation of indoor temperature is established as follows:

$$C_n \frac{\mathrm{d}t_n}{\mathrm{d}\tau} = k_1 F_1(t_r - t_n) - k_2 F_2(t_n - t_0) \quad (36.1.7)$$

where C_n is the heat capacity of heating room, k_2 is the heat transfer coefficient of building envelope, F_2 is the heat transfer area of building envelope, and t_0 is the outdoor temperature.

The Laplace transform of Eq. (36.1.7) is described as follows:

$$(C_n s + k_1 F_1 + k_2 F_2)t_n(s) = k_1 F_1 t_r(s) + k_2 F_2 t_0(s) \quad (36.1.8)$$

The transfer functions of disturbance object are established as follows:

$$G_{f1}(s) = \frac{t_n(s)}{t_0(s)} = \frac{k_2 F_2}{C_w s + k_1 F_1 + k_2 F_2} \quad (36.1.9)$$

$$G_{f2}(s) = \frac{t_{\mathrm{re}}(s)}{t_{\mathrm{n}}(s)} = \frac{K_2}{T_1 s + 1} \quad (36.1.10)$$

36.3 Design of Heating Room Temperature Control System

PID algorithm is used as the master controller of heating room temperature control system. System inertia effect and time delay are eliminated by use of feed-forward controller, which uses outdoor temperature as feed-forward signal. The structure of control system is shown in Fig. 36.1. The heating control system enables eliminate indoor temperature fluctuation caused by outdoor temperature room temperature fluctuation. Overshoot and adjustment time of the control system are decreased.

The system output in the disturbances is described as follows:

$$Y(s) = t_0(s)G_f(s) + t_0(s)G_{xk}(s)G_v(s)G_p(s) \tag{36.2.1}$$

The condition to achieve full compensation for the disturbance is established as follows:

$$G_f(s) + G_{xk}(s)G_v(s)G_p(s) = 0 \tag{36.2.2}$$

In order to achieve full control system anti-interference, transfer function of the feed-forward controller is described as follows:

$$\begin{aligned} G_{xk}(s) &= -\frac{G_f(s)}{G_v(s)G_p(s)} = -\frac{K_2k_2F_2/((C_ws + k_1F_1 + k_2F_2)(T_1s+1))}{k_4K_1/((T_1s+1)(T_2s+1))} \\ &= K_{ff}\frac{T_2s+1}{T_3s+1} \end{aligned} \tag{36.2.3}$$

in which $K_{ff} = -K_2k_2F_2/(K_1k_4)$ $T_3 = C_ws/(k_1F_1 + k_2F_2)$.

The diagram of feed-forward controller is shown in Fig. 36.2.

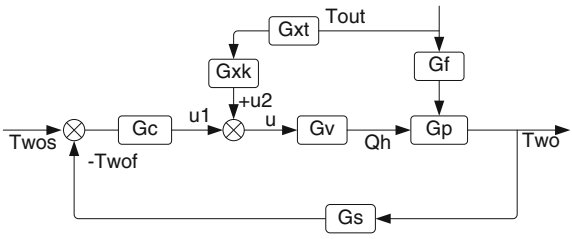

Fig. 36.1 Structure of heating room control system

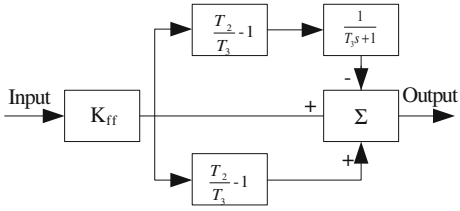

Fig. 36.2 Diagram of feed-forward controller

36.4 Simulation and Discussion of Heating Room Temperature Control System

An actual heating system is taken as the example. A simulation is given by MATLAB/Simulink. System parameters are shown in Table 36.1. Simulation system program of the heating room temperature is established, which is shown in Fig. 36.3.

The indoor temperature is interfered by an outdoor temperature in the 40 min. In order to analyze the comparison, the response curves of return-water temperature with and without dynamic-load compensation are shown in same coordinate system in Fig. 36.4. Simulation results show that the heating room control system with dynamic-load compensation can overcome rapidly disturbance effects of outdoor temperature to indoor temperature in 15 min. The adjustment time of control system is greatly reduced. Its dynamic characteristic is improved well.

Table 36.1 System parameters of heating room temperature control system

Simulation parameter	Unit	Numerical value	Simulation parameter	Unit	Numerical value
Area of room	m^2	120	Heat transfer coefficient of radiator	w $(m^2°C)^{-1}$	7.99
Outdoor temperature	°C	−10	Heat capacity of radiator	J $°C^{-1}$	233,856
Indoor temperature	°C	18	Heat capacity of room	J $°C^{-1}$	460,400
Return-water temperature	°C	50	Heat transfer coefficient of building envelope	w $(m^2 °C)^{-1}$	1.6
Flow rate of radiator	kg s^{-1}	0.16	Area of building envelope	m^2	38

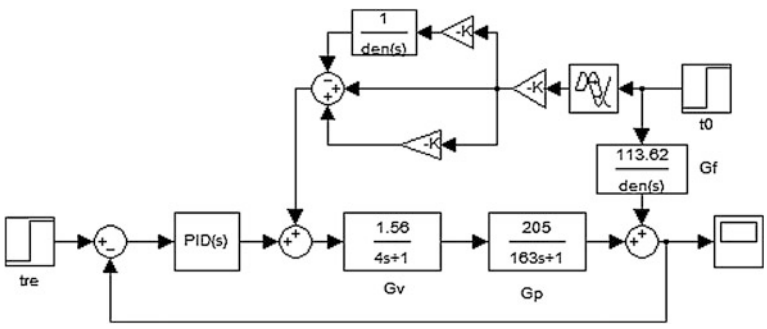

Fig. 36.3 Simulation system program of the heating room temperature

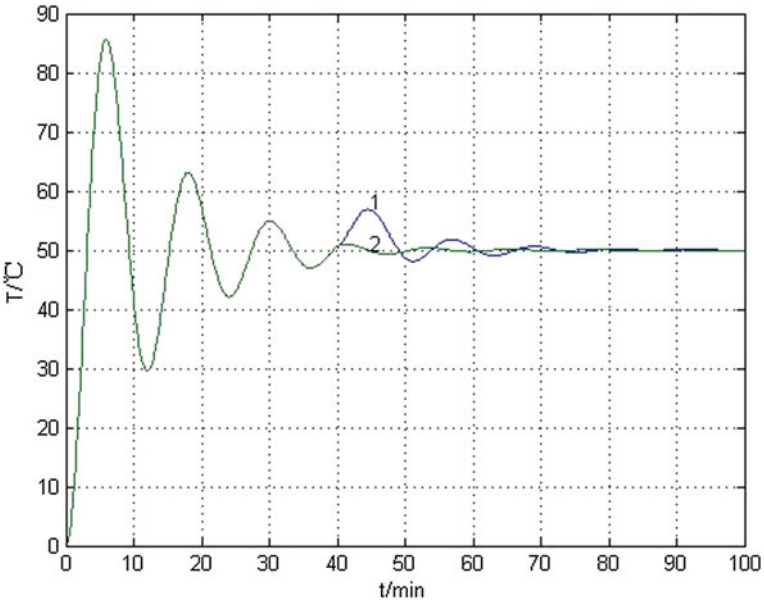

Fig. 36.4 *1* Response curves of return-water temperature without dynamic-load compensation. *2* Response curves of return-water temperature with dynamic-load compensation

36.5 Conclusion

The control system with dynamic-load compensation gives superior performance in terms of temperature regulation and disturbance rejection. The control system has a good response to the stability and accuracy. The adjustment time of control system is greatly reduced. Its dynamic characteristic is improved well. The method overcomes the limitations of simple PID control. The control system has certain application value in the heating room temperature control system.

References

1. Lianzhong L, Zaheeruddin M (2004) A control strategy for energy optimal operation of a direct district heating system. Int J Energy Res 28(7):597–612
2. Yang J-K (2007) The optimization of heating patterns and the research of hot network control strategy in small cities of China. Tongji University, Shanghai
3. Ying-hong DUAN (2008) Research of predictive fuzzy-PID controller in temperature of central air-condition system. J Syst Simul 3:020

Chapter 37
Numerical Study of the Return Air Characteristics in the Stratified Air-Conditioning System with Middle Sidewall Air Return Intakes

Huan Wang, Chen Huang and Qianru Zhang

Abstract For energy efficiency and better IAQ, stratified air distribution (STRAD) systems with low sidewall air supply (LSAS) and middle sidewall air return (MSAR) are even more used nowadays in large-space buildings. Located between the air-conditioning zone (ACZ) and non-air-conditioning zone (NACZ), the air return opening will intake air flow from both sides. In order to study the air flow characteristics near the air return opening computational fluid dynamic (CFD) is used. CFD physical model is built in accordance with the dimension of the reduced-scale model. A steady-state simulation is conducted first for the calculation of the steady temperature and velocity field, and then, the air in ACZ and NACZ is marked separately with the 'Same Property and Different Name' method which is although the gas in both zones has different names, they share the same physical property with the normal air. After that, transient simulation with species transport equations continues to simulate and log the fraction of species in the air return flow. By evaluating the fraction of the species within return air flow, the proportion of return air from NACZ and ACZ can be calculated. By further processing the temperature and cooling capacity of each zone can also be demonstrated. These above mentioned can provide reference to the calculation of the total heat transferred from the NACZ to the ACZ which is critical to the cooling load of a large-space building.

Keywords Same property and different name · Stratified air-conditioning · Numerical simulation study · Middle sidewall return air

H. Wang (✉) · C. Huang · Q. Zhang
University of Shanghai for Science and Technology, Shanghai 200093, China
e-mail: wanghuan4610@gmail.com

A. Li et al. (eds.), *Proceedings of the 8th International Symposium on Heating, Ventilation and Air Conditioning*, Lecture Notes in Electrical Engineering 263,
DOI: 10.1007/978-3-642-39578-9_37,

37.1 Introduction

In large-space buildings, stratified air distribution (STRAD) systems with low sidewall air supply (LSAS) and middle sidewall air return (MSAR) have been widely used for their better performance in energy efficiency and thermal comfort [1]. Located on middle sidewall, the air return openings will intake air from both the non-air-conditioning zone (NACZ) and the air-conditioning zone (ACZ); the temperature and flow rate can determine the cooling capacity of the system. With the computational fluid dynamic (CFD), this study conducted several cases using the Same Property and Different Names (SPDN) method to distinguish the air from different zones, aiming at the flow thermal characteristics near the air return intakes.

STRAD systems used in normal office building have been widely studied and a lot of achievements have been made, including the distribution of temperature, thermal comfort, cooling load capacity calculation, and so on [2–9]. However, the study on the usage of STRAD in large-space buildings, especially about flow characteristics and temperature of return air as well as the impact of location and direction of air return intakes is rarely reported.

37.2 Description of the Object

The research target is the STRAD system of a large space, using the LSAS and MSAR. The air distribution of this system is different from the ordinary system because it sets return air grilles in the middle sidewall of the large space, between the ACZ and the NACZ. This is also where a large temperature gradient exists. The STRAD system always has a large supply air volume, and hence, a large return air volume which has a direct impact on the cooling load, so the study of the where the air flow from, its temperature, and the volume of the return air is of great importance. In order to study the influence of multiple factors more clearly, and verify the simulation better, the research adopts a reduced-scale test chamber to model a typical large space, and the physical model is constructed according to the reduced-scale test chamber.

37.3 Description of the Characteristics of the Thermal Environment in Large Space with LSAS

The downside air supply system is adopted by more and more large-space buildings because of the energy-saving potential and the comfortable sensation it provides. However, some new situations come up when the stratified air-conditioning system with downside air supply and central air return is applied to

the large-space buildings. Firstly, large-space building has high ceilings and heavy cooling load, so the temperature gradient is grater and the temperature of the ceiling can reach 50 °C [10], and the radiant heat transfer between walls become a non-ignorable factor [11]. Secondly, as a result of the small air supply temperature difference and large air volume of the stratified air-conditioning system, usual offices always adopt small return air volume and the upper warm air is exhausted to the outside environment. In the application of the large-space building, considering the large cold capacity needed per square meter, if most of the return air is not handled, the total air volume and the cold capacity will increase. Thirdly, the activity areas of the large space is very small comparing to the whole building, so the main target of the air-conditioning system is to guarantee the comfort of the activity areas. So it is more important to distinguish the thermal stagnant zone (the ACZ) and the NACZ in order to reduce the air-conditioning energy consumption. According to the existed documents, the well-running stratified air-conditioning system can save 30 % more energy than ordinary air-conditioning system [12]. All the above characteristics make the thermal environment in a large space with downside air supply different from the usual air supply system and also reflect the urgency of the research.

37.4 Physical Modeling and Case Configuration

In this study, the large-space thermal comfort laboratory in USST which has the typical size and STAD system is selected as the prototype model (19.8*14*10 m), the scale of the reduced-scale model is set to 1:4. CFD model is built in accord with the reduced-scale model. The reduced scale is 4.9 m long, 3.5 m wide, and 2.5 m high; the distance between two air supply distributors is 1.2 m. The half-cylinder distributor heights 310 mm and diameter is 150 mm. The air return opening is 100 mm in diameter and located 1.125 m high. According to air return openings, the NACZ includes the space above 1.125 m. On the contrary, the ACZ covers the space below. As the whole building is symmetry in width direction, symmetry plane is located in the middle of the space, as shown in Fig. 37.1.

Two directions of return air openings are selected, horizontal intake and downward intake, combined with two different air supply flow rate, 4 cases as listed in Table 37.1 are calculated for the cooling load in NACZ and ACZ.

37.5 CFD Model Validation and Boundary Conditions

The CFD simulation consists 2 parts: steady-state simulation of the distribution of speed and temperature and transient species transport simulation with the SPDN method.

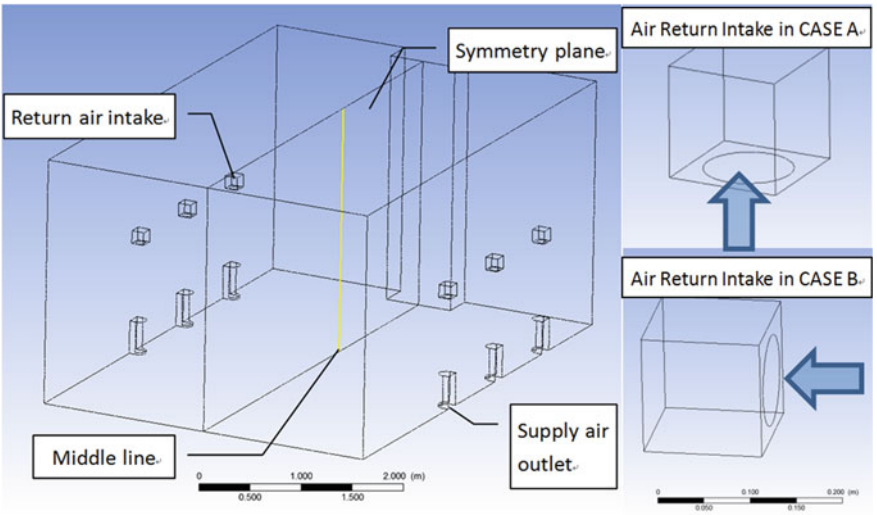

Fig. 37.1 Physical model

Table 37.1 Case list

No.	Description	Wall (W/m^2)	Ceiling (W/m^2)	Supply rate (m/s)	Supply temperature (°C)
Case A-1	Downward return	25	70	0.2	15
Case A-2		25	70	0.4	15
Case B-1	Horizontal return	25	70	0.2	15
Case B-2		25	70	0.4	15

37.5.1 Steady-State Simulation

Steady simulation is used to solve the distribution of temperature and flow distribution for the basic information to conduct transient species transport simulation. Turbulence is described with RNG k-e model which is capable to simulate convective heat transfer of buoyancy-driven airflow as long as reasonable value of y+ is achieved [13, 14]. Boussinesq hypothesis is adopted for density calculation, and enhanced wall treatment is used for near wall calculation. Mesh near outlets and inlets are partially refined and the mesh near walls are adjusted through testing to ensure that the y +value is lower than 10. The size of the mesh reaches 900–1,000 thousand. The S2S model is used to calculate the radiant heat exchange, the emissivity of wall is set to 0.5, ceiling 0.4, and the heat flux is 70 W/m^2 for ceiling and 25 W/m^2 for walls while the floor is set to be adiabatic.

37.5.2 SPDN in the Study of the Return Air Flow Fraction

In the design and calculation of cooling load in large-space building, the return air flow fraction of the air flow from NACZ and ACZ has more guiding significance. Therefore, this study uses the SPDN method to evaluate the return air flow fraction.

The SPDN method is to introduce the species transport equations based on the steady simulation result, and then, the air in the space is marked differently for its location or other characters but share the exact same property, after that, transient simulation begin to capture the flow characters within zone. In this study, 1.125 m height is selected as the interface; then, the above zone is marked as the NACZ air while the below zone is marked as the ACZ air. In the following, transient species transport simulation starts on the result of steady temperature and flow distribution. The transient species transportation simulation aims at the trace the flow and mixing of these two species and records the fraction of each species at the outlet surface. During the transient species transport simulation, only species transport equations are solved for decreasing both the residuals and calculation time.

Through the entire process, SPDN mark is conducted only once, so this process is unsteady, but during the calculation, the outlet fraction of each species can remain relatively constant for a long period of time; therefore, these relatively stable time points are selected as study targets. The determination for a stable time point includes the mass flow rate fluctuation of each species is no more than 1e-4(kg/s2), the other gas concentration in all zones is limited to 1 %, and the point with less mass flow rate fluctuation is set to be the stable time point for each case. After the stable time point is set, the detailed data of the each mesh on the outlet surface is picked out which including temperature, velocity, density, species fraction, and each area size. Here, the character in each cell is considered homogeneous. To calculate the flow rate of each species, Eq. (37.1) is used.

$$\dot{m}_k = \sum_{i=1}^{n} \rho_i \vec{v_i} \vec{A}_i F_k \tag{37.1}$$

where $\dot{m}_k$ refers to the mass flow rate on the outlet surface, ρ is the density, v refers to the vertical speed, A is the area size, F is the mass species fraction, and n is the number of mesh on the surface.

The equation for calculating the temperature of each species refers to

$$T_k = \frac{\sum_{i=1}^{n} \rho_i \vec{v_i} \vec{A}_i F_k \cdot T_i}{\sum_{j=1}^{n} \rho_j \vec{v_j} \vec{A}_j F_k} \tag{37.2}$$

At last, the cooling load is got with equation

$$Q = \dot{m} c_p \cdot (T - 15) \tag{37.3}$$

where $\dot{m}$ is mass flow rate, cp is heat capacity, T is return air temperature, and 15 refers to supply air temperature.

37.6 Analysis of Cases with Different Return Air Direction

The vertical air temperature distribution in each case is demonstrated in Fig. 37.2; as the temperature on each horizontal plain differs very little, the temperature on the middle line of the room is selected to demonstrate the vertical air temperature distribution. Generally, the temperature distribution follows the same tendency, and the slope increases greatly near the height of return openings. One thing has to be point out is that, due to the larger turbulence caused by the horizontal placed air return intakes, the temperature is higher in CASE B. Another phenomenon is that, besides the limited zones close to the return air intakes, the temperature difference between CASE A and CASE B is not very large, which means the impact of the air return intakes does not spread wider space.

37.6.1 Analysis of the Result from SPDN Method

Table 37.2 shows the return air flow rate, temperature, and corresponding cold capacity. By preparation, the research shows that the proportion of the return air is closely related to the direction of return air. The return air of non-air-conditioned area in CASE A accounts for 27 % while in CASE B 49 %. In the stratified

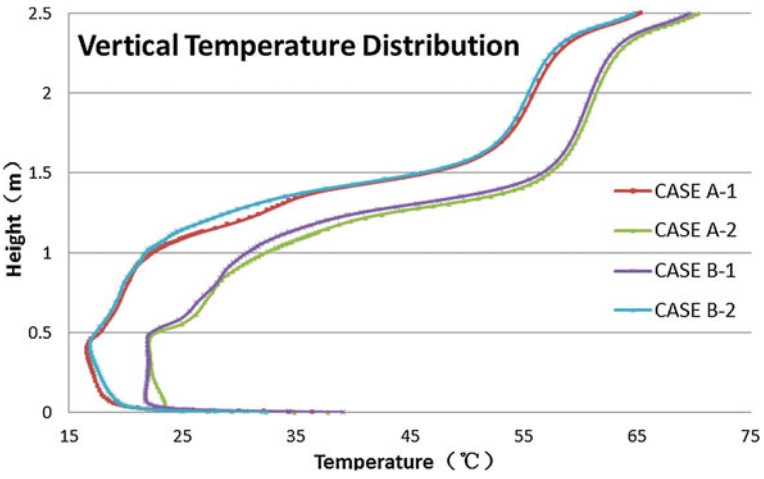

Fig. 37.2 Vertical temperature distribution in the room

Table 37.2 Return air data in cases

		Return air flow rate (kg/s)	Return air fraction	Return air temperature (°C)	Average temperature (°C)	Cooling load (W)	Cooling load fraction
Case A-1	NACZ	0.0134	0.2607	37.268	58.221	300.21	0.2973
	ACZ	0.0380	0.7392	33.565	26.029	709.54	0.7026
	Total			34.753	43.752	1,009.75	
Case A-2	NACZ	0.0297	0.2884	28.151	50.342	392.26	0.3875
	ACZ	0.0732	0.7115	23.425	19.251	619.87	0.6124
	Total			24.788	36.368	1,012.12	
Case B-1	NACZ	0.0250	0.4852	37.811	57.321	572.19	0.5555
	ACZ	0.0265	0.5147	32.205	25.447	457.73	0.4444
	Total			34.978	42.949	1,029.91	
Case B-2	NACZ	0.0500	0.4854	27.952	49.530	650.03	0.6256
	ACZ	0.0529	0.5145	22.312	19.068	388.89	0.3743
	Total			25.063	35.795	1,038.92	

Notes NACZ refers to *non-air-conditioning zone*, while ACZ refers to *air-conditioning zone*

air-conditioning system, the temperature in the NACZ is higher than that of the ACZ apparently, which leads to the higher whole cold capacity of the horizontal air return case than that of the vertical air return case. While in the aspect of the calculated cold capacity, the cold capacity in non-air-conditioned zone is less than that in air-conditioned zone in the vertical air return case, while the opposite in the horizontal case.

The increase in air supply volume will also make the mixing intensity increase evidently. Hence, more heat is transferred from non-air-conditioned zone to the air-conditioned zone. After the supply air volume increases, the cold capacity of the air-conditioned zone declined because of the decrease in the air-conditioned zone temperature while the cold capacity in non-air-conditioned zone increases to a large extent, especially in the horizontal air return case with a large air volume. In terms of the average temperature of the two zones, the average temperature of the horizontal air return cases are all lower than that of the vertical air return cases, which reflects the better uniformity and effectiveness in cold capacity distribution of the horizontal air return cases. But it is necessary to point out that one of the aims of the stratified air-condition system is to guarantee the required temperature of the activity area.

37.7 Conclusion

The research adopts CFD as a tool to construct a mathematical model according to the reduced-scale model of the actual building, mark the air in different areas with SPDN method, introduce the component transport equation, and study the return air composition near the return air grille.

The research also achieves air return composition under several different air volumes and return air grille angles, which provides a reference for the study of return air heat composition and the load calculation of the stratified air-conditioning system with downside air supply.

Acknowledgments This work is financially supported by the Leading Academic Discipline Project of Shanghai Municipal Education Commission (J50502) and the National Natural Science Foundation of China (51108263; 51278302).

References

1. Cheng Y, Niu J, Gao N (2012) Stratified air distribution systems in a large lecture theatre: a numerical method to optimize thermal comfort and maximize energy saving. Energy Build 55:515–525
2. Bauman F (2003) Underfloor air distribution (UFAD) design guide. American Society of Heating, Refrigerating and Air-Conditioning Engineers Inc, Atlanta
3. ASHRAE (2009) Nonresidential cooling and heating load calculations, In: ASHRAE Handbook 2009, Fundamental, ASHRAE Publication, Atlanta, USA, 2009. (Chapter 18)
4. Chen QY, Glicksman L (2003) System performance evaluation and design guideline for displacement ventilation. American Society of Heating, Refrigerating and Air-Conditioning Engineers Inc, Atlanta
5. Loudermilk KJ (1999) Underfloor air distribution solutions for open office applications. ASHRAE Trans 105:605–613
6. Schiavon S, Lee KH, Bauman F, Webster T (2010) Simplified calculation method for design cooling loads in underfloor air distribution (UFAD) systems. Energy Build 43:517–528
7. Kong Q, Yu B (2008) Numerical study on temperature stratification in a room with underfloor air distribution system. Energy Build 40(4):495–502
8. Nielsen P, Hoff L, Pedersen L (1988) Displacement ventilation by different types of diffusers. Conference on effective ventilation
9. Zhang Z, Chen Q (2006) Experimental measurements and numerical simulations of particle transport and distribution in ventilated rooms. Atmos Environ 40:3396–3408
10. Ning C, Weiwu H (2011) Study on a simultaneously solving model for stratified air conditioning under low sidewall air supply system in a large space building. J Refrig 4339:1–6
11. Huang C, Li ML, Zou ZJ et al (2000) Experiment and energy analysis of indoor thermal environment in a large space. Heating Ventilating and Air Conditioning 30(6):52–55
12. Fan CY (2001) Design of air conditioning in large space and project record. China Building Industry Press, Beijing
13. Niu JL, van der Kooi J (1992) Grid-optimization for k–ε turbulence model simulation of natural convection in rooms. In: Proceedings ROOMVENT-92: air distribution in rooms: third international conference, vol. 1, 1992, pp 207–224
14. Chen Q, Srebric J (2002) A procedure for verification, validation, and reporting of indoor environment CFD analyses. HVAC&R Res 8(2):201–216

Chapter 38
Influence of Urban Highway Tunnel Upper Vents Groups Number on Natural Ventilation Efficiency

Zhiyi Huo, Enshen Long and Jun Wang

Abstract For natural ventilation, setting upper vents of urban highway tunnel is one possible method for improving the environment and the outlet of the tunnel. In this present paper, one 1,000 m tunnel is chosen as the analysis object, according to the universal size of road tunnel. The relationship between the number of upper vents groups and pollutant dispersion in the tunnel was analyzed with aid of the subway environment simulation (SES) simulation software. The results show that the urban highway tunnel with upper vents can emit pollutant along the tunnel. Meanwhile, for the same quantity, total area of the vents and a certain vents spans, two vent groups are the best type of ventilation, from which about 50 % pollutant emission can be emitted. In addition, the single group is the worst type of ventilation, from which only 37 % pollutant emission can be emitted.

Keywords Urban highway tunnel · Upper vent · Natural ventilation · Simulation

38.1 Introduction

As tunnels are constructed more and more in the city and people's awareness of energy saving gradually increases, tunnel with natural ventilation is becoming universal. Urban highway tunnel has the characteristics of heavy traffic flow,

Z. Huo
Institute of Building Energy Efficiency and Human settlement,
Sichuan University, Chengdu, China
e-mail: huozhiyi2008@163.com

E. Long (✉) · J. Wang
College of Architecture and Environment, Sichuan University,
Chengdu, China
e-mail: longes2@163.com

J. Wang
e-mail: wangjunhvac@163.com

A. Li et al. (eds.), *Proceedings of the 8th International Symposium on Heating, Ventilation and Air Conditioning*, Lecture Notes in Electrical Engineering 263,
DOI: 10.1007/978-3-642-39578-9_38,

shorter length. Therefore, piston wind can be utilized in the tunnel to improve the air environment. Meanwhile, if all pollutants emit to the atmosphere around the tunnel outlet, the environment may be polluted. In order to solve this problem, a possible chose is setting vents in the roof of the tunnel and the pollutants can be discharged to the outside along the tunnel, which reduces the amount of pollutants exhausting at tunnel outlet. Researches in this area have begun in the past few years before [1–9]. Zhong analyzed the changes of piston wind in the vent and obtained the calculation method of the tunnel's natural ventilation. He also analyzed the distribution of pollutants and the conversion relationship of correlation index between the experimental model and prototype as well by establishing an experimental platform. Hu established one mathematical model of relationship between vent's airflow and carbon monoxide (CO) concentration. In this present study, the effect of urban highway tunnel vents groups number on natural ventilation efficiency is analyzed.

38.2 Model and Methods

With the rapid development of computer technology, the study about highway tunnel ventilation has become more efficient. Meanwhile, many kinds of modeling software have been developed, such as subway environment simulation (SES), train operation and aerodynamic program in tunnel system (TOAPITS), Tehran Metro Environment Control Software (EnCs). Based on the 1D theory of flow analysis and the results of experimental studies, SES has been developed as a 1D design program for subway ventilation systems in the mid-1970s, which has been utilized in many subway design processes and modified and supplemented. The results derived from the SES have high precision.

In order to evaluate the effect of urban highway tunnel vents groups number on natural ventilation efficiency, a simplified road tunnel model is adopted in this study, as shown in Fig. 38.1.

The model has length of 1,000 m and a full-scale cross section of width of 12 m and height of 5 m. There are 15 vents, which are numbered as vent 1, vent 2,…, vent 15. Each vent is 3 m long, 12 m wide, and 4 m high. The vehicle is 5 m long, 2 m wide, and 1.1 m high. Vehicle driving air upward, namely piston wind, realizes the natural ventilation of tunnel. The tunnel has a three-lane highway, which has potential interfering with each other. Assume that vehicles are running side by side is applied for minimize the interfering of vehicles. The schedule of the

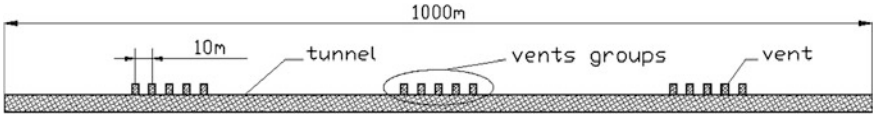

Fig. 38.1 Schematic diagram of tunnel with upper vents groups

vehicle run is as follows. When it runs at a constant speed of 20 km/h ($v = 20$ km/h), traffic is 3,600 a/h. As it runs at a constant speed of 40 km/h (as $v = 40$ km/h), traffic is 5,400 a/h.

38.3 Results and Discussion

The conditions for analysis include that the total number of vents is 15, each vent has area of 36 m^2, and the interval of two neighboring vents is 10 m. Four levels of s of urban highway tunnel vents groups number are considered, containing 1, 2, 3, and 5. Variation of airflow and CO concentration are shown in Figs. 38.2, 38.3, 38.4, and 38.5 for two kinds of car speed.

Figure 38.2a and b show the variations of airflow in the tunnel and vent under the conditions of different speeds. It can be found that the amount of airflow is changing in the tunnel, owing to the exchange between the inside and outside air of tunnel through vents. Some pollutants in the airflow are discharged through vents, which reduces pollutant amount of tunnel. Moreover, some fresh airflows into tunnel to dilute pollutants concentration. Figure 38.2c shows the CO concentration distribution in tunnel. It can be seen that vent 1, vent 2, vent 3, vent 13, vent 14,

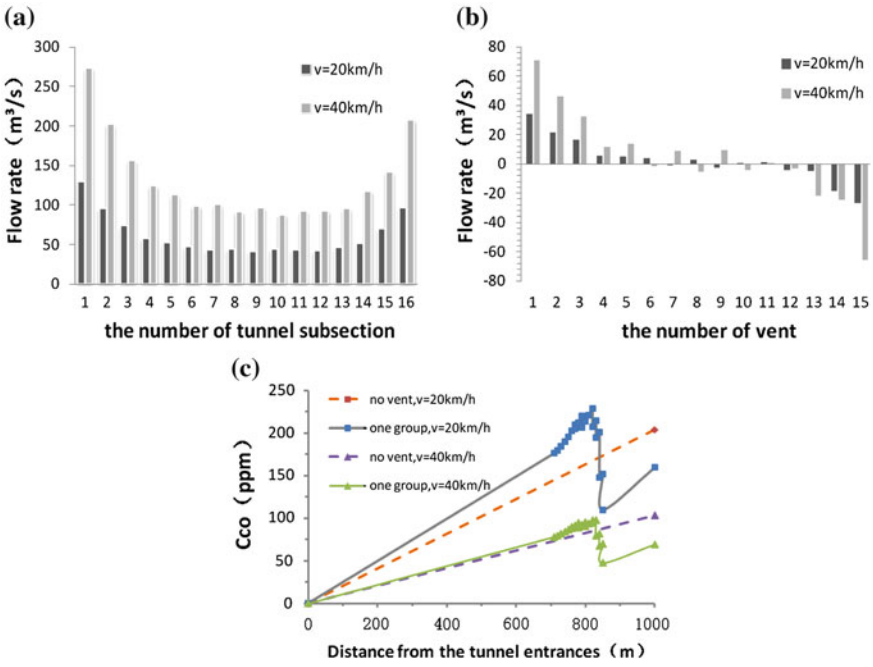

Fig. 38.2 The single vent groups. **a** Airflow in the each tunnel subsection. **b** Airflow in the each vent. **c** CO concentration in tunnel

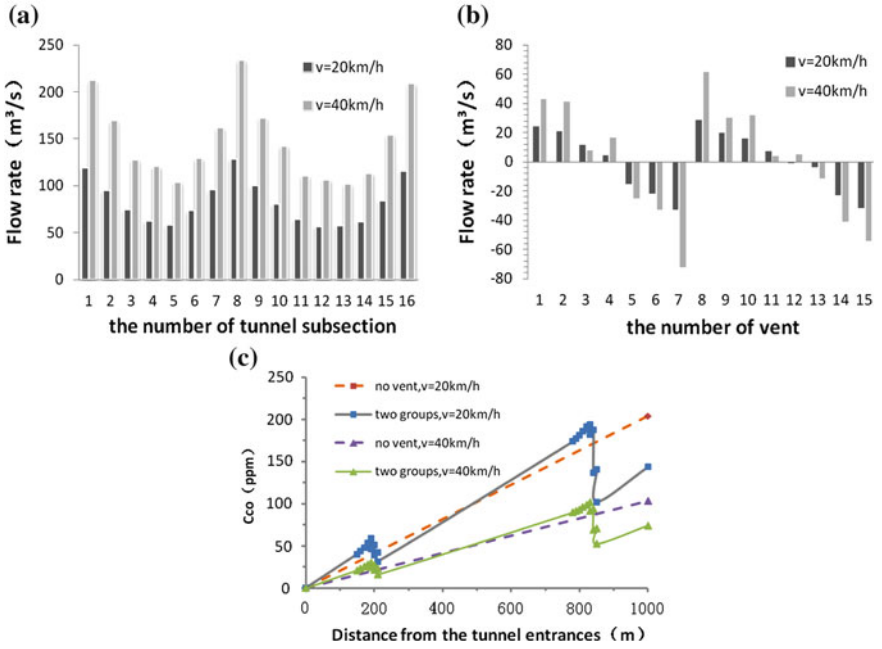

Fig. 38.3 Two vents groups. **a** Airflow in the each tunnel subsection. **b** Airflow in the each vent. **c** CO concentration in tunnel

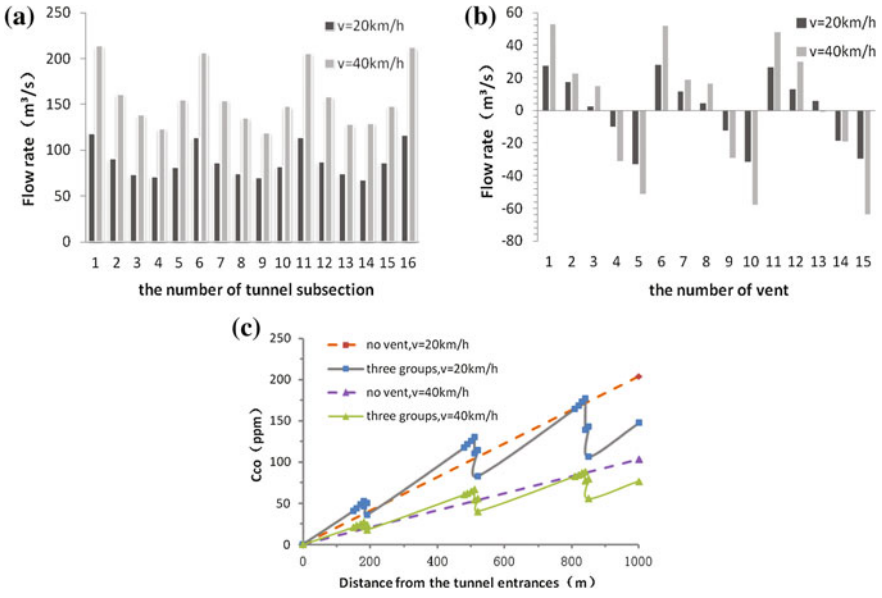

Fig. 38.4 Three vents groups. **a** Airflow in the each tunnel subsection. **b** Airflow in the each vent. **c** CO concentration in tunnel

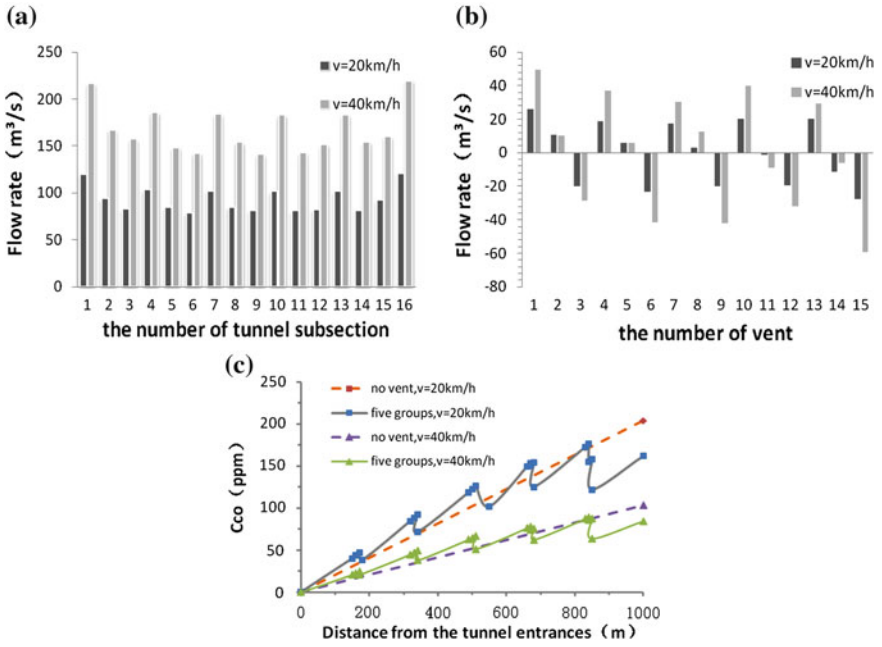

Fig. 38.5 Four vents groups. **a** Airflow in the each tunnel subsection. **b** Airflow in the each vent. **c** CO concentration in tunnel

vent 15 have higher ventilation than others, the vents 1–3 have the air intake effect, the vents 13–15 have the ventilation effect. CO concentration at the outlet of tunnel with upper vents is lower than that of tunnel without upper vents, as increase in airflow makes pollutants be diluted. But the situation is opposite in some segments, because airflow is reduced by ventilation effect of vents.

It can be observed from Fig. 38.3, 38.4, and 38.5 that airflow and CO concentration behave cyclical variations. CO concentration at the outlet of tunnel with upper vents is lower than that of tunnel without upper vents. So, we can draw a conclusion that tunnel having upper vents is conducive to air environment. Meanwhile, in order to determine the best number of urban highway tunnel vents groups, one evaluation index, emission rate of CO through vents, is introduced. Table 38.1 shows that emission of CO (Qco) through outlet of tunnel and that through vents.

It can be seen from Table 38.1 that emission of CO through outlet of tunnel is lower than that of tunnel without upper vents. The maximum emission rate of CO is appearing when the tunnel has two vents groups.

Table 38.1 Emissions of CO (m^3/s) under different number of urban tunnel vents groups

v (km/h)	No vents		Single vent groups		Two vents groups	
	Qco	Emission rate	Qco	Emission rate (%)	Qco	Emission rate (%)
20	0.0288	0	0.01812	37.09	0.01433	50.24
40	0.027	0	0.01685	37.61	0.0133	50.76

v (km/h)	Three vents groups		Five vents groups	
	Qco	Emission rate (%)	Qco	Emission rate (%)
20	0.01504	47.79	0.01726	40.07
40	0.0143	47.05	0.0165	38.88

38.4 Conclusions

The natural ventilation performance of urban highway tunnel under different vents group number was evaluated. The following conclusions can be drawn:

1. Under normal conditions, airflow and wind speed increase with the vehicles speed, but it is inverse for CO concentration.
2. When tunnel has vents groups, airflow and CO concentration behave cyclical variations, which do not change with vehicles speed.
3. The CO concentration get higher along tunnel, but it has abrupt change in tunnel with upper vents.
4. The percentage for maximum emission rate of CO is 50.76 %, when the tunnel has two vents groups.

Acknowledgments The authors gratefully acknowledgment the financial support from China Postdoctoral Science Foundation under Grant No. 2012M511930 and the National Natural Science Foundation of China under Grant No. 51178282.

References

1. Lin CJ, Chuah YK, Liu CW (2008) A study on underground tunnel ventilation for piston effects influenced by draught relief shaft in subway system. Appl Therm Eng 28:372–379
2. Kim JY, Kim KY (2009) Effects of vent shaft location on the ventilation performance in a subway tunnel. J Wind Eng Ind Aerodyn 97:174–179
3. Boulard T, Feuilloley P, Kittas C (1997) Natural ventilation performance of six greenhouse and tunnel types. J Agric Eng Res 67:249–266
4. Ke MT, Cheng TC, Wang WP (2002) Numerical simulation for optimizing the design of subway environmental control system. Build Environ 37:1139–1152
5. Hu LH, Tang F, Yang D, Liu S, Huo R (2010) Longitudinal distributions of CO concentration and difference with temperature field in a tunnel fire smoke flow. Int J Heat Mass Transf 53:2844–2855

6. Li JSM, Chow WK (2003) Numerical studies on performance evaluation of tunnel ventilation safety systems. Tunn Undergr Space Technol 18:435–452
7. Underwood S, Macdonald M (1999) Automatic detection system for a longitudinally ventilated tunnel'. In: Proceedings of tunnel control and instrumentation and communications systems for tunnels, ITC
8. Zhong X, Gao H, ,Gong B (2006) Discussion on natural ventilation action principle of traffic wind force. J Railway Eng Soc 5(Ser. 95), Aug 2006
9. Tong Y, Su R, Gong Y (2011) Study on influence factors about airflow and pollution distribution for road tunnels with shafts under natural ventilation condition. Build Sci 27(6), Jun 2011

Chapter 39
Study on Air Distribution Characteristics of Air Orifice Plate in CRH6 Intercity Rail

Haiying Wang, Chunfang Li and Songtao Hu

Abstract The train industry is developing quickly in China. At the same time, the comfort of carriages is getting more and more attention. As the dimension of carriage is quite limited, the supply air of air-conditioning system should be dispersed in very short distance to avoid draught sensation. Among the existing supplying systems, the orifice plate has the following advantages: short jet flow range, well diffused, and mix flow field. If orifice plate was mounted at the top of the carriage, piston flow can be formed easily and the thermal comfort can be improved. The diameter of hole on the orifice plate and percentage of open area on the plate are important factors affecting its flowing performance. In this paper, we studied the effect of perorate rate on flow characters inside the carriage. The CFD model of CRH6 intercity rail with orifice plate was set up to simulate the air distribution. Experiment was also carried out to verify the reliability of the CFD models. The effect of different open area on uniformity of air distribution was further investigated. The velocities on selected cross sections were compared. The results showed that as the percentage of perforate rate (PR) decreased, the difference of air velocity in the occupant zone became larger, the air distribution tended to worse. It was also found that the flow uniformity were quite similar when the open area was larger than 7.1 %.

Keywords Air distribution · Orifice plate · CFD

H. Wang (✉) · C. Li · S. Hu
Qingdao Technological University, No.11 Fushun Road, Qingdao, China
e-mail: why3305@126.com

A. Li et al. (eds.), *Proceedings of the 8th International Symposium on Heating, Ventilation and Air Conditioning*, Lecture Notes in Electrical Engineering 263,
DOI: 10.1007/978-3-642-39578-9_39,

39.1 Introductions

The train industry in China is developing quickly in recent years. The passenger train is upgrading in the direction of faster and more comfortable. The air-conditioning system installed on train improves the environment of carriage and the competitiveness of the railway transportation [1]. Thermal comfort is one of the important factors evaluating carriage environment. Among the six factors affecting thermal comfort, air temperature, velocity, and their distribution are related to the air supplying systems on train. So, the layout of supplying system is very important to the comfort of the carriage.

In order to improve the air distribution of carriage, a variety of supply systems have been developed based on different carriage structures [2–4]. The orifice plate supply system has the following characters: short jet flow range, well diffused, and mixed flow field [5]. These characters lead to the widely use of orifice plate in air-conditioned spaces, where there are strict requirements on temperature field and velocity field. The carriage holds a lot of people, yet the space is quite limited. To achieve comfort and uniformity of air distribution in carriage, orifice plates would be a good choice. Actually, orifice plate supplying system has been applied in some trains [6]. Studies on orifice supplying system are mainly about the flow resistance and supply plenum [6–8]. Research about the effect of orifice plate structures, like diameter of holes and perforate rate (PR) of the plate, on air distribution is quite limited. In this paper, the effect of PR on air distribution applied in CRH6 intercity train will be studied.

39.2 CFD Modeling

The model of CRH6 carriage along with the orifice supplying system was set up. Then, the model was calculated in FLUENT. Experiment was carried out in an experiment carriage to verify the accuracy of simulation. After that, orifice plate air supplying systems with different PR were further modeled to investigate the effect of PR on air distribution.

39.2.1 Introduction of the Train

The CRH6 has three kinds of carriage: the head carriage, first class carriage, and second class carriage. We studied the head carriage and its total length was 25 m. The carriage is shown in Fig. 39.1. The driver's cab was separated by walls from the passenger car. The air distribution in the passenger car was studied.

Figure 39.2 shows the top view of the air-conditioning system with air conditioners, ducts, and outlets. There were two air-conditioning units installed at the

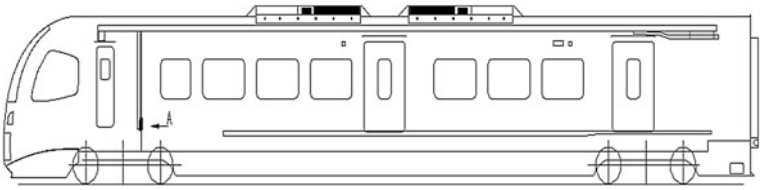

Fig. 39.1 Side view of the carriage

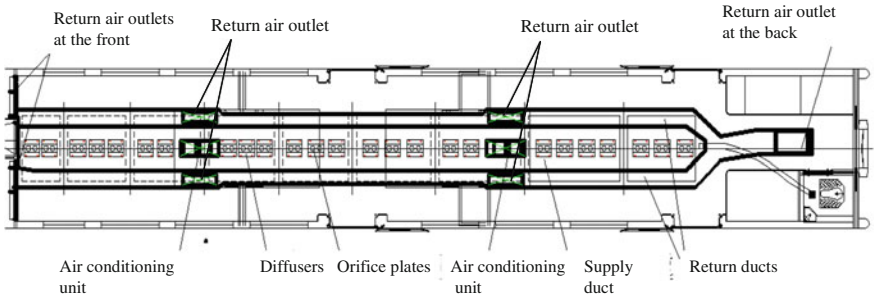

Fig. 39.2 Top view of the air-conditioning system

Fig. 39.3 Profile of the carriage

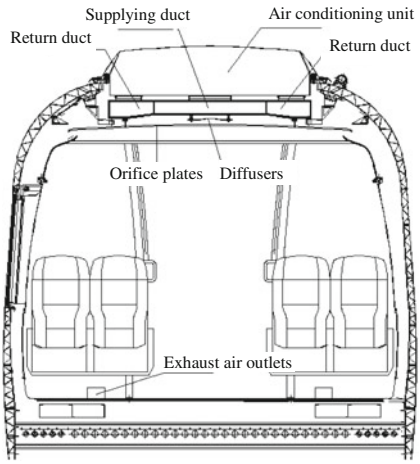

middle top of train. The fresh air and return air flowed by the air-conditioning units to the supplying duct. Then, it passes the diffusers and flows to the plenum as shown in Fig. 39.3. Finally, the air ran through the orifice plated into the carriage. The diffusers were used to distribute the air into the plenum uniformly. The orifice plates were mounted at the bottom of the plenum, so the air flew downward form the middle top of the ceilings.

39.2.2 The CFD Modeling

The physical model of the carriage is set up and meshed in Gambit, see Figs. 39.4 and 39.5. The calculation was made based on the following assumptions [9, 10]:

1. The gas in simulation is incompressible fluid and satisfies the Boussinesq hypothesis, e.g., the changes of fluid density changes affect the buoyancy only.
2. The flow is turbulent flow.
3. The viscosity of fluid is isotropic in all dimensions.
4. The heat dissipation by viscosity work is neglected at low-speed flow.

The total supply air volume designed was 7,000 m^3/h. The fresh air volume was 1600 m^3/h, and the return air volume was 5,400 m^3/h. Air velocity was assigned at the boundary of outlets according to their flow volumes.

The k-ε turbulence model was used in the calculation [11]. For the solution of the model, the finite volume method was used. Because of the limited length of paper, details about the governing equations would not be listed here.

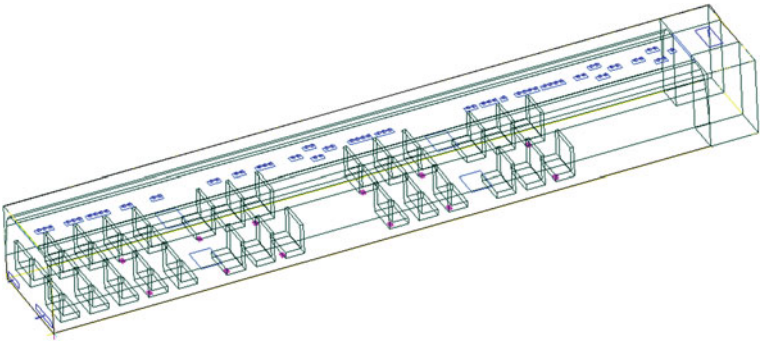

Fig. 39.4 Physical model of the carriage

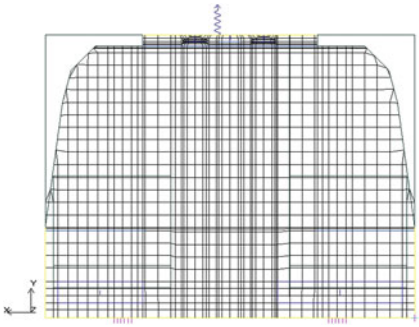

Fig. 39.5 Profile of model meshing

39.3 The Verification of CFD Simulation

In the experimental carriage, the thickness of orifice plates was 3 mm. The diameter of holes was 6 mm. The distance between holes was 32 mm, and the percentage of PR was 2.8 %. The physical model was set according to the information.

Three cross sections inside the carriage are selected to compare the simulation results with the experiments, see Fig. 39.6. Twenty points on each section are chosen, as shown in Fig. 39.7. The height of the points were 0.1 m, 0.5 m, 1.2 m, 1.7 m, corresponding to the height of foot, knee, shoulder, and head of passengers, respectively.

The experiment is carried out in the experimental carriage, which is arranged in the same way with the actual carriage, see Fig. 39.8. Before experiment, the supply air volume and return air volume was adjusted close to the designed values. In the experiment, velocity of the twenty points on each section was tested by the multipoint anemometry system (KANOMAX 6242, Japan).

Figure 39.9 shows the velocity distribution on the three sections, which is from the CFD simulation. The correctness of CFD simulation should be confirmed. The velocity simulated and tested is compared in Fig. 39.10.

From Fig. 39.10, it could be seen that the prediction of CFD is very close to the experimental results. The mean difference between CFD and experiment was 0.052 m/s. Considering the simplification and assumptions in CFD calculation, the calculation was still accurate.

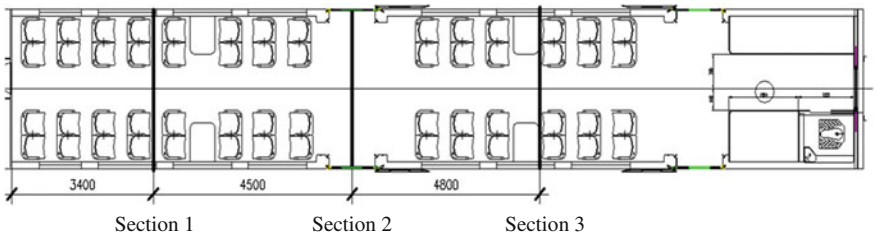

Fig. 39.6 Location of three sections

Fig. 39.7 Location of 20 points on each section

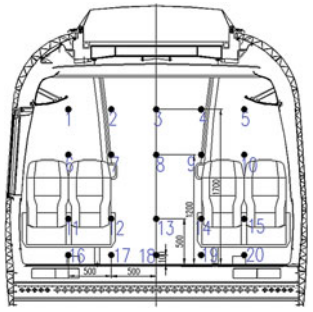

Fig. 39.8 Experimental carriage

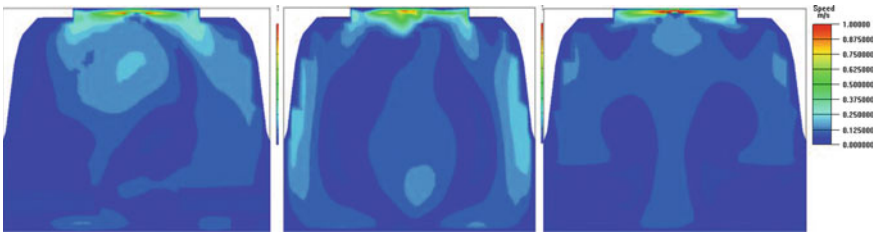

(Section 1) (Section 2) (Section 3)

Fig. 39.9 Velocity contour of the three sections

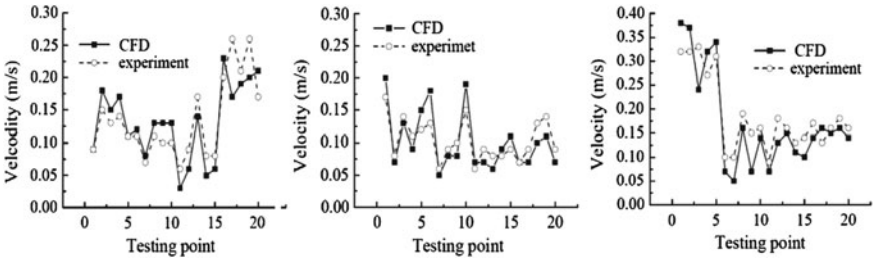

(Section 1) (Section 2) (Section 3)

Fig. 39.10 Comparison of CFD modeling and experiment

The air distributions of the three sections were different. The velocities of section 2 were much more uniform than sections 1 and 3. On section 1, velocity at point 16–20 (the foot position) was larger than the other points. On section 3, the

high velocity points were number 1–5 (the head position). This was caused by the unevenly assigned return/exhaust air outlets. The exhaust air outlet closed to section 1 was located under the seat, while the return air outlet close to section 3 was at the top of the ceiling.

Although the air distributions were not quite the same on the three sections, the total velocity difference was not too large. For 83.8 % points, the velocity was in the range of 0.05–0.2 m/s. This was the advantage of orifice plate supply system.

39.4 The Effect of PR on Air Distribution

In order to make clear the effect of PR (PR) of orifice, we further simulated 4 kinds of arrangement, which is shown in Table 39.1.

In the simulation, the calculation circumstances were kept same, except the PR of orifice plate.

The CFD simulation results for five PR conditions are shown in Fig. 39.11.

The velocity distribution was affected by PR. As PR increased, the velocity fields tended to be more uniform. For three PR conditions (28.3, 14.4, and 7.1 %), the velocity distributions of three sections were quite similar and uniform. The mean velocity of each section was less than 0.17 m/s, which satisfied the thermal comfort requirement of standard [12]. When PR was 2.8 %, the flow speed at foot position on Section 3 increased. When PR was 1.5 %, the flow speeds at foot and head both increased on section 3. As PR decreased, the air speed through the orifices would increase and the mixture of jet flow became worse. According to analysis, the suggested PR should no less than 2.8 %. Since the air distribution changed little when PR was larger than 7.1 %, the reasonable PR should not be too large considering the manufacture and intensity of orifice plate.

Table 39.1 PR of orifice simulated (including the PR already simulated)

The distance between holes (mm)	10	14	20	32	44
PR (%)	28.3	14.4	7.1	2.8	1.5

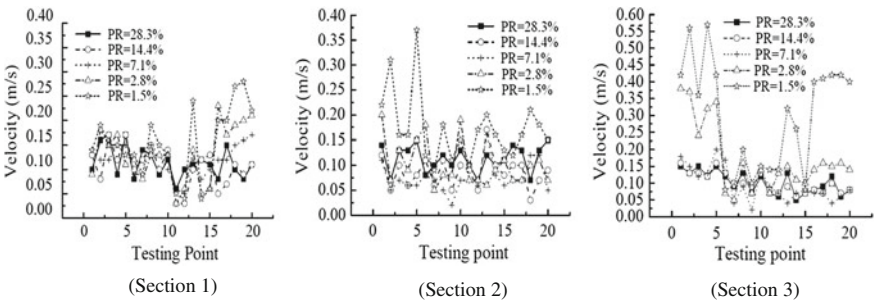

Fig. 39.11 Comparison of air distribution at different PR

39.5 Conclusions

In this paper, we simulated the air distribution of CRH6 carriage. The CFD simulation was verified by experiments. The results showed that PR of orifice plate affected the uniformity of air distribution. When PR was less than 2.8 %, the air distribution in the carriage was not satisfying. When PR was greater than 7.1 %, the air distribution was quite similar and satisfying.

References

1. Zhang G, Lian Z, He J et al (2001) Investigation and analysis of comfortability on air-conditioned passenger cars. Roll Stock 39(9):14–15
2. Lian Z, Zhang G, Ye X (2004) Evaluation of air distribution in an air conditioned railway carriage. J Shanghai Jiaotong Univ 38(6):961–966
3. Tan Y (2001) Structural analysis and test research on static pressure air supply duct. Roll Stock 39(6):11–13
4. Zhou J, Zhou Y (2005) Performance experimentation about supplying, returning air duct of air-conditioning Ruanwo train & research of correlative items. Railway Locomotive Car 25(1):41–43
5. Burhan C, Yahya EA, Ahmet OT (2007) An experimental study on the effects of uniform injection through one perforated surface of a square cylinder on some aerodynamic parameters. Exp Thermal Fluid Sci 31(8):909–915
6. Jianbin Z, Yawei W, Jia C (2011) Experiments on performance of air supply orifice in rail vehicle. J China Railway Soc 33(12):33–37
7. Guohui G, Affa BR (1997) Pressure loss characteristics of orifice and perforated plates. Exp Thermal Fluid Sci 14:160–165
8. Zhu C, Zhang X (2010) Study on flow resistance of supply orifice. In: The HVAC & R conference of China, pp 513–517
9. Zhao B, Li X, Yan Q (2002) Numerical simulation of air jet from perforated panels. Mech Eng 24(1):18–21
10. Wang D, Zhao W, Ma S (2007) Application of CFD numerical simulation in high speed train design. J China Raiway Soc 29(5):64–68
11. Wang F (2004) Computational fluid dynamics analysis—the theory and application of CFD software. Publishing house of Tsinghua University, Beijing
12. The Railway Ministry of China (1988) Designing parameters for air-conditioned train carriage: TB 1951–1987

Chapter 40
Research of the Vertical Movable Exterior Sunshade Devices' Impact on Indoor Natural Ventilation in Guangzhou Area

Xiangyang Jiang, Jiankun Yang, Chongpao Gan and Yonghua Zhang

Abstract Building shading and natural ventilation are the two of traditional and efficient energy-saving technologies at hot summer and warm winter zone. However, building exterior shading may block or guide the air inlet or outlet, which would result in positive or negative effects on natural ventilation. For optimizing the building shading and natural ventilation and to make them better combination, this paper selected a high-rise building in Guangzhou as the research object, then used STAR-CCM+ software to simulate the building indoor ventilation, analyze the indoor ventilation situation, and trend under shading conditions or not, through which the vertical movable exterior sunshade devices' impact on indoor natural ventilation was revealed. At last, this paper summarized the vertical movable exterior sunshade devices' impact on indoor natural ventilation in Guangzhou area.

Keywords Building shading · Indoor natural ventilation · STAR-CCM+ software · Impact

40.1 Introduction

Building shading can prevent unnecessary daylight and reduce solar radiation, which is an effective strategy for reducing overheating in summer season. In summer at hot area, shadings have significant effect on reducing energy consumption and improving indoor environment comfort.

X. Jiang (✉) · J. Yang
Guangzhou Institute of Building Science CO., LTD, Guangzhou, Guangdong, China
e-mail: jxy_gibs@foxmail.com

C. Gan · Y. Zhang
Science and technology plan projects in Guangdong province (2012A010800046, 2012A010800025), The First Construction Engineering Limited Company of China Construction Third Engineering Bureau, Wuhan, Hubei, China

A. Li et al. (eds.), *Proceedings of the 8th International Symposium on Heating, Ventilation and Air Conditioning*, Lecture Notes in Electrical Engineering 263,
DOI: 10.1007/978-3-642-39578-9_40,

Nature ventilation is one of the passive design strategies for improving indoor air quality by fresh air. Most of outstanding green, energy efficient, eco-buildings select the strategy as important design method. Nature ventilation not only can satisfy ventilation requirement in transition season, but also can drastically reduce mechanical ventilation demand (see [1]).

Shading and natural ventilations are both efficient strategies for saving energy. However, correlation between the two strategies should be considered. As building shadings can block the air flow of inlet and outlet of nature ventilation, the efficiency will be declined.

Therefore, research on analyzing correlation between shadings and nature ventilation could provide a logical basis for passive design strategies. This paper selected a high-rise building in Guangzhou and used fluid dynamic model to analyze the effect of the two factors.

40.2 Project Outline

The project selected an office building as research object; its total gross area is 56,215 m^2, and air-conditioned area is 25,079 m^2. Basement is total of 5 floors, ground floor is total of 32 floors, and total building height is 154 m.

The south, the southwest and the west side of the project are installed vertical steel auto-shading systems. The total shading area is 4,500 m^2, There are 1,274 blades in all. Single blade width is 1,000 mm, height is 3,500 mm, and there are 300 control units.

The steel shading system can collect information from sensors for wind and daylight and will analyze for optimized strategies (or can control by manually), and by controlling daylight distribution, the system can conduct a best strategy for saving energy.

The project vertical shading blade detail is shown in Fig. 40.1.

40.3 Methods of Analysis

40.3.1 Basic Idea

The indoor nature ventilation analysis selected computational fluid dynamics (CFD) program for simulation. CFD simulation can help to predict and be used in architecture environment, energy systems, and automobile engineering field. CFD simulation technology can be used for dynamic physical model, for fluid and thermal conduct analyzing model [2].

The project simulation selected STAR-CCM+ 6.04.014 from CD-adapco Company for simulation. The standard k-e turbulent model was used with the finite volume method [3].

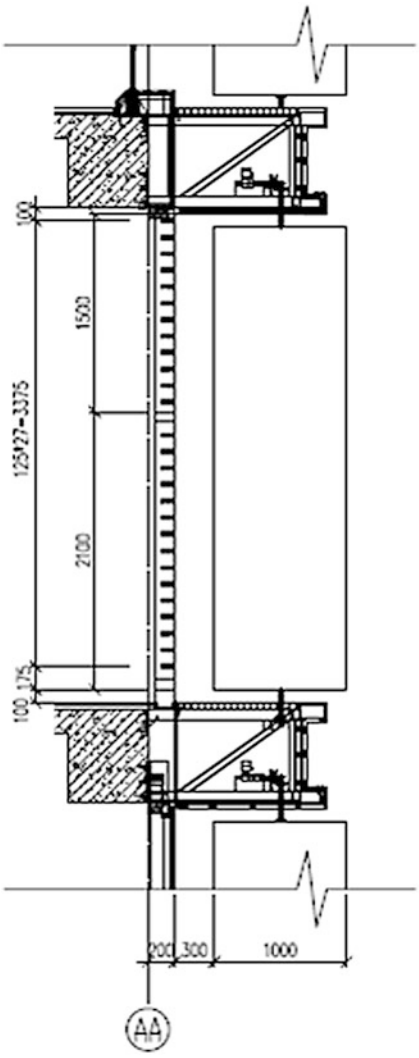

Fig. 40.1 Shading blade detail

40.3.2 Model and Boundary Conditions Set

40.3.2.1 Model Establishment

The project built a model based on project design drawings. Model size is developed to calculate correct air flow. According to different guidelines, model size is 150 × 150 × 4.5 m, and Y-axis of the model is north. Grid number is 246 thousands. Detailed model grid is shown in Figs. 40.2 and 40.3.

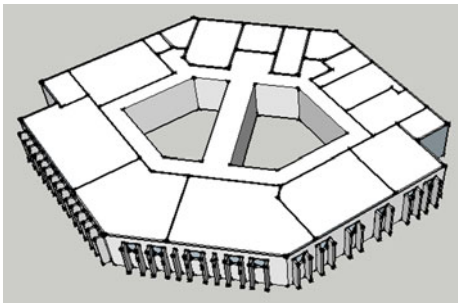

Fig. 40.2 Geometric models

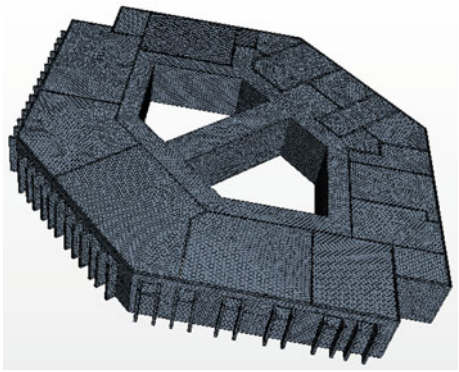

Fig. 40.3 Grid model

40.3.2.2 Boundary Conditions

1. The gradient wind boundary
   Air velocity of building boundaries had been determined based on geological and atmosphere conditions. In different geological condition, air velocity is different. Velocity can be calculated based on the following formula:

$$V_h = V_0 \left(\frac{h}{h_0} \right)^n \tag{40.1}$$

   in which:
   V_h Velocity in height h,m/s;
   V_0 Velocity in height h_0,m/s, generally select air velocity in 10 m height;
   n Index. According to "Building structure load regulation" GB 50009-2001, floor friction can be determined in different grades:
   A Near sea level and coast, lake and desert area, index is 0.12;
   B Country side, forest, and low-density rural and city area, index is 0.16;
   C High-density city area, index is 0.22;
   D High-density and high-rise building area, index is 0.30

The project natural ventilation model used n as 0.22 in simulation.

2. Outlet boundary condition
   In calculation area, pressure setting is same as environment pressure.

40.4 Effects of the Vertical Movable Exterior Sunshade Devices' Impact on Indoor Natural Ventilation

Quantitative analysis has been taken from three aspects such as interior comfort, air quality, and ventilation feasibility.

40.4.1 Thermal Comfort Comparison

Based on simulating different cases, thermal comfort condition in 1.5 m height is as follows. Velocity vector results are shown in Figs. 40.4, 40.5, 40.6, 40.7, 40.8 and 40.9.

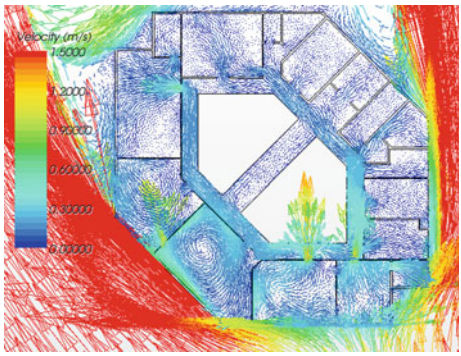

Fig. 40.4 Velocity vector in 1.5 m height (*no shading*)

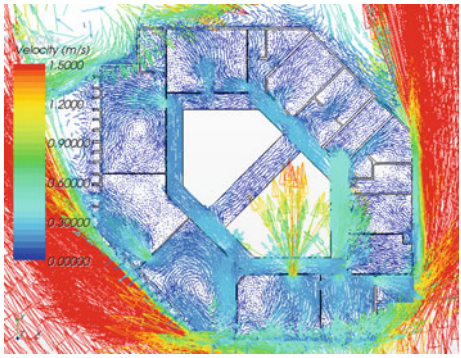

Fig. 40.5 Velocity vector in 1.5 m height (*shading*)

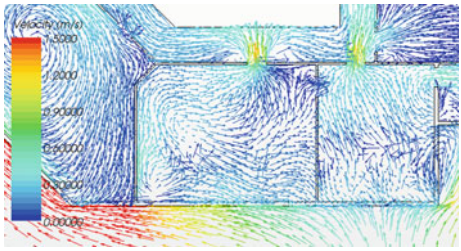

Fig. 40.6 South velocity vector in 1.5 m height (*no shading*)

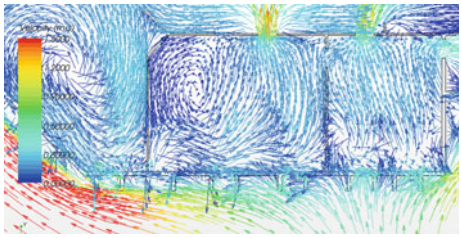

Fig. 40.7 South velocity vector in 1.5 m height (*shading*)

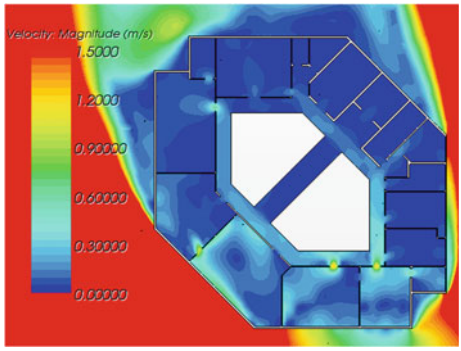

Fig. 40.8 Velocity distribution in 1.5 m height (*no shading*)

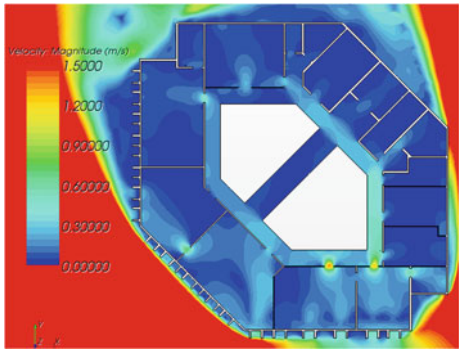

Fig. 40.9 Velocity distribution in 1.5 m height (*shading*)

As can be seen by comparing the project building has an angle with main wind direction of 22.5°, building orientation has a benefit in natural ventilation. Shadings in south, southwest, and west side have a significant effect on inducing air to indoor. Air velocity had been increased 0.2 m/s from no shading. In summer time, main air direction is SSE; office area can have nature ventilation which velocity range is in 0.4–0.8 m/s.

40.4.2 Indoor Air Quality Comparison

According to 1.5 m height age of air distribution result, analysis for indoor air quality is shown in below. Results are shown in Figs. 40.10 and 40.11.

According to comparison, installing exterior shading, age of air can be reduced significantly; maximum reduction can be reached 60s. Exterior shading systems induce wind to indoor and can improve indoor air quality. In summer, wind direction is SSE; indoor air flow can satisfy air quality requirements.

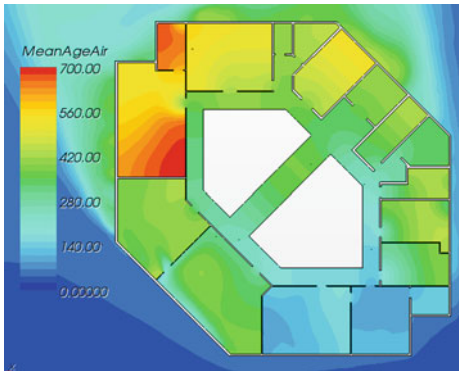

Fig. 40.10 Air age distribution in 1.5 m height (*no shading*)

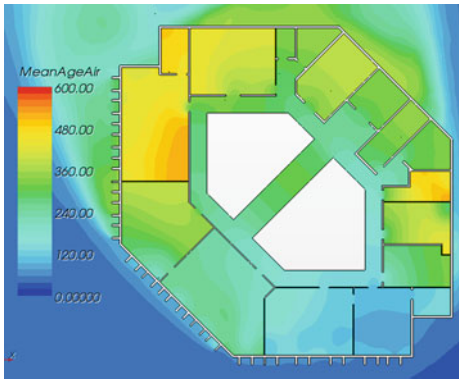

Fig. 40.11 Air age distribution in 1.5 m height (*shading*)

40.4.3 Ventilation Possibility Comparison

From simulation result, 1.5 m height pressure distribution at no exterior shading condition is shown in Figs. 40.12, 40.13, 40.14, 40.15, 40.16 and 40.17. The results show the possibility of ventilation from pressure differences.

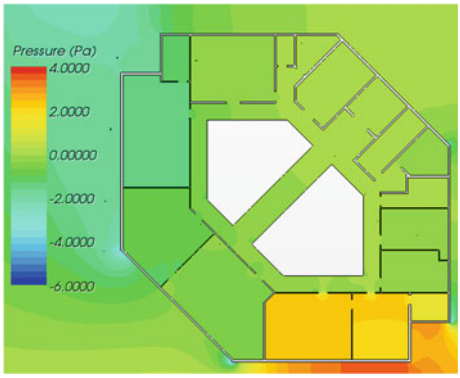

Fig. 40.12 Pressure distribution in 1.5 m height (no shading)

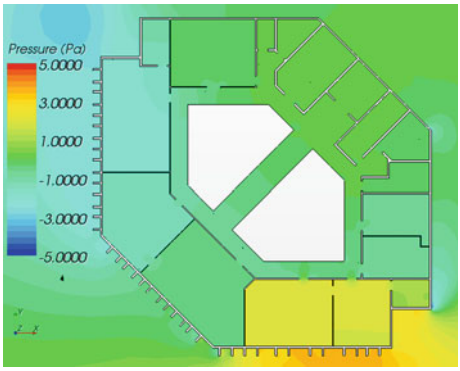

Fig. 40.13 Pressure distribution in 1.5 m height (*shading*)

Fig. 40.14 Pressure distribution of inlet (*no shading*)

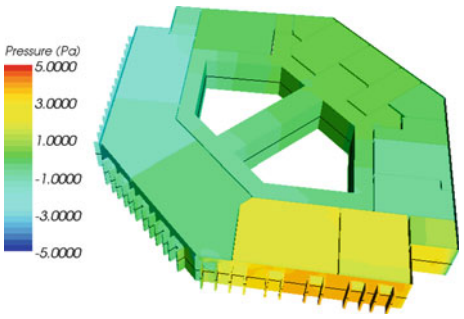

Fig. 40.15 Pressure distribution of inlet (*shading*)

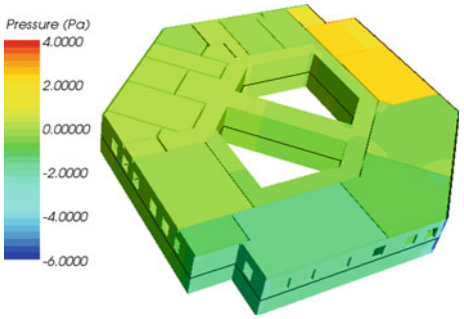

Fig. 40.16 Pressure distribution of outlet (*no shading*)

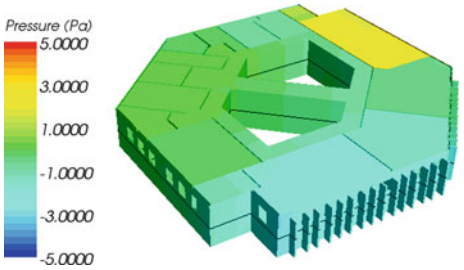

Fig. 40.17 Pressure distribution of outlet (*shading*)

From the comparison, pressure of inlet had been increased; however, pressure of outlet had been decreased. It makes the pressure difference become larger and the indoor, air flow become stronger with exterior shadings. Southeast pressure is in range of 2.0–4.0 Pa; southwest pressure is −1.5 to −0.5 Pa. Most of pressure differences are in average 3.0 Pa or larger, which is sufficient to make nature ventilation in good condition.

40.5 Conclusions

The paper used CFD simulation tool for analyzing nature ventilation in condition of with exterior shading and without. The main conclusions are as follows:

The building orientation and main wind have an angle which can lead outdoor air into indoor environment. Average wind velocity is 0.6 m/s, and pressure difference is 3.0 Pa, which is sufficient to create air flows in office. The corridor design inside of building also has a positive effect for nature ventilation.

The south, the southwest and the west side of the building have been installed exterior shadings for preventing solar radiation and increasing air velocity in office. It also can help to improve air quality and create comfort environment. The exterior shading system has a positive effect on natural ventilation in this project.

References

1. Tang M, Li Z (2007) Research on the influence of louvres on building natural ventilation effect. Tongji University
2. Zhao B, Li X, Hu B, et al (2001) Computational fluid dynamics in the HVAC engineering application. Refrige Air-Condition Elec Mach 22(4):10–14
3. Wang F (2004) The analysis of computational fluid dynamics: CFD principle and application. Tsinghua University Press, Beijing

Chapter 41
Numerical Simulation on Central Exhaust System Design for Residential Kitchen in High-Rise Buildings

Qinghong Zheng, Haichao Wang, Qingqing Chen and Ou Zhang

Abstract According to the problem of insufficient capacity in the central exhaust system of residential kitchen in high-rise buildings, this paper analyzes the reason for the difficulties of the flue exhaust on the basis of field tests on a manufacturer's 33-layer central exhaust system. According to the field test data of 33-layer flue, the CFD technology was applied to simulate the velocity and pressure field distribution on different cross-sectional size of exhaust pipe. In guaranteed the exhaust effect of the most unfavorable loop flue, the paper contrasts and analyzes the flue exhaust effect of a variety of different cross-sectional dimensions, thus to simulate reasonable cross-sectional area of smoke shaft for each floor. This simulation results play an important reference role for the formulation of concentrated exhaust system construction of the new residential kitchen standard atlas of Shaanxi province.

Keywords Residential kitchen · Concentrated exhaust pipe · Numerical simulation · Sectional dimension

41.1 Introduction

In recent years, indoor air quality requirement for people enhances. According to statistics, the vast majority of people spent 70–90 % of their time indoors [1], and indoor combustion process is the main source of indoor particle. In the world, there are 50 % of the developing countries, which 90 % of the pollution mainly depends on the heating or cooking fuel [2]. The kitchen as the largest household environment

Q. Zheng (✉) · H. Wang · Q. Chen
School of Environmental and Municipal Engineering,
Xi'an University of Architecture and Technology, Xi'an, China
e-mail: zhengqinghong@xauat.edu.cn

O. Zhang
Xi'an Architectural Design-Research Institute, Xi'an, China

A. Li et al. (eds.), *Proceedings of the 8th International Symposium on Heating, Ventilation and Air Conditioning*, Lecture Notes in Electrical Engineering 263,
DOI: 10.1007/978-3-642-39578-9_41,

pollutants generated place is always harmful to the health of person in the room. In order not to pollute indoor environment and ensure the dweller's health, it is one of the most priority in the design of indoor ventilation to eliminate indoor air pollution quickly and effectively.

Currently, the kitchen which located in the new high-rise building is installed central exhaust pipe. Equal section exhaust pipe is one of the most common forms in the market. Due to its good exhaust effect, low-cost system, facilitate construction, and other advantages, the central exhaust pipe is widely used in the actual project.

The central exhaust pipe also has some problems. The exhaust system of the previous civilian residential kitchen, due to the influence of the factors such as the flue material, forms and designs parameters, resulting in a lack of exhaust system ability; the flue gas of some of the families did not be removed, even in some high-rise exhaust system, all residential kitchen exhaust rate cannot meet the requirements, as well as flue gas reflux problems, which make the original exhaust system, and the design parameters can no longer meet the requirements of people living in the high-rise buildings. Therefore, people constantly try to improve the effect of smoke exhaust. The standard office of Shaanxi province concentrates on the standard atlas of the original residential kitchen exhaust system building to do a comprehensive revision, and the author participated in this work. The simulation is in this context mainly for new polymer–cement fireproof-type flue exhaust duct system. Hoping on the basis of the theoretical analysis, the simulation combined with the field test data can find ways to solve the problem and then can determine the size of the exhaust shaft cross section for different layers building to ensure that pollutants in the kitchen can be exhausted quickly and efficiently.

41.2 Physical Model

The numerical simulation focused on common building 6-layer, 9-layer, 12-layer, 18-layer, 24-layer, 33-layer exhaust systems, the analog input data are completely same with the experimental test data. Flue story is 3 m. The length of the branch pipe is 680 mm. The diameter of the branch is 150 mm. A deflector and non-return valve is equipped in the outlet of each layer user. For example, the 12-layer model is shown in Fig. 41.1.

41.3 Mathematical Models and Boundary Conditions

41.3.1 Mathematical Models

The simulation choose the air as a fluid medium, the flue gas temperature is not very high in actual kitchen flue and compared to lots of wind pressure the exhaust hood provided, and the effect of the thermo-compression of the flue gas itself is

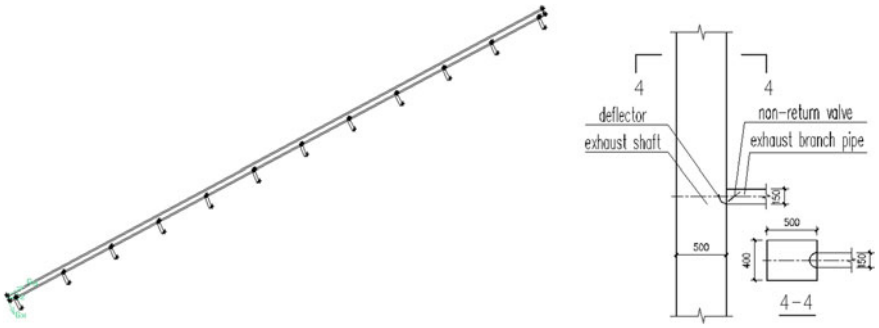

Fig. 41.1 Physical model and local diagram of 12-layer exhaust system

very small, so the simulation does not consider the influence of hot press [3]. For the steady incompressible flow, we use standard k-ε turbulence model to calculate, use standard wall function method in the near-wall region, choose the pressure-coupled equations simple algorithm as the flow field calculation method, and the basic control equation [4, 5] is as follows:

Continuity equation:

$$\frac{\partial u_i}{\partial x_i} = 0$$

Momentum equation:

$$\rho \frac{\partial}{\partial x_j}(u_i u_j) = -\frac{\partial p}{\partial x_i} + \mu \frac{\partial}{\partial x_j}\left(\frac{\partial u_i}{\partial x_j} + \frac{\partial u_j}{\partial x_i}\right) + \rho g_i$$

Turbulent energy transfer equation:

$$\rho \frac{\partial}{\partial x_j}(u_i k) = \frac{\partial}{\partial x_j}\left[\left(\mu + \frac{\mu_t}{\sigma_k}\right)\frac{\partial k}{\partial x_i}\right] + \mu_i \frac{\partial u_j}{\partial x_i}\left(\frac{\partial u_i}{\partial x_j} + \frac{\partial u_j}{\partial x_i}\right) + \rho\varepsilon$$

Dissipation rate of turbulent kinetic energy transfer equation:

$$\frac{\partial}{\partial x_i}(\rho u_i \varepsilon) = \frac{\partial}{\partial x_i}\left[\left(\mu + \frac{\mu_t}{\sigma_k}\right)\frac{\partial \varepsilon}{\partial x_i}\right] + C_{l\varepsilon}\mu_t \frac{\varepsilon}{k}\frac{\partial u_j}{\partial x_i}\left(\frac{\partial u_i}{\partial x_j} + \frac{\partial u_j}{\partial x_i}\right) + C_{2\varepsilon}\rho\frac{\varepsilon^2}{k}$$

where u_i, u_j are speed; i, j refer to tensor subscripts, $i, j = 1,2,3$; ρ is fluid density; μ is viscosity coefficient; ε is turbulent fluctuation kinetic energy dissipation rate; k is turbulent fluctuation kinetic energy; and empirical constants $\sigma_k = 1.0$, $\sigma_t = 1.3$, $C_{l\varepsilon} = 1.44$, $C_{2\varepsilon} = 1.92$, $C_\mu = 0.09$ [6].

Table 41.1 The fitting formula of each floor number

Layer	The fitting formula
33	$P = -0.002X^3 - 0.003X^2 + 0.621X + 246$
24	$P = -0.014X^3 - 0.138X^2 + 1.222X + 230$
18	$P = -0.006X^3 - 0.135X^2 + 1.252X + 209$
12	$P = -0.084X^3 - 1.917X^2 + 7.833X + 182$
9	$P = 0.030X^3 - 0.381X^2 + 3.526X + 186$
6	$P = -0.023X^3 + 1.552X^2 + 14.892X + 190$

where x is the number of floors.

41.3.2 The Setting of the Boundary Condition

When the range hood is close, it is assumed that the valve shut tightly, imports choose the wall type [7]. When user range hood is open, imports set to the pressure inlet boundary condition, total pressure value of the branch flue inlet based on the fitting resulting of flue measured data. The fitting formula of each floor number is shown in Table 41.1.

The main flue outlet is set to pressure outlet boundary condition. The wall is set to no-slip boundary condition in the simulation. The test uses a new polymer–cement fireproof flue. The inner wall of the flue is smooth. With the past experience in design, the roughness takes 1.5 mm [8], based on that values in this model, we choose different roughness height to do the simulation, contrasting the simulation data with the test data. When $k = 1.7$ mm, the simulation values are closer to the experimental values, so we choose $k = 1.7$ mm as the roughness height of this simulation.

The comparison of the test results and the simulation results of different flue wall roughness height are shown in Fig. 41.2. From the figures, we can see that the simulation results are in good agreement with the test results, branch pipe velocity of the test fluctuate in some layers. Because the hood of those layers are imprecise in the installation process, which leading to a certain amount of air leakage.

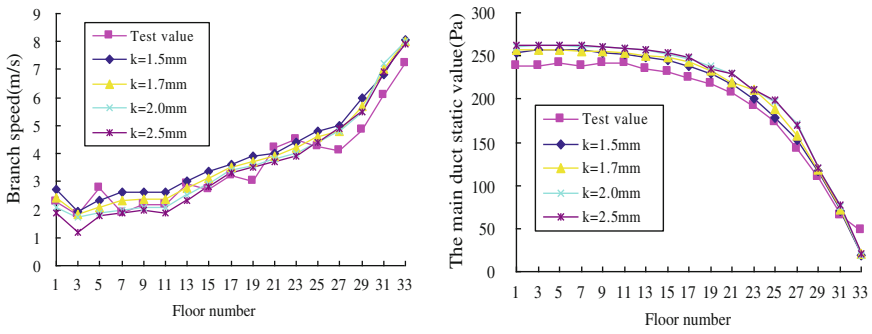

Fig. 41.2 In comparison to simulated data and test data

41.4 The Selection of the Simulated Conditions

41.4.1 The Selection of Operation Rate

In the actual test, we selected several operation rates, 12.1, 30.3, 51.5, 81.8 and 100 %, to do experiments; the test data show, when the operation rate is not the same, the amount of smoke of the same floor varied widely, and with the rise in operation rate, the amount of smoke the decline, the smoke effect weaken. This shows that the reasonable choice of the operation rate is very important in the design. According to the operation data which is recommended in the literature [9], the author combines with the operation rate of the residential kitchen hood investigated by the author themselves, the operation data have been adjusted slightly in this chapter. The selection of the operation rate is shown in Table 41.2.

41.4.2 Determine the Amount of Smoke

Choosing values are recommended by 《HVAC and power technology measures》 [10] (hereinafter referred to as "technical measures") to calculate exhaust volume. Described in the 《technical measures》, the cover mouth suction speed of the exhaust hood should not be less than 0.5 m/s, and the equation for calculating the amount of kitchen exhaust is as follows:

$$L = 3600 \times S \times V$$

where L is exhaust volume (m^3/h); S is cover mouth area (m^2); and V is the suction speed of the cover (m/s), for example, range hood CXW-180, its size is 700 × 400 × 525, and the exhaust volume is 517 m^3/h.

In [11] which discusses the amount of smoke of the range hood shows that when exhaust volume is 250 m^3/h, the range hood can exclude contaminants from kitchen effectively, and considering the economic requirements that flue cross-sectional area should not be too big, the area of the kitchen is 5 m^2; the number of ventilators can up to 16.6 times/h, which meets the requirements of engineering design. Peng [12] studied the collection efficiency of the range hood, thinking that

Table 41.2 The operation rate and operation floor of the different floors

Floor number	Operation rate (%)	Operation floor
6	83.3	1–5
9	77.8	1–7
12	75	1–9
18	72.2	1–13
24	70.8	1–17
33	66.7	1–22

when the standard exhaust volume is 300 m^3/h, it can ensure the smoke effect of kitchen, minimize heat loss of the kitchen in winter.

In summary, we select 250, 300, and 500 m^3/h as the design exhaust volume in this simulation to simulate suitable flue diameter.

41.5 The Simulation Results

In the simulation, we choose the most unfavorable loop, changing the cross-sectional size of the main flue constantly, based on the design exhaust volume of 250, 300, and 500 m^3/h, when one of the condition which the minimum the amount of smoke up to the design exhaust volume, we think the condition meets the exhaust needs. 33-layer simulation results, for example, the operation rate of 33-layer flue is 67 %, selecting the most unfavorable loop, the 1–22 layers are all opening, 22–33 layers are all closing. We choose several flue specifications such as 500 × 450, 500 × 500, 550 × 500, 600 × 540, 600 × 500, 700 × 600, simulating the exhaust volume of branch pipe of every layer, the results are shown in Fig. 41.3.

If calculating with the minimum amount of exhaust volume, based on the minimum of exhaust volume 250, 300, and 500 m^3/h, respectively, from Fig. 41.3, we know that 550 × 500, 600 × 540, and 700 × 600 just meet pipeline specifications. The minimum exhaust volume of 550 × 500 flue branch pipe is 252 m^3/h, the minimum exhaust volume of 600 × 540 flue branch pipe is 318 m^3/h. The minimum exhaust volume of 700 × 600 flue branch pipe is 512 m^3/h. According to this method, we simulate 6-layer, 9-layer, 12-layer, 18-layer, 24-layer exhaust systems, respectively. The results of the simulation are shown in Table 41.3.

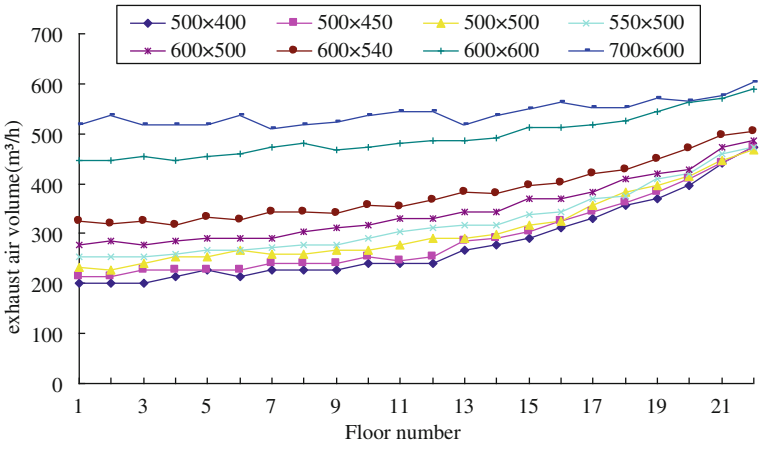

Fig. 41.3 The exhaust volume of each branch pipe of different diameter in 33 layer

Table 41.3 The flue section size

Floor number	Open probability (%)	Duct size (mm)		
		250 m^3/h	300 m^3/h	500 m^3/h
≤6	83.3	230 × 200	250 × 200	300 × 300
6–9	77.8	250 × 250	300 × 250	400 × 350
9–12	75	300 × 300	330 × 300	400 × 400
12–18	72	400 × 320	400 × 350	500 × 500
18–24	71	400 × 380	430 × 400	600 × 600
24–33	67	550 × 500	600 × 540	700 × 600

41.6 Conclusion

The size of the cross-sectional area of shared shaft plays an important role in the emission of gas; the cross-sectional area of shared shaft is too small in the past Atlas, and it cannot meet the smoke needs. This simulation considers the effect of the roughness of the inner wall, minimum exhaust volume, operation rate, to determine the suitable size of the flue, and provide reference for design and production of the flue.

Flue material is better in the market at present, which improve the smoke effect directly, and for the design of the central exhaust system of high-rise residential kitchen, the absolute roughness of the inner wall taken as 1.7 mm is safe.

Acknowledgments This work is supported by the urban and rural construction commission projects of science and technology in Xi'an. The project name is "optimization study on solar energy double drive of the residential kitchen or toilet centralized exhaust system in high-rise buildings".

References

1. Wang JN, Cao SR, Li Z (1988) Human exposure to carbon monoxide and inhalable particulate in Beijing. Biomed Environ Sci 1(1):5–12
2. Naether LP, Smith KR, Leaderer BP (2001) Carbon monoxide as a tracer for assessing exposures to particulate matter in wood and gas cook stove households of highland Guatemala. Environ Sci Technol 35:575–581
3. Gong YF, Chen LP, Guo JJ (2002) The flue gas flow characteristics analysis of residential kitchens. J Nanjing Archit Civil Eng Inst 3:8–12
4. Fluent Incorporated (2002) Fluent 5 Users Guide. Lebanon, N.H., USA
5. Fu DD, Ma YW (2002) Calculation of fluid dynamics. Higher Education Press, China
6. Tao WQ (2001) Numerical heat transfer. Xi'an Jiaotong University Press, China
7. Fan YS, Shao ZM (2011) Numerical simulation on variable pressure exhaust system of residential kitchens. Archit Sci 27(2):103–106
8. Xin YQ, Xu WH (2005) Research on friction loss of equivalent sectional concrete flue. The national air conditioning refrigeration academic conference
9. Chen LP, Gong YF, Guo JJ, Mo Q (2002) Calculation of central exhaust system of residential kitchens. HVAC 32(4):107–109

10. National civil engineering design measures: HVAC Power (2009), China Planning Press, China
11. Xu WH, Shen XF (2001) Research and system design method on residential kitchen exhaust system. Building Energy Environ 1:46–48
12. Peng R (1995) Several problems in the kitchen exhaust ventilation and dust removal. Building Energy Environ 4:42–43

Chapter 42
Applicability of Vapor Transport Theory for Common Wall Types in Mixed Climate Zone of China

Shui Yu, Xu Zhang and Guohui Feng

Abstract To decrease building energy consumption and improve indoor thermal environment, mixed climate zone (MCZ) imitates northern buildings to use immature thermal insulation technology to new or retrofitting buildings; however, it leads to condensation inside or on the surface of building enclosure (BE), which makes building energy consumption increasing, improves fungus growth, deteriorates indoor air quality (IAQ), and lowers durability. Generally, dew-point method and vapor transport theory is used to determine condensation; however, the former method is only used to the surface of BE without considering the influence of heat and air on moisture transfer, and the latter method could be used to the inside of BE without considering the influence of liquid water transfer and vapor transfer on temperature; furthermore, hygrothermal characterization of building materials is usually considered as constant, and in fact, it is variable. Meanwhile, due to capillary condensation existing in porous materials, even though relative humidity (RH) (water vapor pressure ratio) is less than 100 %, condensation also could occur. So the applicability of vapor transport theory is discussed in several common wall types including 240 mm brick wall, 180 mm concrete wall, and 190 mm AAC wall in MCZ in China.

Keywords Vapor transport theory · Relative humidity · Capillary condensation

S. Yu (✉) · G. Feng
School of Municipal and Environmental Engineering, Shenyang Jianzhu University, No.9, Hunnan East Road, Hunnan New District, Shenyang 110168, China
e-mail: yushui19832002@gmail.com

G. Feng
e-mail: fengguohui888@163.com

X. Zhang
College of Mechanical Engineering, Tongji University, Shanghai 200092, China
e-mail: zhangxu-hvac@tongji.edu.cn

A. Li et al. (eds.), *Proceedings of the 8th International Symposium on Heating, Ventilation and Air Conditioning*, Lecture Notes in Electrical Engineering 263,
DOI: 10.1007/978-3-642-39578-9_42,

42.1 Introduction

The characteristic of mixed climate zone (MCZ) in China is low indoor temperature and high relative humidity (RH) in winter, and the risk of condensation and mold on the surface of the building enclosure (BE) is high. Furthermore, the long-term operation of air-conditioning in summer season increases the condensation potential. When the temperature on the interior surface of the external wall is lower than the dew point, the condensation will happen; then, mold grows on the wall surface, which will also deteriorate indoor air quality (IAQ) and harm to people's health. On the other hand, heat flux (HF) through the building envelopes accounts for a great proportion of the total HF [1–3].

At present, most designers or consultants only focus on the thermal performance of buildings based on experiment or simulation analysis without considering moisture effect frequently. However, moisture has a big influence on the thermal characteristic of building materials and heat transfer processing. The history of the research on the couple of heat and moisture (HM) transfer has more than 50 years. There are several models to describe the HM transfer process and solving methods. However, till now, there is no any theory that could cover all situations for HM transfer in porous materials, due to the kinds of assumption and complicated system. Meanwhile, kinds of hygrothermal characteristics need to be input into the models, which probably limit solving the mathematic model [4, 5].

Generally, the simplified one-dimensional computing method is used to calculate the temperature and RH distribution in engineering, which cannot provide the accuracy results; also the effect of moisture on temperature is neglected. In a word, it is fully significant to research the HM transfer through building envelop for improving indoor thermal environment with low energy consumption in the MCZ of China.

Now, there are three best known design tools for evaluating the probability of condensation, including vapor transport theory, the Glaser diagram, and the Kieper diagram. All three methods use simple vapor diffusion equations to get vapor pressure and saturation pressure. If the calculated vapor pressure is above the saturation pressure at any point within the envelope, condensation is indicated. Now, most of designers used vapor transport theory to analyze the practical problem in China, which bases on the following diffusion equation and definitions [6]:

$$T_m = T_{\text{in}} - (T_{\text{in}} - T_{\text{out}}) \cdot \sum_{j=1}^{m-1} R_j \Big/ R_{\text{total}} \quad m = 2, 3, 4 \ldots n \tag{42.1}$$

$$\varphi_m = \frac{P_m}{P_{m,\text{sat}}} = \frac{P_{\text{in}} - \frac{\sum_{j=1}^{m-1} H_j}{H_{\text{total}}}(P_{\text{in}} - P_{\text{out}})}{P_{m,\text{sat}}} \quad m = 2, 3, 4 \ldots n \tag{42.2}$$

42.2 Capillary Condensation

The capillary condensation phenomenon exists in porous materials according to classic theory, as shown in Kelvin Eq. 42.3, where saturation vapor pressure, surface tension, molecular weight of liquid, and density are all inherent properties. Therefore, the variables that govern capillary condensation most are the equilibrium vapor pressure and the mean curvature of the meniscus. When relative pressure of water vapor in pores is up to the corresponding value of r, capillary condensation will occur; similarly, pores will be filled with condensed liquid when desorption starts; when relative pressure is reduced to the corresponding value of r, capillary evaporation will occur [7–9].

$$\ln\left(\frac{P_v}{p_{\text{sat}}}\right) = -\frac{2\sigma M}{\rho r R T}\cos\theta \tag{42.3}$$

where, P_v is the equilibrium vapor pressure, namely saturation vapor pressure on the surface of plane liquid, Pa; P_{sat} is the saturation vapor pressure on the surface of meniscus; σ is the liquid or vapor surface tension, N/m; M is the molecular weight of the liquid, kg/mol; ρ is the density of the liquid, kg/m^3; r is the radius of mean curvature of meniscus, m; R is the ideal gas constant, m^{3}Pa/(K · mol); T is the temperature, K; θ is the contact angle.

Now in China, concrete is used as main building materials. It is necessary to know the limitation of RH permitted in building. Concrete is one kind of porous materials consisting of gel pores and capillary pores. Gel pores are smaller in size with majority being smaller than 10^{-8} m. Capillary pores are larger in size and range from 10^{-8} to 10^{-5} m. Only the capillary pores contribute toward the movement of water through concrete. Parameters are as follows: M is 18.02 g/mol, ρ is 1,000 kg/m^3, θ is 0, R is 8.31 m^{3}Pa/(K · mol), T is 296.15 K, r ranges from 10^{-8} to 10^{-5} m.

Figure 42.1 shows the relationship of critical RH with different r when temperature is 296.15 K according to Eq. 42.3. There is capillary condensation occurring where r is 10^{-8} m when RH reaches to 90 %. When RH is larger than 90 %, there will be more condensation in more small pores. Temperature has a little influence on r when capillary condensation occurs, and only RH has a great influence, especially from 60 to 100 %, as shown in Fig. 42.2.

Pore size distribution of porous materials could be obtained by ASAP 2020. Figure 42.3 shows the principle of the test equipment. To calculate the surface area of eco-stucco, the BET multilayer absorption theory is used. A total surface area S_{total} and a specific surface area S are derived from the following equation:

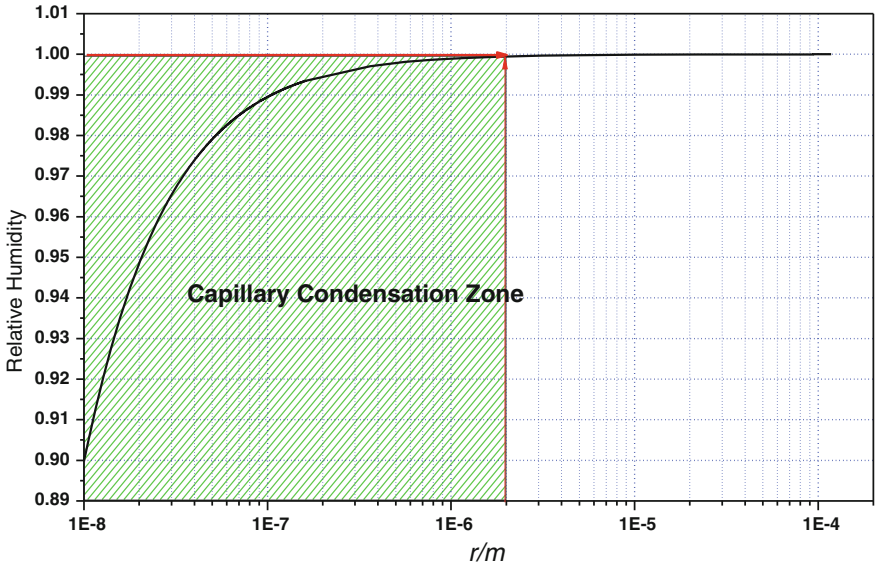

Fig. 42.1 Capillary condensation occurs when r is 10^{-8} m and when RH is larger than 90 %

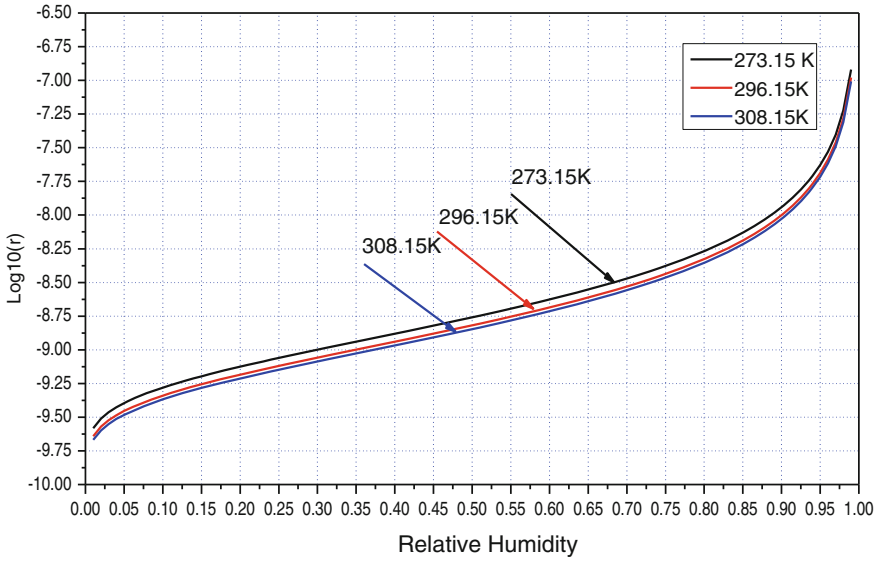

Fig. 42.2 The relationship of r with RH when capillary condensation occurs with different T

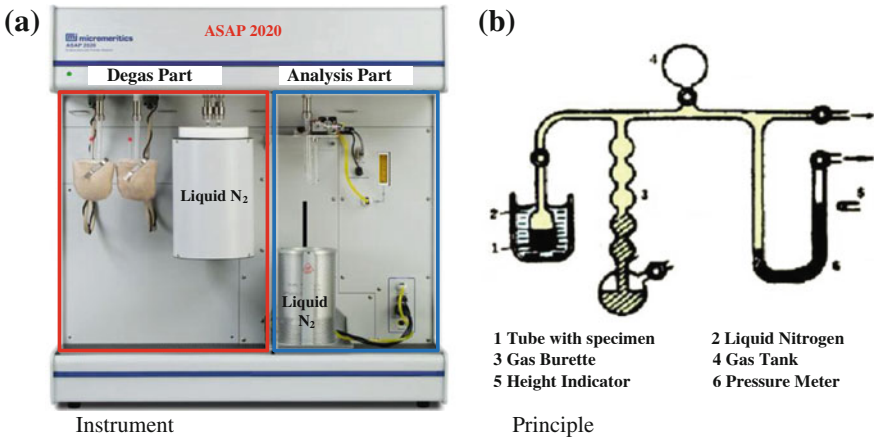

Fig. 42.3 The operating principle of ASAP 2020 instrument

$$S_{\mathrm{BET,total}} = \frac{(v_m N_S)}{V} \tag{42.4}$$

where v_m is the volume in units of the molar volume of the adsorbed gas, N is the Avogadro's number, and s is the adsorption cross-section of the adsorbing species. Here, BET surface area of eco-stucco is 4.3665 m^2/g. Figure 42.4 shows the pore size distribution and cumulative pore volume measured by the ASAP 2020. One may observe two peaks in the distribution of pore size (incremental pore volume);

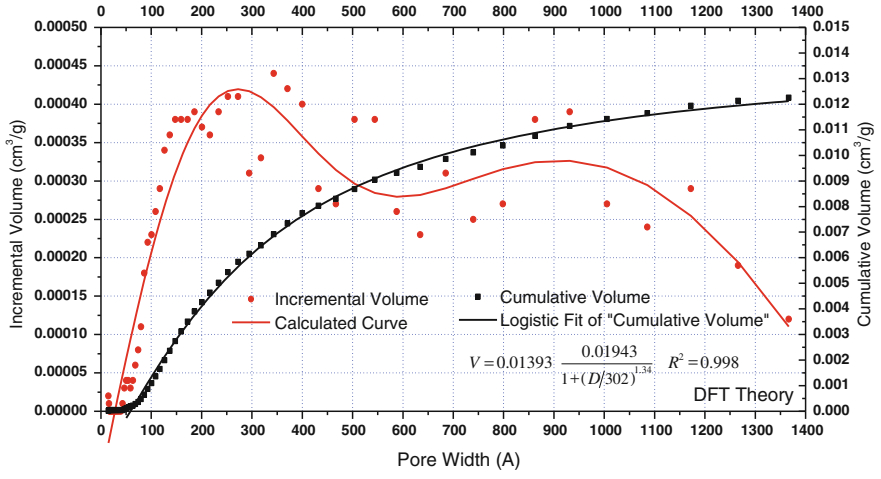

Fig. 42.4 The pore size distribution and cumulative volume of eco-stucco measured with ASAP 2020

Table 42.1 Min RH when capillary condensation occurs for several common building materials [10, 11]

Materials	T	r (m)	RH (%)
Concrete	296.15 K	$10^{-8} \sim 10^{-5}$	90
Sandstone		$10^{-8} \sim 10^{-3}$	
Brick		$10^{-8} \sim 10^{-3}$	
Tuffeau stone		$2 \times 10^{-9} \sim 10^{-5}$	60
Eco-stucco		$5 \times 10^{-9} \sim 10^{-3}$	66

one peak is around 300 Å (3 x 10^{-8} m) and the other is around 950 Å, i.e., in the middle and at the end of micropore region.

Generally, designers or researchers only consider when RH is 100 % which means vapor pressure is equal to or larger than saturation vapor pressure; there is condensation occurring on the surface or inside of the building envelop. And when this happens and condensation quality exceeds the maximum water capacity of materials, vapor retarder should be used or reselect suitable materials avoiding condensation and mold growth. However, due to the capillary condensation phenomenon, condensation will occur before vapor pressure and is larger than saturation vapor pressure. So it is very dangerous without considering capillary condensation when materials are located in the high humidity environment. Table 42.1 shows critical RH of some common building materials.

42.3 Physics Model and Parameters

In MCZ of China, brick wall, concrete wall, and AAC wall is very popular used, so here, three kinds of common wall is applied to analyze the max RH in the wall with comparing with critical RH. Figure 42.5 is the physic model and its materials. Table 42.2 is boundary condition including indoor or outdoor temperature and RH.

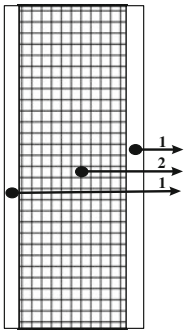

- 1-20mm Cement Mortar
- 2-240mm Brick
- 180mm Concrete
- 190mmAAC

Fig. 42.5 Physics model, materials, and thickness of the wall

Table 42.2 Boundary conditions

	Indoor parameters	Outdoor parameters	Classification
Case 1	Indoor tem: 18 °C	Outdoor tem: −4 ~ 42 °C	① Brick wall
	Indoor RH: 60 %	Outdoor RH: 30 ~ 100 %	② Concrete wall
Case 2	Indoor Tem: 0–30 °C	Outdoor tem: −4 °C	③ AAC wall
	Indoor RH: 30–100 %	Outdoor RH: 75 %	

42.4 Applicability of Vapor Transport Theory

42.4.1 Brick Wall

In general, critical RH of brick and concrete is 90 % when capillary condensation occurs that will lead to liquid transfer. So max RH is calculated depending on vapor transport theory (shown in Eqs. 42.1 and 42.2) in brick wall under two kinds of boundary conditions, and the results are shown in Fig. 42.6, which show the applicability of vapor transport theory in brick wall.

As shown in Fig. 42.6, ① when outdoor temperature is lower than −9.1 °C, or outdoor RH is larger than 90 %, vapor transport theory is not suitable in common size brick wall; ② when outdoor temperature is larger than 12 °C and outdoor RH is lower than 90 %, vapor transport theory is suitable in common size brick wall; and ③ otherwise, the applicability depends on indoor or outdoor temperature and RH.

42.4.2 Concrete Wall

Max RH is calculated depending on vapor transport theory in concrete wall under two kinds of boundary conditions, and the results are shown in Fig. 42.7, which show the applicability of vapor transport theory in concrete wall.

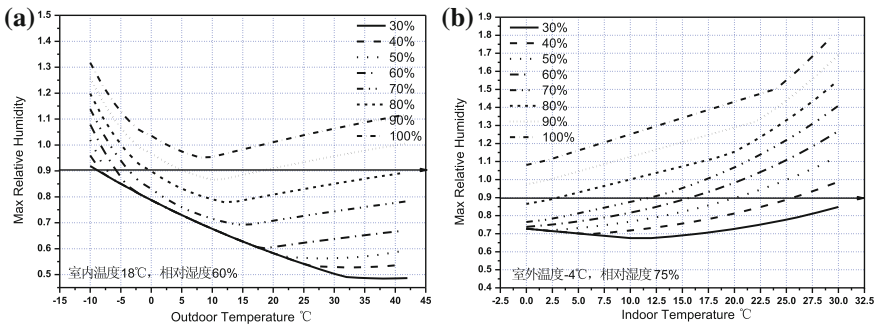

Fig. 42.6 Brick wall: max RH versus indoor temperature

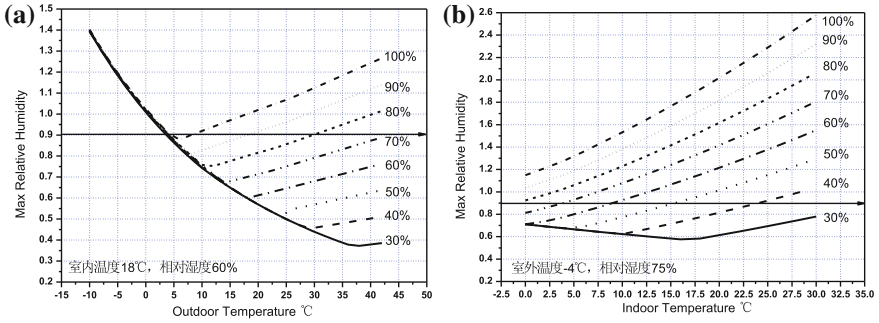

Fig. 42.7 Concrete wall: max RH versus indoor temperature

As shown in Fig. 42.7, ① when outdoor temperature is lower than 3.6 °C, vapor transport theory is not suitable in common size concrete wall; ② otherwise, the applicability depends on indoor or outdoor temperature and RH.

42.4.3 AAC Wall

Max RH is calculated depending on vapor transport theory in AAC wall under two kinds of boundary conditions, and the results are shown in Fig. 42.8, which show the applicability of vapor transport theory in AAC wall.

As shown in Fig. 42.8, ① when outdoor temperature is lower than −3 °C, or outdoor RH is larger than 90 %, vapor transport theory is not suitable in common size AAC wall; ② when indoor RH is larger than 90 %, vapor transport theory is not suitable in common size AAC wall; and ③ otherwise, the applicability depends on indoor or outdoor temperature and RH.

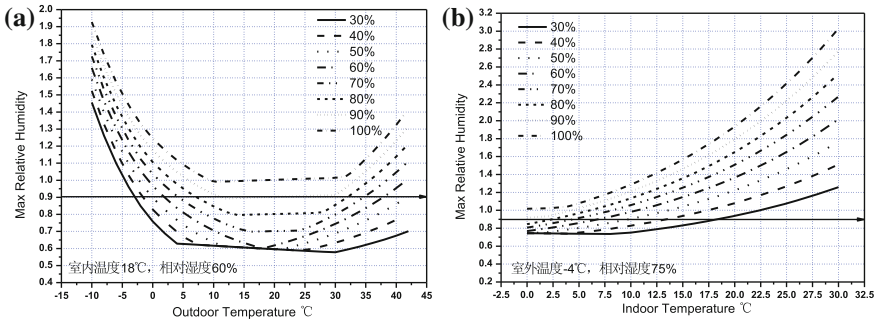

Fig. 42.8 AAC wall: max RH versus indoor temperature

42.5 Conclusions and Discussion

Critical RH in building materials is proposed according to Kelvin theory when capillary condensation occurs, which is the key point to decide the applicability of vapor transport theory. This chapter presents the applicability of vapor transport theory for three common wall types in MCZ in China. However, there are still lots of research work needed to do. The accuracy of critical RH depends on the pore size distribution of porous materials which are lacking. Furthermore, adaptive model of vapor transport theory should be proposed and verified.

Acknowledgments The authors would like to thank both the National Eleventh Five-year Plan for Science and Technology (2006BAJ01A05) of China and Building Energy and Environmental Systems Laboratory at Syracuse University for their financial support to the project.

References

1. Bomberg MT, Shirtliffe CJ (2009) Moisture Control in Buildings: The key factor in mold preventation, Baltimore, MD, pp 16–37
2. Schijndel, A.W.M. van. (2007) Integrated heat air and moisture modeling and simulation: [PhD thesis]. Eindhoven, Technische Universiteit
3. Yu S, Bomberg M, Zhang X (2012) Integrated methodology for evaluation of energy performance of the building enclosures: part 5-application of the proposed hygrothermal characterization. J Build Phys 36(2):178–197
4. Yu S, Bomberg M, Zhang X (2012) Integrated methodology for evaluation of energy performance of the building enclosures: part 4-material characterization for input to hygrothermal models. J Build Phys 35(3):194–212
5. ASHRAE. (2006) A Thermal and Moisture Property Database for Common Building and Insulation Materials, RP-1018, ASHRAE Transactions, Vol. 112(2), pp 485–497
6. Brandt AM (2006) Cement Based Composites: Materials, Mechanical Properties and Performance, E&FN Spon, UK
7. Straube J, Burnett E (2005) Building science for building enclosures. Building Science Press Inc, Westford, Massachusetts, pp 293–365
8. Winslow NM, Shapiro JJ (1959) An instrument for the measurement of pore-size distribution by mercury penetration. ASTM Bull 236:39–54
9. Hunter RJ (2001) Foundations of colloid science, 2nd edn. Oxford University Press, Oxford
10. Miller EE, Miller RD (1995) Theory of capillary flow: I practical implications. Proc Soil Sci Soc Am 19:267–271
11. Miller EE, Miller RD (1955) Theory of capillary flow: II experimental information. Proc Soil Sci Soc Am 19:272–275

Chapter 43
Numerical Simulation and Analysis of Natural Smoke Exhaust for Straight Corridor in a High-Rise Hotel

Wei Shi and Fusheng Gao

Abstract The natural smoke exhaust is acknowledged as a common smoke control manner with simple form and does not require additional energy support either with the complex exhaust facilities. In this paper, the field model fire dynamic simulator (FDS) with a combination of zone model consolidate fire and smoke transport (CFAST) was used to simulate the natural smoke exhaust in a straight corridor of a high-rise hotel, for the purpose of evaluating fire safety of smoke exhaust. There were several factors under discussion, such as the outdoor wind direction, wind speed, seasons, length of corridor, and dimensions of windows. The height of smoke layer interface was used to evaluate the effect of smoke exhaust. The conclusions were obtained as follows. Natural smoke exhaust in winter affects better than summer. With the outdoor wind speed increasing, the windward windows have poor effects on natural smoke exhaust, but the leeward windows work better. Natural smoke exhaust would not ensure evacuation safety in high-rise buildings when the length exceeds 30 m.

Keywords Building fire · Natural smoke exhaust · Straight corridor · FDS · CFAST

W. Shi (✉)
Northeast Petroleum University, Daqing 163318, China
e-mail: sw_dqpi@126.com

F. Gao
Harbin Institute of Technology, Harbin 150001, China
e-mail: fushenggao@126.com

A. Li et al. (eds.), *Proceedings of the 8th International Symposium on Heating, Ventilation and Air Conditioning*, Lecture Notes in Electrical Engineering 263,
DOI: 10.1007/978-3-642-39578-9_43,

43.1 Introduction

When building is on fire, smoke spreads to the corridor and other parts of the building. The corridor is the necessary path to atria or outdoor. The smoke should be exhausted outside in time, which made a significant impact on evacuation of people in the building. The natural smoke exhaust is acknowledged as a common smoke control manner with simple form and does not require additional energy support either with the complex exhaust facilities. In this paper, the field model fire dynamic simulator (FDS) with a combination of zone model consolidate fire and smoke transport (CFAST) was used to simulate the natural smoke exhaust in a straight corridor of the fire floor in a high-rise hotel, for the purpose of evaluating fire safety of smoke exhaust.

The general view of simulation model in 2D was represented in Fig. 43.1. The straight corridor was 56 m in length and 1.8 m in width, with ceiling height of 2.5 m. There were two windows at the ends of the corridor, with the length 1.5 m and the width 1.8 m, which could be open to exhaust smoke. The high-rise hotel was in urban district of Beijing, with the atmospheric parameters shown in Table 43.1. The building had 30 floors, and each floor height was 3 m. The fire room was on the twentieth floor. Fire room was room 1, with the fire source in corner.

Fire development in fire room was simulated by FDS. Heat release rate (HRR) was set as shown in Fig. 43.2 by calculations of FDS, which was transmitted to CFAST. Smoke spread was simulated by CFAST. The simulation time was 1,200 s. The height of smoke layer interface was used to evaluate the effect of smoke exhaust, with the limit of 1.5 m.

The study showed that with the increase in the fire room door's open size, the peak of HRR increased [2]. The corresponding smoke speed, temperature, and concentration of the flue gas would also increase. After the fire, if a non-fire room door opened, it would save a certain amount of smoke. Given the wide range of situations, this chapter only simulates fire room door fully open and non-fire room door fully closed, which was the most adverse condition. With the intent of providing more accurate results, the straight corridor was divided into several regions [3],

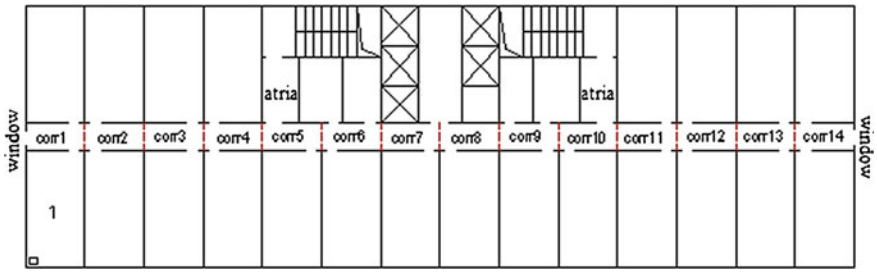

Fig. 43.1 Floor plan of building in simulation

Table 43.1 Parameter of outdoor in Beijing

	Atmospheric pressure (kPa)	Dry bulb temperature (°C)	Relative humidity (%)	Wind velocity in urban area [1] (m/s)
Summer	99.86	30	20	1.5
Winter	102.04	−5	45	2.2

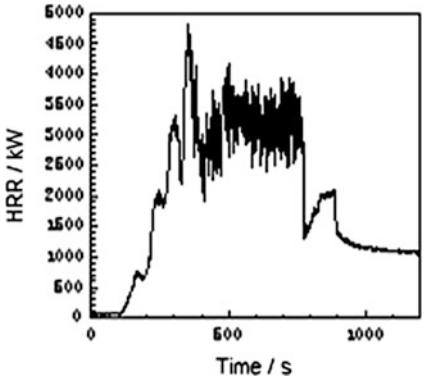

Fig. 43.2 Input parameters of HRR

and contour vents were set between regions. These vents were set with the same dimensions of the length and height of corridor. There were 14 regions divided and named as corr1, corr2 ~ corr14. And all of these were divided as follows: corr1 ~ corr5 called access1, corr6 ~ corr9 called access2, and corr10 ~ corr14 called access3.

There were several factors under discussions, such as the outdoor wind direction, wind speed, season, and length of the corridor. When considering different wind directions, an angle between wind direction and window direction was defined as a wind–window angle, as representation in Fig. 43.3. A1 and A2 were, respectively, for the left and right window–wind angle. And three kinds of wind were defined as follows: (1) A1 = 0°, A2 = 180°; (2) A1 = 180°, A2 = 0°; and (3) A1 = 90°, A2 = 90°. In settings of the simulations, the windows were opened 100 s later when the fire is happened.

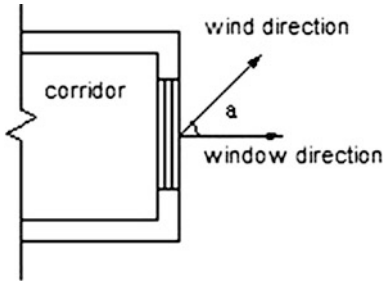

Fig. 43.3 Sketch map of wind–window angle

43.2 Analyzing Simulation Results

43.2.1 Impact of Wind Direction and Velocity

According to the definition of wind–window angle above, different wind conditions outside could be simulated by changing the wind–window angle. In the results, the curves of height of layer interface of areas of access2 almost coincided. The following discussions were major in simulation results of access1 and access3.

With the windows opened to natural exhaust, the simulation results were shown in Fig. 43.4. Under conditions of A1 = 0°, A2 = 180°, the smoke layer interface declined fast at the initial fire. Smoke had spread horizontally to the entire corridor at 200 s. After opening the windows, the height of smoke layer in the left declined slowly because of the negative pressure of the left window. As the fire develops, a large number of high-temperature smokes are generated and gathered in the corridor. At about 400 s, layer height of areas had bottomed out in succession. Then, fire came into a stable status, and the smoke layer height becomes stable too, with a little disturbance. The window on the right was in windward side, and a lot of air could enter into the corridor. The smoke layer of access3 declined toward the bottom since the smoke was cooled. Except corr1, the layer height of the whole corridor was below 1.5 m, which is not an ideal situation for evacuating.

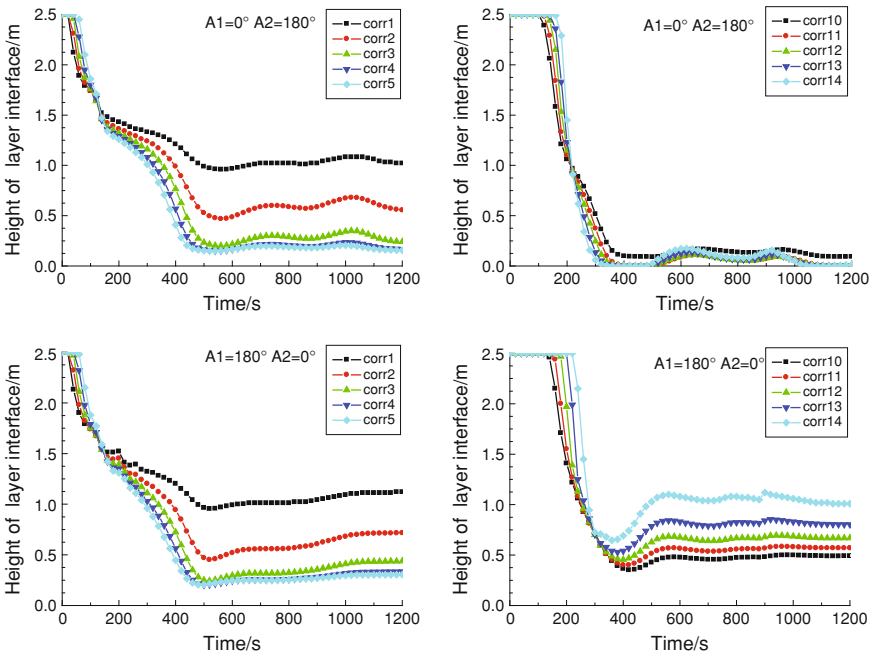

Fig. 43.4 Height of layer interface with different wind directions

Under conditions of A1 = 180°, A2 = 0°, the smoke layer height of access1 was almost similar to the former, but an opposite results in access3. It was because that access3 was far from the fire room and nearby the window. Smoke could exhaust outside in time, which made the smoke layer height lifted. Overall, the smoke exhaust effect was not still satisfactory. With the conditions of A1 = 90°, A2 = 90°, smoke exhaust effect was between the former two.

The velocity of the wind was set to be 2.5 m/s, and two kinds of conditions were applied: (1) A1 = 0°, A2 = 180°; (2) A1 = 180°, A2 = 0°. The results were shown in Fig. 43.5. By comparing these two conditions, smoke exhaust effect of access3 was no good after 400 s. With condition (1), which window was in the windward side, smoke exhaust worse with the wind velocity increased. Because the added velocity would block off the smoke exhaust, the window would lost functioning of exhausting if the wind speed was large enough. Through calculation of the critical wind velocity, it was 2.2 m/s which was less than 2.5 m/s in settings. The window on the right was invalid. This situation would only appear in the non-fire-side corridor but at the windward side. When the fire room was near the windward-side window, a large number of hot smokes made more pressure than that made by the wind, which could achieve smoke exhaust. The conclusions above were obtained also in conditions (2). With condition (2), which window was in the leeward side, smoke exhaust better with larger wind velocity. As analyzing above, the larger the wind velocity in leeward side, the better the smoke exhaust,

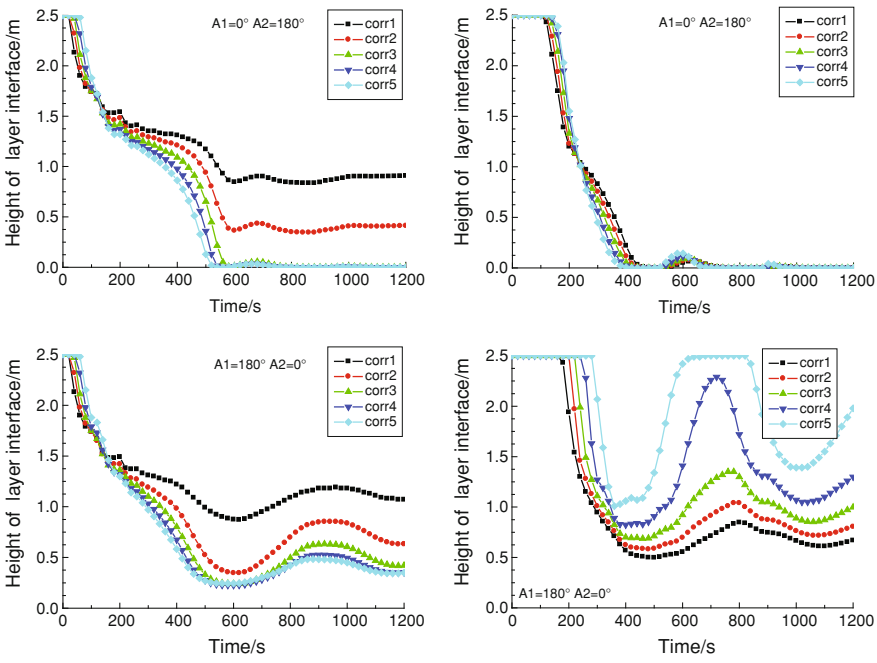

Fig. 43.5 Height of layer interface with different wind velocities (2.5 m/s)

but with the opposite results in the windward side. The smoke exhaust could not guarantee people safe in evacuation.

43.2.2 Impact of Width of the Corridor and Dimensions of Window

The width of the corridor was designed by the number of people on each floor accommodated, which was usually between 1.5 and 2.2 m. The next simulations were made by setting the width as 2.1 m, while changing the window size. The areas of windows meet the related provisions of GB50045-95.

Under conditions A1 = 180°, A2 = 0°, the results were shown in Fig. 43.6. Only by changing the corridor size, smoke effects were not affected much. When the size of the outside windows is changed, the width change made little effect, but when the height (the vertical size of the windows) is increased, the smoke layer interface height is significantly improved. As shown in curves, the height of the window is a sensitive parameter for natural smoke exhaust. With the same area of windows, windows at higher position result in better smoke exhaust. Therefore, in the design of the building, increasing the height of the window in corridor should be under consideration, which could also improve natural smoke effect.

43.2.3 Impact of Seasons

Compared with summer, wind speed in winter is larger, and the outdoor and indoor temperature are lower. Therefore, wind pressure and hot smoke effect are greater than those of the natural smoke in summer. The simulation results showed that the natural smoke effect in winter was much better than the summer. Three different outdoor wind cases and smoke interface height varying with time are shown in Fig. 43.7. Natural smoke effect in winter, though better than the summer, still cannot guarantee the safe evacuation. Smoke layer interface height in the entire process is maintained at less than 1.5 m evacuation, unable to meet the security requirements.

43.2.4 Impact of Length of the Corridor

Simulations above were within the corridor length of 56 m, and the results showed that this condition cannot satisfy the need for safe evacuation. In the next part, corridor length was set to 32, 20 m separately, to simulate the natural smoke effect under conditions A1 = 0°, A2 = 180°. The corridor was also divided by 4 m in

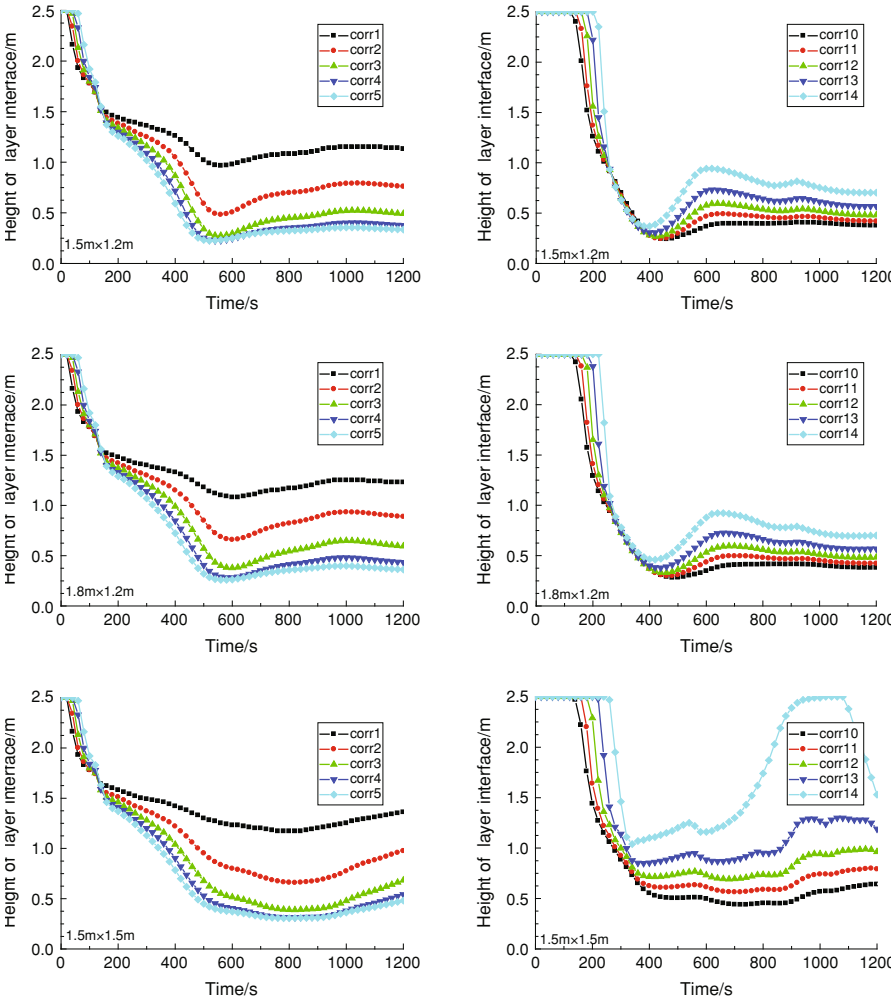

Fig. 43.6 Height of layer interface under different dimensions of window (W × H) with corridor width of 2.1 m

length. The simulation results of 32 m in length were shown in Fig. 43.8. The results showed that the smoke layer interface was significantly higher with corridor length decreased. The main reason is that windows were located at both ends of the straight corridor. With the length decreasing, the two windows made the hot smoke and cold air convect well, so a lot of air could enter the corridor. Heat gas and cold air made mass energy passed quickly, which also made smoke exhaust as soon as possible. There was not much smoke stranded in the middle of the corridor, making smoke affect overall improvement.

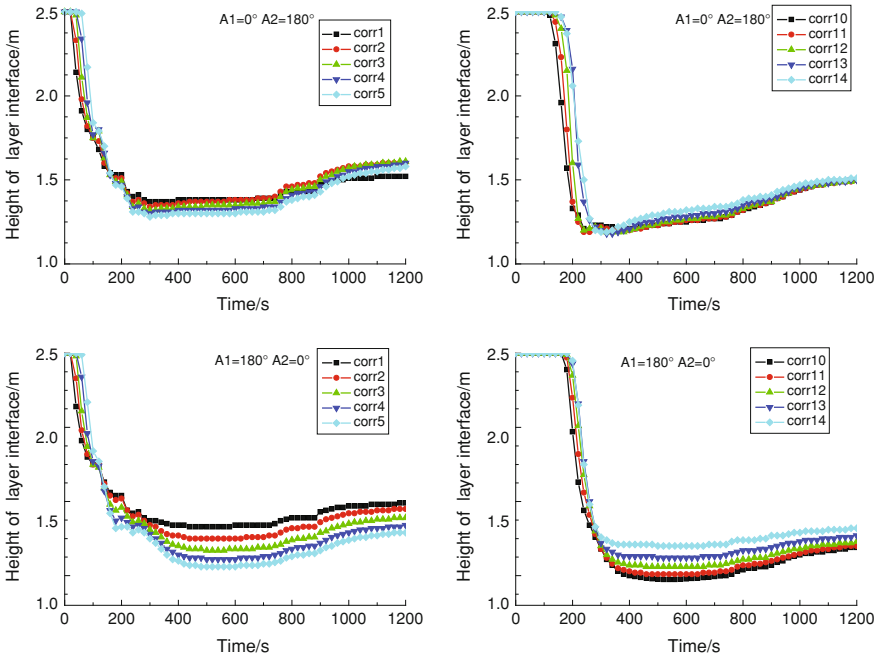

Fig. 43.7 Height of layer interface with different wind directions in winter

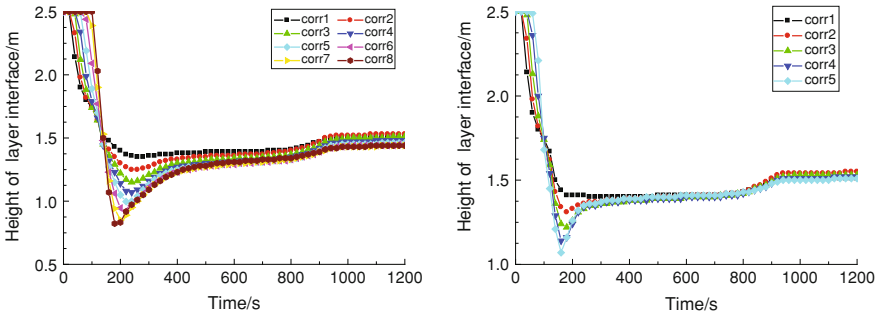

Fig. 43.8 Height of layer interface with different corridor lengths (*left* 32 m, *right* 20 m)

When the length of corridor is decreased to 20 m, the smoke layer interfaces were almost coincide at 1.5 m height, which can ensure the safety of personnel evacuation. With the length of 32 m, smoke layer interfaces were stable at between 1.2 and 1.5 m. Lengths 36 and 40 m were also simulated. The results found that in the length of 36 m, the layer height was stable at 1 m. Length of 40 m, part of the area's smoke layer height decreased between 0.5 and 1 m which

threatened personnel evacuation. As shown in curves that with the corridor more than 30 m in length, using only natural smoke was insufficient to guarantee safe and effective evacuation.

43.3 Conclusions

The conclusions were obtained as follows. Natural smoke exhaust in winter affects better than summer. With the outdoor wind speed increasing, the windward windows have poor effects on natural smoke exhaust, but leeward windows work better. As the wind speeds up, when outside wind speed exceeds a critical wind speed, the windward side of the outdoor windows will lose exhaust function. When considering the dimensions of the outdoor windows, the width change made little effect, but when the height (the vertical size of the windows) is increased, the smoke exhaust was better obviously. Natural smoke exhaust would not ensure safety in high-rise buildings when the length exceeds 30 m.

References

1. Lixing D, Xiaoqing L, Hong Y (2005) Impact of modifying terrain roughness class on theoretic wind pressure of air filtration. HV&AC 35(8):7–9
2. Qiu X (2003) Fire numerical simulation in high-rise building. Dissertation for the Master Degree, Harbin Institute of Technology, Harbin
3. Hu L-H, Huo R, Yao B et al (2003) Preliminary study on engineering method to predict smoke movement in very long-narrow spaces with two closing ends. Fire Saf Sci 12(1):36–39

Chapter 44
Study on Thermal Performance of Insulating Glass Window with Blind Inside

Shengjie Li, Zengfeng Yan and Junzhi Peng

Abstract In this paper, heat transfer theory is used to analyze the basic heat transfer process of insulating glass windows with blind inside, for which a simple mathematical model is established.By using the calculation software for thermal performance of doors, windows and glass curtain wall, the heat transfer coefficient and shading coefficient (SC) of ordinary hollow blind glass window was calculated.The simulation results showed a certain adjustable range for the heat transfer coefficient and SC of insulating glass windows with blind inside. Through the adjustment, different demands of heat insulation, shading and day lighting can be fulfilled.The feature of excellent thermal performance of insulating glass windows with blind inside can be used to fulfill the energy-saving requirement at the present stage and natural day lighting demand. This study can contribute to improve the thermal performance of building envelope and enhance energy conservation level.

Keywords Insulating glass window with blind inside · Mathematical model · Heat transfer coefficient · SC

S. Li (✉) · Z. Yan
Institute of Architecture, Xi'an University of Architecture and Technology, Xi'an 710055, China
e-mail: lishengjie1988@yahoo.com.cn

S. Li · J. Peng
Xiamen Academy of Building Research Group Co., Ltd, Xiamen 361004, China

A. Li et al. (eds.), *Proceedings of the 8th International Symposium on Heating, Ventilation and Air Conditioning*, Lecture Notes in Electrical Engineering 263,
DOI: 10.1007/978-3-642-39578-9_44

44.1 Introduction

With the improvement of building energy-saving requirement, as well as the gradual progressing of building energy efficiency, the requirements for thermal insulation performance of building envelop structure become higher; especially the transparent envelop structure like doors and windows of higher thermal loss, which is about 40–50 % of total energy consumption of building envelope components [1]. Therefore, to enhance the thermal insulation performance of doors and windows so as to reduce energy loss is an important link to improve the indoor thermal environment quality and building energy efficiency level. To meet the needs in different environments in different regions, windows with special functions become a research hotspot. Low-E insulating glass, heat radiation glass, insulating glass with built-in adjustable sunshade films and insulating glass with blind inside have been gradually applied in practical projects. Although insulating glass with blind inside has been applied in some projects, study on heat transfer process for it is relatively backward as well as research analysis on thermal performance for it.

44.2 Insulating Glass Window with Blind Inside

Insulating glass window with blind inside is a kind of built-in sunshade insulating glass product, namely, glass window with blinds built in the insulating glass [2]. With the magnetic-controlled closing device and lifting device, it has functions like lifting the blinds up and down and turning the blinds (Fig. 44.1). The angle of the blind can be adjusted manually and mechanically to control the incoming light and radiation heat so as to control heat insulation and indoor day lighting.

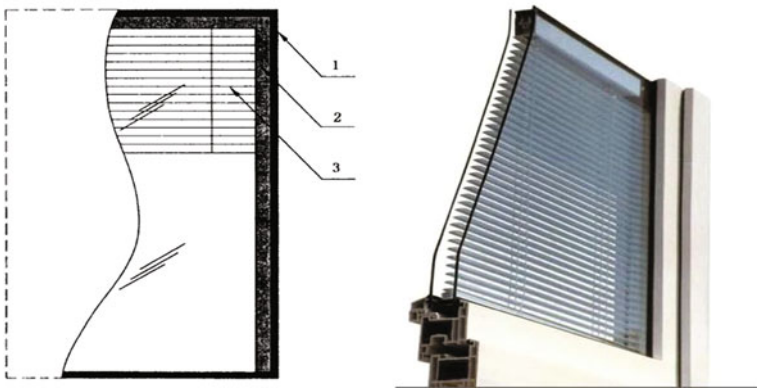

1—sealant; 2—frame; 3—blind;

Fig. 44.1 Insulating glass window with blind inside. *1* Sealant; *2* Frame; *3* Blind

44.3 Heat Transfer Process and Mathematical Model

44.3.1 Heat Transfer Processes

Heat transfer theory is used to analyze the heat transfer processes. There are two kinds of heat sources which can affect indoor heat gain of building with insulating glass window with blind inside. The two kinds of heat sources are solar transmittance thermal and thermal transfer by differ temperature when the glass temperature is higher than the indoor temperature. The heat process is very complex in the hollow layer. There are three heat transfer ways, which are transfer, convection and radiation [3]. For insulating glass window with blind inside when blind close, both of the two gas layer exist convective heat transfer process between the air flow with glass and louvers. Also there is the radiation heat transfer between the glass and blind. Insulating glass window with blind inside have three common conditions of blind inside (Fig. 44.2).

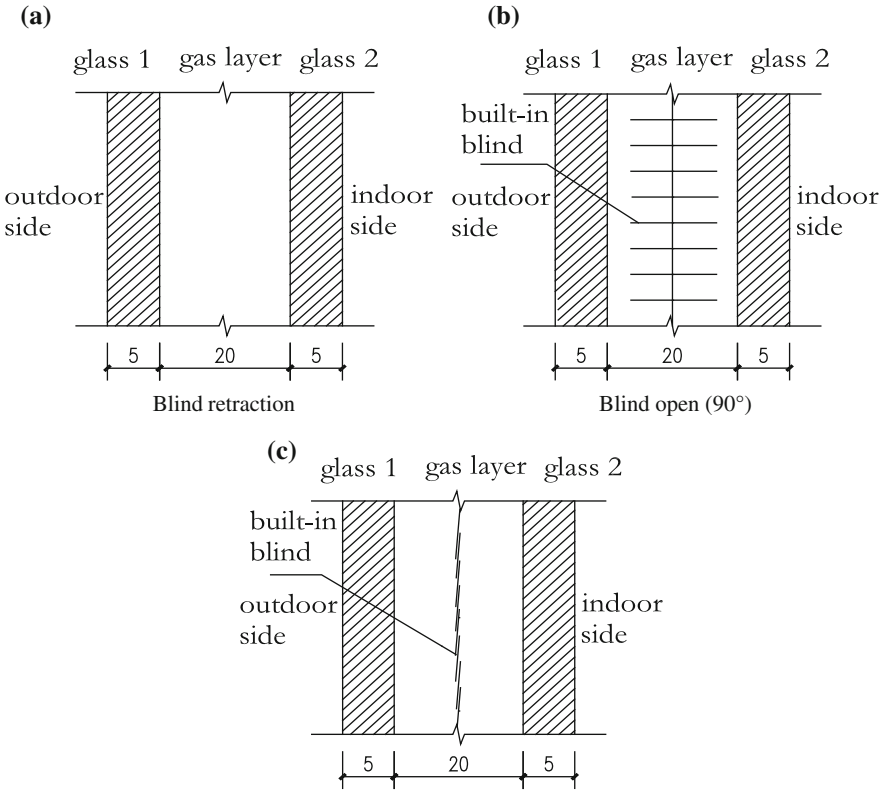

Fig. 44.2 Three status of built-in blind. **a** blind retraction, **b** blind open (90°), and **c** blind closed

When the blind was open at a certain angle, the heat transfer process is much complex in insulating glass window with blind inside. Therefore, there is no detailed analysis in the paper and further study will be in the follow-up research.

44.3.2 Mathematical Model

Based on the heat transfer process analysis of the insulating glass with blind inside, combined with the insulating glass heat transfer calculation principle, the heat transfer mathematical model of insulating glass window with blind inside can be establish. If the shading curtain is placed in between two-layer door and window (or glass curtain wall), the door and window (or glass curtain wall) and shading curtain should be considered as one-layer glass, and the total transmittance, transfer coefficient and visible light transmittance of sunlight should be calculated by multi-layer glass model [4].

44.3.2.1 Mathematical Equation of Heat Transfer Coefficient

When calculating the transfer coefficient [U_g,W/(m^2·K)] of glass system, simple simulation environment conditions should be adopted, taking only indoor and outdoor temperature difference into account without solar radiation [4], thus the transfer coefficient of hollow blind glass can be calculated as followed:

$$U_g = \frac{1}{R_t} \tag{44.1}$$

In formula (44.1), thermal resistance (R_t,m^2·K/W) of glass system should be the sum of the exchange thermal resistance of each layer glass, air layers, built-in blind and inside and outside surface, the calculation formula should be:

$$R_t 1 = \frac{1}{h_{out}} + R_{g1} + R_{a1} + R_b + R_{a2} + R_{g2} + \frac{1}{h_{in}} \tag{44.2}$$

$$R_{t2} = \frac{1}{h_{out}} + R_{g1} + R_{a1} + R_{a2} + R_{g2} + \frac{1}{h_{in}} \tag{44.3}$$

In which:

R_{t1} Thermal resistance of insulating glass with blind inside when blind close (m^2·K/W);

R_{t2} Thermal resistance of insulating glass with blind inside when blind retraction (m^2·K/W);

h_{out} Heat transfer coefficient of external surface air, [W/(m^2·K)];

h_{in} Heat transfer coefficient of internal surface air, [W/(m^2·K)];

R_{g1}, R_{g2} Respectively represents the glass thermal resistance of outer and inner layer of hollow blind glass (m^2·K/W);
R_{a1}, R_{a2} Respectively represents the glass thermal resistance of outer and inner layer of hollow blind glass (m^2·K/W);
R_b Blind thermal resistance of insulating glass with blind inside (m^2·K/W).

44.3.2.2 Mathematical Equation of Shading Coefficient

The insulating glass with blind inside shading coefficient (SC) can be calculated as:

$$SC = \frac{g_t}{0.87} \tag{44.4}$$

The total transmittance (g_t) of sunlight in the formula can be calculated as:

$$g_t = \tau_s + q_{ing1} + q_{inb} + q_{ing2} \tag{44.5}$$

In which:
τ_s Visible light transmittance of insulating glass with blind inside;
q_{ing1} Secondary heat transfer heat flux density of external glass;
q_{inb} Secondary heat transfer heat flux density of built-in blind;
q_{ing2} Secondary heat transfer heat flux density of internal glass.

The secondary heat transfer of each glass layer and blind towards indoor in the above formula should be calculated as;

$$q_{ing1} = \frac{A_{sg1} \cdot R_{outg1}}{R_t} \tag{44.6}$$

$$q_{inb} = \frac{A_{sb} \cdot R_{outb}}{R_t} \tag{44.7}$$

$$q_{ing2} = \frac{A_{sg2} \cdot R_{outg2}}{R_t} \tag{44.8}$$

In which:
R_t Thermal resistance of insulating glass with blind inside system (m^2·K/W);
A_{sg1} Solar radiation absorption ratio of external glass;
A_{sb} Solar radiation absorption ratio of built-in blind;
A_{sg2} Solar radiation absorption ratio of internal glass.

The thermal resistance of each layer of glass and the outdoor side direction of blind should be calculated as;

$$R_{outg1} = \frac{1}{h_{out}} + \frac{1}{2} R_{gg1} \tag{44.9}$$

$$R_{\text{outb}} = \frac{1}{h_{\text{out}}} + R_{\text{gg1}} + R_{\text{a1}} + \frac{1}{2}R_{\text{gb}} \tag{44.10}$$

$$R_{\text{outg2}} = \frac{1}{h_{\text{out}}} + R_{\text{gg1}} + R_{\text{a1}} + R_{\text{gb}} + R_{\text{a2}} + \frac{1}{2}R_{\text{gg2}} \tag{44.11}$$

In which:

R_{outg1} Thermal resistance of outdoor side direction of outer glass (m^2·K/W);
R_{outb} Thermal resistance of outdoor side direction of built-in blind (m^2·K/W);
R_{outg2} Thermal resistance of outdoor side direction of inner glass (m^2·K/W);
R_{gg1} Thermal resistance of external glass (m^2·K/W);
R_{gb} Thermal resistance of built-in blind (m^2·K/W);
R_{a1} Thermal resistance of the air layer between outer glass and built-in blind (m^2·K/W);
R_{a2} Thermal resistance of the air layer between inner glass and built-in blind (m^2·K/W);
R_{gg2} Thermal resistance of internal glass (m^2·K/W).

When calculating the thermal performance of insulating glass windows with blind inside, options can be defined according to the status of blind. When built-in blind is lifted up, the heat transfer process and calculation is considered the same as that of hollow glass. When built-in blind is closed, it can be considered as a layer of glass in between the air layer.

44.4 Simulation Calculation of Thermal Parameter

Aiming to understand the heat transfer coefficient, SC and visible light transmittance of hollow glass with built-in blind in various statuses, analog calculation was conducted by using calculation software for thermal performance of doors, windows and glass curtain wall WINDOW6.3 in this paper. WINDOW6.3 is a software to calculation the windows overall thermal performance which was developed by Lawrence Berkeley National Laboratory. It can calculation the optical and thermal performance of single glass, insulating glass and so on. Many International experts account it is a software that widely used, abundant function and calculate accurate. Two particular statuses were chosen to simplify the analog process.

44.4.1 The Simulation Setting of Boundary Conditions

When simulation the thermal parameters of the glass system you need to set the boundary conditions of the environment. In this simulation, choose china environment boundary conditions.The specific parameter setting as Table 44.1.

Table 44.1 Thermal performance calculation boundary conditions

calculation boundary conditions	Winter calculation standard conditions	Summer calculation standard conditions
Indoor air temperature T_{in}	20 °C	25 °C
Outdoor air temperature T_{out}	−20 °C	30 °C
Indoor convection heat transfer coefficient $h_{c,in}$	3.6 W/(m^2·K)	2.5 W/(m^2·K)
Outdoor convection heat transfer coefficient $h_{c,out}$	16 W/(m^2·K)	16 W/(m^2·K)
Indoor average radiation temperature $T_{rm,in}$	20 °C	25 °C
Outdoor average radiation temperature $T_{rm,out}$	−20 °C	30 °C
Solar irradiance I_s	0 W/m^2	500 W/m^2

44.4.2 Simulation Results

The chosen insulating glass windows with blind inside, thickness of (5 + 20A + 5) mm in the analog calculation is filled with argon with ordinary white glass as inner and outer glass. Results showed that when the blind is lifted, the thermal performance of insulating glass windows with blind inside is close to that of ordinary hollow glass. When the blind is closed, the heat transfer coefficient and SC are both lower. Table 44.2 is the thermal performance of several types of ordinary glass and the simulation numerical results. As shown, in hot summer and warm winter zone, in the hot summer insulating glass windows with blind inside has good heat insulation and sun shading function by effectively blocking the solar radiation into indoor and reducing cooling energy consumption of air-conditioning.

Table 44.2 Thermal performance of common glass [5] and the simulation numerical results

Glass kinds		Heat transfer coefficient K[W/(m^2·K)]	Shading coefficient S_e	Data sources
6 mm transparent glass		5.7	0.93	Shenzhen standard SJG15-2005
Single 6 mm high transmittance Low-E glass		3.6	0.58	Guangdong province standard DBJ15-5-2007
Colorless, transparent insulating glass 6 + 9A + 6		3.0	0.82	Shenzhen standard SJG15-2005
Low-E insulating glass 6 + 9A + 6		2.3	0.5	Shenzhen standard SJG15-2005
Insulating glass window with blind inside	Blind retraction	2.73	0.86	Window6.3 simulation results
	Blind close	1.83	0.15	Window6.3 simulation results

44.5 Conclusion

As know from the simulation analysis, the heat coefficient and SC of hollow glass window respectively ranges within 2.73–1.83 W/(m^2·K) and 0.86–0.15. According to adjust the blind, it can achieve the controllability of the heat transfer coefficient and SC of the insulating glass. And also achieve a good insulation, shading effect. In subsequent research, indoor thermal and optical environments of a room with insulating glass window with blind inside will be test. And will verify the accuracy of the heat transfer model by test.

Acknowledgments This research was financially supported by "Twelfth Five-Year' National Technology Program" (2011BAJ03B06) and the Science and Technology Resource Coordinate Project of Shaanxi Province (2011KTCQ03-07).

References

1. Lin H, Nie X, Wu N (2009) Achieve and development of high efficiency energy saving insulating glass window with blind inside. In: Proceedings of the national Plastic Door and Window Industry Annual Conference,Xian,pp 75–80
2. JG/T 255-2009. Sealed insulating glass unit with shading inside
3. Yihua C, Shizhong S, Zhou Y et al (2006) A mathematical model of thermal channel glazing curtain wall. Build Energ Environ 25(4):10–21
4. JGJ/T 151-2008. Calculation specification for thermal performance of windows, doors and glass curtain-walls
5. Lin Z (2010) High efficiency energy saving window—insulating glass window with blind inside. Shenzhen Arch Civil Eng 7(1):64

Chapter 45
Simulation and Analysis for Laboratory Animal Room Air Environment Security Control System

Xinbo Jiang, Changzhi Yang and Wei Chen

Abstract This paper simulated and analyzed the pressure differential of laboratory animal room by CFD software, under a certain wind speed; the windward-side pressure distribution of laboratory animal room was studied; the windward-side pressure differential distribution function was drawn; the corresponding distribution law and max wind pressure point were found. At the same time, the indoor air pressure among the laboratory animal rooms was simulated when the door opened, to find the air pressure differential which can prevent air flow from low-pressure region to high-pressure region, to determine the air pressure differential between indoor and outdoor, and among the laboratory animal rooms, so as to provide certain reference for making code, construction and design, and to decrease positive pressure air change and save energy based on inside air environment achieves requests.

Keywords Laboratory animal room · Pressure differential · Simulation · Energy save

45.1 Introduction

In order to guarantee the laboratory animal room air environment security, the laboratory animal room must keep a higher (lower) air pressure differential to the next room; this is one of the most important characteristics of the laboratory

X. Jiang · C. Yang (✉)
Hunan University, Yuelu District, Changsha 410008, Hunan, China
e-mail: yang0369@126.com

X. Jiang · W. Chen
University of South China, Zhengxiang District, Hengyang 421001, Hunan, China

A. Li et al. (eds.), *Proceedings of the 8th International Symposium on Heating, Ventilation and Air Conditioning*, Lecture Notes in Electrical Engineering 263,
DOI: 10.1007/978-3-642-39578-9_45,

animal room air-conditioning system to the common air-conditioning system, and it is also one of the most important parts of its cleanness. Table 45.1 is the pressure differential request of the laboratory animal [1].

45.2 Pressure Differential Simulations Between Indoor and Outdoor

When the wind flows on the windward side, the wind pressure would be formed on it; Ref. [2, 3] was made some study on it. The aim of this simulation is that through the study on building's windward-side pressure, one can find the change rule of the windward-side pressure.

45.2.1 Physical Model

As shown in Fig. 45.1, it is the physical model; the building is in center of the area; the volume is 4 × 5 × 15 m. It can be known that the width is 5 times of the building and the length is 10 times of it for the simulation area; it can simulate wind flow to the building in the infinitude space. Based on this conditioning, the calculation area can be set as 80 × 20 × 80 m. The distance between building and left border of calculation area is 38 m, the origin on the left bottom is taken, and the coordinate nearest to the corner of the origin is (38.0, 5.5, 0.0), inlet in the left and outlet in the right.

Table 45.1 The pressure differential request of laboratory animal

Environment	Cleanness corridor	Rooms	Contaminated corridor	Outdoor
Barrier (Pa)	+60	+40	+20	0
Isolation (Pa)	+120	+80	+40	0

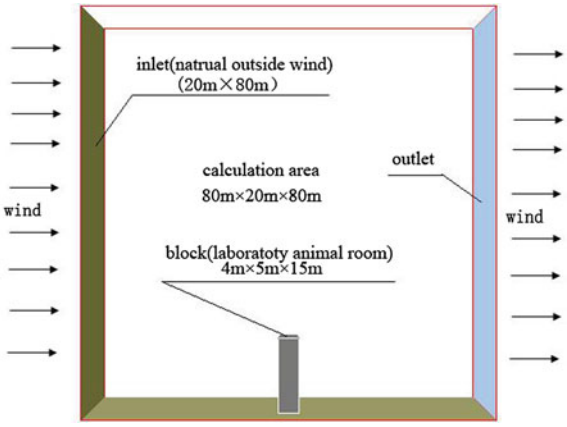

Fig. 45.1 Physical model of the outdoor pressure differential simulation

45.2.2 Mathematics Model and Boundary Condition

This research is related to low velocity of flow, and it can be described by turbulent k–ε equation [4].

The boundary conditions are treated as follow:

1. Boundary condition of the wall

For the wall, boundary condition can be taken as $u = 0, v = 0, w = 0, k = 0, \varepsilon = 0$.

2. Boundary condition of the inlet

The supply air is outdoor wind, and it is a variable with h, and the function [2] is

$$u = u_{10} \times \left(\frac{h}{10}\right)^{a} \tag{45.2.1}$$

In accordance with the geographical location, mean wind velocity of the standard height (always taken as 10 m) is 6 m/s, and the roughness coefficient of the ground is 0.333. So formula (1.1) can be taken as

$$u = 6 \times \left(\frac{h}{10}\right)^{0.333} \tag{45.2.2}$$

$$v = 0 \quad w = 0$$

K, ε of the inlet affected by many factors are always confirmed by experiment. The values are respectively as follow [5]: K = 0.04, $\varepsilon = 0.008$.

Based on the law of conservation of mass:

$$u = -1, v = 0, w = 0.$$

For the boundary condition k, ε, it fits on the second-category boundary conditions:

$$\frac{\partial k}{\partial n} = 0, \quad \frac{\partial \varepsilon}{\partial n} = 0 \tag{45.2.3}$$

45.2.3 Results and Discussion

Figure 45.2 shows velocity and pressure distribution of outdoor pressure differential simulation; the left figure shows the supply air velocity distribution; the right figure shows the pressure distribution; Fig. 45.3 shows the velocity and pressure distribution of the building's windward side. From the Fig. 45.2, we can see that

the velocity of building's windward side becomes larger and larger along the height direction, and the data can be obtained from the simulation value. It also can be seen from Fig. 45.2. In the calculate area, The pressure is kept to be 1 Pa in the most of the area. However, the pressure gradient become bigger near the wall. From Fig. 45.3, we can see that the wind impinged on the wall. Then it was divided into two parts. One part walks along the wall to the bottom with forming a whirlpool. Another part continued walking along the wall toward the upside and, then climbed over the wall from the top. In the figure, it can be clearly seen that a boundary layer separation phenomenon appears at the top of the boundary layer (h = 15 m) and speed of airstreams suddenly increased and it was changed into a negative pressure point. The more detailed description for the phenomenon of boundary layer separation can be found in Ref. [6–8].

According to simulation results, a function of windward-side pressure distribution is fitted as

$$P = -0.0408h^3 + 0.7663h^2 - 2.4746h + 12.1428 \tag{45.2.4}$$

According to function (45.2.4), the location of minimum pressure is in $h = 1.90$ m, the location of maximum pressure is in $h = 10.62$ m, and the value is $P_{\max} = 23.42$ Pa.

45.3 Pressure Simulations Among the Indoor Rooms

As the result of personnel activity, the animals can be overlapping infected. In order to prevent this kind of phenomenon, a differential pressure between the rooms needs to be established, and this prevents the air flow to the low cleanness

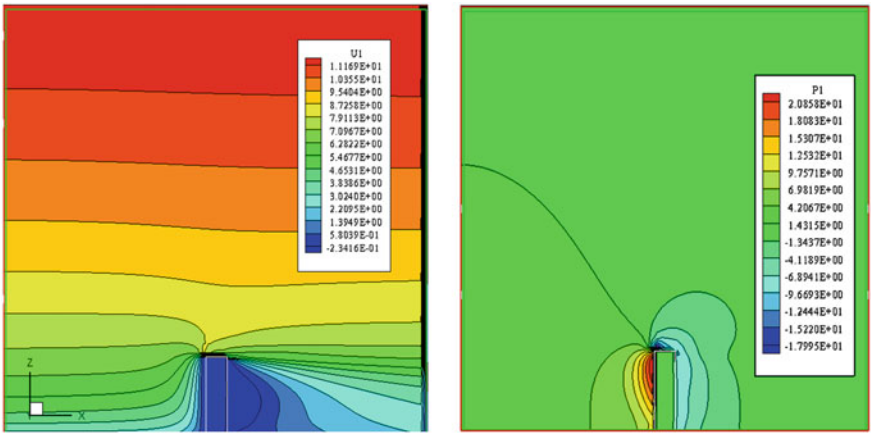

Fig. 45.2 The distribution of outdoor velocity and pressure differential

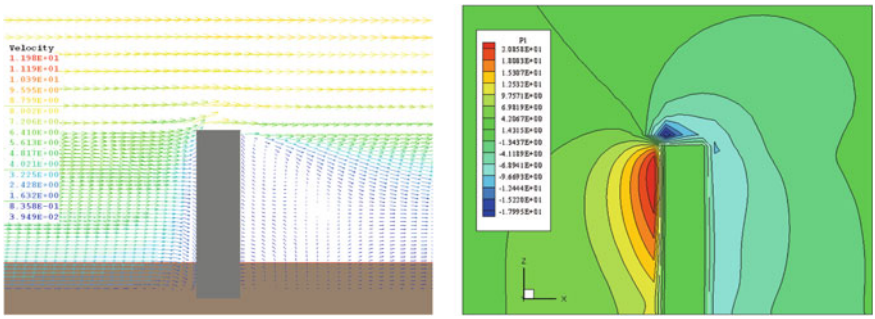

Fig. 45.3 Zoom in the distribution of outdoor velocity and pressure differential

room from the high cleanness room. We can know from Table 45.1, the differential pressure gradient in the barrier environment is 20 Pa, and the pressure gradient in the isolation environment is 40 Pa. Presently simulated two rooms under the differential pressure 20 Pa, two rooms differential pressure change rate when the door is opening.

45.3.1 Physical Model

As shown in Fig. 45.4, a door connects room 1 and room 2, and there are three probes in two rooms—probe 1, probe 2, and probe 3[10,11], which record the parameter change rate such as velocity and pressure. The red one is high-pressure room and the white one is the low-pressure room, and the differential pressure between two rooms is 20 Pa. The trim size of the room is 1.0 × 1.0 × 1.0 m, and the trim size of the door is 0.2 × 1 m; taking the origin on the down basement in

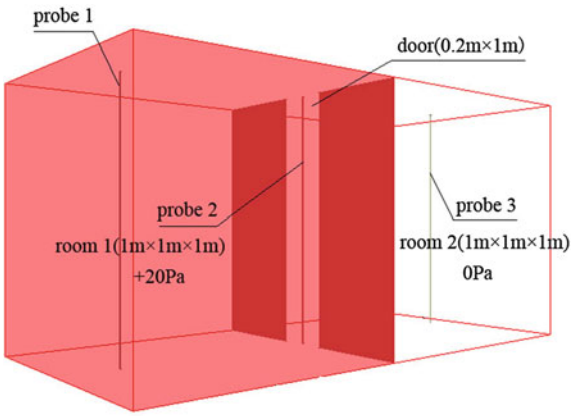

Fig. 45.4 Model of the pressure simulation among the indoor rooms

the left of the red room, the coordinates of the three probes are (0.2, 0.5, 0.0), (0.1, 0.5, 0.0), and (1.8, 0.5, 0.0), respectively.

The turbulent model of the simulation is $k-\varepsilon$ equation [4]. Boundary condition refers to Sect. 2.2

45.3.2 Results and Discussion

Figure 45.5a–f shows the pressure transformation in two rooms. At first, the pressure in room 1 is +20 Pa (relative to atmospheric pressure), and the pressure in room 2 is 0 Pa. When the partition board was pulled out suddenly, air currents driven by the differential pressures, flow from room 1 to room 2, until two rooms balanced.

Figure 45.6 is probe records of pressure changes over time, Fig. 45.6a shows the pressure transformation record taken by probe 1, Fig. 45.6b shows the record taken by probe 2, and Fig. 45.6c shows the record taken by probe 3. In this process, the time step is 0.00001 s. It can be found the pressure transformation in room 1 and room 2 through observing Fig. 45.6a, c. In Fig. 45.6a, the pressure changes from +20 Pa to balance state. After balancing, the pressure continues to decline instead of being static. Then it reaches to 0 Pa. At the same time room 2 has a similar process. Figure 45.6b shows pressure transformation of the door; at first, the pressure is 0 Pa, and with the progress in time, it becomes 15 Pa, and there are fluctuations in the value.

Figure 45.7 shows the velocity of flow produced by 20 Pa differential pressures on the door. It is the point velocity of flow recorded by probes. Figure 45.7a shows the data recorded by probe 1 in room 1, Fig. 45.7b shows the data recorded by probe 2 in room 2, and Fig. 45.7c shows the data recorded by probe 3 in the middle of two rooms. According to this, the formula can be described:

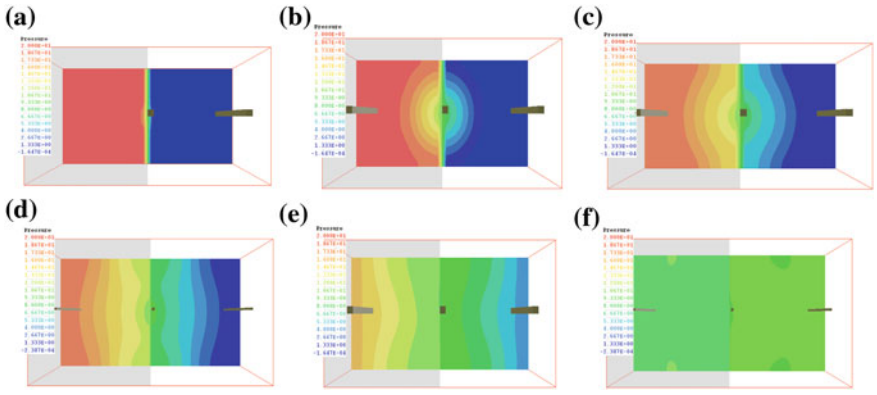

Fig. 45.5 The pressure transformation in two rooms

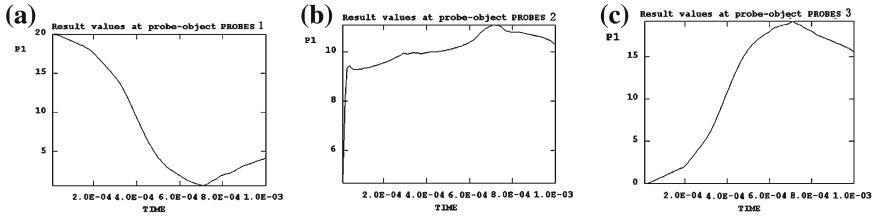

Fig. 45.6 Pressure transformation recorded by probes

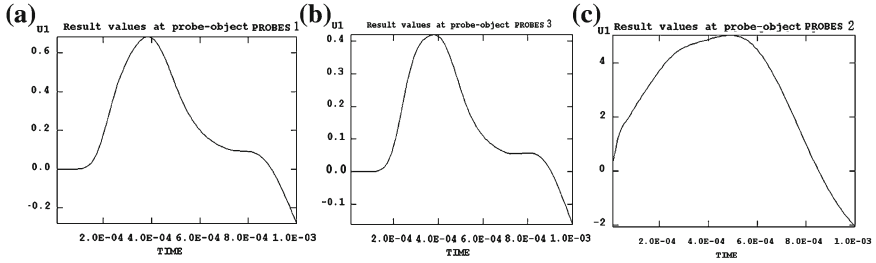

Fig. 45.7 The velocity value recorded by probes

$$v_c = \frac{1}{\sqrt{\xi_1 + \xi_2}} \sqrt{\frac{2\Delta P}{\rho}} = \varphi \sqrt{\frac{2\Delta P}{\rho}} = 0.82 \sqrt{\frac{2 \times 20}{1.2}} = 4.73 \text{ (m/s)} \qquad (45.3.1)$$

It can be seen in Fig. (c), that the maximum velocity of flow is 5 m/s. And the value of the difference is not great. When people walk from the area of low-pressure zone to high-pressure zone, airspeed is generally about 0.14–0.2 m/s; when the value of the differential pressures of two rooms remain in 20 Pa, the resulting value of speed is 5 m/s and can offset the speed produced by walking person. Figs. (a) and (b) show the data recorded by probe in those room, and it can be seen that the rate of change is very similar to two figures; it shows pressure changes that are synchronized; when the pressure diminishes in room 1, the pressure in room 2 immediately increases; the time difference is very small.

45.4 Conclusions

We can draw a conclusion based on the previous analysis:

1. When it is windward, the maximum pressure is always 1/4–1/3 of the top. In that, we should increase the pressure on this point for the safe of the environment of the laboratory animal room.
2. When the rate of the coming natural wind is 6 m/s, we can calculate the max pressure that is around 23.4 Pa. The code regulates differential pressures

between indoor and outside that should be 20–50 Pa in normal situation. Based on the calculated result, if the wind velocity is greater than 6 m/s, then the differential pressures between door and indoor should be greater than 25 Pa for the safe of indoor environment, so that the outside air is unable to permeate into indoor through the windward side.

3. When we set indoor pressure differential gradient as 20 Pa, it can offset the affect of personnel activity, and prevent the low-pressure area from pollutants.
4. Pressure change shocks occur during the simulation, and this is because the simulation process cannot provide continuous pressure. If continuous pressure can provide by high-pressure area, then continuous air currents can flow from high-pressure area to low-pressure area and prevent pollutants from the area of low-pressure to high-pressure infiltration; thus, laboratory animal room security can be guaranteed.

References

1. State Bureau of Quality and Technical (2002) PRC national standards GB14925-2001, Laboratory animal-Requirements of environment and housing facilities 2002 (in Chinese)
2. Zhang X (1984) Structure wind pressure and wind libration. Publishing Company of Tongji University, Shanghai (in Chinese)
3. Wengfei W, Yike L, Yongzheng F (1997) Analyzing numerically the wind pressure distribution on building change with building length. J Baotou Univ Iron Steel Technol 37(1):54–57 (in Chinese)
4. Zhuo W, Iida T, Moriizumi J, Aoyagi T (2001) Simulation of the concentrations and distributions of indoor radon and thoron. Radiat Prot Dosim 93(4):357–368
5. Yamagutsi K (1979) Basic research of indoor air distribution. OSAKA University, Ph.D. Thesis
6. Bao H, Chen P, Wu Y (2003) Prediction of wing boundary layer separation area with turbulent models. J Beijing Polytech Univ 29(2):159–163 (in Chinese)
7. Bao H (1998) Bordering algorithm for solution of boundary layer separation flow. Acta Aerodyn Sinica 16(4):468–472 (in Chinese)
8. Voronin VI, Ulyanov GS, Shvetz AI (1993) Experimental study of supersonic flow past wedges with longitudinal grooves on the windward side. Fluid Dyn 28(2):296–298

Chapter 46
CFD Simulation of the Airflow in Poultry Housing with Wind Shield

Huifeng Zou, Fuhua Yang, Yingchao Fei, Hao Tang, Ying Zhang and Sheng Ye

Abstract The chapter discussed the change of the airflow distribution in poultry housing after installing windshields in summer. We have analyzed the temperature and speed in the poultry housing with windshield by the software Airpak. We got the conclusion through the temperature field and speed field of the poultry housing with windshield in comparison with that in a common longitudinal ventilation poultry housing. The chapter also made a research on an optimized installation height of the wind shield and compared the air distribution when the windshield installation height is 1.6, 1.8, and 2.0 m, respectively. The application of windshield can significantly increase the wind speed and reduce the poultry housing temperature. And the numerical simulation proved that the appropriate installation height should be 1.8 m.

Keywords Poultry housing · Wind shield · Airpak · Numerical simulation

46.1 Introduction

In hot summer, there is much heat inside the poultry housing and the temperature of the poultry housing increases sharply. If the temperature in the poultry housing has not been adjusted appropriately, it will cause the "heat stress" of the chickens which influences the feed intake, daily gain, and laying rate of the chickens. As a result, the feed efficiency decreases. More seriously, the high temperature may

H. Zou · F. Yang (✉) · Y. Fei · H. Tang · Y. Zhang
School of Municipal and Environment Engineering, Shenyang Jianzhu University, Shenyang 110168, China
e-mail: yfh1989@yahoo.com.cn

S. Ye
School of Management, Shenyang Jianzhu University, Shenyang 110168, China
e-mail: yesheng@163.com

A. Li et al. (eds.), *Proceedings of the 8th International Symposium on Heating, Ventilation and Air Conditioning*, Lecture Notes in Electrical Engineering 263,
DOI: 10.1007/978-3-642-39578-9_46,

cause "heat exhaustion" of the chickens, which will lead to mass mortality of the chickens in a short time [1]. This will bring great harm to the poultry industry. In order to reduce the death rate and elimination rate of chickens caused by "heat stress" and enhance the production efficiency of the poultry enterprise, we must take effective measures to create a good living environment for the chickens [2].

Viewing from improving the "air-cooling effect" by reducing the indoor temperature and increasing the air velocity, most domestic poultry housing use the longitudinal ventilation mode in summer [3], namely the water curtain is installed in the air inlet region and 6–8 platoon fans are installed at the end area of the house. The exhaust fans exhaust air, which causes a negative pressure in the poultry housing. Hot air goes through the water curtain, and the temperature of the coming air drops. The air flows longitudinally along the poultry housing and is discharged by the platoon fans. For chickens, the ideal air velocity of the poultry housing in summer is above 2 m/s, which will help to remove excess heat better and keep a good "air-cooling effect". Generally, the air velocity on both sides of the poultry housing is higher than that in the center. The air velocity of the upper edges inside the poultry housing is higher than that near the ground. The difference between two velocities can achieve more than 30 %, and the gap will be even expanded to 200 % in the poultry housing of poor environment [4]. Actually, the cooling effect of the poultry housing is far from what we expected.

The ventilation velocity formula of the poultry housing:

$$\text{Air velocity} = \text{Ventilation volume}/\text{Sectional area}$$

We can get two methods of improving the air velocity in the poultry housing [5]. The two methods are as follows:

1. Improve the ventilation velocity of the poultry housing. The specific manifestations are increasing the amount of the fans or enlarging the model of the fans.
2. Reduce the sectional area. Increasing the amount of the fans or enlarging the model of the fans means the increase of the poultry housing's operating costs. Considering the situation that the profit of the breeding industry is generally low, we should reduce the operation cost of the enterprise. From the perspective of reducing the sectional area, one practice of the breeding enterprise is making a ceiling for the poultry housing, so that the height of the poultry housing has been decreased. Another practice is temporarily installing windshields or windshield curtains every certain distance vertically along the triangle roof.

Therefore, the chapter uses the CFD software Airpak to simulate the common poultry housing and a windshield-installed poultry housing [6]. Comparatively analyzing the two poultry housing from the temperature field and the air velocity field, we get that poultry housing with windshields is better than the common one in improving the indoor air velocity and removing excess heat of the poultry housing. Then, we conducted an optimized research in installation height.

46.2 CFD Model and the Boundary Conditions

46.2.1 Physical Model

The chapter uses a longitudinal ventilation henhouse in North China area as an example. The geometric model of the henhouse (Length × Width × Height) is 56 (X) × 10.6 (Y) × 2.7 (Z) m. There are three rows of poultry cages in the henhouse. The length of the poultry cages is 54.0 m, being symmetrically arranged in the henhouse. The height of "wet curtain inlet" in the sidewall is 0–2.0 m, and the length of "wet curtain inlet" is 5.0 m. The windshield curtains are transversally set every 8 m in the henhouse. The positions of the windshield curtains, the air inlets, and the poultry cages are shown in the Fig. 46.1.

46.2.2 Mathematical Model

The airflow inside the henhouse is a turbulent flow, and the air velocity is generally less than 10 m/s. Therefore, we use k-ε dual-equation turbulent model in Airpak for numerical simulation [7].

We establish the following hypotheses:

1. The airflow is a turbulent flow, which is incompressible.
2. Assume that the flow field has a high Re number, and the turbulent viscidity of the airflow is anisotropic.
3. The airflow is a low velocity flow. So, we can ignore the heat consumption caused by the fluid viscous force.
4. Ignore the influence of the air leakage and assume that the air tightness of the henhouse is excellent.

Based on the hypotheses, the governing equations can be expressed as follows:
Continuity equation:

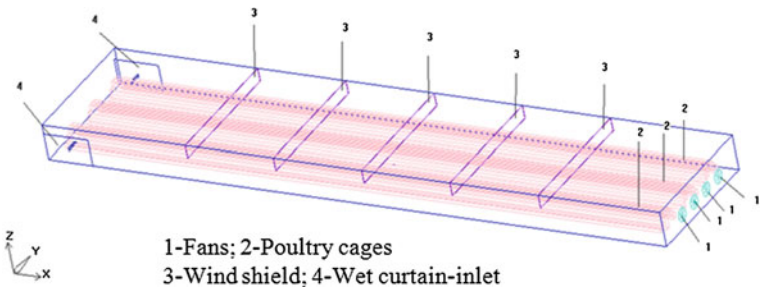

Fig. 46.1 The schematic plot of the longitudinal ventilation henhouse

$$\frac{\partial}{\partial X_i}\left(\rho U_i U_j\right) = -\frac{\partial}{\partial X_i}\left[\mu_t + \mu_\tau\left(\frac{\partial U_i}{\partial X_j} + \frac{\partial U_j}{\partial X_i}\right)\right] + \beta(T_0 T)\rho g; i,j = 1,2,3 \quad (46.2.1)$$

$$\text{Energy equation}: \frac{\partial}{\partial X_i}(\rho U_i T) = -\frac{\partial}{\partial X_i}\left[\left(\frac{\mu_\tau}{\text{Pr}} + \frac{\mu_t}{\sigma_r}\right)\frac{\partial T}{\partial X_i}\right] + \frac{q}{CP_i}; i = 1,2,3 \quad (46.2.2)$$

Turbulent dynamic equation (k equation):

$$\frac{\partial}{\partial X_i}(\rho U_i k) = -\frac{\partial}{\partial X_i}\left(\frac{\mu_t}{\sigma_k}\frac{\partial k}{\partial X_i}\right) + \mu_t\left(\frac{\partial U_i}{\partial X_j} + \frac{\partial U_j}{\partial X_i}\right)\frac{\partial U_i}{\partial X_j} - \rho g + \beta g\frac{\mu_t}{\text{Pr}}\frac{\partial T}{\partial_{X_j}}; i = 1,2,3 \quad (46.2.3)$$

Turbulent kinetic energy dissipation rate equation (ε equation):

$$\frac{\partial}{\partial X_i}(\rho U_i \varepsilon) = -\frac{\partial}{\partial X_j}\left(\frac{\mu_t}{\sigma_k}\frac{\partial \varepsilon}{\partial X_i}\right) + C_1\mu_t\left(\frac{\partial U_i}{\partial X_j} + \frac{\partial U_j}{\partial X_i}\right)\frac{\partial U_i}{\partial X_j} - C_2\frac{\varepsilon^2}{k} + C_3\beta g\frac{\varepsilon\mu_t\partial T}{k\ \text{Pr}\,\partial_{X_i}}; i,j = 1,2,3 \quad (46.2.4)$$

Turbulent viscosity coefficient expression:

$$\mu_t = \frac{C_\mu C_D \rho k^2}{\varepsilon} \quad (46.2.5)$$

In Eqs. (46.2.1)–(46.2.5), g is the acceleration of gravity; k is the turbulent kinetic energy; p is the time-average pressure; Pr is the Prandtl number of adequate turbulent flow; T is the fluid temperature; T_0 is the reference temperature; U_i is the velocity component; $i = 1,2,3$represents the direction of X, Y, Z; ε is the turbulent energy dissipation rate; respectively μ_t and $\mu_\tau$is the viscosity coefficient of the laminar flow and the turbulence; ρ is the fluid density; β is the volumetric expansion coefficient; and $C_1, C_2, C_3, C_\text{D}, C_\mu, \sigma_r, \sigma_k$ are the empirical constants.

46.2.3 The Boundary Conditions

The air inlet is the velocity inlet, and the air outlet is the pressure outlet. According to the total air volume, we choose 5.2 m/s as the air inlet velocity. There is a cooling process when the air goes through the wet curtain. Assume that the air temperature near the inlet is 16 °C and the velocity is 12.3 m/s. The walls and ceiling of the henhouse are set as no-slip surface boundary. The fluid velocity on the fixed boundary equals to the velocity on the wall surface. Considering the heat convection between the outdoor space and indoor space, we use the unstructured grid to divide the model. We use the finite volume method and "simple" algorithm to solve the differential equations discretely.

46.3 The Simulation Results and Analyses

46.3.1 The Influence on the Velocity Field by Adding Wind Shields

The average height of the poultry body is 1.4 m. We choose the height as the standard. The simulation results of air velocity inside the henhouse are shown in Figs. 46.2 and 46.3 [8].

From the Figs. 46.2 and 46.3, we can get that the air velocity inside the henhouse is almost uniform. The outdoor air goes into the henhouse by the negative pressure which is produced by the air exhaust of the fans. The air velocity in the region near the air inlet and the fans is comparatively higher than that in other regions. The velocity is nearly 4 m/s. The minimum velocity in the henhouse is almost 0 m/s. This is because local area becomes the whirlpool area, which is caused by the backflow. We can know from the color distribution that the general average velocity is obviously higher after adding the wind shields.

46.3.2 The Influence on the Temperature Field by Adding Wind Shields

We analyze the change in the temperature field after installing the wind shields. We discuss whether the windshields are conducive to discharge the waste heat and lower the temperature inside the henhouse. The simulations of the temperature distribution in Section $X = 40$ Figs. 46.2 and 46.3.

From the two figures, we can see that the temperature inside the henhouse distributes symmetrically and uniformly. There is no obvious thermal stratification. The temperature near the cages is high. This is because the chickens are the main source of heat release. The temperature near the top of the henhouse is 17 °C, and temperature in the section is basically between 16.3 and 22.6 °C, which conform to the temperature requirement of the henhouse. Comparing the two

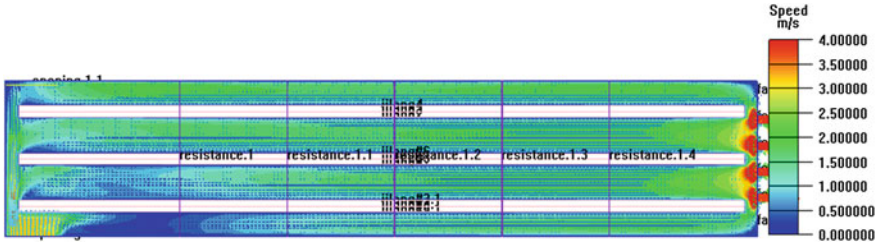

Fig. 46.2 The velocity distribution of section $Z = 1.4$ m with wind shields

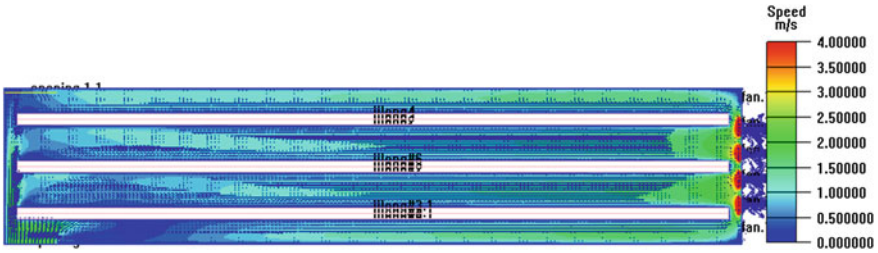

Fig. 46.3 The velocity distribution of section $Z = 1.4$ m without wind shields

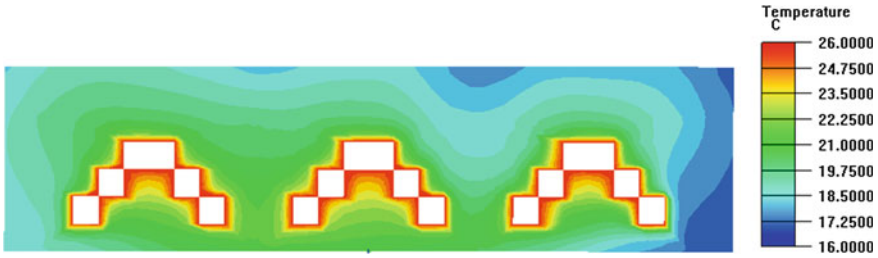

Fig. 46.4 The temperature distribution of section $X = 40$ m with wind shields

figures, we can get that the overall average temperature of the section installing windshields is obviously lower than that with no wind shields. In Fig. 46.5, the temperature at the height of 0.8 m is between 21 and 22.6 °C. In Fig. 46.4, the temperature at the height of 0.8 m is between 17 and 18.7 °C. The phenomenon shows that the installation of the windshields effectively helps to release the heat inside the henhouse and lower the effect of the "heat stress". This greatly improves the growth environment of the chickens.

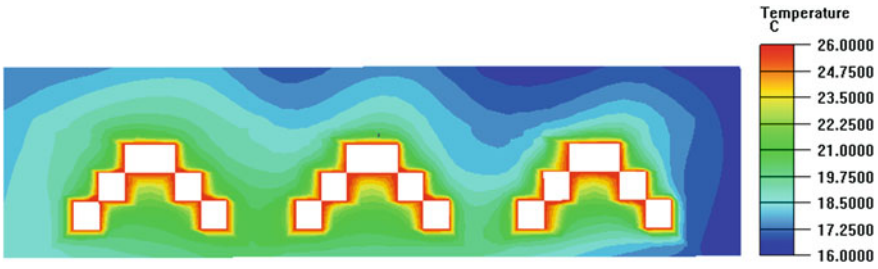

Fig. 46.5 The temperature distribution of section $X = 40$ m without wind shields

46.3.3 The Installation Height Optimization of the Wind Shield

We analyze the air velocity in the henhouse with windshields installed at the height of 1.6, 1.8, and 2.0 m. Set the henhouse length as axis and the henhouse width as the y axis. We get the air velocity of the coordinate points under three different situations from the simulation. The simulation result is show in the Fig. 46.6.

Comparing the three broken lines in the Fig. 46.6, we know that the air velocity increases rapidly along the direction of the henhouse length. The curvature of the curves shows that when the installation height is 1.8 and 2.0 m, the improvement of velocity is obvious and rapid. And when the installation height is 2.0 m, the fluctuation range of the temperature is small. When $X = 4$ m, the size of the air velocity is at the same starting point. When $X = 12$ m, the air velocity of the henhouse with windshields installing at the height of 1.6 m is the maximum (1.786 m/s). These situations show that lower installation height of the windshields is more conducive to improving the air velocity. Throughout the three curves, the average air velocity in the henhouse with windshields installing at the height of 1.6 m is the largest but the internal air velocity distribution of which is not uniform. The gap between the minimum and the maximum air velocity is nearly 3 m/s. The large air velocity in local area leads to a result that the hydrostatic pressure is too high. The air leakage goes into the henhouse easily, which influences the cooling effect of the henhouse. It is disadvantageous to the breeding environment. When the windshields are installed at the height of 2.0 m, the air velocity is too low for the chickens to grow. The maximum air velocity is only 1.4 m/s, far from the air velocity needed by the chickens. Turning to the curve of installation height 1.8 m, the maximum velocity is 3.3 m/s and the average velocity is 2.4 m/s, which satisfies the velocity requirement of the henhouse and cause a certain degree of "air-cooling effect". In conclusion, the windshield installation height of 1.8 m is the most suitable for the growth of the chickens.

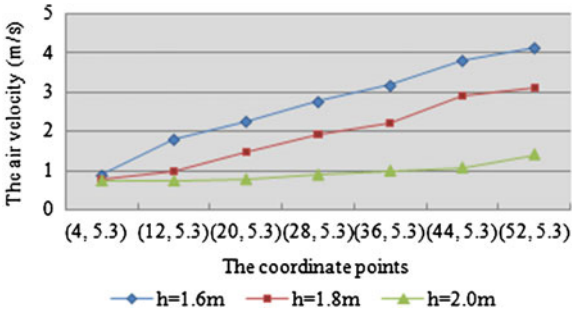

Fig. 46.6 The air velocity of the coordinates in the henhouse

46.4 Conclusion

1. The installation of the windshield can effectively improve the velocity and decrease the temperature inside the henhouse, which enhances the "air-cooling effect" in the hot summer.
2. Based on the simulation analyses, an improper installation height of the windshields will produce a negative effect on the improvement of the henhouse indoor environment.
3. Based on the simulation results, the optimized installation height of the windshields should be determined by the specific dimensions of the henhouse. In this case, a height of 1.8 m is the most suitable for the growth of the chickens.

Acknowledgments This research was supported by the Natural Science Foundation of China (51208313).

References

1. Sun X (2001) Poultry under heat stress. China Poultry 23(16):32–34
2. VonWachenfelt E (1994) Modern techniques give less air pollution in broiler houses. In: Proceedings of the XII world congress on agricultural engineering, Milan CIGR, Meribeke, Belgium, 1994, 590–598
3. Zhang T, Xu Y, Huang Z, Cui Y (1998) Thermal environmental study on high density stacked-cage-raising layer house in summer. J China Agric Univ (15):38–43
4. Zhang T (1997) Environment system study in high density stacked-cage-raising layer house on the tropic climate. Beijing: China Agricultural University, 10, 44–48
5. Wang S, Zhang J, Wang H (2010) The effect of indoor thermal comfort by changing velocity of air inlet. J Shenyang Jianzhu Univ (Natural Sci) (26):166–170
6. Li H (2006) Simulation of humidity and temperature field in ventilated henhouse and study environmental testing. J Inner Mongolia Agricult Univ (5):31–37
7. Tan H (1999) Application of CFD in the thermal environment engineering field in Japan. J HVAC (4):23–28
8. Hauser RH, Filch DW (1988) Measures for measuring ammonia in poultry houses: review and approved practices. J Vet Med 35:579–593

Chapter 47
Research on Built Environmental Characteristics of Double-Skin Facade

Weijie Zhang, Yanyan Li, Dongyuan Gao and Qianqian Zhao

Abstract A new type of double-skin facade (DSF consists of unitary double-breathing-type glass curtain wall with an adjustable outer shade) is suggested and discussed. Instead of ordinary outer wall configuration (with a certain ratio of transparent window to opaque wall), DSF is installed as the whole facade outer wall of a typical office room (one room selected from a typical office building). Characteristic comparison of built environment within the typical office room (located in a certain meteorological region) has been done in detail by simulation work between the ordinary configuration and our new configuration. Characteristic comparison work includes light gain and its distribution characteristics, temperature distribution, even the thermal load and HVAC systematic energy consumption characteristics of the room have been also accomplished and presented. Further, research on regional adaptation has been also done by selecting four different meteorological regions in China from north to south (Harbin, Beijing, Shanghai and Guangzhou). Base on our research work, the advantages of the built environmental characteristics of the DSF can be well obtained and demonstrated.

Keywords Built environment · Characteristic · Double-Skin Facade (DSF) · Adjustable outer shade · Simulation · Comparison · Regional adaptation

47.1 Introduction

Building envelope plays an important role that affects the built environment (mainly including light distribution, temperature distribution) greatly. Glazing windows on facade are often preferred by many architects to achieve better light

W. Zhang (✉) · Y. Li · D. Gao · Q. Zhao
College of Urban Construction, Hebei University of Engineering, Handan 056038, China
e-mail: zhangweijie_5@sina.com

A. Li et al. (eds.), *Proceedings of the 8th International Symposium on Heating, Ventilation and Air Conditioning*, Lecture Notes in Electrical Engineering 263,
DOI: 10.1007/978-3-642-39578-9_47,

gain, artistic facade decoration and better persons' view effect and scope. But on the other hand, this kind of installation is usually opposed by HVAC (Heating, ventilation and Air-Conditioning) engineers, because it may cause large increasing of building thermal load (both heating load in winter and cooling load in summer), may cause large increasing of services energy consumption, and makes the control of built environment more difficult [1]. So in many circumstances, the ratio of window to wall is often limited. If this kind of contradiction be well resolved, both side advantages can be obtained. This kind of research is worth accomplished and of great significance. Double-skin facade (DSF) which has variety excellent characteristics can gain favour with both architects and HVAC engineers [2].

In this paper, a new style of DSF is suggested and discussed. Instead of ordinary outer wall configuration (with a certain ratio of transparent window to opaque wall), DSF with an adjustable outer shade is installed as the whole facade of a typical office room (one room selected from a typical office building). Characteristic comparison of built environment within the typical office room (located in a certain meteorological region) has been done in detail by simulation work between the ordinary configuration and DSF. Characteristic comparison work includes light gain and its distribution characteristics, temperature distribution characteristics, even the thermal load, and HVAC systematic energy consumption characteristics of the room have been also accomplished and presented. Further, research on regional adaptation [3] has been also done by selecting four different meteorological regions in China from north to south (Harbin, Beijing, Shanghai and Guangzhou).

Based on our research work, the advantages of the built environmental characteristics of the new style of DSF can be well obtained and demonstrated. It is convinced that this kind of research work is valuable and helpful to the design work of energy efficient building and green building.

47.2 Establishment of Model Building and Model Room

47.2.1 Model Building

Two kind of model office buildings (A and B) are established, all the configuration dimensions and structural materials of Building A and Building B are the same except the facade configuration. Building A has the ordinary facade configuration, and Building B has the facade configuration with the new style of DSF. Building A and Building B are all five-storey office buildings, the plane area is 994.5 m^2 from first floor to third floor, and the plane area is 982.8 m^2 from fourth floor to fifth floor, floor height of the office building is 3.6 m. The outlook of the Building A is shown in Figs. 47.1 and 47.2. The window dimensions are all 2.4 m $\times$ 2 m. The outlook of the Building B is shown in Figs. 47.3 and 47.4.

Fig. 47.1 Outlook of building A

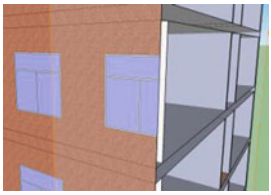

Fig. 47.2 The profile of building A

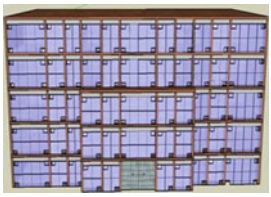

Fig. 47.3 Outlook of bBuilding B

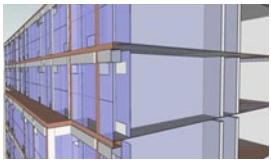

Fig. 47.4 The profile of building B

47.2.2 Model Room

To demonstrate the process and results of simulation work and comparison work, a model Room A from the Building A and a model Room B from the Building B are selected as the objective case. Room A and Room B are at the same position within each building. The outlook of Room A is shown in Figs. 47.5 and 47.6.

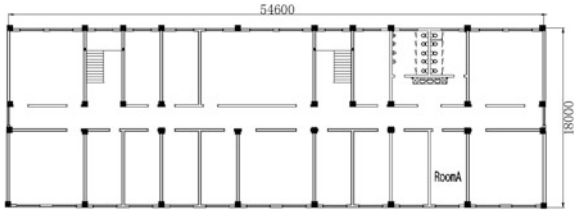

Fig. 47.5 The plan of the fourth floor

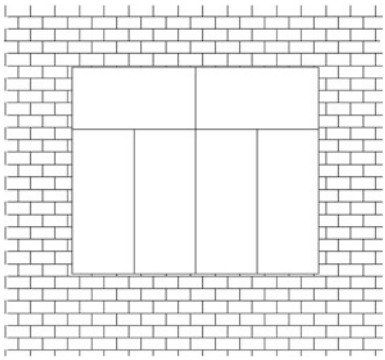

Fig. 47.6 Outlook of the room A

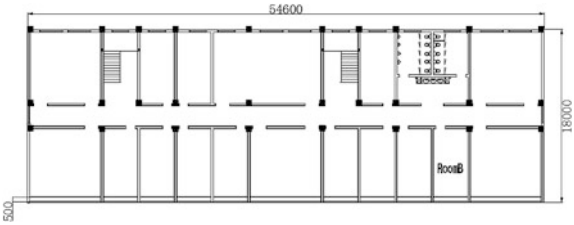

Fig. 47.7 The plan of fourth floor

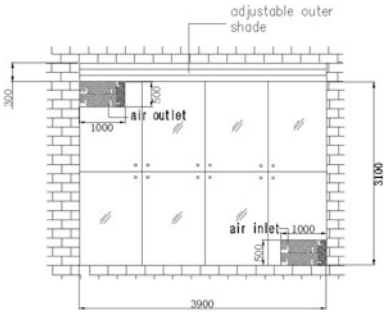

Fig. 47.8 Outlook of room B

The outlook of Room B is shown in Figs. 47.7, 47.8 and 47.9.

This model building B with the new style of DSF is a kind of new building envelope (the double-breathing-type glass curtain wall with an adjustable outer shade). The new building facade (as a part of building envelope) is made up of curtain wall units [4]. The size of the curtain wall unit is 3.9 × 3.1 m. It is made up of two layers of glass curtain wall. Toughened glass is used as outer curtain wall, Low-e glass is used as the inner curtain wall. The interval of two layers of glass curtain wall is 500 mm. Every curtain wall unit has one air inlet and one air outlet. The size of the air inlet and the air outlet is 1.0 m × 0.5 m. The air inlet is at the bottom of the outer curtain wall and the air outlet is at the top of the outer

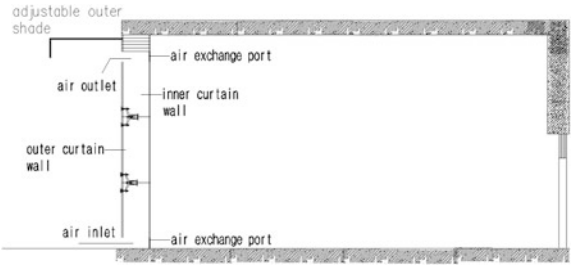

Fig. 47.9 The profile of room B

curtain wall. Every corners of the inner curtain wall has an air exchange port which generally be closed. The size of the air exchange port is 1.0 × 0.5 m.

47.3 Simulation Work

47.3.1 Parameter Descriptions of the Model Room

Parameters of the building envelope are listed in Table 47.1 (Building A) and Table 47.2 (Building B).

Table 47.1 Thermal characteristics of the facade (building A)

Thermal characteristics of the facade	External wall: insulated concrete wall, U-Value = 1.22 W/m^2·k
	Glass: toughened glass, U-Value = 19.3 W/m^2·k
	Density:2,220 kg/m^3
	Cp-value = 830 J/kg·k
	Thermal conductivity: 1.15 W/m·k
	The plane area of room A: 30.42 m^2

Table 47.2 Thermal characteristics of the facade (building B)

Thermal characteristics of the facade	External wall: Insulated concrete wall, U-Value = 1.22 W/m^2·k
	Outer curtain wall: toughened glass, U-Value = 19.3 W/m^2·k
	Absorption coefficient of solar radiation ρ = 0.75
	Solar radiation intensity I = 450 W/m^2
	Density: 2,220 kg/m^3
	Cp-value = 830 J/kg·k
	Thermal conductivity: 1.15 W/m·k
	Inner curtain wall: low-e glass, U-Value = 2.0 W/m^2·k
	The plane area of room B: 30.42 m^2

Table 47.3 Descriptions of the set parameters of the Building B

Environmental temperatures	Outer curtain wall temperature: $t_z = t_w + \frac{\rho I}{U} = 50.9°C$
	where $\rho = 0.75$ I = 450 W/m^2
	tw = 33.6 °C U = 19.3 W/m^2·k
	Surface temperature of inner walls: 26 °C
	Glass emissivity: $\varepsilon = 0.932$
	Wall thickness: 0.42 m Glass thickness: 0.013 m
	Air inlet/air outlet size: 0.5 × 1.0 m
	Air inlet/air outlet mode: closed
The velocity boundary condition	Air inlet velocity: 0
	Turbulence model: NEWκ-ε model

47.3.2 Simulation Work

The simulation of the model room is based on the set parameters of the building which has been obtained by Tables 47.3 and 47.4. Take the set parameters of the building as the input data of CFD simulation. The CFD simulation results are illustrated in Figs. 47.10 and 47.11, which is simulated by Fluent. The thermal load simulation results are illustrated in Fig. 47.14, which is simulated by EnergyPlus software. The natural room temperature simulation results are illustrated in

Table 47.4 Descriptions of the set parameters of the Building A

Environmental temperatures	Outer wall temperature: 33.6 °C
	Inner boundary air temperature: 26 °C
	Glass emissivity: $\varepsilon = 0.932$, window mode: closed
	Wall thickness: 0.42 m, glass thickness: 0.013 m
The velocity boundary condition	Air inlet velocity: 0
	Turbulence model: NEW κ-ε model

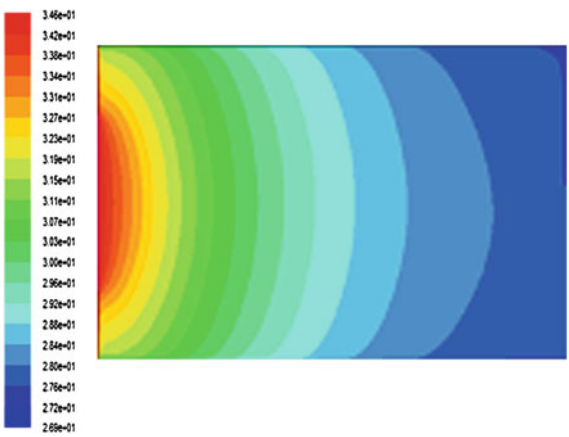

Fig. 47.10 Temperature contour of room A

Fig. 47.11 Temperature contour of room B

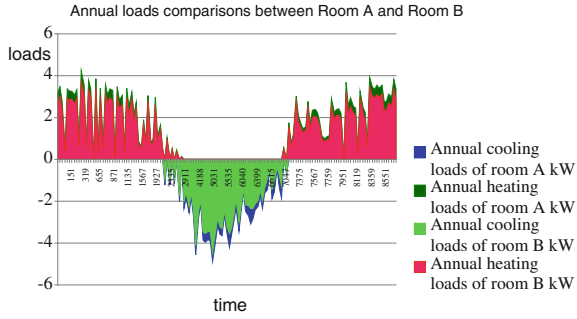

Fig. 47.12 Illumination contour of room A

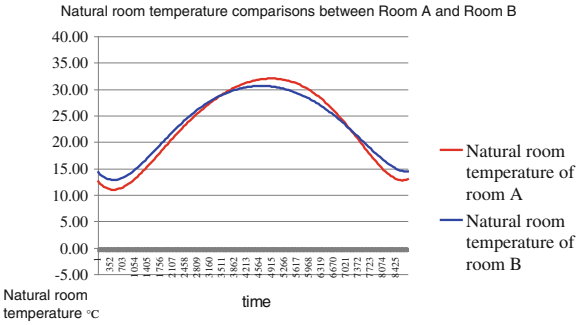

Fig. 47.13 Illumination contour of room B

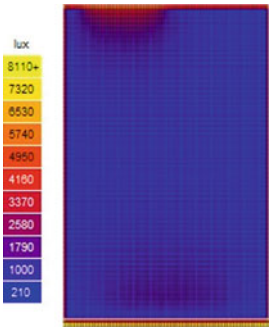

Fig. 47.14 Hourly thermal load of the building in the whole year

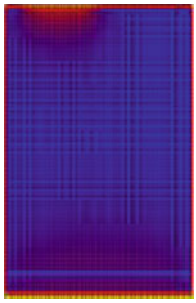

Fig. 47.15 Hourly natural room temperature of the building in the whole year

Fig. 47.15, which is simulated by DeST software. The indoor illumination distribution simulation results are illustrated in Figs. 47.12 and 47.13, which is simulated by Ecotect software [5].

47.3.3 Analysis on Regional Adaptation

Simulation work has been taken within four different regions. The regions are Harbin, Beijing, Shanghai and Guangzhou. The thermal characteristics of the building facade are listed in Table 47.5 .

Simulation results are illustrated in Figs. 47.16, 47.17, 47.18, 47.19, 47.20, 47.21, 47.22, 47.23, 47.24, 47.25, 47.26, 47.27, 47.28, 47.29, 47.30, 47.31, 47.32 and 47.33.

Shanghai Area

Figures 47.16, 47.17, 47.18, 47.19, 47.20 and 47.21.

Harbin Area

Figures 47.22, 47.23, 47.24, 47.25, 47.26 and 47.27

Guangzhou Area

Figures 47.28, 47.29, 47.30, 47.31, 47.32 and 47.33.

Table 47.5 Thermal characteristics of the facade

Summer outdoor meteorological parameters and thermal characteristics of the facade						
	Atmospheric pressure(Pa)	Average wind speed (m/s)	Dry-bulb temperature (°C)	Wall thickness (m)	Wall U-value (W/m^2·k)	Solar radiation intensity I (W/m^2)
Guangzhou	100,287	1.5	34.2	0.12	1.97	175
Shanghai	100,573	3.4	34.6	0.24	1.5	273
Beijing	101,169	2.2	33.6	0.42	1.22	420
Harbin	98,677	2.8	30.6	0.52	0.96	534

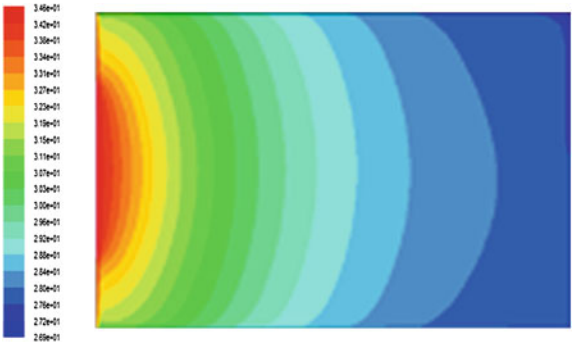

Fig. 47.16 Temperature contour of room A

Fig. 47.17 Temperature contour of room B

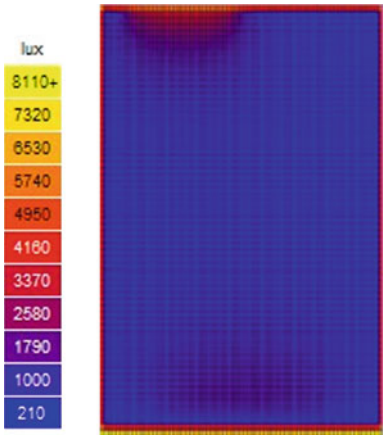

Fig. 47.18 Illumination contour of room A

47.3.4 Comparison Work

For schematic comparison and optimization, three evaluation indexes are employed:

(1) The extreme room natural temperature (either the highest in summer or the lowest in winter) within the typical year.

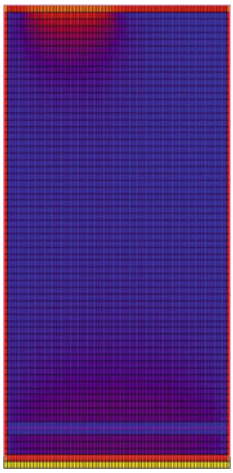

Fig. 47.19 Illumination contour of room B

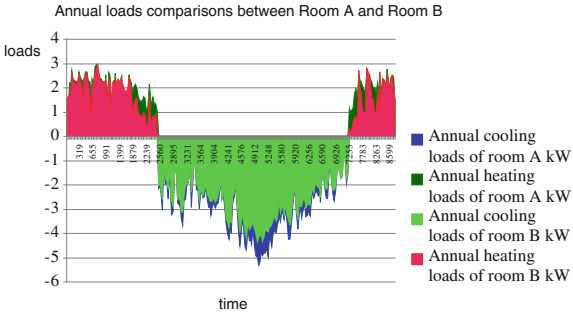

Fig. 47.20 Hourly thermal load of the building in the whole year

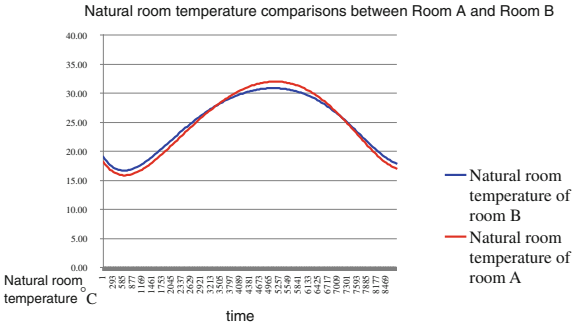

Fig. 47.21 Hourly natural room temperature of the building in the whole year

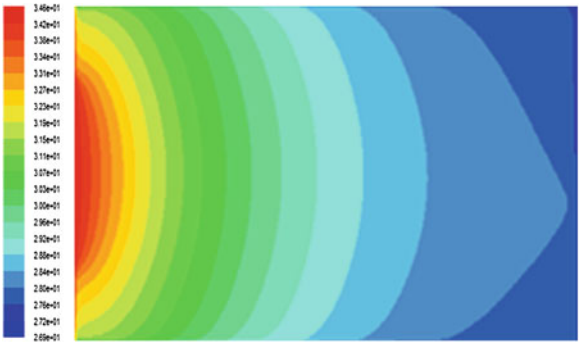

Fig. 47.22 Temperature contour of room A

Fig. 47.23 Temperature contour of room B

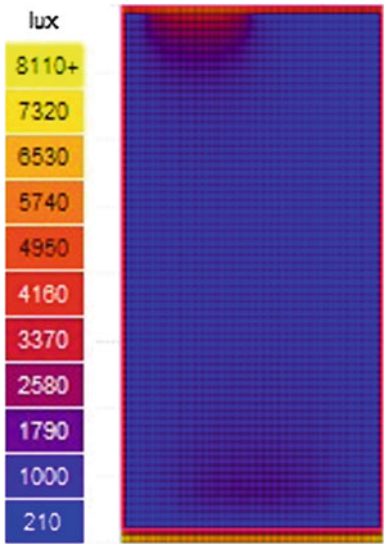

Fig. 47.24 Illumination contour of room A

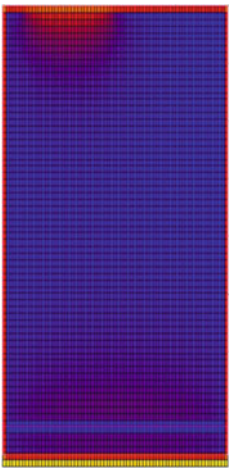

Fig. 47.25 Illumination contour of room B

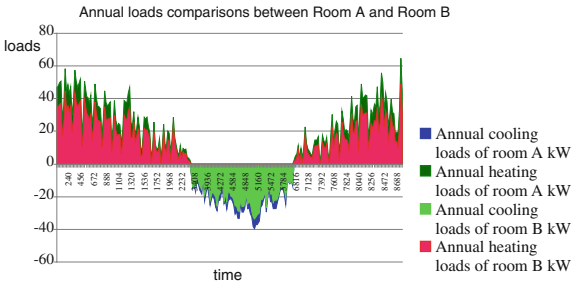

Fig. 47.26 Hourly thermal load of the building in the whole year

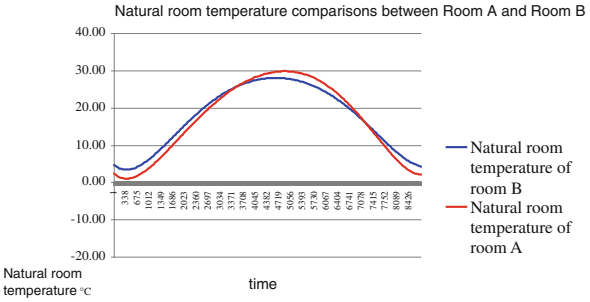

Fig. 47.27 Hourly natural room temperature of the building in the whole year

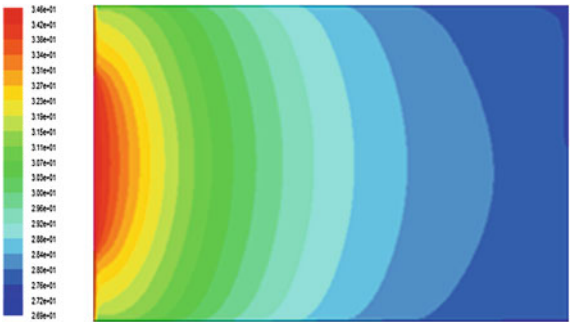

Fig. 47.28 Temperature contour of room A

Fig. 47.29 Temperature contour of room B

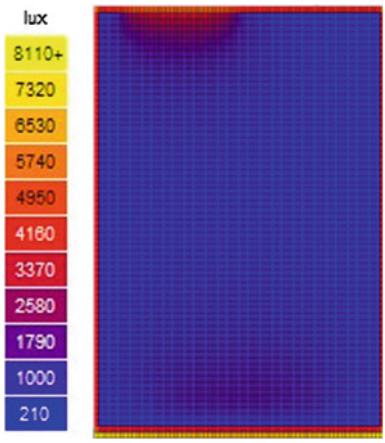

Fig. 47.30 Illumination contour of room A

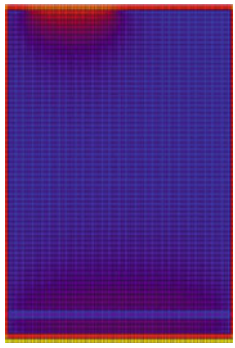

Fig. 47.31 Illumination contour of room B

The comparison of the extreme room natural temperature between Room A (TAmaxs in summer, TAmaxw in winter) and Room B (TBmaxs in summer, TBmaxw in winter) in four different meteorological regions of China is shown in Figs. 47.34 and 47.35.

$$\Delta Tmaxs = TAmaxs - TBmaxs,\ \Delta Tmaxw = TBmaxw - TAmaxw.$$

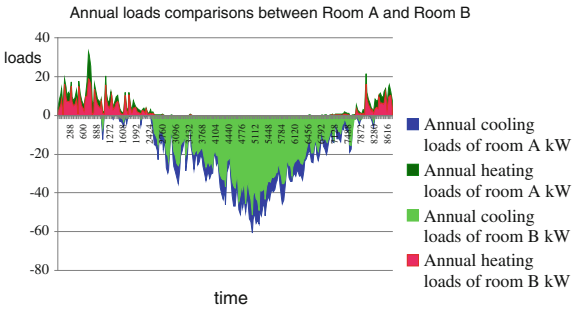

Fig. 47.32 Hourly thermal load of the building in the whole year

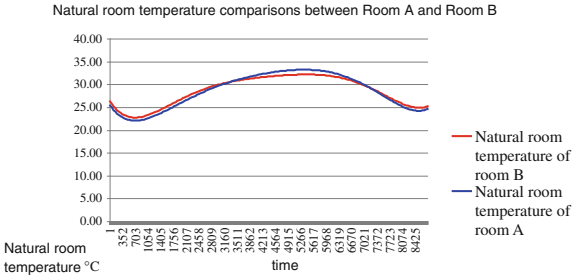

Fig. 47.33 Hourly natural room temperature of the building in the whole year

$$\eta\mathrm{ts} = \Delta\mathrm{Tmaxs}/\mathrm{TAmaxs},\ \eta\mathrm{tw} = \Delta\mathrm{Tmaxw}/\mathrm{TBmaxw}.$$

(2) The extreme room thermal load (either the maximum cooling load in summer or the maximum heating load in winter) within the typical year.

The comparison of the extreme room thermal load between Room A (QAmaxs in summer, QAmaxw in winter) and Room B (QBmaxs in summer, QBmaxw in winter) in four different meteorological regions of China is shown in Figs. 47.36 and 47.37.

$$\Delta\mathrm{Qmaxs} = \mathrm{QAmaxs} - \mathrm{QBmaxs},\ \Delta\mathrm{Qmaxw} = \mathrm{QAmaxw} - \mathrm{QBmaxw}.$$

$$\eta\mathrm{qs} = \Delta\mathrm{Qmaxs}/\mathrm{QAmaxs},\ \eta\mathrm{Qw} = \Delta\mathrm{Qmaxw}/\mathrm{QAmaxw}.$$

(3) The illumination index in the overcast day

The comparison of the illumination index between Room A (LXAmin) and Room B (LXBmin) in four different meteorological regions of China is shown in Fig. 47.38.

$$\Delta\mathrm{LXmin} = \mathrm{LXAmin} - \mathrm{LXBmin},\ \eta = \Delta\mathrm{LXmin}/\mathrm{LXAmin}.$$

Results of indexes comparison between building A and building B within four regions are illustrated in Tables 47.6 and 47.7.

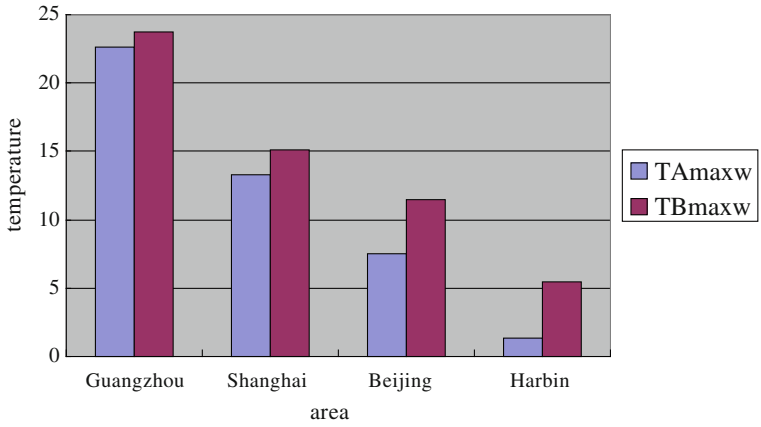

Fig. 47.34 Comparison of extreme temperature (winter)

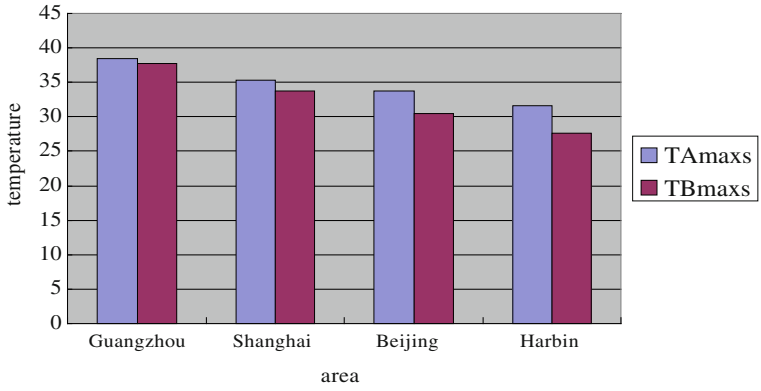

Fig. 47.35 Comparison of extreme temperature (summer)

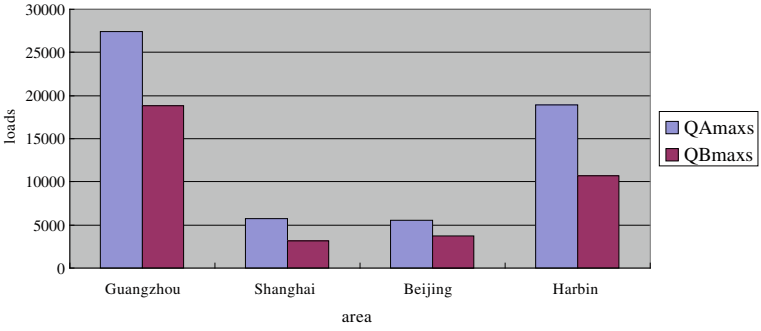

Fig. 47.36 Comparison of extreme cooling loads

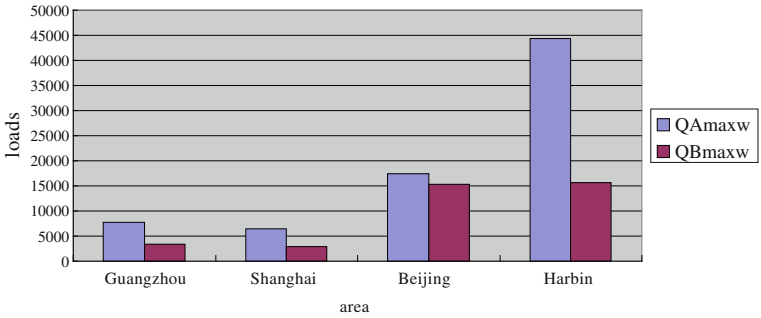

Fig. 47.37 Comparison of extreme heating loads

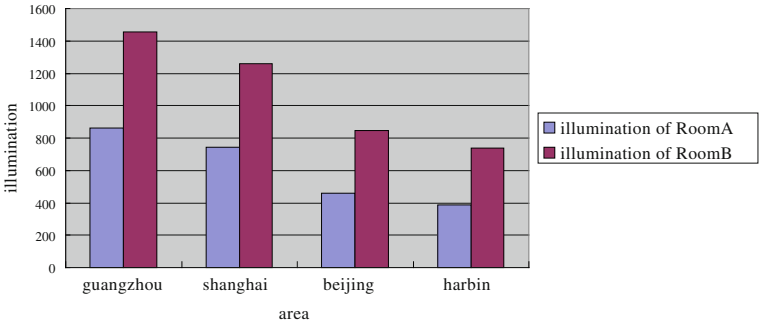

Fig. 47.38 Comparison of average illumination

47.4 Conclusions

From the simulation work and analysis above, some conclusions can be obtained:

1. DSF as a kind of new building envelope not only has better light gain, artistic facade decoration and better persons' view effect and scope, but also has better indoor thermal and environmental characteristics;
2. In most area of China, new kind of building envelope with DSF can obtain a lower natural indoor air temperature in summer, a higher natural indoor air temperature in winter, a less building thermal load both in summer and in winter, and a better indoor light gain which pay off in the reduction in building HVAC energy consumption, all of these benefits can usually offset the extra investment cost of DSF;
3. The improvement extent of the indoor thermal and environmental characteristics by the new kind of building envelope with DSF differs from the different meteorological regions of China. Indeed, based on the corresponding simulation and investigation work, we know that DSF is not adaptable to some

Table 47.6 Results of indexes comparison between building A and building B (summer)

	ΔTmaxs	η ts	Qmaxs	η qs	ΔLxmin	η
Guangzhou	0.55	1.43 %↑	8627	31.47 %↑	596	40.87 %↑
Shanghai	1.5	4.25 %↑	1600	27.73 %↑	516	40.98 %↑
Beijing	3.28	9.72 %↑	3750	47.57 %↑	389	45.98 %↑
Harbin	3.92	12.41 %↑	8198	43.31 %↑	353	47.83 %↑

Table 47.7 Results of indexes comparison between building A and building B (winter)

	ΔTmaxw	η tw (%)	ΔQmaxw	η qw (%)	ΔLxmin	η (%)
Guangzhou	1.06	4.68 ↑	4350	56.86 ↑	596	40.87 ↑
Shanghai	1.85	13.95 ↑	1150	17.76 ↑	516	40.98 ↑
Beijing	2.78	50.26 ↑	3575	20.48 ↑	389	45.98 ↑
Harbin	4.09	70.50 ↑	15627	35.28 ↑	353	47.83 ↑

meteorological regions of China because of its high extra investment cost and its limited energy saving effect;

4. To well obtain and demonstrate the advantages and the regional adaptation of the built environmental characteristics of the new style of DSF, simulation work is necessary and unavoidable in the inception of the design work;
5. DSF which has variety excellent characteristics that can gain favour with both architects and HVAC engineers.

References

1. Steiner I, Ozkan E (2005) An approach for the evaluation of energy and cost efficiency of glass facades. Energy Build 37(6):673–684
2. Heiselberg P, Kalyanova O, Jensen RL (2008) Measurement and Modelling of Air Flow Rate in a Naturally Ventilated Double Skin Facade. The First International Conference on Building Energy and Environment, pp 1895–1903
3. Du P (2003) The study on climatic adaptability of double-skin glass curtain wall in hot-summer and cold-winter zone. Huazhong University of Science & Technology
4. He X, Wan X (2007) Development of double-skin facade's thermal behavior simulation code based on commercial CFD software, Journal of Materials and Metallurgy (1):72–76
5. Yun P (2007) An architectural environment design course on ECOTECT. China Architecture & Building Press, Beijing, China (in chinese)

Part II
Building Information and Management

Chapter 48
Temperature Field Real-Time Diagnosis by Means of Infrared Imaging in Data Elaboration Center

Fabio Favoino, Alfonso Capozzoli and Marco Perino

Abstract Data Elaboration Centers are characterized by high specific energy consumptions, due to the requirements for the working environment of IT machines and their large working loads. This is due to the fact that the control of the indoor air parameters is of paramount importance in order to maintain the servers in safe working conditions. Reliable diagnostic procedures are therefore needed. The work herewith presented proposes an innovative diagnostic method, which makes use of infrared thermal imaging for real-time monitoring of the air temperature field in the proximity to the server air inlet. The method is validated by means of an experimental assessment, with the aim to assess the capability of an industrial infrared camera to evaluate the air temperature field next to the inlet surface of the server racks, in real working conditions. Potential and limitations of this procedure are presented and discussed.

Keywords Diagnostic · Data elaboration center · Hot spot · Infrared imaging

48.1 Introduction

In recent years, data elaboration centers (DEC) have rapidly increased their power requirements. In the last guideline published by ASHRAE [1], a footprint of about 20 kW/m2 of heat dissipation (for all types of servers) was predicted for 2012. Another ASHRAE guideline [2] introduces environmental requirements

F. Favoino
Glass and Facade Technology Research Group, Department of Engineering, University of Cambridge, Trumpington Street CB2 1PZ Cambridge, UK

A. Capozzoli · M. Perino (✉)
TEBE Research Group, Department of Energy, Politecnico di Torino, Corso Duca degli Abruzzi 24 10129 Torino, Italy
e-mail: marco.perino@polito.it

A. Li et al. (eds.), *Proceedings of the 8th International Symposium on Heating, Ventilation and Air Conditioning*, Lecture Notes in Electrical Engineering 263,
DOI: 10.1007/978-3-642-39578-9_48,

(temperature and humidity) for CED, in order to preserve the correct working conditions of the IT equipment accommodated in the racks, thus attempting to minimize their failure risk [2]. Cho et al. [3] highlight how an effective air management results in a decrease in the cooling energy consumption of a CED. Considering the well-established design layout of server rooms, i.e., hot aisle/cold aisle [2], different researchers [3–5] identify two main problems regarding air management: bypass air and recirculation air. These problems cause a decrease in the cooling efficiency and generate a vicious cycle of rising local temperature [3], generally named a "hot spot" phenomenon. In order to increase the energy saving for cooling and decrease the IT equipment failure rate, recirculation and bypass air needs to be minimized [3–6]. For these reasons, a monitoring method which enables a simple and automatic visualization and localization of these phenomena would be of great interest for the IT industry.

In this chapter, a flexible and cost-effective method to monitor the air thermal field in the proximity of server racks in CED is presented. The method is based on the use of IR thermography, robot mounted, and capable of measuring the air thermal field in proximity to the server rack surface, thus enabling to apply a fault detection method for hot/cold spot phenomena.

48.2 IT Inlet Air Temperature Prediction with Infrared Imaging

A novel diagnostic method for monitoring inlet air temperature to IT equipment in a data elaboration center environment is proposed. The work has been carried out as part of a research activity supported by Telecom Italia S.p.A.

The method adopts an IR camera to measure the surface temperature of the rack door, thus giving a measure of the temperature of the inlet air to IT equipment and of the maximum air temperature difference on the cold aisle side. The IR camera makes spot photos of the cold aisles and is mounted on a robot, independently managing the monitoring plan. The main aim of the research is to evaluate how accurate a rack door surface temperature measurement is, by means of an IR camera, in giving a measurement of the inlet air temperature to IT equipment. For this sake, an experimental campaign was planned on two stages: the first one in laboratory was mainly aimed at characterizing the IR camera and the second one in a real CED room was aimed at applying the method in a real CED environment and at trying to generalize the results. The methodology consisted in verifying how the IR temperature measurement (T_{IR}) could reproduce the rack door surface temperatures (T_S), how the surface temperature T_S could give a measure of the air inlet temperature to IT equipment (T_E), and finally, how the T_{IR} could measure the T_E, both in absolute terms and in terms of vertical differences.

48.3 Characterization of the Diagnostic System in Laboratory

Prior to the field monitoring campaign, a first characterization of the diagnostic system was carried out in a climatic chamber in order to verify the accuracy of the infrared measurement system and to understand the potential sources of error. In particular, the purpose of this first experiment was to verify the following:

- the influence of the view angle of the IR camera on the Ts;
- the influence of emissivity of the rack door surface on Ts;
- the ability of the IR camera to measure the T_E at a close distance from the rack door surface;
- the ability of the IR camera to measure the maximum vertical difference in T_E (ΔT_E) at a close distance from the rack door surface.

For this sake, an experimental mock-up, reproducing the cold air surface of a server rack, was built using the net door of a typical rack (wide 60 × 205 cm tall). Different air temperature vertical gradients were obtained by differentially regulating the voltage to electric heating foils (EHF) placed behind the rack door.

The EHF were mounted on a wooden support at 10 cm distance from the rack door. Four axial fans (150 m^3/h each) were included into the wooden surface to suck the air from a controlled environment on one side of the mock-up. The measurement apparatus consisted of the IR camera Optris (spectral range 7.5–13 μm, 48 × 37° field of view (FOV), accuracy ± 2 °C, temperature resolution 0.08 K), and 21 thermocouples measuring at different heights the temperature of the heating foils (6), the temperature of the air between the heating foil, and the rack door (3), the T_S on the rack door (6), and the T_E at 30 cm from the door (6). The thermocouples were previously calibrated against a reference PT100, obtaining an accuracy of ± 0.3 °C. The IR camera was placed at such a distance that the entire server mock-up was inside the field of view of the camera. The IR measurement was performed at different angles moving the camera, from 0° (axis of the IR camera perpendicular to the door surface) to 40°, with steps of 10°. By doing this, the angular distortion of the IR Camera was characterized, and the results are shown in Fig. 48.1 (black color). The average value and the 95 % confidence interval are shown. The subscript α indicates the angle between the axis of the camera and the perpendicular to the rack door. The graph is built in such a way that all the measurements with a different angle are referred to angle 0° measurements. It can be clearly seen that there is a linear dependence between IR temperature and angle in the field of view of the instrument (emissivity $\varepsilon = 1$), with a maximum average error of 1.5 °C at 40° angle, which means 6 % relative error at 25 °C. This linear regression could be used to correct measurements with non-zero angle when the camera is mounted on the robot, even though the correction is only marginal.

The accuracy of the rack door surface temperature measurement (T_S) by means of the IR camera (T_{IR}) is analyzed in Fig. 48.1, looking at the difference T_{IR}–T_S.

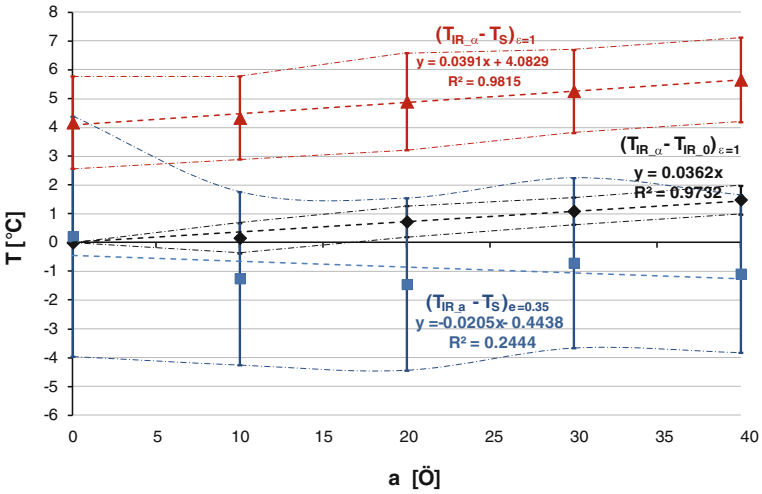

Fig. 48.1 IR camera angular characterization and surface measurement accuracy

The red color is used for measurement with $\varepsilon = 1$, while the blue for $\varepsilon = 0.35$ (emissivity of the rack door). For $\varepsilon = 1$, nearly the same value for the angular distortion index was found (3 % difference), and most importantly, it was found that the IR camera is able to measure the surface temperature with an accuracy of 1.5 °C (confidence interval 95 %), which is quite constant with the angle. When applying the net surface door emissivity, it is noticeable how, even though the average values of T_{IR} are closer to T_S (at 0° angle the value is almost -0.02), the accuracy for IC95 % is between 3 and 4 °C. The accuracy in this case increases with the angle, thus suggesting that the net resolution related to the resolution of the camera needs to be considered. More accurate results are obtained by considering $\varepsilon = 1$.

Another set of measurement was performed in order to analyze the accuracy of the IR camera at measuring the air temperature at 30 cm from the door T_E and the maximum vertical temperature difference ΔT_E by means of T_{IR} and ΔT_{IR}, respectively. More accurate results are obtained when considering $\varepsilon = 1$ (Fig. 48.2), showing really low differences between the measured air temperature T_E and the surface temperature measured with IR (T_{IR}), suggesting that there is an average 4 °C temperature drop between surface and the air passing through it. The accuracy of measuring T_E by means of T_{IR} is of 1.5 °C (confidence interval 95 %).

In order to assess the accuracy of measuring ΔT_E by means of ΔT_{IR}, a graph was drawn using ΔT_{IR} as the x-axis and ΔT_E as the y-axis. Each point on the graph represents the maximum ΔT_{IR} measured with IR camera compared to the maximum ΔT_E measured with the thermocouples. Thus, the proximity of each point to the bisector gives a measure of the accuracy of the diagnostic method.

In order to perform this analysis in the laboratory, only maximum vertical air temperature differences higher than 3 °C were considered. Figure 48.3 shows that

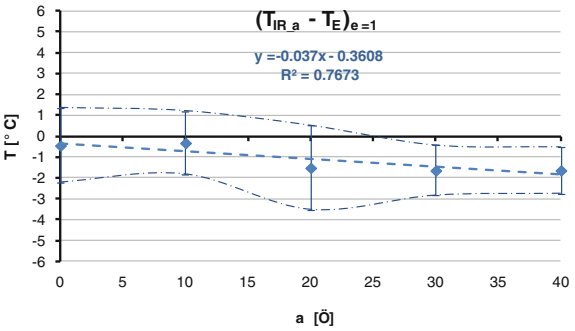

Fig. 48.2 IR camera 30 cm from door air temperature measurement accuracy

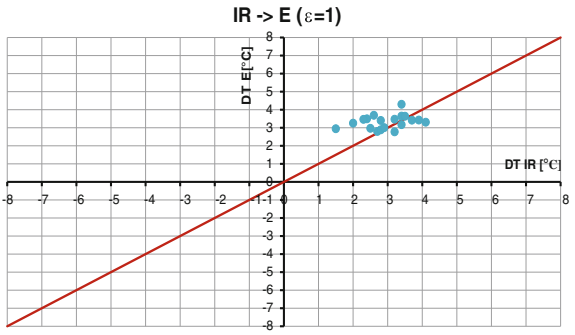

Fig. 48.3 Maximum T_E vertical gradients function of maximum T_{IR} rack door vertical gradients

it is possible to measure ΔT_E by means of ΔT_{IR} with a good accuracy, as all the points are in the first quadrant and close to the bisector. For fault detection purposes, this method could be used to estimate ΔT_E by applying a "safety" factor, taking into account the underestimation of ΔT_E by means of ΔT_{IR}. Furthermore, it was noticed that the accuracy of the measurement increases with the magnitude of the vertical temperature difference. For these reasons, a broader campaign was carried out in a typical CED server room on different types of rack door.

48.4 Field Monitoring Campaign in a CED Room

A monitoring campaign was carried out in a real data center in order to verify the applicability of the method tested in the laboratory, by means the experimental mock-up, in real working conditions. The surface and near air temperature field of the selected racks was monitored during three different campaigns. Each campaign was characterized by a time period of two days and a sampling interval of 5 min. For each rack, eight temperatures have been measured through calibrated thermocouples. These thermocouples have been placed at four different heights on the door surface of the rack (T_S) and in the air at 30 cm from the rack door (T_E). The

selected seven racks are characterized by four different types of texture of the metal door and hole percentages. On the basis of the results of the analysis carried out in the laboratory and of the methodology described above, the analysis of the monitored data was performed:

- by setting the emissivity of the IR camera equal to 1;
- by analyzing, for each rack, the capability of the IR camera to predict ΔT_E by means of ΔT_{IR} and the maximum temperature at the inlet of the IT equipment.

This was done by a comparison between IR and SE measurements made with thermocouples on the surface and in the air. In Fig. 48.4, the relation between the T_{IR} and T_E at the inlet of the IT equipments is shown. A good correlation is observed, although both an underestimation and an overestimation of the air temperature by means the infrared measurements may occur.

In order to evaluate the accuracy of the IR camera at predicting the maximum vertical temperature difference ΔT_E and the maximum values of the air temperature at 30 cm from the door T_E, another set of analyses was performed.

Figure 48.5 shows how ΔT_E is nearly always underestimated by means of the IR camera (only in 1 % of the cases an overestimation is observed), resulting in an average ratio of $\Delta T_E/\Delta T_{IR}$ of 1.32 with an error of 24 %. In the figure, the dashed lines represent the limits of the range of variation of the ratio of $\Delta T_E/\Delta T_{IR,}$ which spans from a maximum value of 2.17 to a minimum of 0.84. Through a frequency analysis, a Gaussian distribution of $\Delta T_E/\Delta T_{IR}$ has been found, and the IC 95 % (i.e., $\mu \pm 1.96\sigma$) is represented with the yellow lines. However, analyzing the cumulative frequency, the value of the ratio is lower than 1.9 in 96 % of the cases.

In Fig. 48.6, the relation between the maximum air temperature at the inlet of the IT equipment and the corresponding temperature measured through the IR

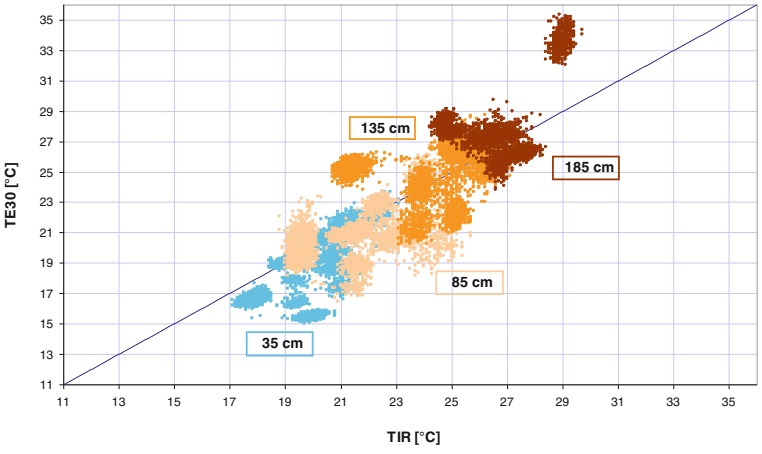

Fig. 48.4 Air temperature TE as a function of superficial temperature TIR rack door for different heights

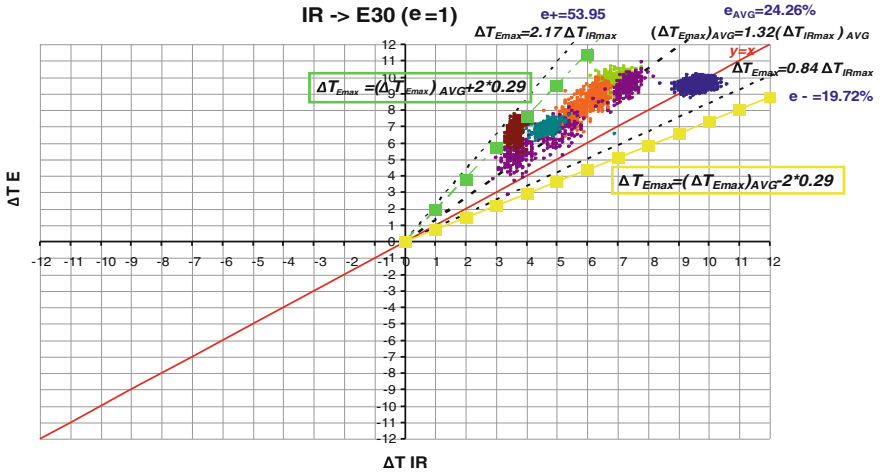

Fig. 48.5 Maximum vertical temperature difference ΔT_E as a function of maximum vertical surface temperature ΔT_{IR} rack door

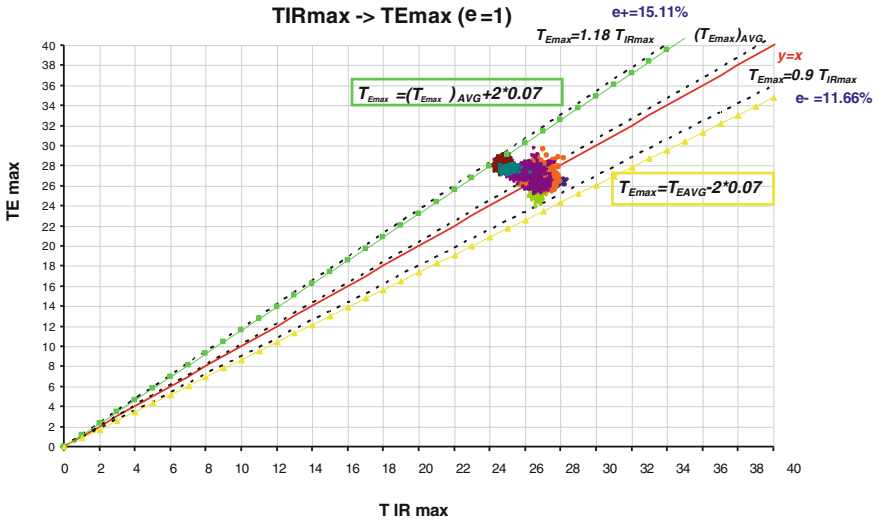

Fig. 48.6 Maximum air temperature T_E as a function of maximum surface temperature T_{IR} rack door

camera is shown. The average value of the ratio T_{Emax}/T_{IRmax} is very close to 1. In 50 % of the observed cases, T_{Emax} is slightly underestimated with an upper limit value of the ratio of 1.18 (error of 15 %). In all the other cases, an underestimation of T_{Emax} by means of infrared camera was found with a lower limit of the ratio of 0.9 (error of 11 %). Analyzing the cumulative frequency, the value of the ratio

T_{Emax}/T_{IRmax} is lower than 0.96 only in 6 % of the observed cases, and it is greater than 1.16 only in 2 % of the cases.

The results of these analyses suggest that a simple fault detection method based on a threshold limit could be adopted to detect hot/cold spot in CED rooms. A safety factor, deduced from the experimental work, can be applied on the infrared measurements to predict the maximum vertical temperature difference and the maximum inlet air temperature to the IT equipments.

As far as T_{Emax} is concerned, when applying a safety factor to correct the underestimated values measured by means of the IR camera, some false positives could be detected. In general, it has been observed that when T_{Emax} is overestimated, the extent of its overestimation is small; hence, a small occurrence of false positives is expected when the security factor is applied.

48.5 Conclusions

In this chapter, the evaluation of an innovative method to estimate the inlet air temperature to IT equipment, on the cold aisle side of a server rack, is presented. The results obtained can be summarized as follows:

- both local air temperature and maximum vertical air temperature differences are strongly correlated to the corresponding surface temperatures, so that the precision of measuring T_E by means of T_{IR} depends most of all on the precision of measuring T_S by means of T_{IR};
- due to the presence of different type of doors in the CED room (different emissivity and different net resolutions), it is more accurate to perform the measurements with $\varepsilon = 1$, improving the accuracy;
- the maximum air temperature difference is always underestimated by the IR measurements. In particular, the maximum ratio $\Delta T_{Emax}/\Delta T_{IRmax}$ observed is 2.17. In 95 % of cases, this ratio is greater than 1.9;
- by means of an IR camera, it is possible to identify the maximum temperature of the inlet air server with a good approximation. In 50 % of cases, the maximum temperature is slightly underestimated. The value of the ratio T_{Emax}/T_{IRmax} in 98 % of cases does not exceed 1.16.

To conclude, by applying the appropriate safety factors, considering a simple threshold limit fault detection algorithm, the proposed method is potentially able to systematically detect the occurrence of any hot/cold spot. Future work will be carried out to validate the above-mentioned fault detection method.

References

1. ASHRAE (2012) Datacom equipment power trends and cooling applications, 2nd edn. ASHRAE TC 9.9
2. ASHRAE (2011) Thermal guidelines for data processing environments—expanded data center classes and usage guidance. ASHRAE TC 9.9
3. Cho Jinkyun, Kim Byungseon (2011) Evaluation of air management system's thermal performance for superior cooling efficiency in high—density data centers. Energy Build 43:2145–2155
4. Fredrik Karlsson J, Moshfegh Bahram (2005) Investigation of indoor climate and power usage in a data center. Energy Build 37:1075–1083
5. Tao Lu, Xiaoshu Lu, Remes Matias, Viljanen Martti (2011) Investigation of air management and energy performance in a data center in Finland: case study. Energy Build 43:3360–3372
6. Sun HS, Lee SE (2006) Case study of data centers' energy performance. Energy Build 38:522–533

Chapter 49
Solar-Based Pre-Heating and Pre-Cooling of Buildings to Reduce Overnight Energy Demand

David Johnston

Abstract This research investigates dynamic control of the interior temperature of buildings, which are largely heated or cooled using solar energy. This can match heating demands to availability of solar energy, reducing demand for non-solar energy. Simulations were used to assess the potential savings. Pre-warming (warming before sunset) was used for a sample building in a cold climate (Beijing), and pre-cooling (cooling before sunset) was used for a sample building in a hot climate (Hong Kong). In each case—heating and cooling—the effectiveness of dynamic temperature control was assessed by comparing the non-solar energy requirement with a baseline, in which a constant temperature was maintained overnight.

Keywords Solar · Pre-warming · Pre-cooling · Setback · Photovoltaic

49.1 Introduction

A number of strategies exist for heating and cooling of buildings, which use solar energy to a greater or lesser extent [1, 2]. In cold climates, where heating is required, the simplest approach is to maintain a constant temperature overnight. The alternative lets the building cool naturally (setback) and raises the temperature in the morning (setback recovery) [3]. This uses less energy over twenty-four hours, but requires a high peak morning demand. Solar heating can provide the peak required for setback recovery after sunrise, whereas overnight heating requires non-solar energy. Therefore, setback is often used in buildings with solar heating systems. Conversely, in hot climates, cooling (air conditioning) is required. The hottest

D. Johnston (✉)
Northumbria University, Newcastle, UK
e-mail: david.johnston@northumbria.ac.uk

A. Li et al. (eds.), *Proceedings of the 8th International Symposium on Heating, Ventilation and Air Conditioning*, Lecture Notes in Electrical Engineering 263,
DOI: 10.1007/978-3-642-39578-9_49,

part of the day is in the afternoon, when solar energy is available to power air conditioning systems. However, thermal storage in the building walls produces a time delay which results in high temperatures continuing after sunset.

In China, east- and west-facing walls receive almost as much radiation as south-facing walls. It is thus advantageous to install solar panels on the east- and west-facing walls, as well as on the south-facing wall, as is common practice in existing solar energy buildings [4]. The solar radiation received by panels in each orientation varies with the time of day, as shown in Fig. 49.1. By comparing these inputs to the daily peaks in heating and cooling, it is possible to determine which panels should provide each function. (At mid-latitudes, heating is required in winter and cooling in summer, so both demands must be met by panels on a single building.)

Based on the above considerations, panels on east-facing walls are used for morning setback recovery, thus augmenting passive solar heating. In cold climates, there is a peak in heating demand, which occurs in the evening, at a time when solar energy is not generally available. Panels on west-facing walls can be used to pre-warm the building, in the period before sunset, heating the interior of the building to the maximum comfortable temperature (set by the thermostat). This allows a comfortable temperature to be maintained during the evening and overnight, with less use of supplementary (non-solar) energy. In hot climates, pre-cooling can be adopted. In the afternoon, the air conditioning reduces the temperature to the lower

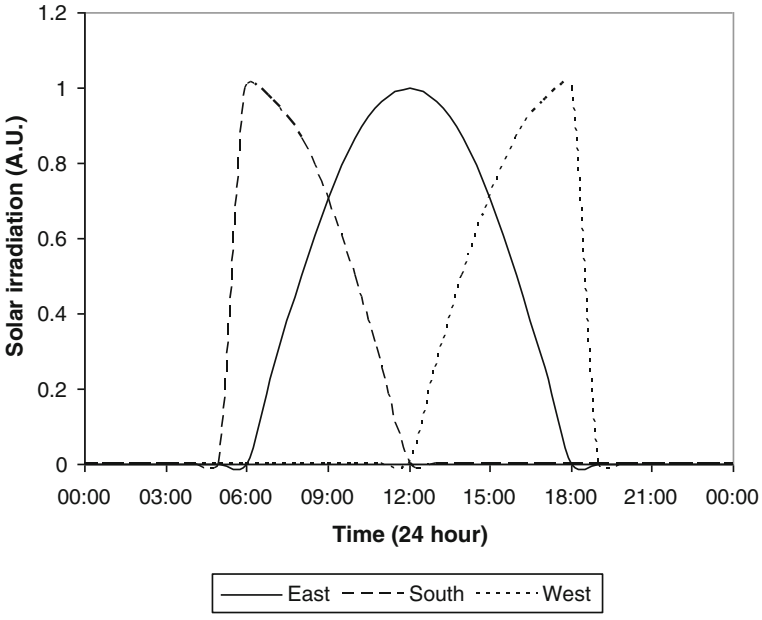

Fig. 49.1 Solar irradiation (clear sky) on panels mounted on east-, south-, and west-facing walls, for a latitude of 31°N (Shanghai) and the optimum tilt for that latitude

end of the comfortable range. After sunset, the building heats naturally, while the exterior temperature is high, and then cools as the exterior temperature falls overnight. This approach shifts the peak energy demand to before sunset, so that solar photovoltaic panels on the west-facing walls can provide the energy required.

49.2 Case Study: Pre-Warming, Beijing

The case study for pre-warming is based on a set of flats comprising a single story of a tower block. The trial day was January 15, based on EnergyPlus weather data for Beijing [5]. Building insulation U-values were those recommended for Beijing in the building standard for northern China—JG26-95 [6]. The baseline for comparison is a simulation in which there is no pre-warming. The thermostatic set point is maintained at 15 °C from late afternoon until late evening, after which the building is allowed to cool naturally to a lower set point of 10 °C. The heating required and the temperature profile are shown in Fig. 49.2. The heat transfers occurring at each part of the day are listed below.

1. Prior to 17:00, the available solar energy is more than sufficient to maintain an interior temperature of 15 °C, and a higher temperature may be attainable.
2. From 17:00 to 18:00, solar heating decreases rapidly, and non-solar heating must increasingly be used.
3. After 18:00 (sunset), non-solar heating meets the entire demand.

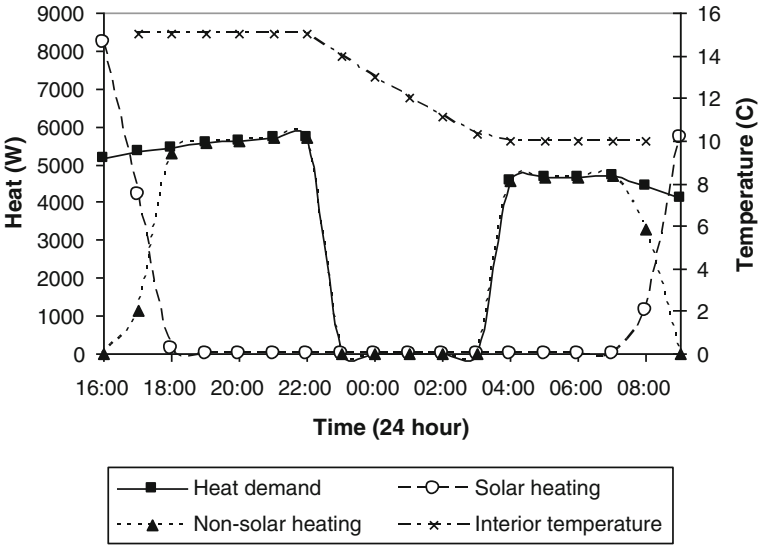

Fig. 49.2 Heating (solar, non-solar, and total demand) and interior temperature for the period from late afternoon, overnight to shortly after sunrise, with no pre-warming. (Beijing, Jan 15)

4. At 22:00, the occupants retire to bed, and the thermostatic set point is reset to 10 °C. The interior temperature is allowed to fall naturally to this value, which it reaches at 04:00.
5. From 04:00 to 08:00, non-solar energy provides the heat necessary to maintain 10 °C.
6. Solar heating increases rapidly from 08:00, and by 09:00, it is more than sufficient to maintain 10 °C. From this time, the surplus solar heating can be used for setback recovery.

Pre-warming is implemented by setting a higher thermostatic set point earlier in the afternoon, when more solar heating is available, allowing the building to cool naturally as the level of solar radiation decreases toward sunset and continues to cool after sunset. A set point of 22 °C is selected for the afternoon period. This is reduced to 15 °C at 18:00 and further to 10 °C at 22:00. The heating required and the temperature profiles are shown in Fig. 49.3. The heat transfers occurring at each part of the day are listed below.

1. Prior to 17:00, the available solar energy is more than sufficient to maintain an interior temperature of 22 °C, and a higher temperature may be attainable.
2. At 18:00, the thermostatic set point is reduced to 15 °C, and the interior temperature is allowed to fall naturally. This temperature is still above the set point at 22:00.

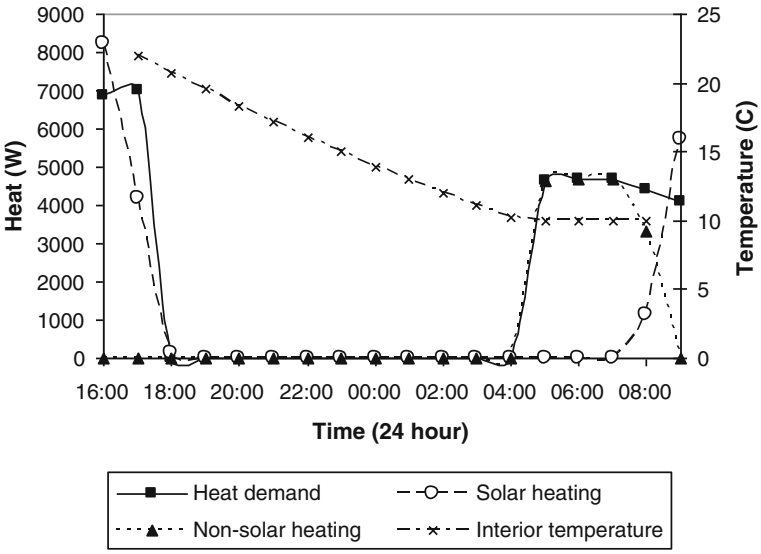

Fig. 49.3 Heating (solar, non-solar, and total demand) and interior temperature for the period from late afternoon, overnight to shortly after sunrise, showing the effects of pre-warming. (Beijing, Jan 15)

3. At 22:00, the thermostatic set point is further reduced to 10 °C, and temperature continues to fall naturally until it reaches 10 °C at 05:00.
4. From 05:00 to 08:00, non-solar energy provides the heat necessary to maintain 10 °C.
5. Solar heating increases rapidly, and from 09:00, it can be used for setback recovery.

The results show that heating demand can be eliminated during the evening and is slightly reduced in the early morning. The heating required to achieve pre-warming is provided during the afternoon, when it is available as solar energy. The demand for non-solar energy was 17 kWh per day, compared to 51 kWh without pre-warming.

49.3 Case Study: Pre-Cooling, Hong Kong

In the hot climate of Hong Kong, cooling is provided by air conditioners, supplied by photovoltaic panels mounted on the building when solar radiation is available, and supplemented by grid-connected electricity. Shading by the wall-mounted solar panels can significantly reduce solar gain, and hence cooling demand, during the hottest parts of the day [4]. In the baseline case, a temperature of 26 °C is maintained throughout the day. The results are shown in Fig. 49.4. The heat transfers occurring at each part of the day are listed below.

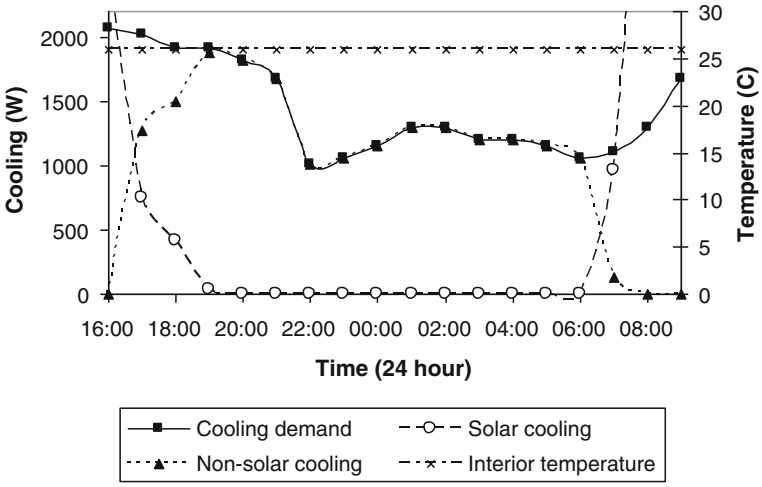

Fig. 49.4 Cooling (solar, non-solar, and total demand) and interior temperature for the period from late afternoon, overnight to shortly after sunrise, with no pre-cooling. (Hong Kong, July 15)

1. Until 16:00, solar energy is sufficient for the air conditioning to maintain an interior temperature of 26 °C.
2. After this time, non-solar energy is required. As high exterior temperatures continue well into the evening, the cooling demand remains high until 22:00.
3. Overnight, the cooling demand reduces to a moderate level, but all of this must be met by non-solar energy.
4. From 07:00, the cooling demand increases, but the solar energy available increases more rapidly and can supply all of the demand for the remainder of the morning.

Where pre-cooling is adopted, a thermostatic set point of 22 °C is maintained during the afternoon. The air conditioning can maintain this, based solely on solar energy, until 14:00, after which the set point is increased to 26 °C. The results are shown in Fig. 49.5. The heat transfers occurring at each part of the day are listed below.

1. After 14:00, solar energy allows the air conditioning to provide some cooling, and the temperature rises at a moderate rate.
2. After 18:00, there is no solar input and the air conditioning provides no cooling. The interior temperature rises naturally at a slightly higher rate, reaching 26 °C at 02:00.
3. From 02:00 to 07:00, non-solar energy is used to maintain a temperature of 26 °C.
4. After 07:00, solar energy is more than sufficient to maintain a temperature of 26 °C.

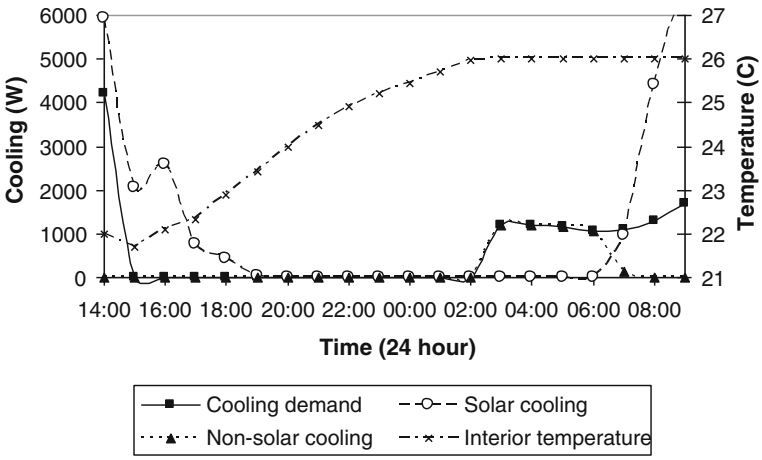

Fig. 49.5 Cooling (solar, non-solar, and total demand) and interior temperature for the period from late afternoon, overnight to shortly after sunrise, showing the effects of pre-cooling. (Hong Kong, July 15)

The results show that cooling demand can be eliminated during the evening and is significantly reduced in the early morning. The air conditioning required to achieve pre-cooling is provided during the afternoon, when it is available from solar energy. The demand for non-solar energy was 5 kWh per day, compared to 19 kWh without pre-cooling.

49.4 Conclusions

The results show that, when solar energy is used to power the heating and air conditioning systems, the non-solar energy required for heating and cooling can be reduced by a factor of three or four by adopting dynamic control of the interior temperature. The simulations show that the non-solar demand (both heating and cooling) can be eliminated during the evening, but only reduced in the early morning. This is because the interior temperature reaches the overnight set point at approximately 02:00–05:00 (depending on the conditions). Increasing the thermal time constant could extend the natural heating/cooling period until sunrise, at which point, solar energy could be used, and non-solar energy would not be required. This could be implemented by improving the building insulation or by increasing the thermal mass.

References

1. Tiwari G (2003) Solar energy: fundamentals, design, modelling and applications. Alpha Science International, UK
2. Zhai XQ, Wang RZ, Dai YJ, Wu JY, Xu YX, Ma Q (2007) Solar integrated energy system for a green building. Energ Build 39(8):985–993
3. Kreider J (2000) Handbook of heating, ventilation and air conditioning. CRC Press, US
4. Johnston D (2007) Solar energy systems installed on Chinese-style buildings. Energ Build 39:385–392
5. EnergyPlus weather data (2007) (Source: Solar and Wind Energy Resource Availability)
6. http://www.eere.energy.gov/buildings/energyplus/cfm/weather_data.cfm

Chapter 50
Building Energy Benchmarking Between the United States and China: Methods and Challenges

Tianzhen Hong, Le Yang, Jianjun Xia and Wei Feng

Abstract Currently, buildings in the U.S. account for more than 40 % of total primary energy. In China, the same figure is 20 %. Detailed building energy analysis and benchmarking based on energy monitoring are becoming vitally important for the evaluation of energy-efficient technologies and related policy making. This paper focuses on methods and challenges in energy benchmarking of office buildings between the U.S. and China, based on the experiences and outcomes of a joint research project under the U.S.–China Clean Energy Research Center for Building Energy Efficiency (CERC-BEE). First, benchmarking methods were presented, including data analysis methods, required data, building selection criteria, and a standard data model for building energy use. Annual electricity use benchmarking was performed from a sample of selected office buildings in both countries, with the aim of identifying and understanding the main discrepancies and key driving factors. Benchmarking challenges were then summarized and discussed, and some potential solutions were proposed, including the process of building selection, data collection and clean-up, and specific analysis techniques. Recommendations were proposed for future work to improve the process and outcomes of building energy benchmarking between the two countries.

Keywords Benchmarking · Buildings · China · Data analysis · Data model · Energy data · United States

T. Hong (✉)
Simulation Research Group, Lawrence Berkeley National Laboratory (LBNL), Berkeley, USA
e-mail: thong@lbl.gov

T. Hong · W. Feng
Lawrence Berkeley National Laboratory (LBNL), 1 Cyclotron Road, Berkeley CA 94720, USA

L. Yang · J. Xia
Tsinghua University, Beijing 100084, China

A. Li et al. (eds.), *Proceedings of the 8th International Symposium on Heating, Ventilation and Air Conditioning*, Lecture Notes in Electrical Engineering 263,
DOI: 10.1007/978-3-642-39578-9_50,

50.1 Introduction

In 2010, China and the U.S. accounted for 20 and 19 % of the global energy consumption respectively—more than any other country [1]. In the U.S., the building sector is the largest energy consumer and contributor to climate change, responsible for about 41 % of the U.S. primary energy use and 8 % of the world's CO_2 emissions [2, 3]. China is the second largest building energy user in the world, ranking first in residential energy consumption and third in commercial energy consumption [4]. Buildings account for more than 20 % of China's total primary energy consumption, and the percentage is increasing [5]. In the world, buildings are responsible for more than 40 % of global energy use and one-third of global greenhouse gas emissions [6]. Most existing buildings have operation issues or deficiency, and it has been demonstrated that the problems of building energy performance are pervasive and well known [7].

In the building sector, two distinct scenarios apply: buildings in China have lower design efficiency levels but also lower needs for energy use and buildings in the U.S. have higher design efficiency levels but also higher needs for energy use [8]. Generally, U.S. buildings use more energy than Chinese buildings. This is mainly driven by the differences in building design, operation, and occupant behavior. Chinese buildings are usually conditioned with zonal systems such as fan coil units and operate in a part-time, part-space mode—only occupied spaces during occupied times are conditioned. While U.S. buildings, with central built-up variable air volume (VAV) systems serving multiple zones, typically operate in a full-time, full-space mode—the whole building is conditioned most of the time, including unoccupied hours with thermostat setback [9]. Thus, while buildings in the world's two largest economies have large energy-saving potential, different energy-saving measures will apply.

Six factors directly influencing building energy use are climate, building envelope, building equipment, operation and maintenance, occupants' behavior, and indoor environmental conditions [10]. In order to make policies that promote building energy savings, it is crucial to gain a better knowledge of these driving factors as well as the major discrepancies of energy use between buildings in the two countries. To achieve this goal, detailed building energy analysis and benchmarking based on energy monitoring system (EMS) is becoming increasingly important.

A joint research project was conducted between Lawrence Berkeley National Laboratory (LBNL), USA, and Tsinghua University, China, from 2011 to 2013, under the U.S.–China Clean Energy Research Center for Building Energy Efficiency (CERC-BEE). The goal was to understand the driving forces behind the discrepancies in building energy use between the two countries; identify gaps and deficiencies of current building energy monitoring, data collection, and analysis; and create knowledge and tools to collect and analyze good building energy data to provide valuable and actionable information for key stakeholders.

However, building energy benchmarking has always been a difficult task. Though lots of efforts were made in detailed analysis and benchmarking of several buildings in this project, this paper mainly focuses on the methods and challenges during this study, to provide recommendations to improve the process and methodologies of building energy benchmarking in the future.

50.2 Benchmarking Methods

50.2.1 Data Analysis Methods

In order to understand the driving forces behind the discrepancies in building energy use between the two countries, benchmarking should be based on three levels:

1. Energy consumption of the whole building.
2. Energy consumption of major end uses, including lighting, plug-loads, data centers and kitchens if present, elevators, domestic hot water, and HVAC systems (chillers, boilers, cooling towers, fans, pumps, direct expansion (DX) units, and radiators), etc.
3. Performance of systems and components, including some indexes like chiller coefficients of performance, water transport factors, energy efficiency of air handling units (AHUs), and central plants, etc.

As for specific methods, energy profiling (including annual, monthly, weekly, and daily energy use patterns of the whole building and major end uses) is essential for individual building analysis and benchmarking. Energy profiling yields important information such as energy use per square meter or per capita, working days versus non-working days (holidays, weekends), base-to-peak loads, etc.

Additionally, benchmarking should include not only the buildings in the project portfolio, but also typical buildings of the same type in both countries.

50.2.2 Required Data

With a clear knowledge of the goal, results, and data analysis methods to obtain the results, it is important to know what kind of data is required. First of all, detailed descriptions of building information should be collected, including not only basic information like building type, location, vintage, climate zone, floor area, conditioned floor area, operating hours, number of occupants, number of floors, etc., but also descriptions of the building envelope, HVAC systems, lighting systems, plug-load equipment, as well as control and monitoring systems. Some of

the basic information is of significant importance to energy analysis and benchmarking.

Measurements of the monitoring system should include three types of data:

1. Total building energy use, broken down into major end uses for various fuel types (see Sect. 2.1);
2. Operating conditions of HVAC systems and equipment, for example, chilled/hot water flow rates and corresponding supply and return water temperatures;
3. Indoor and outdoor environmental conditions, such as air temperature and humidity, outdoor wind speed and direction, solar radiation, etc.

In order to fulfill analysis with different time scales and at typical time periods, at least one complete year's valid data with a sampling frequency of at least one hour are required.

Considering the difficulty in data acquisition in reality, data described in (1) is particularly important and necessary for basic energy benchmarking, while data in (2) and (3) are also important but optional.

50.2.3 Building Selection Criteria

Typical buildings from the two countries selected in this study should meet the following criteria as much as possible:

1. Medium- to large-size office buildings were preferred, as they are the most common types of commercial buildings (referred to as "public buildings" in China). The end uses of such buildings can be more easily clarified as there are not so many special devices or complicated systems as in other building types, such as hospitals and shopping malls.
2. Required data discussed in Sect. 2.2 are available.
3. Overview of the monitoring system showing the hierarchy of sub-metering is available.
4. High-level description of Building Management System (BMS)—what data points are available.

50.2.4 Energy Data Model

After detailed and valid data are collected, it is necessary to analyze energy usage based on different end uses. Contributions were made during this project to develop a uniform data model, certified by the ISO Standard 12655, Energy Performance of Buildings—presentation of measured energy use of buildings [11] as shown in Fig. 50.1.

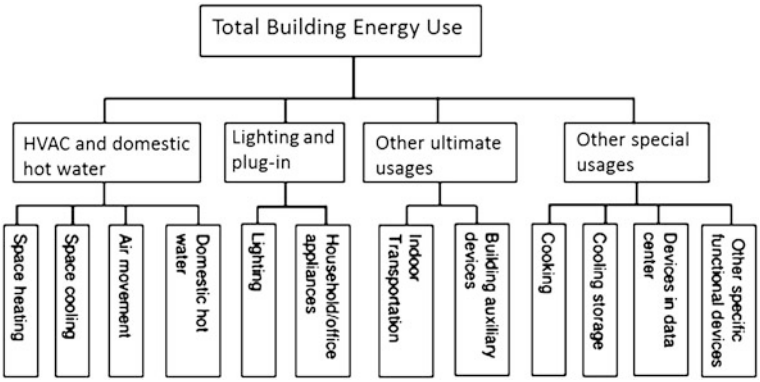

Fig. 50.1 Data model of energy use in buildings

This model follows a tree structure, from total energy use down to each major end use. End uses in both the first and second tiers are described clearly in this standard. Ideally, it can be applied in most buildings, and benchmarking can be performed across buildings based on these detailed end uses.

50.3 Benchmarking Case Study

50.3.1 Introduction of Selected Buildings

A dozen office buildings in the U.S. and China were selected for this project. Four of them, for which the data collection and initial analysis have been completed, were used for benchmarking. Table 50.1 summarizes some basic information of these buildings.

Building A is a large, mixed-use commercial office building with some restaurants, stores, and a bank. It consists of a tall main building with large glass curtain walls and an annex. Building B is a government administrative office building, served by decentralized cooling systems and district heating with radiators, without any other air side equipment. Building C is a mixed-use building with a library wing (9,000 m^2) and an office wing (7,000 m^2) and is served by district cooling and heating systems. Only the office wing is considered in this study. Building D is the oldest among these four buildings, with metal panel walls without insulation and leaky, single-pane, clear-glass windows. It is served by various DX HVAC systems.

Table 50.1 Basic information of the case study buildings

Name	Building A	Building B	Building C	Building D
Location	Beijing, China	Beijing, China	Merced, California, U.S.	Berkeley, California, U.S.
IECC climate zone	Zone 4B	Zone 4B	Zone 3B	Zone 3C
Year of construction	1989	1987	2005	1960
Floor area (m^2)	54,490	39,211	16,000 (7,000 for the office wing)	8,316
Operation hours	M–F 7 a.m.–6 p.m.	M–F 6 a.m.–6 p.m.	M–F 7 a.m.–6 p.m.	M–F 7 a.m.– 6 p.m.
HVAC	Water-cooled chiller, district heating, VAV + CAV systems	Decentralized AC for cooling, district heating	District cooling, district heating, VAV systems	Local electric cooling and gas-boiler heating packaged DX systems
Monitoring platform	iSagy	iSagy	EPP (Energy performance platform)	Pulse energy
Data time-interval	1 h	1 h	15 min	15 min

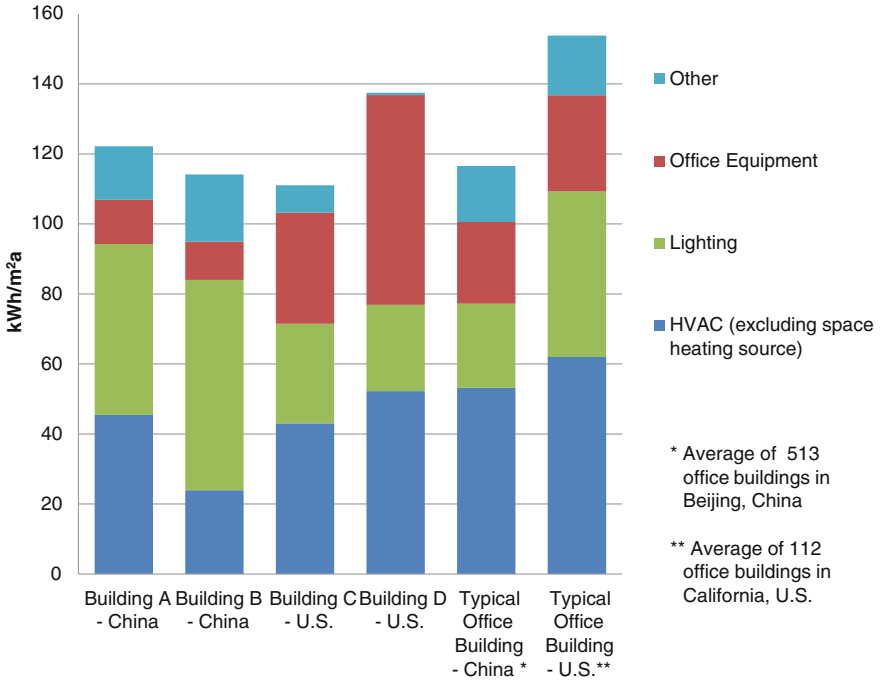

Fig. 50.2 Comparison of annual electricity consumption of the case-study buildings and typical office buildings in China and the U.S.

50.3.2 Benchmarking of Case Study Buildings

Energy benchmarking was conducted among the selected buildings based on annual, monthly, weekly, and daily time scales. However, in this paper, only the annual analysis is presented as an example.

As shown in Fig. 50.2, the annual total electricity consumption intensity of each building is broken down into four major subcategories, which slightly distinguish from the first tier end uses in Fig. 50.1, due to the inadequate sub-metering in some buildings. Typical office buildings in both countries were also included in this benchmarking. The typical Chinese office building is the average of 513 office buildings in Beijing, China [12], while the typical U.S. office building is the average of 112 office buildings in California, U.S.[1]

Because of the lack of gas metering for space heating in the Chinese buildings served by the city-wide district heating systems, only electricity was considered, and space heating source energy was not included in the HVAC category. However, energy used by equipment related to space heating (pumps, AHUs, etc.) is

[1] California Commercial End-Use Survey, http://energyiq.lbl.gov/.

still included. The subcategory "Other" in Fig. 50.1 describes energy-using devices such as elevators, data centers, kitchen equipment, hot water boilers, water supplying, and draining pumps. However, in Building D, some special equipment which should have been categorized as "Other" was actually included in "Office Equipment", due to the lack of sub-metering.

For total annual electricity use, Buildings A and B performed similar to the typical Chinese office building. However, the two U.S. buildings, particularly Building C, consumed much less than the typical U.S. office building, mainly due to more efficient lighting and HVAC systems.

In terms of HVAC performance, Building B consumed the least electricity, indicating that decentralized HVAC systems may perform more efficiently than centralized HVAC systems. Building D, though located in a mild climate, consumed more HVAC energy than the Chinese buildings, which may be caused by several factors. First, Building D's indoor temperature set point for cooling is 21–22 °C, lower than Building A's 24–26 °C. Second, Building D's old, leaky, and uninsulated envelope results in much higher cooling and heating loads. Finally, in general, more ventilation air is provided in U.S. buildings. U.S. ventilation standards are more stringent than that of China, leading to more electricity use to condition outdoor air.

As for lighting, the Chinese buildings consume much more energy than the U.S. buildings. This may be a combination of design and operation: lighting power, occupant density, operation mode of lights, and utilization of natural light. According to real-time data, Building B's lighting system consumes more electricity not only during daytime, but also at nighttime, contributing to the greatest lighting energy use among the buildings. On the other hand, Building D's single-pane windows introduce more natural light, and its lighting system has undergone some retrofits. Occupancy sensors in Buildings C and D turn off lights when occupants leave the office. However, the typical office building in the U.S. consumes more lighting energy than the typical building in China, demonstrating that in general, lights in most U.S. office buildings are on for most of the time and without occupancy sensor control.

The two U.S. buildings, particularly Building D, consume much more electricity by office equipment than the two Chinese buildings. Many computers in Building D are left on or in standby mode at night for remote log on, data backup, system operating, or security software updates. This building also has more personal fans, heaters, and desktop task lights, leading to higher energy use.

Generally, more energy-saving potential was identified from lighting measures for the two Chinese buildings and from office equipment measures for the two U.S. buildings. There are various reasons for these discrepancies. More buildings with detailed information are needed to figure out common discrepancies and their key driving factors and retrofit measures.

50.4 Challenges and Discussion

50.4.1 Building Selection

50.4.1.1 Lack of Data

A large number of commercial buildings in the U.S. have some kind of EMS installed. The newer buildings with Leadership in Energy and Environmental Design (LEED) certification require building monitoring as a part of the commissioning process. However, many buildings that claim to have EMS lack detailed component-level measurements, so hourly or sub-hourly data were unavailable in most buildings.

It is common to see a lack of data for environmental and HVAC operating conditions in buildings with EMS, especially in China. Some buildings installed with energy management and control systems that can monitor and control indoor conditions as well as energy end uses in real time are unfortunately not connected to a monitoring system to store the data for a long period of time. More seriously, there is a lack of heating energy data for Chinese buildings served by city district heating systems. All of these problems set limitation to building selection in this project, and the selected buildings may not meet all criteria.

50.4.1.2 Data Sharing and Communication

The willingness of building owners to share data and communicate with building managers are also barriers to energy benchmarking. First, many owners are worried about privacy and security concerning real-time data. Second, such an energy-saving project may not be on the high priority list of building owners and managers. Therefore, energy data and detailed information about the whole building, systems, and even particular equipment may not be available. These problems have to be overcome by personal communication, site visits, nondisclosure agreements, the promise to share analysis results and identify retrofit measures, and sometimes even by government mandatory policies. It is important to convince building owners and managers of the benefits of such an energy-saving project and inform them of their responsibilities and the kind of information they may provide throughout the project.

50.4.2 Data Collection and Clean-Up

50.4.2.1 Data Retrieval

Even when access to building information databases is permitted by the operators/managers, it is still a labor-intensive procedure to download or export the data.

Some systems require software written in specific computer languages to retrieve and export data, which may add complications. Moreover, downloaded datasets may change unnoticed when the same operations are conducted repeatedly.

More importantly, although raw data may be sampled over short intervals by EMS, such as five-minute intervals or even less, the frequency of the data available for download can be different, depending on what time intervals are used for post-processing of the raw data. In this project, 15-minute-interval data were downloaded for the two U.S. buildings and hourly data for the two Chinese buildings.

The difficulty and reliability of data retrieval and the availability of data at certain intervals depend on the EMS. The features of some existing systems were reviewed in some studies [13, 14]. Improvements to data retrieval, downloading, and exporting features would ease data acquisition and contribute to data with smaller time steps and fewer manual errors.

50.4.2.2 Naming of Data Points

Poor naming conventions of data points in some EMSs have led to confusion, incompleteness, and other mistakes in data collection. Consistent and clear naming conventions for data points are becoming more crucial as computerized systems containing hundreds of data points are deployed in commercial buildings. Well-chosen data point names can provide useful information about installed systems and make it easier to monitor, retrieve and download, analyze, maintain, modify, and interconnect data from various building systems [15].

50.4.2.3 Data Quality

Most selected buildings have some missing data, and there seems to be no pattern to describe which meters might lose data and when. Meter instability may cause occasional individual missing data, while large sets of missing data may be caused by the retrofit of either the monitoring system itself or energy service system (like HVAC or lighting). Data loss may also be caused by power failure in the buildings, during which the meters do not measure, the connection is lost, and even the computer is out of power. Avoiding these problems requires higher quality meters, sensors, nonstop operation of the monitoring system, and better emergency measures or backup systems when power is out and connection is lost.

Even if the data obtained are complete, data quality may suffer, mainly due to un-calibrated or broken meters and sensors. Some invalid data—such as negative values and abnormal spikes—can easily be detected, while some seemingly normal data may actually be inaccurate, considering the error of measurement. Higher quality meters and sensors, along with more frequent maintenance, would avoid these problems.

It is possible for missing or invalid data to appear during the downloading and exporting process, especially when exporting a large set of data at one time. A higher quality data transmission system may avoid this possibility.

50.4.2.4 Data Clean-up

To get the data in workable order for analysis, missing or invalid data should be replaced with data during time periods or days that were similar to the invalid points, taking weather conditions into account. For example, a few missing data could be replaced by the previous or following proper data, or their average. Several hours' missing data could be replaced by data of the same time period from the previous or following day, taking into account weekdays and weekends, respectively. The same applies to missing or invalid data from even longer period.

50.4.3 Specific Analysis Challenges

50.4.3.1 Mixed-Use Building

In reality, most buildings are mixed-use buildings to some extent, and thus separating spaces with different usages (office, retail, library, etc.) is a big challenge. For buildings with large spaces for one type of usage and only small spaces for other usages, such as Building A and B which have small restaurant areas, it can be unnecessary and sometimes impossible to separate. While for buildings with comparative spaces of different types, a nearly half-library and half-office building, there should be a way to separate the spaces. Take Building C for example, the energy use of the office wing can be calculated by multiplying the energy use of the whole building by the area ratio of the office wing, in this case 7/16.

50.4.3.2 District Cooling/Heating System

District systems are common for heating in Chinese buildings, and buildings that are part of a campus network for American buildings. Thus, related energy use data particularly for individual buildings are unavailable, in terms of equipment such as chillers, boilers, pumps, and cooling towers.

However, there is a way to estimate such energy use. First, calculate the ratio of the cooling/heating load consumed by the individual building to that supplied by the plant. Then, multiply this ratio by the energy consumed by the plant to get a rough estimate of the building's energy consumption associated with heating/cooling. Such an estimation method was applied to Building C during this study. However, it is still impossible to estimate heating source energy for Chinese buildings served by district heating systems.

50.4.3.3 End uses Comparison

Though the ISO standard data model was proposed, each building has its own particular sub-metering system that is not compliant with the ISO standard. It is hard to take full advantage of the data model to categorize and compare energy use at various end-use levels thoroughly.

Separating mixed end uses is always a big challenge. In some cases, there are certain methods within the monitoring system to separate mixed end uses, such as lighting and plug-loads. For example, the Optimization of Adjustment Algorithm [16] is adopted for the EMS in Building A and B. In some other cases, total consumption of mixed end uses and the consumption of one specific end use are metered, and thus the energy consumption of the other end uses can be calculated. However, when neither of the above methods is applied to a building, comparison can be difficult. In most buildings, public service and special equipment are usually not metered separately. Take Building D for example, equipment in the kitchens and data center are mixed with office equipment, leading to the difficulty in comparison based on major subcategories.

Besides, the lack of gas metering of space heating in Chinese buildings makes the HVAC energy benchmarking insufficient, due to the exclusion of not only the space heating source energy, but also the terminal reheat in VAV systems commonly used in the U.S. buildings.

50.4.3.4 Normalization of Energy Use

Energy use normalized by floor area, number of occupants, operating hours or cooling/heating degree days (CDD/HDD) is important for benchmarking. However, the related data may not be accurate despite being available. For example, floor area is a key factor for calculating energy use intensity and benchmarking, but the real definition of it varies a lot in different references about some buildings. Whether garage, restaurants, podiums, or any other special spaces are included, and whether walls are considered, can be confusing, especially for buildings with spaces for different usages. Moreover, air conditioning floor area is even more complicated and less reliable. Therefore, the inaccuracy of floor area may lead to incorrect conclusions from benchmarking.

The number of occupants and operating hours provided by building managers may be inaccurate or out of date, since it changes with time. The reliability of CDD/HDD data also needs consideration, as it was calculated with some approximation methods. Consequently, deeper benchmarking cannot be conducted precisely with normalized energy use.

50.4.3.5 Typical Buildings

Acquiring energy use data for typical buildings of the same type as case buildings throughout a country is a big challenge for benchmarking. Though there are some national or state surveys on energy consumption for lots of buildings of each main type, only annual data based on a few major subcategories are available, limiting the depth of benchmarking between case buildings and typical buildings. The accuracy of average energy use based on such databases depends highly on the number, variation and typicality of surveyed buildings, and how thoroughly the survey was conducted. A good example is given by the deviation of the lighting energy comparison between case buildings from that between typical buildings in both countries.

50.5 Conclusions

Building energy benchmarking is becoming crucially important for energy savings in the U.S. and China. Based on the actual experience and outcomes of energy benchmarking between several office buildings in the two countries, benchmarking methods and challenges were discussed in this chapter. Some basic recommendations for future benchmarking work are summarized as follows:

1. Install well-designed EMSs at the beginning of building construction and improve the features of the whole system, to get complete and valid required data, so that benchmarking based on the standard data model can be conducted. Specifically, the U.S. buildings should focus more on detailed sub-metering for different end uses and data quality, while Chinese buildings should install more sensors and meters for environmental conditions and HVAC monitoring, add district heating information and related data, and increase the time resolution of data available for download.
2. Include more buildings and other building types in energy benchmarking to identify and understand common discrepancies and their driving factors and feasible retrofit measures. More emphasis should be put on communication with building owners and facility managers, to gain better knowledge about the building characteristics and operation.
3. Increase the accuracy and reliability of some key data related to building energy benchmarking, such as floor area, operating hours, and so on.

Acknowledgments This work was supported by the U.S.–China Clean Energy Research Center for Building Energy Efficiency. The authors appreciate the building owners, facility managers, and a few LBNL researchers for providing building data and related information for the project.

References

1. U.S. Department of Energy (2012) 2011 buildings energy data book. D&R International, USA
2. U.S. Department of Energy (2010). Energy efficiency trends in residential and commercial buildings
3. Architecture 2030 (2011) 2030 challenge for products: critical points
4. Eom J, Clark LE, Kim SH (2012) China's building energy use: a long-term perspective based on a detailed assessment. PNNL Report, PNNL-21073
5. THUBERC (2011) Annual report on China's building energy development. Tsinghua University, Beijing (in Chinese)
6. UNEP (2009) Buildings and climate change, summary for decision-makers
7. Mills E, Bourassa N et al (2005) The cost effectiveness of commissioning new and existing commercial buildings: Lessons from 224 buildings. In: Proceedings of the 2005 national conference on building commissioning
8. Hong T (2009) A close look at the China Design Standard for energy efficiency of public buildings. Energy Build 41:426–435
9. Jiang Y (2012) China gives green light to building energy reductions combining energy conversation technologies with green lifestyle. IEA ECBCS News, 55
10. IEA (2009–2012) ECBCS Annex 53: total energy use in buildings—analysis and evaluation methods
11. ISO (2012) Standard 12655: energy performance of buildings—presentation of real energy use of buildings
12. 2007 Beijing Municipal Government Office Buildings and Large Public Building Energy Consumption Statistical Summary (in Chinese)
13. Motegi N, Piette MA et al (2003) Web-based energy information systems for energy management and demand response in commercial buildings. Lawrence Berkeley National Laboratory, Technical Report, LBNL-52510
14. Granderson J, Piette MA et al (2009) Building energy information systems: state of the technology and user case studies. Lawrence Berkeley National Laboratory, Technical Report, LBNL-2899E
15. Butler JF, Veelenturf R (2010) Point naming standards. ASHRAE J B16–20 (Nov)
16. Wang X (2010) Studies on key technology of sub-metering in commercial buildings. Dissertation for the doctoral degree. Tsinghua University, Beijing (in Chinese)

Chapter 51
Oversizing Analysis of HVAC System in Prototypical Commercial Buildings

Yuebin Yu, Haorong Li, Denchai Woradechjumroen and Daihong Yu

Abstract Oversizing of heating ventilation and air-conditioning equipment becomes an intractable fault once the building system is designed and constructed. It imposes control challenges, impacts the indoor air condition, increases energy consumption, and reduces the equipment life span. As a system-level fault, it is difficult to duplicate and quantify in an experimental environment. This study analyzes the oversizing issues in prototypical commercial buildings. Data of system operations from 12 retail stores in different climatic regions in the US are collected. We applied three parameters, including cycling number, run-time fraction, and maximum cycling number, to capture the oversizing signature of a RTU based on the annual design conditions. Two different effective dead-band temperatures are adopted to evaluate the potential uncertainty. The findings can be used to assess the oversizing level of RTUs, quantify the average energy penalty of sample buildings, and guide future design. More importantly, the methodology can be automated and applied in smart building management systems for soft-repairing of an oversizing issue.

Keywords Oversizing · Retail stores · Real-time measurements · Energy penalty · Optimization · Smart building management

51.1 Introduction

Commercial buildings accounted for 19 % of total energy consumption in the USA in 2009 [1]. From the survey in 2003 [2], 4.9 million commercial buildings covered 72 billion ft^2 of floor space—an increase of 28 % in buildings and 40 %

Y. Yu (✉) · H. Li · D. Woradechjumroen · D. Yu
University of Nebraska-Lincoln, 1110 S 67th ST, PKI-104F,
Omaha, NE 68182, USA
e-mail: yuebin.yu@unl.edu

A. Li et al. (eds.), *Proceedings of the 8th International Symposium on Heating, Ventilation and Air Conditioning*, Lecture Notes in Electrical Engineering 263,
DOI: 10.1007/978-3-642-39578-9_51,

in floor space since 1979. Specifically, based on US Commercial Sector Primary Energy in 2006 [3], heating, ventilation, air-conditioning, and refrigeration systems (HVAC&R) accounted for about 50 % of the total energy use in commercial buildings. Approximately, 30 % of total energy was consumed on space cooling and space heating by HVAC systems. Thus, HVAC&R systems are considerably important areas to be analyzed in order to reduce waste energy use in commercial buildings. Among them, rooftop units (RTUs) consumed approximately 62 % of total energy to heat and cool commercial buildings in the USA [4]. For small commercial offices and retail stores, RTUs accounted for 50 % of total energy use [5]. The energy penalty of oversizing RTUs has been significantly concerned since 1998. Previous researchers (e.g., [6–8]) evaluated and/or surveyed the performance of RTU in terms of oversizing at field tests. Only two of the prior studies [6, 9] processed data from the engineering design point of view; however, no previous study analyzed and evaluated the performance of a RTU in terms of the level of oversizing and average energy penalty based on annual design condition for both cooling and heating modes.

The analysis of commercial buildings in this study is preceded through the data obtained by the advanced internet protocol, i.e., BACnet, a data communication protocol for building automation and control networks. The weather data and RTU performance data are analyzed from 12 retail stores at different climates by the program described below to compute the waste energy consumption occurring from the oversized RTUs. The accuracy of the proposed programming calculation is evaluated using *N-analysis method* to validate part load ratio (PLR) in terms of uncertainty (within $\pm$ 16.99 % for all RTUs). The findings can be applied as smart building technologies for improving the building operation visibility and efficiency [10–12].

51.2 Background

As a compact air-conditioning unit, a RTU comprises mainly a complete vapor compression cycle, a furnace heater, and a fan. The performance of a RTU can be evaluated by analyzing the operation of the compressor and the furnace heater. The units are usually selected to handle the maximum zone heating and cooling load at design weather condition. In addition, designers tend to apply safety factors in sizing the equipment. Since design condition only occurs about 2.5–5 % of the time each year, for most of the time, the units are running at partial load conditions. With the simplest RTUs, the components are at constant capacity, speed, and volume. The discrepancy between the overall heating/cooling capacity and the variable thermal load is balanced by turning on and off the compressor and heater with an on/off controller. When multiple stage units are used, the control can have some more level of flexibility.

To avoid frequent on/off and heating/cooling mode change, a dead band is usually applied on the control variable. Cycling RTUs on and off, even switching

between heating and cooling, in daily operation becomes necessary. Oversizing refers to the scenario when a system can provide much higher capacity than needed for the peak load. The symptom of oversizing in RTUs is reflected by the frequent on/off and staging operation during the design conditions. The penalty due to oversizing includes the extreme control challenges for stable indoor air environment, high indoor relative humidity, additional energy consumption, and premature equipment failure. The signature of RTU oversizing can be captured by evaluating the cycling times per hour during peak load condition.

51.3 Methodology

Data in 45 big-box retail stores in the USA were downloaded from October 2010 to October 2011 through BACnet protocol. The stores are in 7 different climatic regions and 12 stores from the total are selected for this study. All machines can be categorized into 4 different models with various capacities as follows: (1) one-stage compressor for cooling and two-stage gas furnace for heating; (2) two-stage compressor for cooling and two-stage gas furnace for heating; (3) two-stage compressor for cooling and two-stage gas furnace for heating; and (4) two-stage compressor for cooling and two-stage gas furnace for heating.

The trended data from BAS were filtered first with only related variables remained. The cleaned data are as follows: (1) recorded time stamps are in the form as MM/DD/YYYY HH:MM:SS; (2) average outdoor air temperatures (OAT) are obtained in English unit (°F); and (3) the status records of RTU compressors at time stamps (1 = turned on, 0 = turned off).

With the cleaned yearlong data from 2010 to 2011, the following variables are further prepared for analysis: (1) the start time (t_{start}) of all compressor cycles of both cooling and heating mode along the year; (2) the stop time (t_{stop}) of all compressor cycles of both cooling and heating mode along the year; (3) the selected design condition of an outdoor temperature in each location based on ASHRAE Fundamentals, annual heating 99 % DB and 1 % cooling DB/WB [13]; and (4) the effect of a dead-band temperature (EDBT, °C) as the lowest limited temperature for a cooling mode, whereas the maximum limited temperature for a heating mode.

Figure 51.1 illustrates the data analysis process applied in this study.

The overall data analysis methodology is further interpreted as six steps:

Step 1. Selecting AOAT for the given store location;
Step 2. Selecting EDBT 1.39 and 4.17 °C to obtain the solution of set-1 ($S1$) and set-2 ($S2$), respectively;
Step 3. Comparing average RTF of $S1$ with $S2$ in terms of uncertainty;
Step 4. Calibrating l_{on} and l_{cycle} of cycles for $S1$ and $S2$; $S3$ and $S4$ are calibrated sets of $S1$ and $S2$ by using N-analysis, respectively;

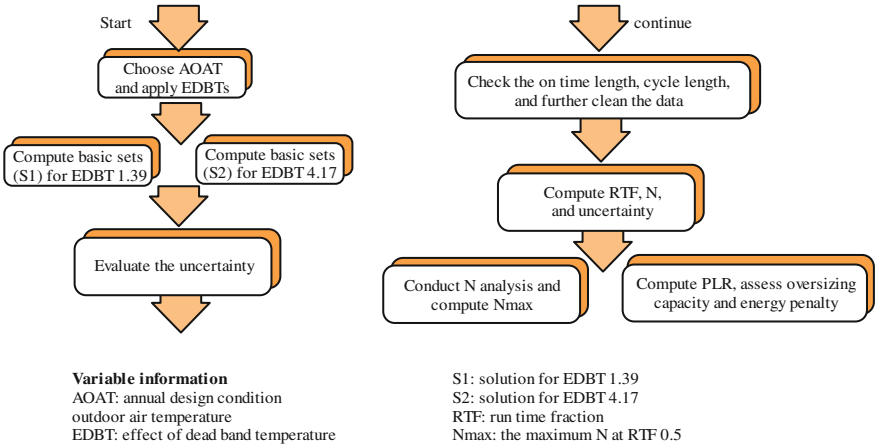

Fig. 51.1 Illustration of the analysis program

Step 5. Computing the final solution of set-3 (*S*3) in terms of uncertainty by comparing *S*3 with *S*4;

Step 6. Applying *S*3 to compute oversized capacities and average energy penalties using PLR. The results can be fed directly into a smart building management for optimal control [12].

With above information, the calculation is carried out for the cycles of each stage compressor in peak design conditions. Table 51.1 collects the definitions and calculation equations of the variables included in the analysis.

Table 51.1 Definition of parameters for calculation of heating/cooling cycle

Parameters	Equations or conditions	Units
l_{on} (duration of on status of a compressor)	$l_{\text{on}} = \left\lvert t_{\text{start}} - t_{\text{stop}} \right\rvert$ (51.1)	hour
l_{off} (duration of off status of a compressor)	$l_{\text{off}} = \left\lvert t_{\text{start,next\_cycle}} - t_{\text{stop}} \right\rvert$ (51.2)	hour
l_{cycle} (total duration for a cycle)	$l_{\text{cycle}} = l_{\text{on}} + l_{\text{off}}$ (51.3)	hour
N (a number of cycles occur in an hour)	$N = \frac{1}{l_{\text{cycle}}}$ (51.4)	cycle per hour
RTF (run-time fraction)	$\text{RTF} = \frac{l_{\text{on}}}{l_{\text{off}}}$ (51.5)	dimensionless
PLR (part load ratio)	$\text{PLR} = \text{RTF} - \frac{\tau}{l_{\text{cycle}}}\left(1 - e^{\frac{-l_{\text{on}}}{\tau}}\right)$ (51.6)	dimensionless
τ (time constant, duration)	$\tau = 60$	second
AOAT (annual design condition of outdoor air temperature)	99 % heating DB 1 % cooling DB/WB	°C
EDBT (the effect of dead-band temperature)	Cooling condition $\geq$ AOAT − EDBT (51.7) Heating condition $\leq$ AOAT-EDBT (51.8)	°C

51.4 Implementation and Analysis

The methodology is applied on the trended data of the RTUs. The quantification of oversizing is evaluated through the on/off status of compressors and furnace heaters. Ideally, at peak conditions, a properly sized compressor should run continuously without cycling during this period.

51.4.1 Implementation

The analysis methodology is applied to all TRUs in the 12 retail stores. As an example, for the 22 RTUs in Store I at Boise, Idaho, AOAT at 35 °C is selected for step 1. After that, l_{on} and l_{off} of all cycles in the range of the specified temperatures are calculated for obtaining RTF and N of $S1$ and $S2$, when EDBT is set as 1.39 and 4.17 °C, respectively. The duration of temperatures, which are higher than 33.6 °C, is not over 6 h, and therefore, l_{cycle} and l_{on} occurring within this duration should not be over 6 h for $S1$. Similarly, the duration of $S2$ is set not over 10 h. The durations of l_{cycle} and l_{on} are used to examine the complete cycles of the results.

Figures 51.2 and 51.3 illustrate the results (on/off status and l_{on}) for the cooling mode of compressor RTU No.5 located in Store I by using *EDBT* 1.39 and 4.17 °C, on 7/25, 2011, respectively. The different results are demonstrated through comparing Fig. 51.2 with Fig. 51.3. Area 1 in Fig. 51.2 shows the 5 complete cycles occurring between time 15:36 and 19:12. The results in this area can be approximated the same as the results of Area 3 in Fig. 51.3 for the same period because l_{on} of those cycles is not varied. This comparison shows that there

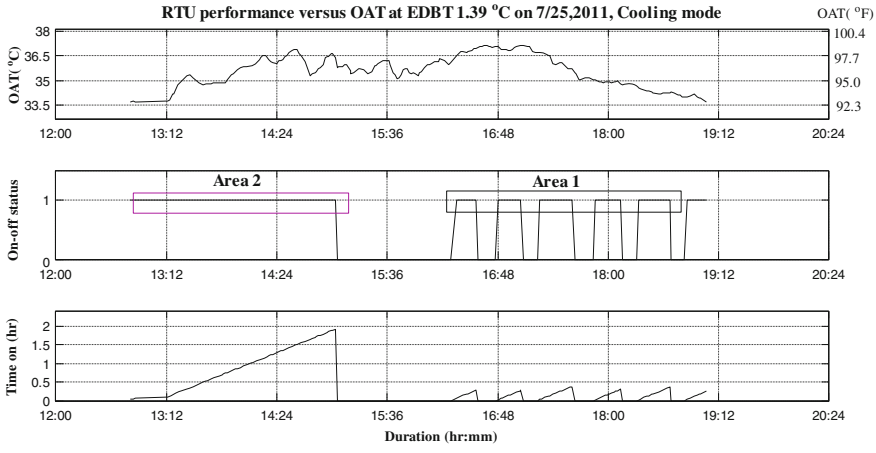

Fig. 51.2 The cycles of a cooling mode of RTU No.5 in store I with *EDBT* = 1.39 °C

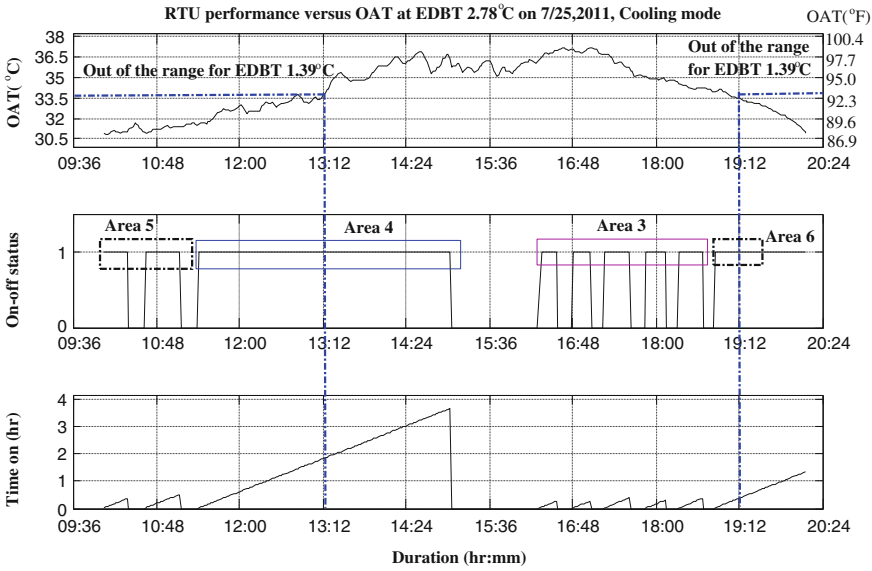

Fig. 51.3 The cycles of a cooling mode of RTU No.5 in store I with $EDBT = 4.17$ °C

is no variation due to the different EDBTs for this period. On the other hand, a cycle is affected by the selection of EDBT in Area 2 since the same cycle is longer in Area 4 when EDBT is 4.17 °C as shown in Fig. 51.3. As a result of this variation, l_{on} of this cycle is approximately changed from 2 to 4 h, so this difference between Area 2 and Area 4 leads to the variation of an average maximum RTF. Since the range of specific temperatures is longer for EDBT 4.17 °C, Area 5 in Fig. 51.3 shows two more cycles, which do not exist with EDBT 1.39 °C. Similar incidences as Area 4 and Area 5 also result in the variation of the average maximum RTF at the peak condition in terms of uncertainty. Area 6 is another example of the difference affected by the dead-band temperature. However, the cycle of this area is not included because it cannot be computed by the program due to the incomplete cycle. Consequently, Area 6 does not result in any change on the average maximum RTF. The comparison of RTF between EDBT 1.39 and 4.17 °C is tabulated in Table 51.2 for all RTUs in Store I.

Comparing RTF of $S1$ with $S2$, the uncertainty of results occurs due to the selection of different EDBT from the thermostat of a RTU. The uncertainty could lead to incomplete cycles because RTF and N of a cycle out of the specific range of temperatures are not captured. Moreover, the variation of cycles could affect N and RTF and lead to the change of evaluation for RTUs in the analysis. This uncertainty can be used as a self-validation measure to assess the accuracy of the proposed methodology when EDBT 4.17 °C is selected in the program. This self-validation is more accurate when RTUs are properly sized. The uncertainties of all 12 stores are within ±30 % for all mode operations. RTF results found till Step 3

Table 51.2 Results of *RTF* and uncertainty in store I

Store I (RTF)	Cooling mode				Heating mode				Uncertainty of 2 stages (St) in both modes (%)			
RTU no.	Stage1 (EDBT, °C)		Stage2 (EDBT, °C)		Stage 1 (EDBT, °C)		Stage 2 (EDBT, °C)		Cooling mode		Heating mode	
	1.39	4.17	1.39	4.17	1.39	4.17	1.39	4.17	St1	St2	St1	St2
1	0.995	0.921	*	*	0	0	0	0	7.44	–	–	–
2	0.679	0.655	*	*	0.397	0.356	*	*	3.53	–	10.33	–
3	0.640	0.610	*	*	0	0	*	*	4.68	–	–	–
4	0.604	0.590	*	*	0.378	0.322	*	*	2.30	–	14.81	–
5	0.631	0.691	0.261	0.235	0.519	0.445	0.483	0.519	−9.50	9.96	14.26	−7.45
6	0.937	0.948	0.642	0.642	0.165	0.151	0	0	−1.17	0	8.48	–
7	0.600	0.540	0.659	0.550	0	0	0	0	10.00	16.51	–	–
8	0.967	0.928	0.452	0.345	0	0	0	0	4.03	23.67	–	–
9	0.996	0.998	0.904	0.742	0.350	0.286	0	0	−0.2	17.92	18.29	–
10	0.808	0.729	0.680	0.592	0.505	0.398	0	0	9.77	12.94	21.08	–
11	0.997	0.980	0.605	0.450	0	0	0	0	1.71	24.62	–	–
12	0.591	0.603	0.413	0.325	0.805	0.734	0	0	2.03	21.31	8.82	–
13	0.771	0.665	0.878	0.873	0.112	0.072	0	0	13.75	0.57	24.71	–
14	0.818	0.808	0.425	0.538	0	0	0	0	1.22	−20.9	–	–
15	0.394	0.349	0.197	_	0.973	_	0	0	11.42	–	–	–
16	0.423	0.400	0.321	0.297	0.311	_	0	0	5.44	7.48	–	–
17	0.999	0.996	0.831	0.633	0.382	0.292	0	0	0.30	23.83	23.56	–
18	0.960	0.929	0.539	0.474	0.603	0.530	0	0	3.23	12.06	12.11	–
19	0.693	0.655	0.249	0.269	0.631	0.550	0	0	5.48	−8.03	12.84	–
20	0.613	0.679	*	*	0.537	0.406	*	*	−10.7	–	24.39	–
21	0.581	0.503	*	*	0.704	0.620	0	0	13.43	–	11.93	–
22	*	*	*	*	0.704	0.614	*	*	–	–	12.78	–

Note The symbol * means without a mode operation and – refers to no uncertainty due to *

could be used as a correction factor for equipment sizing in commercial buildings because many HVAC designers normally amplify the load calculation by 20–25 % for safe as an acceptable practice [8]. However, they are not accurate enough to directly implement in a smart building management system for real-time optimization.

51.4.2 N-Analysis

In this section, l_{on} and l_{cycle} are used to calibrate solution 2 (*S*2) and conduct N_{max} analysis. Based on the results with EDBT 4.17 °C in the previous section, this range of OAT is approximately equivalent to the field measurements in previous studies. The relation between *N* and RTF was processed by two equations, which were proposed by several researchers [14, 15].

These two equations are also applied to compute maximum cycle rate per hour (N_{max}) in order to validate results on quantifying the oversizing of RTUs. Henderson et al. [15] proposed N_{max}, which is the regressed maximum cycle per hour occurring at RTF = 0.5, to describe the performance of a thermostat of an air-conditioner. Second equation was proposed by Miller et al. [14]. The correlation between *N* and RTF of 9 heat pumps was described by the proposed variables called beta (β) and alpha (α) in the different pattern. The two equations are given below:

$$N = 4N_{max}\mathrm{RTF}(1 - \mathrm{RTF}) \tag{51.9}$$

$$N = \frac{4\beta \cdot \mathrm{RTF}(1 - \mathrm{RTF})}{1 + \alpha \cdot \mathrm{RTF}} \tag{51.10}$$

where β is equivalent to N_{max} when α is zero. The term α is essential since a RTU capacity in terms of RTF is dependent on outdoor temperatures. Also, α is affected by the variation of outdoor temperatures to RTU capacity, so α is proportional to RTF.

Figure 51.4 illustrates the application of Eqs. 51.9 and 51.10 of RTU No.2 in Store I obtained from EDBT 1.39 °C. For cooling mode, the blue curve is fitted in the pattern of β and α, whereas the black curve is fitted by the deduction of term α to calculate N_{max} compared with previous studies. For heating mode, the blue curve is a plot based on original data and the black curve excludes the influence of OAT. The parameter N_{max} from the black curve is used to explain the level of oversized capacity with *N* and RTF both considered.

Compared to RTF, the uncertainty of N_{max} with EDBT 1.39 and 4.17 °C is much lower with value in ±11.6 %. Table 51.3 illustrates the results obtained from *N*-analysis to validate the accuracy in terms of uncertainty. This method is more robust than the validation by RTF uncertainty because RTF is proportional to OAT, whereas N_{max} is obtained excluding the effect of OAT. Thus, N_{max} is more constant and accurate than RTF; the uncertainty of N_{max} is within ±11.6 % for this

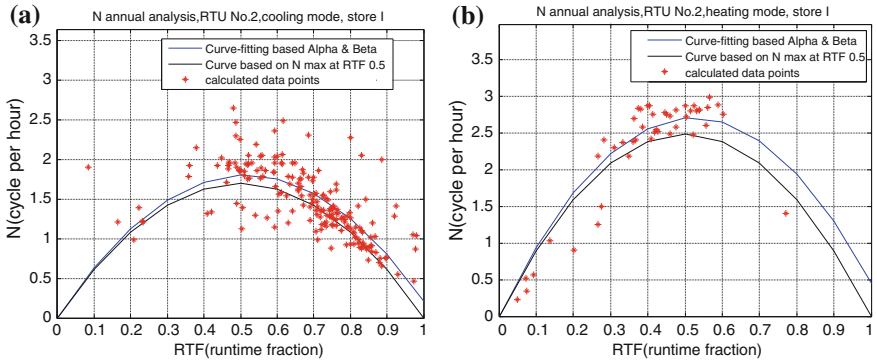

Fig. 51.4 *N* versus *RTF* of RTU No.2 in Store I. **a** Cooling mode. **b** Heating mode

store and within ±17.9 % for all stores. However, the limitation of *N*-analysis occurs when EDBT 4.17 °C cannot be used to compute $N_{\max}$.

51.4.3 Average Energy Penalty Analysis Along a Year

PLR, as given by Eq. 51.6, is the parameter to quantify the actual load of a RTU in a peak condition. This value can be validated by using *N*-analysis. The results for oversizing quantification by using validated PLR are more accurate than using average RTF. The equations used to quantify the oversize capacity and energy penalty are given as follows:

$$Q_{\text{over}} = Q \cdot (1 - \text{PLR}) \tag{51.11}$$

$$Q_{\text{pnt}} = Q \cdot \frac{(1 - \text{PLR})}{\text{EER}} \tag{51.12}$$

where Q is the capacity of a RTU, W or Btu/hour, and EER (Btu/W–h) is the energy efficiency ratio of a RTU. The subscripts *over* and *pnt* denote the oversized capacity and energy penalty, respectively.

The energy penalty using Eq. 51.12 is for cooling mode only. When heating mode is concerned, EER should be replaced by AFUE (annual fuel utilization efficiency).

$$Q_{\text{pnt}} = Q \cdot \frac{(1 - \text{PLR})}{\text{AFUE}} \tag{51.13}$$

For simplicity, EER and AFUE of a RTU are assumed as 10 Btu/W–h and 80 %, respectively, in order to evaluate the energy penalties. The results for 12 stores are collected in Table 51.4.

Table 51.3 The comparison of N_{max} between *EDBT* 1.39 °C and 4.17 °C by step 4 in Store I

Store I (N_{max})	Cooling mode (cycle per hour)				Heating mode (cycle per hour)				Uncertainty of 2 stages (St) in both modes (%)			
RTU no.	Stage1 (EDBT, °C)		Stage2 (EDBT, °C)		Stage 1 (EDBT, °C)		Stage 2 (EDBT, °C)		Cooling mode		Heating mode	
	1.39	4.17	1.39	4.17	1.39	4.17	1.39	4.17	St1	St2	St1	St2
1	2.15	2.38	*	*	0	0	0	0	9.67	–	–	–
2	1.58	1.72	*	*	1.98	2.16	*	*	8.23	–	9.09	–
3	2.22	2.35	*	*	0	0	*	*	5.86	–	–	–
4	1.31	1.33	*	*	1.90	1.74	*	*	1.53	–	−8.42	–
5	1.75	1.62	0.22	0.24	0.51	0.56	–	0.04	−7.43	9.09	9.80	–
6	0.14	0.15	0.15	0.16	0.26	0.28	0	0	7.14	6.67	7.70	–
7	0.17	0.18	1.12	1.12	0	0	0	0	5.88	0	–	–
8	0.12	0.13	1.01	1.09	0	0	0	0	8.33	7.92	–	–
9	–	–	0.12	0.13	0.68	0.76	0	0	–	8.33	8.82	–
10	1.70	1.53	0.59	0.65	2.10	2.33	0	0	10.00	10.17	10.95	–
11	0.17	0.18	1.05	1.09	0	0	0	0	5.88	3.81	–	–
12	0.165	0.173	0.931	1.039	0.505	0.452	0	0	4.85	11.60	10.50	–
13	2.45	2.25	0.49	0.51	0.29	0.30	0	0	8.16	4.08	3.33	–
14	3.09	2.97	1.50	1.34	0	0	0	0	−3.97	−10.67	–	–
15	0.16	0.17	0.17	–	0.37	–	0	0	6.25	–	–	–
16	0.35	0.25	1.05	1.15	0.24	–	0	0	−2.86	9.52	–	–
17	–	–	0.235	0.214	0.85	0.77	0	0	–	−8.94	−9.42	–
18	0.261	0.286	0.91	1.01	0.51	0.52	0	0	9.56	10.99	1.96	–
19	–	–	0.178	0.197	0.266	0.281	0	0	–	10.67	5.64	–
20	1.51	1.65	*	*	1.25	1.27	*	*	9.27	–	1.6	–
21	1.89	2.09	*	*	–	0.28	0	0	10.58	–	–	–
22	*	*	*	*	0.88	0.83	*	*	–	–	−5.68	–

Note The symbol—means Nmax cannot be computed by data due to not enough points and * is also without a mode operation, whereas—means no uncertainty due to – and *

Table 51.4 Summary of oversizing capacity and peak energy penalty for 12 retail stores

Store	Range of N_{max} (cycle/hour)		Oversized capacities (%)		Total capacities (Tons, MBH)		Peak energy penalty (kW)	
	cooling	heating	cooling	heating	cooling	heating	cooling	heating
A	0.57–5.75	0.64–4.05	100.11	398.69	320	3778.8	192.16	1,106.12
B	0.48–3.95	*	39.19	*	209	2753.2	70.62	*
C	0.59–2.77	0.51–4.14	14.65	224.29	235	2449.5	34.66	620.30
D	0.61–3.07	0.48–1.61	88.89	631.45	218	2741.1	123.11	872.66
E	0.24–4.65	0.68–4.05	247.19	261.43	289	3611.0	226.41	802.44
F	0.58–3.22	0.27–1.63	71.47	198.15	241	2903.0	120.54	635.44
G	0.48–4.05	0.72–5.63	87.90	367.41	172	2685.2	90.94	772.81
H	0.85–3.17	0.44–1.97	67.52	199.99	197	2928.2	91.89	593.74
I	0.13–2.97	0.00–2.33	50.43	236.49	177.5	2848.0	71.41	732.87
J	0.61–3.85	0.29–2.04	94.12	383.38	177	4738.4	102.98	1,375.99
K	0.52–3.22	0.37–3.29	70.09	225.16	226	3326.7	111.76	25.14
L	*	0.19–3.08	*	166.62	185	3997.4	*	914.66

The range of N_{max} varies from 0.13 to 5.75 cycles per hour for a cooling mode, while the range of a heating mode is between 0.00 and 5.63 cycle per hour. The oversized capacity of the RTUs has an average value of 84 % for cooling and 299 % for heating. The lowest peak energy penalty for the 12 stores is 34.66 kW in a cooling mode and 25.14 kW in a heating mode, while the highest peak energy penalty is 226.41 kW in a cooling mode and 1,375.99 kW in a heating mode.

51.5 Conclusion and Discussion

This study presents the systematic analysis of oversized capacities and energy penalties of RTUs for 12 retail stores. To avoid the errors by using simple RTF, *N*-analysis is proposed to calibrate the solution and uncertainty. N_{max} at annual design condition is introduced to exclude the effect of OAT in evaluating the compressor performance. Comparing N_{max} obtained from EDBT 1.39 °C with EDBT 4.17 °C, the uncertainty of this value is within ±17.9 % for all RTUs. Since N_{max} describes the performance of a RTU based on both *N* and RTF, this validation demonstrates the improved accuracy. In addition, *N*-analysis is further applied to compute PLR as a function of *N* and RTF. The average oversized capacities and penalty energy of RTUs can be computed by PLR for both cooling and heating mode. These accurate and robust results can be used as a tool to enhance the process of building load calculation. Additionally, the oversized capacities lead to the concept of smart building management. Another program will be built to automatically assist and adjust the control of each RTU in stores. The aim of this future study is to minimize waste energy consumption consumed by RTUs in retail stores without extra investment such as RTUs replacement and variable feed drive application.

References

1. U.S. DOE (2006) Energy Information Administration (EIA). Annual Energy Review 2009
2. U.S. DOE (2006) Energy Information Administration (EIA). Commercial Buildings Energy Consumption Survey 2003
3. U.S. DOE (2010) Energy efficiency and renewable energy, energy efficiency trends in residential and commercial buildings, Buildings Energy Data Book
4. Breuker M, Rossi T, Braun J (2000) Smart maintenance of rooftop units. ASHRAE J 42:41–47
5. Rivers N (2005) Management of energy usage in a supermarket refrigeration systems, The Institute of Refrigeration session 2004–2005
6. Djunaedy E, Van Den Wymelenberg K, Acker B, Thimmanna H (2011) Oversizing of HVAC system: signatures and penalties. Energ Buildings 43(2–3):468–475
7. Jacobs P, Conlon T (2002) State-of-the-art review whole building, building envelope, and HVAC component and system simulation and design tools—part1: whole-building and building envelope simulation design tools, Project FC05-99OR22674
8. Felts DR, Bailey P (2000) The state of affairs—packaged cooling equipment in California. In: Proceedings of American Council for an Energy-Efficient Economy, vol 3, pp 137–148
9. Scharn BK (2012) Investigation of over-sized rooftop units in a big box retail application. Master Thesis of Architectural Engineering, University of Nebraska at Lincoln, NE
10. Yu D, Li H, Yu Y (2011) A gray-box based virtual supply airflow meter in rooftop air-conditioning units. J Therm Sci Eng Appl 3(1):1–7
11. Yu Y, Liu M, Li H, Yu D, Loftness V (2012) Synergization of air handling units for high energy efficiency in office buildings: implement methodology and performance evaluation. Energ Buildings 54:426–435
12. Li H, Yu D, Braun JE (2011) A review of virtual sensing technology and application in building systems. Int J HVAC&R Res 17(5):619–627
13. ASHARE (2009) ASHRAE Handbook-fundamentals
14. Miller RS, Jaster H (1985) Performance of air-source heat pump, Project 1495-1 Final Report, EPRI EM-4226, NOV. 1985
15. Henderson H, Raustad R, Rengarajan K (1991) Measuring thermostat and air conditioner performance in Florida homes (FSEC-RR-24-91). Florida Solar Energy Center, Florida, USA

Chapter 52
Analysis on CO_2 Emissions of Construction Industry in China Based on Life Cycle Assessment

Xilong Cong, Hailin Mu, Huanan Li and Changzheng Liu

Abstract Construction industry has a great contribution to energy consumption and CO_2 emissions in the world. In this paper, CO_2 emissions of construction industry are calculated based on the method of life cycle assessment (LCA) from 2004 to 2010. According to life cycle theory, building life cycle is divided into four parts, namely building materials production, construction, operation and maintenance, and demolition waste. For the convenience of statistical analysis, the constructing, building maintenance, and demolition waste were merged into one part named the new construction. The results present the macrobuilding CO_2 emissions were 3.7 billion tons, accounting for 44.7 % of the China's CO_2 emissions in 2010. Among the macrobuilding CO_2 emissions, the averaged annual percentage of materials production, new construction, and operation phase were 40, 3, and 57 %, respectively.

Keywords LCA · Construction industry · CO_2 emissions

52.1 Introduction

As we know that today local and global environmental world are facing major environmental situation, i.e., global warming, ozone layer depletion, waste accumulation, etc. According to the relevant documents, the global climate is changing rapidly. So it is high time for us to mitigate these undesirable problems arising from our modern way of lifestyle to save our environment and our world.

X. Cong · H. Mu (✉) · H. Li
College of Energy and Power Engineering, Dalian University of Technology, Dalian, China
e-mail: congxl@126.com

C. Liu (✉)
Dalian Test and Control Institute, Dalian, China
e-mail: congxl@126.com

A. Li et al. (eds.), *Proceedings of the 8th International Symposium on Heating, Ventilation and Air Conditioning*, Lecture Notes in Electrical Engineering 263,
DOI: 10.1007/978-3-642-39578-9_52,

Building has always played a crucial important role in the energy consumption and CO_2 emissions around the world. According to the "building and climate change: decision makers" which are published by United Nations Environment Programme Sustainable Buildings and Climate Initiative (UNEP-SBCI) in 2009 [1], the construction field energy consumption accounts for about 40 % of global energy consumption and about 1/3 of greenhouse gas is related to the construction. Statistics from the US Energy Information Administration combined the annual energy required to operate dwelling and commercial buildings with the embodied energy of industry-produced building materials like concrete, ceramic, glass, steel, etc. and revealed buildings to be the largest energy-consuming and greenhouse-gas-emitting sector.

In recent years with rapid economic growth, urbanization area increasing and the continuous improvement of living standards, building total amount continuously increases, and building energy consumption rise sharply. The generalized building energy consumption accounts for about 45 % of the energy consumption of the whole society in China [2].

52.2 Building Life Cycle CO_2 Emissions Evaluation

In order to overcome the increasing concern of today's resource depletion and to address environmental considerations in both developed and developing countries, life cycle assessment (LCA) can be applied to decision making in order to improve sustainability in the construction industry.

According to the international standards of series ISO 14040, LCA is a technique that compiles an inventory of relevant inputs and outputs in the entire life cycle of a product (or service), evaluating the potential environmental impacts associated with these inputs and outputs [3]. It consists of four parts: objective and scope definition; inventory analysis; impact assessment; and interpretation.

1. The objective and scope definition involves establishing the functional unit, defining system boundaries and making inventory data.
2. Numbered lists should use the "numbered item" style. The life cycle inventory analysis (LCI) is a process that quantifies relevant inputs and outputs of the product, i.e., energy, raw material, and air emissions.
3. The life cycle impact assessment (LCIA) involves assigning environmental impacts of material and energy to different environmental impact categories and calculating the contribution of the constituents for different environmental indicators by characterization factor.
4. The interpretation deals with the interpretation of results from LCI and LCIA which includes the identification, determination, check, and results.

LCA is internationally acknowledged as a standardized environmental assessment methodology, and it is widely used in many sectors, including construction industry. Building life cycle is a process that buildings go though from cradle to

grave, including building materials production, construction, operation and maintenance, and demolition waste. As the energy consumption is quite different in each stage of building life cycle, the calculation about CO_2 emissions should be based on the building's entire life cycle. While many studies have examined building life cycle at the microlevel, little research has been done about environmental effect of buildings at the macrolevel [4, 5]. So the macrobuilding CO_2 emissions which based on life cycle would be analyzed and computed in this paper.

52.2.1 System Boundaries

Building life cycle CO_2 emissions includes four stages: building materials production, construction, operation and maintenance, and demolition waste [6]. The schematic representation of the building life cycle was indicated in Fig. 52.1.

In the building materials production phase, four kinds of building materials have been taken into account: steel, cement, glass, and timber and the CO_2 emissions come mainly from the use of energy during the production of the materials.

The building construction stage is the continuation of building materials processing in the building entire life cycle. The CO_2 emissions in this stage came from the use of the energy in the construction process, which includes the use of mechanical equipment and the transportation of the construction site.

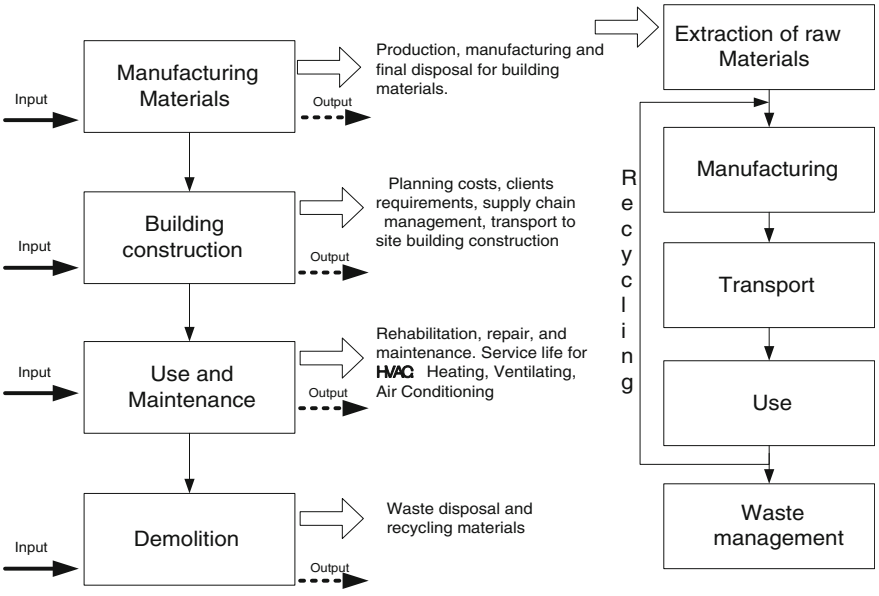

Fig. 52.1 Schematic representation of the building life cycle

The CO_2 emissions during operation phase came mainly from the use of energy in the course of utilization of buildings. The energy in this phase includes space heating (energy for heating system and electricity for operating the ventilation system), domestic hot water, household electricity, and electricity for facility management purposes.

The building demolition stage includes the site operation of building demolition and the transportation and disposal of construction waste. The CO_2 emissions in this stage come mainly from the fuel oil consumption of machinery and the waste treatment.

52.2.2 Construction Industry CO_2 Emissions Calculation

According to the above, the CO_2 emissions of the construction industry came mainly from four parts: building materials production, building constructing, operation and maintenance, and demolition.

From a macrolevel perspective, the building constructing, building maintenance, and the demolition are occurred in the construction industry. For convenience of statistical analysis, the three were merged into one part named the new construction. So the CO_2 emissions of the construction industry were simplified to three sources: materials production, new construction, and operation phase. The sum of the CO_2 emissions in the materials production, new construction, and operation phase is called construction industry CO_2 emissions and can be expressed as

$$CE_{total} = CE_{mp} + CE_{nc} + CE_{op} \tag{52.1}$$

where CE_{total} = the total CO_2 emissions in the construction industry; CE_{mp} = CO_2 emissions of materials production; CE_{nc} = CO_2 emissions of new construction; and CE_{op} = CO_2 emissions of operation phase

52.2.2.1 Materials Production

According to the data from China construction industry statistics yearbook, there are four building materials considered in this paper (steel, cement, timber, and glass). The CO_2 emissions of the materials production can be expressed as

$$CE_{mp} = f_i \times m_i \tag{52.2}$$

where f_i = CO_2 emissions factors of material (i) per unit quantity, the data about CO_2 emissions factors were shown in Table 52.1; and m_i = quantity of building material (i).

Table 52.1 CO_2 emissions factors in 2004–2010

Time	Steel [7] t/t	Cement [8] t/t	Glass [9] t/weight boxes	Timber [10] t/m^3
2004	2.03	0.83	0.42	−0.84
2005	2.03	0.75	0.42	−0.84
2006	2.00	0.73	0.41	−0.84
2007	1.87	0.71	0.40	−0.84
2008	1.84	0.68	0.40	−0.84
2009	1.83	0.63	0.39	−0.84
2010	1.81	0.61	0.39	−0.84

Note Timber is considered as environment-friendly materials due to its carbon fixation in this paper. The carbon storage content of per unit timber is 0.25 t/m^3, and CO_2 emissions factor is 0.072 t/m^3 in the whole production process [11]
Source Arrangement of related relevant literature [7–11]

52.2.2.2 New Construction

The CO_2 emissions in the new construction phase can be expressed as

$$CE_{nc} = C_i \times EC_i \times 44/12 \tag{52.3}$$

where C_i = carbon emissions coefficients of energy (i) per standard coal; EC_i = energy consumption in the new construction phase.

Energy consumption data for the new construction phase were obtained from the China Energy Statistical Yearbook. The fuel data included coal (raw coal, cleaned coal, and other washed coal), coking products (coke, coke oven gas, and other coking products), petroleum products (gasoline, kerosene, diesel oil, fuel oil, LPG, and other petroleum products), natural gas, and electricity. All the carbon emissions coefficients were provided by IPCC except electricity. The carbon emissions coefficients of electricity took 0.26 kg(c)/kg based on the Chinese academy of Engineering.

52.2.2.3 Operation Phase

The CO_2 emissions in the operation phase can be expressed as

$$CE_{op} = C_j \times EC_j \times 44/12 \tag{52.4}$$

where C_j = carbon emissions coefficients of energy (j) per standard coal and EC_j = energy consumption in the new construction phase (Ditto).

Considering the differences of heating means between the north and south, building types and lifestyle between urban and rural, and energy-consuming equipment between residential buildings and public buildings, the energy consumption of the operation phase were divided into four parts: heating energy consumption for northern cities, urban residential energy consumption (except

heating), public building energy consumption (except heating), and rural residential energy consumption [12]. When calculating the energy consumption of transport, storage, and post in the public building, only electricity was considered.

52.3 Results and Discussion

The CO_2 emissions of construction industry were calculated and compared with the China's total CO_2 emissions in Fig. 52.2. The data about the China's total CO_2 emissions came from CDICA.

The proportion of the CO_2 emissions of construction industry in national CO_2 emissions increased quickly, especially in 2010, the proportion reached 44.7 %. Figure 52.3 shows the proportions of materials production, new construction, and operation phase in the total national building CO_2 emissions, which remained relatively stable. The CO_2 emissions came from operation phase accounted for the highest proportion (51–60 %), followed by materials production (36–45 %) and new construction occupied the least proportion (3–4 %).

The CO_2 emissions of operation phase were composed of northern heating zones, urban residential, rural residential and public buildings, and the proportions of each part in the operation phase were shown in Fig. 52.4. The proportions of the CO_2 emissions of northern heating zones, urban residential, rural residential and public buildings in the operation phase show little change in 2004–2010. The averaged annual proportions of the parts were 26, 24, 20, and 30 %, respectively. The rapid growth of building sector CO_2 emissions and the rapid development of construction industry had been associated with the improvement of living standards. In recent years, with the national income rising, the people's requirements

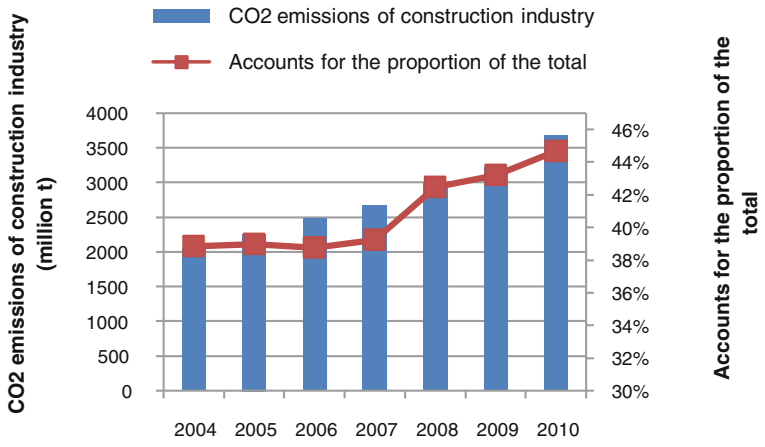

Fig. 52.2 The CO_2 emissions of construction industry and the proportion in national

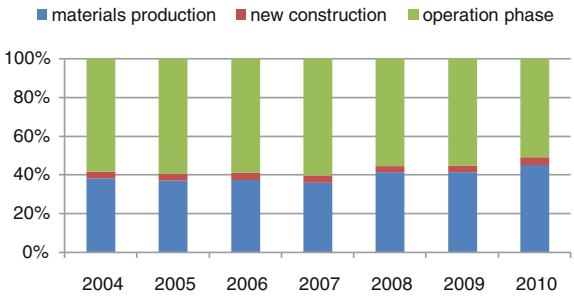

Fig. 52.3 Composition of building sector CO_2 emissions in China

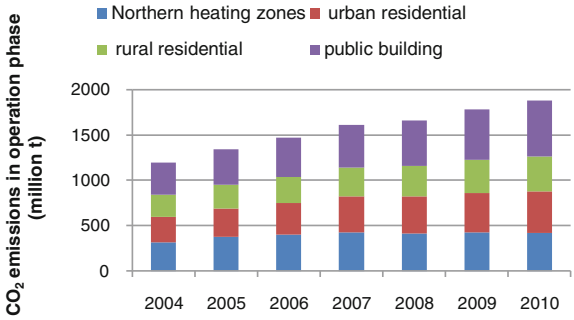

Fig. 52.4 Composition of CO_2 emissions of the operation phase

for the living conditions are becoming higher and higher, more and more household appliances are used, and the area of residence and public building is increasing quickly and all this contributed to sustained growth in CO_2 emissions of building operation stage. Meanwhile, as the floor space of buildings under construction expands every year, building materials consumption increases continually which resulted in the rapid growth in CO_2 emissions of materials production.

52.4 Conclusions

This study has assessed the CO_2 emissions of construction industry in china (2004–2010) by applying life cycle analysis methods. The macrobuilding CO_2 emissions were divided into three parts: materials production, new construction, and operation phase. The construction industry had the highest CO_2 emissions in various industries, especially in 2010, the emissions account for 44.7 % of the country's CO_2 emissions. Hence, the importance and urgency of developing low-carbon building should be realized.

The CO_2 emissions of materials production were an important part of macrobuilding CO_2 emissions, which account for about 40 % of total building CO_2

emissions. Therefore, improving energy efficiency of building materials industries and decreasing consumption of building materials are very important measures to reduce CO_2 emissions of construction industry. The CO_2 emissions of new construction phase account for only 3–4 % of the total building CO_2 emissions. However, this phase is a key point in the lifecycle of building which had a significant impact on building materials production phase, and building operation phase. The type and quantity of building materials and the thermal performance of buildings were decided in the new construction phase. The CO_2 emissions of building operation phase were the largest component in the construction industry, which account for about 57 % of the total building CO_2 emissions.

Acknowledgments This work was financially supported by the National Natural Science Foundation of China (71273039).

References

1. SBCI N (2009) Buildings and climate change: a summary for decision-makers. http://www.unep.org/SBCI/pdfs/SBCI-BCCSummary.pdf
2. Li XJ, Jiang Y (2006) Pondering over the Situation of domestic generalized building energy consumption. Architectural J 7:30–33
3. ISO 14040 (1997) Life cycle assessment-principles and framework, Geneva
4. Sharma A, Saxena A, Sethi M, Shree V, Varun (2011) Life cycle assessment of buildings: a review. Renew Sustain Energ Rev 15:871–875. doi:10.1016/j.rser.2010.09.008
5. Asif M, Muneer T, Kelley R (2007) Life cycle assessment: a case study of a dwelling home in Scotland. Build Environ 42:1391–1394. doi:10.1016/j.buildenv.2005.11.023
6. Ortiz O, Castells F, Sonnemann G (2009) Sustainability in the construction industry: a review of recent developments based on LCA. Constr Build Mater 23:28–39. doi:10.1016/j.conbuildmat.2007.11.012
7. Zhao YQ, Li XC, Li GJ (2012) Current Situation of CO2 emission and point sources distribution in China's iron and steel industry. J Iron Steel Res 24:1–4
8. Xu R, Wu XY, Cui YS (2012) CO2 emission status and outlook of Chinese cement industry. Cement grinding technology exchanges conference and exhibition both at home and abroad
9. Tian HL (2011) Research on the sustainable development of flat glass industry from the perspective of low carbon economy. Tianjin University of Technology
10. Yang QM (2009) Quantificational life cycle assessment of environmental impact of construction productions. Tianjin University, Tianjin
11. Yan PF, Yang J (2007) An improved method of environmental impact assessment and application. Environment and Sustainable Development: 10–12
12. Building energy conservation and research center at Tsinghua University (2011) China's building energy conservation annual development report. China building industry press, Beijing

Chapter 53
Indicator-Based Energy Diagnosis for Cooling Water System

Cheng Chang, Yiming Feng, Xuedong Tian and Qingpeng Wei

Abstract The performance of the cooling water system strongly affects the energy efficiency of centralized chiller plant. However, many cooling water systems are not well operated. Energy diagnosis is necessary to enhance the system efficiency. The existing energy diagnosis methods rely on expert experience and are time-consuming and expensive. Therefore, this chapter presents an indicator-based diagnosis method for the cooling water systems. In this method, four indicators are defined to quantitatively evaluate the performance of the system. These indicators can be calculated by a standard process. By reading the indicators, building managers and operators can easily find the energy-waste problems and estimate the energy-saving potential. This method has been applied in a large-scale commercial building in Hong Kong. This application is presented in detail to show this method.

Keywords Cooling water system · Energy diagnosis · Energy performance indicator

53.1 Introduction

In large-scale buildings, the central cooling water systems (CWS) circulate the cooling water between the cooling towers and the chillers. The performance of the CWS strongly affects the energy consumption of cooling water pumps and cooling towers. Moreover, it has significant influence on the chiller efficiency. However, in many buildings, the CWS are not well operated. The ratios of cooling energy to

C. Chang (✉) · Y. Feng · X. Tian · Q. Wei
Department of Building Science and Technology, Tsinghua University,
100084 Beijing, China
e-mail: changs04@mails.tsinghua.edu.cn

A. Li et al. (eds.), *Proceedings of the 8th International Symposium on Heating, Ventilation and Air Conditioning*, Lecture Notes in Electrical Engineering 263,
DOI: 10.1007/978-3-642-39578-9_53,

cooling water pump power (kW/kW) should reach 70 in the climate of Beijing, but an on-site survey shows that the ratios in most buildings are much lower than that. Thus, optimization of the cooling water system is one of the major approaches to improve building energy efficiency.

Many diagnosis methods have been put forward to raise the energy efficiency of the CWS [1, 2]. Those methods can bring significant energy-saving benefit. However, they still have some disadvantages. First, the success of diagnosis highly relies on the expert experience. Different experts may make different conclusions. Second, the diagnosis process is complicated. It is hard to learn for building managers and operators. Though expert plays an important role in energy-saving diagnosis, it is also important to let the building managers and operators understand and continuously watch the performance of their systems. Finally, existing energy diagnosis method is time-consuming and expensive, so it is difficult to afford the diagnosis through the building lifecycle.

This chapter therefore presents an indicator-based energy diagnosis method for the CWS. Based on the analysis of the 4-stage energy efficiency losses in the CWS, energy performance indicators (EPIs) are given to quantitatively evaluate the energy-waste problems. EPIs can be calculated automatically. By observing these EPIs, building managers and operators can easily master the performance of the CWS. This method is applied in a large-scale office building in Hong Kong. This application is introduced in detail as an example to illustrate this method.

53.2 Energy Performance Indicators of CWS

53.2.1 4-stage Energy Efficiency Losses in CWS

An ideal CWS should have following four characteristics. First, the pump size is proper for the system. Second, given a set point of cooling water flow rate or pressure differential, the operating number and frequency of the pumps are optimized to satisfy the set point as well as reach the highest pump efficiency. Third, there is no unnecessary resistance in the CWS. Fourth, the CWS should have proper cooling water flow rate set point, which optimizes the total efficiency of chillers and cooling water pumps.

In real buildings, problems may exist in the aforementioned four aspects, called 4-stage losses of energy efficiency, including (1) pump size selection; (2) pump group control; (3) water resistance; and (4) cooling water flow rate set point. Problems in the first two aspects influence pump efficiency and those in the third aspect affect pump head, while those in the last aspect have impact on both pump power and chiller power.

Table 53.1 EPIs of CWS

EPIs	Contents
Pump size indicator	Evaluate the pump size selection
Pipe resistance indicator	Evaluate the pipe resistance
Pump group control indicator	Evaluate the group control of pumps
Cooling water flow rate indicator	Evaluate the cooling water flow rate

53.2.2 Energy Performance Indicators

Energy performance indicators (EPIs) are used to find and quantitatively evaluate the energy efficiency losses in the CWS. According to the 4-stage energy efficiency losses, the indicators are presented and shown in Table 53.1.

The value of EPI equals to the ratio of the energy consumption under ideal condition to that under current condition. For instance, the cooling water flow rate indicator equals to the ratio of the total energy consumption of chillers and pumps under optimized cooling water flow rate to that under current water flow rate. Therefore, if the EPI equals to 1.0, there is no problem in that aspect. The further the EPI is away from 1.0, the higher the energy-saving potential is.

53.3 Description of the Case System

The CWS under study serves an 80,600 m^2 large-scale office tower in Hong Kong. The building needs 24-hour air-conditioning all year round. The configuration of this system is shown in Fig 53.1. It has four large centrifugal chillers and two small screw chillers. All chillers adopt constant-speed compressors. The cooling water pumps and cooling towers are all constant speed. The operating number of pumps and towers corresponds to that of chillers.

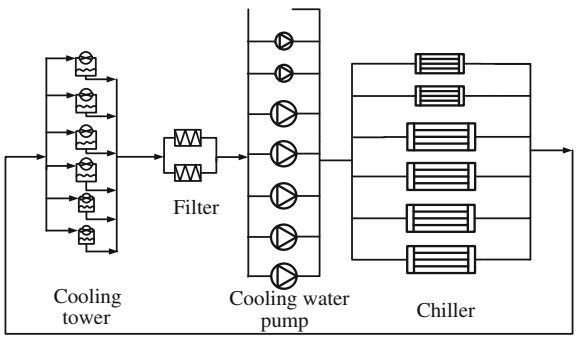

Fig. 53.1 Configuration of the cooling water system

The operating data of this system are recorded in the building management system (BMS). However, these data are not well utilized for the analysis of the system performance.

53.4 Indicator-Based Diagnosis

53.4.1 Outline

As shown in Fig. 53.2, the indicator-based diagnosis includes four steps. The first step is collecting related operating data logs and organizing them into standard forms. The second step is making the equipment models. Third, the EPIs are calculated. Forth, conclusions are made according to the EPIs.

53.4.2 Data Collection

Both equipment modeling and EPI calculation need to use the operating data logs. BMS in the buildings usually measures and records the important operating data of several years. Therefore, the data needed here can be summarized from the data logs stored in BMS. If some kinds of data cannot be found in BMS, on-site measurement is required.

In the case building, several kinds of operating data are collected, including the cooling water flow rate, temperature, chiller power, cooling production. All the data are organized in standard forms. The time step of each data log is 1 h.

53.4.3 Modeling

Three equipment models are used in this process, including the pump group model, the hydraulic network model, and the chiller model. Given the operating number and frequency of the pumps, the pump group model calculates the pressure

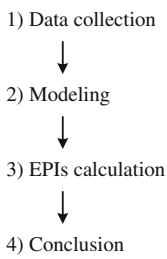

Fig. 53.2 Outline of indicator-based diagnosis

differential water flow rate curve of the pump group. The hydraulic network model estimates the total resistance value of the network, calculating the pressure drop and flow rate of each branch. The chiller model calculates the chiller power and COP under given working condition. All the models are semi-empirical. The parameters in these models are fitted by the operating data logs. The details of these models can be found in the literature [3] and is not repeated here.

53.4.4 Indicator Calculation

53.4.4.1 Pump Size Indicator

The cooling water pump is selected with rated flow rate and pressure differential. The pump reaches its highest efficiency at the rated working point. However, in real buildings, the actual flow rate and pressure differential are commonly different from the design values. Therefore, the pumps do not work at their rated points and the pump efficiencies decrease. The pump size indicator equals to the ratio of the pump power under the situation that the pumps are well selected to that under the current situation. This indicator shows how much pump power can be saved if the pumps are well selected.

In the case building, the rated cooling water flow rate of the large pump is 109 L/s, while the actual flow rate is 136 L/s. It means that the pump is little bit oversized. The rated efficiency of the pump is 64.5 %, while current efficiency is 61.6 %. The pump efficiency loss caused by the oversizing problem is 2.9 %.

The pump size indicator in the case building is 0.955, calculated in Eq. (53.1). It shows that the pump power will reduce to 95.5 % of the current value if the pumps are reselected.

$$\text{Indicator}_{\text{pump\_size\_selection}} = \frac{61.6\,\%}{64.5\,\%} = 0.955 \tag{53.1}$$

53.4.4.2 Pipe Resistance Indicator

Problems like valves at wrong openings bring unexpected hydraulic resistance in the cooling water system. Well-maintained system should avoid these problems to save pump head. The pipe resistance indicator equals to the ratio of the pump power with ideal pipe resistance to that with current pipe resistance.

The ideal pipe resistance is calculated according to design manual. In the case system, the current pipe resistance is 6.2 m H_2O higher than the calculated ideal pipe resistance. Further on-site measurement showed that 2.7 m H_2O head and 3.5 m H_2O head are consumed, respectively, by two balancing valves which are wrongly adjusted. The pipe resistance indicator is calculated to be 0.746, showing that 25.4 % of the pump power can be saved by adjusting the two valves.

53.4.4.3 Pump Group Control Indicator

By choosing the best operating pump number and frequency, the optimized pump group control strategy can increase the pump efficiency without any change in the overall flow rate and pressure differential. The pump group control indicator equals to the ratio of the pump power under the ideal group control to that under current control strategy.

According to the pump sample and the data logs of water flow rate and pump head, the current pump efficiency can be calculated. In the case system, the current pump efficiency ranges from 47.8 to 64.5 %. Based on the pump group model, if the ideal group control strategy is applied, the pump efficiency can be maintained at 64.5 %. The pump power will reduce to 94.8 % of the current value; thus, the pump group control indicator equals to 0.948.

53.4.4.4 Cooling Water Flow Rate Indicator

Cooling water flow rate influences not only the pump power, but also the chiller power. Higher cooling water flow rate increases the pump power but meanwhile decreases the chiller power, so there is a best flow rate under given working condition to achieve the overall optimal efficiency of chillers and pumps.

The optimal flow rate can be determined in following steps. First, the possible range of the cooling water flow rate is calculated. The cooling water flow rate through the chiller condenser should be higher than half and lower than 1.5 times of the rated value. Second, the water flow rate is traversed within the possible range with certain step. The total power of chillers and pumps under each water flow rate is calculated based on the equipment models. Then, the optimal flow rate for this situation can be chosen.

The comparisons between current values and optimized values of condensing water flow rate and the total power of chillers and pumps in typical working situations are shown in Figs. 53.3 and 53.4. The optimized flow rate is about 70 % of the current flow rate, and the optimized power is about 95 % of the current power.

The annual power consumption of chillers and pumps can be reduced to 95.1 % of the current value after the optimization of water flow rate set point. The cooling water flow rate indicator in the case building is 0.951.

53.4.5 Diagnosis Conclusion

The values of the EPIs of the case cooling water system are shown in Table 53.2.

Pipe resistance indicator is the lowest among the 4 indicators. The saving potential accounts for 25 % of the current pump power. It has been put into the

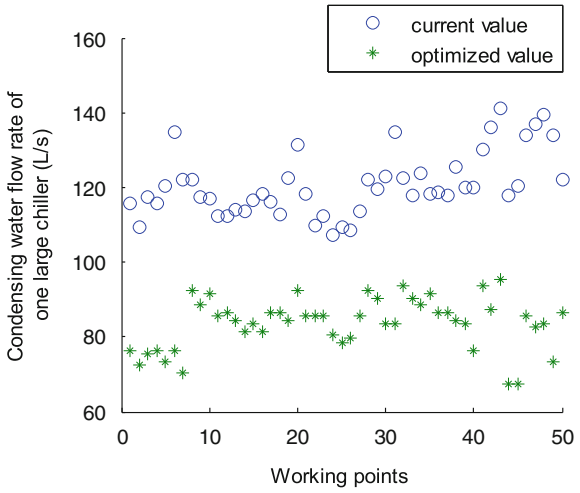

Fig. 53.3 Current water flow rate and optimized water flow rate

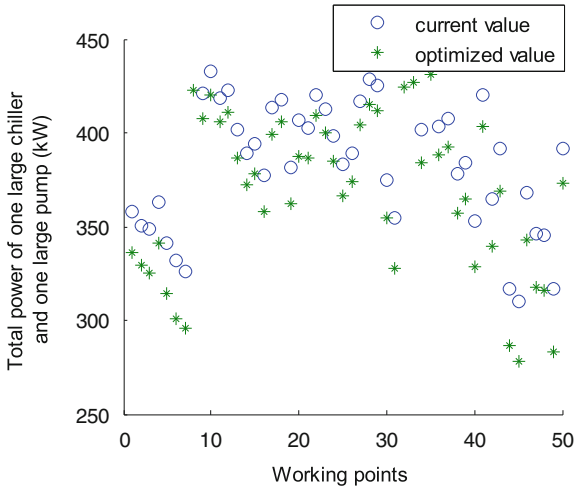

Fig. 53.4 Current power and optimized power of chillers and pumps

Table 53.2 Values of EPIs in the case cooling water system

EPIs	Contents
Pump size indicator	0.955
Pipe resistance indicator	0.746
Pump group control indicator	0.948
Cooling water flow rate indicator	0.951

proposal of this year that the balancing valves should be fully opened and the pump impellers should be trimmed down accordingly to fit the lower hydraulic resistance.

The saving potentials shown by the other three indicators are all around 5 %, the same level as the error of modeling and measurement. Therefore, no retrofits are suggested to do on these three aspects.

53.5 Conclusions and Discussion

To enhance the efficiency of the cooling water systems, this chapter presents an indicator-based diagnosis method. The energy performance indicators can be calculated by a standard process. By reading the indicators, building managers and operators can easily find the energy-waste problems and know the energy-saving potentials. Real application shows that this method can achieve reliable diagnosis result in a streamlined progress.

Many operating data are used in this method. Most of the data logs are from the BMS. The quality of the data strongly affects the reliability of the diagnosis result. Thus, the validation of the BMS data is necessary for this method.

Besides cooling water system, the idea of indicator-based diagnosis can also be applied to other subsystems of HVAC.

References

1. Energy Systems Laboratory at Texas A and M University and University of Nebraska (2002) Continuous Commissioning SM Guidebook for Federal Energy Managers. Federal Energy Management Program, Washington D.C
2. Xu K, Wang G, Wang Z et al (2009) Integrated system optimization through continuous commissioning. Energy Eng 106:7–25
3. Cheng C, Qingpeng W, Xin W (2011) Assessing chilled water system retrofit through data-log-based simulation. In: Proceedings of Building Simulation Conference, Sydney, 2011

Chapter 54
The Energy Consumption Analysis for the Windows with External Shading Influenced on the Green Building

Guohui Feng, Qinhong Zhang, Shuai Sha and Zhichao Wang

Abstract Window is a major factor affecting air-conditioning load. It brings heat conduction and convection caused by temperature difference, as well as the heat transferring by sun radiation, which has greater impact on air-conditioning load. The concept of building external shading is elaborated in this paper. The energy consumption of windows with exterior shading has an influence on the consumption of buildings. By employing the Ecotect ecological building design software, the external shading of office buildings in Fuzhou and Shenyang, is analyzed. The results show that active external shading is better for the Shenyang area building; for the Fuzhou area, the 0.4-m-level sun shields are most effective in energy-saving. External shading by geographical factors provided reasonable suggestions for the preparation and revision of the Green Building Evaluation Standard.

Keywords External shading · Overhang · Activities shading · Energy consumption · Ecotect

54.1 Introduction

The general term 5.2.9 in Fujian Province Green Building Evaluation Standard (DBJ/T13-118-2010) [1] points out that fixed or adjustable external shading facilities should be used on exterior windows (including the curtain walls), skylights and translucent roof. And the shading facilities should be convenient for operating and maintaining. With the development of technology and building energy efficiency requirements, the term 5.2.9 should be adjusted to the controls.

G. Feng (✉) · Q. Zhang · S. Sha · Z. Wang
School of Municipal and Environment Engineering, Shenyang Jianzhu University, Shenyang 110168, China
e-mail: fengguohui888@163.com

A. Li et al. (eds.), *Proceedings of the 8th International Symposium on Heating, Ventilation and Air Conditioning*, Lecture Notes in Electrical Engineering 263,
DOI: 10.1007/978-3-642-39578-9_54,

Fujian Province region spans in two climate zones, one is hot summer and warm winter and another is hot summer and cold winter. Summer time is long with hot weather, high indoor temperature, and strong sense of baking. Such living conditions should be considered to reduce the sun's radiant heat gain effectively so as to reduce the sun sunshine through rate [2, 3]. Strong summer sunshine through the window glass will cause indoor occupants uncomfortable, and it also increased air-conditioning load significantly. It is more common to set a curtain inside the window for shading. But the curtain which blocks the direct sunlight can also keep out the scattering light and affects the natural lighting, and for the air-conditioning load, the impact is not big. Setting the shade facilities outside, the window is an effective method to reduce indoor air-conditioning load. Therefore, we analyze the impact of external shading for green building indoor energy consumption.

54.2 Energy-Saving Theoretical Analysis of Building External Shading

(1) The different lengths visor analysis of indoor system energy consumption.

We apply the building outside shading coefficient calculation method A.0.1. which is described in "Design Standard for Energy Efficiency of Public buildings (GB 50189-2005)". The outside shading coefficient of level and vertical visors should be determined according to the following formula:

$$\text{The level visor}: \mathrm{SD}_H = a_h \mathrm{PF}^2 + b_h \mathrm{PF} + 1 \tag{54.1}$$

$$\text{The vertical visor}: \ \mathrm{SD}_V = a_v \mathrm{PF}^2 + b_v \mathrm{PF} + 1 \tag{54.2}$$

$$\text{Visor outside carry coefficient}: \mathrm{PF} = \frac{A}{B} \tag{54.3}$$

The comment:

SD_H	Level visor summer exterior shading coefficient;
SD_V	Vertical visor summer exterior shading coefficient;
PF	Visor outside carry coefficient, when the PF $>$ 1, take PF $=$ 1;
$a_h b_h a_v b_v$	Calculation coefficient, according to the Table A.0.1;
A	Visor outside carry length (Fig. 54.1);
B	The sun visor distance from roots to the window edge (Fig. 54.1)

(1) External shading can more effectively hide solar radiation than the inner one. The solar radiation heat absorbed by external shading device itself discharged into the outdoor by convection. It avoided the defect of inner shading effectively.
(2) For south or close to the south window, because height angle of the sun is higher, setting horizontal visor shade is appropriate. This method can form lots of shade area, and it can achieve good shading effect in reducing the south wall surface temperature and preventing sun irradiate window directly.

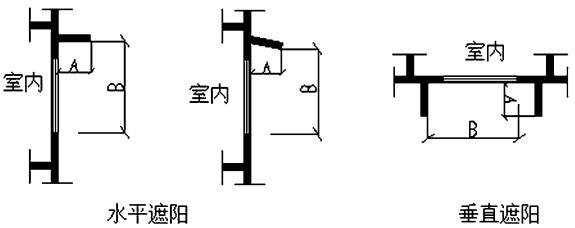

Fig. 54.1 Outside shade carry coefficient (FP) calculation diagram

This chapter chooses level placed visor whose width and the windows are the same as wide B is 2.5 m. We apply the shading coefficient limit for cold region in "Design Standard for Energy Efficiency of Public Buildings (GB 50189-2005)". Due to the Shenyang is cold region, the standard for shading coefficient limit is not explicitly stated. The length of the external visor in the south in this model is calculated.

$$\begin{aligned} \text{The level visor}: \ \mathrm{SD}_H &= a_h \mathrm{PF}^2 + b_h \mathrm{PF} + 1 \\ \mathrm{SD}_H &= 0.63\mathrm{PF}^2 - 0.99\mathrm{PF} + 1 \\ \mathrm{PF} &= 0.41 \\ \mathrm{PF} &= A/B = 0.41 \end{aligned} \tag{54.4}$$

The size of the external visor in the south is 2.5 m × 0.82 m. By employing the analysis software, the energy consumption of the room can also be obtained. Considering the size of the window, the indoor solar radiation heat gain is compared when the length of the visor are 0.0 m, 0.2 m, 0.4 m, 0.6 m, 0.8 m, 1.0 m and 1.2 m, respectively. The 0.0 m is the equipment energy consumption with no shade device. Assume that all other conditions do not change and calculate the system energy consumption with different visor's length.

54.3 Energy-Saving Simulation Analysis of External Shading

54.3.1 Ecotect Simulation Software

The Ecotect ecological building design software was developed by SquareOne company in British. It is mainly used in the design stage. It can be easily used in the design process of any stage to evaluate the design and has the high speed, strong intuitive and technical advantages. It also can combine series of precise analysis software for further analysis [4]. Ecotect is the most comprehensive of the most innovative architectural analysis software. It can provide friendly three-dimensional modeling design interfaces, and a wide range of USES performance analysis and simulation function.

54.3.2 The Simulation Model

54.3.2.1 East–West Level External Shading

East–West Level External Shading in Shenyang

Figure 54.2 shows that Shenyang office building uses the east–west visor for shade, the original parameters of the construction are constant, and shape coefficient is $S = 0.3$, Simulated architectural east–west window size is 2.5 × 2.5 m. Other buildings have the same heat transfer coefficient. The indoor energy diagram of east–west visor is shown in Fig. 54.3.

The Fig. 54.3 shows that the summer decline trend is not very obvious, 1.2 m visor will also increase indoor load, and the consumption of all sizes basically shows a rising state. Summer load is lower than south shading, because of the sun latitude and high angle, so in Shenyang, there is no need to do something fixed shading for east–west. Adjustable external shading in the south is advised.

East–West Level External Shading in Fuzhou

The literature shows that Fuzhou region will have a significant amount of sunlight, so analysis of Fuzhou area is for the east–west horizontal visor; the original parameters of construction are constant, shape coefficient is $S = 0.3$, and other buildings have the same heat transfer coefficient.

The indoor energy consumption with different length east–west visor in Fuzhou is shown in Fig. 54.4.

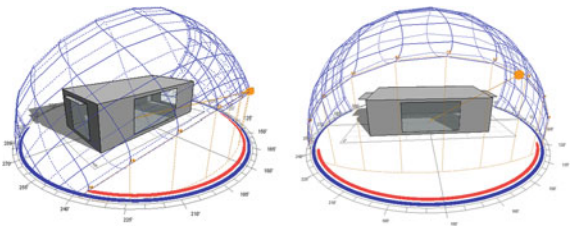

Fig. 54.2 Shenyang one office building using east–west shade

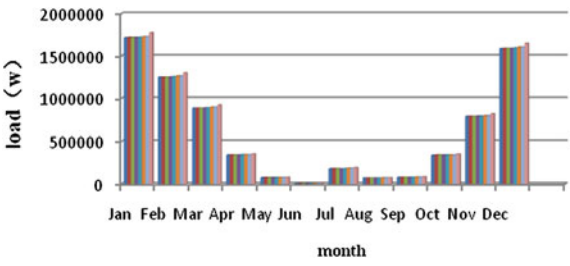

Fig. 54.3 Different length of east–west visor for indoor energy consumption in Shenyang area

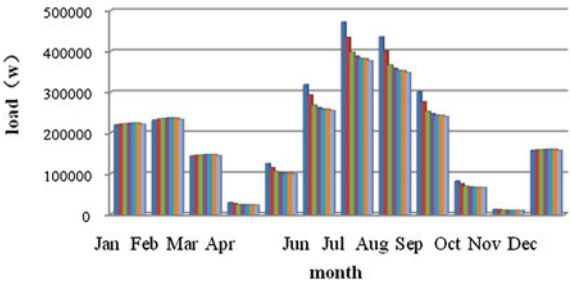

Fig. 54.4 Different length of east–west indoor shade energy consumption in Fuzhou region

Figure 54.4 shows that the building indoor load is downward trend, although the trend of decline is not obvious in 11th and 12th month because it is cold in winter and visor will keep out sunshine. But the others will appear obvious decline.

The Figure 54.5 shows that Fuzhou region for shading level will have a great impact. 0.4-m-level shade for system energy saves up to 17.30 %, 0.6 m energy-saving rate is 17.47 %, 0.8 m energy-saving rate is 18.31 %, and 1.2 m energy-saving rate is 19.01 %. The results show that for this building in Fuzhou, the longer the length of the visor, the more obvious the effect of the energy-saving is. Considering both the energy-saving effect and the material cost, the visor of 0.4 m is chosen finally. This is mainly because the energy-saving effect of 1.2 m visor is no more than that of the 0.4 m visor. Moreover, when the length of the visor is more than 0.4 m, it will affect the architectural appearance.

The results show that for this building in Fuzhou, when the visor length is 0.4 m, the effect of the south shading and east–west shading is good and they cost less. When the area of the southeast windows are the same as the south one, the effect of the southeast shading is better. This is due to the geographical location of Fuzhou area that in general will have west sunshine. So in the green building design, we should pay attention to the problem and we should reduce as far as possible on the west sunshine when we design it. At the same time, we can increase the weight of shading, the shade will be changed into control items, and it is better to Fuzhou region for shading.

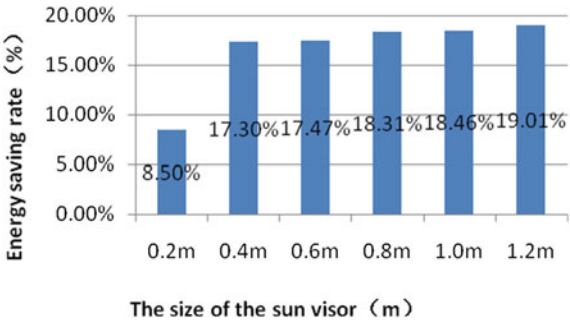

Fig. 54.5 Fuzhou different length visor for indoor system energy-saving rate

54.4 The Influence of Natural Lighting

According to "Standard for Daylighting design of buildings (GB/T50033-2001)", for the design of the architecture's lighting, we should make full use of natural light. It will create a good environment and save the energy. There are different climate zones for different regions. The value of the lowest indoor illumination factor for daylight natural light is shown in the Table 54.1.

In the section, the level of 0.4 m to cut off the sunshine outdoor hot is the best, and according to the conclusion, we build the model in Fig. 1.11 to prove the level of the sun visor for the impact of natural light in the room.

According to normal weather simulation, considering that the function is the office building, analysis of the height is 600 mm local simulation, indoor lighting coefficient is about 4–20 %, and the distribution is not uniform, it is because the south window is larger; therefore, in the south, indoor lighting coefficient value is bigger. Indoor lighting coefficient and natural light are shown in Figs. 54.6 and 54.7.

The building is located in Fuzhou that belongs to area IV. In accordance with "Standard for Daylighting Design of Buildings (GB/T50033-2001)", the lowest design coefficient is 2 %, and the indoor natural light critical illumination values is 100 lx. The simulation result shows that the lowest lighting coefficient of architecture is from 4% to 20 %, and the natural light indoor critical illumination values is about 180–900 lx. The office lighting level is III. All these meet the requirement of the meeting room, office and screen studio.

Table 54.1 Office building lighting coefficient standard value

Lighting level	Room name	The minimum coefficient of lighting $C_{\min}$ (%)	Critical natural light indoor illumination l_x
II	Design room, drawing room	3	150
III	Office, screen studio	2	100

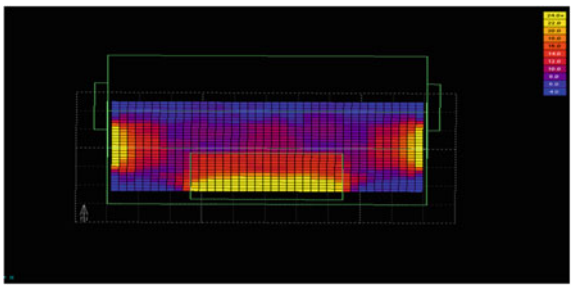

Fig. 54.6 Office building day lighting simulation in Fuzhou region

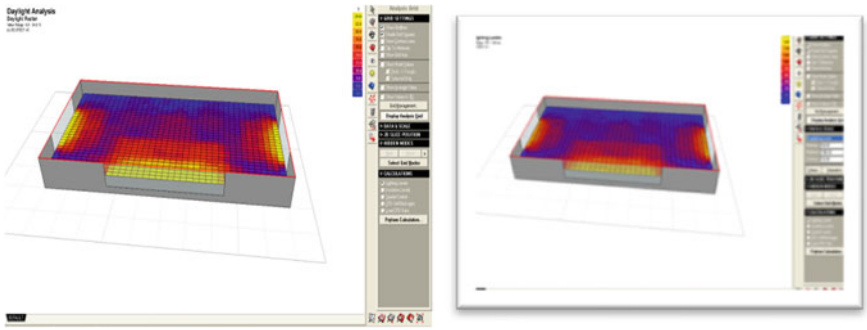

Fig. 54.7 Two-dimensional indoor day lighting factor/natural light chart

54.5 Summary

(1). The use of green building exterior shading technology is strongly advocated, and exterior shading terms can be more effective shielding of solar radiation energy than inner shade.
(2). The office buildings 0.4-m visor shading is better and has a good economy and convenient construction in Fuzhou area. In green building design, we focus on the problem of shining from west in Fuzhou region and try not to pay attention to building orientation like just south and north in green building design, while we should increase the weight of shading items, change the shading items into control, and consider the impact of shading and natural lighting.

Acknowledgments This study is supported by National Science and Technology Pillar Program during the 12th Five-Year Plan Period (2011BAJ05B02).

References

1. Fujian Province Green Building Evaluation Standard DBJ/T 13-118-2010 [S] China Building Industry Press, Fujian, 2010
2. Guillemin A, Molten A (2002) Energy efficient controller for shading devices self adapting to the user wishes. Build Environ 34(11):1091–1097
3. Jay S B, Steve F (2001) Alternative strategies for sun shading. Environ Des Constr (9):24
4. Yun P (2007) ECOTECTBuilding environment design tutorial. China Building Industry Press, Beijing

Chapter 55
Survey of Window-Opening Behavior of Severe Cold Area in Winter and Relevant Energy Consumption Analysis

Kailiang Huang, Guohui Feng, Lei Zhao, Shasha Chang and Mingzhi Jiang

Abstract In severe cold area with district heating, residents generally rely on window-opening behavior to improve indoor air quality, while heat loss becomes serious due to great temperature difference of inside and outside. Firstly, this paper acquired the basic information of Shenyang residential window-opening behavior though means of questionnaire. The second step is a comprehensive analysis using tracer gas measurement, computational fluid dynamics, and empirical models to acquire air change rate for typical rooms under conditions including window-opening custom and meteorological parameters. Based on all that, ventilation mass of a family apartment is predicted, and furthermore, we determined the ratio of the energy consumption to window-opening behavior in the coldest month. The research shows that most residents in Shenyang pay attention to indoor air quality and has window-opening behavior for certain time, and the present residential ventilation strategy is not only energy unfriendly but also unhealthy. This study provides important fundamental information for further ventilation strategy optimization in serve cold zone in China.

Keywords Window-opening · Severe cold area · Energy consumption · Air change rate

K. Huang
Faculty of Urban Construction and Environmental Engineering, Chongqing University, Chongqing 400030, China

K. Huang · G. Feng (✉) · L. Zhao · S. Chang · M. Jiang
School of Municipal and Environment Engineering, Shenyang Jianzhu University, Shenyang 110168, China
e-mail: fengguohui888@163.com

A. Li et al. (eds.), *Proceedings of the 8th International Symposium on Heating, Ventilation and Air Conditioning*, Lecture Notes in Electrical Engineering 263,
DOI: 10.1007/978-3-642-39578-9_55,

55.1 Introduction

Along with the improvement in economic society and new desire of people's living standard, more and more people start to care about indoor air quality and personal health, especially for northern residents who only care about indoor temperature in the past [1–4]. Consequently, building energy consumption tends to increase continually and occupy the lion's share in total energy consumption. Hence, some kinds of works become significant for the present building energy consumption situation, like survey of factors and potential factors pushing building energy consumption and the relevant fundamental information.

In China's severe cold area with district heating, residents generally rely on window-opening behavior to improve indoor air quality, while heat loss becomes serious due to great temperature difference in inside and outside [3]. Bringing in fresh air by opening window not only makes heat loss in short time but also leads to substandard indoor environment in severe cold city residential buildings. Fresh air system is generally not considered in district heating residential buildings. If windows are always kept closed, the indoor air quality will turn bad because of large amounts of pollutants produced by construction material and human body. At last, sick building syndrome appears among residents [5, 6].

Tracer gas measurement, empirical models, and computational fluid dynamics (CFD) have been widely used to study single-sided ventilation with limited accuracy [7–9]. Wang' research shows the differences between the empirical model predictions and CFD and/or the experimental data were less than 25 % [8]. In fact, direct measuring velocity at the opening and laser Doppler anemometry are also able to perform experimental measurements. For typical velocity measurements, such as hot wire anemometry, the equipment size will pose a limitation on the number of positions that can be measured [8]. Laser Doppler anemometry is usually very expensive and can only detect the velocity at one point each time [10]. Note that tracer gas measurement is useful for steady room conditions, and it can still work for variable indoor environment if enough test points are established to achieve desirable average indoor tracer gas concentration [11, 12].

This investigation intended to understand window-opening behavior in severe cold area in winter, acquire the related fundamental information, and finally calculate the ratio of the energy consumption of window-opening with a comprehensive analysis method.

55.2 Survey of Window-Opening Behavior

55.2.1 Survey Sample Information

Shenyang, the surveyed provincial capital of Liaoning Province, which lies in north latitude 41.7° and east longitude 123.4°, is the most prosperous and biggest city of northeast serve cold district in China. Its HDD18 is 3929, and the average

temperature of heating period is −4.5 °C. The sample of 511 house apartments comes from interview from 12 communities and 2 subways of Shenyang City. Specifically, the surveyed residential buildings include old buildings constructed before 2005, accounting for 50.5 %, and new buildings, accounting for 50.5 %. They are located in 3 typical districts of Shenyang and include types of tall buildings, multistory building, and very few villas. Most of the interviewed residents are office workers with a family of 2–3 members and lives in a 60–100 m^2 house apartment. The survey team is composed of 12 trained members of Shenyang Jianzhu University, and the survived date is in January, 2013, because this time is suitable to report the winter situation. We record date by inquiring people outside the community gate and send out questionnaire in the subways during the time of waiting train.

55.2.2 Results of Questionnaire

Through the statistical data, we find that 76.9 % of the residents in Shenyang have feelings of satisfied temperature, with a bit hot and very hot feelings and 23.1 % of the residents are not satisfied with the heating temperature. It is interesting to find that even heating for the house is poor, there are still 70.2 % who keeps the habit of opening window. The specific ratio of opening-window behavior to all 511 samples and those with poor indoor temperature are seen in Figs. 55.1 and 55.2.

Shenyang has implemented the policy of energy saving reconstruction since 2005 for old buildings toward exterior wall and window. Consequently, the survey reveals that only 12.4 % of the samples use window of single glass. Push–pull window and Pulley casement windows takes the vast majority of the surveyed windows. For ventilation habit, only 13.2 % of the residents would open opposite windows to have cross-ventilation, owing to the fact that great air change rate in a short time causes a dramatic temperature degradation. In the survey of window-opening size, 80.2 % of residents tend to open half of the window and less, so in the second step, 30° is adopted for analysis. Ventilation frequency in a day and the last time is shown in Figs. 55.3 and 55.4. We can find that most people prefer opening window for only one time and it lasts within half an hour. In the later experiment, we find indoor temperature would drop to an unacceptable level within half an hour and that explained their choices.

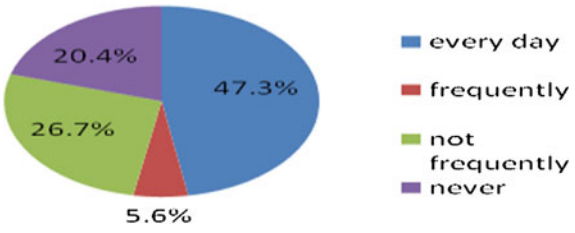

Fig. 55.1 Ratio of opening-window behavior for all samples

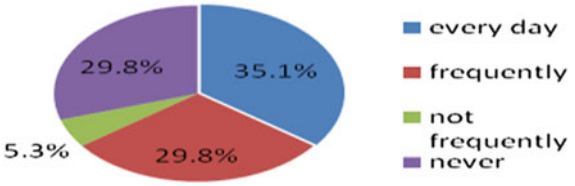

Fig. 55.2 Ratio of opening-window behavior for poor heating house

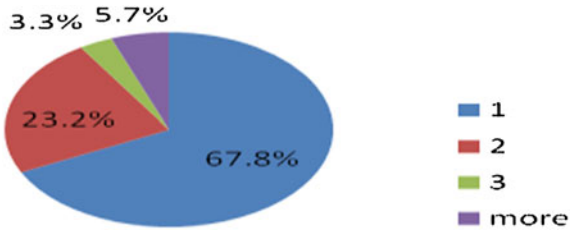

Fig. 55.3 Ratio of opening-window frequency for all samples

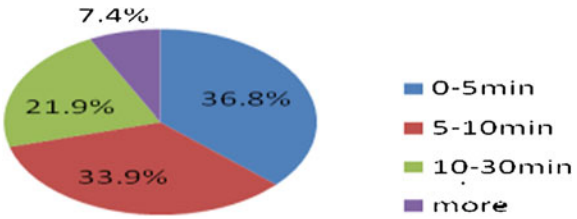

Fig. 55.4 Ratio of opening-window time for all samples

Appraisal of subjective indoor air quality is divided into 4 levels: satisfactory, ordinary, not satisfactory, and bad with sick building syndrome. 66.8 % of surveyed residents have ordinary feeling of their house on indoor air quality and no more than 10 % complains about the air. It is deduced that people can accept one time window-opening in a day though it is not sufficient for ventilation requirement [13].

55.3 Description of Experimental Setup and Test

Concentration decay method as a tracer gas is frequently used to calculate air change rate in the previous study [14]. The condition of evenly distribution is very hard to achieve in real buildings. Charlesworth indicated that one could overcome this problem by measuring the tracer gas concentration at several locations and by assuming that the mean of these concentrations is representative for the average concentration in the entire enclosure [15] and that methodology is supported by Hooff's CFD and experimental research, in which the average concentration based on the concentrations at the four individual locations is almost equal to the volume-averaged concentration in a large stadium [16]. The mass conservation for tracer gas is depicted in Eq. (55.1).

$$\frac{dC}{dt} = \frac{u}{v}(C_{out} - C) \tag{55.1}$$

where C is the concentration of tracer gas, C_{out} is the outside concentration of the tracer gas, u is the ventilation rate, and V is the volume of the space. The ventilation flow can be determined as Eq. (55.2).

$$u = \left[\ln(C_{i,1} - C_{out}) - \ln(C_{i,2} - C_{out})\right]\frac{V}{t} \tag{55.2}$$

The air change rate in 2 min can be represented in Eq. (55.3).

$$ACR = 30\left[\ln(C_{i,1} - C_{out}) - \ln(C_{i,2} - C_{out})\right] \tag{55.3}$$

CO_2 was chosen as the tracer gas in our present research as it is safe, does not cost much, and satisfies accuracy requirements [16, 17].The indoor CO_2 concentrations were measured using CO_2 concentration sensors of Telaire 7001 with a range of 0–10000 ppm, a measuring accuracy of ± 5 %, and a reaction time of less than 1 min. To calculate air change rate of different indoor spaces, a sleeping room of 3.3 × 3.4 × 3 m, a sitting room of (4.5 × 6.1 + 3 × 3.7 m) × 3 m, and a kitchen of 3 × 2.5 × 3 m are tested with four evenly distributed test points. The temperatures of these test points and the outside environment were recorded automatically with temperature and humidity auto recorder with measuring accuracy of ± 0.3 °C. Windward opening with nearly vertical condition is considered in our study.

All the start concentration of the present study is above 2000 ppm, selected in Hooff's research [16], because the great indoor and outdoor temperature difference may lead to a quick air exchange and that is not appropriate for sufficient test time requirement. The sleeping room takes 4020 ppm as a start because we want to observe a longer time for this most time occupied place at home. Figures 55.5, 55.6, and 55.7 show the concentration decay curves at the sleeping room, sitting room, and kitchen. Compared to the sitting room, concentration decay curves of the sleeping room and kitchen have more drastic degradations during the first 8 min. Additionally, the degradation for kitchen is the most drastic even it is similar to the sleeping room. These differences for them can be explained by the same window-opening size and space differences.

55.4 Simulation and a Comprehensive Analysis

55.4.1 Simulation Model

A former CFD model by Visagavel [13] has been used in the simulation with improved consideration of energy conservation equation since temperature is not considered in Visagavel' work. SIMPLE and SIMPLEC algorithms are used to

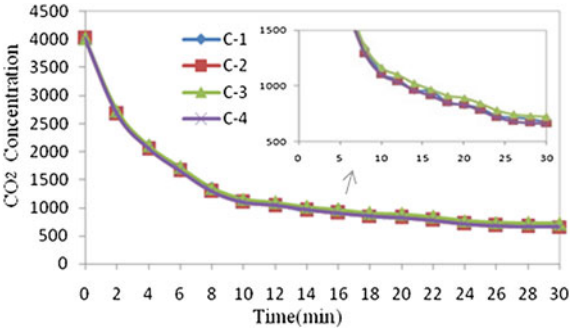

Fig. 55.5 CO_2 concentration decay curve of the sleeping room

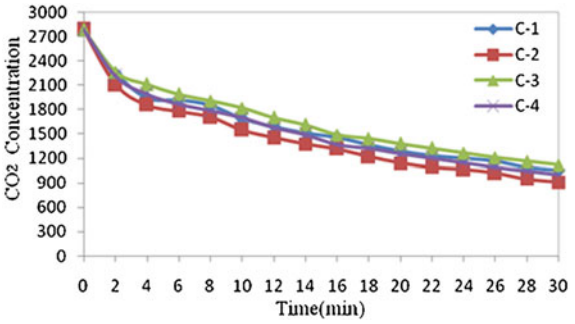

Fig. 55.6 CO_2 concentration decay curve of the sitting room

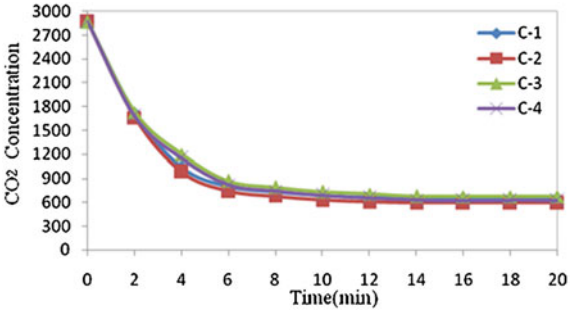

Fig. 55.7 CO_2 concentration decay curve of the kitchen

solve these equations. Steady, k- e turbulence model, and incompressible flow of a constant property fluid under Boussinesq's approximation have been considered. Figure 55.8 shows the two-dimensional computational domain in which L is the length of the room space, H is the height, and w is the window-opening size.

The model information is referred to document [13], and the boundary conditions to solve the problem are as follows: (1) No slip boundary condition($u = 0$, $v = 0$) is applied on the floor (south surface, SS)and the building surface (S), and zero-pressure boundary condition ($p = 0$) is applied on the right surface (RS); (2) LS is specified as velocity inlet, NS is specified as symmetry, and SS and S as

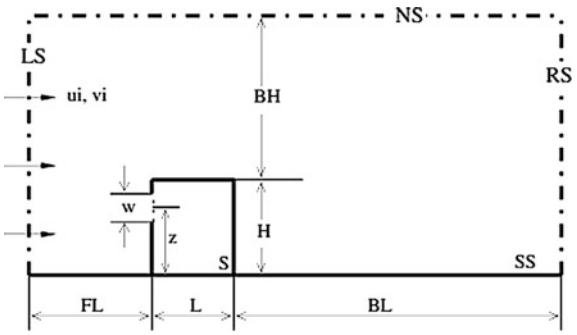

Fig. 55.8 Domain of the CFD model

wall and RS as pressure outlet boundary; (3) floor is set to be a heat source, and the other surface is considered to be insulated except the left wall has heat transfer. The model is solved numerically using the Fluent 6.3 CFD software. The ventilation rate is compared with experimental and empirical model results in the comprehensive analysis.

55.4.2 A Comprehensive Analysis

The window-opening works as inlet and outlet at the same time, and a part of thermal and mass exchange is due to turbulent diffusion, so it is not straightforward to calculate air change rate. A widely used method without taking into account turbulent diffusion is selected by integrating the time-averaged normal velocities over the opening area.

$$u = \frac{1}{2}\sum_{c}^{\text{opening}} |V_c.n_c|A_c \tag{55.4}$$

where v_c is the velocity vector, n_c is the unitary vector normal to the opening, and A_c is the area of the cell c belonging to the opening.

The calculated results of simulation and model are shown in Fig. 55.9. We can see that the simulation gives good results and its trend line resembles the experimental result with reliable value of R^2. Some of the experimental ACR have bad performance in its trend line. Two reasons about the deflection are deduced: (1) Outside wind is not rigidly consistent though repeated tests have been done; (2) turbulent diffusion of the opening and changing temperature conditions would make the deviation happen.

Few empirical models have been proposed to calculate the overall air change rate of single-sided ventilation resulting from the combination of stack and wind effects, among which Warren's correlation has been proved to obtain best agreement of measured and calculated air change rate [7]. The stack-driven single-sided ventilation is based on analytical considerations in Warren's correlation, and the

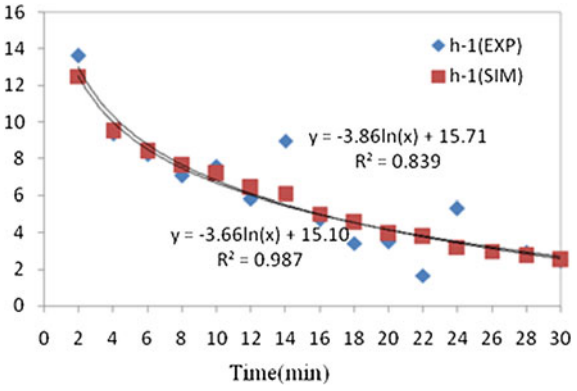

Fig. 55.9 Simulated and experimental change curve of ACR in two minutes

other one for wind-driven single-sided ventilation is based on experiments carried out in two full-scale buildings. The two equations are as follows:

$$q_{\text{stack}} = \frac{1}{3} A_{\text{eff}} C_d \sqrt{\frac{\Delta T H_g}{T_{\text{av}}}} \tag{55.5}$$

$$q_{\text{wind}} = 0.025 A_{\text{eff}} V_{\text{wind}} \tag{55.6}$$

where, q_{stack} and q_{wind} are the airflow rates due to stack and wind, respectively, C_d is the discharge coefficient, A_{eff} is the effective flow area of the opening, ΔT is the outdoor–indoor temperature difference, H is the opening height, g is the gravitational acceleration, T_{av} is the average temperature between outdoor and v_{wind} is the wind speed.

The air change rates of stack and wind effects by Warren's correlation are determined and compared to results from experiment and simulation in Table 55.1. The time periods are set to be 5 and 10 min which are frequently adopted in the survey of window-opening behavior. It is seen that stack effect is prominent in both 5 and 10 min and shows degradation in the 5–10 min. This is due to the higher temperature of indoor and outside and its change along with time. The results of experiment, simulation, and empirical models do not deviate from the average value clearly with the biggest deviation of 8.5 and 9.6 % for 0–5 and 0–10 min, respectively. Several literatures have implied that both simulation and empirical models are promising in calculating the air change rate, but the uncertainty makes them in need of validation [9, 16]. The accuracy of developed

Table 55.1 Air change rate of experiment, simulation, and empirical models

Time (min)	Average wind Speed (m/s)	Experiment (h-1)	Simulation (h-1)	Stack (h-1)	Average (h-1)	Wind (h-1)
0–5	1.9	10.8	11.6	12.7	11.7	8.1
0–10	1.9	8.8	9.2	10.3	9.4	8.1

Table 55.2 Heating index and ratio of opening-window heat consumption

Floor number	≤3	4–8	9–13	≥14
Index of heating period (W/m2)	20.1	17.2	15.9	13.9
Index of coldest month (W/m2)	42.0	36.1	33.4	29.2
House heat consumption for a day (KJ)	362.9×10^3	311.9×10^3	288.6×10^3	252.3×10^3
Opening-window heat consumption for 10 min (KJ)	5992.5	5992.5	5992.5	5992.5
Ratio for 1 time (%)	1.7	1.9	2.0	2.3
Ratio for 2 time (%)	3.4	3.8	4.0	4.6

trace gas decay method has been proved by the comparison, and then, the results are used for prediction of the ratio of the energy consumption to window-opening behavior.

Since the outside temperature of the former test is around −12 °C which is the average temperature of the coldest month in Shenyang, the ratio of the energy consumption to window-opening behavior can be easily predicted with two assumptions:(1) The heat consumption for the building is averaged on every family;(2) outdoor temperature is averaged; (3) only the mentioned sleeping room, sitting room, and kitchen have opening behavior for a 100 m^2 house. In the standard for severe cold and cold zones, the building heating index is based on average heating period temperature [13], and the index can be easily achieved through ratio calculation. The energy consumption of window-opening behavior is calculated by Eq. (55.7).

$$Q = \sum t \cdot \mathrm{ACR}_i \cdot \rho \cdot C_p(T_i - T_{\mathrm{out}}) \tag{55.7}$$

In Eq. (55.7), ρ is the density of air, C_p is specific heat of air, and T_i is indoor average temperature in each tiny period.

The times of air change in 10 min for sleeping room, sitting room, and kitchen are 1.47, 0.6, and 2.06, respectively. It means 10 min of ventilation fully meet standard of 0.5–1.0 in an hour [13]. Table 55.2 shows specific information of opening-window heat consumption ratio in total heat consumption.

55.5 Conclusions

This chapter surveyed the window-opening behavior of a serve cold city—Shenyang in the northeast of China. The comprehensive analysis is proved to be reliable without clear deviation. Finally, the ratio of the energy consumption to window-opening behavior is predicted.

Most residents in Shenyang pay attention to indoor air quality and have window-opening behavior for certain time. Even heating for the house is poor, there are still 70.2 % who keeps the habit of opening window. 66.8 % of surveyed residents have ordinary feeling of their house on indoor air quality and no more than 10 % complains about the air quality. The developed tracer gas decay method suits for calculating air change rate in the changing conditions, and room space has clear influence on the value. The air change in 10 min in the tested spaces brings in enough fresh air, and more ventilation would make unnecessary heat loss. The results of experiment, simulation, and empirical models do not deviate from the average value clearly with the biggest deviation of 8.5 and 9.6 % for ventilation of 0–5 and 0–10 min, respectively. Energy consumption of window-opening in winter is worth of attention even it is usually neglected in the building design. 10 min of ventilation for 2 times would make opening-window heat consumption ratio in total heat consumption to be 4.6 % or more.

Acknowledgments This study is supported by National Science and Technology Pillar Program during the 12th Five-Year Plan Period (2012BAJ26B02).

References

1. National Bureau of Statistics of China, China Statistical Yearbooks (1999–2010), China Statistics Press, Beijing, 1999–2010
2. China building energy efficiency annual development report- Building energy conservation and research centre of Tsinghua University. China building industry press, Beijing, (2010)
3. Li Jingmei, Lin Fu, Hongfa Di (2008) Test and analysis of window opening heat loss in heating residential buildings. J HVAC 38(3):111–113
4. Wang Y, Wu G (2008) Improvement performance evaluation of winter ventilation's influence on indoor air quality. J Saf Environ 38(3):111–113
5. Xu Z, Xiang Z, Jun W (2012) Study on fresh air volume in residential buildings. J HVAC 42(7):27–32
6. Lee SC, Li WM, Ao CH (2002) Investigation of indoor air quality at residential homes in Hong Kong-case study. Atmos Environ 36:225–237
7. Caciolo M, Stabat P, Marchio D (2011) Full scale experimental study of single-sided ventilation: analysis of stack and wind effects. Energy Build 43:1765–1773
8. Wang H, Chen Q (2012) A new empirical model for predicting single-sided, wind-driven natural ventilation in buildings. Energy Build 54:386–394
9. Caciolo M, Stabat P, Marchio D (2012) Numerical simulation of single-sided ventilation using RANS and LES and comparison with full-scale experiments. Build Environ 50:202–213
10. Buchhave P, George WK Jr (1979) The measurement of turbulence with the laser-Doppler anemometer. Annu Rev Fluid Mech 11:443–503
11. Lagus P, Persily AK (1985) A review of tracer-gas techniques for measuring airflows in buildings. ASHRAE Trans 91(2B):1075
12. Sherman MH (1990) Tracer gas techniques for measuring ventilation in a single zone. Build Environ 25(4):365–374
13. Design standard for energy efficiency of residential buildings in severe cold and cold zones. JGJ 26—2010. China building industry press, Beijing, (2010)

14. van Hooff T, Blocken B (2012) Full-scale measurements of indoor environmental conditions and natural ventilation in a large semi-enclosed stadium: Possibilities and limitations for CFD validation. J Wind Eng Ind Aerodyn 104(106):330–341
15. Charlesworth PS (1988) Air exchange rate and airtightness measurement techniques-an applications guide. Air Infiltration and Ventilation Centre, Coventry
16. van Hooff T, Blocken B (2013) CFD evaluation of natural ventilation of indoor environments by the concentration decay meth od: CO2 gas dispersion from a semi-enclosed stadium. Build Environ 61:1–17
17. Roulet CA, Foradini F (2000) Simple and cheap air change rate measurement using CO2 concentration decays. Int J Vent Volume 1(1):39–44

Chapter 56
A Study on the Household Heat Metering with Dynamic Temperature Method

Xiangli Li, Renjin Wang, Lin Duanmu and Lixin Hu

Abstract In this paper, the dynamic temperature method was used to establish heat consumption allocation model of residential buildings and a new household heat metering was proposed. The public heat consumption and variable heat consumption were described. According to the envelope characteristics of the residential buildings and then based on the thermal balance analysis of room and envelope, the formulas of effective heat consumption and heat consumption allocation coefficient were derived in this paper. In the derivation process of the effective heat consumption, frequency-domain regression model, plate heat-storage model, and transparent envelope's steady-state heat transfer model were involved. Finally, these models were validated by the data from energy efficiency inspection of a low-energy building in Dalian City. Test results showed that, in the calculation of the accumulated heat consumption compared with the measured values, the cumulative 14 h later, the relative error remains below 10 %; the cumulative 17 h later, the relative error remained about 6 %. It is basically satisfied the engineering requirements.

Keywords Household heat metering · Dynamic temperature method · Heat sharing

56.1 Introduction

Heat metering heating system has a history of 80 years in Europe. Practice shows that the heat metering system can save energy by 10–25 % than the traditional system [1]. However, the development of heat metering system is currently

X. Li (✉) · R. Wang · L. Duanmu
Faculty of Infrastructure Engineering, Dalian University of Technology, Dalian 116024, China
e-mail: lxl@dlut.edu.cn

L. Hu
Civil Air Defence Administrative Office of Underground Construction Engineering Crossing the Street, Jiamusi 154002 Heilongjiang, China

A. Li et al. (eds.), *Proceedings of the 8th International Symposium on Heating, Ventilation and Air Conditioning*, Lecture Notes in Electrical Engineering 263,
DOI: 10.1007/978-3-642-39578-9_56,

hampered by many factors and limited only to pilot project without large-scale application.

The shortcoming of traditional heat consumption allocation model is the lack of fairness. The initial investment, the cost of installation, and maintenance is very high and exceeds the psychological expectation of the heating enterprises and users. This also hinders heat measurement technology's large-scale promotion. For the current problems, a reasonable approach is setting a heat meter for each unit or building and then allocates the heat consumption to each user. There are many allocation models such as temperature method and time-off method. Traditional temperature method has weaknesses mainly in the processing of solar radiation and indoor-free heat. Other heat allocation methods are not yet mature [2, 3]. There are many other heat consumption calculation methods, such as time method, neural networks, and software modeling [4]. However, these methods are not based on the role of envelope or just give the correction factor of the building-corner users. It is not appropriate to give the static correction factor because each user's heating condition is changing all the time.

This paper is aimed to build a fair and reasonable dynamic heat allocation system in order to solve the problem. At the same time, meteorological parameters and indoor temperature are measured, transfer function method is used to complete heat-loss calculation, and the dynamic heat consumption allocation model based on the envelope's non-steady heat transfer model is derived.

56.2 Heat Consumption Allocation Model

Under heating conditions, the users of building corner (including the bottom user, the top user, and the users close to gable) contact directly with the outdoor environment and this is resulted that the building-corner users need much more heat than other users. However, building is a whole system; just the existence of building-corner users ensures much smaller heat consumption of other users. Therefore, the heat consumption of the building-corner users should be shared by all users. Based on this idea, three concepts are introduced in this paper: public heat consumption, variable heat consumption, and effective heat consumption [5].

Public heat consumption means the heat consumed by the envelopment of building corner. It does not only include the heat consumption of building floor, roof, and gable, but also the heat gained from the solar radiation. The heat consumption of building-corner envelop, seemingly, is consumed by the building-corner users, but from the point of the whole building, it is consumed to maintain the whole thermal environment. This part of heat loss should be shared by all users. Besides, the location of each user is different; thus, the heat obtained from solar radiation is much different, and this part of heat should be shared by all users. So, it should be attributed to the part of public heat consumption. At the same time, it should be noted that the existence of solar radiation may reduce the heat consumption of each user, so the heat obtained from the solar radiation should be removed from the public heat consumption.

Variable heat consumption means the part of heat which is used to maintain the user's own thermal environment without relating to other users. It includes the heat consumption of windows, gable walls, roof and floor, and adjacent rooms. In the heating conditions, the indoor thermal environment of each user is different, so the heating load is also not the same. In this case, the heat consumed is only used to meet each user's own request and other users benefit nothing at all. So, this part of heat should be undertaken by each user independently [5].

The relationship of each kind of heat consumption can be illustrated by the heat-allocating figure as shown in Fig. 56.1.

56.3 Mathematical Models

Under the action of internal and external disturbances, heat exchange between indoor and outdoor occurs through the envelope as a result of which forms the cold and heat load. According to the characteristics of envelope's heat transfer, the process will be divided into three categories [6]. In this paper, based on unsteady heat transfer of non-transparent envelope, heat gained from endothermic of transparent envelope, and heat gained form transmission, a mathematical model was created, respectively. In addition, previous studies show that the disturbance of indoor staff and equipment has little influence on heat consumption, so this paper does not consider the indoor-free heat.

56.3.1 Frequency-Domain Regression Model

Directly calculating root method is the most popular method to calculate the coefficient of transfer (CTF), because of the complexity of calculation, and there is

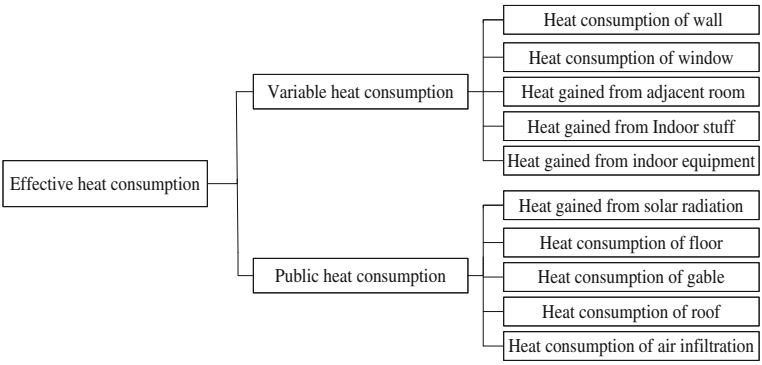

Fig. 56.1 Heat-allocating system

a possibility of losing root; basically, it is hardly to realize this method through programming. Therefore, scholars at home and abroad have proposed different methods, such as state-space method and frequency-domain regression method. The latter method is used to calculate the CTF in this paper [7].

56.3.2 Steady-State Heat Transfer Model of Transparent Envelope

Transparent envelope mainly refers to the transparent parts of windows or doors. Under outdoor weather conditions, the steady-state heat transfer model of transparent envelope in this paper includes two parts: one is the heat flowing through the envelope generated by the action of the indoor and outdoor temperature difference, and the other one is the heat gained from the solar radiation absorbed by envelope. Generally, the thickness of windows is about 4 mm to 6 mm, thermal conductivity is 0.76 J/(m s k), and the density is 2,500 kg/m^3. So, the heat-storage characteristics of glass have not been taken into account. The heat transfer formula of the glass is as follows:

$$Q_{\text{win,con}} = F \times K(t_l - t_n) \tag{56.1}$$

where F is the area of window, m^2; K is the heat transfer coefficient of window, W/(m^{2}K); t_n is the indoor temperature, °C; t_l is the indoor temperature, °C.

When solar radiation goes through the glass, some of the energy will be absorbed as a result of which making the glass temperature increasing, and then transfer heat indoors or outdoors. The heat transferred can be calculated by the following formulas:

$$q_{\text{win,absorp}} = N \times q_{\text{rad,ver}} \times \tau \tag{56.2}$$

$$N = \frac{R_w}{R_w + R_n}. \tag{56.3}$$

where τ is the absorption rate of glass, N is the ratio transferred to the interior after glass's absorbing the solar radiation, R_w is the convection coefficient of the outer surface of glass, W/(m^{2}K), R_n is the convection coefficient of the inner surface of glass, W/(m^{2}K).

56.3.3 Hypothetical Model of Plate Heat Storage

The solar radiation turns into heat completely after going through windows into the room. However, this part of energy does not directly impact on the current heat load, but is firstly absorbed by the envelope and furniture which raises the

temperature of envelope and furniture. Then, the indoor temperature rises gradually by convective heat transfer.

The internal structure of different buildings varies widely, and the indoor furniture is also different from each other. So, it is difficult to accurately calculate the process of solar radiation's absorption. In order to reflect the process of solar radiation's transmission and absorption in room, this paper proposes the following assumptions: Suppose there is a horizontal plate indoors and its area is 1.7 times the transparent envelope. All of the solar radiation transmitting into room has been absorbed by the plate. Then, the indoor thermal environment is gradually impacted by convection heat transfer of the flat's surface. In the calculation, the plate's area is 1.7 times the window's area. The material of plate is assumed to be as the same as the structure of interior wall. The calculating process shows in the following formulas:

$$T_{\mathrm{in,rad}}(\tau_{\mathrm{n}}) = T_{\mathrm{in}}(\tau_{\mathrm{n}}) + \alpha I/\alpha_{\mathrm{out}} \tag{56.4}$$

$$\mathrm{Q}_{\mathrm{flat}}(\tau_{\mathrm{n}}) = \sum_{i=1}^{r} b_i T_{\mathrm{in,rad}}(\tau_{\mathrm{n}} - i) - \sum_{i=1}^{m} d_i Q_{\mathrm{flat}}(\tau_{\mathrm{n}} - i) - \sum_{i=0}^{r} c_i T_{\mathrm{in}}(\tau_{\mathrm{n}} - i) \tag{56.5}$$

where α_{out} is the heat transfer coefficient of plate's surface, W/(m^{2}K); α is the absorption rate of the plate's surface; $\mathrm{Q}_{\mathrm{flat}}(\tau_{\mathrm{n}})$ is the heat transferred by plate at current time, W/m^2; $T_{\mathrm{in}}(\tau_{\mathrm{n}})$ is the indoor air temperature at time of τ_{n}, °C; $T_{\mathrm{in,rad}}(\tau_{\mathrm{n}} - \mathrm{i})$ is the indoor air integrated temperature at time of $\tau_{\mathrm{n}} - \mathrm{i}$, °C; $\mathrm{Q}_{\mathrm{flat}}(\tau_{\mathrm{n}} - \mathrm{i})$ is the transient heat transferred by plate at time of $\tau_{\mathrm{n}} - \mathrm{i}$, W/m^2.

56.4 Actual Measurement Program and Data Analysis

In order to verify the heat consumption allocation system and the model, a practice low-energy consumption building in Dalian was measured. The area of the building is 3,612.0 m^2, the height is 27.5 m, and there are eight storys. The thermal parameters of envelope can be seen in Table 56.1.

The measurement is divided into three periods. First, the commissioning phase of heating system, which is from December 14 to December 22, 2009; then, the first test phase, from December 23 to December 31, 2009; the second test phase, from February 2 to February 6, 2010. Outdoor air temperature range is 0–11.9 °C

Table 56.1 Thermal parameters of envelope

Envelope	Heat transfer coefficient [W/(m^2 K)]
Outer wall	0.25
Window	1.3
Ceiling	0.15
Outdoor	1.3
Interior wall	2.0

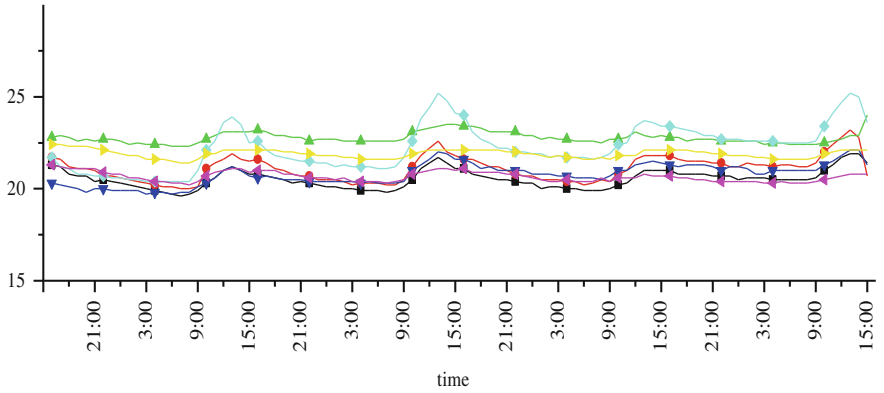

Fig. 56.2 Hourly indoor temperature of the rooms in the first floor

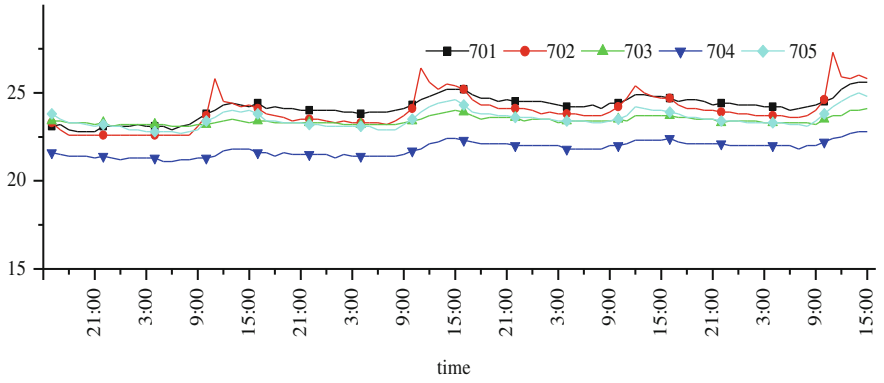

Fig. 56.3 Hourly indoor temperature of the rooms in the standard layer

The indoor hourly temperature of the building is shown in Figs. 56.2 and 56.3. The heating design temperature is 20 °C. During the measuring period, the room temperature is 20–25 °C, which meets the design requirements. Based on the actual situation of the building, the southern windows than walls is 0.46, and the northern windows than walls is 0.32. Because of the larger area of the southern windows, a large majority of solar radiation goes through indoor room as a result of which the indoor temperature is very high from 11:00 to 15:00 in the daytime. When the indoor temperature is not affected by the solar radiation, it can meet the design standard and the required range of the design specification.

56.5 Model Verification

According to this heat consumption allocation model, the comparison of a unit's cumulative values of calculated and measured is shown in Figs. 56.4 and 56.5.

It can be seen from Figs. 56.5 and 56.6, the relative error of calculated and measured cumulative values is about 10 and 6 % in the former 14 and 17 h, respectively. Before 14 h, the dynamic change difference of the calculated and measured values is obvious and cannot be eliminated in a short time. After 14 h, the relative error of the cumulated load begins to stabilize and stays less than 6 %. According to the proposed heat consumption model, the cumulative heat consumption allocation coefficient of each user is finally calculated which is shown in Fig. 56.6.

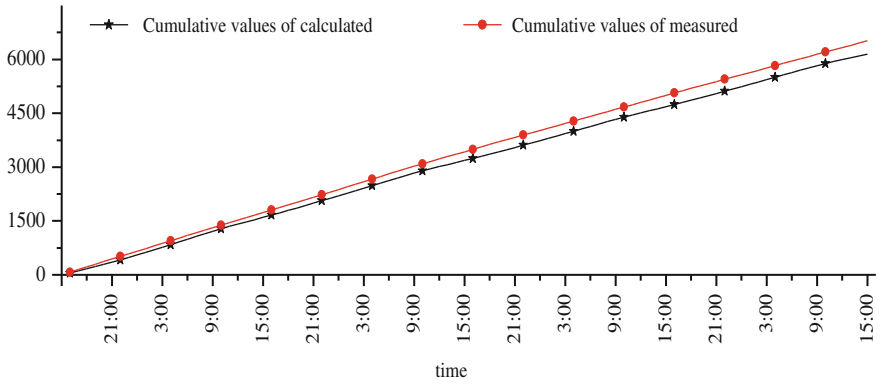

Fig. 56.4 Cumulative values of calculated and measured

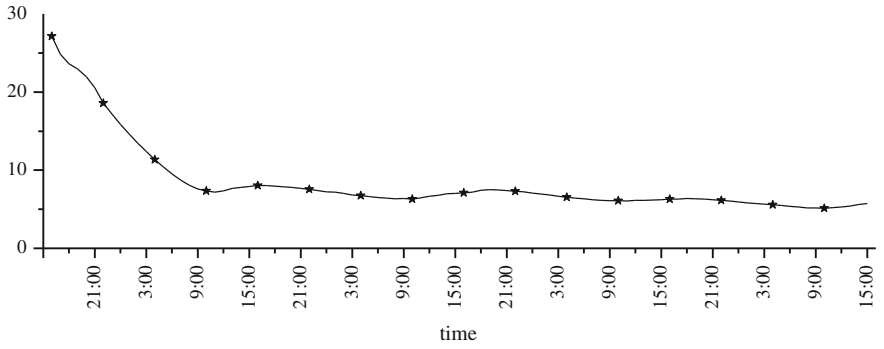

Fig. 56.5 Relative error of cumulative values of calculated and measured

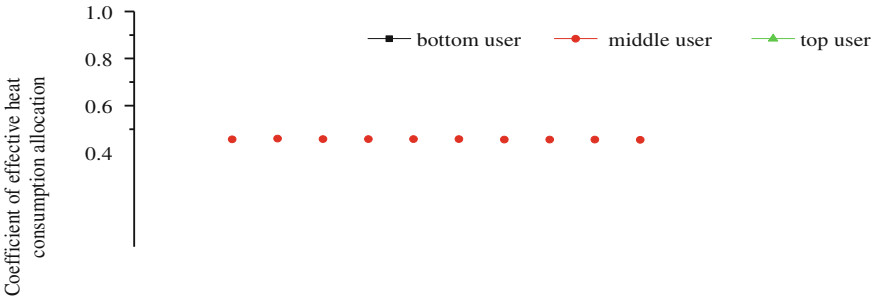

Fig. 56.6 Coefficient of effective heat consumption allocation

It can be seen from Fig. 56.5 that each user's effective heat consumption allocation coefficient goes stable after 14 h, and the coefficient of bottom user, middle user, and top user is at 0.3, 0.45, and 0.23, respectively. The reason is that in the testing process, each user's pipe valves are not change and there is no other thermal disturbance in the interior room. Therefore, each user's allocation coefficient stays stable and is realistic. The area of middle users, top users, and bottom users is 410, 205, and 289 m^2, respectively. The user on the first floor is allocated a larger proportion of heat consumption.

56.6 Conclusions

1. An effective heat consumption allocation model is established in this paper. Compared with the measured value, the calculation error is about 10 % at the beginning 14 h and it is 6 % after 18 h, which is basically consistent with the measured values. The calculating precise is enough for the heat measurement.
2. The only input parameter is indoor temperature for each heat user, so we just need to install some thermometers in the heating room. Compared to other allocation programs, the investment is greatly reduced.
3. In this paper, a hypothesis of plate's heat storage is proposed to calculate the absorption and transformation processes of indoor solar radiation. The error can be kept below 10 % comparing the calculating values and measured values.

Acknowledgments The authors appreciate the financial support of the National Science & Technology Pillar Program during the 12th Five-year Plan Period, No. 2012BAJ04B03-02.

References

1. Xu W, Zou Y (2000) Temperature control and heat metering of heating system. China plan press, Beijing
2. Fang X, Jiang Y, Wang X (2005) Heat metering allocation system based on indoor temperature method. J HV@AC 35(05):112–115
3. Song W, Wei L (2006) Dynamic simulation software for room temperature and heating load of household heat metering systems. J HV@AC 36(2):108–111
4. Liu L, Fu L, Jiang Y (2011) Major issues and solutions in the heat-metering reform in China. Renew Sustain Energy Rev 15:673–680
5. Li G, Feng G, Shang J et al (2007) Research on heat consumption allocation model. Shenyang Univ Archit (Nat Sci) 23(5):802–805
6. Yan Q, Shi W, Tian C (2010) Air conditioning and refrigeration technology. China Building Industry Press, Beijing
7. Chen Y, Wang S (2004) New method for unsteady heat transfer of building envelope. Science Press, Beijing

Chapter 57
A Survey on Energy Consumption in Rural Households in Three Regions of China

Zhengwu Yang, Pengfei Si, Xiangyang Rong, Yueshen Fan and Xiaodan Min

Abstract A survey focusing on energy consumption in rural households in three typical areas of China was conducted in the form of questionnaire. Nearly 800 households were sampled in the survey. The purpose of the survey was to find out some unreasonable energy consumptions and offer some practical solutions. The results indicate that: firstly, in rural areas, energy consumption level is quite low, meanwhile, the non-commercial energy consumption accounts for a large percent, and this even occupies more than 90 % in Pu'er; secondly, the use ratio of solar energy in rural households is very low and has no correlation with availability of local solar energy resources, for example in Xinzhou, the use rate of solar water heating is less than 5 %; thirdly, in rural areas of Xinzhou, household energy consumption per capita is 1.24 times of the national rural average, and it is less than the average in Jingzhou and Pu'er. Fourthly, the use ratio of energy-saving lamp is lower than 50 % in all three areas; finally, there is a certain correlation between income level and commercial energy consumption, and the correlation coefficient for each area is 0.36697, 0.29312, and 0.45456, respectively.

Keywords Rural building · Energy consumption · Energy conservation · Commercial energy

Z. Yang · P. Si (✉) · X. Rong · X. Min
China Southwest Architectural Design and Research Institute Corp. Ltd, Chengdu 610041 Sichuan, People's Republic of China
e-mail: 175987342@163.com

P. Si · Y. Fan
School of Environmental and Municipal Engineering, Xi'an University of Architecture and Technology, Xi'an 710055 Shaanxi, People's Republic of China

A. Li et al. (eds.), *Proceedings of the 8th International Symposium on Heating, Ventilation and Air Conditioning*, Lecture Notes in Electrical Engineering 263,
DOI: 10.1007/978-3-642-39578-9_57,

57.1 Introduction

It was agreed that energy should be the main context of sustainable development [1]. Energy consumption in China has been increasing rapidly due to recent economic growth and development. This leads to serious environmental problems such as global warming, air pollution, and acid rain [2]. As we all know, China has a population of 1.3 billions, among which nearly 800 millions people live in rural areas. The construction areas are about 25 billion square meters in rural areas [3]. With the increasing construction of the rural infrastructure during the process of building a new socialist countryside, energy consumption will become one of the most dramatic and realistic issues that may restrict the sustainable development of rural areas. In this paper, we will obtain some conclusions though investigating and analyzing energy consumption in three typical regions of China.

57.2 The Methods of Survey

Considering the rationality and typicality of data, in accordance with geographical characteristics and the distribution of energy and resources in three typical areas of China, household energy consumption in rural residential buildings has been investigated and studied in this article. The three regions have significant different climatic conditions. They have different resources enrichment, such as rich coal resources in Xinzhou, rich water resources in Jingzhou, and rich forest resources in Pu'er.

The samples of survey are as follows: 267 families from 81 villages of three counties of Xinzhou of Shanxi Province, 289 families from 39 villages of two counties of Pu'er of Yunnan Province, and 241 families from 57 villages of one county of Jingzhou of Hubei Province. More than 900 samples were distributed, and a total of 797 valid samples were returned. The items within the questionnaire are shown in Table 57.1. In order to minimize bias, target visiting was conducted to obtain data from some typical households.

Table 57.1 Items of the questionnaire sheet

Number of household members	Biomass consumption	Main stove type for space heating	Main lamp type for lighting
Income	Liquefied petroleum gas consumption	Main fuel for space heating	Owning appliance type
Source of income	Natural gas consumption	The use of passive solar house	
Ways of energy consumption	Electricity consumption	Main fuel for water heating	
Coal consumption	Main fuel for cooking	Owning air-conditioning	

57.3 Survey Results

57.3.1 Energy Consumption

Energy consumption level and its proportion in the three regions were shown in Table 57.2. The results indicate that in rural areas, energy consumption level is quite low; meanwhile, the non-commercial energy consumption accounts for a large percent, and this even occupies more than 90 % in Pu'er.

57.3.2 Heating

Pu'er is located in south of China and belongs to warm region according to the classification of the architecture heat supply, and that is non-heating region. As the survey shown, in Pu'er, 85.47 % of households do not have space heating, 12.42 % of households use brazier for space heating, and 2.11 % use electricity; Jingzhou, located in the Yangtze River region, belongs to hot summer and cold winter region. From the survey, 29.46 % of households use brazier for space heating, 26.56 % use electricity, and 30.71 % use air-conditioning, 6.22 % use charcoal stoves and the rest 7.05 % do not have space heating; Xinzhou is in cold region where 70.78 % of households use charcoal stoves and kang for space heating, 21.74 % use small boiler, and the rest 7.48 % only use kang.

From the survey, we find that Xinzhou is rich in solar energy resources. In Xinzhou, winter is very cold, but no one use passive solar houses for space heating. According to the measured data about passive solar houses in rural areas of Dalian City, energy consumption in space heating was annually cut down by 50 % [4]. It shows that solar energy can be taken full advantage of in space heating in Xinzhou rural areas, and there is great potential in the popularity of passive solar houses, which is also very significant to construction energy conservation in this region.

Table 57.2 Energy consumption level and its proportion of the three regions

Single energy	Pu'er		Jingzhou		Xinzhou	
	Per capita coal equivalent kgce	Proportion (%)	Per capita coal equivalent kgce	Proportion (%)	Per capita coal equivalent kgce	Proportion (%)
Biomass fuel	336.97	94.013	124.24	43.567	149.38	18.604
Coal consumption	7.65	2.134	108.24	37.956	634.76	79.055
Electricity	12.12	3.381	14.31	5.018	9.53	1.87
Liquefied petroleum gas	1.69	0.472	38.38	13.459	9.27	1.154
Commercial energy	21.46	5.987	160.93	56.433	653.56	81.396
Total energy	358.43	–	285.17	–	802.93	–

57.3.3 Heating Water

From the survey, we get the conclusion that in households of Xinzhou, the main ways of energy consumption for heating water are coal and electricity; 75.65 % of households use coal or electricity or a combination of the two ways; in Jingzhou, 21.58 % of households use electricity, 26.14 % use solar energy, and 27.80 % use briquette; in Pu'er, 87.19 % of households use biomass fuels, electricity as well as a combination of both.

57.3.4 Cooking

In Xinzhou, 66.67 % of households use raw coal and electricity for cooking, and the rest 33.33 % use a combination of various resources (including biomass fuels, liquefied petroleum gas, electricity, original coal) for cooking; in Pu'er, 97.24 % of households only use biomass fuels and electricity for cooking; The main ways of energy consumption for cooking in Jingzhou are mainly liquefied petroleum gas, electricity, biomass fuel, and briquette of which the percentages are as follows: electricity is 23.24 %, liquefied petroleum gas 13.69 %, briquette 14.11 %, and a combination of various energy consumption is about 48.96 %.

57.3.5 Lighting

The electricity consumption for lighting accounts for about 12 % of the total electricity consumption in China. Analysts pointed out that with the development of economy and the improvement of people's living standards, China's electricity consumption for lighting will increase further. Luminous efficiency of energy-saving lamp is five times of incandescent lamp.

In the same condition, energy-saving lamp can save 80 % of the electric energy than incandescent lamp [5]. However, in Fig. 57.1, the use rate of energy-saving lamp is relatively low, and less than 50 % of households have energy-saving lamp in the three regions. Particularly, in rural areas of Pu'er, less than 5 % of households use energy-saving lamp. On the contrary, the use rate of incandescent lamp is very high: about 50 % of households in Xinzhou, about 30 % in Jingzhou, and more than 90 % in Pu'er. Obviously, in the three rural areas, the use rate of incandescent lamp is more than that of energy-saving lamp. Just as some statistical data shown, the use rate of incandescent lamp in small- and medium-sized cities is generally more than 50 %, and in rural areas, it is greater.

Through investigation, we find out that this phenomenon was mainly caused by three reasons as follows: Firstly, residents are used to incandescent lamp; secondly, the incandescent lamps in use are in good condition; thirdly, energy-saving lamp is more expensive. Actually, in January 21, 2008, Ministry of Finance,

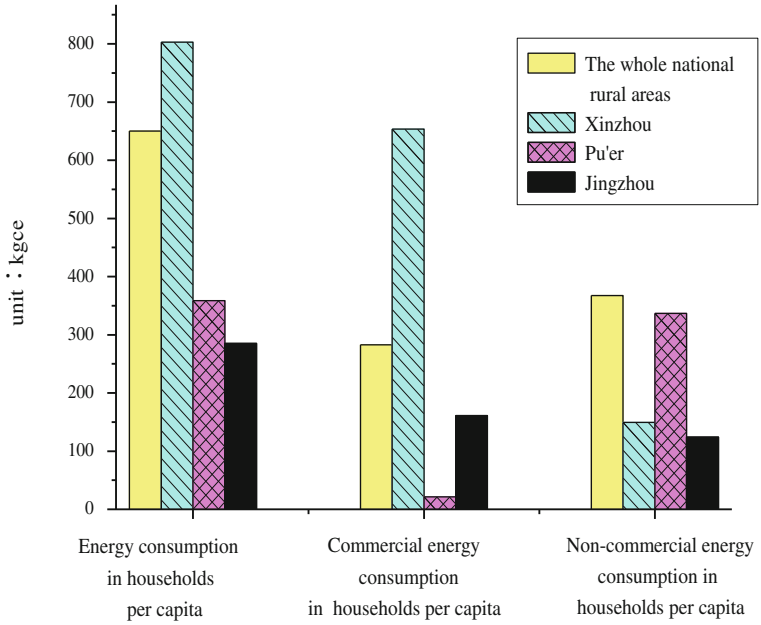

Fig. 57.1 The comparison between the surveyed regions and the whole national rural areas on energy consumption

Commission of National Development and Rehabilitation jointly issued Provisional Administrative Measures of Financial Subsidy on the Promotion of Efficient Lighting Products, saying that urban and rural residents will be given 50 % of the price as subsidy. In other words, the successful tendered enterprises will sell energy-saving lamp all on half-price in the market [5]. However, the surveyed data imply that this policy has not been introduced to the surveyed regions so far.

57.4 Discussion

Table 57.3 shows the situation about energy consumption in China's countries during 2005 and 2006, from which we can see that in rural areas of China commercial energy in households in 2006 equals to 226 million tons of coal equivalent, non-commercial energy consumption in households can be equivalent to 275 million tons of coal equivalent, and the total household energy consumption can equal to around 520 million tons of coal equivalent. With the standard of 800 millions agricultural populations, we can calculate that household energy consumption per capita is 650 kgce, commercial energy consumption in households per capita is 282.5 kgce, and non-commercial energy consumption in households per capita is 367.5 kgce. The comparison of energy consumption level between the three surveyed regions and the whole national rural areas is shown in Fig. 57.1.

Table 57.3 The situation of energy consumption in China's rural areas (unit: 10,000 tons of coal equivalent)

		2005			2006		
		Total	In households	For produce	Total	In households	For produce
Non-commercial energy	Coal	38,260	16,684	21,576	47,327	17,722	29,605
	Oil	8,041	1,220	68,521	7,895	1,535	6,360
	Electricity	9,999	3,398	6,601	9,180	3,352	5,828
	Total	56,300	21,602	34,998	64,402	22,609	41,793
Commercial energy	Firewood	13,597	10,310	3,287	13,457	9,686	3,771
	Straw	15,962	15,960	–	17,791	17,791	–
	Total	29,557	26,270	3287	31,248	27,477	3,771
Total		86,983	48,698	38285	97,545	51,981	45,564

From the figure, we can see that household energy consumption of Jingzhou and Pu'er per capita is less than the national rural average, while Xinzhou's is 1.24 times of the national rural level on average, but all are lower than the national average 1,090 kgce in 1995 and less than 50 % of the world average level 2,060 kgce [6]. In addition, non-commercial energy consumption per capital of Pu'er is close to the national rural level on average, while commercial energy consumption per capital is even low than it. Commercial energy consumption of Jingzhou is up to 56.43 % in all of the energy consumption, while of which Pu'er occupies only 5.99 %. Obviously, within short period, it is unrealistic that commercial energy meets the need of household energy consumption in some rural areas.

In Fig. 57.2, there is a certain correlation between income level per capita and commercial energy consumption. The monadic linear equations for Xinzhou,

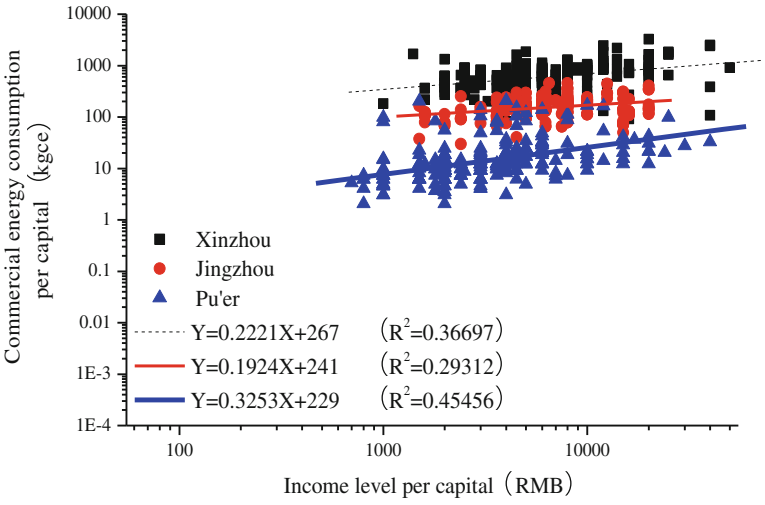

Fig. 57.2 Separate regression analysis between income per capita and commercial energy consumption per capita in the surveyed regions

Jingzhou, and Pu'er are $Y = 0.2221X + 267$, $Y = 0.1924X + 241$, and $Y = 0.3253X + 229$, respectively, and the correlation coefficients are 0.36697, 0.29312, and 0.45456, respectively.

57.5 Conclusions

1. Energy consumption in households of China's rural areas largely dependent on biomass fuel of which combustion efficiency is merely about 25 % (http://www.zgnyb.com/). It results in more serious energy loss, and high emission of carbon. However, it is unrealistic that commercial energy meets the need of energy in households in some rural areas. Therefore, the government should take some actions to change the extensive form of energy consumption gradually, such as the promotion of biogas technology and biohydrogen production technology and the improvement of utilization rate of energy in rural areas.
2. In Xinzhou, energy consumption per capita is greater than the national rural average, and energy consumption per capita in Jingzhou and Pu'er is lower than the national rural average.
3. If we do a deep research in each province, we find that there is still some correlation between income level and commercial energy consumption per capita.
4. The use rate of energy-saving lamp for lighting is also low.

References

1. Lo SM, Zhao CM, Cheng WY (2006) Perceptions of building professionals on sustainable development: a comparative study between Hong Kong and Shenyang. Energy Build 38:1327–1334
2. Yoshino H, Yoshino Y, Zhang Q, Mochida A, Li N, Li Z, Miyasaka H (2006) Indoor thermal environment and energy saving for urban residential buildings in China. Energy Build 38:1308–1319
3. Zhang L (2008) the status, problems and solutions in the promotion of energy-saving technologies of construction in rural areas. Resour Living Environ 4:59–62
4. Chen B (2008) Passive solar heating technology. Building energy-saving Research Center of Tsinghua University, Research report about annual development of China's energy conservation, Beijing, pp 170—173
5. Fang M (2008) "Incandescent Time" will end Construction Science and Technology (16):17–21
6. Wu Y-h, Cao B et al (2008) Studies on current rural energy resources utilization and bioenergy development in Northwest Yunnan—the case study on Lanping and Shangri-La Counties. China J Nat Resour 23(5):781–789

Chapter 58
Research on Improving the Engineering Applicability of On–Off Time–Area Method

Shuyi Qi, Hua Yang, Guoqiang Xia, Chunhua Sun and Dan Chen

Abstract In order to improve the engineering applicability of on–off time–area method, this chapter first carried on tracing collection of existed building thermal measurement transformation users' data of heating performance in Shijiazhuang and other three cities in the heating season 2010–2011. Then it brings up the empirical formula of opening ratio compensation factor. Combined with typical users' heating data of practical engineering, the heat of all users has been calculated and shared again. Result shows that heat-sharing can reflect users' real heat demand more accurately. To some extent, empirical formula of opening ratio compensation factor improved the accuracy and fairness of measurement. At the same time, it provides a theoretical basis for the applicability of on–off time–area method.

Keywords On–off time–area method · Opening time ratio · Compensation factor technology of apportionment · Heat metering

58.1 Introduction

"Technical Specification For Heat Metering" pointed out that our country can adopt four kinds of heat metering method now: radiator heat allocation meter method, flow temperature method, on–off time–area method, and household heat meter method. To some extent, all of these four methods can measure user's heat consumption correctly. However, in view of our traditional apartment, poor water quality and other characteristics, these measurement methods have limitations more or less. If we can do some proper modification and correction of these methods in practical application, accuracy and fairness of metering will be further improved.

S. Qi · H. Yang (✉) · G. Xia · C. Sun · D. Chen
School of Energy and Environmental Engineering, Hebei University of Technology, Tianjin, China
e-mail: y8h8@163.com

A. Li et al. (eds.), *Proceedings of the 8th International Symposium on Heating, Ventilation and Air Conditioning*, Lecture Notes in Electrical Engineering 263,
DOI: 10.1007/978-3-642-39578-9_58,

Early in 2002, Hebei University of Technology had presented a new heat metering heating system in accordance with on–off time–area method: Q Type Heating Control System [1, 2]. In view of the system, it was studied in different angles by a number of researchers. Theoretical analysis and experimental study about heat-sharing technology of on–off time–area method which is based on the pattern of on–off heating are mentioned in the literature [3]. Meanwhile, the literature proved that the heat-sharing method is available on technology. In the literature [4–6], test about opening ratio in different locations of room based on experiment has been checked out. By carrying out some correction to opening ratio, the fairness of on–off time–area method can be improved to some degree.

In 2010–2011 heating season, on–off time–area method began to spread in many cities of Hebei province, like Shijiazhuang, Xingtai, Tangshan, Hengshui, and so on. A large number of engineering data and experimental data show that the method can fairly and reasonably reflect the condition of most heat application in some instances. However, it is unavailable to consumers whose virtual operation is heavily deviated from design. Therefore, this article re-submits an empirical formula of opening ratio compensation factor, and it is verified with the actual running data.

58.2 Applicability of On–Off Time–Area Method

The on–off time–area method is a new heat-sharing technology which is based on the *Q* type heating system. Its working principle: according to various users' corrected opening ratio and heat area, the building's total heat meter will carry on heat-sharing by hour. Then it will send the data to each user's heat meter to accumulate and display.

However, the method of current system is available mainly in response to the users whose condition is not far deviated from design. That is to say that in the situations of radiator area matches the designed heating load, the user does not change the radiator and no hydraulic disorder and conduit jam occur; on–off time–area method can fairly reflect the user's actual consumption. The actual running data yet show that there are always some users working relatively far from the design conditions; therefore, there will be deviation of fairness about heat-sharing.

58.3 Application Research About On–Off Time–Area Method on Improving Engineering Applicability

In 2010, Shijiazhuang, Xingtai, Hengshui, Tangshan, Langfang, and other major cities of Hebei Province carried out a wide range of heat-metering reform, which was based on on–off time–area method. This chapter selects parts of communities

of some cities which have the typical significance and collects its actual heating data of the 2010–2011 heating season. At the same time, analysis has been carried out based on the running data of this heat season.

Through field surveys, users' reflection, and experiments of Mount Everest international and Ya Qingyuan District of Shijiazhuang, the following phenomena have been found, which will cause heat-sharing unfairness in actual project.

- Individual users change the type or increase the area of the radiator.
- User's radiator area in unfavorable positions does not match load requirements.
- Blockage of the pipe and radiator short circuit due to the poor quality of heating water.

58.3.1 Opening Ratio Correction

In view of users' increase radiator area, changing radiator type, pipe plug, and so on, calculating the values of compensation factor in different conditions, on this basis, taking the indoor temperature tn of users into account, and correcting and fitting opening ratio, the chapter puts forward to the opening time ratio correction coefficient calculation formula (58.1) which is available to variety of conditions.

$$\text{Compensation factor} = d \times \left(\frac{t_{\text{gi}}}{t_{\text{gz}}}\right)^{a} \times \left(\frac{t_{\text{hi}}}{t_{\text{hz}}}\right)^{b} \times e^{\left(\frac{t_{\text{ni}}}{t_{\text{npj}}}\right)^{\text{C}}} \times \left(\frac{t_{\text{ni}}}{t_{\text{npj}}}\right)^{f} \tag{58.1}$$

In the formula,

t_{gi} User's supply water temperature (°C);
t_{hi} User's return water temperature (°C);
t_{gz} Total meter's supply water temperature (°C);
t_{hz} Total meter's return water temperature (°C);
t_{ni} User's indoor temperature (°C);
t_{npj} User's average indoor temperature (°C).

Taking theoretical calculation and experimental measurement data into the formula (58.1), obtained each unknown.

Get: $a = 1.2$, $b = 0.345$, $c = 1.6$, $d = 0.366$, $f = 2.1$

Then

$$\text{compensation factor} = 0.366 \times \left(\frac{t_{\text{gi}}}{t_{\text{gz}}}\right)^{1.2} \times \left(\frac{t_{\text{hi}}}{t_{\text{hz}}}\right)^{0.345} \times e^{\left(\frac{t_{\text{ni}}}{t_{\text{npj}}}\right)^{1.6}} \times \left(\frac{t_{\text{ni}}}{t_{\text{npj}}}\right)^{2.1} \tag{58.2}$$

58.3.2 Correction Formula Validation

The author contrasted the following four heat-sharing methods: hour sharing method (apportion computing per hour), accumulated sharing method (apportion computing per heat season), opening ratio sharing method without correcting, and corrected opening ratio sharing method. Through the comparison of different algorithms of households per unit area per unit temperature heat consumption, the chapter finally gives a comparative analysis and judgment to the four sharing effects. Figure 58.1 shows that the sharing results, which use the above four methods, of each user in the same unit of one six-story residential building of Shijiazhuang.

58.3.2.1 Change the Radiator Size

From Fig. 58.1, it is obviously known the results of these three sharing methods, hour sharing method, accumulated sharing method, and opening ratio sharing method without correcting. The Figure shows users (like 302 and 502) who instead of floor radiant heating method by themselves have a lower unit area, unit temperature heat consumption than others. It apparently violates the principle of equality of the user's same retaining structure of unit area, unit temperature heat consumption values. The result shows roughly equivalent by corrected opening ratio sharing method, especially for the users, who were replaced to floor radiant heating by themselves. After correction, the values almost improved equally to the average.

58.3.2.2 Influence of Location Factor

In actual heating project, the users, who live in the top or corner, have a high opening radio due to the disadvantage in location and mismatch in radiator area, compared to the users who live in the middle of the building. Therefore, the heat-sharing is unfair. Through the theoretical derivation combined with practical engineering data, this section analyzed the impact of location on opening ratio and further verified the applicability of the correction formula.

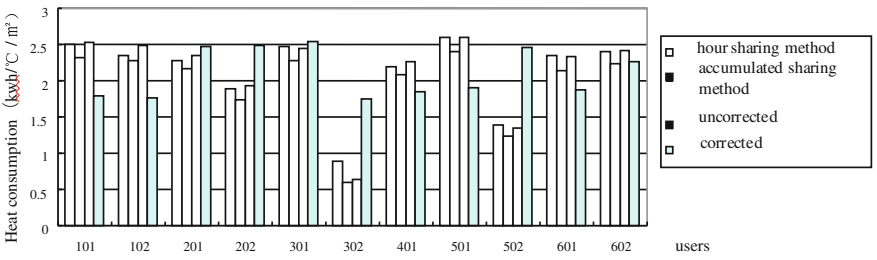

Fig. 58.1 Heat consumption of unit area and unit temperature of different sharing methods

Table 58.1 Sketch map of typical room

User 4	User 2	
	User 1	
User 3		
Unit 1	Unit 2	Unit 3

This paper chooses four typical households of one community of building No.17 in Shijiazhuang to analyze. The number 1 household (No.17-1-601) belongs to middle-level user. The number 2 household (No.17-1-401) belongs to top-level user without gable. The number 3 household (No.17-1-301) belongs to middle-level user with gable. The number 4 household (No.17-1-601) belongs to top-level with gable, Specific locations are shown in the Table 58.1.

Data of the four users, such as supply water temperature, return water temperature, indoor temperature, and according to formula (58.2), were measured and recorded to calculate the corrected opening ratio. The result is shown in Fig. 58.2.

From Fig. 58.2, it can be seen that, corrected opening ratio decreased the impact of location factor, and it is almost equal to the heat demand of the users. Therefore, it will be in a considerable extent to compensate for the impact of adverse location to opening ratio by formula (58.2) and improve the fairness of heat-sharing.

58.3.2.3 The Situation of Pipe Blockage

In field survey, the phenomenon has been found that the blockage of pipe in building No. 17, unit 3 of one community is serious, and the user of No. 201, unit 3 of this building has blockage of pipe too. For the user of No. 602, unit 3, the heat radiator was replaced with floor radiant heating privately..

Due to the pipe blockage of building No. 17, unit 3, each user's valve opening ratio is almost equal to 1, and the indoor temperature is low. There is almost no difference among these users. The heats of accumulate sharing method and

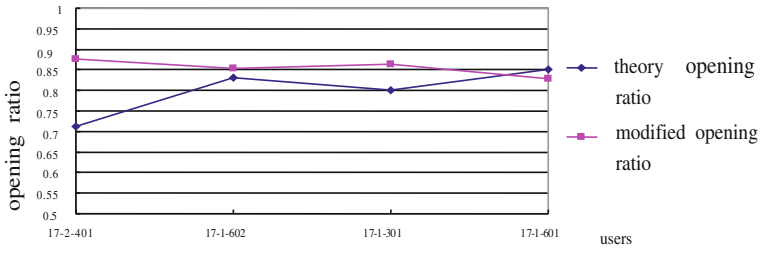

Fig. 58.2 Comparison of theory and modified opening ratio

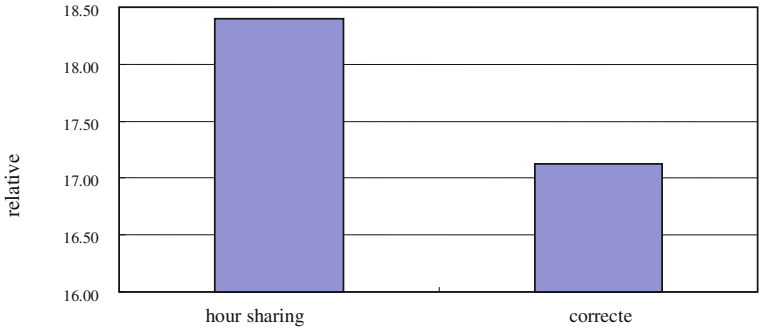

Fig. 58.3 Relative deviation with different sharing methods

opening ratio sharing method without correcting are almost same. By analyzing the relative deviation (Fig. 58.3), it can be known that the corrected opening ratio sharing method not only corrects the blockage of pipe but also the users who reform to floor radiant heating secretly. Therefore, it can decrease the unfairness of heat-sharing when the conditions were changed.

58.4 Conclusions

On–off time–area method is one of the measurements referred to in "Technical Specification For Heat Metering". It can correctly calculate the user's heat consumption to a certain extent, but there are some problems of engineering applicability. This paper has a further research in response to the above questions and draws the following conclusions:

Pointed to the phenomena of fewer users reform, the type and area of heat radiator privately and blockage of pipe and heat radiator short circuit in actual project, the method of corrected opening ratio has been brought up through theoretical derivation combined with practical engineering data and configured the following formula through fitting regression:

$$\text{Compensation factor} = 0.366 \times \left(\frac{t_{gi}}{t_{gz}}\right)^{1.2} \times \left(\frac{t_{hi}}{t_{hz}}\right)^{0.345} \times e^{\left(\frac{t_{ni}}{t_{npj}}\right)^{1.6}} \times \left(\frac{t_{ni}}{t_{npj}}\right)^{2.1} \tag{58.3}$$

By analyzing the unit area unit, temperature heat consumption through the four following methods: hour sharing method, accumulated sharing method, opening ratio sharing method without correcting, and corrected opening ratio sharing method, it was proved that the empirical formula of opening ratio compensation

factor can reflect the fairness and reasonableness on heat-sharing. It can avoid many problems of actual project and provide theoretical basis to improve the reform of household heat metering.

References

1. Qi C, Wu J, Wang X (2003) Measurement and room temperature control of integrated intelligent heat meter. China: 03242120.6, 2004. 9.29 (Date of Application:2003.3.18)
2. Qi C, Gao J, Fang L et al (2004) New intelligent heat metering control system. HVAC 34(10):103–105
3. Gao Y (2006) Numerical simulation of influence of Step Changed Heat Source on indoor environment in a heating room. Hebei University of Technology, Tianjin
4. Zhang K (2009) Improvement of heating allocation method based on on–off value regulation mode of heat supply. Hebei University of Technology, Tianjin
5. Feng D (2010) Compensation factor of Q system used for residence building. Hebei University of Technology, Tianjin
6. Yang H, Chen D, Xia G et al (2011) Theoretical research of the accumulative open time ratio base on on–off valve regulation mode of heat supply. ICEE IV:364–367

Chapter 59
Based on AHP and Fuzzy Comprehensive Evaluation of Residential Life Decision-Making Framework for Research

Wei Yuan, Jianyong Yang and Zhenying Zhu

Abstract A series of analytic hierarchy process (AHP) and the comprehensive fuzzy analysis are adopted to establish the mathematical model to analyze the formation of cell architecture design in this article. The concept of the full life cycle design methods, design principles, design purpose, design technique are explained. The general framework of the cell design is established. The cell design ideas has a certain practical significance.

Keywords Whole life cycle · Analytic hierarchy process · Fuzzy comprehensive evaluation · Architectural design

59.1 Introduction

Traditional architectural design process is often segmented considering the various stages of the construction. The design often focuses on the efficiency of the construction, the duration of the work and the cost [1]. Introduction of the concept of life cycle makes traditional architectural design extend to all aspects of the building, including plan, design, construction, management, demolition, and material recycling. The architectural design of the full life cycle of the building has a significant influence on the building. However, in recent years, there is few residential architectural design of the full life cycle. Further research is needed.

W. Yuan · J. Yang (✉) · Z. Zhu
Jiangxi University of Science and Technology, HongQi Road 86,
Ganzhou 341000 Jiangxi, China
e-mail: 258023555@qq.com

A. Li et al. (eds.), *Proceedings of the 8th International Symposium on Heating, Ventilation and Air Conditioning*, Lecture Notes in Electrical Engineering 263,
DOI: 10.1007/978-3-642-39578-9_59,

59.2 Conception

The architectural design is the core of the building. Concrete is the crystallization of human wisdom. The entire life cycle of the building design is an important stage. It relates to the full life cycle of the building. It can be divided into many steps as below: planning, design, construction, operation, maintenance, construction materials recycling. So architectural design must contains all these steps.

Analytic hierarchy process (AHP) is a combination of qualitative and quantitative analysis to determine the parameters of the weight of the analytical methods [2]. It is characterized by less information with in-depth analysis of the complex decision-making problem. Mathematical model is applied to analyze the factor and its internal relationship. So this method can provide a simple way of decision-making for the complex problem [3].

The fuzzy comprehensive evaluation method is a kind of use of the membership fuzzy math theory qualitative evaluation into quantitative evaluation of the comprehensive evaluation method. It has a clear clue to solve the fuzzy and difficult problem [4].

All phases of residential life design stage also need to take into account the full life cycle of the entire building, including building structure planning, design, construction, operation, maintenance, and construction materials recycling [5]. All aspects of the building in specific circumstances Appropriate method which meet the requirement of the entire life cycle is sought [6–8].

Including general structural design of residential life design stage, durable design life cycle, acoustic design, safety design, aesthetic design, design of the health, as well as the structure and material reuse and recycling design. According to the literature, the author summarizing come to their corresponding content such as the general structure design [9–14].

59.2.1 General Structure Design

The general structure of the design is also a core part of the basis of the architectural design, in accordance with its design content is divided into the design of building structures, fire-resistant design, and seismic design.

59.2.2 Durable Design Life Cycle

Durable design is essential to achieve the investment, service time requirements, as well as the security requirements of the building. And its contents include environment, material quality requirements, protective measures, construction measures, maintenance, and trial period.

59.2.3 Acoustic Design

Acoustic design for a building consists of planning and construction. The built environment should meet the needs of users or the national design standard generally including: building materials, design purposes, structural measures.

59.2.4 Safety Design

One of the most basic purposes of the building is to provide a safe shelter to the people to withstand natural disasters, and the people who live and work within which felt a certain security. Security design is very important, and general safety design includes structure security design, fire safety design, design of the safety and health, construction safety planning, the venue safety design, design security.

59.2.5 Aesthetic Design

With the development of modern society, people become increasingly improve. Constructions are basic unit in a city. It often reflects the characteristics and cultural connotation of a city. The aesthetic design is becoming increasingly important in the cell environment, and aesthetic design includes the exterior of the building, district planning, and landscaping.

59.2.6 Health Design

Health conditions are closely related to people's health, which often determines the district is good or bad. Of residential building, health and hygiene are a very important design content, mainly including environmental facilities, lighting ventilation, dirty clean division, and sewage measures.

59.2.7 Recycling Design

There is serious pollution problem in modern construction. Recycling economic investment in the design of the whole life cycle, is also a very important part which generally includes: reuse of the structure, reuse of materials, reuse of the district planning.

The whole life cycle design can be divided. We can draw a schematic diagram for the whole life cycle design, as shown in Fig. 59.1 (Table 59.1).

Calculated the λ_{max}

$$\lambda_{max} = \sum_{i=1}^{n} \frac{(AW)_i}{W_i} \tag{59.2.1}$$

Judgment matrix processing

(a) Consistency index (CI)

$$CI = \frac{\lambda_{max} - n}{n - 1} \tag{59.2.2}$$

The formula: n—average to determine the order of the matrix

(b) Consistency ratio (CR)

$$CR = \frac{CI}{RI} \tag{59.2.3}$$

The formula: RI—average random CI, from Table 59.2 that investigation to take.

When CR < 0.1, general that judgment matrix consistency could be accepted.

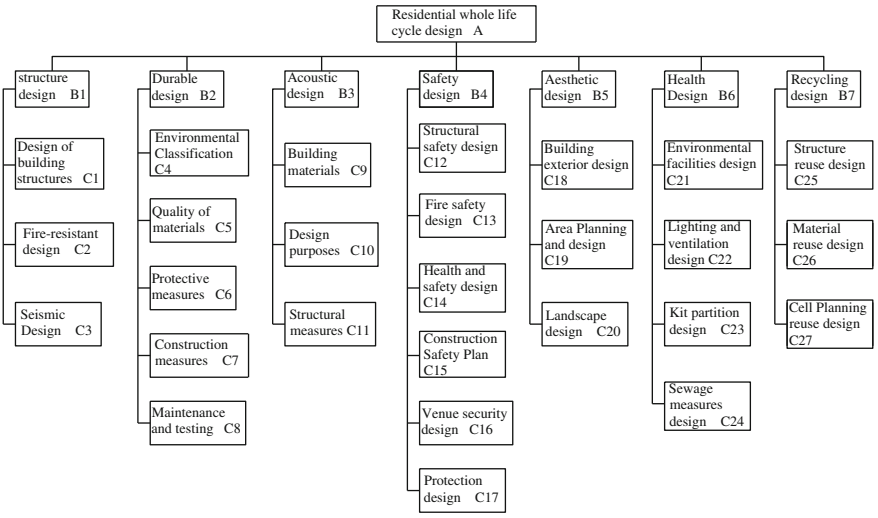

Fig. 59.1 Residential life cycle design framework

Table 59.1 1–9 comparative scale method table

Definition	Explain	R
Equally important	The two factors have the same importance	1
Slightly important	Slightly important factors than the other factor	3
Obviously important	The factors are obviously important than the other factor	5
The most important	The most important factors than the other factor	7
Absolutely important	The factors that are absolutely important than the other factor	9
The 2, 4, 6, 8, said the intermediate values of the adjacent judgments		

In order to know the cell design requirements and the comfort needs of the human body, many experts, scholars in universities and institutes have been investigated and consulted in Ganzhou, Nanchang and Ji'an. The factors used in the design decisions of cell life cycle were evaluated based on their own experience. The comparison matrix, weight vector, consistency and so on are analyzed by using the MATLAB software. (Tables 59.3, 59.4, 59.5, 59.6, 59.7, 59.8, 59.9, 59.10).

Calculated using the formula $W_i = u_i \times r_i$, the right to sub-items heavy weight accumulated to establish the right to reset W_c, reuse fuzzy comprehensive evaluation formula $E_{pw} = E_p \times W$, to calculate the weighted average evaluation value E_{pw}.

Table 59.2 Average random consistency index

n	1	2	3	4	5	6	7	8	9	10	11
RI	0	0	0.58	0.90	1.12	1.24	1.32	1.41	1.45	1.49	1.51

Table 59.3 The matrix A–B

A	B1	B2	B3	B4	B5	B6	B7	Weights	Normalized	Consistency test
B1	1	3	6	3	6	6	5	0.7711	0.3793	$\lambda_{max} = 7.5012$
B2	1/3	1	5	2	5	5	6	0.4896	0.2408	RI(7) = 1.32
B3	1/6	1/5	1	1/5	2	1/3	2	0.1048	0.0515	
B4	1/3	1/2	5	1	5	3	3	0.3376	0.1661	CR = 0.0633 < 0.1
B5	1/6	1/5	1/2	1/5	1	1/2	2	0.0895	0.0440	
B6	1/6	1/5	3	1/3	2	1	3	0.1635	0.0804	
B7	1/5	1/6	1/2	1/3	1/2	1/3	1	0.0769	0.0378	

Table 59.4 The matrix B1–C

B1	C1	C2	C3	Weights	Normalized	Consistency test
C1	1	5	3	0.9161	0.6370	$\lambda_{max} = 3.0385$
C2	1/5	1	1/3	0.1506	0.1047	RI(3) = 0.58
C3	1/3	3	1	0.3715	0.2583	CR = 0.0332 < 0.1

Table 59.5 The matrix B2–C

B2	C4	C5	C6	C7	C8	Weights	Normalized	Consistency test
C4	1	1/4	3	4	5	−0.4353	0.2514	$\lambda_{max} = 5.3131$
C5	4	1	4	5	5	−0.8604	0.4969	
C6	1/3	1/4	1	3	2	−0.2104	0.1215	RI(5) = 1.12
C7	1/4	1/5	1/3	1	1/2	−0.0964	0.0557	CR = 0.0699 < 0.1
C8	1/5	1/5	1/2	2	1	−0.1292	0.0746	

Table 59.6 The matrix B3–C

B3	C9	C10	C11	Weights	Normalized	Consistency test
C9	1	5	1/3	0.3662	0.2655	$\lambda_{max} = 3.0291$
C10	1/5	1	1/9	0.0868	0.0629	RI(3) = 0.58
C11	3	9	1	0.9265	0.6716	CR = 0.0251 < 0.1

Table 59.7 The matrix B4–C

B4	C12	C13	C14	C15	C16	C17	Weights	Normalized	Consistency test
C12	1	5	7	3	4	5	−0.8641	0.453382	$\lambda_{max} = 6.3066$
C13	1/5	1	2	1/2	3	2	−0.2575	0.135107	
C14	1/7	1/2	1	1/2	1/2	1/2	−0.111	0.05824	RI(6) = 1.24
C15	1/3	2	2	1	2	3	−0.3487	0.182958	CR = 0.0494
C16	1/4	1/3	2	1/2	1	1/2	−0.1482	0.077759	< 0.1
C17	1/5	1/2	2	1/3	2	1	−0.1764	0.092555	

Table 59.8 The matrix B5–C

B5	C18	C19	C20	Weights	Normalized	Consistency test
C18	1	5	3	−0.9281	0.6483	$\lambda_{max} = 3.0037$
C19	1/5	1	1/2	−0.1747	0.1220	RI(3) = 0.58
C20	1/3	2	1	−0.3288	0.2297	CR = 0.0032 < 0.1

Table 59.9 The matrix B6–C

B6	C21	C22	C23	C24	Weights	Normalized	Consistency test
C21	1	6	4	3	0.8770	0.5417	$\lambda_{max} = 4.1389$
C22	1/6	1	1/4	1/5	0.0920	0.0568	
C23	1/4	4	1	1/2	0.2507	0.1548	RI(4) = 0.90
C24	1/3	5	2	1	0.3994	0.2467	CR = 0.0514 < 0.1

Table 59.10 The matrix B7–C

B7	C25	C26	C27	Weights	Normalized	Consistency test
C25	1	5	3	−0.9281	0.6483	$\lambda_{max} = 3.0037$
C26	1/5	1	1/2	−0.1747	0.1220	RI(3) = 0.58
C27	1/3	2	1	−0.3288	0.2297	CR = 0.0032 < 0.1

59.3 The Example Analysis

There is a residential project in Nanchang, with an total area of 125,491 m^2. And there is underground garage with two storeys. Rooms on the ground floor along the street are used for the commercial use.

Expert evaluation method is used to evaluate the entire life cycle design individually in the programs with scoring 0–10 points. 10 point is the highest, and 0 is the lowest. The statistics results are given in Tables 59.11, 59.12.

According to the fuzzy comprehensive evaluation method, the two programs were evaluated.

Its sub-items corresponding weight relative to the overall evaluation factors set could be calculated as follows:

$$W_C = W_{A-B} \times W_{B-C} \tag{59.3.1}$$

Therefore, we could draw the C overall evaluation factors set as shown in Table 59.13.

According to the fuzzy comprehensive evaluation formula

$$E = \sum_{t=1}^{27} (W_t \times R_t) \tag{59.3.2}$$

Therefore, we can conclude that:

$$E_1 = 0.2416 \times 7 + 0.0.397 \times 6 + \cdots + 0.0101 \times 4 = 5.7891$$
$$E_2 = 0.2416 \times 5 + 0.0.397 \times 5 + \cdots + 0.0101 \times 4 = 5.3896.$$

Table 59.11 Option one

Project	Score	Project	Score	Project	Score	Project	Score
C1	7	C8	7	C15	5	C22	4
C2	6	C9	8	C16	6	C23	3
C3	4	C10	6	C17	5	C24	3
C4	4	C11	6	C18	6	C25	4
C5	7	C12	6	C19	5	C26	3
C6	6	C13	5	C20	6	C27	4
C7	3	C14	3	C21	4		

Table 59.12 Option two

Project	Score	Project	Score	Project	Score	Project	Score
C1	5	C8	6	C15	7	C22	6
C2	5	C9	5	C16	7	C23	7
C3	6	C10	6	C17	5	C24	5
C4	4	C11	4	C18	3	C25	5
C5	5	C12	7	C19	8	C26	7
C6	4	C13	4	C20	3	C27	4
C7	5	C14	5	C21	6		

Table 59.13 The overall evaluation of comprehensive factors

Project	Weight coefficient	Project	Weight coefficient	Project	Weight coefficient	Project	Weight coefficient
C1	0.2416	C8	0.0180	C15	0.0304	C22	0.0304
C2	0.0397	C9	0.0137	C16	0.0129	C23	0.0129
C3	0.0980	C10	0.0032	C17	0.0154	C24	0.0154
C4	0.0605	C11	0.0346	C18	0.0285	C25	0.0285
C5	0.1197	C12	0.0753	C19	0.0054	C26	0.0054
C6	0.0293	C13	0.0224	C20	0.0101	C27	0.0101
C7	0.0134	C14	0.0097	C21	0.0436		

Accordingly, $E_1 = 5.7891 > E_2 = 5.3896$, the first program is better than the second program, after evaluation confirmed by experts and the economic effect, selected Option 1 for the district program implementation.

59.4 Conclusion

(a) The AHP is introduced to the residential life design decision-making stage. It helps to solve comprehensive problems in decision-making stage. Various factors are considered to provide a theoretical basis for the decision makers in the decision-making stage.
(b) The various factors of the decision-making phase comparison matrix parameters selected by expert evaluation method, and there, the method is a certain degree of vagueness, but its accuracy will continue to improve with the increase in the number of evaluation experts.
(c) AHP and fuzzy comprehensive evaluation of the cell whole life can be programed. The evaluators can use the program to get the results. It is simple and easy to operate.
(d) The AHP and fuzzy analysis method of the residential whole life cycle design increases the reliability and accuracy of the evaluation results and solves complex issues in new ways.

References

1. Chen A, Ma J (2005) Whole life design methods and keys issues of bridges. Symposium of youth forum for China highway science and technology. Beijing: China Communications Press, 168–184.
2. Saaty TL, Vargas LG (2001) Models, methods, concepts and applications of the analytic hierarchy process. Kluwer Academic
3. Golden BL, Wasil EA, Harker PT (1989) The analytic hierarchy process applications and studies, Springer, Berlin
4. Ho HP, Chang CT (2013) On the location selection problem using analytic hierarchy process and multi-choice goal programming. Int J Syst Sci Jan:94–108
5. Bratianu C, Orzea I (2012) Knowledge strategies analysis by using the analytic hierarchy process. IUP J Knowl Manage 10(2):p7–21
6. Xu S (1988) The principles of the analytic hierarchy process. Tianjin University Press
7. Jin L, Wei Y, Ding J (2004) Fuzzy comprehensive evaluation model based on improved analytic hierarchy process. J Hydraul Eng
8. Luo Z, Yang S (2004) Comparative study on several scales in AHP. Syst Eng Theory Pract 24(9)
9. Gao Y (2008) Study of sustainable housing by theory of the whole life cycle. Arch J
10. Zhen L, Tai H (2003) Energy efficient building life-cycle-oriented design method. Arch J (2003.03)
11. Ma J, Chen A, He J (2007) The bridge whole life overall design framework for research. J Tongji Univ (Nat Sci) (2007.8)
12. Shao X, Peng J, Yan B (2006) The bridge life design framework. HighWay (2006.1)
13. Ministry of Construction of the People's Republic of China (1994) Urban Residential Area Planning and Design. GB50180—93 (1994.2)
14. Liu W, Zhang W, Li J (2000) Using the analytic hierarchy—fuzzy evaluation of the safety evaluation of water inrush. J China Coal Soc (2000.6)

Chapter 60
Survey on HVAC Energy Consumption Status and Indoor Environment Quality Test for Hotel Buildings in Guangzhou

Yonghua Zhang, Jiankun Yang and Xiangyang Jiang

Abstract This paper investigates and analyzes energy consumption of thirteen hotel buildings in Guangzhou and tests the indoor temperature, relative humidity, internal illuminance, and carbon dioxide density. Be difference from other public buildings, hotel buildings in Guangzhou have both air-conditioning system in summer and heating system in winter. Hot water system is running continuously all year round. Through survey, that hotel building's cooling and heating sources scheme consist of water chillers + air-source heat pumps, water chillers + oil-fired (gas-fired) boilers, water chillers + oil-fired (gas-fired) boilers + air-source heat pumps, and water chillers +direct-fired LiBr absorption refrigeration machine + water source heat pump. By statistics, the power consumption per unit area is from 87.27 to 229.80 kWh/(m^2.a), and the HVAC power consumption per unit area is from 21.25 to 119.84 kWh/(m^2.a). HVAC system consumes about from 16.0 to 71.6 % power. A comprehensive energy consumption of the 13 hotel buildings in Guangzhou is obtained by converting consumption of oil, gas and power to coal equivalent. The comprehensive energy consumption for unit area is from 19.74 to 65.67 kgce/(m^2.a), and the HVAC energy consumption per unit area is from 7.58 to 47.27 kgce/(m^2.a). HVAC system consumes about from 38.1 to 84.4 % comprehensive energy. In the end, analyzes the causes for energy consumption difference. Puts forward some problems existed in HVAC system and indoor environment quality and some approaches for improving energy utilization.

Keywords Hotel buildings · HVAC energy consumption · Comprehensive energy consumption · Indoor environment quality

Y. Zhang (✉) · J. Yang · X. Jiang
Guangzhou Institute of Building Science CO., LTD, Guangzhou, China
e-mail: zhangyonghua525@163.com

J. Yang
e-mail: yangjiankun2000@tom.com

X. Jiang
e-mail: jxy_gibs@foxmail.com

A. Li et al. (eds.), *Proceedings of the 8th International Symposium on Heating, Ventilation and Air Conditioning*, Lecture Notes in Electrical Engineering 263,
DOI: 10.1007/978-3-642-39578-9_60,

60.1 Introduction

Energy resources and environment are the two difficult problems facing the world today. The energy is beneficial to the people's livelihood, the sustainable development of economy and society, and the national security, which are the basis of human survival and the lifeblood of industrial production. As sustained growth of energy supply which provides an important support for economic and social development, at the same time, resource constraint and the pressure of environmental protection have become an important factor restricting the sustainable and healthy development of China's economy and society. In the recent ten years, the total energy production and consumption grew continually because of the development of economic and the progress of society. At present, China's energy consumption is still dominated by coal. Due to the limited reserves and the destructive effect to the environment, it led to the double pressure of energy supply and environmental protection. The consumption of building energy plays a decisive role in the total social energy consumption; the ratio is generally 30–40 % in the developed countries. Statistical data show that, in 2009, the country's total energy consumption is 306,647 tce and the building energy consumption is 78,523 tce, which accounts for 25.6 % of the total energy consumption [1].

Guangzhou is located in the Zhujiang Delta and has a high level of urbanization and a lot of restaurant buildings. In the 1980s, the first batch of five-star hotel appeared in Guangzhou, such as White Swan Hotel, Garden Hotel, and China World Hotel. With the further development of the economy of Guangzhou city, the hotel building in Guangzhou city is also showing unprecedented development, especially in the 2010 Asian Games. Facing the emphasis on the improvement of people's living standards and energy saving, building energy costs as the important part of the cost of hotels and restaurants, has accounted for about 10 % of the turnover of the hotels, and the operators pay more and more attention on it. White Swan Hotel and Guangdong Guest Hotel are conducting a comprehensive energy-saving reconstruction. HVAC system and hot water system is the key of building energy saving for hotels. Through the investigation and survey for energy characteristics, energy consumption situation (especially HVAC energy consumption) and the indoor environment of 13 hotels in Guangzhou city provide basic data and technical support for solving the problems of large consumption in air-conditioning energy, low efficiency in the operation of air-conditioning system, and the poor quality of the indoor environment.

60.2 The General Situation for the Hotel Buildings

There are 9 high-rise buildings and 4 super high-rise buildings in the researched 13 buildings, the construction time is between 1952 and 2011, the structure is mainly in reinforced concrete structure, and the building area is in between 11,400 and

14,700 square meters. There are four in nine buildings have 1–4 layer of basement, and 3 buildings have not set the basement, they are mainly distributed in Yuexiu district (at most 8), Tianhe district, Haizhuqu district, and Liwan district. There are 5 five-star hotels account for 38.5 %, 5 four-star hotels account for 38.5 %, 2 three-star hotels account for 15.4 %, and 1 hotel has no star accounts for 7.7 %. The investigation includes the basic information (building area, building layers, star status, and construction time, whether there is a subentry metering), energy consumption, and the indoor environmental conditions (Table 60.1).

60.3 Analysis of the Hotel Buildings' Energy Consumption and Indoor Environment

60.3.1 Analysis of the Hotel Buildings' Energy Consumption

60.3.1.1 The Characteristics of the Hotel Buildings' Energy Consumption

1. Guangzhou is located in the south of the hot summer and warm winter area which needs a long time to cool in hot summer. The hotel buildings are different from the office buildings and the shopping arcades, which have a short heating period in winter, and they need to supply domestic hot water for guest rooms in all the year round. So hotel buildings in Guangzhou include cold source and heat source system.
2. Air-conditioning system contains all-air system and fan-coil plus fresh air system. Most of the guest rooms use the fan-coil plus fresh air system, part of the large conference rooms, restaurants, lobbies, and other large regions of space with full air system.
3. Air-conditioning system works throughout 24 h; the guests go out at daytime and live at night, led to the hotels' cold consumption did not differ in day and night.
4. In order to make the guests can use the hot water anytime, they need to supply domestic hot water in a whole year, so hot water circulating pump works continuously for 24 h; the DHW energy consumption in the proportion of the total energy consumption is very large.
5. The buildings provide with a steam boiler to heating in winter and supply domestic hot water, and the fuel consumption accounts for a large proportion in the total energy cost of the hotels.
6. The contribution for decreasing the annual air-conditioning energy is not obvious to improve the insulation of the building envelope in the southern region, even the building energy consumption would be increased, just like to wear a thick cotton-padded jacket in summer; people can make full use of sunshade and natural ventilation in order to reduce the energy [2].

Table 60.1 Basic information of building samples

Construction code	Cold and heat source	Age of building	Area	Star	Stores		Type
					Under	Below	
A	Water chillers + air-source heat pumps	1952	20,451	4	8	1	High-rise
B	Water chillers + air-source heat pumps	1994	11,400	4	9	1	High-rise
C	Water chillers + boilers	1968	36,475	3	26	1	High-rise
D	Water chillers + air-source heat pumps + boilers	1988	60,000	4	25	1	High-rise
E	Water chillers + boilers	1976	48,519	5	34	0	super high-rise
F	Water chillers + LiBr absorption refrigeration machine	1961	147,000	5	9	1	High-rise
G	Water chillers + LiBr absorption refrigeration machine	1991	20,000	3	14	2	High-rise
H	Water chillers +direct-fired LiBr absorption refrigeration machine + boilers + water source heat pumps	2006	122,867	5	37	2	Super high-rise
I	Water chillers + boilers	2011	77,439	5	26	4	High-rise
J	Water chillers +direct-fired LiBr absorption refrigeration machine + boilers	1972	60,647.8	4	8	0	High-rise
K	Water chillers + boilers	1982	110,000	5	28	1	Super high-rise
L	Water chillers + boilers	1999	58,000	4	35	2	Super high-rise
M	Water chillers + boilers	1984	40,000	–	18	0	High-rise

60.3.1.2 Cold Source and Heat Source

Through survey, hotel building's cooling and heating sources scheme consist of water chillers + air-source heat pumps, water chillers + oil-fired (gas-fired) boilers, water chillers + oil-fired (gas-fired) boilers + air-source heat pumps, and water chillers + direct-fired LiBr absorption refrigeration machine + water source heat pump. Cold source system is responsible for providing air-conditioning with cold quantity, and hot source system is responsible for two contents: one is the heating indoor and the other is supplying living hot water.

Due to the use of the characteristics of hotel buildings, energy structure mainly has 5 kinds: the power, flash steam, natural gas, pipeline gas, and diesel, wherein the power energy is the main energy in buildings. According to the research result, the power energy accounts for total building energy is 20.7–100 % in 13 hotels construction. The proportion can be showed in Fig. 60.1.

60.3.1.3 Analysis of the Hotel Buildings' Electricity Consumption

In this research, only A, B, H, and L, four buildings, install a separate measurement instruments for air-conditioning electricity, and the four buildings' air-conditioning electricity adopts the monthly data copy by construction managers. According to the following method to calculate the air-conditioning electricity for those in which cannot provide that: (1) The analysis reveals that the lighting, power, and other basic loads are stable throughout the year, but the air-conditioning load will vary with the seasons, (2) Setting up the minimum consumption as the basic load in transition seasons, the part higher than the lowest power consumption is the air-conditioning electricity consumption [3].

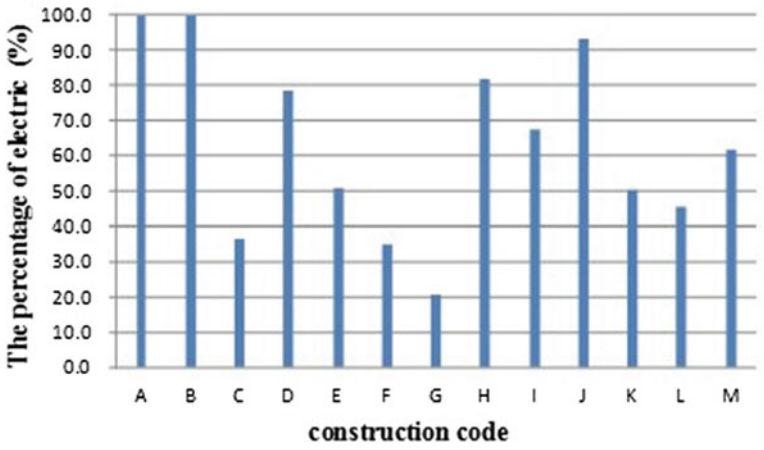

Fig. 60.1 The percentage of electric energy in buildings

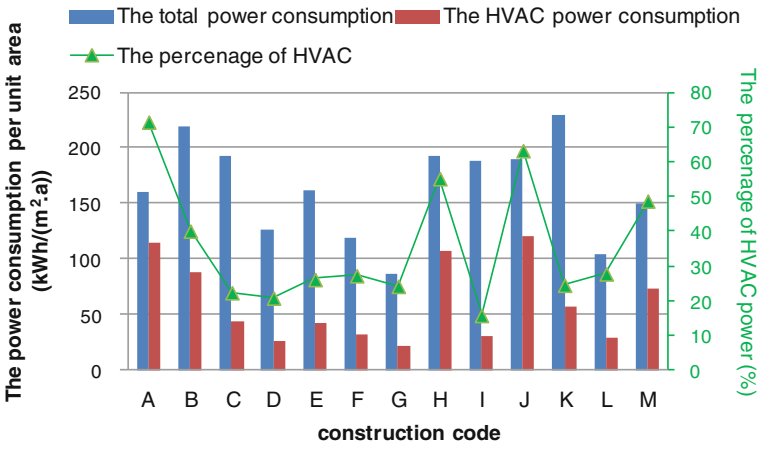

Fig. 60.2 The power consumption and percentage of HVAC power consumption

As you can see in Fig. 60.2, there is a lager difference between different buildings in unit area building total power consumption and unit area HVAC power consumption. These factors relate to hotel buildings star, architectural design, the heat and cold source form, the occupancy rate, and the level of mangers' energy saving. The total power consumption per unit area is from 87.27 to 229.80 kWh/(m^2.a), averaged 165.51 kWh/(m^2.a). And the HVAC power consumption per unit area is from 21.25 to 119.84 kWh/(m^2.a), averaged 58.31 kWh/(m^2.a). HVAC system consumes about from 16.0 to 71.6 % power, averaged 35.2 %.

60.3.1.4 Analysis of the Hotel Buildings' Comprehensive Energy Consumption

Only two buildings all use of electric energy in the researched 13 hotel buildings, and the other 11 buildings also use other types of energy in addition to electric energy, accounted for 84.6 % of the number of samples. These flash steam, fuel, and gas use in the buildings as air-conditioning heating energy and construction; this part should be considered in the energy consumption of heating air-conditioning, and thus, air-conditioning include electricity consumption, flash steam, fuel, gas, and other energy resources (Fig. 60.3).

Converting oil, gas, and power to coal equivalent obtains comprehensive energy consumption of the thirteen hotel buildings in Guangzhou. Similar to power consumption, there is a lager difference between different hotel buildings in unit area building total comprehensive energy consumption and unit area HVAC comprehensive energy consumption. By statistics, the comprehensive energy consumption for unit area is from 19.74 to 65.67 kgce/(m^2.a), averaged

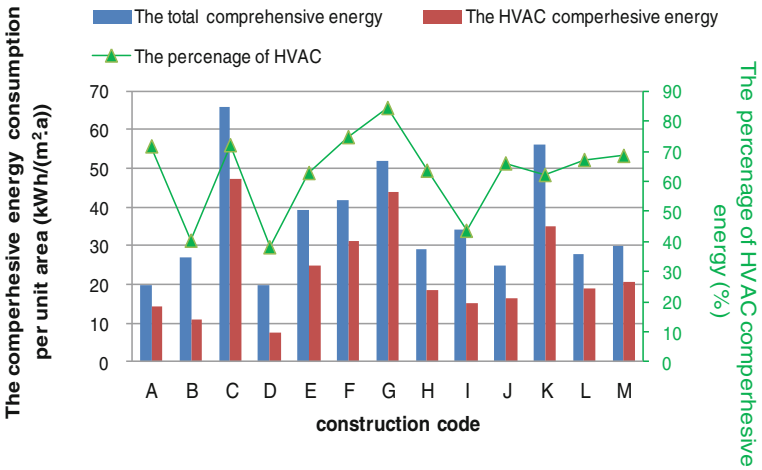

Fig. 60.3 The comprehensive energy consumption and the percentage of HVAC comprehensive energy consumption

37.05 kgce/(m^2.a), and the HVAC energy consumption per unit area is from 7.58 to 47.27 kgce/(m^2.a), averaged 23.88 kgce/(m^2.a). HVAC system consumes about from 38.1 to 84.4 % comprehensive energy, averaged 64.4 %.

Through the analysis for building power energy consumption and building comprehensive energy consumption can be seen: when only considering the electric energy consumption, HVAC electricity consumption accounts for 35.2 % with total power in the 13 hotel buildings. But in considering the other energy sources in addition to electric energy, HVAC energy consumption accounted for the proportion of total energy consumption of 64.4 %. A lot of literature data only statistic electric power for building energy statistics, ignoring the power outside the electric energy when doing the calculation of air-conditioning energy consumption, resulting the energy data are not correct. From the comprehensive energy consumption data, HVAC energy consumption accounted for the proportion of total energy consumption of 64.4 %, so energy saving of HVAC system is very potential, which is the key of building energy saving.

60.3.2 Analysis of the Testing Results for Indoor Environment

In order to know the condition of indoor environmental of the hotel buildings, nine of the buildings to be tested, and each building selects at least eight rooms for testing; test parameters include temperature, humidity, carbon dioxide concentration, and illumination. Temperature and humidity can reflect the situation of

Table 60.2 The test result of indoor environment parameters of hotel buildings in Guangzhou

Construction code	Temperature (°C)	Relative humidity (%)	Carbon dioxide density (ppm)	Illuminance (lx)
A	24.2–26.6	61.8–74.5	523–593	73.7–405.9
B	20.2–24.8	45.3–62.4	460–661	22.8–493.7
C	22.0–26.0	60.0–70.0	385–538	18.9–30.3
F	23.4–26.4	62.5–74.7	547–675	81.0–164.4
G	24.2–27.2	64.3–75.3	615–716	39.4–199.2
H	22.1–24.7	52.3–69.1	403–479	51.0–132.1
I	21.7–26.3	48.3–54.2	514–790	77.6–131.8
J	20.4–24.6	23.4–47.7	669–956	117.0–475.0
M	22.5–26.5	62.4–84.9	467–606	28.3–977.3

indoor thermal environment directly; determining the indoor temperature and humidity is in accordance with the energy-saving requirements. Carbon dioxide concentration testing can reflect the quantity of fresh air to meet the indoor sanitation requirements. Luminance is reflected in architectural lighting level and the contribution degree of indoor air-conditioning cooling load. The test adopts these following instruments: digital temperature and humidity recorder (HC-2), carbon dioxide tester (SWEMA Airtest4), and illuminometer (T-10). The result of test is shown in Table 60.2.

60.3.2.1 Temperature and Relative Humidity

Indoor temperature in summer is 20.2°–27.2° for the tested building. The test results show that one more area's indoor temperature is less than 26° in summer which is not met regulations that public building indoor temperature is not lower than 26° from the state council, and all the test area's indoor temperature is less than 26° in three of these buildings. Hotel buildings often reduce the indoor temperature at the expense of energy saving to meet their guests who come from home and abroad and are very high requirements of the indoor temperature.

The test find out that the average indoor relative humidity is from 23.4 to 84.9 %, which basically meet the requirements of indoor humidity from "Indoor air quality standard" GB/T 18883-2002, but humidity is too low for a small amount of room. Lower indoor humidity will cause that air-conditioning consumes more dehumidification load.

60.3.2.2 Carbon Dioxide Density

From the test result of the carbon dioxide concentration of, the control to fresh air volume is reasonable in these hotel buildings, which have not found the phenomenon of carbon dioxide concentrations exceed the standard. In the research

found that building fresh air volume in Guangzhou city is basically rely on building managers to adjust air valve manually to open or controlled by the automatic control system of building equipment, which is mainly based on human judgment whether is open or not. Hotel buildings are suggested to install CO_2 concentration monitoring system to control the quantity of the fresh air by monitoring the CO_2 level.

60.3.2.3 Luminance

Luminance is 18.9 lx–493.7 lx. It is common appeared in guest room illumination, which is lower than the standard in "architectural lighting design" GB 50034-2004. At the same time, the survey found that room lighting power density mounting is low, the cooling load is small in hotel building rooms caused by lighting fever.

60.4 Conclusions

The main energies of hotel buildings in Guangzhou are electric energy, flash steam, gas and fuel oil, etc. Electric energy is the most primary energy form of hotel buildings which accounted for 20.7–100 % in building total energy consumption. The most common cold and heat source method is water chillers + boilers.

For the hotels in Guangzhou, the mean power consumption per unit area is 165.51 kWh/(m^2.a), and their HVAC system consumes about 35.2 % power. The mean comprehensive energy consumption per unit area is 37.05 kgce/(m^2.a), and their HVAC system consumes about 64.4 % comprehensive energy consumption. Thus, the HVAC system for hotel buildings is the most primary energy consumption system.

The situation for indoor environment: indoor temperature is generally lower than the requirement of public building energy efficiency which requires 26 °C; relative humidity and carbon dioxide concentration can meet the "indoor air quality standards" GB/T 18883-2002; indoor illumination is generally lower than the standard involved in "architectural lighting design "GB 50034-2004.

Acknowledgments This work is supported by the science and technology plan projects in Guangdong province of China (2012A010800025, 2012A010800046)

References

1. Yonhua Z (2012) Preparation of the PCM Roof brick and Study on Its Thermal Insulation Properties. Master thesis, University of Guangzhou, Guangdong, China
2. Guolun Q, Haiyang T, Wei H, Shaoling CH (2012) Research and application integration of applicable technology for energy efficiency reformation of air-conditioning system in star hotels in south China-Energy efficiency reformation scheme of air conditioning and ventilation system in Guangzhou White Swan Hotel. HV&AC 46(1):1–6
3. Yan W, An'gui L, Shuhai S, Zhichao W (2009) Survey on energy consumption status and field test of temperature and humidity for public buildings in Xi'an in summer. HV&AC 39(7):76–80

Chapter 61
The Influence of Human's Behavior on Energy-Efficient Technologies Promotion in China

Cui Li, Zhengrong Li, Wangxiang Yao and Yuyang Wang

Abstract High-Energy-efficient products and technologies are important to promote energy saving and CO_2 emission reduction. However, it is argued that the popular promotion of these technologies is affected by the behavior of human beings. Based on Behavior Model theory, six questions on energy-efficient technologies are designed to study the influence of human's behavior on energy-efficient products accepted and policies implemented. A large number of questionnaire surveys were done, the internal and external factors of residents' behavior are analyzed. The key factors of residents' approval are found in SPSS software. Comparing to the external factors, the statistical results show that the internal factors of residents' behavior play an important role for the energy-efficient technologies promotion, especially for the different age, gender, degree groups. So according to the researches, some suggestions are given to encourage people to accept energy-efficient products and related policies.

Keywords Behavior · Questionnaires survey · Energy efficiency · Energy-efficient technology · Energy-efficient policy

61.1 Introduction

Energy-saving and emission reduction have becoming a hot issue in today's world, which are closely bound up with the every citizen's life. With the improvement in residents' living standards and the rapid urbanization in the country, people's energy consumption in China is increasing now. Data from the statistical yearbook of 2012 have shown that energy consumption for living in 2010 accounted for

C. Li · Z. Li (✉) · W. Yao · Y. Wang
College of Mechanical and Energy Engineering, Tongji University,
Shanghai 20092, China
e-mail: lizhengrong@tongji.edu.cn

A. Li et al. (eds.), *Proceedings of the 8th International Symposium on Heating, Ventilation and Air Conditioning*, Lecture Notes in Electrical Engineering 263,
DOI: 10.1007/978-3-642-39578-9_61,

10.6 % of total energy consumption [1]. Due to the higher energy consumption and the larger energy-saving potential in daily activities, the man-made guiding and scientific guidance of energy usage have given the energy-saving potential of behaviour based on the statistical work, and it is about 15–20 % [2]; there are 107 million ton raw coal saving and 200 million ton CO_2 emission reduction at the same time; the benefits of both economy and environments are significant [3]. So it is urgent that the energy use behaviour of residents needs to be improved immediately.

In daily life, such as household electrical appliances purchased and used, energy usage habits will affect household energy consumption. The understanding and participation in energy-efficient policies will directly affect their behaviour and then affect the domestic energy consumption costs. The impact of users' behaviour on the promotion of energy-saving technologies is researched here. Six questions on energy-efficient technologies are designed to study the influence factors of residents' behaviour. The choices of the different groups are shown, and the supports for different energy-efficient technologies are analyzed. Then, the regularity of residents' behaviour effecting on implementation of energy-saving measure is predicted using SPSS software. Some suggestions on how to encourage people to accept energy-efficient products are given out.

61.2 Method and Researches

Behavioural science and behavioural psychology are introduced to study energy use behaviour, and psychology and motivation of individual activity are often discussed by questionnaire survey.

61.2.1 Behavior Model Theory

Human behaviour is the comprehensive results of knowledge, attitudes, needs, incentives, and others. The behaviour model theory describes that the behaviour of people depends on both the personal needs and the environmental factors [4], that is $B = f(P, E)$. When the rules of human behaviour are predicted, both factors should be considered simultaneously, not only individual's own situations deeply understood, but also the individual's specific environment wholly analyzed. So the factors of residents' behaviour which impact the promotion of energy-efficient technology are summarized as internal (it is mainly about P) and external factors (it is about E). Here, the internal factors mainly refer to people's inherent factors, such as age, education level, gender, income, and some other factors such as psychology, knowledge, and attitudes are included. The external factors are mainly about the ambit environments, like cultural factors, policies.

61.2.2 The Features of Behavioral Energy-Saving

Both advanced technologies utilized and energy use behaviour changed measures can realize energy efficiency in buildings. Behaviour energy-saving is a simple and easy way, and it does not require any capital investment and just need to change energy usage in daily life, and energy-savings are remarkable. Meanwhile, technical energy conservation usually requires additional investment, and the energy-saving effects are not effective immediately. The characteristics of behaviour energy-saving have attracted many scholars' attention in domestic and abroad. The researches of behaviour energy-saving started early in European countries, some specialized research projects have been set up yet, and there are many researches on the impact factors of household energy usage, energy-saving achieved by changing users' behaviour [5]. The research results have shown that information feedback of household energy consumption bills can contribute to more behaviour energy-savings [6]. Domestic energy usage purposes and relevant information intervened can reduce household energy consumption. [7]. Household energy consumption bills and demand side management also can affect energy use behaviour [8]. In the meantime, the researches of behaviour energy-saving in China are comparably scarce, and many of the researches are merely descriptive study [9]. Some researchers are mainly on phenomena of household energy usage survey [10]. Others are mainly on the choice characteristics of household energy usage [11]. All these studies are comparably unitary. Therefore, more studies are needed to explore people' behaviour on energy conservation.

61.3 Overview on the Investigation Background

In order to formulate energy-efficient products market, "Measures for the Administration of Energy Efficiency Labelling" was implemented by Chinese government and the first batch of products like refrigerators and air conditioners are used in 2005. The labelling program arms at informing energy efficiency to the end-users and to encourage them to select energy-efficient product. For these, a new policy on exchanging old domestic appliances was implemented in some regions of China in 2009. Residents who changed their old appliances were principally given a subsidy for 10 % of the new appliances' price, and five categories of products, such as TVs, refrigerators, washing machines, air conditioners, computers, are included.

At the same time, some energy efficiency trainings are held at some small and middle schools of Shanghai, and the exchange program is also implemented in Shanghai as the first batch. However, what are the results of energy-efficient products and related policies implemented? In order to found the answers, a large number of questionnaires are surveyed between teachers coming from small and middle schools and civil servants from the government in Shanghai. The survey

Table 61.1 The basic data from the surveyed persons

Variable	Levels	Number	Percentage
Income	Less than 2,000 RMB	12	4
	2,000–5,000 RMB	73	21
	5,000–10,000 RMB	176	52
	More than 10,000 RMB	76	23
Gender	Male	157	47
	Female	180	53
Age	Less than 30 years old	103	31
	30–50 years old	207	61
	More than 50 years old	27	8
Degree	Junior college	131	39
	Bachelor's degree	194	57
	Master's degree	12	4

started at the end of November, 2009, the total number of samples is 400, and the available number is 349.90 % of them own their houses independently, 61 % have bachelor or higher degree, 73 % whose household income is more than five thousand, and the basic data for the surveyed persons are shown in Table 61.1.

61.4 Results and Analysis

Six questions on energy-efficient technologies are designed to study the awareness of energy-efficient products and the participation of energy-saving policy. One question is about the awareness of energy efficiency, and the question aims at researching the people's recognition and response toward energy efficiency. Three questions regard policies which have been implemented in Shanghai now, such as energy-efficient labels of electrical appliances and the policy of electric appliance exchange. The other two questions are about the choices of energy-efficient measure and the support of building retrofitting. The questions and results of the questionnaire surveys are shown in Table 61.2, and then, the factors which influence human's behaviour are analysed in terms of *P* and *E*. The key factors will be compared with each other, and the implementation regularity of energy-efficient measures with behaviour influence is predicted using SPSS software. According to software' requirement, the parameters like residents' age, gender, degree, and household income are defined as independent variables and the awareness of energy efficiency, measure choice, energy efficiency labels, and appliance exchange programs are defined as dependent variables.

Table 61.2 Questions and results of questionnaire survey

Questions	Answers			
	A	B	C	D
Awareness of energy efficiency (Q_{I})	Know nothing 13 %	Know a little 47 %	Never concerned 2 %	More attention 38 %
The reasons for energy efficiency's awareness ($Q_{\mathrm{I}'}$)	Household energy bill 32 %	Colleague's intercommunion 11 %	Office mandatory requirements 17 %	Media/ Newspaper reports 40 %
Measure choice of energy-saving (Q_{II})	Behavioural energy-saving 34 %	Technical energy-saving 54 %	Both of measures 12 %	—
The support of building retrofitting (Q_{III})	Compulsive and agree 43 %	Don't know and not agree 14 %	Know and agree 43 %	—
The concerned of labelling program (Q_{IV})	Never concerned 16 %	Little concerned 31 %	Bought label appliance 44 %	Will buy 9 %
The understanding of labelling program (Q_{V})	Not know 34 %	Kwon related with energy efficiency 57 %	Know every rank index 9 %	—
Concerned of exchange program (Q_{VI})	Never heard 2 %	Have exchanged 50 %	Will exchange 15 %	Won't exchange 33 %

61.4.1 The Results for the Same E *(External Factors)*

61.4.1.1 The Different Choices for the Same Level of Energy Efficiency's Awareness

The effect of energy-saving awareness on approval of energy-efficient technologies and policy is researched. The results of Q_{II} and Q_{IV} for the same level of energy efficiency's awareness are analysed, and four types of measure choice results got under different levels of awareness are shown in Fig. 61.1. The results of labelling program concerned are shown in Fig. 61.2.

The choices for behavioural energy-saving are from 31 to 35 % and the technical is from 53 to 57 %, but under every level of awareness, statistical results show that they are very different for measure choice, except for the level of Never Concerned. The reason for the Never Concerned group in Fig. 61.1 is mainly about the surveyed people's energy-efficient knowledge.

On the same level of Q_{I} conditions, the results for concerned labelling program are also very different for every level. The more they paid attention to energy efficiency, the more they will buy the labelled appliances in the future. The less they paid attention to energy efficiency, the less they concerned about labelling

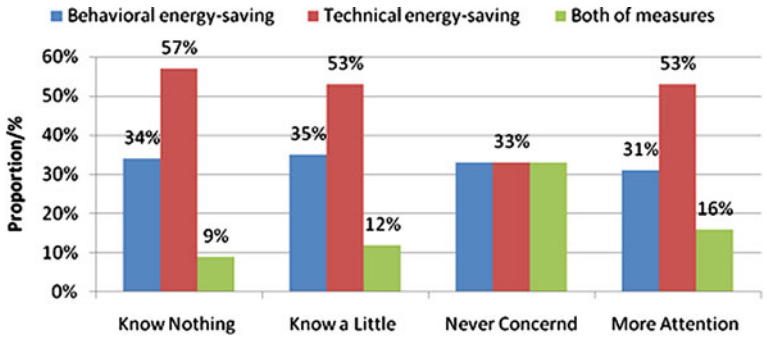

Fig. 61.1 The measure choice of energy saving under the same level of energy efficiency' awareness

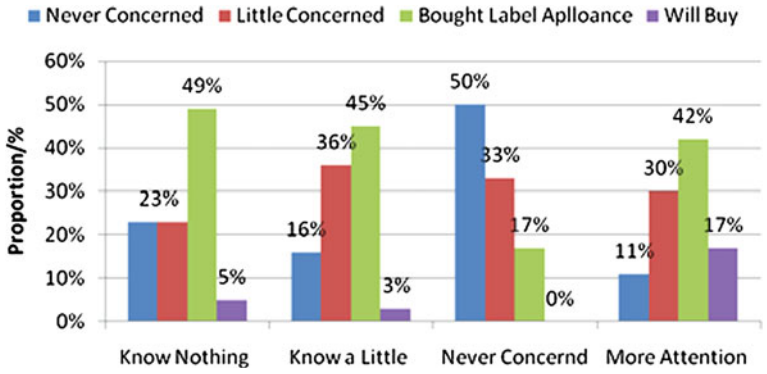

Fig. 61.2 The concerned of labeling program under the same level of energy efficiency' awareness

program. So we can know that awareness of energy efficiency has an effect on energy efficiency labelling program.

61.4.1.2 The Different Choices for the Same Level of Energy-Efficient Technology

With the same external environment background, the effects of Q_{II} on Q_{III} and Q_{IV} on Q_V are analysed. The statistical results are indicated in Figs. 61.3 and 61.4, and they are very different for the support of building retrofitting under every energy-saving measure group, especially for both measure groups, the choice is 82 %, and it is about 30 percent than the other two groups. The stronger awareness of energy efficiency leads to the choices of building retrofitting similar to behaviour and technology groups.

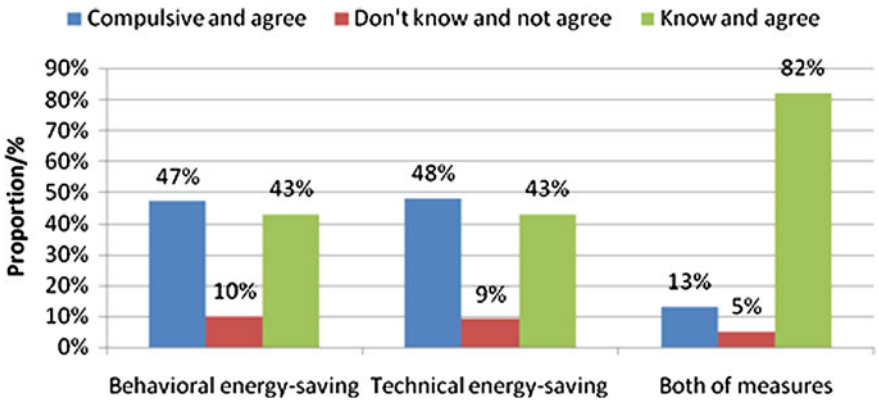

Fig. 61.3 Building retrofitting's support under the same energy-saving measure choice

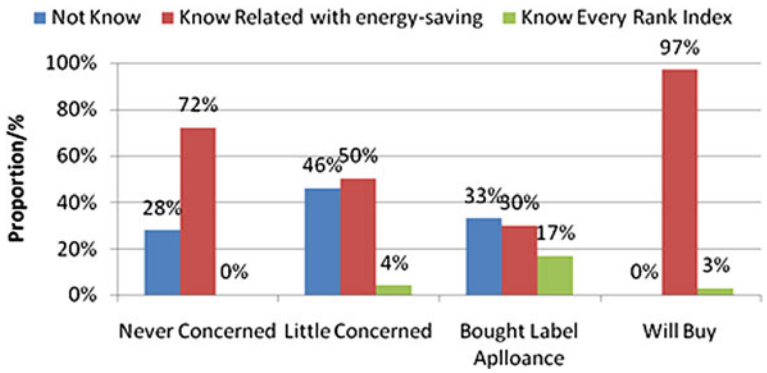

Fig. 61.4 The understanding of labeling program under the same labeling concerned

On the different conditions of Q_{IV}, the choices for the Know Relation with energy-saving are from 17 to 97 %, the Not know group are from 0 to 46 %, and the Know Every Rank Index group are from 0 to 17 %. For the same level of labelling concerned, the choices are also very different, especially for the Will buy group. So we can know that there are different choices for the same level of energy-efficient technology.

61.4.2 The Results for the Same **P** *(Internal Factors)*

The internal factors of residents' behaviour are mainly about the person's characteristics such as age, gender, education, and income, so for the same group, it

will have a different approval of energy-efficient technologies. What is the effect on energy-efficient technology utilized and related policies implemented? The questions Q_{I}, Q_{II}, and Q_{VI} are selected for future study.

61.4.2.1 Internal Factor of Behaviour Effect on Energy-Efficient Technology Approval

The influence of behaviour internal factor on Q_{I} is researched, and Fig. 61.5 expressly shows the gender, income, age, and education degree effect on energy-saving awareness. From figure (a), we can see that the choices of energy efficiency' awareness are very different and the female group is also different, although the two groups are so similar. From figure (b), (c), and (d), we can know that the results are very different too for every income group, degree group, and age group. There are some interesting phenomena, such as the distribution of the less than two thousand income group, the master's degree group, and the older group, awareness of energy efficiency is poor for lower income group and the older group, and it is opposite for the higher education degree group.

The same residents' group for their attitudes or preferences leads to different choice of Q_{II}. From Fig. 61.6, we know that many groups more prefer behaviour energy-saving, especially for female, the two–five thousand income, the Lower Education Degree group, and the 30–50 age group. The reason for female pays more attention on behaviour energy efficiency may be because of housekeeping. We can infer that the highest income group does not like to invest money on energy-saving.

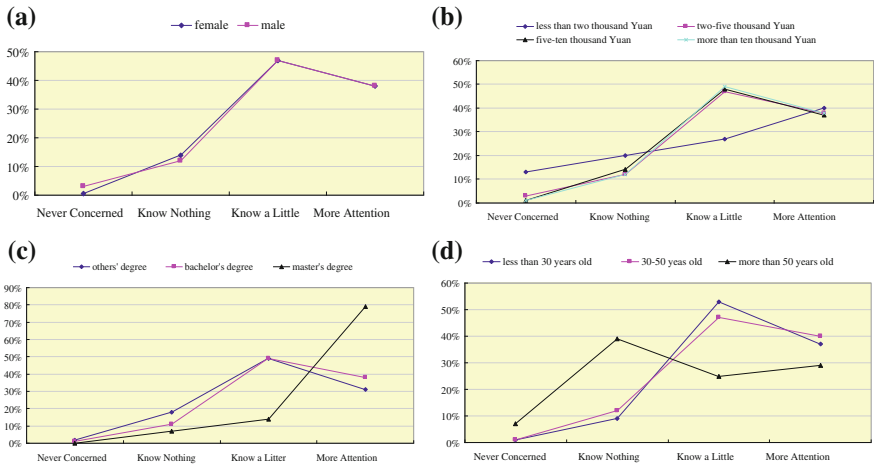

Fig. 61.5 Internal factor of behaviour effect on awareness of energy efficiency

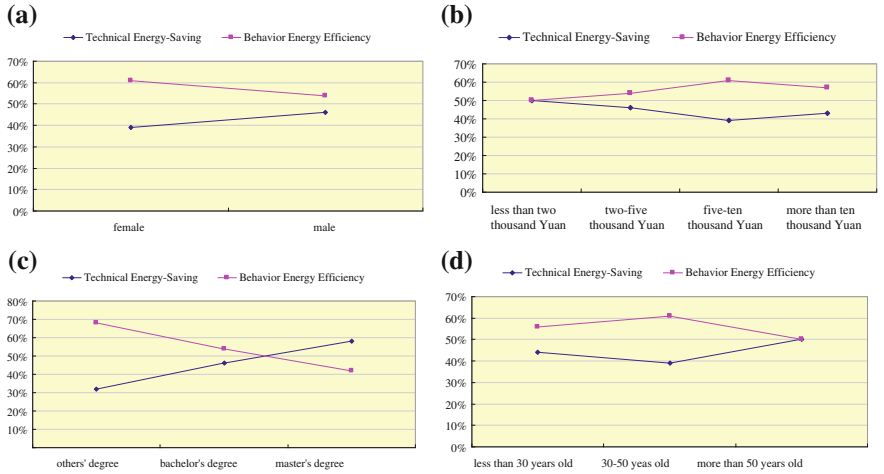

Fig. 61.6 Internal factor of behaviour effect on measure choice of energy efficiency

61.4.2.2 Internal Factor of Behaviour Effect on Energy-Efficient Policies Implementation

The internal factors which effect on the implementation of Q_{VI} are analyzed in Fig. 61.7. On the one hand, for every group, the choices are very different. On the other hand, we know that the percentage of the Have Exchanged group is higher for female, and it is lower for the Less Than Two Thousand Income group and the Master's Degree groups. The distribution of the different age groups is so similar, the Less Than Two Thousand and the Master's Degree are so different.

61.4.3 The Key Factor of Energy-Efficient Technologies Promotion

Base on the above results, the influence of behaviour external and internal factors on energy-efficient technology and related policies have be analyzed.

And then SPSS software will be used to analyse the key factors which effect on the energy-efficient technology promotion.

The one-way ANOVA analysis is used to estimate the factors such as income, degree, age, and gender effect on energy-efficient technology select, the sig. level is 0.1, the statistical results are shown in Table 61.3. From the results we can see that different income levels have significant influence on the labelling program concerned, and different education degree have an effect on the energy efficiency' awareness and labelling program, so does the age factor. But different genders have no striking difference on energy-efficient technology promotion.

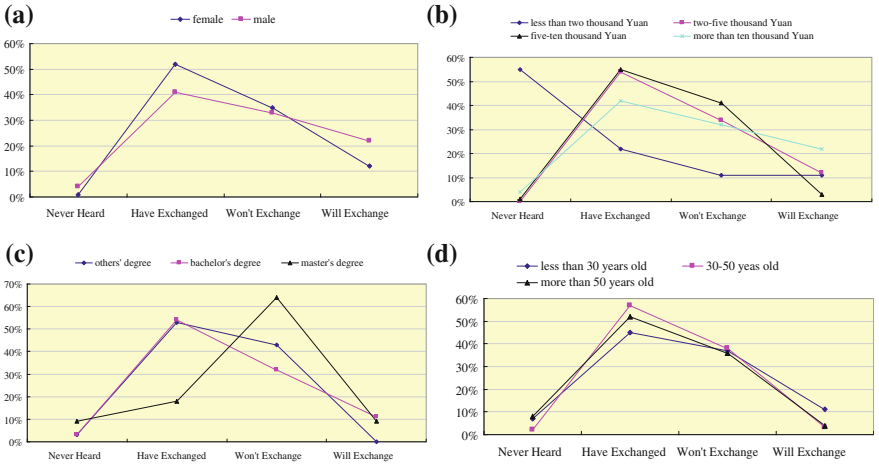

Fig. 61.7 internal factor of behaviour effect on concerned of exchange program

Table 61.3 The analyses results of ANOVA

		Income		Degree		Age		Gender	
		Mean squares	Sig.	Mean squares	Sig.	Mean squares	Sig.	Mean squares	Sig.
Q_{I}	Between group	3.811	0.219	7.007	0.017	16.109	0.000	0.001	0.978
	With group	285.127		281.931		272.828		288.937	
	Total	288.938		288.938		288.938		288.938	
Q_{II}	Between group	1.931	0.185	0.355	0.643	1.189	0.227	0.132	0.566
	With group	132.627		134.203		133.369		134.425	
	Total	134.558		134.558		134.558		134.558	
Q_{IV}	Between group	20.706	0.000	6.354	0.013	12.200	0.000	0.045	0.805
	With group	225.454		239.806		233.961		246.115	
	Total	246.160		246.160		246.160		246.160	
Q_{VI}	Between group	0.701	0.738	1.788	0.198	0.869	0.456	0.405	0.393
	With group	184.605		183.517		184.437		184.901	
	Total	185.306		185.306		185.306		185.306	

61.5 Conclusions

Base on the Behavior Model theory, the influence of behavior on awareness of energy-efficient technologies and participation of related policies are studied in this paper, and the selected results for the same people group and the same level energy efficiency are then analyzed, the conclusions are as follows:

1. Under the same energy–saving levels the choices of energy-efficient measures and the attention of labeling program concerned are coincided, the results are very different, especially for the Behavior Energy Efficiency and the Technical groups, although both of the two measure choices are similar. On the same level of attentions of labeling program, the results of label understanding are also very different.
2. For the same question, different personal factors of behavior effecting on awareness of energy efficiency and implementation of related policies are very different, like age, gender, degree and home income, especially for the Female group, the Lower Income group, the older group and the Masters' Degree group. Comparing to the external factor of behavior, the internal factors on energy-efficient technologies promotion are more obvious.
3. House income is the bigger influence factor for different energy-efficient measures promotion, and then is the degree.

Acknowledgments The authors gratefully acknowledge our friends and their colleagues who help do the surveys, and they come from JingAn Primary and secondary schools, XiangYang primary school, ShangHai primary school, QiuZhi primary school, ShiJie primary school, ChangEr primary school, HuaJing primary school and so on.

References

1. Compiled by National Bureau of Statistics of China (2009) China Statistical Yearbook 2009. China Statistics Press
2. Yong W, Long W (2009) Building energy efficient management. China Building Industry Press, Beijing
3. The Ministry of science and Technology of the People's Republic of China (2008) Handbook of energy conservation and emission reduction of national
4. Wang J (1987) Behavioral science. Zhejiang Publishing House
5. Belk R, Painter J, Semenik R (1982) A study of factors influencing energy conservation behavior. Adv Consum Res 306–312
6. Wood G, Newborough M (2007) Energy-use information transfer for intelligent homes: Enabling energy conservation with central and local displays. Energy Build 39:495–503
7. Abrahamse W, Steg L, Vlek C, Rothengatter T (2007) The effect of tailored information, goal setting, and tailored feedback on household energy use, energy-related behaviors, and behavioral antecedents. Environ Psychol 27:265–276
8. Dullecka U, Kaufmann S (2004) Do customer information programs reduce household electricity demand?—the Irish program. Energy Policy 32:1025–1032
9. Feng Y (2009) Urban residents' energy efficiency awareness and states. China Statistics. Hot Spots Interview 15–16
10. Zheng Y (2008) Study on Residents' Households Energy Use Saving Shanghai. Shanghai Energy Conserv 4:31–33
11. Guo Q (2007) The economic analysis and policy study of the public's energy conservation behaviour. Shandong University

Chapter 62
The Method of Field Date Collection and Date Validity for Energy Efficiency Diagnosis in Heat Pump Operating

Zhanwei Wang, Zhiwei Wang and Zengfeng Yan

Abstract Energy efficiency diagnosis in heat pump operating is a necessary means to ensure that the heat pump has energy-efficient operation, but existing conditions of field operational date collection and collected date accuracy are always bottlenecks for field date collection. This paper presents the basic criteria of field date collection and determines what parameters are needed for energy efficiency diagnosis in heat pump operating, based on the first law of thermodynamics and basic principle of heat transfer. These parameters include evaporation/condensation pressure of refrigerant in heat pump system; temperature, pressure, and flow rate of water entering/leaving the evaporator; temperature, pressure, and flow rate of water entering/leaving the condenser; and power consumption of the heat pump/water pump. Combining the experience of date collection from some fields and the technical demands measuring basic parameters, the authors of this paper present the comprehensive method combining the online in situ instruments with necessary portable instruments for the field measurement and also provide the criterion of date collection validity. Taking a typical heat pump system as case study, we describe a general date collection method and implementation steps in this paper. The results show that the method proposed in this paper is simple and effective.

Keywords Field date collection · Online in situ measurement · Date validity · Energy efficiency diagnosis · Heat pump operating

Z. Wang (✉) · Z. Wang
School of Environmental and Municipal Engineering, Xi'an University of Architecture & Technology, Xi'an 710055 Shaanxi, China
e-mail: 731173775@qq.com

Z. Wang
e-mail: wzhiwei-atu@163.com

Z. Yan
School of Architecture, Xi'an University of Architecture & Technology, Xi'an 710055 Shaanxi, China

A. Li et al. (eds.), *Proceedings of the 8th International Symposium on Heating, Ventilation and Air Conditioning*, Lecture Notes in Electrical Engineering 263,
DOI: 10.1007/978-3-642-39578-9_62,

62.1 Introduction

According to the investigation, the existing buildings in China have an area of up to over 40 billion square meters, more than 90 % of which belong to the highly energy-consuming buildings. The building energy consumption in the whole country has amounted to over 28 % of the end use of energy of the whole society, and about 65 % of building energy consumption serves for heating and air-conditioning [1]. Heat pump system is the main energy-consuming equipment of heating and air-conditioning. So there is an important significance for the energy efficiency diagnosis in heat pump operating. However, the model of energy efficiency diagnosis needs some heat pump operating parameters including evaporation/condensation pressure of refrigerant in heat pump system; temperature, pressure, and flow rate of water entering/leaving the evaporator; temperature, pressure, and flow rate of water entering/leaving the condenser; and power consumption of the heat pump/water pump [2]. Using online in situ instruments installed on the system and pipelines adequately is a very simple and encouraged method. But sometimes, these instruments in the field have so large measuring errors when the range of instruments is too wide, or these instruments are damaged or scaling. So the results came out by these parameters must be wrong. So what must be done is to check the date collection validity. But the method which is used to judge whether these parameters measured in the field are effective or not is still lacking. In order to fill this gap, the authors of this paper combine the experience of date collection from some fields and the technical demand measuring basic parameters, then present the comprehensive method combining the online in situ instruments with necessary portable instruments for the field measurement, and also provide the criterion of date collection validity. Meanwhile, we present some methods of field date collection. The criterion presented in this paper is energy imbalance rate (EIR). The value of EIR must be not more than a specific value. If the value of EIR is more than the specific value, what must be done is to find which parameters measured in the field are not effective, and the next step is to correct these parameters. Taking a typical heat pump system as case study, we describe a general date collection method and implementation steps in this paper.

62.2 The Method of Field Date Collection and Date Validity

62.2.1 Energy Efficiency Diagnostic Model in Heat Pump Operating

Depending on thermodynamic analysis of heat pump's refrigeration cycle and heat transfer analysis of its heat exchangers, we have developed the approximate white

box model which is different from the gray box model [3] and black box model [4] for energy efficiency diagnosis in heat pump operating.

62.2.1.1 The Energy Efficiency Diagnostic Model of Compressor

Analyzing the refrigeration cycle in the side of refrigerant, we judge if the compressor have non-energy-saving fault by comparing the COP between the actual refrigerating cycle and theory refrigeration cycle. The formulas calculating COP of the actual refrigerating cycle (ε_{acu}) and COP of the theory refrigeration cycle (ε_{th}) can be written as

$$\varepsilon_{th} = \frac{h_1 - h_4}{h_2 - h_1} \quad \text{and} \quad \varepsilon_{acu} = \frac{m_e c_p (t_{ei} - t_{eo})}{P_{in}} \quad \text{summer} \tag{62.1}$$

$$\varepsilon_{th} = \frac{h_2 - h_3}{h_2 - h_1} \quad \text{and} \quad \varepsilon_{acu} = \frac{m_c c_p (t_{co} - t_{ci})}{P_{in}} \quad \text{winter} \tag{62.2}$$

where h_1/h_2 stands for inlet/outlet enthalpy of compressor, and h_3/h_4 ($h_3 = h_4$) stands for inlet/outlet enthalpy of expansion valve in theoretic refrigeration cycle. Reading data from online pressure and temperature meters attached on condenser and evaporator in refrigerant side, the $h_1 \sim h_4$ can be approximately obtained from theoretic refrigeration cycle's $\lg p \sim h$ diagram (see Fig. 62.1). t_{ei}/t_{eo} stands for inlet/outlet water temperature of evaporator, t_{ci}/t_{co} stands for inlet/outlet water temperature of condenser, m_e/m_c is water flow rate through evaporator/condenser, c_p is water-specific heat capacity, P_{in} is input power of compressor. These parameters ($t_{ei,}$ $t_{eo,}$ $m_{e,}$ P_{in}, etc.) can be often read from online working meters on site.

We can judge if the compressor has non-energy-saving fault by the value of η, and η can be written as

$$\eta = \varepsilon_{acu}/\varepsilon_{th} \tag{62.3}$$

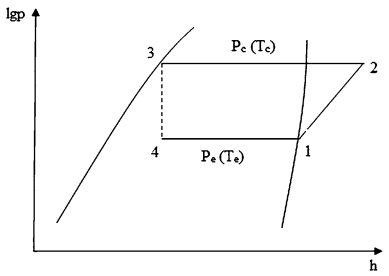

Fig. 62.1 Theoretic refrigeration cycle

62.2.1.2 The Energy Efficiency Diagnostic Model of Condenser/Evaporator

According to the heat balance equation and heat transfer equation, we have

$$Q = mc_p\Delta t = KF\Delta t_m \tag{62.4}$$

where Q is gaining/discharging heat rate, Δt is water temperature difference of heat exchanger's inlet and outlet, K is the overall heat transfer coefficient of condenser/evaporator, F is the overall heat transfer area of condenser/evaporator, Δt_m is the logarithmic average temperature difference of heat transfer between refrigerant and water.

Based on the formula (62.4), we can calculate the K or KF of condenser/evaporator, respectively, below

$$K_c = \frac{m_c c_p \ln\left(\frac{t_c - t_{ci}}{t_c - t_{co}}\right)}{F_c} \quad \text{or} \quad K_c F_c = m_c c_p \ln\left(\frac{t_c - t_{ci}}{t_c - t_{co}}\right) \tag{62.5}$$

$$K_e = \frac{m_e c_p \ln\left(\frac{t_{ei} - t_e}{t_{eo} - t_e}\right)}{F_e} \quad \text{or} \quad K_e F_e = m_e c_p \ln\left(\frac{t_{ei} - t_e}{t_{eo} - t_e}\right) \tag{62.6}$$

where t_c/t_e is the condensation/evaporation temperature, t_{ci}/t_{co} is the inlet/outlet temperature of cooling water, t_{ei}/t_{eo} is the inlet/outlet temperature of chilled water, m_c/m_e is the cooling/chilled water mass flow rate. When F is known, the K can be calculated; when F is unknown, the KF can be calculated. We take For KF as the fault judgment rule of heat transfer performance, and the fault judgment rule of flow resistance is similar to that of heat transfer performance decline.

According to the above analysis, we need these parameters including evaporation/condensation pressure of refrigerant in heat pump system; and temperature, pressure, and flow rate of water entering/leaving the evaporator; temperature, pressure, and flow rate of water entering/leaving the condenser; and power consumption of the heat pump/water pump.

62.2.2 The Method of Field Date Collection and Date Validity

62.2.2.1 The Demand Measuring These Parameters in the Field

We recommend using online measuring instruments of field to measure necessary parameters, because it will be convenient and economical. In order to ensure the result of energy efficiency diagnosis in heat pump operating is right, we must ensure the validity of these parameters. So the precision of these measuring instruments should not be inferior to the rule presented by Table 62.1 [5–9]. And

Table 62.1 The demand of precision of these measuring instruments

Name of measuring instrument	Precision
Thermometer	1.0
Piezometer	2.5
Flow meter	2.0
Electric energy meter	2.0

the range of thermometer, piezometer, and flow meter should not be oversize or undersize. It is best to make the measured value lie within the range 1/3 $\sim$ 2/3 of the full scale of measuring instruments.

But measuring instruments are often scaling, or their precision is too low, or their range is not appropriate, or they are damaged, or there are not some instruments in the field. In this case, we cannot ensure if the values of the parameters measured by these instruments are valid. So we need some necessary portable instruments to measure and correct, and the precision and range of portable instruments should meet above-mentioned demand. In this case, the method of field date collection is presented under contents detailedly.

When we measure temperature of water entering/leaving the condenser and temperature of water entering/leaving the evaporator, we cannot influence normal operation of equipments. So we recommend using thermocouples to measure the wall temperature of pipelines in which the chilled water and chilling water flow, and it will be necessary to break some thermal insulation layers sometimes. We should put measure points on the straight pipes of full-section pipe flow, and the measure points should be far away from the valves and elbows. On the straight pipes selected by us, we need to find a transversal surface as a measuring section and then cut off a circle thermal insulation layers, then uniformly put four measure points of thermocouple on every transversal surface along the appearance perimeter. And we need to encase the thermocouple probe with thermal insulation material firmly and measure the temperature of four measure points. Combining the empirical thermal resistance of the pipeline material with the mean value of four measure points, we can gain temperature of water entering/leaving the evaporator and condenser [9].

If there are not flow meters measuring the chilling water and chilled water in the field, we suggest using ultrasonic flow meters. And the ultrasonic flow meters should be put on the straight pipes of full-section pipe flow [9]. Combining the real-time power of chilled water pump and chilling water pump, we can also calculate the flow rate by water pump performance curve or table.

62.2.2.2 The Method of Field Date Collection and Date Validity for Energy Efficiency Diagnosis in Heat Pump Operating

EIR can well reflect date validity. EIR should not be more than 10 % in the engineering [10]. We can judge that the dates are invalid, when EIR is more than 10 %. EIR can be expressed as

$$\left|\frac{(Q_e + P_{\text{in}}) - Q_c}{Q_e + P_{\text{in}}}\right| \tag{62.7}$$

Criterion of date collection validity can be written as

$$\left|\frac{(Q_e + P_{\text{in}}) - Q_c}{Q_e + P_{\text{in}}}\right| \leq 0.1 \tag{62.8}$$

where Q and P can be calculated by following formulas

$$Q = m\, c_p \Delta t \tag{62.9}$$

$$P = \sqrt{3} UI \times \partial \tag{62.10}$$

where Q stands for quantity of heat, P stands for rate of power, the value of P can be also measured by electric energy meter, U stands for voltage, I stands for electric current, and ∂ stands for power factor.

Firstly, we use online instruments to measure these parameters for energy efficiency diagnosis in heat pump operating. If some instruments are absent, the corresponding portable instruments which meet the demand presented by the above contents must be used. And the time interval measuring each group of data is set 10 $\sim$ 30 min [5–9, 11–13]. It will be best to measure each group of data at the same time as far as possible. And we measure these parameters when the heat pump system is operating. Then, we calculate EIR of each group of data by Eq. (62.7). Data are valid only when its EIR is less than 10 %.

We can use these parameters for energy efficiency diagnosis in heat pump operating, when the EIR of these parameters is less than 10 %. What must be paid attention to is that the number of group of valid data should not be less than 15. The implementation steps of the method of field date collection and date validity are summarized in the Fig. 62.2.

62.3 Method Application Case

62.3.1 Outline of Project

The project used by this paper is groundwater source heat pump system located in Huize community of Hanzhong. The total air-conditioning area of this community is about 43,600 m^2. In this field, there are these instruments which measure evaporation/condensation pressure and temperature of refrigerant, and the temperature of chilling water entering/leaving the condenser, and the temperature of chilled water leaving the evaporator, and power consumption of the heat pump/water pump, but these instruments which measure the temperature of chilled water entering the evaporator and the flow rate of chilling/chilled water are absent. These existing instruments meet the demand presented above.

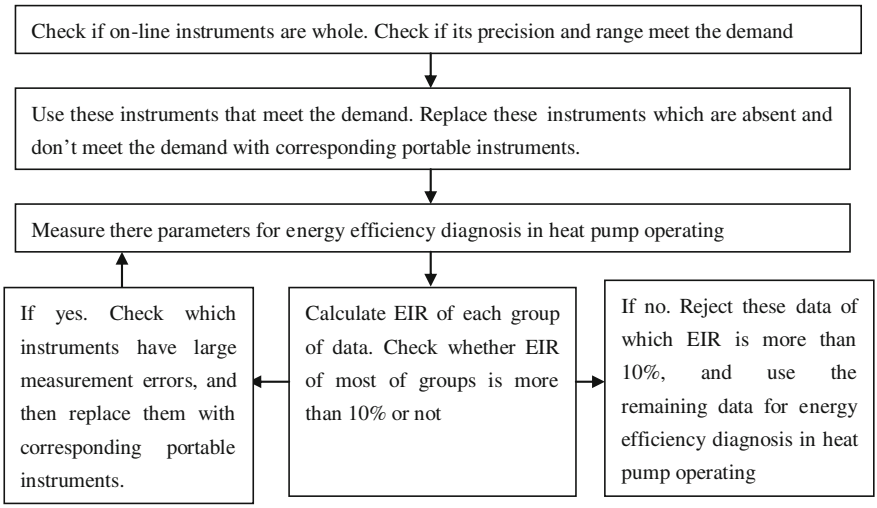

Fig. 62.2 The implementation steps of the method of field date collection and date validity

62.3.2 Data Collection

According to the method and implementation steps presented above, we put thermocouples on the straight pipes of full-section pipe flow of chilled water entering the heat pump system to measure its temperature. We combine real-time power of chilling water pump and chilled water pump measured by the electric energy meters with water pump performance table to determine their flow rate. We totally measure 20 groups of data in a day of winter of 2012, and the time interval of each group of data is 30 min. According to the measured results, we determine the flow rate of chilling water is 290 m^3/h, and the flow rate of chilled water is 120 m^3/h.

62.3.3 Results of EIR

According to the implementation steps presented by Fig. 62.2, we calculate EIR of 20 groups of data with formula (62.7) and compare the values of EIR before correction with EIR after correction. The result is presented in Fig. 62.3. What is paid attention to is that rated flow of chilling water pump and chilled water pump is used to calculate EIR before correction, and that the actual flow rate determined by measurement is used after correction. And the rated flow of chilling water pump and chilled water pump is 187 m^3/h and 200 m^3/h, respectively.

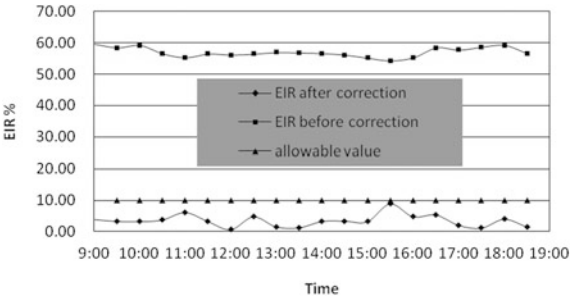

Fig. 62.3 Comparison between EIR before correction and EIR after correction

62.3.4 Discussion

According to the Fig. 62.3, the EIR is more than 50 % which is far greater than 10 %, if we do not correct the flow rate of chilling water and chilled water, so these data have very large errors and cannot be used for energy efficiency diagnosis in heat pump operating. EIR of these data corrected by portable instruments is all less than 10 %, so these data can be used for energy efficiency diagnosis in heat pump operating. And the diagnostic results should be right. According to this case study, the method of field date collection and date validity presented in this paper is feasible.

62.4 Conclusions

Combining the experience of date collection from some fields with the technical demand measuring basic parameters, the authors of this paper successfully present the comprehensive method combining the online in situ instruments with necessary portable instruments for the field measurement and also provide the criterion of date collection validity. The criterion presented in this paper is EIR. Taking a typical heat pump system as case study, we describe a general date collection method and implementation steps in this paper. And the results show that the method is simple and effective. Only these data which meet the demand of EIR are valid and can be used for energy efficiency diagnosis in heat pump operating, and the results are right only in this way. Field date collection and date validity is not only the precondition of energy efficiency diagnosis in heat pump operating, but also is the precondition to improve performance of heat pump system and keep it high-efficient operating status.

Acknowledgments This study is financially supported by "Twelfth Five-Year National Science and Technology Support Programme" (2011BAJ03B06) and 2011 Shaanxi Scientific and Technological Innovation Project (2011KTCQ03-07) and 2012 Xi'an Scientific and Technological Project (CX12187①).

References

1. Center of Science and Technology of Construction, Ministry of Housing and Urban-Rural Development, P.R.China (2011) Building energy project efficiency development report(2010 Year). China Architecture & Building Press, Beijing (In Chinese)
2. Wang Z, Wang Z, Yan Z (2013) A fault diagnosis model and its application in chiller operating. Appl Mech Mater 291–294:1851–1856
3. Lee TS (2004) Thermodynamic modeling and experimental validation of screw liquid chillers. ASHRAE Trans 110(1):206–216
4. Swider DJ (2003) A comparison of empirically based steady-state models for vapor-compression liquid chillers. Appl Therm Eng 23(5):539–556
5. GB/T 16664-1996 (1996) Monitoring and testing method for energy saving of power supply distribution system of industrial enterprise
6. GB/T 1666-1996 (1996) Monitoring and testing method for energy saving of motor-pump liquid transport system
7. GB/T 15912-1995 (1995)Monitoring and testing method for energy saving of single-stage reciprocating refrigerating unit and its refrigeration system
8. GB/T 16665-1996 (1996) Monitoring and testing method for energy saving of air compressor unit and air distribution system
9. GB/T 15910-1995 (1995) Monitoring and testing method for energy saving of heat transmission and distribution system
10. Leming L, Yufei T, Jianzheng W, Zhu T (2007) Engineering thermodynamics (fifth edition). China Architecture & Building Press, Beijing (In Chinese)
11. GB/T 15316-2009 General principles for monitoring and testing of energy saving
12. Xiumu F, Jiang Y, Zhang J (2007) Architectural environment testing technology. China Architecture & Building Press, Beijing (In Chinese)
13. Lu C (2001) Thermal parameters measurement and processing, 2nd edn. Tsinghua University Press, Beijing (In Chinese)

Chapter 63
Discussion on a Running Control Strategy Suitable for Evaporative Cooling Straight-Flow Air-Conditioning System

Zhixiang Wu, Zhuan Xue, Rengang Wang and Yuan Qu

Abstract A running control strategy was proposed based on tremendous analysis of the running regulation of straight-flow air-conditioning system. By adjusting parameters in sub-regulation and control mechanism modular linkage, the coupling characteristic of each adjustment factor to the system can be eased. The running control strategy can greatly improve the running stability of the evaporative cooling straight-flow air-conditioning system and thus make the system more energetic efficient.

Keywords Evaporative cooling straight-flow air-conditioning technology · Evaporative cooling air-conditioning · Intelligent control linkage · Energy saving

63.1 Introduction

The current research about the equipment development, application area, and unit performance of the evaporative cooling straight-flow air-conditioning system is more in-depth and comprehensive. However, the research on running control of that air-conditioning system is lagging behind. This is due to the weak running applicability of the existing evaporative cooling straight-flow air-conditioning system, especially for the constant volume system. The poor energy-saving effect has affected the promotion and application of that air-conditioning system. In this case, using variable air volume conditioning system will benefit the existing running control from no feasible and effective regulation strategy suitable for that air-conditioning system. Therefore, the research on the running control strategy of evaporative cooling straight-flow air-conditioning system is extremely necessary.

Z. Wu (✉) · Z. Xue · R. Wang · Y. Qu
Xi'an Polytechnic University, Xi'an 710048, China
e-mail: wzx1040@126.com

A. Li et al. (eds.), *Proceedings of the 8th International Symposium on Heating, Ventilation and Air Conditioning*, Lecture Notes in Electrical Engineering 263,
DOI: 10.1007/978-3-642-39578-9_63,

63.2 Evaporative Cooling Straight-Flow Air-Conditioning System and Its Running Control Features

Since water passes the packing and contacts in the evaporative cooling air-conditioning system with unsaturated air directly, the system uses the latent heat of evaporation of the water to cool down the processed air [1]. Therefore, the outdoor air meteorological parameters have a great impact on the air-conditioning system. Moreover, the evaporative cooling all air-conditioning system and the traditional mechanical refrigeration air-conditioning system have distinctive differences in the refrigeration principle, the form of system, operation mode, and application areas. As a result, the running control strategy of traditional air-conditioning system cannot be applied to the evaporative cooling air-conditioning system.

63.2.1 The Influential Factor of Running

While evaporative cooling straight-flow conditioning system is running, the outdoor meteorological parameters' effect on cooling cannot be ignored, the process ($W_1 \rightarrow W_2$) stands for indirect evaporative cooling (IEC), and the process ($W_2 \rightarrow O$) stands for direct evaporative cooling (DEC). Cooling efficiency formula:

$$\eta_1 = \frac{T_g\_T_o}{T_g\_T_s} \quad \eta_2 = \frac{T_g\_T_{g1}}{T_g\_T_s}$$

Here, η_1 is DEC efficiency, η_2 is IEC efficiency, T_g is outdoor dry bulb temperature, T_{g1} is indirect section outlet temperature, T_o is temperature of the supplied air, and T_s is wet bulb temperature.

Obviously, the outdoor dry bulb temperature and the wet bulb temperature play leading roles in the cooling efficiency of the unit. The change of outdoor conditional point will affect the supply air-conditional point. Some existing research has shown that influence factors of the evaporative cooling air-conditioning units efficiency are also included the outdoor air wet and dry bulb temperature, barometric pressure, relative humidity, face velocity of the filler, shower density and shower temperature, namely wet bulb temperature. However, the related factors of the molded evaporative cooling air-conditioning unit cannot be easily changed. Besides, the outdoor meteorological parameters cannot be controlled. In this point of view, only shower density, shower temperature, and face velocity of the filler are adjustable. The existing evaporative cooling air-conditioning system all use recycled water; therefore, only the face velocity of the filler and leaching water are adjustable.

63.2.2 Running Control Regulation Characteristics

For the air-conditioning system, the essence of running control strategy is to regulate the cooling capacity which is fed into by the unit, by means of that to maintain the stability of the indoor temperature and humidity environment [2]. At the same time, the supply air-conditional point of the evaporative cooling direct air-conditioning system reached saturation as a result of the isenthalpic humidification and cooling process. The actual running the relative humidity of supply air-conditional point exceeds 80 %, and the process is affected by outdoor meteorological parameters and unit's own factors. In this case, the final conditional point of the treated air is uncertain. The air-conditioning system becomes difficult to achieve accurate regulation of supply air temperature, and the relative humidity regulation is even more difficult. If the evaporative cooling straight-flow conditioning system is applied, the most effective way to control the temperature is to adjust the volume in all, each adjustment factor and functional segment have larger correlation and will affect the adjustment effect for the combined application of IEC, DEC segment.

63.3 The Running Control Strategy of Evaporative Cooling Straight-Flow Air-Conditioning System

The running control factors of evaporative cooling straight-flow air-conditioning system have the characteristics of large correlation and strong coupling. A suitable air supply point range should be applied according to the air-conditional point, temperature, and humidity design requirements and cooling efficiency of the air condition. Herein, we propose the running control strategy which mainly use the air grading adjustment and regard shower water regulation as auxiliary. When the air volume controls reach the limit and the leaching of water is then adjusted [3], this running control strategy improved the applicability of the air-conditioning system and is energetic saving.

63.3.1 Analysis of the Control Strategy and Determination of Air-Conditional Point Range

63.3.1.1 Analysis of the Control Strategy

Changes in the face velocity of the filler and the shower density will affect supply air-conditional point for the evaporative cooling air-conditioning unit. Studies have shown that shower density and face velocity of the filler have the best combination value, which leads to the highest cooling efficiency [4]. However, the

drawback is the lower circulating pump power. If the unit adopts frequency regulation, the energy-saving effect becomes not obvious, and the costs of operation and investment will increase. At most time, the wind speed is adjusted from the maximum to the minimum, and the adjustment of the leaching water has less pronounced impact on air-conditional point. Therefore, the leaching water is not adjusted while adjusting the air volume. Since the application areas have less demanding on temperature and humidity, ensuring the supply air temperature to meet the design requirements is the key to the running control of air-conditioning system.

As for the running of evaporative cooling straight-flow air-conditioning system, influential factors are more complicated and strongly coupled. The coupling and relevance of the influential factors have been resolved by subsection and prioritization control to the adjustment parameters. Meanwhile, sub-file adjustment to the blower would enhance the adaptability of the unit running, improving the life of the equipment and reducing the running costs of the system. In addition, the intelligent linkage control module can also replace the artificial initial debugging aspect of evaporative cooling straight-flow air-conditioning air system, which have greatly saved the manpower input and improved the applicability of the system.

63.3.1.2 Determination of Air-Conditional Point Range

According to the maximum of the unit, minimum air volume of the unit, and indoor temperature, the temperature range of supply air-conditional point ($T_{min} < T_o < T_{max}$), T_{min} stands for the web bulb temperature of the outdoor point W_2; after that, according to the design requirements of indoor temperature and humidity, the range of indoor temperature and humidity can be determined; finally, according to ε, the range of supply air-conditional point can be determined. The approximate triangular region is shown in Fig. 63.1 (Bounded by O_2, O'_1 and O, O'_1 stands for supply air-conditional point under the lowest efficiency of DEC, W stands for outdoor conditional air point.).

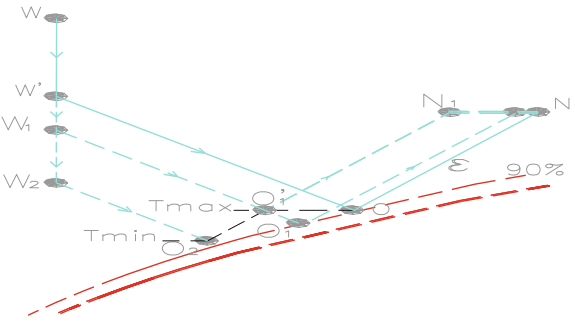

Fig. 63.1 Air-conditioning system air handling control analysis chart (IEC + DEC)

63.3.1.3 The Feasibility of the Determined Supply Air Range

The common industrial and civil constructions usually have no strict accuracy requirements on indoor relative humidity when applying the evaporative cooling straight-flow air-conditioning system. Therefore, the indoor relative humidity could be set within a certain range and combined with the indoor set temperature to determine the range of indoor conditional point (N_1–N in Fig. 63.1). The range of supply air temperature (T_{min}–T_{max} in Fig. 63.1), based on the unit supply air temperature, could be determined by the maximum air volume and the lowest supply air temperature determined by the minimum air volume. The minimum relative humidity of the air supply conditional point could also be determined according to ε and N_1. In this way, the lowest cooling efficiency of the unit is guaranteed and the range can be determined.

63.3.2 The Intelligent Linkage Control Module

The adjustment factors of the running of the evaporative cooling straight-flow air-conditioning system have the characteristic of strong correlation and coupling, the intelligent control linkage control module can solve the problem by adjusting the unit, out door monitor parameters, and indoor monitor parameters [2]. The overall running schematic diagram of the intelligent linkage control module is shown in Fig. 63.2, and the running flowchart of the intelligent linkage control module is shown in Fig. 63.3.

63.3.2.1 The Monitor Parameters and Its Effects

The running control of the air-conditioning unit is mainly adjusted by the fan speed and pump start/stop, so the running control primarily bases on the indoor temperature and humidity change. The monitor value of outdoor dry bulb temperature and the monitor value of unit outlet dry bulb temperature are regarded as auxiliary regulation. For example, the outdoor dry bulb temperature control point of the indirect segment start/stop can be achieved through, design and calculation, shown as W′ in Fig. 63.1. To adjust the blower, which bases on the monitor value of unit outlet temperature and the set value of indoor temperature, as well as the IEC pump, which based on the minimum air value, the fan speed is set as the classified regulation.

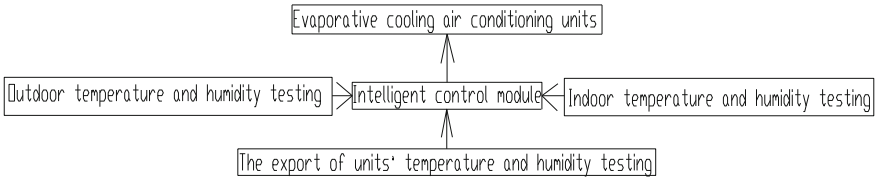

Fig. 63.2 The overall running schematic diagram of the intelligent linkage control module

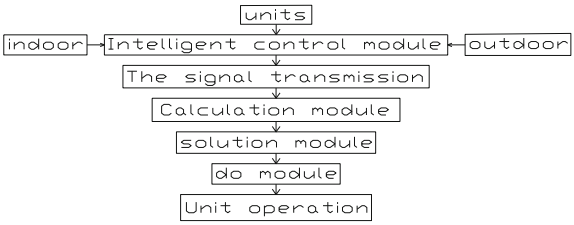

Fig. 63.3 The running flowchart of the intelligent linkage control module

63.3.2.2 The Intelligent Module

Conditioning functions mainly include data storage, configuration, analysis, and processing functions. The data storage configuration module can store and set the relevant parameters, while the intelligent programming can calculate and analyze the monitoring data and then draw the best adjustment program. For example, the required air volume can be calculated according to the set indoor temperature and the monitor value of supply air temperature, and then the regulation scheme could be chosen by comparing the required air volume and actual air. In addition, the module has a selection function for constant air system and variable air volume system.

63.3.2.3 The Linkage Control

The linkage control could be achieved by adjusting secondary side fan, blower, exhaust unit, and start/stop pump. In other words, the intelligent module control can demonstrate a certain proportion of adjustment to the blower and exhaust fan, the secondary side fan and blower, blower and pump (IEC and DEC) start/stop.

63.3.3 The Running Control and Regulation of the System

Take IEC + DEC straight-flow air-conditioning system as an example. First, according to the original design parameters, maximum air temperature (T_{max}), the lowest supply air temperature (T_{min}), IEC running boundaries temperature ($T_{W'}$), minimum air volume (L_{min}), and the minimum quantity of shower (Q_{min}), the adjustable parameters of the intelligent linkage control module could be manually set. If the air volume of the unit is adjusted to the minimum while the indoor temperature still deviates from the set value, the system under working conditions could have the blower open alone. The system plays the role of ventilation and cooling until the system turns off the fan.

Specific adjustment process is shown in Fig. 63.4. The air-conditioning system is assumed to run under the full load condition, with the running of the system, when the detected temperature of the room is higher than the set value (The dashed

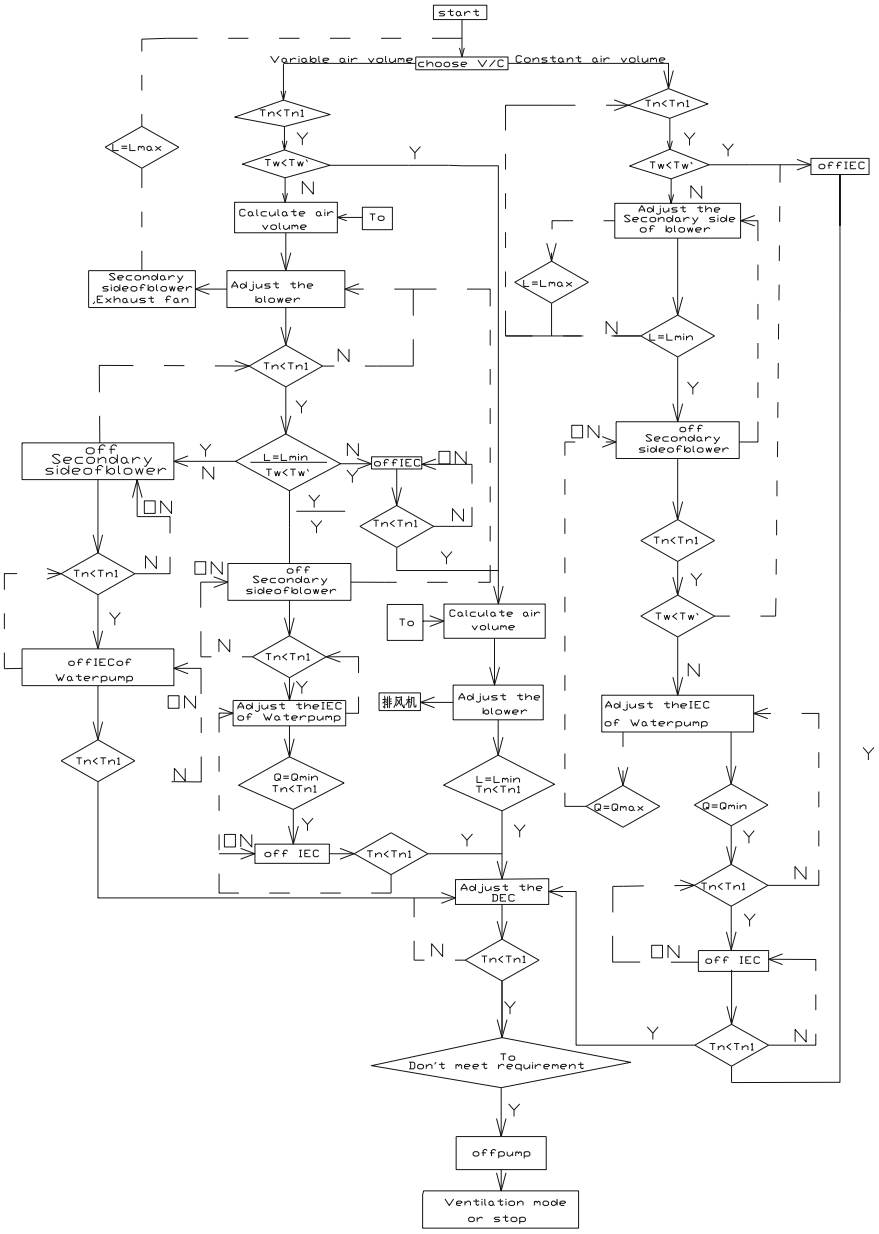

Fig. 63.4 The control process of intelligent control linkage adjustment module (IEC + DEC) (T_{n1} is monitor temperature, T_n is indoor set temperature, T_o is air-conditional point temperature, L is air volume, and Q is leaching water.)

line stands for the adjustment process.). The regulation eventually makes the indoor temperature and humidity near the set value. In addition, the regulation maintains the stability of indoor environment.

63.4 Conclusions

The VAV control system, which based on the running features and combined with its own characteristics, is needed for the evaporative cooling straight-flow air-conditioning system. The VAV control system can make the indoor temperature stay relatively stable in the presence of the frequent indoor temperature fluctuation. The proposed strategy takes air volume regulation as primary and leaching water as auxiliary control. The intelligent linkage control strategy solved the coupling characteristic of each adjustment factor to the system and improved the applicability of the straight-flow air-conditioning system, energy efficiency.

In theory, the author proposed a solution strategy for the running and regulation of the air-conditioning system. In a certain sense, this control strategy provides a guide for future researches on enriching the theoretical system of evaporative cooling air-conditioning system running control.

References

1. Huang X (2010) Evaporative cooling air conditioning theory and application. China Building Industry Press, Beijing
2. Zhang ZH (2009) Construction equipment management system. People's Communications Press, Beijing
3. Malli A, Seyf HR, Layeghi M, Sharifian S, Behravesh H (2011) Investigating the performance of cellulosic evaporative cooling pads. Energy Convers Manage 52:2598–2603
4. Riangvilaikul B, Kumar S (2010) Numerical study of a novel dew point evaporative cooling system. Energy Build 42:2241–2250

Chapter 64
The Research of Applying TOPSIS Combined with Grey Relational Analysis Approach for Building Energy Consumption Evaluation

Ying Li, Guohui Feng, Liang Yu, Qiang Li and Mengyun Sun

Abstract In this paper, besides defining the positive "ideal building," an approach combined TOPSIS with grey relational analysis method is introduced into the field of architecture. This improved method can reflect the exact energy consumption close degree of each building for evaluation to the positive "ideal building" from both aspects of position distance and shape similarity. Due to the energy consumption relative closeness degree of buildings to the positive "ideal building," not only each building energy consumption level can be determined precisely to rank multiple existing building energy consumption levels, but the qualities of each building index can be assessed effectively. At last, taking a simple evaluation system as an example, three urban building energy consumption levels are compared through the selected system. Through the case analysis, the superiority and effectiveness of the new method for building energy consumption evaluation are proved.

Keywords TOPSIS · Grey relational analysis · Positive "ideal building" · Building energy consumption evaluation

64.1 Introduction

In the current situation that building energy consumption evaluation has been got more attention, more and more scholars devote themselves to the building energy consumption evaluation research [1, 2]. With regard to the research of evaluation method, fuzzy comprehensive evaluation method is used by almost all of the estimators to evaluate the target architecture [3–7] in spite of the fact that this method mainly aims at evaluating a single building energy consumption level and

Y. Li · G. Feng (✉) · L. Yu · Q. Li · M. Sun
School of Municipal and Environment Engineering, Shenyang Jianzhu University, Shenyang 110168, China
e-mail: fengguohui888@163.com

A. Li et al. (eds.), *Proceedings of the 8th International Symposium on Heating, Ventilation and Air Conditioning*, Lecture Notes in Electrical Engineering 263,
DOI: 10.1007/978-3-642-39578-9_64,

it is unable to make contrast analysis and evaluation of more than two building energy consumption level [8, 9].

Evaluation of building energy consumption not only aims at making judgment of a single building energy consumption level, more meticulous judgments of multiple building energy consumption level are more necessary [10–13]. Therefore, it is important, in particular, to make contrast analysis and evaluation of multiple building energy consumption level through adoption of the more effective and specific evaluation method.

64.2 The Basic Principle of TOPSIS and Grey Correlation Analysis Method

64.2.1 Introduction of TOPSIS

TOPSIS with its full name of technique for order preference by similarity to ideal solution, which is a kind of more effective multi-index decision-making method, once used in comprehensive evaluation of industrial economic benefit [1]. The ultimate principle is that taking ideal solution and negative ideal solution of multi-index problem to get the two distances, which are close to the ideal solution and far away from negative ideal solution as judging basis. Thus, strengths and weaknesses of program evaluation, based on the relatively close degree of target program to optimal decision, can be made [2].

64.2.2 Introduction of GRA

Grey relational analysis is a kind of selection method, which is based on the corresponding changes with the alteration of time and other objects in the process of development, among the factors of alternatives and ideal alternative. Its basic principle is that adopting the closeness degree among curves as measurement levels of correlation degree, on the basis of analyzing and comparing the closeness degree of curve geometric shape and geometrical relationship of the plan data sequence. Therefore, a quantitative measure for multiple target project decision is provided by the method of GRA.

64.3 A New Method Combined TOPSIS with GRA

The method of TOPSIS and GRA own their respective advantages and disadvantages. Curve position relation of alternative data can be better reflected by TOPSIS using distance scale, which cannot reflect the differences of internal

various factors change trend between alternatives and ideal scheme clearly. Because of the adoption of original data sample, when information acquisition is limited, it is difficult to guarantee the accuracy of the decision result. The method of GRA is appropriate for the evaluation environment of incomplete information, reflecting the changes of data curves and similarity of curve geometric shape between alternatives and ideal scheme. In order to make more effective evaluation of the energy consumption level of buildings and get more accurate evaluation results, now, the two methods are combined, avoiding their own disadvantages. Thus, a new optimal and improved solution approach and model of program approximation ideal solution are presented to make contrast evaluation of multiple building energy consumption level.

64.3.1 Improvement of Method of TOPSIS Based on GRA

The method of TOPSIS is commonly used for decision analysis of system engineering that has a number of schemes and multiple targets. Generally, the building energy consumption for evaluation is objective, so that building energy consumption evaluation is just a single system. In view of characteristics of the research objects, the best and worst schemes are constructed. The best scheme is the case that all indexes affected the building energy consumption fully comply with the relevant criterions, and the worst scheme is that almost all of indexes affected the building energy consumption do not conform to the relevant norms.

Record the indexes, which fully comply with the relevant criterions, as 10, the ones that do not conform to standards, as 1, and so on. By doing so, all elements contained within decision matrix are the numerals from 1 to 10. Thus, the original data that have wide gap in the numerical size can be used directly.

64.3.2 Steps of Improved Method of TOPSIS Based on GRA

The steps of model establishment through improved method of TOPSIS based on GRA:

1. Determine the index weights. Different methods can be chosen to determine the index weights.
2. Standardize the decision matrix through the method of vector normalization.

$$a_{ij} = f_{ij} / \sqrt{\sum_{j=1}^{m} F_{ij}^2} \tag{64.1}$$

3. Determine weighted standardization judgment matrix.
4. Determine the positive "ideal building" F^* and negative "ideal building" F^0:

$$F^* = ((\max_i a_{ij} | j \in J) \text{ or } (\min_i a_{ij} | j \in J^0))^T \tag{64.2}$$

$$F^0 = ((\min_i a_{ij} | j \in J) \text{ or } (\max_i a_{ij} | j \in J^0))^T \tag{64.3}$$

5. Calculate the distance of each buildings for evaluating to the positive and negative "ideal building", $L_2(i)$ and $L_2^0(i)$.

The distance of building for evaluating to the positive "ideal building" about index j:

$$L_2(i) = \sqrt{\sum_{j=1}^{m} \left(a_{ij} - 10\right)^2}, \quad 1 \le i \le \mathrm{n} \tag{64.4}$$

The distance of building for evaluating to the negative "ideal building" about index j:

$$L_2^0(i) = \sqrt{\sum_{j=1}^{m} \left(a_{ij} - 1\right)^2}, \quad 1 \le i \le \mathrm{n} \tag{64.5}$$

6. Calculate the grey correlation degrees of each buildings for evaluating to the positive and negative "ideal building" by weight vectors, R_i^+ and R_i^-.

The grey relational coefficients of each building for evaluating to the positive and negative "ideal building" about index j:

$$r_{ij}^+ = \frac{m + \zeta M}{\Delta_i(k) + \zeta M}, \quad \zeta \in (0, 1) \tag{64.6}$$

$$r_{ij}^- = \frac{m + \zeta M}{\Delta_i(k) + \zeta M}, \quad \zeta \in (0, 1) \tag{64.7}$$

$\Delta_i(k) = \left|u_0^+ - u_i(k)\right|$, $\Delta_i(k) = \left|u_0^- - u_i(k)\right|$, $m = \min_i \min_k \Delta_i(k)$, $M = \max_i \max_k \Delta_i(k)$. Generally, the value of resolution ratio ζ is 0.5.

$$R_i^+ = \sum_{j=1}^{n} W_j \, r_{ij}^+, \quad i = (1, 2, \ldots, m) \tag{64.8}$$

$$R_i^- = \sum_{j=1}^{n} W_j \, r_{ij}^-, \quad i = (1, 2, \ldots, m) \tag{64.9}$$

7. Nondimensionalize the Euclidean distance values and Grey correlation values:

$$M_{\text{new}} = \frac{M_i}{\max\limits_{1 \le i \le n} (M_i)}, \quad i = (1, 2, \ldots, m) \tag{64.10}$$

M_i represents $L_2(i)$, $L_2^0(i)$, R_i^+ and R_i^-.

8. Calculate the energy consumption similar closeness degrees, taking $\alpha_1 + \alpha_2 = 1$:

$$S_i^+ = \alpha_1 L_2^0(i) + \alpha_2 R_i^+, \quad i = (1, 2, \ldots, m) \tag{64.11}$$

$$S_i^- = \alpha_1 L_2(i) + \alpha_2 R_i^-, \quad i = (1, 2, \ldots, m) \tag{64.12}$$

The value of S_i^+ indicates the closeness degree of the building energy consumption for evaluating to the positive "ideal building" energy consumption, and the higher value of S_i^+ shows that the building energy consumption is lower. The value of S_i^- indicates the closeness degree of the building energy consumption for evaluating to the negative "ideal building" energy consumption, and the higher value of S_i^- shows that the building energy consumption is higher.

9. Calculate the relative similarity degrees of buildings for evaluating to the positive "ideal building":

$$C_i^* = \frac{S_i^+}{S_i^+ + S_i^-}, \quad i = (1, 2, \ldots, m) \tag{64.13}$$

10. Sort building energy consumption levels for evaluating through the calculated closeness degrees. Higher value shows that the corresponding building energy consumption is lower.

64.4 Case Analysis

This study selects three urban public buildings recorded as building A, B and C and takes the evaluation system shown in Table 64.1 as an example. Then, the weight of each index in the system is determined by the method of ANP.

The decision matrix: $X_{ij} = \begin{pmatrix} 7 & 6 & 6 & 6 & 5 & 3 & 6 & 3 & 3 & 2 & 5 & 5 & 3 \\ 7 & 6 & 5 & 3 & 5 & 6 & 6 & 2 & 4 & 2 & 4 & 5 & 4 \\ 6 & 7 & 7 & 5 & 4 & 4 & 4 & 4 & 3 & 1 & 3 & 5 & 4 \end{pmatrix}^T$

The calculated weighted normalized matrix:

$$X = w\,X_{ij} = \begin{pmatrix} 0.1806 & 0.1507 & 0.1986 & 0.8791 & 0.2373 & 0.1198 & 0.1715 & 0.1602 & 0.1130 & 0.0605 & 0.1695 & 0.1594 & 0.0848 \\ 0.2077 & 0.1507 & 0.1863 & 0.5062 & 0.2373 & 0.1931 & 0.1715 & 0.1498 & 0.1625 & 0.0605 & 0.1130 & 0.1594 & 0.1272 \\ 0.1806 & 0.1777 & 0.2118 & 0.7017 & 0.2286 & 0.1409 & 0.1122 & 0.1718 & 0.1130 & 0.0305 & 0.0887 & 0.1594 & 0.1272 \end{pmatrix}^T$$

The ideal solution:

$$F^+ = (0.2077 \quad 0.1777 \quad 0.2118 \quad 0.8791 \quad 0.2373 \quad 0.1931 \quad 0.1715 \quad 0.1718 \quad 0.1625 \quad 0.0305 \quad 0.1695 \quad 0.1594 \quad 0.1272)^T$$

The negative ideal solution:

$$F^0 = (0.1806 \quad 0.1507 \quad 0.1863 \quad 0.5062 \quad 0.2286 \quad 0.1409 \quad 0.1122 \quad 0.1498 \quad 0.1130 \quad 0.0305 \quad 0.0887 \quad 0.01594 \quad 0.0848)^T$$

The distances of building A, B, and C to the positive and negative "ideal building" is calculated by the formula (64.4) and (64.5), and shown in Figs. 64.1, 64.2.

Table 64.1 Public building energy consumption evaluation index system and weight value of indexes

Indexes and weights value of evaluation system		Public buildings		
		A	B	C
Construction factors B1	Maintenance structures C11 (0.0618)	7	7	6
	Thermal insulation C12 (0.0515)	6	6	7
	Energy saving design C13 (0.0704)	6	5	7
Equipment factors B2	HVAC C21 (0.3890)	6	3	5
	Illuminating system C22 (0.0752)	5	5	4
	Dynamical system C23 (0.0692)	3	6	4
	Other equipments C24 (0.0346)	6	6	4
New energy utilization factors B3	Application of solar energy C31 (0.0520)	3	2	4
	The use of natural ventilation C32 (0.0417)	3	4	3
	The use of other renewable energy C33 (0.0334)	2	2	1
Operation and management factors B4	Operation regulation C41 (0.0492)	5	4	3
	System maintenance and repair C42 (0.0370)	5	5	5
	Employee skills C43 (0.0350)	3	4	4

The grey relational coefficients of building A, B, and C to the positive and negative "ideal building" is calculated by the formula (64.6)–(64.9), and shown in Figs. 64.3, 64.4.

The relative similarity degree of building A, B, and C to "ideal building" is calculated by the formula (64.11)–(64.13), and shown in Fig. 64.5, taking $\alpha_1 = \alpha_2 = 0.5$:

Finally, the comprehensive ranking for energy consumption of the three public buildings is obtained and the final outcome of the energy consumption level of the three building, from high to low, is building C, building A and building B.

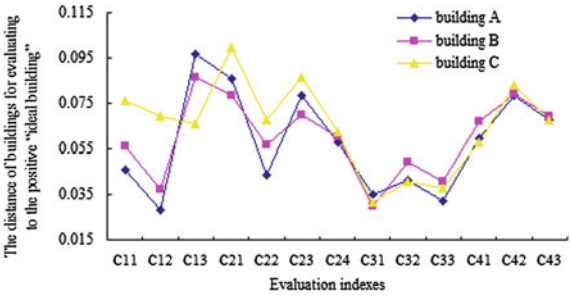

Fig. 64.1 The distance of building A, B, and C to the positive "ideal building"

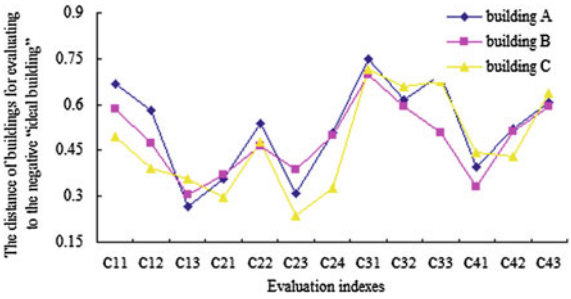

Fig. 64.2 The distance of building A, B, and C to the negative "ideal building"

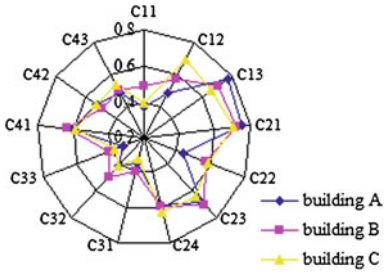

Fig. 64.3 Grey relational coefficient of building A, B, and C to the positive "ideal building"

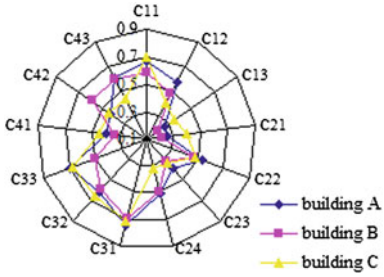

Fig. 64.4 Grey relational coefficient of building A, B, and C to the negative "ideal building"

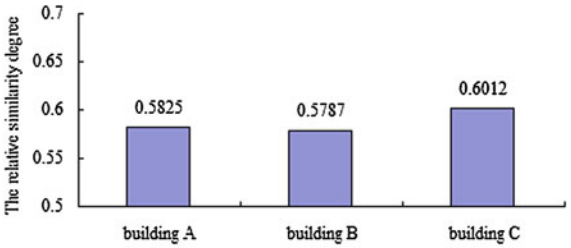

Fig. 64.5 The relative similarity degree of building A, B and C to "ideal building"

64.5 Conclusion

Through the case analysis, the feasibility of TOPSIS and GRA as an approach of building energy consumption evaluation is confirmed, convincingly. This improved method can reflect the exact energy consumption closeness degrees of each building for evaluating to the positive "ideal building" from both aspects of position distance and shape similarity. Due to the energy consumption relative closeness degrees of buildings to positive "ideal building," based on the calculated similarity nearness degree, not only can each building energy consumption level be determined precisely in order to rank multiple existing building energy consumption levels, but the qualities of each building indexes can be assessed, effectively. In view of the above, this approach is practical, more than that, it can provide theoretical basis for energy saving renovation work.

Acknowledgments This study is supported by National Science & Technology Pillar Program during the 12th Five-Year Plan Period (2011BAJ05B02).

References

1. Czogala E, Roubens M (1989) Approach to multi-criteria decision making problems using probabilistic set theory. Eur J Oper Res 43(3):263–266
2. Fan Z, You T (2002) TOPSIS method for multiple attribute decision between intervals. J Northeast Univ (Nat Sci Ed) 23(9):840–843

3. Liu S, Guo T, Dang Y (2004) Grey system theory and application, 3rd edn. Science Press, Peking
4. Lu Y (1997) Construction system engineering. Tsinghua University press, Peking
5. Kale A (2003) Comparison between polystyrenes and fiberglass roof insulation in warm and cold climates. Renew Energy 28:603–611
6. Corgnati SP, Corrado V, Filippi M (2008) A method for heating consumption assessment in existing buildings: a field survey concerning 120 Italian schools. Energy Build 40(5):801–809
7. Toftum J, Andersen RV, Jensen KJ (2009) Occupant performance and building energy consumption with different philosophies of determining acceptable thermal conditions. Build Environ 44(10):2009–2016
8. Lu F (2003) An improved TOPSIS method. Stat Decis 7(3):78–79
9. Hu Y (2002) Improvement of TOPSIS method used in comprehensive evaluation. Pract Theor Math 32(4):572–575
10. Xia Y, Wu Q (2004) A hybrid TOPSIS method for multiple attribute decision making problem. J Syst Eng 19(6):630–634
11. Luo D (2005) The analysis method of grey decision problem. The Yellow River water conservancy press, Zhengzhou, p 112
12. Luo D, Liu S (2005) Research of grey relational decision method. Chinese J Manage Sci 13(1):101–106
13. Olson DL (2004) Comparison of weights in TOPSIS models. Math Comput Model 40:721–727

Chapter 65
Analysis of Energy Saving Potential of a Low-Energy Building in China

Shuaifei Wang, Xiang Zhou, Guangyu Cao, Yangjun Wu and Xu Zhang

Abstract The objective of this study is to set up a road map for Chinese low-energy buildings with regards to technology solutions and economic perspectives. By simulation and calculation, different energy-efficient solutions were developed for a typical two floors villa in Chinese hot summer and cold winter zone. The energy-saving strategy adopted in this study can be summarized as: reducing demand; using high-efficient HVAC system; better control strategy; using renewable energy. By the careful design of building envelope, HVAC system and control strategy, the yearly energy consumption can be reduced by 90 % compared with the baseline of energy consumption in agreement with current Chinese building code. Proper use of renewable energy can be very helpful to achieve the final goal of low-energy building.

Keywords Hot summer and cold winter climate zone · Low-energy building · Energy-saving potential

65.1 Introduction

The building sector in the European Union (EU) is attributed to more than 40 % of energy consumption of the whole society energy usage [1]. Meanwhile, as a developing country, Chinese building sector contributes to more than 20 % of the national whole energy consumption, and the number grows with the rapid

S. Wang · X. Zhou (✉) · Y. Wu · X. Zhang
School of Mechanical Engineering, Tongji University, 4800 Caoan Road, Shanghai, China
e-mail: zhouxiang@tongji.edu.cn

G. Cao
VTT Technical Research Centre of Finland, Espo, Finland

A. Li et al. (eds.), *Proceedings of the 8th International Symposium on Heating, Ventilation and Air Conditioning*, Lecture Notes in Electrical Engineering 263,
DOI: 10.1007/978-3-642-39578-9_65,

development of China [2]. How to balance the energy consumption and indoor environmental quality are becoming more and more important, especially in low energy, passive, and zero energy buildings.

Nowadays, different countries in the EU are trying to improve their national building codes and striving to reach a higher performance. In some EU countries, a limited primary energy coefficient about 100 kWh/m^{2}a was set as a goal for the complete building services technology presented by Voss et al. The energy performance of building directive (EPBD) has been guiding these different improvements in the EU since 2006. Each country in Europe is developing new solutions to achieve low-energy buildings to meet the requirement of EBPD and the goal of nearly zero energy building by 2020. It is indicated that by the year 2020, building sector will cover 45 % of Chinese whole energy consumption [2], which would be a serious impediment for China's economic and urban development. So it is urgent for us to explore low-energy building in China. China has just started its journey on low-energy building. Lessons can be learned from the implementation of low-energy building in Europe.

This study chose a typical two floors villa building in Chinese hot summer and cold winter climate zone as the Demo building and analyzed its energy-saving potential regarding technology solutions and economic perspectives through simulation and calculation considering different energy efficient solutions.

65.2 Design Parameters of the Demo Building

The building is located in Changxing, Huzhou, Zhejiang Province, China, which is oceanic climate zone. The rain is well-distributed in each season. Sunlight and water resources are abundant.

General information of the building: this building has 2 floors. The building area is 274 m^2, and air-conditioned area is 153 m^2. Shape coefficient of the building is 0.50 and ratio of window area to wall area is 0.12 (Fig. 65.1).

Indoor design parameters: summer temperature 26 °C; winter temperature 18 °C; relative humidity: 50 %.

Outdoor parameters: outdoor average wind speed: winter 2.3 m/s; summer 2.2 m/s; winter air-conditioning calculation temperature: −4 °C; summer air-conditioning calculation temperature: 35.7 °C; winter heating calculating temperature: −1 °C. Outdoor yearly average relative humidity is 78 % [3].

This study first calculated the detailed heating and cooling load of the Demo building. Building Envelope 1 was set based on the current Chinese building code JGJ134-2010 Design Standard for Energy Efficiency of Residential Buildings in Hot Summer and Cold Winter Zone.

Exterior wall construction: 22 mm thermal insulation material and reinforced concrete, K = 1.0 W/m^{2}K. Roof: cellular concrete, reinforced concrete and 14 mm thermal insulation material, K = 0.6 W/m^{2}K. External window: K = 2.8 W/m^{2}K. Shading coefficient is 0.9 [4].

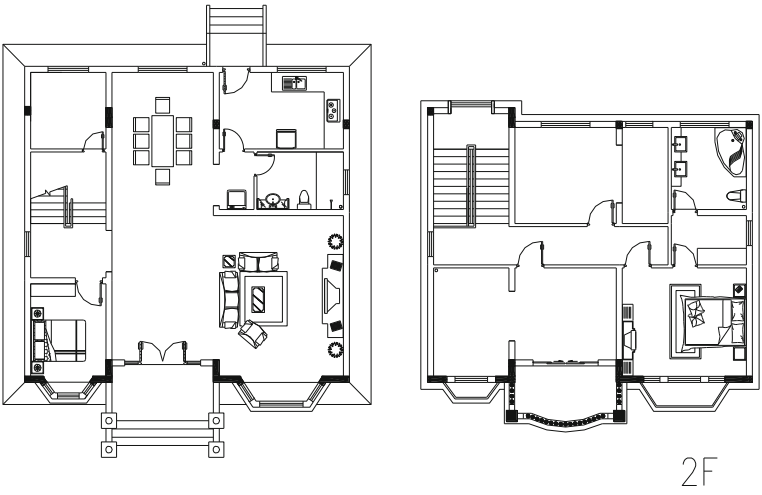

Fig. 65.1 Architectural plan of demonstration building

Air-conditioning season was set from June 15 to August 31 and heating season was December 1 to February 28 next year, in agreement with Chinese building code GB50736-2012 Code for Design of Heating, Ventilation and Air Conditioning for Residential Buildings. Air change rate was set as 0.5/h [5].

This study used designer's simulation toolkit (DeST) to calculate the cooling and heating load. The model of a two floors villa was built based on current Chinese building energy saving standards. And the calculation is based on hourly climate parameters from Chinese Building Thermal Environment Dedicated Meteorological Data Set [6], as shown in Fig. 65.2.

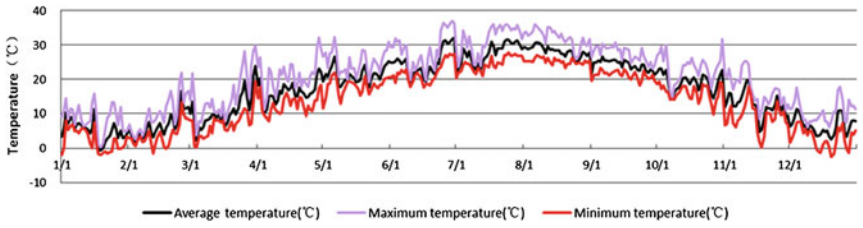

Fig. 65.2 Daily temperature of Hangzhou

65.3 Energy-Saving Potential Analysis of the Demo Building

65.3.1 Strategy of Building Energy Saving

Based on current Chinese energy-saving standard and referred to European energy efficient standards, the energy-saving design could be done from the following 4 aspects:

- Reduce demand with better envelope
- Use high-efficient cooling and heating system/sources
- Behavior-related energy saving
- Use renewable energy

65.3.2 Reduce Demand

The most effective strategy of reducing heating and cooling load is to use better envelope. Increase thermal insulation of the building envelope could reduce the building energy consumption significantly. In this study, three cases with different envelope systems were studied and simulated. Envelope 1 and Envelope 3 were set based on Chinese and European building codes. Since the energy saving effect would be lesser after the thermal insulation of building envelope was extended to a certain level and the construction cost would rise at the same time, Envelope 2 was set as a medium level considering local climate and economy.

In the material database of DeST, we established three new building envelope systems. In the three cases, heat transfer coefficient of the building envelope and window shading coefficient varied, while other conditions stayed fixed. The calculation results were shown in Table 65.1.

From the results, we could see no matter how building envelope changes, the heating load in winter is still more than the cooling load in summer. Part of the reason was that heating season time is half a month longer than air-conditioning season, and the enthalpy difference was larger in winter. Fresh air covered the major load.

Table 65.1 Simulation results of different envelope systems

	Envelope 1	Envelope 2	Envelope 3
Wall K value (W/m^2K)	1.0	0.5	0.3
Roof K value (W/m^2K)	0.6	0.5	0.3
External window K value (W/m^2K)	2.8	1.8	1.2
External window Sc	0.9	0.6	0.3
Total heating load (kWh)	7,277	5,012	4,309
Total cooling load (kWh)	3,048	2,620	1,845
Envelope cost (Yuan)	38,600	86,000	163,000

Table 65.2 Energy saving of heat exchanger

	Original fresh air load (kWh)	Fresh air load after heat recovery (kWh)
Winter	2,759	855
Summer	447	165
Total	3,206	1,020

In order to reduce heating/cooling fresh air load, we chose a total heat exchanger for air heat recovery. Enthalpy exchange efficiencies were 63 % for cooling and 69 % for heating with an airflow of 100 m^3/h. Energy-saving potential of heat exchanger was shown in Table 65.2. As shown in Table 65.2, the fresh air load in winter was larger than that in summer. Heat exchanger is much more efficient and economical in winter. Natural ventilation could also be used to reduce the fresh air load effectively in transit seasons. Therefore, we set a criterion for natural ventilation to reduce cooling load. When the outdoor temperature ranged from 16 to 28 °C, natural ventilation was used to reduce cooling fresh air load.

Figure 65.3 showed the cooling and heating load when the different strategies were applied to save energy.

65.3.3 Use High-Efficiency Heating and Cooling Sources

This study compared air source heat pump (ASHP), ground source heat pump (GSHP) and other systems, at last we chose GSHP as the heating and cooling sources. Figure 65.4 showed the cooling and heating efficiency of GSHP system in summer and winter.

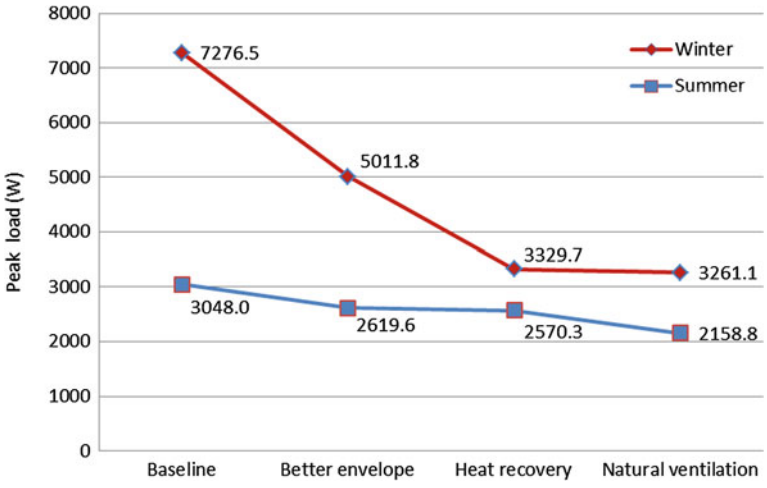

Fig. 65.3 Cooling and heating load after different energy saving means applied

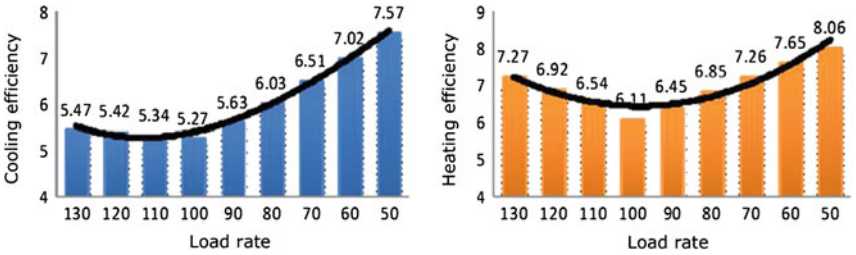

Fig. 65.4 Cooling and heating efficiency of GSHP system

Considering the efficiency of variable refrigerant volume (VRV) system is the highest when the load rate is 50 %, this indicates that a VRV may be very suitable for perennial operation under partial load for the villa use, and thus, this study adopts a VRV-terminal system, which is combined with the usage of a GSHP system.

65.3.4 Behavior Energy Saving

People's behavior can be directly linked to building energy saving. For example, a VRV-terminal system could be opened and closed conveniently by the occupants, which might provide a chance to save energy by the occupants' behavior. So we designed a specific air-conditioning schedule to consider the occupation of different rooms at different time.

A specific schedule with previous settings for different rooms was set as shown in Table 65.3.

Energy consumption following the air-conditioning schedule was shown in Table 65.4.

Table 65.3 Air-conditioning schedule

Room	Number	Air-conditioning time
Living room	1	8:00–22:00
Bedroom	3	22:00–8:00

Table 65.4 Energy consumption following the air-conditioning schedule

Energy consumption	GSHP (kWh)	After independent regulation (kWh)
Winter	465	247
Summer	353	166
Total	818	413

Table 65.5 Energy produced by solar energy

	Energy saving of solar thermal panel (kWh)	Energy generation of photovoltaic panel (kWh)
Winter	72	134
Summer	0	221
Total	72	355

65.3.5 Renewable Energy

Solar energy could be used to generate power and produce hot water to preheat the supply water of GSHP. Table 65.5 showed the energy-saving potential of solar energy. The roof area can be used in the south was 41.3 m^2. 5 m^2 photovoltaic panel with the efficiency of 13 % and 10 m^2 solar thermal panel with the efficiency of 70 % were installed on the roof.

65.4 Energy-Saving Road Map

The step by step Energy-saving strategies for low-energy building were shown in Table 65.6.

Table 65.6 The road map of energy saving design

Cases	Energy saving strategies
1	Baseline
2	Building envelope with external thermal insulation and traditional air-conditioning system (cooling efficiency: 2.3; heating efficiency: 1.9)
3	Optimized building envelope with external thermal insulation and traditional air-conditioning system
4	Optimized building envelope with external thermal insulation, total heat exchanger and traditional air-conditioning system
5	Optimized building envelope with external thermal insulation, total heat exchanger, natural ventilation and traditional air-conditioning system
6	Optimized building envelope with external thermal insulation, total heat exchanger, natural ventilation and ASHP with VRV
7	Optimized building envelope with external thermal insulation, total heat exchanger, natural ventilation and GSHP with VRV
8	Optimized building envelope with external thermal insulation, total heat exchanger, natural ventilation, GSHP with VRV and independent control
9	Optimized building envelope with external thermal insulation, total heat exchanger, natural ventilation, GSHP with VRV, independent control and solar thermal panel
10	Optimized building envelope with external thermal insulation, total heat exchanger, natural ventilation, GSHP with VRV, independent control, solar thermal panel and photovoltaic panel

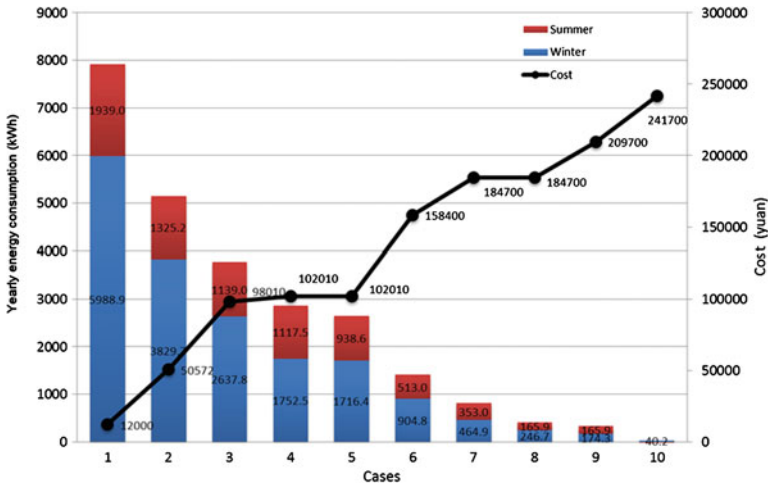

Fig. 65.5 Energy consumption and economical costs considering different solutions

Energy consumption and economical costs of every case in Table 65.6 was carefully simulated and calculated based on hourly cooling and heating load of the demonstration building through a whole year. The results were shown in Fig. 65.5.

65.5 Conclusions

Low-energy building is achievable in Chinese hot summer and cold winter zone. Improving insulation of building envelope system can reduce heating and cooling demand significantly. Better envelope contributes more to the reduction of heating load in winter than to cooling load in summer. It is not enough to follow current Chinese building code if the goal is to achieve low-energy building. However, considering the cost efficiency of increasing the thickness of the envelope insulation and the long summer in Chinese hot summer and cold winter zone, it is not economically feasible to improve the envelope to the level which is recommended in European standards. High-efficiency HVAC system contributes significantly to the reduction of HVAC system energy consumption, and it performs better with efficient terminal system. It is important to leave a chance for independent regulation for residential buildings considering the occupation coefficient of different rooms.

By carefully design of the building envelope, HVAC system, and control strategy, the yearly energy consumption can be reduced by 90 % compared with the baseline refer to current Chinese building code. Renewable energy can be proper used to achieve the final goal of low-energy building.

Acknowledgments This research was supported by the Fundamental Research Funds for the Central Universities under contract 2011KJ025, the science research project of MHURC—Ministry of Housing and Urban–Rural Construction under contract 2011-R1-8 and by the State Key Laboratory of Pollution Control and Resource Reuse Foundation of China under contract PCRRF09010.

References

1. Femenias P (2004) Demonstration projects for sustainable building. Ph.D thesis, Chalmers University of technology, Goteborg, Sweden
2. Centre for Energy Saving Studies, Tsinghua University (2012) Annual report on China Building energy efficiency. China architecture and building press
3. Lu Yaoqing (2007) Handbook of practical heating and air conditioning design. China architecture and building press
4. Ministry of housing and urban-rural development of the People's Republic of China (2010) JGJ 134-2010, Design standard for energy efficiency of residential buildings in hot summer and cold winter zone. China architecture and building press
5. Ministry of housing and urban-rural development of the People's Republic of China (2012) GB 50376-2012, Design standard for heating, ventilation and air conditioning of residential buildings. China architecture and building press
6. Meteorological Information Center of the China (2005) China building thermal environment dedicated meteorological data set. China architecture and building press

Chapter 66
Evolutionary Game Theory Analysis of the Role of Government Regulation on the Rural Energy Efficiency Construction

Mingling Zhai and Xu Zhang

Abstract Energy efficiency construction in rural areas is of great significance to society. There will be a lot of social benefits and economic positive externalities. Because of positive externalities, the energy-saving products' cost is higher than the traditional products' cost. The famers have a very low income, and they are price-sensitive. There is always a market failure. According to the consumer features of the farmers summarized, the asymmetric 2×2 noncooperative repeated game between the government and the farmers is analyzed through the method of evolutionary game theory. The game model is used to research the government regulatory role for promoting the energy-efficient construction after the implementation of incentives. Then, the game equilibrium is obtained which is evolutionary stable strategy (ESS) and is uncertain and dependent on the initial states of the game. According to the game conclusion, the game equilibrium and parameters of the game were given. The government that is dominant in the game and with higher level of rationality should guide the farmers with a lower level of rationality to reach the Pareto optimal Nash equilibrium.

Keywords Rural energy efficient · Consumer behaviors of farmers · Asymmetric game · Evolutionary game · Theory · Government policies

66.1 Introduction

The government attaches considerable importance to the energy efficiency construction of the new socialist countryside in China. The major policies are to improve the energy utilization status in rural areas, improve rural energy

M. Zhai · X. Zhang (✉)
Department of HVAC and Thermal Engineering, Tongji University, No.1239 Siping Road Shanghai, Shanghai 200092, China
e-mail: zhangxu-hvac@tongji.edu.cn

A. Li et al. (eds.), *Proceedings of the 8th International Symposium on Heating, Ventilation and Air Conditioning*, Lecture Notes in Electrical Engineering 263,
DOI: 10.1007/978-3-642-39578-9_66,

efficiency, increase rural renewable energy utilization and get sustainable development. There were some detailed plans to promote the development of rural energy utilization in China's "11th Five-Year Plan" of energy development and "11th Five-Year Plan" of renewable energy development. In the Key Technologies R&D Program of China during the 12th Five-Year Plan Period, there are many resources used to improve the rural energy efficiency construction and promote the development of rural energy-saving and emission reduction.

Energy efficiency construction in rural areas is of great significance to society. There will be a lot of social benefits such as conserving resources, improving the environment, economic growth and increasing employment. There are a lot of economic positive externalities. Externality refers to someone's the economic behavior bringing an economic impact on others or the society. There are positive externalities and negative externalities. Positive externalities refer to someone's economic activities benefiting others or the community but the beneficiaries not having to undertake the cost. Negative externalities refer to someone's economic activities harming others or the society but the behavioral agent not having to undertake the cost. Precisely because of positive externalities, the energy-saving product's cost is higher than the traditional product's cost. But the energy-saving product can bring social benefits. Especially, in rural areas, because people have a very low income and they are price-sensitive, there will be a market failure. Then, the positive externalities have to be internalized [1, 2].

To promote the energy efficiency construction, there are many researches of energy conservation and incentive mechanism and the game theory analysis [2–4]. But there are very less researches, through the method of game theory analysis, of the government regulatory role for promoting the energy efficiency construction after the implementation of incentives. Once there are some loopholes in the relevant works of the government, energy-saving products developers will make speculations that they maybe sell inferior products instead of high-quality products. The energy-saving products in the rural market are full of price elasticity of demand and consumers are dominant in the market. Once there are the fraudulent behaviors, the rural market of energy-saving products built painstakingly will be directly destroyed. Therefore, I make this game theory analysis between the government and the farmers to get a solution to these problems.

66.2 Consumer Behaviors Features of the Farmers in China

The features are shown as below [5–7]

1. The farmers restrain their consumer behaviors due to thrifty tradition, very low income and the lack of material wealth. They have to continue their everyday life and maintain the family normal activity with very low expected income.

They have to face all kinds of uncertainties. So a part of their income exists in the form of precautionary savings then the consumer behaviors are restrained.
2. The farmers' consumer behaviors have obvious characteristics of mental accounts. Different sources of income and expenditures for different purposes will be allocated according to their different mental accounts. Once one of the accounts is spent too much beyond mental budgeting, the farmers will stop their consumer activities.
3. Income threshold effect. Once the farmers' income is above a certain threshold, they will increase the demand for some consumer goods that they were not interested in or did not consume when their income did not increase.
4. Consumer characteristics of the village community like significant herd mentality, obvious consumption comparison phenomena and rare individualized consumer and so on. In acquaintance society, rural household's commodity consumptions are affected by the commodity's reputation very much especial the consumptions of household appliances, motorcycles and other big-ticket goods.

66.3 The Asymmetric Game Theory Analysis Between the Government and the Farmers

66.3.1 Basic Assumptions

1. According to research purposes, I select the government and the farmers as the game players. The government formulates the policies of energy-saving incentives and constraints. The government supervises energy-saving products developers' production and guides the farmers' behavior of consumer energy-saving products. The farmers, as a group, respond to the government policies and actions according to their own interest objectives.
2. There are two strategies of the government which are strict supervision of energy-saving products developers' production (shorthanded for strict behavior) and the opposite behavior (shorthanded for relax behavior). When the government does not adopt strict behavior, there will be some substandard products instead of qualified products sold to the farmers. There are two strategies of the farmers that purchasing energy-saving products and purchasing traditional products which are not energy-saving products or not so energy-efficient.
3. The opportunities to gain information for the two game players are equal and symmetrical. The two players can study and understand their income under the different strategies by analyzing the information. This game is a static game and a noncooperative repeated game. The decisions of the government's adopting a strict policy or not and the farmer's purchasing the energy-saving products or not are made at the same time.

4. They are of both bounded rationality. Although the government is close to completely rational, the government will still appear lax regulation when implementing the policies so the government can be seen as bounded rationality. The farmer's skills of getting and analyzing information are limited so the famers can be seen as bounded rationality. The degree of each farmer's bounded rationality is same.
5. The government and the farmers are independent. The government does not mandate any consumer economic behavior of the farmers. The government officers and the farmers are not relatives and do not have other related interests. The supervising officers will not deliberately relax the supervision of energy-saving products' production because of any personal interests. The supervising officers will not create difficulties to the qualified products deliberately to increase their costs. But there will be regulatory loopholes in the government's work due to its bounded rationality.

66.3.2 Game Theory Model

Let us consider the 2×2 noncooperative repeated game. Stage game payoff matrix is shown in Table 66.1.

The meanings of the different letters in Table 66.1 are shown below. x, $1-x$ = the proportions of purchasing energy-saving products and purchasing traditional products for the farmers. y, $1-y$ = the proportions of strict behavior and relax behavior for the government. a_1 = the use value of energy-saving products. a_2 = the monetary value of energy-saving products that the farmers paid. a_3 = the income of the farmers using energy-saving products. a_4 = the value of the psychological benefits because of energy-saving products bringing actual energy savings to the farmers. a_5 = the use value of traditional products. a_6 = the monetary value of energy-saving products that the farmers paid. a_7 = the value of the psychological benefits of farmers because they are not deceived. C = the genuine proportion in energy-saving products bought by the farmers when there are loopholes in the government's work. Assume that C is only decided by the degree of government's work loopholes. b_1 = government's tax revenue from the sale of relevant products. b_2 = administrative costs increased because the government takes the strict behavior instead of the relax behavior. b_3 = the social benefits like energy conservation and emission reduction because of energy-saving

Table 66.1 Stage payoff matrix of the asymmetric game between the government and the famers

Farmers	Government	
	Strict (y)	Relax ($1-y$)
Purchasing energy-saving products (x)	$a_1 - a_2 + a_3 + a_4$, $b_1 - b_2 + b_3 - b_4$	$(a_1 - a_2 + a_3 + a_4)c + (a_5 - a_2)(1-c)$, $b_1 - b_4 - b_6(1-c) + b_3c$
Purchasing traditional products ($1-x$)	$a_5 - a_6$, $b_1 - b_2 + b_5$	$a_5 - a_6 + a_7(1-c)$, $b_1 + b_5 - b_6(1-c)$

products using. b_4 = the expense paid in order to stimulate the consumptions of energy-saving products. b_5 = the revenue obtained by punishing dishonest behavior when implementing strict policies. b_6 = the value of the loss of the government's reputation when there are loopholes in the government's work.

66.3.3 Evolutionary Game Theory Analysis

Traditional game theory analysis is based on the assumption of complete rationality. Under this hypothesis, the game players have common knowledge that everyone is completely rational and everyone has the ability to judge and reason. They cannot make mistakes, and they are not impetuous. The players must be absolutely rational. However, such high requirements are difficult to meet in the real world. It is impossible for a real person or group even if the government to make no mistakes. Therefore, Maynard Smith and Price introduced the concept of evolutionary stable strategy (ESS) and established the evolutionary game theory that was based on the assumption of bounded rationality [8, 9]. Then, the game players did not have the perfect ability to judge and reason. Maybe they cannot take the optimal strategy at the first time, but they can get ESS through learning and imitating other one. The results obtained through the method of evolutionary game theory analysis are more realistic and persuasive.

ESS can be achieved through the game players' adjustment process of learning and imitating. ESS can still resume after the interference of error and deviation from initial ESS. The t times repeated game between the two players is simulated by dynamic simulation equations.

66.3.3.1 The Farmers' Benefit Analysis

The payoff of the strategy of purchasing energy-saving products is calculated as follows:

$$\pi_{11} = y(a_1 - a_2 + a_3 + a_4) + (1 - y)[(a_1 - a_2 + a_3 + a_4)c + (a_5 - a_2)(1 - c)]. \tag{66.1}$$

The payoff of the strategy of purchasing traditional products is calculated as follows:

$$\pi_{12} = y(a_5 - a_6) + (1 - y)[a_5 - a_6 + a_7(1 - c)]. \tag{66.2}$$

The average payoff is calculated as follows:

$$\pi_1 = x\pi_{11} + (1 - x)\pi_{12} \tag{66.3}$$

The farmers' dynamic simulation equation is shown below.

$$F(x) = \frac{dx}{dt} = x(\pi_{11} - \pi_1)\frac{dy}{dx} = x(1-x)[(a_6 - a_2 - a_7) + c(a_1 + a_3 + a_4 - a_5 + a_7) + y(1-c)(a_1 + a_3 + a_4 - a_5 + a_7)] \tag{66.4}$$

Make $F(x) = 0$, I get $x_1 = 0$, $x_2 = 1$, $y^* = 1 - \frac{a_1 - a_2 + a_3 + a_4 - (a_5 - a_6)}{(1-c)(a_1 + a_3 + a_4 - a_5 + a_7)}$.

According to the theorem of calculus and ESS, the x obtained is the ESS when $F'(x) < 0$.

When $y^* = 1 - \frac{a_1 - a_2 + a_3 + a_4 - (a_5 - a_6)}{(1-c)(a_1 + a_3 + a_4 - a_5 + a_7)}$ $\left(0 < \frac{a_1 - a_2 + a_3 + a_4 - (a_5 - a_6)}{(1-c)(a_1 + a_3 + a_4 - a_5 + a_7)} < 1\right)$, it is always right that $F(x) = 0$. The values of the proportions of purchasing energy-saving products(x) and purchasing traditional products $(1 - x)$ are stable. When $y > y^*$, only $x_2 = 1$ is the ESS which means when government implements a strict policy to a greater extent than a certain value farmers will take the strategy of purchasing energy-saving products. When $y < y^*$, only $x_1 = 0$ is the ESS which means when the government's work loopholes reaches a certain level the farmers will lose confidence in the government supervision work and take the strategy of purchasing energy-saving products.

66.3.3.2 The Government's Benefit Analysis

The payoff of strict policies strategy is calculated as follows:

$$\pi_{21} = x(b_1 - b_2 + b_3 - b_4) + (1-x)(b_1 - b_2 + b_5). \tag{66.5}$$

The payoff of relax policies strategy is calculated as follows:

$$\pi_{22} = x(b_1 - b_4 - b_6(1-c) + b_3 c) + (1-x)(b_1 + b_5 - b_6(1-c)). \tag{66.6}$$

The average payment is calculated as follows:

$$\pi_2 = y\pi_{21} + (1-y)\pi_{22}. \tag{66.7}$$

The Government's dynamic simulation equation is shown below.

$$\begin{aligned} F(y) = \frac{dy}{dt} &= y(\pi_{21} - \pi_2) \\ &= y(1-y)[b_6(1-c) - b_2 + x b_3(1-c)] \end{aligned} \tag{66.8}$$

Make $F(y) = 0$, I get $y_1 = 0$, $y_2 = 1$, $x^* = \frac{b_2 - b_6(1-c)}{b_3(1-c)}$

According to the theorem of calculus and ESS the y obtained is the ESS when $F'(y) < 0$.

When $x^* = \frac{b_2 - b_6(1-c)}{b_3(1-c)}$ $\left(0 < \frac{b_2 - b_6(1-c)}{b_3(1-c)} < 1\right)$, it is always right that $F(y) = 0$ then the values of the proportions of strict policies (y) and relax policies $(1 - y)$ are stable. When $x > x^*$, only $y_2 = 1$ is the ESS that means when farmers adopt the

strategy of purchasing energy-saving products to a greater extent than a certain value the government will be confident in the prospects for the promoting energy-saving products and take strict policies strategy. When $x < x^*$, only $y_1 = 0$ is the ESS that means when farmers adopt the strategy of purchasing traditional products to a greater extent than a certain value the government will work slack and take relax policies strategy due to energy conservation promotion work with little success.

The trend of asymmetric evolutionary game between the two players is shown in Fig. 66.1.

In Fig. 66.1, the two points (1,1) and (0,0) are both ESSs. Which one will be the final equilibrium is decided by the game's initial state. When it falls in area III, the game will be converged to the Pareto optimal equilibrium point (1,1). When it falls in area I, the game will be converged to the Pareto suboptimal equilibrium point (0,0). When it falls in area II or IV, the trend of the evolutionary game is uncertain. Maybe the game is converged to point (1,1) or the game is converged to point (0,0).

x^* and y^* are the threshold values of the asymmetric game. When the initial state point of the asymmetric game gets close to these two values, the state's slight changes will affect the final result of the game. Evolutionary game is sensitive to initial state. When the initial state point of the asymmetric game falls within a certain area, the final state of the game is very relatively certain. The result of evolutionary game is dependent on the initial states.

66.3.4 Analysis of the Degree of Game Players' Bounded Rationality

This asymmetric game is different from traditional asymmetric game because of game players' unequal bounded rationality degree. The government has more information about the different strategies, relevant payoffs and game structure and has abundant administrative resources. So the government is close to completely rational and dominates in the game. The farmers' ability to learn and analyze is worse than the government and the farmers do not have enough information and

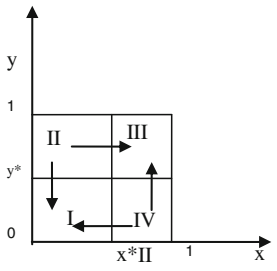

Fig. 66.1 Phase diagram of the asymmetric game between the government and the famers

resources so their rational degree is lower than the government. Liu Dehai pointed out that according to the theory of Stackelberg leader model in a game between an individual and a "experienced" group with the higher degree of rational, the individual game player which is the government in my paper should guide the farmers with a lower level of rationality to reach the Pareto optimal Nash equilibrium through the constantly repeated game process of trial and error by locking Pareto optimal state Nash equilibrium. Pareto optimal state Nash equilibrium is ($x = 1$, $y = 1$).

66.3.5 Policies Recommendations

As the above analysis if the game is desired to reach the Pareto optimal equilibrium, it is need to make x^*, y^* as small as possible. It is need to meet the conditions $0 < \frac{b_2 - b_6(1-c)}{b_3(1-c)} < 1$ and $0 < \frac{a_1 - a_2 + a_3 + a_4 - (a_5 - a_6)}{(1-c)(a_1 + a_3 + a_4 - a_5 + a_7)} < 1$.

Because of $x^* = \frac{b_2 - b_6(1-c)}{b_3(1-c)}$, it can be concluded that it is necessary to increase $b6$, $b3$ and reduce $b2$ to make x^* sufficiently small. Relevant policies recommendations are as shown below. First, the government should adjust the relevant regulatory authorities' work to increase work efficiency and reduce work cost. Second, the government should increase the investment in energy-saving technologies, make an increase in the energy-saving products' standard and cultivate the farmers' awareness of energy saving and emission reduction and make energy-saving benefits arising from the use of energy-saving products. Third, establish an independent third party to strictly supervise the government's work.

Because of $y^* = 1 - \frac{a_1 - a_2 + a_3 + a_4 - (a_5 - a_6)}{(1-c)(a_1 + a_3 + a_4 - a_5 + a_7)}$, it can be concluded that it is necessary to increase a_1, a_3, a_4, a_6, c and reduce a_5, a_7, a_2 to make y^* sufficiently small. Relevant policies recommendations are shown below. First, promote the energy-saving product development efforts to increase the use value of energy-saving products. Second, promote the farmers' awareness of energy saving to increase the present value of the energy-saving benefits. Praise for active farmers to purchase energy-saving products and set a good example to increase their psychological gains. Third, increase the tax lever adjustment to traditional non-energy-saving products. Increase incentives for the farmers to purchase energy-saving products. Fourth, increase the farmers' income to increase their demand for energy-saving products. Fifth, improve the efficiency of the government's work to reduce the risk of a fault. Increase the protection of consumer rights. Reduce the farmers' deceived psychological loss.

66.4 Conclusions

1. A summary of the feature of consumer behavior of farmers is made that the game theory model to promote the using of energy-saving products in rural areas is based on.
2. The ESS is achieved through the game players' adjustment process of learning and imitating in the evolutionary game theory under the hypothesis of bounded rationality. The results will be more realistic and persuasive.
3. By analyzing the game benefits of both players, a Pareto optimal Nash equilibrium of the game is found. Analysis of relevant government policies is done, and relevant recommendations are provided based on the analysis of the game.
4. As a party with a higher degree of rational the government should take, the initiative to make foresight decisions to guide the farmers with a lower degree of rational. The government should make reasonable policies and create a good environment for the farmers to consume the energy-saving products.
5. The evolutionary game analysis is done on the basis of the actual situation appropriately simplified. This study provides an idea how to analyze this kind of problem. Analysis of specific cases could be done after the work of surveying the data and figuring out clearly income.

Acknowledgments The study is supported by Key Technologies R&D Program of China during the 12th Five-Year Plan Period (No.2011BAJ08B09 and No.2011BAJ08B10).

References

1. Cai W, Wu Y (2007) Demand-oriented incentive mechanism design for energy efficiency of large-scale public buildings. HV&AC 37(8):23–27
2. Xu W, Liu X (2009) Evolutionary game analysis on incentive policy to buildings energy efficiency. J Wuhan Univ Technol (Transp Sci Eng) 33(1):184–187
3. Liu X, Wu Y, Li Q (2010) Incentive mechanism design for the promotion of biomass energy application in rural building. Build Sci 26(12):68–72
4. Lin M (2011) On analysis of stakeholder's game behavior in green building of new rural development. Shanxi Archit 37(3):230–232
5. Liu Z (2006) The study on present farmers' consumption behavior. Financ Econ 215:75–83
6. Yang X, Sun H (2010) Multiple perspectives analysis of peasant household consumption behavior. J Chongqing Technol Bus Univ (West Forum) 20(3):61–68
7. Yang Z (2011) The relationship between the social security and consumption expenditures in rural areas. Econ Manage 25(6):28–34
8. Xie S (2001) Evolutionary game theory under bounded rationality. J Shanghai Univ Financ Econ 10:3–9
9. Xie S (2006) Economic game theory. Fudan University Press, Shanghai